



MacArtney, Adrienne (2018) Atmosphere crust coupling and carbon sequestration on early Mars. PhD thesis.

<http://theses.gla.ac.uk/9006/>

Copyright and moral rights for this work are retained by the author

A copy can be downloaded for personal non-commercial research or study, without prior permission or charge

This work cannot be reproduced or quoted extensively from without first obtaining permission in writing from the author

The content must not be changed in any way or sold commercially in any format or medium without the formal permission of the author

When referring to this work, full bibliographic details including the author, title, awarding institution and date of the thesis must be given

Enlighten:Theses
<http://theses.gla.ac.uk/>
theses@gla.ac.uk

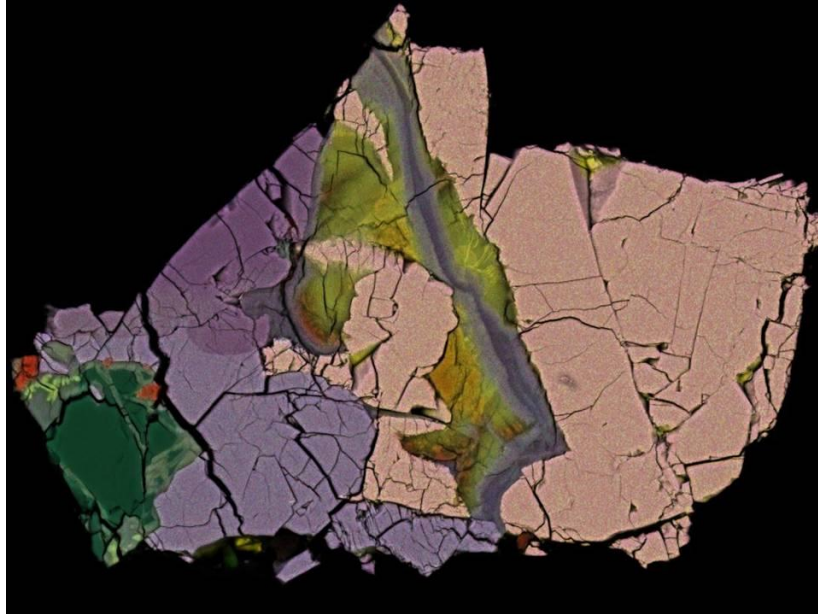
ATMOSPHERE - CRUST COUPLING AND CARBON SEQUESTRATION

ON EARLY MARS

By

Adrienne MacArtney

B.Sc. (Honours) Geosciences, Open University, 2013.



Submitted in partial fulfilment of the requirements for the degree of

Doctor of Philosophy

at the

UNIVERSITY OF GLASGOW

2018

© Adrienne MacArtney All rights reserved.

The author hereby grants to the University of Glasgow permission to reproduce and redistribute publicly paper and electronic copies of this thesis document in whole or in any part in any medium now known or hereafter created.

Signature of Author:

16th January 2018

Abstract

Evidence exists for great volumes of water on early Mars. Liquid surface water requires a much denser atmosphere than modern Mars possesses, probably predominantly composed of CO₂. Such significant volumes of CO₂ and water in the presence of basalt should have produced vast concentrations of carbonate minerals, yet little carbonate has been discovered thus far. These 'missing carbonates' comprise the Mars carbonate conundrum. This thesis provides insight to the conundrum via three distinct lines of investigation. Firstly, using engineering to expand our ability to locate carbonates on the Martian surface. A Micro-Optic UltraSonic Exfoliator (MOUSE) was designed and built that was tested on a range of rock types and wavelengths. Using ultrasonics demonstrates many advantages over the rock abrasion tool currently used on Mars rovers, including a smoother grind finish and a lower rate of tool tip wear when using tungsten carbide. Secondly, carbonates present in our only samples of the Martian regolith on Earth, meteorites, were studied. Carbonates found in Martian meteorites can provide a record of aqueous and atmospheric conditions extending back over 4.5 billion years. This thesis observes carbonates in two meteorites, ALH 84001 and Lafayette, representing early Mars and more recent Mars respectively, and finds evidence for two types of carbonate replacing glass in ALH 84001. The aqueously altered minerals of these two meteorites were compared with those found in the terrestrial ophiolites of Leka (Norway), and Semail (United Arab Emirates), and these ophiolites were assessed for suitability as Mars analogues. Chemically zoned carbonate rosettes similar to those in ALH 84001 are found in the Semail ophiolite samples. No carbonates were identified in Leka samples, but extensive serpentinisation was present. Finally, this thesis sought to replicate alteration processes and products that are recorded by Martian meteorites within a Mars analogue laboratory environment. The effects of differing initial atmospheric and mineral compositions were explored, specifically the comparison of CO₂ and SO₂ with basalt versus CO₂ with olivine.

These three interdisciplinary strands of investigation provide some novel tools, ideas and evidence to help solve the Mars carbonate conundrum.

Dedication

This PhD is dedicated to Debbie Brown

Where it all began.

And to a rabbit who looked after me.

Acknowledgements

This work was funded by the UK Space Agency (UKSA) through the Science and Technologies Facilities Council (STFC). I hope most sincerely that this thesis is a good return on their investment in me, and that they might be proud of its contribution to the fields of space engineering and geochemistry.

I would like to thank my supervisors, Professor Martin Lee and Dr Patrick Harkness, for offering me the opportunity to research such a fantastic project, engaging in climate challenges both terrestrial and Martian. Their ongoing support, advice and wisdom have been invaluable in helping navigate the politics and intricacies of early career academia.

Keith Bateman and Dr Chris Rochelle from the British Geological Survey have my deepest appreciation for equipment provision, laboratory space, ICPMS processing, extensive technical advice and proof reading of chapter 4. Gratitude is also extended to John Faithful from the Huntarian museum, Glasgow, for supplying many mineral samples, and ongoing encouragement. Essential engineering collaboration was provided by Dr Xuan Li. Further, appreciation to Peter Chung, from the school of geographical and Earth sciences, University of Glasgow, for scanning electron microscope support, and thin section support by John Gillece. I would also like to thank the staff at the CARBFIX project in Iceland for the site tour, discussions and highlighting the SULFIX work to me. An amaze balls thank you to Dr Caroline Smith from the Natural History museum, London, for ongoing loans of Mars meteorite samples. Semail ophiolite samples were kindly donated by Dr Alicja Lacinsk.

Thank you to Dr Elisabeth Streit Falk, Pol Knops, Loredana Bessone, Professor Charles Cockell, Professor Martin McCoustra, Dr Mario Toubes, Tasha Nicholson, Dr Claire Cousins, Jane MacArthur, Dr Paul Niles, Dr Susan Fitzner, Dr Zita Martins, Ania Losiak, Sapphire Wanmer, Dr Florent Caste, Dr Natasha Vasiliki Almeida, Lotta Kemppinen, Dr Terry-Ann Suer, Kristin Johnson, Dr Rebecca Skuce, Dr Jaime Toney and Dr Charity Phillips-Lander for all their assistance; from

discussions on minerals, ophiolites and space exploration, to giving a hug and a space to cry.

Good advice, friendship, support, coffee and ice cream have come from a number of people; principally, Robert MacDonald (the big yin), Professor Susan Waldron, Bevis Evans Teush (my partner at Wild Orbit Films), Kenny Roberts, Kirsty Shona Hill and Dr Cristina Persano. A beautiful Jewel deserves my thanks, and fellow jail mate Nick Thomas has been a mainstay of affection, support, patience and loving kindness. I am also grateful to my mother, Margaret, for proof reading many pages of troublesome rock and mineral names, and supporting me when it all got harsh and tiresome. I would also have struggled more than I did without the practical and emotional support of Mike Cavin, the wee rabbit. Thanks also to Steve Webster, for providing me space, shelter and fine single malt in a remote Hebridean croft, where many of these pages were written.

I also remember that I would not have a PhD, nor even a BSc, if it were not for the financial support of the Open University, the patient guidance and care of Alison Tossell, and the friendship of Steph Patterson, Shana Ellis, Cindy Courtillier and especially Tammy Michelle, along with the love of Deb Patterson. My unapologetic background prior to the PhD was sex work. Without the friendship, laughter, affection, cocktails and enormous support of a great many sex workers who will go unnamed, I would not have held together and achieved what I have. They are my family, and will always have my open and vociferous support. It is important to never forget where you come from. I would also like to acknowledge the encouragement of all the Science Hooker followers: the encouragement really makes all the difference.

A final, sparkling, super special thank you to Dr Sarah Rugheimer, an intellectual fireball glued together with love, compassion and care. I hope all PhD students are fortunate enough to find such a valuable and supportive inspiration to guide them through the research rocks, and provide bridges into further academia.

For anyone I may have inadvertently left out, it is due to my temporary myopic absorption, and not due to any lack of love or appreciation.

Thesis contents

	Page
Chapter 1:	7 – 71
Introduction.	
Chapter 2:	72 – 153
The effects of ultrasonics on Mars rover rock abrasion tool performance.	
Chapter 3:	154 – 274
Terrestrial ophiolite carbonates as Martian analogues.	
Chapter 4:	275 – 389
Experimental reproduction of Martian type carbonates and clays.	
Chapter 5:	390 – 405
Conclusions.	
Appendix 1:	406 – 419
Mineral spectral data.	
Appendix 2:	420
Rock abrasion tool stepper motor Arduino code.	
Appendix 3:	421 – 435
Scanning Electron Microscope Standards.	
Appendix 4:	436 – 463
Quantitative Scanning Electron Microscope analysis.	
Appendix 5:	464 – 481
IC – ICPMS data.	
Appendix 6:	482 – 485
Saturation indices.	

Chapter 1

Introduction.

Introduction contents.

	Page
1.1 The Mars carbonate conundrum.	9 - 12
1.2 What are carbonate minerals?	13 - 20
1.2.1 Carbonate mineral structure and classification.	13 - 15
1.2.2 Carbonate mineral formation processes.	16 - 19
1.2.3 Importance of carbonate minerals for planetary evolution.	19 - 20
1.3 Terrestrial warming and carbon sequestration: lessons from Mars.	20 - 28
1.4 Mineral and landed mission maps of Mars.	28 - 33
1.5 Solution to the Mars carbonate conundrum 1: Locating Mars carbonates.	34 - 35
1.6 Solution to the Mars carbonate conundrum 2: Terrestrial analogues.	36 - 38
1.7 Solution to the Mars carbonate conundrum 3: Experimental mineralogy.	38 - 45
1.7.1 Experiments replicating Mars: Water.	41
1.7.2 Experiments replicating Mars: Olivine and CO ₂ .	42 - 44
1.7.3 Experiments replicating Mars: Sulphur.	44 - 45
1.8 The structure of the thesis.	45 - 55
1.8.1 Effects of ultrasonics on rover rock abrasion tool performance.	46 - 47
1.8.2 Terrestrial ophiolites as Mars carbonation analogues.	48 - 51
1.8.3 Experimental reproduction of Martian type carbonates and clays.	51 - 53
1.9 References.	53 – 70

1.1 The Mars carbonate conundrum.

Evidence exists for great volumes of water on early Mars. Liquid surface water requires a much denser atmosphere than modern Mars possesses, probably predominantly composed of CO₂. Such significant volumes of CO₂ and water in the presence of basalt should have produced vast concentrations of carbonate minerals, yet little carbonate has been discovered thus far. These ‘missing carbonates’ comprise the Mars carbonate conundrum and are the central focus of this thesis.

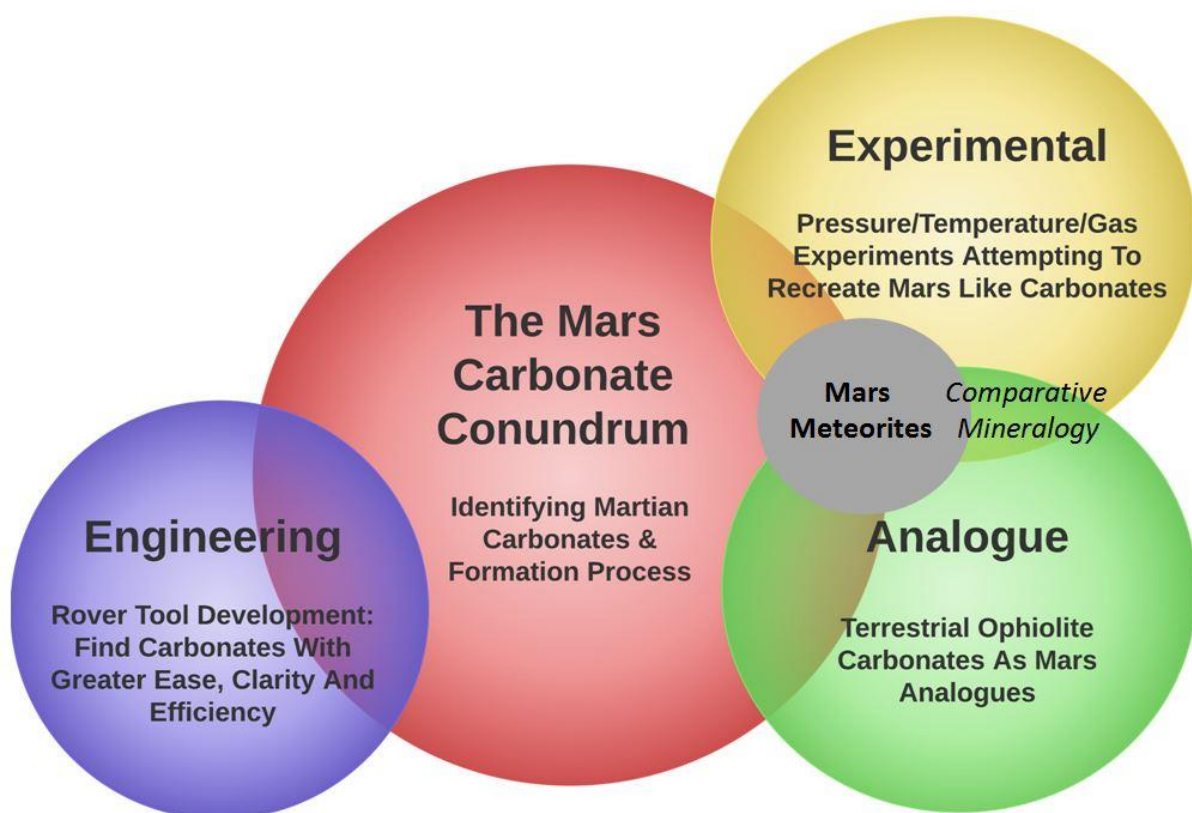


Figure 1.1. The carbonate conundrum that this PhD thesis seeks to address (red circle), along with the different spheres of research used to approach this question. These spheres of research correspond to the three main thesis chapters: engineering (chapter 2), analogues (chapter 3), and experimental (chapter 4). Overlapping circles indicate where chapter and research content overlap and support each other, allowing for comparative mineralogy.

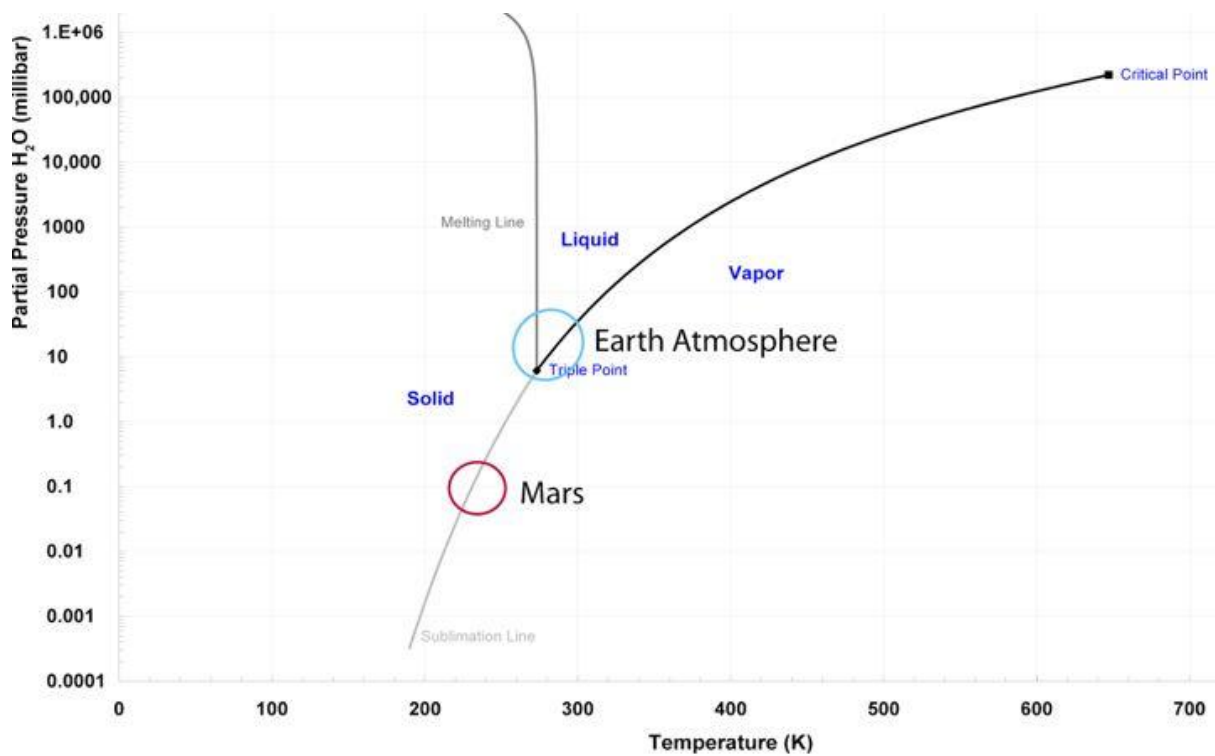


Figure 1.2. Phase diagram of the stability of water on Earth and Mars. *Courtesy of Paul B Niles, personal communication, March 2017.*

The temperature and pressures prevalent on modern Mars do not support liquid water. Pure water will sublime directly from the solid (ice) phase into the gas phase with seasonal and diurnal fluctuations of temperature (Fig. 1.2).

Salt in water, called brine, allows liquid water to be stable at much lower temperatures and plays an important role in Martian hydrodynamics. When frozen the term cryobrine is used. Many species of brine are possible on Mars, including brines of sulphate, chloride, perchloride and carbonate (Möhlmann & Thomsen, 2011). Despite this possibility of brine, evidence for liquid water on modern Mars remains minimal; however, surface features, topography and geomorphology indicate that water may have played a major role in the Martian past (Fig. 1.3).



Figure 1.3. Topography of Osuga Valles indicates a geological past with a significant water component. Taken with the High Resolution Stereo Camera on Mars Express. Red = High elevation. Blue = Low elevation. (Website 1).

For such significant amounts of water to be present on the Martian surface then there must have been a much thicker atmosphere at some point in the planet's past, possibly multiple bars of pressure (Pollack & Kasting, 1987; Forget & Pierrehumbert, 1997). Some researchers suggest a more cautious estimate of <1 bar pressure, but still greater than the modern 0.006 bars pressure (Carr, 1999; Edwards & Ehlmann, 2015). In either case, this atmosphere is now lost. The sun was fainter by ~25 % during early (Noachian) Mars history (Gough, 1981), exacerbating the need for a thicker warming atmosphere to permit liquid water to create the observed surface features. An early thick Mars atmosphere is further supported by the isotopic studies of nitrogen in Martian soil, atmosphere, and meteorites (Wong *et al.* 2013). The modern surface of Mars is enriched in heavy nitrogen (^{15}N) to levels supporting an initial partial pressure indicative of a multiple bar atmosphere (Wong *et al.* 2013; McElroy *et al.* 1976).

The precise composition of this early atmosphere is not currently known. An atmosphere composed solely of CO_2 is unable to produce a wet early Mars regardless of pressure (Kasting, 1991) and SO_2 is required (Pollack & Kasting, 1987; Yung *et al.* 1997; Halevy *et al.* 2007). CO_2 and SO_2 are the two gases scrutinised the most in this study, although methane (CH_4) is another important atmospheric

Page | 11

gas that can exert significant control over surface water stability and is investigated extensively by other studies (Kite *et al.* 2017; Wordsworth *et al.* 2017).

Some of this early atmosphere was lost to space via the solar wind induced sputtering (Jakosky *et al.* 1994) and impact induced erosion (Brain & Jakosky, 1998). Some was stored as CO₂ 'dry ice' in the Martian poles (Phillips *et al.* 2011). But some was also stored as carbonate minerals in the planet's crust (Ehlmann *et al.* 2008).

Assuming a thick atmosphere allowing for surface liquid water to form the observed surface features, water in contact with the basaltic Martian surface would be expected to precipitate significant volumes of carbonates, perhaps analogous to terrestrial archean deposition of massive carbonates under an early Earth atmosphere of ~60 bars of CO₂ and in the presence of liquid water (Holland, 1978).

No such massive carbonate formations have been located on Mars, instead, massive sulphate beds have been found. In Meridiani the average composition appears to be ~40 % sulphates, 10 % hematite and the remainder siliciclastic particles (Clark *et al.* 2005). That massive sulphates are present is not in itself surprising considering Tharsis volcanism which would output SO₂, H₂O, CO₂ and minor H₂S, HCL, HF (Bullock & Moore, 2007). SO₂ gas has a short atmospheric residence time and would oxidise to H₂SO₄ aerosols, and in order for a thick early Martian atmosphere to exist and persist it must have been dominated by CO₂ (Bullock & Moore, 2007).

Determining how much CO₂ was stored as carbonate minerals, locating these carbonates on the Martian surface, determining the species of carbonate and the precise formation processes involved all constitute elements of the Mars carbonate conundrum and are the focus of this thesis.

1.2 What are carbonate minerals?

1.2.1 Carbonate mineral structure and classification.

A carbonate is a salt, possessing the ionic structure CO_3^{2-} , consisting of a strong covalent double bond to one oxygen atom and single bonds to the other two oxygen atoms (Fig. 1.4. A, B). A carbonate mineral is any mineral with this ion in its structure. Most carbonate minerals consist of the carbonate ion combining with a metal cation (Fig. 1.4. C, D), commonly iron (Fe), magnesium (Mg), potassium (K), sodium (Na), calcium (Ca), but also a wide variety of less common elements.

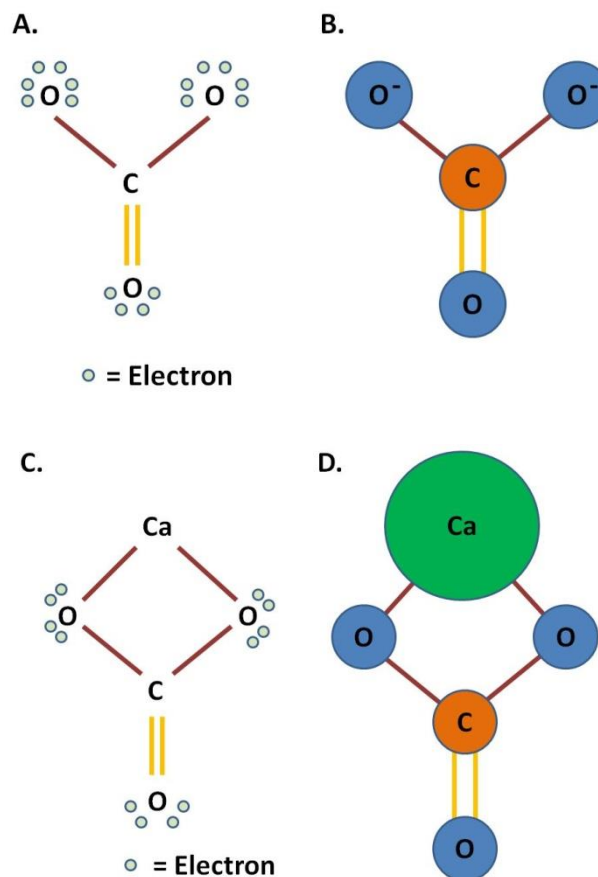


Figure 1.4. Example of how a metal cation, in this case Ca^{2+} bonds with a carbonate salt (CO_3^{2-}) to form a carbonate mineral. **A.** Lewis structure of CO_3^{2-} **B.** Atomic structure of CO_3^{2-} **C.** Lewis structure of CaCO_3 **D.** Atomic structure of CaCO_3 . Atomic angles are not represented.

The carbonate molecule can then combine with others to form lattice structures. Sometimes sparsely populated metals can be included within a carbonate lattice sandwiched between non-metal bearing carbonate lattices, Pb being associated with cerussite, Cu₂ with malachite, Cu₃ with azurite, Zn with smithsonite etc. Calcium carbonate, for example, consists of regularly alternating lattice layers of carbonate and calcium, whereas dolomite consists of alternating lattice layers of carbonate, calcium, carbonate, magnesium, carbonate, calcium, and so on. In systems where multiple metal elements are available, the metal cations in the carbonate mineral structure can be exchangeable. Two of the major crystalline structural polymorphs of calcium carbonate are calcite and aragonite (Fig. 1.5), calcite being rhombohedral and aragonite being orthorhombic. Calcite is more stable than aragonite, and over time aragonite can rearrange its structure to become calcite. Sea creatures often prefer using aragonite as opposed calcite in their shell structures due to aragonite being more resistant to stress in high energy environments, although this preference changes in low pH waters as aragonite is more prone to dissolution in acidic waters. Anthropogenic climate change and increased ocean CO₂ uptake is increasing ocean acidity and raising the calcite and aragonite saturation horizons in the oceans by 1 to 2 m per year (Feely *et al.* 2012).

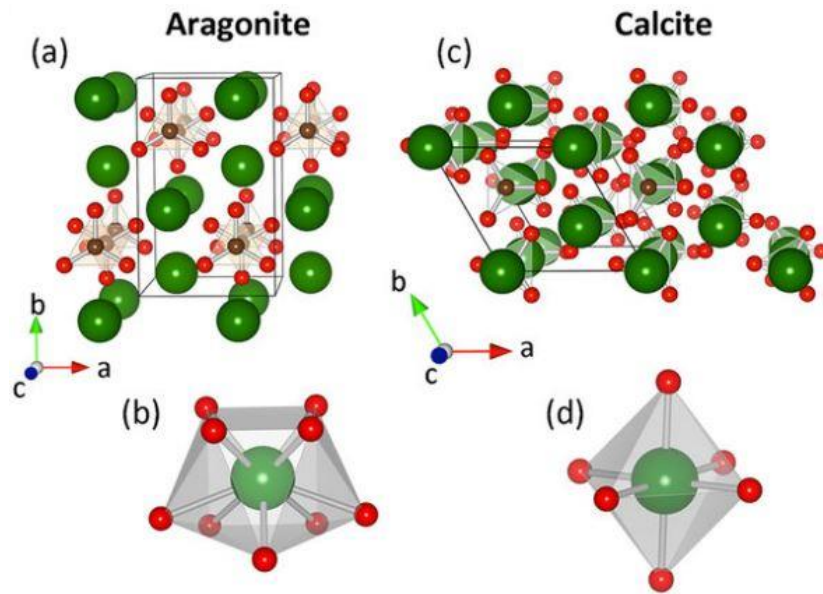


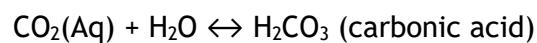
Figure 1.5. Differences in crystal structure between calcite and aragonite. Green = Ca, Red = O, Brown = C. **A.** Aragonite in a lattice structure. **B.** Aragonite possesses 9 connections with O atoms. **C.** Calcite in a lattice structure. **D.** Calcite possesses 6 connections with O atoms (Soldati *et al.* 2016).

Carbonates fall into class 5 of the Dana mineralogy index (Gaines *et al.* 1997), which subdivides the carbonates into acid, anhydrous, hydrated, hydroxyl, halogen and compound classes. Most carbonates under consideration in this work fall under the anhydrous (class 14) carbonates, such as calcite, dolomite, magnesite, siderite etc. The author is currently compiling a series of reference books combining idealised mineral spectra from INCA SEM software and combining this with basic mineral data for all 4714 minerals in the Dana index, the most relevant of these with respect to this thesis have been compiled into appendix 1.

The different polymorphs of calcium carbonate can be difficult to identify in thin section light microscopy, but they all possess high relief, colourless and are grainy in plane polarised light, with perfect cleavage. When viewed in thin section between crossed polarisers they have high interference colours.

1.2.2 Carbonate mineral formation processes.

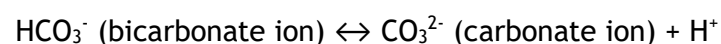
Biom mineralised carbonate shell formation is a process whereby sea creatures such as molluscs and foraminifera secrete carbonate and small amounts of protein to form exoskeletons. CO₂ atmospheric gas dissolves from the atmosphere into seawater and one of the products is free carbonate ions CO₃²⁻ (equation 1.3) which sea creatures can combine with Ca²⁺ cations available in the water to form carbonate exoskeletons. These exoskeletons consist of an inner pearly layer of calcified nacre, a middle layer of prismatic carbonate and an outer layer of proteinaceous periosteum (Horne, 2016). When these creatures die, their skeletons can collect in vast volumes on the seafloor, potentially becoming stratigraphic layers of chalk, limestone or marble if buried.



Equation 1.1



Equation 1.2



Equation 1.3

Abiotic carbonate formation can also occur in seawater, and freshwater (e.g. caves), with the carbonate ions combining with metal cations abiotically and sinking via gravitational settling into limestone sediment, although most marine carbonate formation is biotic (Morse *et al.* 2007). Outside of oceanic environments, CO₂ can dissolve into rainwater, forming carbonate ions (equations 1.1, 1.2, 1.3), which then react with silicate rocks in the Earth's crust, causing them to release metal cations such as calcium, which combine with the carbonate

ions in the rainwater. These carbonates can precipitate out of the fluid, often crystallising in cracks, fissures and interstitial rock pore spaces (Matter & Keleman, 2009). This process is referred to as mineral carbonation.

The mineral products resulting from abiotic carbonation of basic/mafic rocks will vary dependent on the $p\text{CO}_2$ regime of the interacting fluid, with low $p\text{CO}_2$ producing secondary calcites, clays, zeolites (Neuhoff *et al.* 1999) and high $p\text{CO}_2$ producing secondary Fe, Mg-, and Ca-carbonates; both regimes can produce quartz/chalcedony (Rogers *et al.* 2006). A useful simplification of mineral carbonation is that to proceed, three 'ingredients' are required, forming a 'carbonation triangle' (Fig. 1.6).

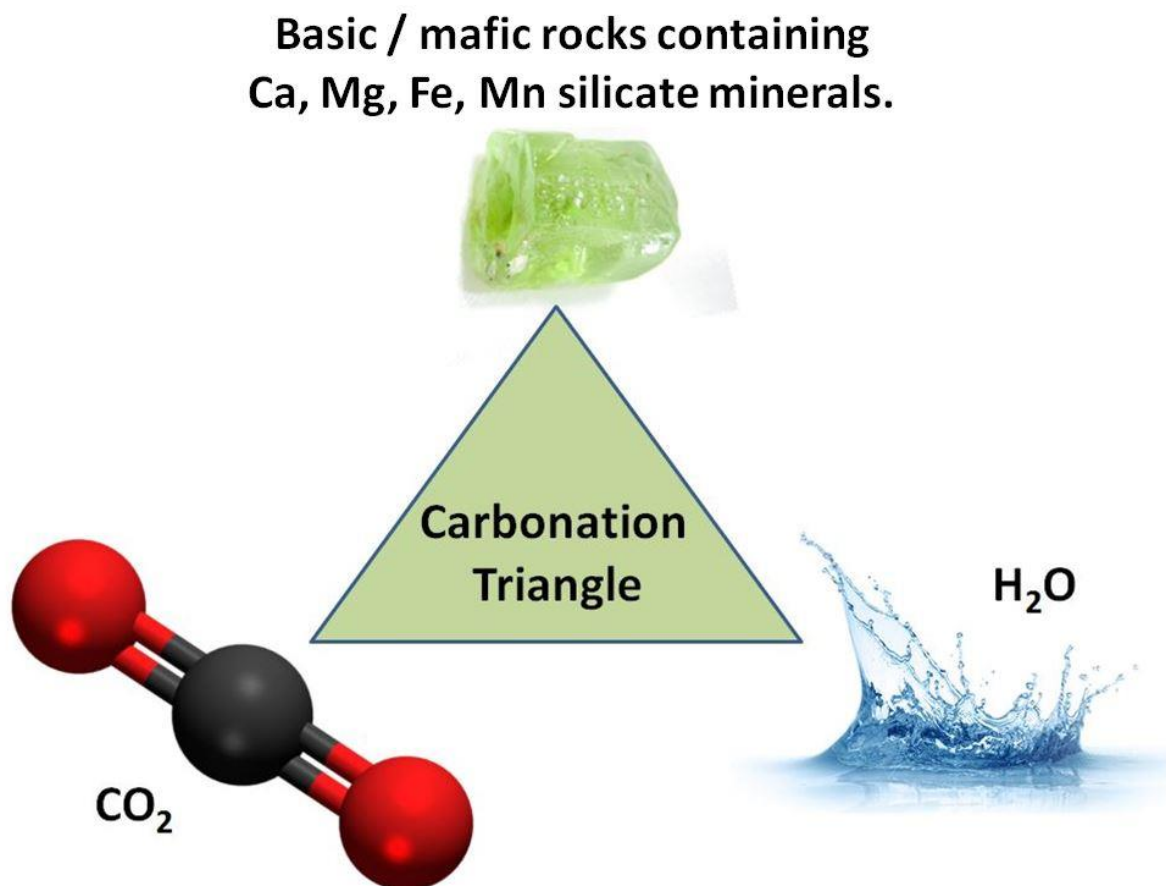
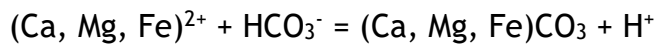


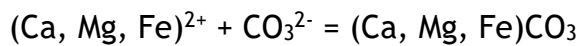
Figure 1.6. The carbonation triangle. Basic minerals, CO_2 and H_2O are the fundamental ingredients needed for mineral carbon sequestration to proceed.

Whether carbonates form within rocks is highly dependent on the fluid pH, as carbonates dissolve in acidic environments. When CO₂ dissolves in liquid water, the solution becomes acidified via the increase in dissociated protons (equations 1.2, 1.3). When this slightly acidic water comes into contact with silicate rocks it causes them to release divalent cations such as magnesium, calcium and iron into solution, which further increase fluid acidity by combining with bicarbonate ions:



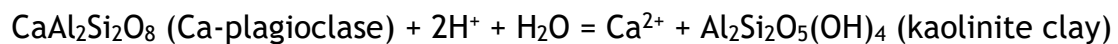
Equation 1.4

Or a neutral combination:



Equation 1.5

This excess of H⁺ must be removed from the system if stable carbonate minerals are to form, and this can occur via Ca-plagioclase dissolution and clay formation:



Equation 1.6

Incorporation of water into precipitated mineral structures demands volumetric expansion, often >44% (Keleman *et al.* 2011), which causes cracking (Keleman & Hirth, 2012) and exposure of fresh mineral surfaces for continued reaction (Keleman & Matter, 2008):

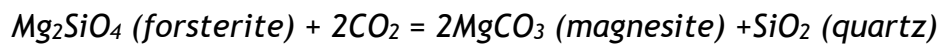


Equation 1.7

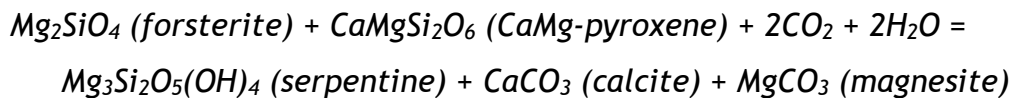
In addition to serpentinisation and hydration of silicates, shown in equation 1.6 and 1.7, carbon from CO₂ becomes incorporated into the structure of secondary minerals deposited in veins, i.e. simple carbonation of olivine (equation

Page | 18

1.8) and carbonation of a mixture of olivine and pyroxene (equation 1.9) (Keleman & Hirth, 2012):



Equation 1.8



Equation 1.9

The variety available on such equations is nearly endless in complex natural systems and the equations above are merely a few simple examples. When peridotite carbonation proceeds to completion i.e. 100% magnesite and quartz, it is known as a lisvenite (Keleman & Hirth, 2012). Neutralization of water acidity by equation 1.5 commonly proceeds beyond neutral pH on Earth, with hyperalkaline waters (pH>11) reaching the Earth's surface in the form of travertine springs (Pentecost, 1995; Keleman & Matter, 2008; Blank et al. 2009; Arcilla *et al.* 2011).

It is not known whether travertine springs do or have ever existed on Mars. Equations 1.1 to 1.9 provide a simplified representation of how CO₂ can be naturally removed, or 'scrubbed', from a planet's short atmospheric residence time reservoirs and into long residence time geological storage.

1.2.3 Importance of carbonate minerals for planetary evolution.

The weathering of silicate rocks, serpentinisation and the formation of carbonate minerals is an important factor controlling planetary atmospheric CO₂ levels, influencing atmospheric composition, density, surface pressure and temperature. This is called the silicate-carbonate cycle (Urey reaction). On Earth, for example, silicate continental weathering associated with the Himalayan uplift ~50 Ma ago with concomitant CO₂ drawdown as a consequence of (predominantly biological) carbonate formation and burial caused major cenozoic global cooling initiating glaciation (Garzzone, 2008). Himalayan silicate weathering and

associated carbonate formation continues to act as a negative feedback offsetting current anthropogenic global warming (Walker *et al.* 1981; France-Lanord & Derry, 1997). In reverse, when carbonate minerals become exposed to acidic conditions or temperatures high enough to cause them to melt, they release CO₂ back into the atmosphere (IEAGHG, 2005).

Yet carbonate minerals do not just play an important role in controlling terrestrial climate evolution. Any planet that contains basic/mafic minerals, CO₂ and water will likely form carbonate minerals, particularly when sources of heat are available such as volcanism and meteorite impacts. Carbonate formation will then adjust the planet's atmosphere; even minor changes in thin atmospheres can cause major planetary system adjustments. The drawdown of atmospheric CO₂ by the formation of carbonate minerals is a mainstream theory of how at least part of a hypothesised multi-bar early Mars atmosphere was lost ~4000 Ma ago (Pollack & Kasting, 1987; Leshin *et al.* 1998; Chassefière & Leblanc, 2004; Halevy *et al.* 2011 and others).

Investigating the validity and evidence associated with this theory is the principal goal of this study, achieved via developing a new rover tool to advance the search for carbonates on Mars (chapter 2), studying terrestrial ophiolite analogues of Mars carbonates (chapter 3), and controlled laboratory experiments attempting to replicate carbonates in Martian meteorites (chapter 4).

1.3 Terrestrial warming and carbon sequestration lessons from Mars.

Mineral carbon sequestration is emerging as a potentially effective method of terrestrial carbon capture and storage (Park *et al.* 2003; Xu *et al.* 2004; Schuiling & Krijgsman, 2006; Oelkers *et al.* 2008). The precipitation of carbonate minerals that are stable over millions of years potentially has a long-term advantage over other carbon capture and storage (CCS) methods. The technology is currently at the pilot stage, deployed in only a handful of countries, with many

unresolved questions regarding the science and technology of industrial mineral carbonation.

Natural processes of mineral carbon sequestration have recently been observed on Mars (Edwards & Ehlmann, 2015) and may have been partly responsible for the loss of the planet's early atmosphere. Mutual knowledge transfer across seemingly diverse scientific disciplines may be the key to resolving many of the outstanding questions involved in coping with terrestrial climate change and associated carbon management, as well as advancing our understanding of the evolution of planetary bodies within our Solar System. Although many studies have compared Martian features with their terrestrial counterparts (see section 1.6), there has been little evaluation of how recent geological and geochemical discoveries on Mars can inform terrestrial carbon capture and storage technology.

There exists overwhelming consensus within the scientific community that climate change is occurring and that global warming is real (Anderegg *et al.* 2010; Cook *et al.* 2013; Doran & Zimmerman, 2009; Oreskes, 2014). Furthermore, over 200 scientific organisations formally state that they believe the rapid rate of warming is predominantly anthropogenic (The Governor's Office of Planning and Research, 2011). A primary mechanism for this planetary warming is the rise in atmospheric CO₂, which backscatters infrared radiation emitted from Earth's interior, returning some of it to the surface and lower atmosphere (Andrews, 2010). Atmospheric CO₂ abundance is currently increasing almost exponentially (NOAA, 2014), and is higher now than at any point since the late Pliocene and early Pleistocene 3.6 to 2.2 million years ago (Naish *et al.* 2009; Schneider & Schneider, 2010). Sources of CO₂ can be divided into natural such as volcanic eruptions, ocean-atmosphere exchange, decomposition, soil respiration, and anthropogenic such as industrial burning of fossil fuels, agriculture, cement production, transport and waste decomposition.

The negative effects of global warming are multitude: rising sea levels caused by ocean heat expansion and melting terrestrial ice deposits threaten to flood low altitude communities (Simonović, 2012), as well as creating storms of

higher frequency and ferocity (O’Gorman, 2010). Droughts are increasing in size and intensity with arid areas expanding; this affects food security by damaging arable land (Verstraete, 2008). The rise in temperature adjusts habitat, disrupting predator-prey and plant-insect dynamics when one species is affected by warming and not the other (Parmesan, 2006). Longer, warmer summers have increased disease carrying mosquito populations (Benitez, 2009; Epstein, 2005). The full effects of climate change and global warming are still being resolved, yet the harmful implications appear to outweigh any potential benefits, both ecologically, financially and socially (IPCC, 2007).

Governments are beginning to act on climate change. In 1992 the Rio Earth summit was held and the UN Framework on Climate Change (UNFCCC) incorporated into the ‘Rio charter’, which now has 195 member states, or parties and 1 regional economic integration organisation (United Nations, 2014, A). Every year since there has been a Conference of Parties (COP), most recently COP21 in Paris. These summits are becoming increasingly legally binding to member parties. In 1997 the Kyoto Protocol differentiated responsibility between developed and developing nations and set internationally binding emissions reduction targets which were adopted into COP7 in 2001 and entered into force in 2005 (United Nations, 2014, B). The overall goal is to keep average global temperatures beneath a 2°C rise from pre-industrial revolution values.

Greenhouse gas emissions (GHC’s) can be reduced by a nation in many ways. The obvious method would be to lower industrial activity, but the economic loss associated is undesirable, especially in economically developing regions. ‘Cleaner’ alternative technologies for power production can be expanded, such as wind, solar, tidal and other renewable energy sources, although the investment in infrastructure, social acceptance and old technology decommissioning replete with business transfer are lengthy and ambitious affairs. Purely fiscal disincentives can be used such as carbon taxes, as well as incentives such as carbon credits, both of which promote economic restructuring towards lower emissions (Arazmuradov, 2015). However, despite climate summit pledges and increasingly legally binding international carbon laws it is becoming doubtful whether we will manage to remain beneath the 2°C rise in average global temperature (Johansson *et al.*

2015). Other technologies and geoengineering methods are being considered more carefully.

Carbon capture and storage (CCS) is one such area of geoengineering. Certain types of CCS have been operating for many years and their efficacy tried, tested and well characterized such as storage in underground depleted oil and gas reservoirs. Other types remain in the pilot scale stage, whereby the basic concepts have been demonstrated to be valid but the full array of chemical and ecological effects remain unresolved. One of these CCS pilot scale technologies is called mineral carbon sequestration (MCS). In MCS a heated fluid supercritical in CO₂ is injected down a borehole to the desired rock formation, usually a porous olivine rich rock type with an impermeable cap rock above for containment. When the aqueous fluid contacts silicate rocks it can cause them to release cations which react with the CO₂ to precipitate a variety of secondary minerals such as carbonates; this chemical reaction is called carbonation (Keleman & Matter, 2008). These carbonates are stable over geological time scales potentially providing a long-term advantage over alternative CCS methods. However, many questions on the carbonation process remain inadequately answered, such as fully understanding the reaction pathways and mineral-CO₂ interactions, especially the changes of mineral surface morphology (Shao *et al.* 2010). Other questions arise in implementing the pathways with sufficient speed to be industrially applicable, and in quantifying CO₂ mineralisation capacities and rates more precisely (Goldberg *et al.* 2008). Further research is clearly required to advance mineral carbon sequestration into a mainstream commercially viable solution for carbon management.

Carbonates, carbonation and mineral weathering processes on the planet Mars have been extensively studied over the last few decades, and many of the findings and lines of inquiry are directly relevant to MCS and CCS development on Earth. Industrial and scientific connections and collaboration remain sparse between the terrestrial carbon management and Mars research communities, and considerable scope exists for exchange of this hard-won knowledge.

Current carbon capture and storage technology.

CCS is not a single uniform technique. A brief review of key CO₂ capture and storage methods are presented to highlight the diversity of the technology, and to assist in understanding where mineral carbon sequestration fits in to the wider CCS landscape.

CO₂ capture techniques.

Air capture technology began emerging ~2009 through the company 'Global Thermostat' and remains at the pilot scale. The technique uses amines (types of ammonia that have had their hydrogen atoms substituted) that bind with CO₂ to produce carbamate molecules (Goeppert *et al.* 2012).

Post-combustion CO₂ capture is undertaken at the point of industrial effluence, and via a range of processes.

- Aqueous amine solvents, commonly monoethanolamine, can be used to absorb the CO₂. Solvent and CO₂ are later dissociated from the weakly bonded solution using heat and the CO₂ gas compressed ready for storage (Wang *et al.* 2011).
- Solid sorbents such as carbonates, polymeric resins, silica and zeolites absorb CO₂ and later go through a desorption process unique to the material selected (Samanta *et al.* 2012).
- A variety of membranes can be placed at the industrial exhaust and filter out CO₂ (Favre, 2011).
- Oxyfuel combustion is where a fuel is combusted in pure (~95%) oxygen instead of air, which provides a flue gas composed of CO₂, H₂O and impurities such as Hg, S and N. These impurities can be treated and removed during compression prior to storage. In comparison to pre- and

post-combustion technologies this technique requires the additional infrastructure of a cryogenic Air Separation Unit (ASU) and a CO₂ purification unit.

- Cryogenics can be used on high volume CO₂ exhausts and is usually combined with oxyfuel combustion and/or membrane technology. CO₂ condenses at -56.6 °C at 1 atmosphere and can therefore be condensed out of an effluent and removed, although this technique is costly (Scholes *et al.* 2013).

Pre-combustion CO₂ capture converts solid, liquid or gas fuels into a synthesis (syn) gas mixture of H and CO₂, usually through an Integrated Gasification Combined Cycle (IGCC) or reforming. Many of the methods described for post-combustion are also applied to pre-combustion, such as the use of porous membranes (Franz *et al.* 2014) and cryogenics (Atsonios *et al.* 2013).

CO₂ storage techniques.

- **Deep geological formations** can be used to store CO₂ by injecting fluid supercritical in CO₂ down a borehole into depleted oil and gas reservoirs, unminable coal beds, saline aquifers or permeable sandstone layers (Rutqvist, 2012). As the injected CO₂ fluid possesses a tendency to migrate back up towards the Earth's surface, these injection sites must have an impermeable cap rock formation above the target injection layer in order to trap the injected fluid.
- **Ocean water injection** involves pumping CO₂ directly into the ocean either from onshore pipelines or from a ship. The ocean is a vastly greater carbon reservoir (~40, 000 GtC) than the atmosphere (~750 GtC) (Houghton *et al.* 1995); however, this storage method increases ocean acidity. Ocean acidity dissolves carbonate, thinning the shells of sea creatures, as well as

interrupting the communication soundscapes of marine wildlife (Ilyina *et al.* 2006). Although this storage technique may play a useful part in offsetting anthropogenic climate change, it comes with considerable drawbacks.

- **Mineral carbon sequestration** is the transformation of atmospheric CO₂ gas into carbonate minerals. It can happen either as a natural process or through geoengineering.

Natural mineral carbon sequestration.

Mineral carbon sequestration proceeds naturally on Earth, in low temperature environments, over geological time scales. This process is an essential component of the global carbon cycle, with significant atmospheric CO₂ removal via silicate weathering partly balancing volcanic CO₂ output. Rock types do not react uniformly to mineral carbonation. Those with high olivine content such as ultra-basic peridotites exhumed from the mantle and out of chemical equilibrium with their new environment alter most efficiently (Keleman *et al.* 2011). Ophiolites, where oceanic crust has been obducted onto the continent, e.g. Oman, are a good example of carbonating peridotite. Alternatively, basalt can carbonate, albeit less efficiently than peridotite, however, if the region affected is great enough, such as large igneous provinces (LIPs) like the Siberian and Indian Deccan traps, then basalt becomes an important natural carbonation rock type too.

Geoengineered mineral carbon sequestration.

MSC is already in use in some pre-combustion carbon capture techniques, where mineral groups such as serpentines are carbonated at a solid-gas steam mediated interface (Larachi *et al.* 2012). What remains at an experimental pilot scale, however, is in-situ post-combustion mineral carbon sequestration within natural rock formations.

The problem with natural mineral carbon sequestration as a mechanism to offset anthropogenic climate change is that it sequesters carbon too slowly (i.e., over geological time scales). Pilot scale test sites in Iceland (Matter *et al.* 2009), the United States (McGrail *et al.* 2011) and elsewhere, are now seeking to accelerate the mineralisation process. This can be achieved by injecting water, super critical in CO₂, down boreholes to the desired rock formation. The carbonation process works optimally ~185°C (Keleman & Matter, 2008) which is initially achieved by pre-injection heat input. Carbonation is exothermic (Matter & Keleman, 2009) and rocks are naturally heated at depth (to a degree that depends on the local geothermal gradient); as a result, the carbonation reaction can remain at a near optimal temperature subsurface.

There has been rapid progress in understanding, testing and developing geoengineered MCS, with kinetic databases being developed for minerals associated with MCS (Oelkers & Declercq, 2014). However, many research questions need answering in more detail before MCS can be employed at a scale that is sufficient to tackle global climate change and so be deployed as a mainstream commercially viable solution for carbon management. This research development includes creating a more robust experimental and empirical cataloguing of the reaction pathways; implementing these pathways with sufficient speed to be industrially applicable; quantitatively estimating CO₂ mineralisation capacities and rates more precisely. Perhaps surprisingly, current research on the planet Mars may assist this advancement.

Terrestrial lessons from Martian atmosphere loss.

There is a near endless variety of ways that unpicking the chemical evolution of one planet might better inform geoengineering actions on our own. For example, understanding the long term fate of Martian carbonates and how they interact with the atmosphere and hydrosphere might teach us how effective this form of carbon storage might be on Earth and what the large scale long term feedbacks are.

Analysing the carbonates found on Mars, looking at the reaction pathways and how they have changed over geological time and how concentrations of carbon have changed spatially across the planet may help us to better understand the process of mineral carbon sequestration, from modelling to application. New carbonate types might be discovered that provide clues about carbon based minerals we think exist on Earth but have yet to be discovered (Wilson, 2015).

Currently there is little communication between Mars scientists and Earth climate change specialists. By combining the knowledge of these two groups, we may be able to control our global climate problems by using the rock reservoir as a thermostat using mineral carbon sequestration.

1.4 Exploration of Mars and instrumentation for locating carbonates.

No crewed mission to Mars has yet been attempted and for the moment all “in-situ” data from the planet comes from remotely operated instrumentation. Early efforts to send instruments to Mars began in 1960, when the USSR launched the two ‘Marsnik’ probes, or ‘Korabl/Sputnik 4 and 5’ in Russian, each weighing 460kg, but unfortunately both failed before reaching Earth orbit (Lundquist, 2009), and brought dangerous radioactive debris back to Earth (Wasson, 1964). Marsnik was followed by a string of failed USSR attempts in 1962 with Sputnik 22 (Korabl 11), Sputnik 23 (Mars 1) and Sputnik 24 (Korabl 13) all failing before reaching Mars (NASA, 2016a). Most missions to Mars have failed; testimony to the difficulty and high precision engineering involved. For the sake of brevity, only mission successes will be discussed in this section. A full list of Mars missions is presented below (Fig. 1.5):

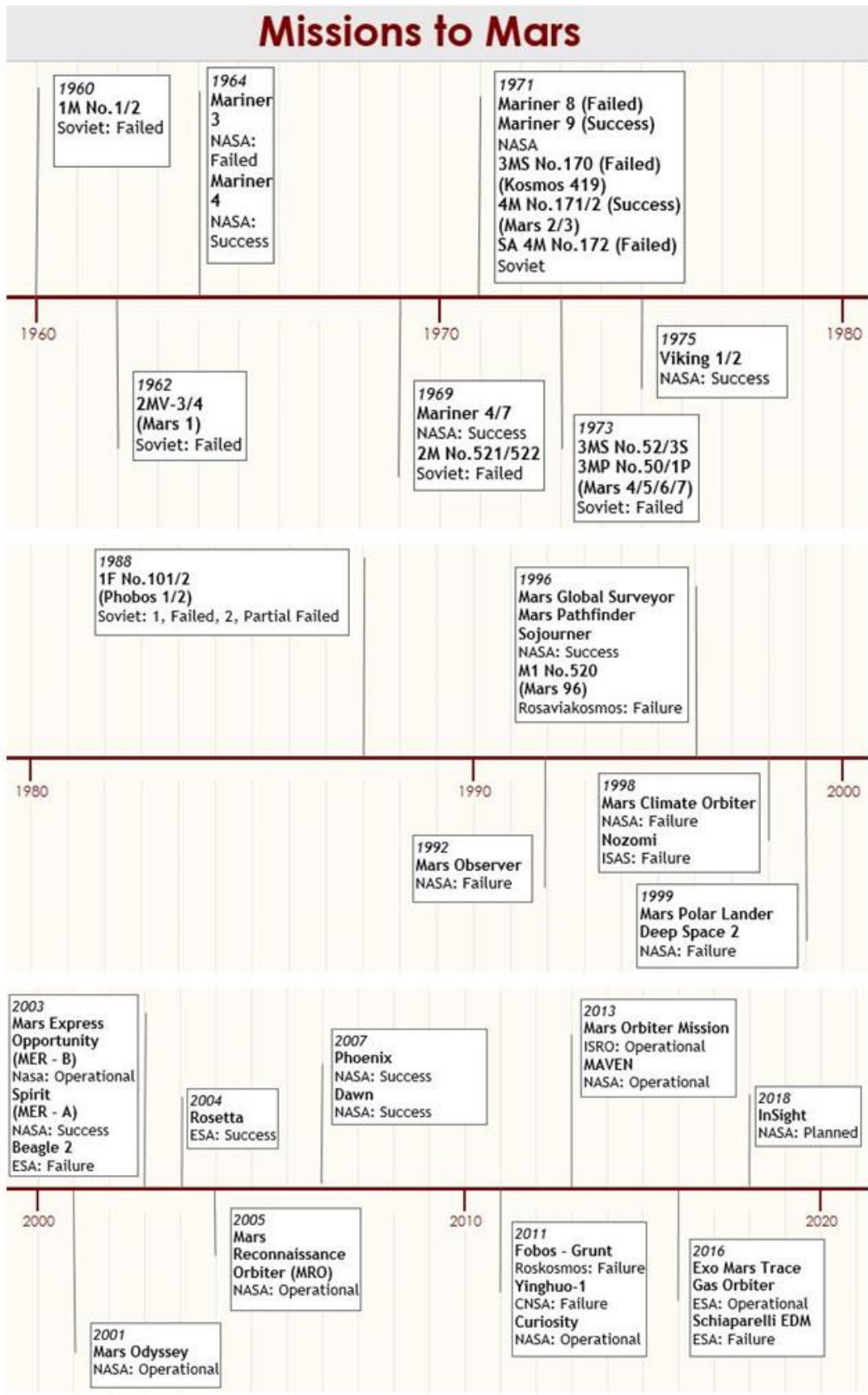


Figure 1.7. Missions to Mars. All dates are launch dates only.

The first successful mission to Mars took place in 1964 by NASA's Mariner 4 (Fig. 1.7), collecting photos of the Martian surface during a flyby. Mariner 4 was followed in 1969 by another two flyby missions from Mariners 6 and 7 (NASA, 1969). The Mariner missions are important as they were the first time the Martian polar ice had been investigated. The missions discovered that large quantities of CO₂ ice was present at the poles (NASA, 2016B). The existence of water, whether liquid or solid, on the surface or subsurface became suspected (Pimentel *et al.* 1974), and through spectral analysis CO₂ was predicted to dominate the atmosphere. The Mariner 6/7 mission spectral data also raised the hypothesis that carbonates existed on the Martian surface (Calvin *et al.* 1994).

In 1971 the USSR missions Mars 2 and 3 were the first to land on Mars and were identical spacecraft. Mars 2 crashed into the surface, but Mars 3 landed successfully, measuring temperature, atmospheric data and 20 seconds of video stream before all contact failed (2M 522, 1969, Fig. 1.7). This data has contributed to attempts to model the solar wind interaction with Mars (Slavin, 1991), and early information about the planet's magnetosphere (Russell, 1978). The following year, NASA's Mariner 9 began orbiting Mars and obtained considerably higher resolution photography than all previous missions, documenting basins, gullies, and geomorphological features indicative of past water flow on the planet (NASA, 1976), and documenting electron density profiles of the ionosphere during dust storms (Withers *et al.* 2015).

Following a great many failed missions, the NASA Viking missions of 1975/6 successfully sent landers and orbiters to Mars. The Viking missions involved searching for signs of life via on board experiments, monitoring weather, taking colour photographs and mapping the surface (Soffen, 1976). The Viking missions analysed the Martian soil and dust, finding mineral carbonate a near ubiquitous component and this has since been verified many times with estimates of 2 to 5 wt. % carbonate in the dust which could potentially account for multiple bars of sequestered CO₂ (Bandfield *et al.* 2003), at least partially answering some of the Mars carbonate conundrum.

In 1996, after 20 years characterised by mostly unsuccessful Soviet missions and a hiatus in Western missions, the Mars Global Surveyor (MGS) successfully reached Mars and remains in a low altitude near polar orbit. The MGS carries high resolution wide angle cameras that build daily global maps. MGS discovered that Mars had no magnetosphere via magnetometer readings, and it can be inferred that a great deal of any early atmosphere would have been lost to space, stripped away by the solar wind.

The first mission to land a rover on the Mars surface was the Pathfinder mission, also in 1996. The rover module of the mission was called Sojourner, and the rover successfully operated for about a year on the Martian surface and was the first to carry chemical analysis instrumentation (Golombek, 1997). The rover landed at the mouth of the outflow channel of Ares Vallis and a key part of its mission was to analyse the geology for water reaction, including carbonate formation (Golombek *et al.* 1999).

In 2001 the NASA mission Mars Odyssey successfully placed an orbiter around Mars (Saunders *et al.* 2001), its function was to act as a communication centre for future missions to the planet. Two years later ESA launched the Mars Express orbiter, which also carried the UK Beagle 2 lander. The lander failed, but the Mars Express orbiter continues to transmit data.

The next rovers on Mars were NASA's Spirit and Opportunity, in 2003 (Squyres, 2005). Termed the Mars Exploration Rovers (MER) they are particularly important to this work as they were the first missions to carry tools on board capable of analysing the interior of Mars rocks. These tools were mounted on an extendable arm called an Instrument Deployment Device (IDD) (Baumgartner *et al.*, 2005), which consists of a Mössbauer Spectrometer (Klingelhöfer *et al.* 2003), an Alpha Particle X-ray Spectrometer (APXS) (Rieder *et al.* 2003), a Microscopic Imager (Herkenhoff *et al.* 2003) and a Rock Abrasion Tool (RAT) (Gorevan *et al.* 2003). The RAT has diamond resin pads that grind in a 40 mm circle to a depth of 5 mm. The spectrometers analyse the dust as the grind proceeds, and the end grind is documented by the microscopic imager. The RAT also contains four magnets that

seek to identify any magnetic minerals in the Martian dust and soil (Madsen *et al.* 2003).

In 2005 the NASA Mars Reconnaissance Orbiter (MRO) successfully made Mars orbit. The MRO carried on board a High Resolution Imaging Science Experiment (HiRISE), which allows photography of extremely fine details gully and crater features (McEwen *et al.* 2007). It also has the Compact Reconnaissance Imaging Spectrometer for Mars (CRISM), which has allowed planet wide spectral analysis of surface chemistry, including the mapping of carbonates and serpentinised silicates (Murchie *et al.* 2007). The MRO Shallow Radar (SHARAD) emits radar at 15-25 MHz over a 0.3-3km horizontal resolution and 10-15m depth, and this is capable of locating near surface water ice, and allowing calculation of dielectric contents of overlying materials (Stuurman *et al.* 2016).

In 2011 NASA launched the Mars Science Laboratory (MSL)/Curiosity rover, landing on Mars in 2012 (Grotzinger *et al.* 2012). Like the MER missions the curiosity rover carried an IDD, RAT and microscopic imager which assists grinding away surface rock weathering so as to observe the pristine rock beneath. In addition it carried three spectrometers for mineral and soil element identification. One of these spectrometers is a Laser-Induced Breakdown Spectroscopy (LIBS), mounted within a 'chemcam' instrument suite (Maurice *et al.* 2012) replete with a laser and camera. MSL also has the ability to scoop soil into a quadrupole mass spectral analysis chamber called a Sample Analysis at Mars suite (Mahaffy *et al.* 2012). Curiosity also carries a Environmental Monitoring Station for weather, temperature, pressure measurements (Gómez-Elvira *et al.* 2012) and a Dynamic Albedo of Neutrons (DAN) capable of measuring underground hydrogen content to a depth of one metre, thus assessing potential subsurface water and hydration (Mitrofanov *et al.* 2012). Finally, MSL also carried the Chemistry & Mineralogy (CheMin) tool, which could conduct x-ray fluorescence/X - ray diffraction, identifying mineralogy and quantitative phase abundances for soil and dust (Blake *et al.* 2012). Curiosity landed at Gale crater (Fig. 1.8.F) and one of its mission objectives was to search for minerals such as carbonates, clays and sulphates associated with an aqueous early Mars (Grotzinger *et al.* 2012).

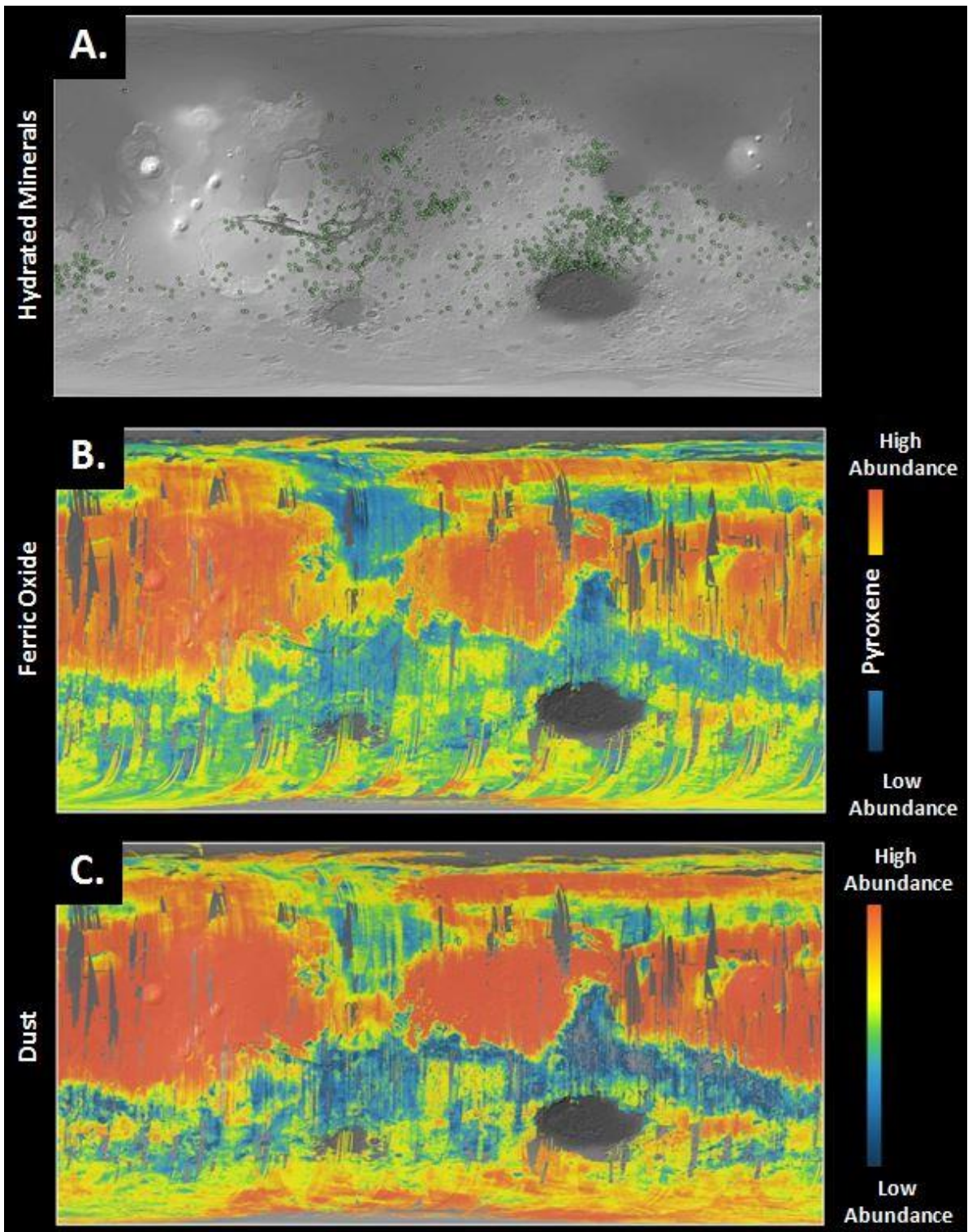
The basaltic terrain around Gale crater is unusually alkaline and fractionated compared to the Fe rich Al poor tholeiitic basalts of the majority of Martian terrain and thought to stem from a more water rich mantle source (Grotzinger, 2013). Amorphous soil content was analysed and emitted CO₂ during analysis thought to stem from a carbonate origin beneath the XRD detection limit of 2% (Grotzinger, 2013). The curiosity mission is ongoing in its search for carbonates (Fig. 1.7), although a lack of carbonate discoveries and a surfeit of hydrated Ca sulphates appears to be a theme (Nachon *et al.* 2014).

An exciting future mission is the InSight lander which is the first mission to Mars equipped with seismic monitoring capability (Banerdt *et al.* 2012). The launch was initially planned for a 2016, now rescheduled for a 2018. One of the points of interest from a carbonate discovery view point is that because carbonate minerals have a much lower density of ~2.2 to 2.8 gm/cm³ compared to basaltic rocks average density of ~2.8 to 3.0 gm/cm³ (EduMine, 2017) it may be possible to detect subsurface carbonates.

Chapter 2 of this thesis seeks to further this history of Mars exploration and the search for carbonates by improving upon the design of the Mars rover rock abrasion tool. The RAT currently uses standard common grinding techniques, analogous to revolving diamond sand paper. Part of the research contained in this thesis is adding ultrasonic vibrations to the RAT to improve the efficiency and grinding capability, ultimately aiding in the search to find potentially 'missing' carbonates and hence solve the Mars carbonate conundrum.

1.5

Mineral and landed mission maps of Mars.



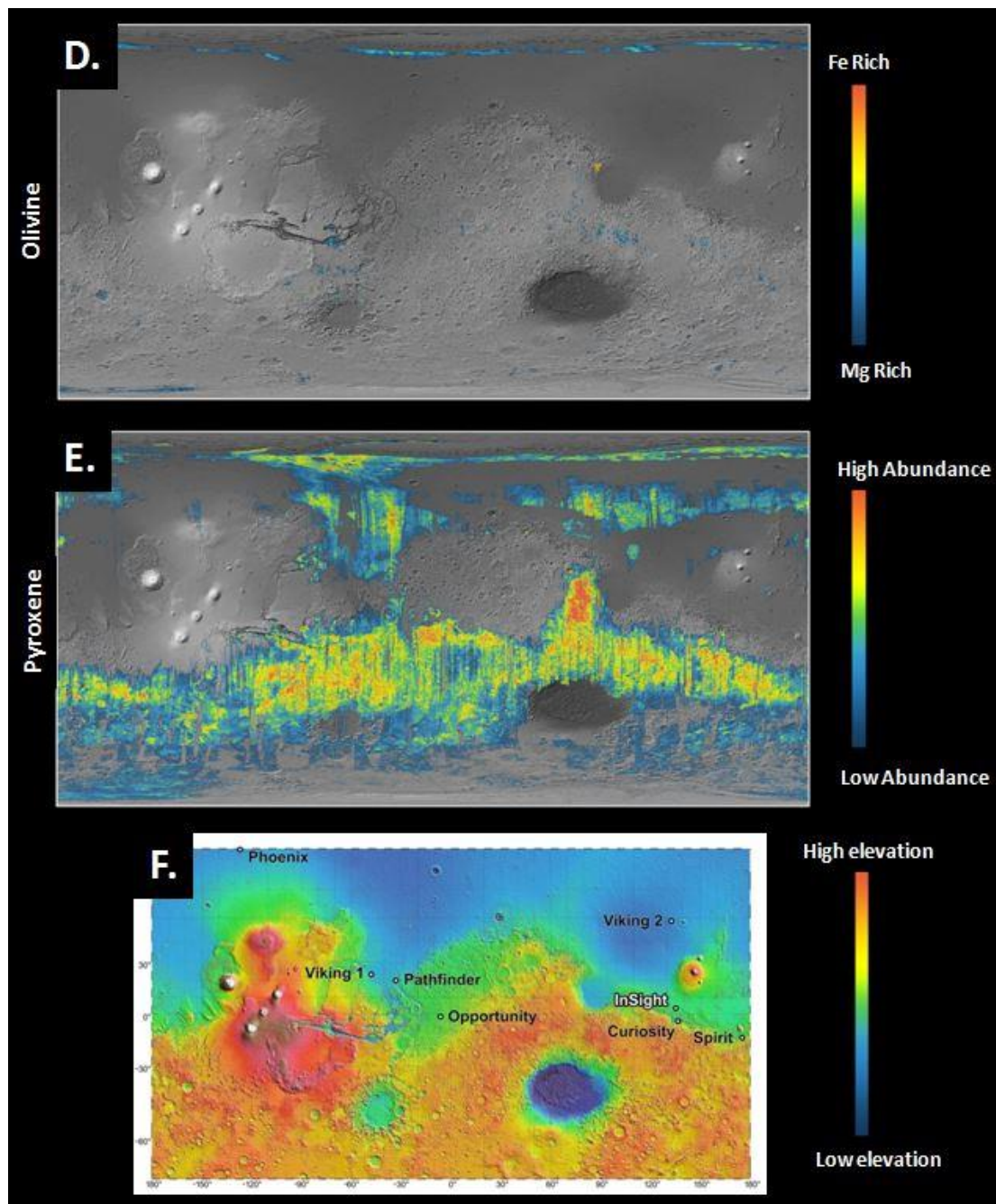


Figure 1.8. Distribution of minerals of interest to mineral carbon sequestration on Mars, overlain onto a NASA Mars Orbiter Laser Altimeter (MOLA) map. The distribution shows a high abundance of Fe oxide and dust in the Northern lowlands (B, C) and high abundance of pyroxene and hydrated minerals in the Southern highlands (A, E). **A.** Hydrated minerals. **B.** Ferric oxides. **C.** Dust. **D.** Olivine. **E.** Pyroxene. Credit: ESA/CNES/CNRS/IAS/Université Paris-Sud, Orsay. **F.** Principle Mars landed mission sites. Credit: JPL - Caltech/NASA.

1.6 Solution to the Mars carbonate conundrum 1: Terrestrial analogues.

*It is impossible to know any one phenomena unless in relation to another.
(Dickson, 2004).*

This statement can be viewed as equally 'true' within both philosophical epistemology, quantum physics or empirical planetary exploration. Knowledge of Y is conducive, if not essential, to the understanding of X. X is meaningless in isolation and the contrast between Y and X is the foundation for every scatter plot in academia. So it is with planetary science, with comparison and contrast of appropriately similar terrestrial minerals with Martian ones allowing for inference and support for hypothesis of early Mars environmental conditions, fluid chemistry and crust-atmosphere exchange. Terrestrial analogue studies form the backbone support of nearly all planetary missions (Preston & Dartnell, 2014). A terrestrial analogue can be selected for one or many specific similarities with a target planet environment, such as geology, fluid chemistry or habitability. Clearly defining the criteria which makes a proposed analogue appropriate for the target is essential.

No single terrestrial analogue is suitable to match the entire history of Mars, and particular terrestrial sites might be selected to represent different epochs in Martian history. Common terrestrial sites used as Martian analogues include:

- **Río Tinto (Iberian Pyritic Belt)** is used as an analogue for Martian iron leaching, sulphur deposition, heavy metal concentrations and the microbial utilisation of iron (Amils *et al.* 2006).
- **Yellowstone National Park, Wyoming, USA** possesses hydrothermal systems studied as both an analogue of early terrestrial and Martian potential microbial formation sites, as well as using the systems as test sites for Mars mission instrument spectroscopy and mineral identification (Bishop *et al.* 2004).
- **Acidic saline lake systems (SW Australia, Kansas USA etc.)** possess low pH <1 contain evaporites with extensive sulphates, Al - Fe - Si rich ground

waters, acidophilic microbial communities and a lack of carbonates (Benison & LaClair, 2004; Benison & Bowen, 2006). These sulphate rich-carbonate poor-environment makes them an interesting analogue of Amazonian Mars and ties into the carbonate conundrum by asking whether acidic sulphur may have dissolved pre-existing carbonate deposits (Benison & LaClair, 2004; Benison & Bowen, 2006).

- **Dry Valleys of Antarctica (McMurdo)** appear barren and have been used as fluvial, glacial and microbiological analogues of Mars (Doran *et al.* 2010; McKay *et al.* 2005). They are arid, cold, icy environments possessing little fluvial activity but produce geomorphological features similar to those observed on Mars. Such analogue environments have led some researchers to conclude there was no era of significant water flow on Mars, hence no need for thick atmospheres and carbonate deposition (Arcone *et al.* 2002; Head & Marchant, 2014). Further, liquid water can exist even in near-surface temperatures below the freezing point of water (~ -14 to -30°C), as ice sheeting can act as an insulating surface barrier allowing for subsurface liquid water, with obvious analogues for water environments in a cold early Mars. Potential Mars mission instrumentation testing is also conducted in Antarctica's dry valleys, such as ground-penetrating radar for subsurface ice and water (Arcone *et al.* 2002).
- **Chilean altiplano (Atacama)** possesses an extremely arid environment that has been used extensively as a Martian analogue site for microbiology (Bull & Asenjo, 2013; Barbieri & Cavalazzi, 2014), geomorphology (Irwin *et al.* 2014), evaporite salt and brine mineralogy including sulphates, jarosite and redox coupling (Escudero *et al.* 2013).
- **Semail ophiolite Oman** is one of the most common ophiolites cited as a Martian analogue (Clenet, 2009; Greenberger *et al.* 2015) for its rich combination of Mars-like mafic primary olivine rich mineralogy of basalt, gabbro and peridotite and secondary mineralogy of serpentinisation with concomitant methane and hydrogen gas production. The formation of carbonates, sulphates, evaporites and highly alkaline travertine springs also

make it an exciting analogue for Mars carbon processes. Other ophiolites used as Mars analogues include the Chimaera seep and Tekirova ophiolites of Turkey (Etiope *et al.* 2011; Etiope *et al.* 2013), the Leka ophiolite in Norway (Daae *et al.* 2013), Tablelands Ophiolite in Gros Morne National Park Canada (Szponar *et al.* 2013), Del Puerto Ophiolite in California (Blank *et al.* 2009), Bay of Islands ophiolite in Newfoundland (Suen & Frey, 1979) and the Maizuru Terrane in Japan (Sugawara *et al.* 2014).

In chapter 3 of this thesis the author initially attempted to gain samples from the Leka ophiolite with the purpose of using them as analogues for Martian carbonate formation processes. However, rock samples from the fieldwork showed extensive serpentinisation but little mineral carbonate. The British Geological Survey provided samples from the Oman ophiolite with well-developed serpentinisation, clays and carbonates filling fractures and these have been used as an analogue for carbonate veins found in the Martian meteorites.

1.7 Solution to the Mars carbonate conundrum 2: Experimental mineralogy.

Controlled laboratory simulations of Mars environments and reactions therein provide a crucial aspect of quantifiable ground truthing to both Mars exploration observations and instrumentation results, as well as to terrestrial analogue results relating to Martian conditions.

Laboratory experiments will never accurately replicate real planetary conditions in all their rich complexity (White & Brantley, 2003) and this is both an advantage and a drawback. The advantage is that by reducing variables to a known and calibrated few, that any changes in the system can be traced to causal variables with relatively high confidence (Lasaga, 1998); one that is unobtainable in real planetary environments where many thousands of variables interact organically and stochastically. By simplifying the natural system to an understandable, data manageable and mathematically approachable level it is

possible to observe the fundamental principles of a system, with noise reduced to a minimum (Maher *et al.* 2009). The drawback is that this simplification of variables means that laboratory data will never truly simulate natural planetary conditions, but remain an approximation (Holland & Turekian, 2011). As an example, mineral dissolution rates tend to be orders of magnitude slower in natural systems compared to laboratory simulations (Renforth *et al.* 2015), due to a natural system complexity not replicable in the laboratory.

The skill of the experimenter is to include enough experimental variables and measurements to reasonably reflect actual dynamics whilst avoiding unnecessary data clutter.

Laboratory simulations of geological processes, specifically mineral reactions, are challenging to represent in real systems due to the long time frames involved in the real systems (Krevor & Lackner, 2011). In comparison, short lived biological or water chemistry responses can be considered as operating in partial equilibrium and observable in their entirety in experimental real time (Morel & Hering, 1993). The former is attempting to provoke and simulate dynamics that occur over geological epochs within a time frame restricted by grant and project timings of months, or years at best. Where biological experiments have recourse to techniques such as adding enzymes to catalyse reactions, the geochemist is restricted to relying on increasing pressure or temperature, or both, in order to speed up reaction time; high water to rock ratio also aids reaction, as can using highly acidic or alkaline solutions.

An increase in pressure, temperature and water volume is effective in inducing mineral change to within academically useful timeframes, however, if the goal is to simulate low pressure, cold or arid environmental mineral changes as is often the case in early planetary environments such as Mars, then the resulting mineral suites and monitored fluid dynamics will not be perfect replicas of those observed by “in-situ” planetary missions.

This is where geochemical modelling can help, acting as a further validation to the experiment data. A wide range of geochemical modelling packages are available, such as PHREEQC (USGS, 2017) and Geochemist Workbench (The

Geochemist's Workbench, 2017), that can act as a validation check to the petrological and fluid chemistry experiment data results.

The objective of controlled laboratory simulations, much like the objectives of terrestrial analogues, is to create informed approximations of Mars conditions, from which inferences and generalised trends can be discerned. These advantages and drawbacks are important to bear in mind when contrasting and comparing “in-situ”, analogue and laboratory data and conclusions.

Below is a brief review of valuable laboratory simulations of specific aspects of the Martian environment relevant to crust - atmosphere coupling and the loss of the early Martian atmosphere via mineral carbonate formation. Also included are sulphur experiments seeking to explore the possible role of late acidifying planetary reactions on Mars that may have removed large carbonate deposits and thus potentially resolve a Martian carbonate conundrum.

Table 1.1. A collection of important laboratory analogue experiments attempting to recreate conditions relevant to either terrestrial mineral weathering conditions or a variety of Martian conditions including brines and sulphur.

Reference	Target	Time (Days)	Temperature (°C)	Aqueous Phase	Gas Phase	Mineral Phase	Pressure (Bars)
Giammar <i>et al.</i> 2005.	Terrestrial	1/7/10/14	30/95	H ₂ O + MgCl ₂ + NaHCO ₃	CO ₂	Forsterite Olivine	1/100
Giammar <i>et al.</i> 2005.	Terrestrial	1/7/10/14/26	30/95	H ₂ O	CO ₂	Forsterite Olivine	1/100
Chen & Brantley, 2000.	Terrestrial	0.4 (5 hours)	65	HCl + H ₂ O	Air	Forsterite Olivine	1
Gysi & Stefansson, 2012.	Terrestrial	125	75 to 250	H ₂ O	CO ₂	Basaltic glass	10/25
Qafoku <i>et al.</i> 2014.	Terrestrial	124	35/50/80	H ₂ O	CO ₂	Forsterite Olivine	91.19
Schaefer <i>et al.</i> 2014	Terrestrial	48/98	90	H ₂ O	CO ₂ + SO ₂ + O ₂	Basalt	100
Luce <i>et al.</i> 1972.	Terrestrial	0.66 to 4.16	25	H ₂ O + HNO ₃ /KOH	Air	Forsterite Olivine	1
Lafay <i>et al.</i> 2012	Terrestrial	1 to 90	150/200	NaOH	Air	Forsterite Olivine	5/16
Malvoisin <i>et al.</i> 2012.	Terrestrial	8.3 to 500	250/270/300/350	H ₂ O + NaCl	Air	Forsterite Olivine	500
Hausrath & Brantley, 2010.	Mars	56	34/22/6/-9	H ₂ O/CaCl ₂ + NaCl + H ₂ O	N ₂ /Na-Ca-Cl/air	Forsterite/fayalite or basalt	1
Golden <i>et al.</i> 2012.	Mars	10 to 12	80	H ₂ SO ₄	Air	Forsterite Olivine/siderite or basalt	1
Baker <i>et al.</i> 2000.	Mars	4 to 7	23/75	H ₂ O	CO ₂	Basalt	1 to 2
Dehouck <i>et al.</i> 2013	Mars	90	45	H ₂ O	CO ₂ /H ₂ O ₂ /air	Forsterite Olivine	1.5
Tosca <i>et al.</i> 2004	Mars	14	25	H ₂ O + HCL + H ₂ SO ₄	Air	Basalt	1
Schwensen <i>et al.</i> 2017.	Mars	4 to 7	23/75/200/400	H ₂ O + CO ₂	CO ₂ /H ₂ O + CO ₂	Basalt	1/2/500/1000
Moore & Bullock, 1999.	Mars	30/90/270	35	H ₂ O	Modern Mars mix	Olivine/pyroxene/plagioclase/basalt	Unstated
Booth <i>et al.</i> 1982.	Mars	2	25 to -94	H ₂ O	H ₂ O + O ₂ + SO ₂ + CO ₂	Olivine/tholeiite basalt	0.025 (SO ₂)/0.1 (CO ₂)
Mukhin <i>et al.</i> 1996.	Mars	0.5	Room to 200	-	Degassed	Ca/Mg carbonate + Mg sulphate	Vacuum (1.3 x 10 ⁻¹¹)

1.7.1 Experiments replicating Mars: Water.

The stability of surface water on Mars is complex to determine, yet plays a critical role in the process of atmospheric removal of CO₂ via carbonate mineralisation. Laboratory simulations of water formation in modern Mars conditions support the theoretical possibility of liquid water on the Martian surface (Kuznetz & Gan, 2002).

Experiments on the evaporation rate of pure water under modern Martian conditions of 0°C and 0.007 bar produce average evaporation rates of 0.73 ± 0.14 mm/h (Sears & Moore, 2005). It is proposed that water on Mars, whether modern or ancient, would be brine in order to be temporarily stable and to flow, due to the hyper aridity and water under-saturation in the atmosphere (Martínez & Renno, 2013). Brine ice possesses a lower melting point than pure water ice. Laboratory experiments of the evaporation of brine at temperatures between 0 to -26°C show that brine is both liquid at colder temperatures but also evaporates much more slowly at 0.04 mm/h compared to pure water (Sears & Chittenden, 2005). Evaporation rates are also heavily influenced by wind and insolation.

1.7.2 Experiments replicating Mars: Olivine and CO₂.

A great wealth of literature and controlled laboratory experiments exist exploring the reactions of olivine and CO₂, usually in a fluid filled titanium lined reaction vessel with a gas component (table 1.1). The combination of olivine, CO₂ and water leads to a vast array of interdependent dissolution - precipitation and reduction - oxidation pathways. Quantitatively exploring and documenting these reactions and their products is fundamental to understanding:

- Carbonate formation for the curtailment of terrestrial global warming and investigation of planetary atmosphere loss, such as occurred on Mars.
- Industrial production and processing of commercially valuable secondary gas and mineral products from an olivine feedstock.
- High pressure and temperature deep mantle - core dynamics of planets.

Curtailment of terrestrial global warming and investigation of planetary atmosphere loss such as on Mars covers a plethora of experiments. Table 1.1 highlights a range of literature exploring CO₂, water and olivine experiments conducted at a range of temperatures and pressure. This research has the specific aim of addressing either terrestrial climate change and attempts to simulate conditions such as deep saline aquifer storage and sequestration of CO₂ (Giammar *et al.* 2005; Chen & Brantley, 2000; Luce *et al.* 1972); or Martian questions such as the dissolution rates of olivine and other basaltic minerals under low temperature or brine conditions (Hausrath & Brantley, 2010), diagenesis (Schwensler *et al.* 2017), Martian hydrothermal conditions (Baker *et al.* 2000) or the formation of brine and sulphate mineralogy via controlled replications of the modern Mars atmosphere (Moore & Bullock, 1999; Booth *et al.* 1982; Mukhin *et al.* 1996).

Industrial production of secondary gas and mineral products using an olivine feedstock seeks to utilize and enhance the natural reactions of olivine to CO₂ and water, such as serpentinisation, carbonate formation and production of abiogenic methane and other hydrocarbon gases along with metals. Such experiments can use a wide range of conditions from 300 °C and 500 bar (Berndt *et al.* 1996), producing dihydrogen (H₂) from the conversion of Fe² to Fe³ in magnetite, along with ethane, propane and the production of graphite (Berndt *et al.* 1996). Many lessons learnt from these industrial experiments can shed light on planetary and Martian topics.

The topic of commercial abiogenic methane production is of particular interest to Mars research as methane can be used as a metabolic energy source for chemosynthetic microbes (Russell *et al.* 2010). Several researchers have proposed that methane release from serpentinised olivine is a robust mechanism for both the creation of life on early Earth (Russell *et al.* 2010) and a source of energy for life past or present on Mars (Oze & Sharma, 2005; Atreya *et al.* 2007). Serpentinisation being the hydrolysis of ferromagnesian silicates such as olivine and pyroxene, forming hydrated secondary minerals such as antigorite, crysotile, brucite etc.

Methane has been detected via orbital Mars Express measurements at 10 ± 5 ppbv global average in the modern Mars atmosphere (Formisano *et al.* 2004), albeit with diurnal, seasonal and spatial variations between 0 to 30 ppbv (Formisano *et al.* 2004; Geminale *et al.* 2008). It is difficult to distinguish abiotic from biotic methane production from remote sensing instrumentation, with H₂/CH₄ ratios being deemed unreliable (Lang *et al.* 2012).

Controlled laboratory experiments are a useful means of validating abiotic methane release from serpentinisation under Martian conditions. These experiments indicate the absolute importance of magnetite abundance in the initial mineralogy for determining methane volume production (Oze *et al.* 2012).

Caution in calculating rates and volume of methane production via rock serpentinisation based on laboratory experiments have been voiced by some researchers who have used isotopic carbon tracing to suggest that the majority of

the abiotic methane data recorded in such experiments may in fact be experimental artefacts caused by H₂ rich vapour phases in the experimental reaction systems and background contamination sources (McCollom, 2016). Such examples highlight the need to be aware of the possibility of artefacts in all experiments seeking to replicate planetary conditions.

High pressure and temperature deep mantle - core dynamics of planets utilises experimental mineralogy on water immersed peridotites with a CO₂ gas at very high pressures and temperatures, such as 27000 bars and 1160 °C (Brey & Green, 1977). Although interesting, such olivine and CO₂ experiments will not be reviewed here as they are not relevant to the lower pressures and temperatures of Martian surface and near-surface environments.

1.7.3 Experiments replicating Mars: Sulphur.

Sulphur can occur as mineral sulphides (S²⁻) such as pyrite, pyrrhotite and sphalerite, or alternatively as sulphates (SO₄²⁻) which are salts and esters of sulphuric acid such as anhydrite, gypsum, jarosite and alunite. There are widespread Mg- and Ca- and local Fe³⁺- sulphates on Mars (King & McLennan, 2010). This widespread sulphur on Mars may have come from an Fe-(Ni-)S core that extensively degassed and erupted (King & McLennan, 2010; Halevy & Head, 2014). Such sulphur core and mantle outgassing may have added significantly to the density of an early atmosphere in the form of H₂SO₄- aerosols, thus supporting the possibility of early surface liquid water flow (Halevy & Head, 2014). Sulphur plays an extremely important role in Martian geochemistry, both past and present. Sulphur minerals have been observed via remote sensing satellites and rovers, as well as in a wide range of Martian meteorites (Farquhar *et al.* 2000). The dominant atmospheric species are SO₂ and H₂S and these can become deposited at the Martian surface as both oxidised and reduced minerals (Farquhar *et al.* 2000). The widespread deposition of sulphates on the Martian surface and associated late stage acidity could explain the removal of pre-existing carbonate deposits.

Early laboratory controlled environment experiments on the role of sulphur on Mars sought to investigate the 7-9% SO₃ contents on the Viking lander regolith measurements (Booth *et al.* 1982) and whether these were from evaporitic deposition or SO₂ interaction with silicates. Later researchers used chambered experiments using SO₂ gas to monitor the photo-decomposition of carbonates and sulphates on Mars, forwarding photo-decomposition as a possible solution to the Mars carbonate conundrum (Mukhin *et al.* 1996); they conclude that ultra-violet light dissociating carbonates into atmospheric CO₂ is a plausible mechanism to explain the loss of major early Hesperian carbonate beds.

The experiment conducted in chapter 3 uses sulphur both in the forms of an SO₂ gas component, as well as using pyrite as an initial mineralogy in some of the experiment runs. The effect of sulphur on olivine dissolution and carbonate formation is key to understanding the carbonate conundrum.

1.8 Structure of the thesis.

This thesis does not solve the Mars carbonate conundrum. The question of the potential existence and fate of large carbonate reservoirs on Mars remains a tantalising playground of ideas, theories and lines of enquiry, continuing to divide the scientific community (Edwards & Ehlmann, 2015; Lee *et al.* 2016). Some researchers propose hypothetical solutions to the carbonate loss, such as widescale SO₂ output during Tharsis volcanism and the subsequent H₂SO₄ production removed the carbonate sedimentary layers or prevented significant carbonate precipitation (Bullock & Moore, 2007) and seek evidence to support this. Other researchers doubt whether the carbonate conundrum is even a valid question and that perhaps no massive atmosphere draw down into carbonate minerals occurred; that carbon loss to space via CO photo dissociation combined with minimal carbonate deposition is adequate to explain Martian terrain and chemistry (Hu *et al.* 2015). What this thesis aims to achieve is to provide a broad and interdisciplinary framework with which to approach the carbonate conundrum. An approach combining technical engineering, geochemical modelling, laboratory

experimentation and physical planetary sample observation in the form of Martian meteorites. It is an approach that synthesises pre - existing work on the carbonate conundrum, but also provides a wide angled framework that other researchers might adopt and build on, especially developing rover instrumentation with specific geological and geochemical questions and hypothesis in mind. This approach to the Mars carbonate conundrum is divided into three complementary lines of enquiry, which form the three principal thesis chapters, supported by this introduction and a conclusion.

- **Engineering:** The effects of ultrasonics on Mars rover rock abrasion tool performance.
- **Analogue:** Terrestrial ophiolites as Mars carbonation analogues.
- **Experimental:** Laboratory reproduction of Martian type carbonates and clays.

1.8.1 Effects of ultrasonics on rover rock abrasion tool performance.

Objectives.

The first part of the thesis acts as a practical engineering counterweight to the observational, analogue and geochemical aspects of the earlier chapters. Understanding the history of Martian atmosphere, water, CO₂ and carbonates as investigated in the previous chapters is only possible if the carbonates can be physically located and identified on the planet. Locating carbonates on Mars requires efficient tools mounted on any remote equipment such as rovers. This chapter determines whether ultrasonic assisted grinding as yet unused in Mars exploration performs better than the currently used common grinding techniques; assessing both a NASA rock abrasion tool (RAT) type diamond resin grinding tip and a tungsten carbide cutting tip. Objectives under investigation include:

- A. Post grind surface roughness.
- B. Power consumption.
- C. Thrust force.
- D. Material removal rate.

Carbonates can be found “in-situ” either via satellite, landers or rovers. The Mars rovers contain a suite of instruments for analysing rock samples and identifying minerals, for example the Chemistry and Mineralogy (CheMin) X-ray diffraction (XRD) (Bish *et al.* 2013). However, the Mars surface is dusty and weathered. In order to remove the outer oxidised and reacted surfaces of rocks to view their pristine interior requires targeted mechanical abrasion. To achieve this abrasion current Mars rovers use an instrument called the rock abrasion tool (RAT) which uses two diamond resin pads which mechanically grind to an arbitrary depth of 5 mm into the rock (Gorevan *et al.* 2003). The smoother the resulting surface grind is, the better the rover imaging systems can identify features, such as delicate weathered veins hosting carbonates and clays, for further analysis.

In this methodical chapter a new prototype rover abrasion tool called the Micro-Optic UltraSonic Exfoliator (MOUSE) is designed, modelled, constructed and a diamond resin very similar to the NASA rock abrasion resin developed. The prototype tool uses ultrasonics with the aim of enhancing Mars rover grind surface smoothness. Ultrasonics have repeatedly and consistently demonstrated smoother surface grinds compared to their common grinding counterparts in terrestrial industrial applications of ultrasonics (Brehl & Dow, 2008; Agarwal, 2015). It is hoped this rapidly evolving technology can be applied to rock grinds on Mars, assisting in the search for carbonate minerals.

1.8.2 Terrestrial ophiolites as Mars carbonate analogues.

Objectives.

- A. To review Mars geology, specifically the interaction of water and CO₂ with the planets crust through geological time.
- B. To analyse carbonates and hydrous minerals in two Martian meteorites, ALH 84001 and Lafayette. These meteorites representing early and recent Mars respectively. To highlight the differences and similarities between the two samples and how this relates to objective A.
- C. To analyse carbonates and hydrous minerals in terrestrial ophiolites. To compare and contrast the results with the Martian meteorites of objective B, and relate both terrestrial and Martian samples in the context of objective A.

Ophiolites are terrestrial sea floor that has been obducted onto continental crust. Composed dominantly of basalt, gabbro and peridotite, with high mineral olivine content, ophiolites are strongly out of equilibrium with the surface environment and highly reactive as a consequence; this reactivity is termed retrograde metamorphism. Olivine and pyroxenes react with water, forming secondary minerals including carbonate and clays, which tend to form in rock fractures, pore spaces and other lines of weakness in the rocks. Ophiolites and exposed olivine rich igneous intrusions and global mineral weathering account for $\sim 3 \times 10^9$ Kg draw down of atmospheric carbon, or $\sim 1.11 \times 10^{10}$ Kg draw down of terrestrial atmospheric CO₂ (IPCC, 2013) and are therefore an important part of our planet's carbon budget (Fig. 1.9). The Oman ophiolite alone sequesters $\sim 10^7$ to $\sim 10^8$ kg yr⁻¹ of CO₂ (Kelemen & Matter, 2008).

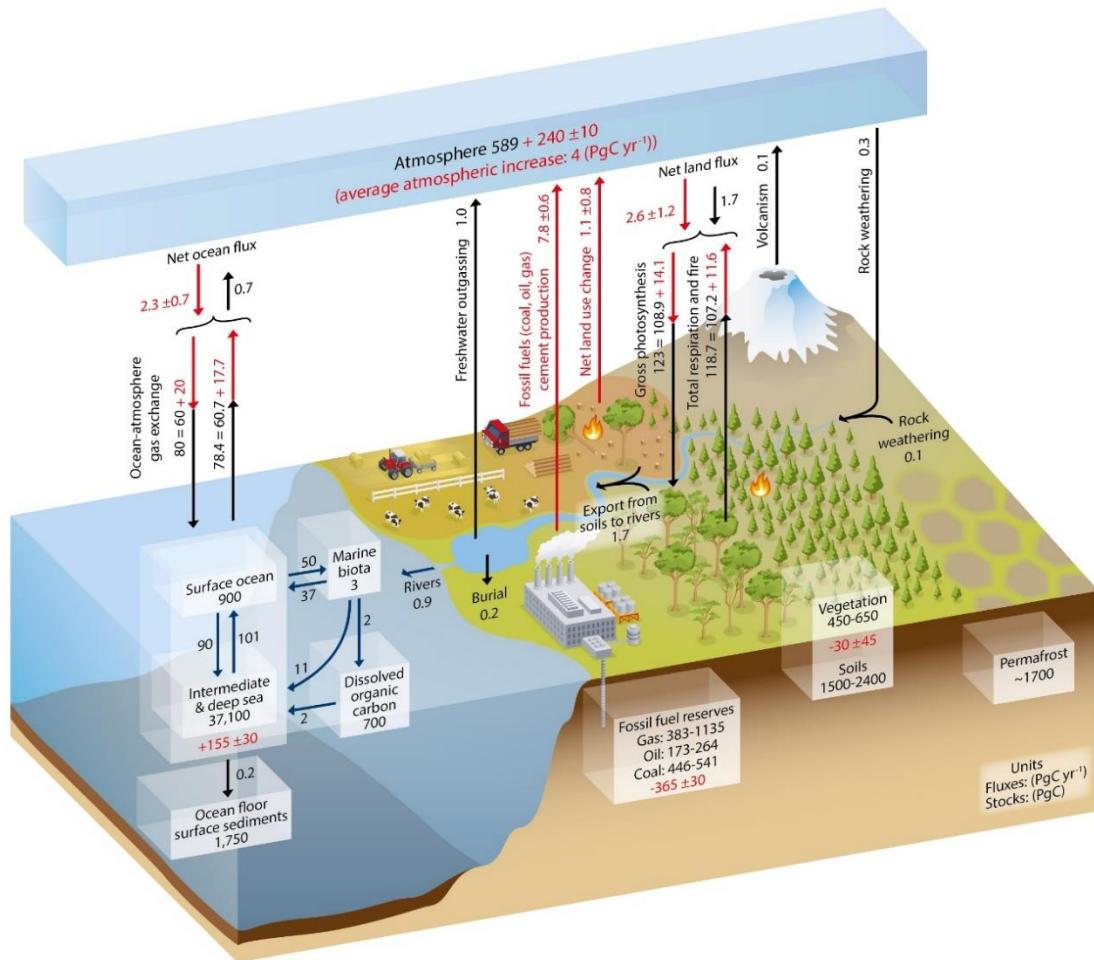


Figure 1.9. Terrestrial global carbon budget from the IPCC 2013 report (IPCC, 2013). Rock weathering draws down 0.3 PgC yr⁻¹ from the atmosphere via mineral carbon sequestration, more than compensating for the 0.1 PgC yr⁻¹ released into the atmosphere by volcanoes and 0.1 PgC yr⁻¹ by fresh water outgassing.

Mafic, olivine rich ophiolites are similar in composition to many Martian rocks and can therefore act as analogues. The surface of Mars is predominantly basaltic (McSween *et al.* 2009) with carbonates, clays and other hydrous minerals having been discovered by both satellites (Calvin *et al.* 1994), rovers (Morris *et al.* 2010), landers (Hecht *et al.* 2009) and in Martian meteorites (Grady *et al.* 1995). There has not yet been any sample return missions of Martian rocks, therefore detailed mineralogical comparative work relies significantly on the Martian meteorites, and a terrestrial analogue to compare these meteorites to is helpful.

This broad third chapter blends a literature review with applied quantitative observation of Martian meteorite and terrestrial ophiolite carbonates, with particular attention paid to the oscillating zonations in the carbonates, contrasting and comparing terrestrial and Martian carbonate zonations. The review aspect covers the geology of Mars with a focus on carbonate and clay minerals, it also discusses CO₂ and water in current and past Mars, along with an analysis of the lines of evidence used to assess the CO₂ and water histories. Particular attention is paid to the Martian meteorites, as these provide us with the only Martian carbonates we can observe under the microscope. Sulphur is also covered in review, as acidic environments are important in accounting for carbonate inventories. Terrestrial ophiolites, their typical fluid chemistry and carbonate types are briefly summarised. The quantitative analysis aspect of the chapter begins by observing carbonates in two famous Martian meteorites of very different ages.

- A. **ALH 84001:** A 4100 Ma old orthopyroxenite (Mittlefehldt, 1994) with a relatively high abundance (~1 wt. %) of chemically and physically varied carbonates compared to younger Martian meteorites (Lapen *et al.*, 2010). This carbonate abundance in the older meteorite may be an indication of a greater abundance of water on early Mars compared to young Mars.
- B. **Lafayette:** A 1300 Ma old olivine clinopyroxenite (Swindle & Olson, 2004). The meteorite possesses veins of clay and hydrated minerals including ferroan saponite, iddingsite, goethite, Fe rich smectite and carbonate which has replaced olivine, pyroxene and high Si glass (Vicenzi & Eiler, 1998; Treiman *et al.* 1993; Tomkinson *et al.* 2013). The carbonate is not as extensive, varied or zoned as in the older ALH 84001; this difference is probably due to less availability of water on Mars ~633 ± 23 Ma ago when the Lafayette carbonates formed (Borg & Drake, 2005) compared to ~4100 Ma ago. However, the intimate association of the carbonate with other hydrous phases, combined with the dating of the clays to 633 ± 23 Ma ago (Borg &

Drake, 2005) demonstrates that water has remained available on Mars until at least this age.

These meteorites are selected to represent the change in carbonate mineralogy, and by proxy water and CO₂, through geological time on Mars. The results of the meteorite analysis work are then compared to terrestrial ophiolites of Semail, Oman and Leka, Norway.

1.8.3 Experimental reproduction of Martian type carbonates and clays.

Objectives.

- A. To observe how compositionally identical minerals react with differing gases that chemically represent a simplified Mars atmosphere. Specific focus is on carbonate and sulphate mineral formation. Gases used:
 - CO₂
 - CO₂:SO₂ (2:1) initial atmosphere.
- B. To observe the evolution of mineralogy and fluid chemistry during carbonate and sulphate formation under identical gas conditions (CO₂ or CO₂:SO₂) but differing initial mineralogy. Initial minerals and rock types used:
 - Olivine (Mg,Fe²⁺)₂SiO₄ (Fo ~50%).
 - Basalt (Glass & olivine rich).
 - Basalt (Glass & olivine rich) with pyrrhotite.
- C. To compare the results of objectives D and E with the results from objectives B and C, the Martian meteorite samples ALH 84001 and Lafayette, representing early and modern Mars and the terrestrial ophiolites; ultimately synthesising all data from chapters 2 and 3 within the context of Martian geological and atmospheric history, objective A.

- D. To test whether Mars meteorite olivine alteration sequences form via isovolumetric replacement of primary minerals or via dissolution and precipitation of secondary minerals into fractures and pore spaces.
- E. To assess whether South African hortonolite is a more suitable Martian olivine analogue than San Carlos olivine.
- F. To observe the effects on mineral alteration and fluid chemistry when sulphur (either as a gas or mineral) is added into a traditional CO₂ Mars analogue system.

When studying carbonates in Martian meteorites, or by remote observation, the precise formation conditions can only be inferred from analytical data, and a formation environment hypothesis proposed, not known. A powerful way to support such hypothesis is to use precise laboratory environments that attempt to recreate the same type of carbonates observed within Martian samples within a controlled and accurately known set of conditions. The analogue maxim being:

If laboratory carbonates are physically and chemically similar to Martian carbonates then similar formation environmental conditions can be inferred.

This concise chapter uses closed batch reactor vessels under fixed pressure and temperature conditions, while varying the atmospheric gas mix and water immersed mineral composition. The resulting minerals and the dataset of evolving fluid chemistry are compared with the two Martian meteorites, ALH 84001 and Lafayette, described in the previous chapter. A great number of difficulties and flaws beset such experimental replications of secondary mineral formation. The minerals observed “in-situ” on Mars and in meteorite samples formed over geological time frames, and attempting to recreate these minerals precisely on a laboratory time scale measured in weeks or months is problematic; the goal is to create approximations rather than identical replicas. Both advantages and disadvantages exist in having a minimal number of environmental controlling factors. The main advantage is that it becomes easier to attribute mineral, chemical and system changes to specific environmental factors and known system variables. The main disadvantage is that by having so few environmental factors in

the laboratory it is impossible to fully recreate the wide panoply and rich diversity of natural aqueous systems.

1.9 References

- Adeoye J. T., Menefee A. H., Xiong W., Wells R. K., Skemer P., Giammar D. E., Ellis B. R. (2017). Effect of transport limitations and fluid properties on reaction products in fractures of unaltered and serpentinized basalt exposed to high PCO₂ fluids. *International Journal of Greenhouse Gas Control Volume 63*:310-320.
- Agarwal S. (2015). On the mechanism and mechanics of material removal in ultrasonic machining. *International Journal of Machine Tools and Manufacture 96*:1-14.
- Amils R., González-Toril E., Fernández-Remolar D., Gómez F., Aguilera A., Rodríguez N., Malki M., García-Moyano A., Fairén A. G., de la Fuente V., Sanz J. L. (2006). Extreme environments as Mars terrestrial analogs: The Rio Tinto case. *Planetary and Space Science 55*(3):370-381.
- Anderegg W. R. L., Prall J. W., Harold J., Schneider S. H. (2010). Expert credibility in climate change. *Proceedings of the National Academy of Sciences 107*(27):12107-12109.
- Andrews D. G. (2010). *An introduction to atmospheric physics*. 2nd ed. New York: Cambridge University Press. 6-7.
- Arcilla C. A., Pascua C. S., Alexander W. R. (2011). Hyperalkaline groundwaters and tectonism in the Philippines: significance to natural carbon capture and sequestration. *Energy Procedia 4*:5093-5101.
- Arcone S. A., Prentice M. L., Delaney A. J. (2002). Stratigraphic profiling with ground-penetrating radar in permafrost: A review of possible analogs for Mars. *Journal of Geophysical Research: Planets 107*(E11):18-1-18-14.
- Atreya S. K., Mahaffy P. R., Wong A. (2007). Methane and related trace species on Mars: Origin, loss, implications for life, and habitability. *Planetary and Space Science 55*(3):358-369.
- Atsonios K., Panopoulos K. D., Doukelis A., Koumanakos A., Kakaras E. (2013). Cryogenic method for H₂ and CH₄ recovery from a rich CO₂ stream in pre-combustion carbon capture and storage schemes. *Energy 53*:106-113.
- Arazmuradov A. (2015). Economic prospect on carbon emissions in commonwealth of independent states. *Economic Change and Restructuring 1*-33.

- Baker L. L., Agenbrood D. J., Wood S. A. (2000). Experimental hydrothermal alteration of a martian analog basalt: Implications for martian meteorites. *Meteoritics & Planetary Science* 35(1):31-38.
- Bandfield J. L., Glotch T. D., Christensen P. R. (2003). Spectroscopic Identification of Carbonate Minerals in the Martian Dust. *Science* 301(5636):1084-1087.
- Banerdt W. B., Smrekar S., Alkalai L., Hoffman T., Warwick R., Hurst K., Folkner W., Lognonné P., Spohn T., Asmar S., Banfield D., Boschi L., Christensen U., Dehant V., Giardini D., Goetz W., Golombek M., Grott M., Hudson T., Johnson C., Kargl G., Kobayashi N., Maki J., Mimoun D., Mocquet A., Morgan P., Panning M., Pike W. T., Tromp J., van Zoest T., Weber R., Wieczorek M., Insight Team. (2012). InSight: An Integrated Exploration of the Interior of Mars. *43rd Lunar and Planetary Science Conference* 1659:2838.
- Barbieri R., Cavalazzi B. (2014). How Do Modern Extreme Hydrothermal Environments Inform the Identification of Martian Habitability? The Case of the El Tatio Geyser Field. *Challenges* 5(2):430-443.
- Bauer A., Velde B. D. (2014). *Geochemistry at the Earth's Surface: Movement of Chemical Elements*. London: Springer. 286.
- Baumgartner E. T., Bonitz R. G., Melko J. P., Shiraishi L. R., Chris L. P. (2005). The Mars Exploration Rover instrument positioning system. *IEEE Aerospace Conference*: 1-19. DOI: 10.1109/AERO.2005.1559295
- Benison K. C., LaClair D. A. (2004). Modern and Ancient Extremely Acid Saline Deposits: Terrestrial Analogs for Martian Environments? *Astrobiology* 3(3):609-618.
- Benison K. C., Bowen B. B. (2006). Acid saline lake systems give clues about past environments and the search for life on Mars. *Icarus* 183:225-229.
- Benitez M. A. (2009). Climate change could affect mosquito-borne diseases in Asia. *The Lancet* 373(9669):1070.
- Berndt M. E., Allen D. E., Seyfried W. E. (1996). Reduction of CO₂ during serpentinization of olivine at 300 °C and 500 bar. *Geology* 24(4):351-354.
- Bish D. L., Blake D. F., Vaniman D. T., Chipera S. J., Morris R. V., Ming D. W., Treiman A. H., Sarrazin P., Morrison S. M., Downs R. T., Achilles C. N., Yen A. S., Bristow T. F., Crisp J. A., Morookian J. M., Farmer J. D., Rampe E. B., Stolper E. M., Spanovich N., MSL Science Team. (2013). X-ray Diffraction Results from Mars Science Laboratory: Mineralogy of Rocknest at Gale Crater. *Science* 341(6153):1238932.

- Bishop J. L., Murad E., Lane M. D., Mancinelli R. L. (2004). Multiple techniques for mineral identification on Mars: a study of hydrothermal rocks as potential analogues for astrobiology sites on Mars. *Icarus* 169(2):311-323.
- Blake D., Vaniman D., Achilles C., Anderson R., Bish D., Bristow T., Chen C., Chipera S., Crisp J., Des Marais D., Downs R. T., Farmer J., Feldman S., Fonda M., Gailhanou M., Ma H., Ming D. W., Morris R. V., Sarrazin P., Stolper E., Treiman A., Yen A. (2012). Characterization and Calibration of the CheMin Mineralogical Instrument on Mars Science Laboratory. *Space Science Reviews* 170(1-4):341-399.
- Blank J. G., Green S. J., 1, Blake D., Valley J. W., Kita N. T., Treiman A., Dobson P. F. (2009). An alkaline spring system within the Del Puerto Ophiolite (California, USA): A Mars analog site. *Planetary and Space Science* 57(5-6):533-540.
- Booth M. C., Gibson E. K., Kotra R. (1982). Chemical Weathering on Mars: Interactions of Sulfur Dioxide with Olivine and Olivine Tholeiite in Simulated Martian Environments. *Lunar and Planetary Science* XIII:55-56.
- Borg L., Drake M. J. (2005). A review of meteorite evidence for the timing of magmatism and of surface or near-surface liquid water on Mars. *Journal of Geophysical Research* 110:E12S03.
- Brain D. A., Jakosky B. M. (1998). Atmospheric loss since the onset of the Martian geologic record: Combined role of impact erosion and sputtering. *Journal of Geophysical Research: Planets* 103(E10):22689-22694.
- Brehl D. E., Dow T. A. (2008) Review of vibration-assisted machining. *Precision Engineering* 32(3):153-172.
- Brey G., Green D. H. (1977). Systematic study of liquidus phase relations in olivine melilitite +H₂O +CO₂ at high pressures and petrogenesis of an olivine melilitite magma. *Contributions to Mineralogy and Petrology* 61(2):141-162.
- Bull A. T., Asenjo J. A. (2013). Microbiology of hyper-arid environments: recent insights from the Atacama Desert, Chile. *Antonie van Leeuwenhoek* 103(6):1173-1179.
- Bullock M. A., Moore J. M. (2007). Atmospheric conditions on early Mars and the missing layered carbonates. *Geophysical Research Letters* 34:(19).
- Calvin W. M., King T. V. V., Clark R. N. (1994). Hydrous carbonates on Mars?: Evidence from Mariner 6/7 infrared spectrometer and ground-based telescopic spectra. *Journal of Geophysical Research: Planets* 99(E7):14659-14675.
- Carr M. H. (1999). Retention of an atmosphere on early Mars. *Journal of Geophysical Research: Planets* 104(E9):21897-21909.

- Chassefière E., Leblanc F. (2004). Mars atmospheric escape and evolution; interaction with the solar wind. *Planetary and Space Science* 52(11):1039-1058.
- Chen Y., Brantley S. L. (2000). Dissolution of forsteritic olivine at 65 °C and 2<pH<5. *Chemical Geology* 165(3-4):267-281.
- Clark B. C., Morris R. V., McLennan S. M., Gellert R., Jolliff B., Knoll A. H., Squyres S. W., Lowenstein T. K., Ming D. W., Tosca N. J., Yen A., Christensen P. R., Gorevan S., Brückner J., Calvin W., Dreibus G., Farrand W., Klingelhofer G., Waenke H., Zipfel J., Bell J. F., Grotzinger J., McSween H. Y., Rieder R. (2005). Chemistry and mineralogy of outcrops at Meridiani Planum. *Earth and Planetary Science Letters* 240:73-94.
- Clenet H. (2009). *Téledétection hyperspectrale : minéralogie et pétrologie, application au volcan Syrtis Major (Mars) et à l'ophiolite d'Oman*. Laboratoire Dynamique Terrestre et Planétaire, UMR.
- Cook J., Nuccitelli D., Green S. A., Richardson M., Winkler B., Painting R., Way R., Jacobs P., Skuce A. (2013). Quantifying the consensus on anthropogenic global warming in the scientific literature. *Environmental Research Letters* 8(2):024024.
- Daae F. L., Økland I., Dahle H., Jørgensen S. L., Thorseth I. H., Pedersen R. B. (2013). Microbial life associated with low-temperature alteration of ultramafic rocks in the Leka ophiolite complex. *Geobiology* 11(4):318-339.
- Dehouck E., Gaudin A., Mangold N., Lajaunie L., Dauzères A., Le Menn E. (2013). Weathering of olivine under CO₂ atmosphere: A Martian perspective. *44th Lunar and Planetary Science Conference 2017*.
- Dickson M. (2004). A view from nowhere: quantum reference frames and uncertainty. *Studies in History and Philosophy of Science Part B: Studies in History and Philosophy of Modern Physics*. 35(2):195-220.
- Doran P. T., Zimmerman M. K. (2009) Examining the scientific consensus on climate change. *Eos, Transactions, American Geophysical Union* 90(3):22-23.
- Doran P. T., Lyons W. B., McKnight D. M. (2010). *Life in Antarctic Deserts and other Cold Dry Environments: Astrobiological Analogs*. Cambridge: Cambridge University Press.
- EduMine. (2017). *Average Specific Gravity of Various Rock Types*. Available: <http://www.edumine.com/xtoolkit/tables/sgtables.htm>
- Edwards C. S., Ehlmann B. L. (2015). Carbon sequestration on Mars. *Geology* 43:863-866.
- Ehlmann B. L., Mustard J. F., Murchie S. L., Poulet F., Bishop J. L., Brown A. J., Calvin W. M., Clark R. N., Des Marais D. J., Milliken R. E., Roach L. H., Roush T. L., Swayze G. A., Wray J. J. (2008). *Science* 322(5909):1828-1832.

- Epstein P. R. (2005). Climate change and human health. *The New England Journal of Medicine* 353:1433-1436.
- Escudero L. V., Bijman J., Chong G., Pueyo J. J., Demergasso C. S. (2013). Geochemistry and Microbiology in an Acidic, High Altitude (4,000 m) Salt Flat – High Andes, Northern Chile. *Advanced Materials Research* 825:28-32.
- Etiopie G., Schoell M., Hosgörmez H. (2011). Abiotic methane flux from the Chimaera seep and Tekirova ophiolites (Turkey): Understanding gas exhalation from low temperature serpentinization and implications for Mars. *Earth and Planetary Science Letters* 310(1-2):96-104.
- Etiopie G., Ehlmann B. L., Schoell M. (2013). Low temperature production and exhalation of methane from serpentinized rocks on Earth: A potential analog for methane production on Mars. *Icarus* 224(2):276-285.
- Farquhar J., Savarino J., Jackson T. L., Thiemens M. H. (2000). Evidence of atmospheric sulphur in the Martian regolith from sulphur isotopes in meteorites. *Nature* 404:50-52.
- Favre E. (2011). Membrane processes and post-combustion carbon dioxide capture: challenges and prospects. *Chemical Engineering Journal* 171(3):782-793.
- Feely R. A., Sabine C. L., Byrne R. H., Millero F. J., Dickson A. G., Wanninkhof R., Murata A., Miller L. A., Greeley D. (2012). Decadal changes in the aragonite and calcite saturation state of the Pacific Ocean. *Global Biogeochemical Cycles* 26(3).
- Forget F., Pierrehumbert R. T. (1997). Warming Early Mars with Carbon Dioxide Clouds That Scatter Infrared Radiation. *Science* 278(5341):1273-1276.
- Formisano V., Atreya S., Encrenaz T., Ignatiev N., Giuranna M. (2004). Detection of Methane in the Atmosphere of Mars. *Science* 306(5702):1758-1761.
- France-Lanord C., Derry L. A. (1997). Organic carbon burial forcing of the carbon cycle from Himalayan erosion. *Nature* 390:65-67.
- Franz J., Maas P., Scherer V. (2014). Economic evaluation of pre-combustion CO₂ capture in IGCC power plants by porous ceramic membranes. *Applied Energy* 130:532-542.
- Gaines R. V., Skinner H. C. W., Foord E. E., Mason B., Rosenzweig A., King V. T., Dowty E. (1997). *Dana's New Mineralogy*. 8th ed. New York: Wiley-Interscience.
- Garzzone C. N. (2008). Surface uplift of Tibet and Cenozoic global cooling. *Geology* 36(12):1003-1004.
- Geminale A., Formisano V., Giuranna M. (2008). Methane in Martian atmosphere: Average spatial, diurnal, and seasonal behaviour. *Planetary and Space Science* 56(9):1194-1203.

- Giammar D. E., Bruant R. G., Peters C. A. (2005). Forsterite dissolution and magnesite precipitation at conditions relevant for deep saline aquifer storage and sequestration of carbon dioxide. *Chemical Geology* 217(3-4):257-276.
- Goeppert A., Czaun M., Suyra Prakash G. K., Olah G. A. (2012). Air as the renewable carbon source of the future: an overview of CO₂ capture from the atmosphere. *Energy & Environmental Science* 5:7833.
- Goldberg D. S., Takahashi T., Slagle A. L. (2008). Carbon dioxide in deep-sea basalt. *Proceedings of the National Academy of Sciences of the United States of America* 105(29):9920-9925.
- Golden D. C., Ming D. W., Hausrath E. M., Morris R. V., Niles P. B., Achilles C. N., Ross D. K., Cooper B. L., Gonzalez C. P., Mertzman S. A. (2012). Dissolution of olivine, siderite, and basalt at 80 °C in 0.1 M H₂SO₄ in a flow through process: Insights into acidic weathering on Mars. *43rd Lunar and Planetary Science Conference* 2521.
- Golombek M. P. (1997). The Mars Pathfinder Mission. *Journal of Geophysical Research: Planets* 102(E2):3953-3965.
- Golombek M. P., Anderson R. C., Barnes Jeffrey R., Bell III J. R., Bridges N. T., Britt D. T., Brückner J., Cook R. A., Crisp J. A., Economou T., Folkner W. M., Greely R., Haberle R. M., Hargraves R. B., Harris J. A., Haldemann A. F. C., Herkenhoff K. E., Hviid S. F., Jaumann R., Johnson J. R., Kалlemeyn P. H., Keller H. U., Kirk R. L., Knudsen J. M., Larsen S., Lemmon M. T., Madsen M. B., Magalhães J. A., Maki J. N., Malin M. C., Manning R. M., Matijevic J., McSween H. Y., Moore H. J., Murchie S. L., Murphy J. R., Parker T. J., Reider R., Rivellini T. P., Schofield J. T., Seiff A., Singer R. B., Smith P. H., Soderblom L. A., Spencer D. A., Stoker C. R., Sullivan R., Thomas N., Thurman S. W., Tomasko M. G., Vaughn R. M., Wänke H., Wilson G. R. (1999). Overview of the mars pathfinder mission : launch through landing, surface operations, data sheets, and science results. *Journal of Geophysical Research* 104(E4):8523-8553.
- Gómez-Elvira J., Armiens C., Castañer L., Domínguez M., Genzer M., Gómez F., Haberle R. M., Harri A. M., Jiménez V., Kahanpää H., Kowalski L., Lepinette A., Martín J., Martínez-Frías J., McEwan I., Mora L., Moreno J., Navarro S., de Pablo M. A., Peinado V., Peña A., Polkko J., Ramos M., Renno N. O., Ricart J., Richardson M., Rodríguez-Manfredi J., Romeral J., Sebastián E., Serrano J., de la Torre Juárez M., Torres J., Torrero F., Urquí R., Vázquez L., Velasco T., Verdasca J., Zorzano M. P., Martín-Torres J. (2012). REMS: the environmental sensor suite for the Mars Science Laboratory rover. *Space Science Reviews* 170(1):583-640.
- Gorevan S. P., Myrick T., Davis K., Chau J. J., Bartlett P., Mukherjee S., Anderson R., Squyres S. W., Arvidson R. E., Madsen M. B., Bertelsen P., Goetz W., Binau C. S., Richter L. (2003). Rock Abrasion Tool: Mars Exploration Rover Mission. *Journal of Geophysical Research* 108(E12):8068. DOI: 10.1029/2003JE002061.

- Gough D. O. (1981). Solar interior structure and luminosity variations. *Solar Physics* 74(1):21-34.
- Grady M. M., Wright I. P., Douglas C., Pillinger C. T. (1995). Carbonates in Martian Meteorites - A Reappraisal. *Meteoritics* 30(5):511.
- Greenberger R. N., Mustard J. F., Cloutis E. A., Pratt L. M., Sauer P. E., Mann P., Turner K., Dyar M. D., Bish D. L. (2015). Serpentinization, iron oxidation, and aqueous conditions in an ophiolite: Implications for hydrogen production and habitability on Mars. *Earth and Planetary Science Letters* 416:21-34.
- Grotzinger J. P., Crisp J., Vasavada A. R., Anderson R. C., Baker C. J., Barry R., Blake D. F., Conrad P., Edgett K. S., Ferdowski B., Gellert R., Gilbert J. B., Golombek M., Gómez-Elvira J., Hassler D. M., Jandura L., Litvak M., Mahaffy P., Maki J., Meyer M., Malin M. C., Mitrofanov I., Simmonds J. J., Vaniman D., Welch R. V., Wiens R. C. (2012). Mars Science Laboratory Mission and Science Investigation. *Space Science Reviews* 170(1):5-56.
- Grotzinger J. P. (2013). Analysis of Surface Materials by the Curiosity Mars Rover. *Science* 341(6153):1475.
- Gysi A. P., Stefansson A. (2012). Mineralogical aspects of CO₂ sequestration during hydrothermal basalt alteration - An experimental study at 75 to 250 °C and elevated pCO₂. *Chemical Geology* 306-307:146-159.
- Halevy I., Zuber M. T., Schrag D. P. (2007). A Sulfur Dioxide Climate Feedback on Early Mars. *Science* 318(5858):1903-1907.
- Halevy I., Fischer W. W., Eiler J. M. (2011). Carbonates in the Martian meteorite Allan Hills 84001 formed at 18 ± 4 °C in a near-surface aqueous environment. *Proceedings of the National Academy of Sciences* 108(41):16895-16899.
- Halevy I., Head J. W. (2014). Episodic warming of early Mars by punctuated volcanism. *Nature Geoscience* 7:865-868.
- Haug T. A., Munz I. A., Kleiv R. A. (2011). Importance of dissolution and precipitation kinetics for mineral carbonation. *Energy Procedia* 4:5029-5036.
- Hausrath E. M., Brantley S. L. (2010). Basalt and olivine dissolution under cold, salty, and acidic conditions: What can we learn about recent aqueous weathering on Mars? *Journal of Geophysical Research: Planets* 115(E12).
- Head J. W., Marchant D. R. (2014). The climate history of early Mars: insights from the Antarctic McMurdo Dry Valleys hydrologic system. *Antarctic Science* 26(6): 774-800.
- Hecht M. H., Kounaves S. P., Quinn R. C., West S. J., S. M. M. Young S. M. M., Ming D. W., Catling D. C., Clark B. C., Boynton W. V., Hoffman J., DeFlores L. P., Gospodinova K., Kapit J.,

- Smith P. H. (2009). Detection of Perchlorate and the Soluble Chemistry of Martian Soil at the Phoenix Lander Site. *Science* 325(5936):64-67.
- Herkenhoff K. E., Squyres S. W., Bell J. F., Maki J. N., Arneson H. M., Bertelsen P., Brown D. I., Collins S. A., Dingizian A., Elliott S. T., Goetz W., Hagerott E. C., Hayes A. G., Johnson M. J., Kirk R. L., McLennan S., Morris R. V., Scherr L. M., Schwochert M. A., Shiraishi L. R., Smith G. H., Soderblom L. A., Sohl-Dickstein J. N., Wadsworth M. V. (2003). Athena Microscopic Imager Investigation. *Journal of Geophysical Research* 108(E12):8065. DOI:10.1029/2003JE002076.
- Holland H. D. (1978). *The Chemistry of the Atmospheres and Oceans*. John Wiley, New York.
- Holland H. D., Turekian K. K. (2011). *Geochemistry of Earth Surface Features: From the Treatise on Geochemistry*. Academic Press. London: 235.
- Horne F. (2016). How are seashells created? Or any other shell, such as a snail's or a turtle's? *Scientific American*. Available: <https://www.scientificamerican.com/article/how-are-seashells-created/>
- Houghton J. T., Meira Filho L. G., Callander B. A., Harris N., Kattenberg A., Maskell K. (1995). Contribution of Working Group I to the Second Assessment Report of the Intergovernmental Panel on Climate Change. *IPCC, Climate Change 1995: The Science of Climate Change*. Cambridge: Cambridge University Press.
- Hu R., Kass D. M., Ehlmann B. L., Yung Y. L. (2015). Tracing the fate of carbon and the atmospheric evolution of Mars. *Nature Communications* 6:10003.
- IEAGHG. (2005). A review of natural CO₂ occurrences and releases and their relevance to CO₂ storage. *International Energy Agency Green House Gas Research and Development 2005/08*. Available: http://www.ieaghg.org/docs/General_Docs/Reports/2005-8.pdf
- Ilyina T., Zeebe R., Brewer P. (2006). Changed in underwater sound propagation caused by ocean acidification. *IOP Conference Series: Earth and Environmental Science* 6:462007.
- IPCC. (2007). *Fourth Assessment Report: Climate Change*. Available: https://www.ipcc.ch/publications_and_data/ar4/syr/en/mains3-3-1.html
- IPCC. (2013). *Climate Change 2013: The Physical Science Basis*. Available: <http://www.ipcc.ch/report/ar5/wg1/>.
- Irwin R. P., Tooth S., Craddock R. A., Howard A. D., Baptist de Latour A. (2014). Origin and development of theater-headed valleys in the Atacama Desert, northern Chile: Morphological analogs to martian valley networks. *Icarus* 243:296-310.

- Jakosky B. M., Pepin R. O., Johnson R. E., Fox J. L. (1994). Mars Atmospheric Loss and Isotopic Fractionation by Solar-Wind-Induced Sputtering and Photochemical Escape. *Icarus* 111(2):271-288.
- Johansson D. J. A., O'Neill B. C., Tebaldi C., Häggström O. (2015). Equilibrium climate sensitivity in light of observations over the warming hiatus. *Nature Climate Change* 5:449-453.
- Kasting J. F. (1991). CO₂ condensation and the climate of early Mars. *Icarus* 94:1-13.
- Kelemen P. B., Matter J. (2008). In situ carbonation of peridotite for CO₂ storage. *Proceedings of the National Academy of Sciences* 105(45):17295-17300.
- Kelemen P., Matter J., Streit E., Rudge J., Curry W., Blusztajn J. (2011). Rates and Mechanisms of Mineral Carbonation in Peridotite: Natural Processes and Recipes for Enhanced, in situ CO₂ Capture and Storage. *Annual Review Of Earth And Planetary Sciences* 39:545-576.
- Kelemen P. B., Hirth G. (2012). Reaction-driven cracking during retrograde metamorphism: Olivine hydration and carbonation. *Earth and Planetary Science Letters* 345-348:81-89.
- King P. L., McLennan S. M. (2010). Sulfur on Mars. *Elements* 6(2).
- Kite E. S., Gao P., Goldblatt C., Mischna M. A., Mayer D. P., Yung Y. L. (2017). Methane bursts as a trigger for intermittent lake-forming climates on post-Noachian Mars. *Nature Geoscience* 10:737-740.
- Klingelhöfer G., Morris R. V., Bernhardt B., Rodionov D., De Souza P. A., Squyres S. W., Foh J., Kankeleit E., Bonnes U., Gellert R., Schröder C., Linkin S., Evlanov E., Zubkov B., Prilutski O. (2003). Athena MIMOS II Mössbauer Spectrometer Investigation. *Journal of Geophysical Research* 108(E12):8067. DOI: 10.1029/2003JE002138.
- Krevor S. C. M., Lackner K. S. (2011). Enhancing serpentine dissolution kinetics for mineral carbon dioxide sequestration. *International Journal of Greenhouse Gas Control* 5(4):1073-1080.
- Kuznetz L. H., Gan D. C. (2002). On the existence and stability of liquid water on the surface of mars today. *Astrobiology* 2(2):183-95.
- Lafay R., Montes-Hernandez G., Janots E., Chiriac R., Findling N., Toche F. (2012). Mineral replacement rate of olivine by chrysotile and brucite under high alkaline conditions. *Journal of Crystal Growth* 347(1):62-72.
- Lang S. Q., Früh-Green G. L., Kelley D. S., Lilley M. D., Proskurowski G., Reeves E. P. (2012). H₂/CH₄ ratios cannot reliably distinguish abiotic vs. biotic methane in natural hydrothermal systems. *Proceedings of the National Academy of Sciences* 109(47):E3210.

- Lapen T., Righter M., Brandon A., Debaille V., Beard B., Shafer J., Peslier A. (2010). A Younger Age for ALH 84001 and Its Geochemical Link to Shergottite Sources in Mars. *Science* 328(5976):347-351.
- Larachi F., Gravel J. P., Grandjean B. P. A., Beaudoin G. (2012). Role of steam, hydrogen and pre-treatment in chrysotile gas-solid carbonation: opportunities for pre-combustion CO₂ capture. *International Journal of Greenhouse Gas Control* 6:69-76.
- Lasaga A. C. (1998). *Kinetic Theory in the Earth Sciences*. Princeton University Press, Princeton, NJ: 781.
- Lee M. R., Tomkinson T., Mark D. F., Smith C. L. (2016). Carbon sequestration on Mars. *Geology* 44(6):E388.
- Leshin L. A., McKeegan K. D., Carpenter P. K., Harvey R. P. (1998). Oxygen Isotopic Constraints on the Genesis of Carbonates from Martian Meteorite ALH84001. *Geochimica et Cosmochimica Acta* 62(1):3-13.
- Luce R. W., Bartlett R. W., Parks G. A. (1972). Dissolution kinetics of magnesium silicates. *Geochimica et Cosmochimica Acta* 36(1):35-50.
- Lundquist C. A. (2009). A sputnik IV saga. *Acta Astronautica* 65(11):1530-1536.
- Madsen M. B., Bertelsen P., Goetz W., Binau C. S., Olsen M., Folkmann F., Gunnlaugsson H. P., Kinch K. M., Knudsen J. M., Merrison J., Nørnberg P., Squyres S. W., Yen A. S., Rademacher J. D., Gorevan S., Myrick T., Bartlett P. (2003). Magnetic Properties Experiments on the Mars Exploration Rover mission. *Journal of Geophysical Research: Planets* 108(E12).
- Mahaffy P. R., Webster C. R., Cabane M., Conrad P. G., Coll P., Atreya S. K., Arvey R., Barciniak M., Benna M., Bleacher L., Brinckerhoff W. B., Eigenbrode J. L., Carignan D., Cascia M., Chalmers R. A., Dworkin J. P., Errigo T., Everson P., Franz H., Farley R., Feng S., Frazier G., Freissinet C., Glavin D. P., Harpold D. N., Hawk D., Holmes V., Johnson C. S., Jones A., Jordan P., Kellogg J., Lewis J., Lyness E., Malespin C. A., Martin D. K., Maurer J., McAdam A. C., McLennan D., Nolan T. J., Noriega M., Pavlov A. A., Prats B., Raaen E., Sheinman O., Sheppard D., Smith J., Stern J. C., Tan F., Trainer M., Ming D. W., Morris R. V., Jones J., Gundersen C., Steele A., Wray J., Botta O., Leshin L. A., Owen T., Battel S., Jakosky B. M., Manning H., Squyres S., Navarro-González R., McKay C. P., Raulin F., Sternberg R., Buch A., Sorensen P., Kline-Schoder R., Coscia D., Szopa C., Teinturier S., Baffes C., Feldman J., Flesch G., Forouhar S., Garcia R., Keymeulen D., Woodward S., Block B. P., Arnett K., Miller R., Edmonson C., Gorevan S., Mumm E. (2012). The Sample Analysis at Mars Investigation and Instrument Suite. *Space Science Reviews* 170(1):401-478.

- Maher K., Steefel C. I., White A. F., Stonestrom D. A. (2009). The Role of Reaction Affinity and Secondary Minerals in Regulating Chemical Weathering Rates at the Santa Cruz Soil Chronosequence, California. *Geochimica et Cosmochimica Acta* 73(10):2804-2831.
- Malvoisin B., Brunet F., Carlut J., Rouméjon S., Cannat M. (2012). Serpentinization of oceanic peridotites: 2. Kinetics and processes of San Carlos olivine hydrothermal alteration. *Journal of Geophysical Research: Solid Earth* 117:B4.
- Martínez G. M., Renno N. O. (2013). Water and Brines on Mars: Current Evidence and Implications for MSL. *Space Science Reviews* 175(1):29-51.
- Matter J. M., Broecker W. S., Stute M., Gislason S. R., Oelkers E. H., Stefánsson A., Wolff-Boenisch D., Gunnlaugsson E., Axelsson G., Björnsson G. (2009). Permanent carbon dioxide storage into basalt: The CarbFix pilot project, Iceland. *Energy Procedia* 1(1):3641-3646.
- Matter J. M., Keleman P. (2009). Permanent storage of carbon dioxide in geological reservoirs by mineral carbonation. *Nature Geoscience* 2:837-841.
- Maurice S., Wiens R. C., Saccoccio M., Barraclough B., Gasnault O., Forni O., Mangold N., Baratoux D., Bender S., Berger G., Bernardin J., Berthé M., Bridges N., Blaney D., Bouyé M., Caïs P., Clark B., Clegg S., Cousin A., Cremers D., Cros A., DeFlores L., Derycke C., Dingler B., Dromart G., Dubois B., Dupieux M., Durand E., d'Uston L., Fabre C., Faure B., Gaboriaud A., Gharsa T., Herkenhoff K., Kan E., Kirkland L., Kouach D., Lacour J. L., Langevin Y., Lasue J., Le Mouélic S., Lescure M., Lewin E., Limonadi D., Manhès G., Mauchien P., McKay C., Meslin P. Y., Michel Y., Miller E., Newsom H. E., Orttner G., Paillet A., Parès L., Parot Y., Pérez R., Pinet F., Poitrasson P., Quertier B., Sallé B., Sotin C., Sautter V., Séran H., Simmonds J. J., Sirven J. B., Stiglich R., Striebig N., Thocaven J. J., Toplis M. J., Vaniman D. (2012). The ChemCam Instrument Suite on the Mars Science Laboratory (MSL) Rover: Science Objectives and Mast Unit Description. *Space Science Reviews* 170(1):95-166.
- McCullom T. M. (2016). Abiotic methane formation during experimental serpentinization of olivine. *Proceedings of the National Academy of Sciences* 113(49):13965-13970.
- McElroy M. B., Yung Y. L., Nier A. O. (1976). Isotopic Composition of Nitrogen: Implications for the Past History of Mars' Atmosphere. *Science* 194(4260).
- McEwen A. S., Eliason E. M., Bergstrom J. W., Bridges N. T., Hansen C. J., Delamere W. A., Grant J. A., Gulick V. C., Herkenhoff K. E., Keszthelyi L., Kirk R. L., Mellon M. T., Squyres S. W., Thomas N., Weitz C. M. (2007). Mars Reconnaissance Orbiter's High Resolution Imaging Science Experiment (HiRISE). *Journal of Geophysical Research: Planets* 112(E5).
- McGrail B. P., Spang F. A., Sullivan E. C., Bacon D. H., Hund G. (2011). The Wallula basalt sequestration pilot project. *Energy Procedia* 4:5653-5660.

- McKay C. P., Andersen D. T., Pollard W. H., Heldmann J. L., Doran P. T., Fritsen C. H., Priscu J. C. (2005). Water on Mars and Life, Part III. Aqueous Environments and the Implications for Life, 9 Polar Lakes, Streams, and Springs as Analogs for the Hydrological Cycle on Mars. Volume 4 of the series *Advances in Astrobiology and Biogeophysics*. Springer 219-233.
- McSween H. Y., Taylor G. J., Wyatt M. B. (2009). Elemental Composition of the Martian Crust. *Science* 324(5928):736-739.
- Mitrofanov I. G., Litvak M. L., Varenikov A. B., Barmakov Y. N., Behar A., Bobrovniksky Y. I., Bogolubov E. P., Boynton W. V., Harshman K., Kan E., Kozyrev A. S., Kuzmin R. O., Malakhov A. V., Mokrousov M. I., Ponomareva S. N., Ryzhkov V. I., Sanin A. B., Smirnov G. A., Shvetsov V. N., Timoshenko G. N., Tomilina T. M., Tret'yakov V. I., Vostrukhin a. a. (2012). Dynamic Albedo of Neutrons (DAN) Experiment Onboard NASA's Mars Science Laboratory. *Space Science Reviews* 170(1):559-582.
- Mittlefehldt D. W. (1994). ALH84001, a cumulate orthopyroxenite member of the martian meteorite clan. *Meteoritics & Planetary Science* 29(2):214-221.
- Möhlmann D., Thomsen K. (2011). Properties of cryobrines on Mars. *Icarus* 212(1):123-130.
- Moore J. M., Bullock M. A. (1999). Experimental studies of Mars-analog brines. *Journal of Geophysical Research: Planets* 104(E9):21925-21934.
- Morel F. M. M., Hering J. G. (1993). *Principals and applications of aquatic chemistry*. John Wiley & Sons Inc. New York: 41.
- Morris R. V., Ruff S. W., Gellert R., Ming D. W., Arvidson R. E., Clark B. C., Golden D. C., Siebach K., Klingelhöfer G., Schröder C., Fleischer I., Yen A. S., Squyres S. W. (2010). Identification of Carbonate-Rich Outcrops on Mars by the Spirit Rover. *Science* 329(5990):421-424.
- Morse J. W., Arvidson R. S., Lüttge A. (2007). Calcium Carbonate Formation and Dissolution. *Chemical reviews* 107(2):342-381.
- Mukhin L. M., Koscheev A. P., Dikov Yu P., Huth J., Wanke H. (1996). Experimental simulations of the photodecomposition of carbonates and sulphates on Mars. *Nature* 379.6561:141-3.
- Murchie S., Arvidson R., Bedini P., Beisser K., Bibring J. P., Bishop J., Boldt J., Cavender P., Choo T., Clancy R. T., Darlington E. H., Des Marais D., Espiritu R., Fort D., Green R., Guinness E., Hayes J., Hash C., Heffernan K., Hemmler J., Heyler G., Humm D., Hutcheson J., Izenberg N., Lee R., Lees J., Lohr D., Malaret E., Martin T., McGovern J. A., McGuire P., Morris R., Mustard J., Pelkey S., Rhodes E., Robinson M., Roush T., Schaefer E., Seagrave G., Seelos F., Silverglate P., Slavney S., Smith M., Shyong W. J., Strohbahn K., Taylor H., Thompson P., Tossman B., Wirzburger M., Wolff M. (2007). Compact Reconnaissance Imaging Spectrometer for Mars (CRISM) on Mars Reconnaissance Orbiter (MRO). *Journal of Geophysical Research: Planets* 112(E5).

- Nachon M., Clegg S. M., Mangold N., Schröder S., Kah L. C., Dromart G., Ollila A., Johnson J. R., Oehler D. Z., Bridges J. C., Le Mouélic S., Forni O., Wiens R. C., Anderson R. B., Blaney D. L., Bell J. F., Clark B., Cousin A., Dyar M. D., Ehlmann B., Fabre C., Gasnault O., Grotzinger J., Lasue J., Lewin E., Léveillé R., McLennan S., Maurice S., Meslin P. Y., Rapin W., Rice M., Squyres S. W., Stack K., Sumner D. Y., Vaniman D., Wellington D. (2014). Calcium sulfate veins characterized by ChemCam/Curiosity at Gale crater, Mars. *Journal of Geophysical Research: Planets* 119(9):1991-2016.
- Naish T., Powell R., Levy R., Wilson G., Scherer R., Talarico F., Krissek L., Niessen F., Pompilio M., Wilson T., Carter L., DeConto R., Huybers P., McKay R., Pollard D., Ross J., Winter D., Barrett P., Browne G., Cody R., Cowan E., Crampton J., Dunbar G., Dunbar N., Florindo F., Gebhardt C., Graham I., Hannah M., Hansaraj D., Harwood D., Helling D., Henrys S., Hinnov L., Kuhn G., Kyle P., Läufer A., Maffioli P., Magens D., Mandernack K., McIntosh W., Millan C., Morin R., Ohneiser C., Paulsen T., Persico D., Raine I., Reed J., Riesselman C., Sagnotti L., Schmitt D., Sjunneskog C., Strong P., Taviani M., Vogel S., Wilch T., Williams T. (2009). Obliquity-paced Pliocene West Antarctic ice sheet oscillations. *Nature* 458:322-328.
- NASA (1969). Mariner Mars 1969 Launches - NASA-NEWS-RELEASE-69-26.
- NASA. (1976). Mars as viewed by Mariner 9 : a pictorial presentation by the Mariner 9 television team and the planetology program principal investigators. *Washington: Scientific and Technical Information Office, National Aeronautics and Space Administration* SP:329.
- NASA. (2016)a. A Chronology of Mars Exploration. Available: <http://history.nasa.gov/marschro.htm>
- NASA. (2016)b. Mariner 7. Available: <http://nssdc.gsfc.nasa.gov/nmc/spacecraftDisplay.do?id=1969-030A>
- National Oceanic and Atmospheric Administration (NOAA). (2014). *Trends in Atmospheric Carbon Dioxide*. Available: <http://www.esrl.noaa.gov/gmd/ccgg/trends/history.html>
- Neuhoff P. S., Fridriksson T., Arnorsson S., Bird D. K. (1999). Porosity evolution and mineral paragenesis of basaltic lavas at Teigarhorn, Eastern Iceland. *American Journal of Science* 299:467-501.
- Oelkers E. H., Gislason S. R., Matter J. (2008). Mineral Carbonation of CO₂. *Elements* 4(5).
- Oelkers E. H., Declercq J. (2014). *CarbFix Report 4 PHREEQC mineral dissolution kinetics database*. Available: https://www.or.is/sites/or.is/files/kinetic_database.pdf
- O’Gorman P. A. (2010). Understanding the varied response of the extra tropical storm tracks to climate change. *Proceedings of the National Academy of Sciences of the United States of America (PNAS)* 107(45):19176-19180.

- Oreskes N. (2004). Beyond the ivory tower: The scientific consensus on climate change. *Science* 306(5702):1686.
- Oze C., Sharma M. (2005). Have olivine, will gas: Serpentinization and the abiogenic production of methane on Mars. *Geophysical Research Letters: Planets* 32(10).
- Oze C., Jones L. C., Goldsmith J. I., Rosenbauer R. J. (2012). Differentiating biotic from abiotic methane genesis in hydrothermally active planetary surfaces. *Proceedings of the National Academy of Sciences* 109(25):9750-9754.
- Park A. A., Jadhav R., Fan L. S. (2003). CO₂ Mineral Sequestration: Chemically Enhanced Aqueous Carbonation of Serpentine. *The Canadian Journal of Chemical Engineering* 81:885-890.
- Parmesan C. (2006). Ecological and evolutionary responses to recent climate change. *Annual Review of Ecology: Evolution and Systematics* 37:637-669.
- Pentecost A. (1995). The quaternary travertine deposits of Europe and Asia Minor. *Quaternary Science Reviews* 14(10):1005-1028.
- Phillips R. J., Davis B. J., Tanaka K. L., Byrne S., Mellon M. T., Putzig N. E., Haberle R. M., Kahre M. A., Campbell B. A., Carter L. M., Smith I. B., Holt J. W., Smrekar S. E., Nunes D. C., Plaut J. J., Egan A. F., Titus T. N., Seu R. (2011). Massive CO₂ Ice Deposits Sequestered in the South Polar Layered Deposits of Mars. *Science* 332(6031).
- Pimentel G. C., Forney P. B., Herr K. C. (1974). Evidence about hydrate and solid water in the Martian surface from the 1969 Mariner Infrared Spectrometer. *Journal of Geophysical Research* 79(11): 1623-1634.
- Pollack J. B., Kasting J. F. (1987). The case for a wet, warm climate on early Mars. *Icarus* 71(2):203-224.
- Preston L. J., Dartnell L. R. (2014). Planetary habitability: lessons learned from terrestrial analogues. *International Journal of Astrobiology* 13(1):81-98.
- Quafoku O., Hu J., Hess N. J., Hu M. Y., Ilton E. S., Feng J., Arey B. W., Felmy A. R. (2014). Formation of submicron magnesite during reaction of natural forsterite in H₂O saturated supercritical CO₂. *Geochimica et Cosmochimica Acta* 134:197-209.
- Renforth P., Pogge von Strandmann P. A. E., Henderson G. M. (2015). The dissolution of olivine added to soil: Implications for enhanced weathering. *Applied Geochemistry* 61:109-118.
- Rieder R., Gellert R., Brückner J., Klingelhöfer G., Dreibus G., Yen A., Squyres S. W. (2003). The New Athena Alpha Particle X-ray Spectrometer for the Mars Exploration Rovers. *Journal of Geophysical Research* 108(E12):8066. DOI: 10.1029/2003JE002150.

- Rogers K. L., Neuhoﬀ P. S., Pedersen A. K., Bird D. K. (2006). CO₂ metasomatism in a basalt-hosted petroleum reservoir, Nuussuaq, West Greenland. *Lithos* 92(1-2):55-82.
- Russell C. T. (1978). The magnetic field of Mars: Mars 3 evidence re-examined. *Geophysical Research Letters* 5(1):81-84.
- Russell M. J., Hall A. J., Martin W. (2010). Serpentinization as a source of energy at the origin of life. *Geobiology* 8(5):355-371.
- Rutqvist J. (2012). The geomechanics of CO₂ storage in deep sedimentary formations. *Geotechnical and Geological Engineering* 30(3):525-551.
- Samanta A., Zhao A., Shimizu G. K. H., Sarkar P., Gupta R. (2012). Post-combustion CO₂ capture using solid sorbents: a review. *Industrial & Engineering Chemistry Research* 51:1438-1463.
- Saunders R. S., Arvidson R. E., Badhwar G. D., Boynton W. V., Christensen P. R., Cucinotta F. A., Feldman W. C., Gibbs R. G., Kloss C., Landano M. R., Mase R. A., McSmith G. W., Meyer M. A., Mitrofanov I. G., Pace G. D., Plaut J. J., Sidney W. P., Spencer D. A., Thompson T. W., Zeitlin C. J. (2001). *2001 Mars Odyssey Mission Summary*. Springer Netherlands 1-36 ISBN 978-94-015-6958-3.
- Schaeﬀ H. T., Horner J. A., Owen A. T., Thompson C. J., Loring J. S., McGrail B. P. (2014). Mineralization of Basalts in the CO₂-H₂O-SO₂-O₂ System. *Environmental Science & Technology Letters* 48(9):5298-5305.
- Schneider B., Schneider R. (2010). Palaeoclimate: Global warmth with little extra CO₂. *Nature Geoscience* 3:6-7.
- Scholes C. A., Ho M. T., Wiley D. E., Stevens G. W., Kentish S. E. (2013). Cost competitive membrane-cryogenic post-combustion carbon capture. *International Journal of Greenhouse Gas Control* 17:341-348.
- Schuiling R. D., Krijgsman P. (2006). Enhanced Weathering: An Effective and Cheap Tool to Sequester CO₂. *Climate Change* 74(1):349-354.
- Schwensler S. P., Bridges J. C., Miller M. A., Hicks L. J., Ott U., Filiberto J., Chavez C., Smith H., Treiman A. H., Kelley S. P., Moore J. M., Swindle T. D., Bullock M. A. (2017). Diagenesis on Mars: insights into noble gas pathways and newly formed mineral assemblages from long term experiments. *48th Lunar and Planetary Science Conference XLVIII* 1344.
- Sears D. W.G., Chittenden J. D. (2005). On laboratory simulation and the temperature dependence of the evaporation rate of brine on Mars. *Geophysical Research Letters: Planets* 32(23).
- Sears D. W. G., Moore S. R. (2005). On laboratory simulation and the evaporation rate of water on Mars. *Geophysical Research Letters* 32(16).

- Shao H., Ray J. R., Jun Y. (2010). Dissolution and precipitation of clay minerals under geologic CO₂ sequestration conditions: CO₂-brine-phlogopite interactions. *Environmental Science and Technology* 44(15):5999-6005.
- Simonović S. P. (2012). *Floods in a Changing Climate*. Cambridge: Cambridge University Press.
- Sissmann O., Brunet F., Martinez I., Guyot F., Verlaguet A., Piquier Y., Daval D. (2014). Enhanced Olivine Carbonation within a Basalt as Compared to Single-Phase Experiments: Reevaluating the Potential of CO₂ Mineral Sequestration. *Environmental Science and Technology Letters* 48(10):5512-5519.
- Squyres S. W. (2005). *Roving Mars: Spirit, Opportunity and the exploration of the red planet*. New York: Hyperion.
- Slavin J. A. (1991). The solar wind interaction with Mars: Mariner 4, Mars 2, Mars 3, Mars 5, and Phobos 2 observations of bow shock position and shape. *Journal of Geophysical Research* 96.
- Soffen G. A. (1976). Scientific Results of the Viking Missions. *Science* 194(4271):1274-1276.
- Soldati A. L., Jacob D. E., Glatzel P., Swarbrick J. C., Geck J. (2016). Element substitution by living organisms: the case of manganese in mollusc shell aragonite. *Nature Scientific Reports* 6: 22514 DOI: 10.1038/srep22514
- Stuurman C. M., Osinski G. R., Holt J. W., Levy J. S., Brothers T. C., Kerrigan M., Campbell B. A. (2016). SHARAD detection and characterization of subsurface water ice deposits in Utopia Planitia, Mars. *Geophysical Research Letters* 43(18):9484-9491.
- Suen C. J., Frey F. A. (1979). Bay of Islands ophiolite suite, Newfoundland: Petrologic and geochemical characteristics with emphasis on rare earth element geochemistry. *Earth and Planetary Science Letters* 45(2):337-348.
- Sugawara H., Sakakibara M., Ikehara M. (2014). Recrystallized microbial trace fossils from metamorphosed Permian basalt, southwestern Japan. *Planetary and Space Science* 95:79-83.
- Swindle T., Olson E. (2004). Ar-40-Ar-39 studies of whole rock nakhlites: Evidence for the timing of formation and aqueous alteration on Mars. *Meteoritics & Planetary Science* 39(5):755-766.
- Szponar N., Brazelton W. J., Schrenk M. O., Bower D. M., Steele A., Morrill P. L. (2013). Geochemistry of a continental site of serpentinization, the Tablelands Ophiolite, Gros Morne National Park: A Mars analogue. *Icarus* 224(2):286-296.
- The Geochemist's Workbench. (2017). *The Geochemist's Workbench*. Available: <https://www.gwb.com/>

- The Governor's Office of Planning and Research (2011). *List of Worldwide Scientific Organizations*. Available: https://www.opr.ca.gov/s_listoforganizations.php
- Tomkinson T., Lee M. R., Mark D. F., Smith C. L. (2013). Sequestration of Martian CO₂ by mineral carbonation. *Nature Communications* 4:2662.
- Tosca N. J., McLennan S. M., Lindsley D. H., Schoonen M. A. A. (2004). Acid-sulfate weathering of synthetic Martian basalt: The acid fog model revisited. *Journal of Geophysical Research: Planets* 109(E5).
- Treiman A. H., Barrett R. A., Gooding J. L. (1993). Preterrestrial aqueous alteration of the Lafayette (SNC) meteorite. *Meteoritics & Planetary Science* 28(1):86-97.
- United Nations Framework Convention on Climate Change. (2014, A). *Status of Ratification of the Convention*. Available: http://unfccc.int/essential_background/convention/status_of_ratification/items/2631.php
- United Nations Framework Convention on Climate Change. (2014, B). *Kyoto Protocol*. Available: http://unfccc.int/kyoto_protocol/items/2830.php
- USGS. (2017). *PHREEQC (Version 3) A Computer Program for Speciation, Batch-Reaction, One-Dimensional Transport, and Inverse Geochemical Calculations*. Available: https://wwwbrr.cr.usgs.gov/projects/GWC_coupled/phreeqc/
- Verstraete M. M., Brink A. B., Scholes R. J., Beniston M., Smith M. S. (2008). Climate change and desertification: Where do we stand, where should we go? *Global and Planetary Change* 64(3-4):105-110.
- Vicenzi E. P., Eiler J. (1998). Oxygen-isotopic composition and high-resolution secondary ion mass spectrometry imaging of Martian carbonate in Lafayette meteorite. *Meteoritics & Planetary Science* 33(S4):A159-A160.
- Walker J. C. G., Hays P. B., Kasting J. F. (1981). A negative feedback mechanism for the long-term stabilization of Earth's surface temperature. *Journal of Geophysical Research: Oceans* 86(C10):9776-9782.
- Wang M., Lawal A., Stephenson P., Sidders J., Ranshaw C. (2011). Post-combustion CO₂ capture with chemical absorption: a state of the art review. *Chemical Engineering Research and Design* 89(9):1609-1624.
- Wasson J. T. (1964). Radioactivity in Sputnik 4 fragment. *Journal of Geophysical Research* 69(11):2223-2230.
- Website 1. (2014). ESA/DLR/FU Berlin. *Osuga Valles Topography*. Available: http://www.esa.int/spaceinimages/Images/2014/04/Osuga_Valles_topography

- Wells R. K., Xiong W., Giammar D., Skemer P. (2017). Dissolution and surface roughening of Columbia River flood basalt at geologic carbon sequestration conditions. *Chemical Geology* 467:100-109.
- White A. F., Brantley S. L. (2003). The effect of time on the weathering of silicate minerals: why do weathering rates differ in the laboratory and field? *Chemical Geology* 202(3-4):479-506.
- Wilson E. K. (2015). *Worldwide Hunt For Missing Carbon Minerals Begins*. Available: <http://cen.acs.org/articles/93/web/2015/12/Worldwide-Hunt-Missing-Carbon-Minerals.html?type=paidArticleContent>
- Withers P., Weiner S., Ferreri N. (2015). Recovery and validation of Mars ionospheric electron density profiles from Mariner 9. *Earth, Planets and Space* 67(1):1-12.
- Wong M. H., Atreya S. K., Mahaffy P. N., Franz H. B., Malespin C., Trainer M. G., Stern J. C., Conrad P. G., Manning H. L. K., Pepin R. O., Becker R. H., McKay C. P., Owen T. C., Navarro-González R., Jones J. H., Jakosky B. M., Steele A. (2013). Isotopes of nitrogen on Mars: Atmospheric measurements by Curiosity's mass spectrometer. *Geophysical Research Letters* 40(23):6033-6037.
- Wordsworth R., Kalugina Y., Lokshantov S., Vigasin A., Ehlmann B., Head J., Sanders C., Wang H. (2017). Transient reducing greenhouse warming on early Mars. *Geophysical Research Letters* 44(2):665-671.
- Xu T., Apps J. A., Pruess K. (2004). Numerical simulation of CO₂ disposal by mineral trapping in deep aquifers. *Applied Geochemistry* 19(6):917-936.
- Yung Y. L., Nair H., Gerstell M. F. (1997). CO₂ Greenhouse in the Early Martian Atmosphere: SO₂ Inhibits Condensation. *Icarus* 130(1):222-224.

Chapter 2

The effects of ultrasonics on Mars rover rock abrasion tool performance.

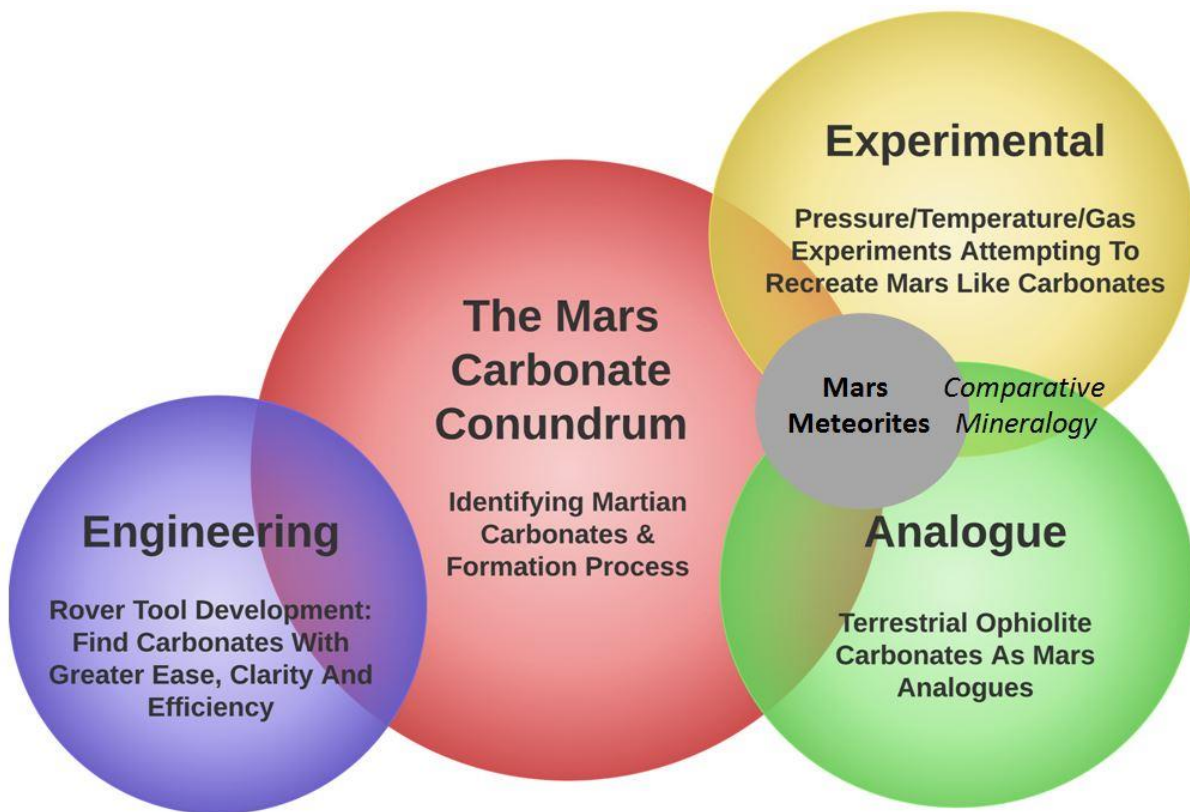


Figure 2.1. The carbonate conundrum that this PhD thesis seeks to address (red circle), along with the different spheres of research used to approach this question. These spheres of research correspond to the three main thesis chapters: engineering (chapter 2), analogues (chapter 3), and experimental (chapter 4). Overlapping circles indicate where chapter and research content overlap and support each other, allowing for comparative mineralogy.

Chapter 2 contents.

	Page
2.1 Key points.	75
2.2 Abstract.	76
2.3 Abbreviations.	77 - 78
2.4 Introduction.	79 - 112
2.4.1 What is ultrasonic?	82 - 92
2.4.2 The Mars rover rock abrasion tool (RAT).	93 - 97
2.4.3 Developing a diamond resin.	97 - 100
2.4.4 The mock RAT.	100 - 102
2.4.5 Developing the Micro Optic UltraSonic Exfoliator (MOUSE).	103 - 111
2.4.6 Experiment aim.	112
2.5 Methods.	113 - 121
2.5.1 The ultrasonic rig.	113
2.5.2 Rock types.	113 - 115
2.5.3 Weight on bit.	116
2.5.4 Wave amplitude.	116
2.5.5 Experiment design.	117
2.5.6 Time.	118
2.5.7 Surface roughness.	118 - 121
2.6 Results.	122 - 139
2.6.1 Surface roughness.	122 - 129
2.6.2 Power consumption.	129 - 132
2.6.3 Thrust force.	133 - 136
2.6.4 Material removal rate.	136 - 138
2.6.5 Error.	138 - 139
2.7 Discussion.	140 - 148
2.7.1 Surface roughness.	140 - 143
2.7.2 Power consumption.	144 - 146
2.7.3 Thrust force.	147 - 148
2.7.4 Material removal rate.	148
2.8 Conclusions.	149 - 150
2.9 Acknowledgements.	150
2.10 References.	151 - 155

2.1 Key points.

1. **Surface roughness.** Ultrasonic grinding can enhance rock surface smoothness compared to current Mars rover common grinding rotary techniques. Smoother surfaces permit clearer image data, making geological analysis easier, and ultimately increasing science return per mission.
2. **Power consumption.** Surface smoothness results differed little between using 2.1 μm or 4.0 μm wavelength. However, power consumption is considerably higher at 4.0 μm . Increased weight on bit made no significant difference to surface smoothness but did consume more power. Less power consumption on grinding operations allow a rover to operate over a wider range of conditions, and for a longer time period.
3. **Tool tip wear rate.** On current Mars rover grinding operations diamond resin wears down relatively quickly. A hard-wearing tungsten carbide tool tip possessing virtually negligible wear is a suitable and better performing alternative when using ultrasonic vibrations. This research contrasts diamond resin and tungsten carbide tips under a variety of variables.
4. **Material removal rate.** Reducing grinding time on the Mars rovers would allow greater time for travel, or other instrument deployments, increasing data yield per mission. The use of ultrasonic assisted grinding could potentially penetrate rock at a faster rate than the common rotary grinding techniques that the Mars rovers currently employ, although this was not sufficiently demonstrated in this study's experimental time scales.

2.2 Abstract.

The Mars exploration Athena science goal is to explore areas where water may have been present, and investigate the palaeo-environmental conditions of these areas in relation to the existence of life. The Rock Abrasion Tool (RAT) is one of four key Athena instruments mounted on the Spirit, Opportunity and Curiosity Mars Exploration Rovers. Exposed rock surfaces weather and chemically alter over time. If the geological history of a landing site is to be constructed, then it is important to analyse the unweathered rock interior as clearly as possible. The role of the rock abrasion tool is to substitute for a geology hammer, removing the weathered and chemically altered outer surface of rocks to view the pristine interior. The RAT uses a diamond resin common grinding technique, producing a 5 mm depth grind with a relatively high surface roughness, achieved over several hours per grind and consuming approximately 11 Watts. This study investigates the benefits of replacing the common grinding techniques currently employed on the RAT with ultrasonic assisted grinding, to make smoother surfaces. The research explores using both ultrasonically excited diamond resin tips and hard wearing tungsten carbide tips. A prototype Micro-Optic UltraSonic Exfoliator (MOUSE) is tested on a range of rock types and demonstrates many advantages over common grinding. These advantages include a smoother grind finish, a lower rate of tool tip wear when using tungsten carbide and fewer moving parts. The study also demonstrates that higher weight on bit load and/or higher ultrasonic wavelengths do not correlate with enhanced surface smoothness when using ultrasonics; therefore low ultrasonic wave lengths, low power and low weight on bit loads can produce very smooth rock grinds. Faster penetration rates can potentially be achieved using ultrasonic grinding; however, this would require further investigation to demonstrate clearly.

2.3 Abbreviations

APXS	Alpha particle X-ray spectrometer
CG	Common grinding
CMIF	Complex modal indicator function
ED	Eigenvalue decomposition
EMA	Exploratory modal analysis
FEA	Finite element analysis
FFT	Fast Fourier transform
FOS	Full scale output
<i>f_{res}</i>	Resonant frequency
FRF	Frequency response function
IDD	Instrument deployment device
ITAR	International traffic in arms regulations
MER	Mars exploration rover
MAHLI	<i>Mars hand lens imager</i>
MI	Microscopic imager
MOUSE	Micro optic ultrasonic exfoliator
MRR	Material removal rate
PVD	Plasma vapour deposition
Ra	Roughness average
RAT	Rock abrasion tool
RPM	Revolutions per minute
RUG	Rotary ultrasonic grinding
RUM	Rotary ultrasonic machining
Rz	Roughness root mean square
SGE	Specific grinding energy
SR	Surface roughness
SVD	Singular value decomposition
TWR	Tool wear rate
UVC	Ultrasonic vibration cutting
UAD	Ultrasonic assisted drilling

UAG	Ultrasonic assisted grinding
UAM	Ultrasonic assisted machining
VAM	Vibration assisted machining
WOB	Weight on bit

2.4 Introduction

When operating in the field, one of the most essential tools at the geologist's disposal is the rock hammer. It is by breaking a rock open and exposing the fresh surface beneath the dusty, oxidised and weathered exterior, that fundamental rock and mineral identification occurs. Usually a geologist would break open many rocks around a location, slowly building up a picture of the local geology. For a human geologist on Earth, breaking rocks with a hammer is a relatively simple, yet essential, science task. On Mars, there is no human presence; therefore exposing fresh rock surfaces for geological analysis requires a great deal of technological design and mission time. The more efficient the process of remotely exposing fresh rock surfaces on other planets can become, the greater the science return will be from each mission. This study demonstrates some of the potential advantages of utilising ultrasonics onboard Mars rovers, testing the addition of ultrasonics on both a traditional diamond resin tool tip and on a solid tungsten carbide tool tip. The results may enhance current rock exposure technology.

The principal tool used to expose fresh rock surfaces on the Mars exploration rovers (MER) has been a small mechanical grinder called the rock abrasion tool, affectionately known as the RAT (Fig. 2.2). This instrument, designed for the Athena payload of 2003 by Honeybee Robotics, can grind a 45 mm wide hole to a depth of 5 mm into a hard rock surface, with an average grind time of two hours for 5 mm of basalt rock penetration (Squyres *et al.* 2003). Once fresh rock is exposed by the RAT then other instruments mounted on the arm of the instrument deployment device (IDD), such as the Mössbauer spectrometer (Klingelhöfer *et al.* 2003), microscopic imager (MI) or *Mars Hand Lens Imager (MAHLI)* (Herkenhoff *et al.* 2003) and Alpha Particle X-ray Spectrometer (APXS) (Rieder *et al.* 2003), can begin analysing the less weathered interior, thereby adding information to local geological history and planetary development processes.

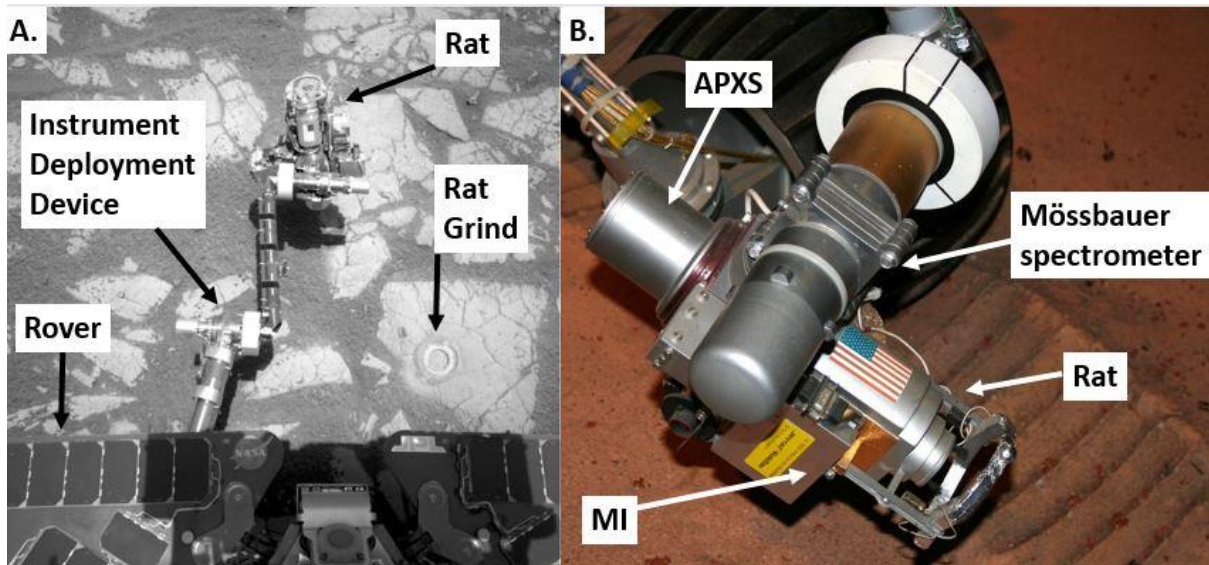


Figure 2.2. The rock abrasion tool (RAT). Built by Honeybee Robotics Ltd. **A.** The RAT is mounted on an instrument deployment device (IDD) arm. **B.** The RAT operates in conjunction with a microscopic image (MI), an Alpha Particle X-ray Spectrometer (APXS) and a Mössbauer spectrometer. *Credit: A. Website 1. B. Website 2.*

The RAT also provides an approximation of rock physical properties (density, hardness etc.) by comparing the machine engineering data during grinding operations on Mars (current, torque, penetration rate, temperature and encoder readouts) with those in a terrestrial ‘standards’ database tailored to the RAT (Bartlett *et al.* 2005; Thomson *et al.* 2013; Thomson *et al.* 2014). Any rock mechanical failures (such as faults and fractures) are useful as they provide information on the target rock’s mass strength, aiding rock type identification (Hoek & Brown, 1997). One key measurement used is ‘Specific Grind Energy’ (SGE), which is the energy consumed per cubic mm of rock removed, expressed as J/mm^3 (Thomson *et al.* 2013, Thomson *et al.* 2014). SGE on the RAT is calculated via MI images of RAT rate of progress in the final 0.25 mm of a designated grind, and the observed value extrapolated. A terrestrial standards rock database provides ideal SGE for the RAT to compare against for each rock type encountered, thus allowing the rock type to be inferred (Bartlett *et al.* 2005). Environmental factors, such as accounting for the Mars gravity, are included within these SGE calculations.

Because the MI is one of the key instruments of the IDD, the smoother a target rock surface can be polished during the grinding procedure, the clearer the MI images of petrologic features such as weathering veins, grain size and inclusions will be; as well as allowing a greater degree of accuracy in the SGE calculations. Weathered rock veins can provide important clues about the role rock weathering and mineral carbon sequestration played in the loss of a hypothesised early Mars atmosphere. Further, if these veins are hydrothermal in nature, they may provide evidence for assessing past habitability and life on Mars. Such improved imagery would greatly add value to the science return of any mission. In its current state, the RAT is effective at penetration, but does not produce particularly smooth surface finishes (Fig. 2.3).

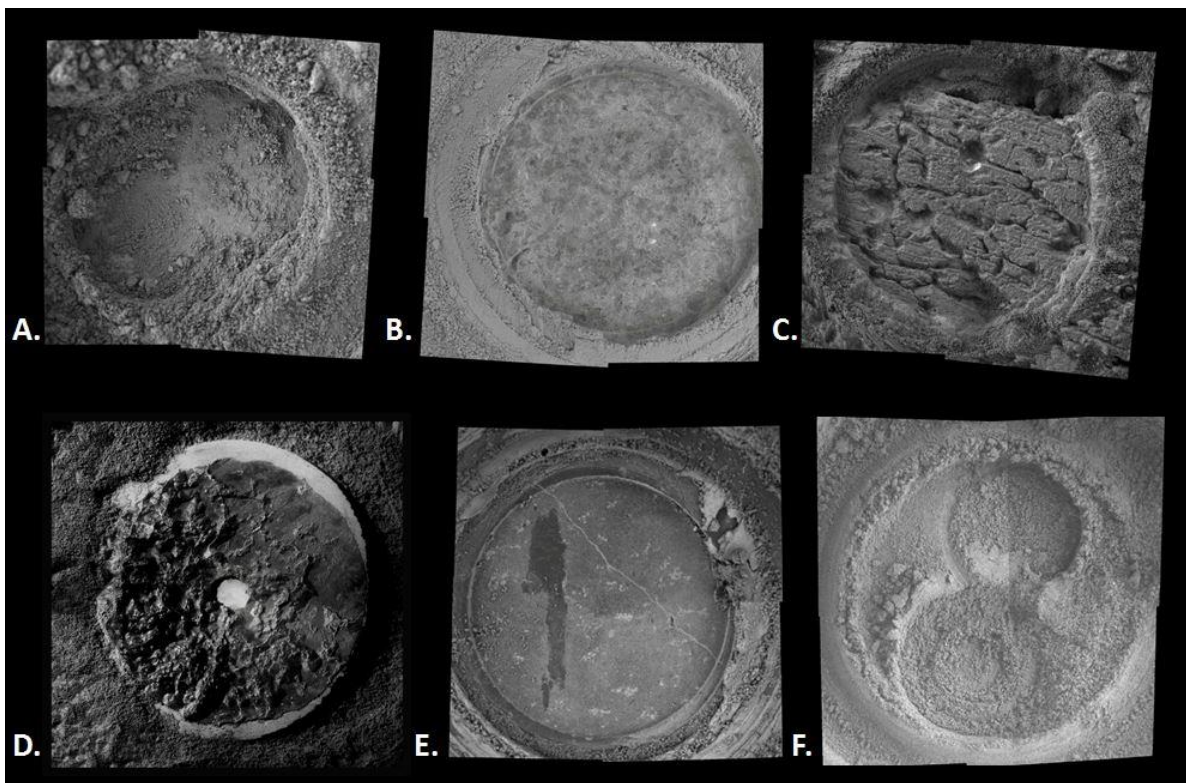


Figure 2.3. 45 mm diameter RAT grinds acquired via the microscopic imager. **A.** 8.9 mm deep grind into “Clovis” rock by the Spirit rover. **B.** Grind into “Champagne” rock by the Spirit rover. **C.** Grind into “Manitoba” rock by the Opportunity rover. **D.** Grind into “Grasburg” rock by the Opportunity rover. **E.** A relatively smooth grind showing rock vein structure on sol 85 of the Spirit rover

mission. **F.** Grind into “Progress” rock by Spirit rover. The resin has entirely worn away by this point (sol 830), leaving only brush and metal stub rotation. *Credit: NASA A. Website 3. B. Website 4. C. Website 5. D. Website 6. E. Website 7. F. Website 8.*

This research investigates how the introduction of ultrasonic vibrations into grinding processes affects the end result, primarily with respect to an improved surface smoothness (lower roughness), but also observing power consumption, optimum weight on bit, force dynamics, tool tip wear and rate of advancement into the rock. These variables will be tested on three different rock types, intended to encompass the range of rock strengths and mineral properties that a rover might encounter on Mars.

2.4.1 What is ultrasonic?

Ultrasonics is the application of ultrasound waves, which act as a time varying vibratory force upon a target. This vibratory force is often called acoustics. Ultrasound waves are simply regular sound waves but with a higher (ultra) frequency (Fig. 2.4). Ultrasonics has a wide and ever growing number of applications, from ultrasound imaging and sonography in hospitals (Eyding *et al.* 2002), to cleaning objects by disintegrating dirt (Spier, 1961), to communication and military applications (Vig, 1993). Specifically, within the field of grinding and polishing there exists a plethora of terminology (often overlapping), and application, which will be reviewed briefly.

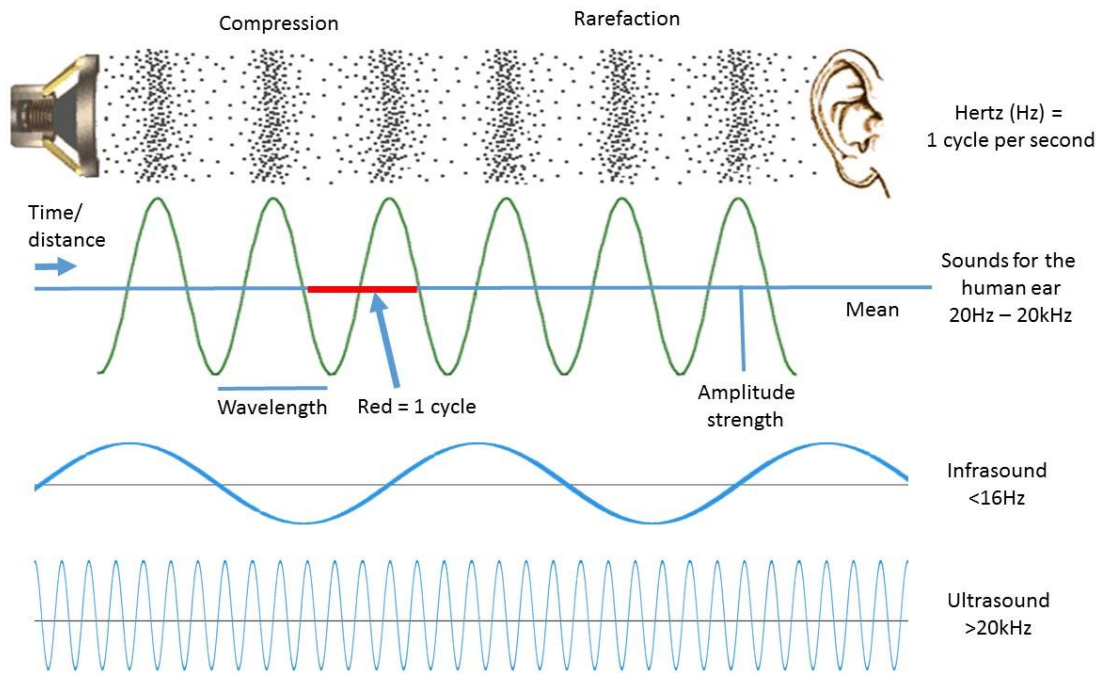


Figure 2.4. Components of sound waves and the value boundaries between wave types.

Frequency (Hz) can be defined as the number of cycles per unit of time. Amplitude (m) can be defined as half the oscillation amplitude (from zero, or oscillation mean, to wave peak). Wave length (λ or lambda, SI unit m) can be defined as the distance between two equal states in a wavelength. λ is a function of velocity (m/s) and frequency (equation 2.1), where c is velocity and f is frequency. For f to be ultrasonic (>20 kHz) velocity must be high, or the wavelength small, or both (equation 2.2).

$$\lambda = c/f$$

Equation 2.1

$$f = c/\lambda$$

Equation 2.2

The atoms that comprise solids can be made to vibrate in a variety of motions, directions and patterns. These atomic kinetics are sometimes referred to as excitation modes. Assuming the stress and tension of the vibratory force does not exceed the brittle deformation limit of the material excited, and then the material will oscillate at the atomic and particle level. The applied mechanical force will displace the particle from its resting equilibrium state and restoration forces return it in a cyclical motion. In a larger scale of wave propagation, earthquake waves pass through solids in several different ways, or modes. The principal wave mode types in a solid are:

- Longitudinal waves (P waves) which oscillate parallel to the direction of motion.
- Transverse waves (shear or S waves) which oscillate perpendicular to the direction of motion.
- Surface waves (Rayleigh waves) that possess an elliptical and symmetrical motion.
- Lamb waves (symmetric and asymmetric) and Love (sideways Rayleigh) plate waves.
- Stoneley or Scholte (leaky Rayleigh waves).
- Sezawa antisymmetric waves (Website 9).

Longitudinal (P), transverse (S), Rayleigh and Love waves are the most commonly used in ultrasonics (Fig. 2.5). The developed rig presented here utilises a longitudinal wave mode.

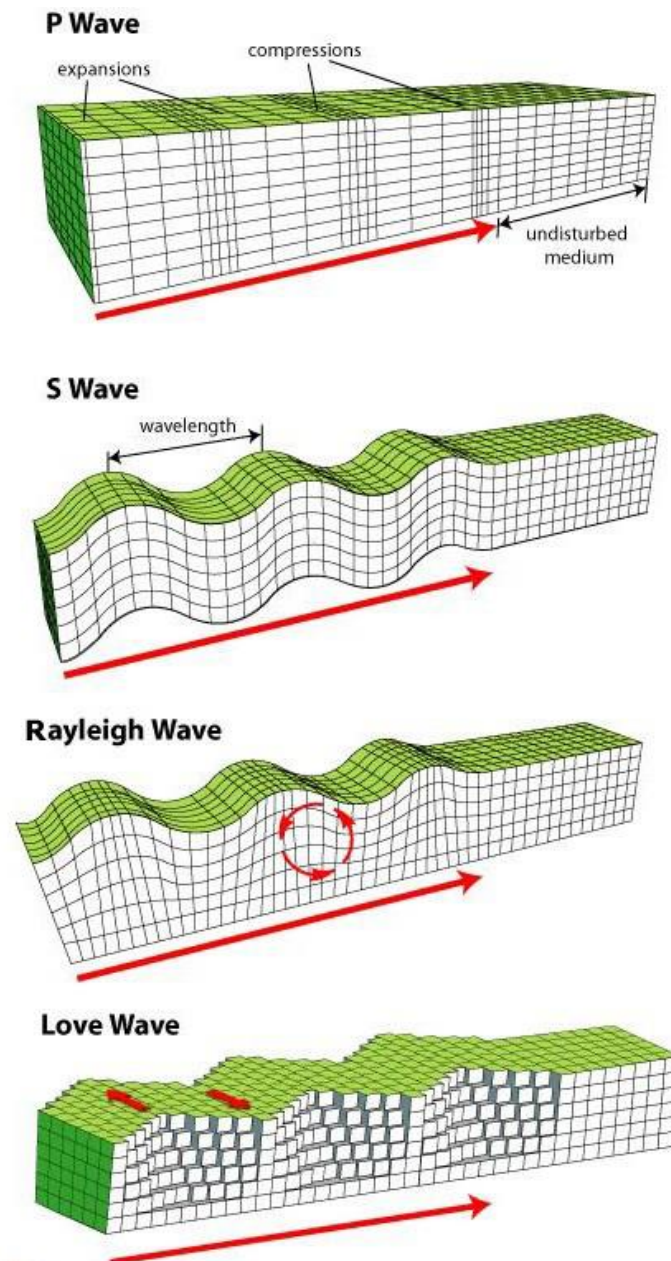


Figure 2.5. Principal wave modes in a solid medium. *Credit: Website 10.*

Vibration assisted machining (VAM)/ultrasonic assisted machining (UAM) (Xu & Zhang, 2015) is a technique harnessing ultrasonic kinetics and can be applied to ultrasonic assisted drilling (UAD) (Li, 2014), ultrasonic assisted grinding (UAG) (Chen *et al.* 2013; Wang *et al.* 2014) and ultrasonic vibration cutting (UVC) (Li *et al.* 2013). Both one-dimensional (linear) and two-dimensional (orbital) tool paths are possible using these machining techniques. Of considerable interest to Mars rover tool grinding research, is that by reducing force during the VAM process, a

Page | 83

smoother surface finish and reduced tool tip wear is possible (Brehl & Dow, 2008). The subdivision of VAM that this research is concerned with is UAG, in which an abrasive composite, usually diamond resin, rotates upon a target material. The individual diamonds, when embedded in a composite resin, are ultrasonically oscillating in a more complex lateral pattern compared with non-ultrasonic techniques (common grinding), and this complex ultrasonic pattern means the diamonds travel a greater distance and cover a greater surface area than with common grinding (Fig. 2.6). This greater area coverage helps provide an increased target surface smoothness, by causing a greater amount of abrasion per rotation pass on a target area.

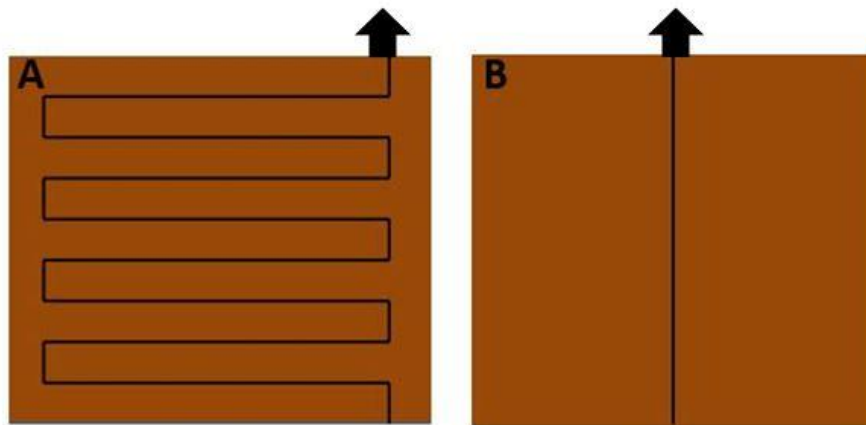


Figure 2.6. Single diamond track (black line) for **A.** Ultrasonic assisted grinding **B.** Common grinding.

One of the most aggressive types of grinding is UAM (Fig. 2.7) and is when a relatively sharp tool piece is ultrasonically vibrated and dragged over a surface whilst under weight on bit (WOB) force. The oscillatory impacts between the tool tip and target caused by the ultrasonic vibration, create a series of very small serrated troughs and peaks. The post-machining surface roughness (SR) and tool wear rate (TWR) will depend upon the target material hardness and initial SR, as well as on grit size and composition, water grit ratio of the slurry, rate of tool motion across the target and the ultrasonic resonant frequency (f_{res}) of vibration (Teimouri *et al.* 2015).

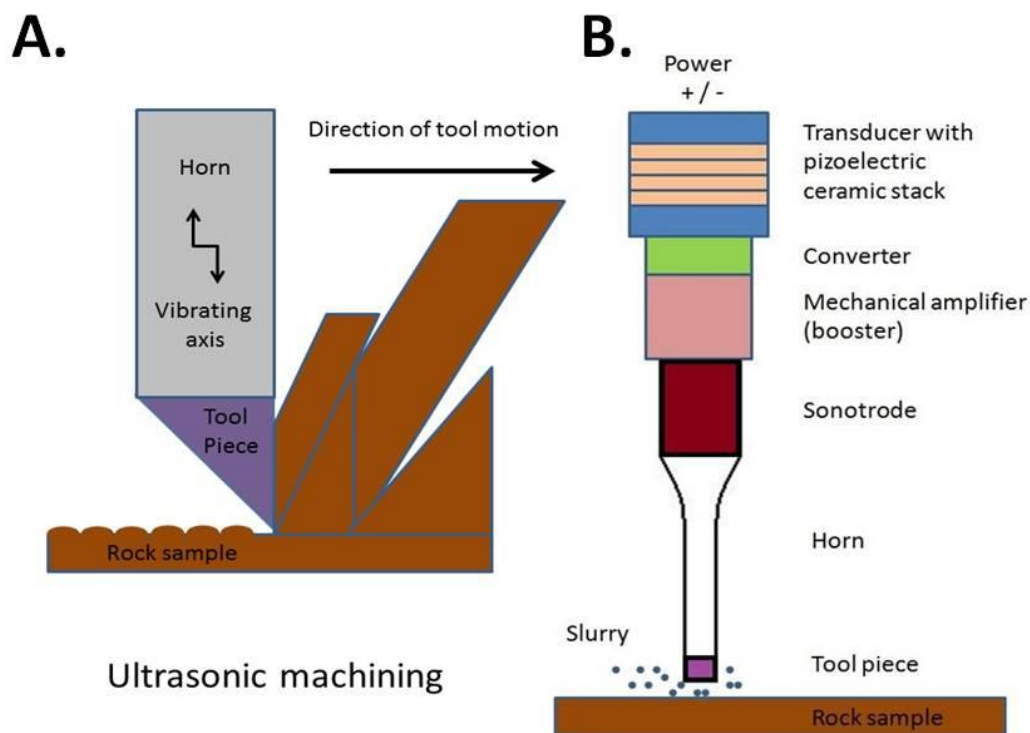


Figure 2.7. Principal and components of ultrasonic machining. In all varieties of ultrasonic machining a horn vibrates ultrasonic frequency. This horn may have **A.** A sharpened tool piece that chisels the target surface away or **B.** The horn tip can be blunt and a fluid slurry passes between to tool tip and target surface (B. and Fig. 2.8).

The tool piece does not in theory need to be sharp, depending on the target material and purpose of machining. Even a flat, blunt tool tip will smooth the target area via ultrasonic vibration of the slurry, which will form microscopic cracks and chips in the target surface (Fig. 2.8). As a rule, the blunter the tool tip, the slower the target material removal rate (MRR) is, although precise modelling and theory of UAM MRR is still poorly understood (Agarwal, 2015). At ultrasonic f_{res} 20-50 kHz the MRR is theoretically proportional to the square root of f_{res} (Agarwal, 2015). The force of an individual slurry grain impact can be expressed by equation 2.3 (Kalpakjian, 2008).

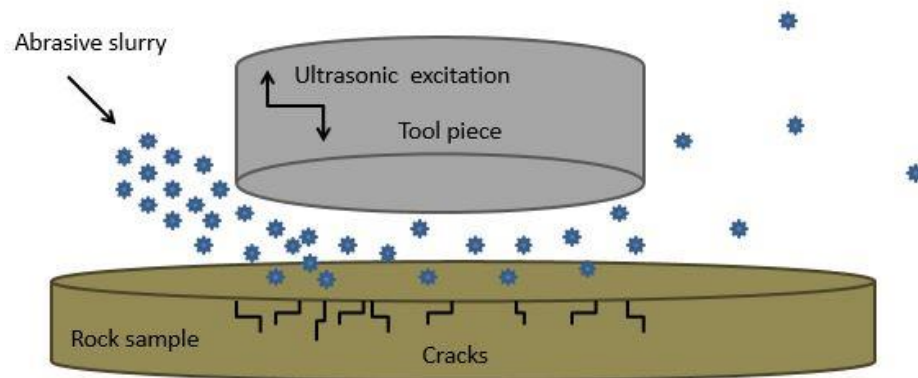


Figure 2.8. Illustrating how the abrasive grit particles in the slurry crack and smooth a target surface.

$$F = 2mv/t$$

Equation 2.3

Force (F), particle mass (m), particle velocity (v), time duration of particle contact with target (t).

This experiment uses a mix of techniques depending on the tool tip used. When the experiment is assessing the results of using diamond resin tips, a type of rotational UAG is occurring, with the diamonds grinding the target surface. When the experiment is assessing the results of using tungsten carbide tips, a type of rotational UAM is occurring. However, the terminology used in the literature is extremely imprecise, overlapping and often contradictory. Neither the UAG nor UAM used in this experiment employs slurry, as it is impractical on a Mars rover. However, only a small proportion of the MRR is attributable to the slurry grain impacts. The bulk of the MRR is from tool impact on the target (Agarwal, 2015). The UAM presented in this work exclusively uses tool impact for material removal and MRR is proportional to material removed per impact and the cycle frequency of impacts.

The formation of ultrasonic waves can occur by either piezoelectric (accumulated charge in a material, Fig 2.9) or electrostatic restoration (Manthey *et al.* 1992). This experiment uses piezoelectrics and therefore only this type will be discussed. Piezoelectric ultrasonics consists of a transducer with a piezoelectric stack, usually composed of a ceramic set of rings or discs stacked on top of each other. The size and shape of these ceramic rings varies depending on the ultrasonic tool, but are usually a vertical maximum of ~30 mm (Website 11).

The ceramic discs have non-centrosymmetric crystals within their structure, usually either zirconate titanate (ZrTiO_3), a perovskite material called lead zirconate titanate ($\text{Pb}[\text{Zr}_x\text{Ti}_{1-x}]\text{O}_3$ ($0 \leq x \leq 1$)) or barium titanate (BaTiO_3), and formerly quartz (SiO_2) (Website 12), which possesses an inherent fixed pyroelectric dipolarity (Fig. 2.9). The crystals align in uniform directional polarity by the introduction of an electric charge to the system during ceramic formation.

Electrodes of silver, or plasma vapour deposition (PVD) which is where an ionised gas (such as silicon nitride) thinly coats an electrode, are then connected to the ceramic discs above and below, through which a rapidly alternating positive and negative charge is pulsed. Alternatively, a monocharged current can be switched on and off. The alternating current polarity interacts with the ceramic fixed polarity, by either attracting or repelling the inherent ceramic crystal polar charge, which causes mechanical expansion or contraction and energy in the form of physical oscillations. If performed rapidly, these oscillations produce waves at ultrasonic frequency (>20 kHz). The conversion of electrical energy to mechanical oscillation is the converter component (Fig. 2.7), after which the physical oscillations are amplified. This sandwich style transducer-converter was first developed by Paul Langevin in 1917 and used quartz; but modern transducers of this style, as used in this research are still called the Langevin type (Uchino, 2010).

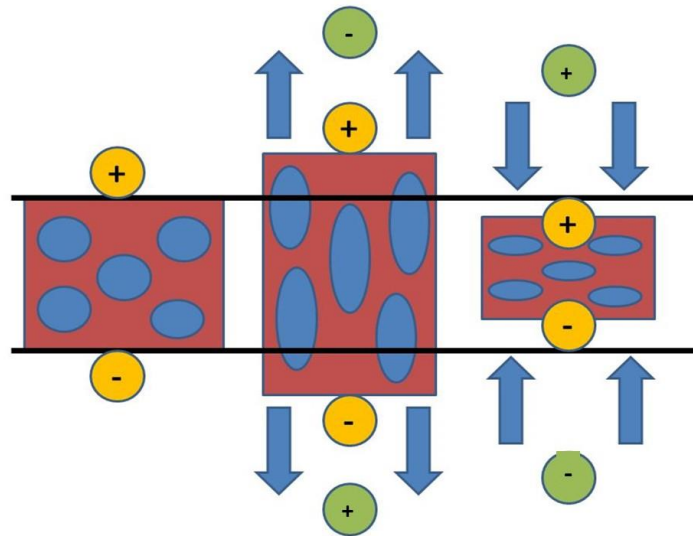


Figure 2.9. Illustration of how a piezoelectric stack generates ultrasonic oscillations. The ceramic (red) has aligned crystals within the structure (blue circles), which possess fixed inherent dipolar charge (yellow circles). An external electric charge is introduced and alternated rapidly, causing the crystals in the ceramic to be attracted or repulsed from the current, thus mechanically distorting the ceramic shape and producing physical waves. If repeated rapidly enough, the waves emit at ultrasonic frequency.

Once the ultrasonic wave is formed by the converter, there are several amplifier designs which operate at various ultrasonic frequencies, or can shift between frequencies. Generally these amplifiers consist of a transformer, a bridge rectifier, a signal generator and a driver circuit (Basa *et al.* 2012). Once amplified, the oscillations are transmitted into a horn, sometimes referred to as a wave guide or sonotrode, usually made from titanium, aluminium or steel. The geometry of the horn controls how the ultrasonic waves propagate, and is specific to the intended tool application and target material. They are usually cylindrical, tapered and possessing exponential shaped steps (Nad, 2010). As the horn tapers and narrows, the waves become increasingly amplified, focussed and effective, analogous to when waves approach a beach shore and the total energy remains near constant, but the wave height (amplitude) and energy per unit volume increases as the depth of water reduces. Ultrasonic horn material is selected to possess low damping capacity, aiding amplification during wave guiding. This

ultrasonic energy focus as a function of surface area reduction comes to a point at the tool tip, whatever material this may be composed from. Because the horn acts as the conduit between transducer and tool tip, it is very important that the horn matches the resonance frequency of the transducer, otherwise the two will be out of synchronisation and the effect will create inharmonious ripples reverberating back into the oncoming waves, dissipating energy potential and propagation. Using the beach analogy once more, if the horn is out of resonance with the transducer, this is similar to refractory waves refracting at angles along a shoreline and bouncing back out to sea to disrupt the incoming waves, reducing their power through resistive losses.

Linear UAG or UAM operations are not practical when considering the complexities and environment of Mars rover operations. Another practice is termed rotary ultrasonic machining (RUM) and rotary ultrasonic grinding (RUG), where a spinning diamond resin disc or tool tip rotates a fixed position and is lowered onto the target material, or the material is raised to the disc/tool contact (Fig. 2.10). The mechanistic principal of causing the individual diamonds to ultrasonically vibrate is the same as described above, just operating within a compact circular geospatial area. Industrial studies on materials such as carbon fibre reinforced plastic have shown RUM to be more efficient than grinding without ultrasonics, in terms of material removal rate, surface roughness, torque and force (Ning *et al.* 2016). The current Mars rover RAT is essentially a complex and versatile version of this rotary style, but without the ultrasonic assistance. It is simply a mechanically rotating diamond resin, utilising common grinding (CG). This research seeks to quantify and explore the advantages and disadvantages of using RUM and RUG in rover RAT technology. Our prototype ultrasonic tool is called the Micro Optic UltraSonic Exfoliator (MOUSE).

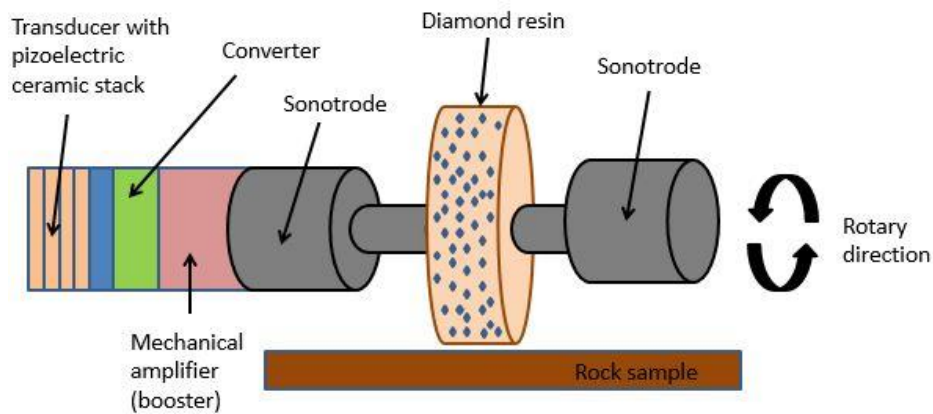


Figure 2.10. Principal and components of rotational ultrasonic grinding (UAG).

In order to know whether an ultrasonic tool, such as the MOUSE, has produced a smoother surface/lower surface roughness than the RAT, it is important to first characterise the current RAT capabilities. Contact with Honeybee Robotics was initiated in 2013; however US-UK International Traffic in Arms Regulations (ITAR) shipping restrictions and intellectual property concerns restricted collaboration. There exists a rather limited literature pool on the specific technical details of RAT construction, detailed below.

2.4.2 The Mars rover rock abrasion tool (RAT)

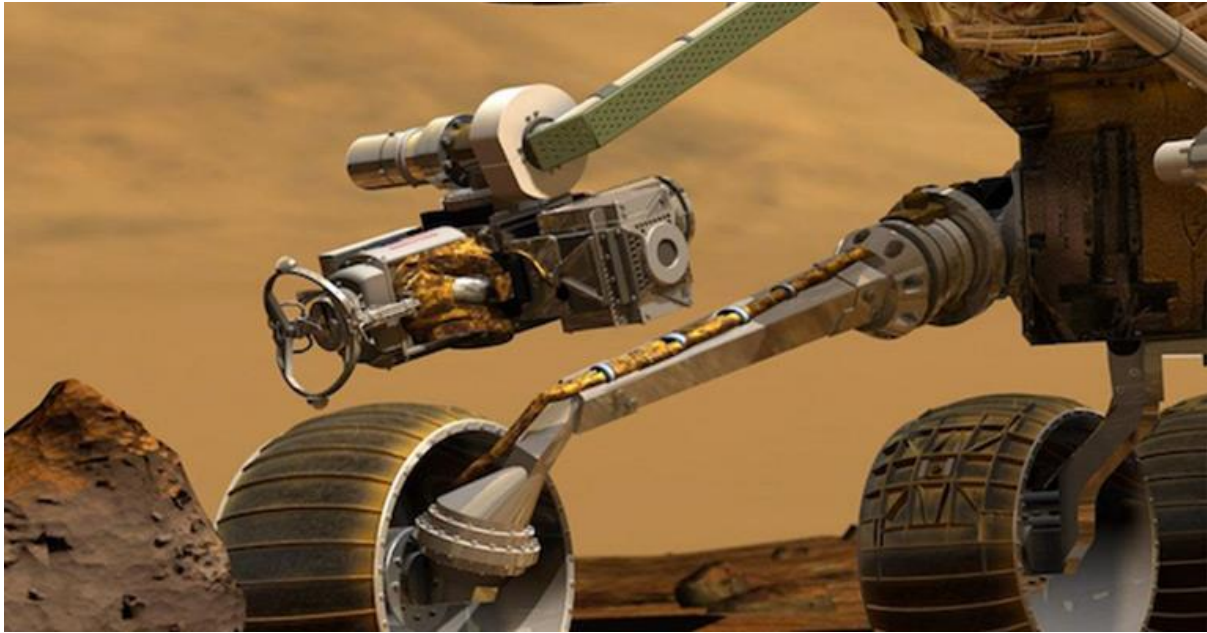


Figure 2.11. Artist's impression of the RAT mounted on the Curiosity rover. *Credit: Honeybee Robotics (Website 13).*

The RAT (Fig. 2.11) is a relatively complex machine with three motors and a great many moving parts. The RAT weighs 685g, has a diameter of 85 mm and a length of 128 mm, with a combined draw of 8 - 11 W. It has a bus voltage of 27 V to 34 V for a 3 hour grind (Myrick *et al.* 2004), and a mean voltage draw of 25.6 V (Thomason *et al.* 2013). Amp draw can be calculated by equation 2.4, and the RAT possesses an amp draw of 296-324 milliamps.

$$I_{(A)} = P_{(W)} / V_{(V)}$$

Equation 2.4

$I_{(A)}$ = Current (Amps), $P_{(W)}$ = Power (Watts), $V_{(V)}$ = Potential difference (Volts)

The RAT components are mostly composed from albernet, an aluminium beryllium alloy of low density and high modulus, with moving parts sealed by Teflon V to limit dust affecting operations (Myrick *et al.* 2004). The RAT is positioned onto the desired target rock by the instrument deployment device (IDD) arm, and is kept in parallel position in relation to the target rock with the aid of

Page | 91

two small spikes and a stabilising framework called butterfly wings (Fig. 2.12). Once in position the IDD places the RAT under a 5N preload (Myrick *et al.* 2004). The RAT has three DC brushed motor actuators to operate its diamond resin common grinding technique.

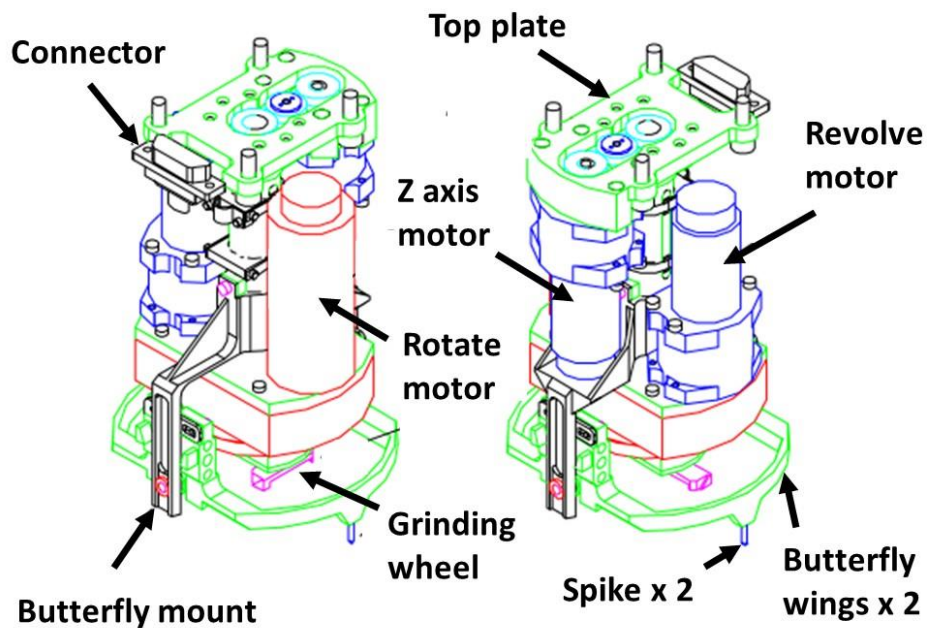


Figure 2.12. Schematic of the Mars rover RAT. *Modified from the MER datasheet, NASA/Cornell (Website 14).*

The rotate motor (Fig. 2.12) is a 3000 repetitions per minute (rpm) motor termed the ‘rotate’ or ‘grind’ motor depending on the author, and is responsible for abrasive torque. It is the fastest rpm motor on the RAT. This rotate motor operates two spindles which are positioned opposite each other at 11.11 mm from the motor axis. One connects to a grinding paddle 23.37 mm in length and 6.35 mm wide (Fig. 2.13). The paddle has two prongs of diamond resin 1.5 x 2.6 x 6.65 mm, which are mounted on either end and these resin prongs wear down as grinding progresses (Website 13). The other spindle connects to a small wire brush (Fig. 2.13) which aids removal of excavated rock material, which might damage and block the grinding procedure.

The revolve motor (Fig. 2.12) moves the whole rotate motor grinding operation in a slow 360 degree revolution around the central point between the brush and the resin grinding paddle (Fig. 2.13). This slow revolution of the rotate motor extends the total grind area from the 23.37 mm paddle length, to a grinding circle of 45 mm diameter (Gorevan *et al.* 2003). This secondary revolve is essential because the diamond resin pads are only small squares on the tips of the paddles and without the revolve motor would not produce a full area ground circle but only a circle outline ~2 to 3 mm wide. The speed of rotation varies between 1 to 2 rpm and is part of a closed loop system, where rotate motor rpm is inversely proportional to the current draw of the rotate motor and thus varies with resin on rock resistance dynamics (Myrick *et al.* 2004).

The Z axis motor (Fig. 2.12) advances the entire grinding operation towards the target rock at a speed of 0.05 mm per revolution of the revolve motor (Gorevan *et al.* 2003). The Z axis advancement therefore depends on the rotate motor rpm, which in turn depends on current draw and resistance from the target rock as described above. Such variation in Z axis advancement can thus contribute mechanical data that can be used to identify rock types by comparing rover tool data against a terrestrial database of ideal Z axis advancement in specific rock types (Bartlett *et al.* 2005; Thomson *et al.* 2013; Thomson *et al.* 2014). The maximum rock penetration depth is an arbitrarily selected 5 mm (Gorevan *et al.* 2003) and this depth is a balance between attempting to be deep enough to penetrate a weathered rock crust and being shallow enough to gain quality MI images, operational time per rock grind and rover power use. To achieve a 5 mm deep grind at 0.05 mm advancement per 1 rpm revolve motor revolution, would take 100 minutes or 1 hour 40 minutes, not accounting for rock resistance.

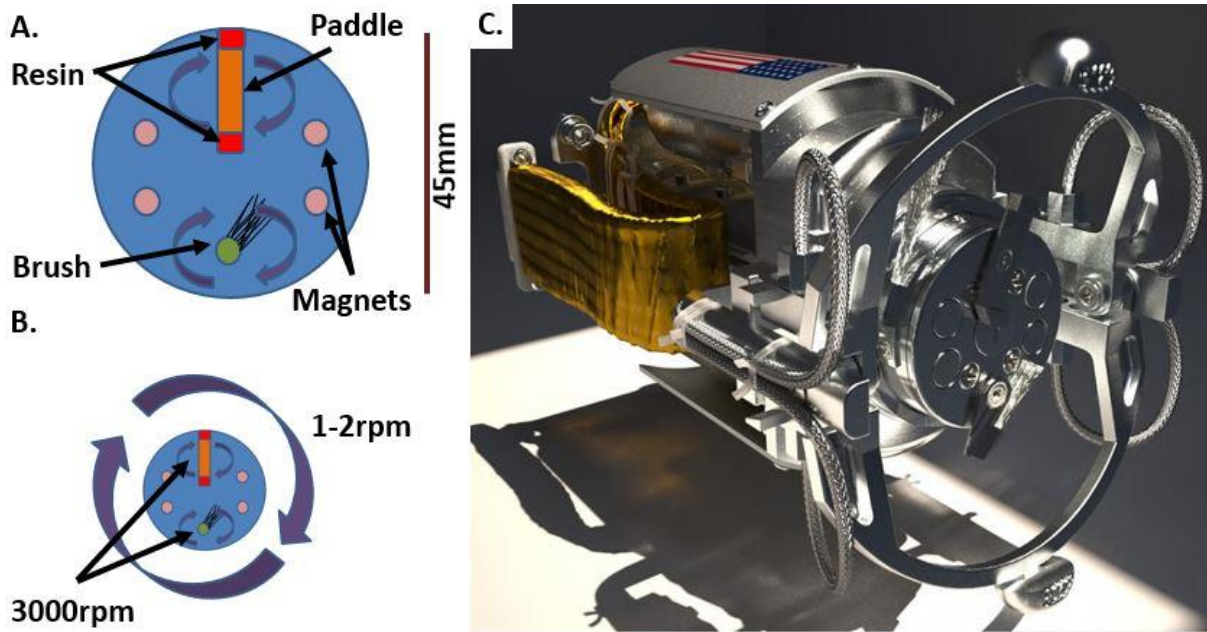


Figure 2.13. The Mars rover RAT. **A.** Schematic demonstrating how the rotate motor causes two spindles to rotate at 3000 rpm. One spindle has a paddle with the diamond resin tips mounted on either end; the other spindle has a wire brush. Magnets are for dust data collections. **B.** Schematic of how the revolve motor causes the entire face to revolve 360 degrees at 1 to 2 rpm around the central point between the brush and the paddle. **C.** A demonstration RAT showing the components described in A and B. *Credit: Honeybee Robotics.*

The relatively slow Z axis advancement rate is designed not to heat up and thereby physically or chemically alter the rock target; although it can be argued the rotate motors 3000 rpm paddle damage this aspiration. The four samarium - cobalt magnets ($\text{Sm}_2\text{Co}_{17}$) each possess a different strength (Fig. 2.13) and are used to analyse the amount of ferromagnetic metals in the dust released from the grinding operation (Seah *et al.* 1993). These magnets will not be discussed further here as it is tangential to the topic of grinding.

Initially, it appeared necessary to design and construct a replica of the RAT to assess performance so an ultrasonic comparison could be made. This did not include replicating the weight or size of the RAT, only the resin, motor configuration, power, speed and torque. Once complete, a set of grinds on

differing rock types were conducted and the final surface measured for surface roughness. Ultimately, it was decided that assessing fundamentally different rig and grinding mechanisms against each did not provide an acceptably robust set of constraints; or a quantitative enough comparison. What was needed and eventually developed was a like for like experiment comparing ultrasonics against common grinding under identical experimental conditions. Nevertheless, the process of designing and building a mock RAT proved insightful in learning functional and mechanistic problems associated with the current rover technology and it is therefore included for discussion.

2.4.3 Developing a diamond resin

The concept of diamond resin is to embed diamonds, usually synthetic and which possess a Mohs hardness of 10 (the highest), into a matrix compound of materials possessing lesser hardness. Natural diamonds are slightly harder than synthetic ones but are structurally less uniform and predictable under stress (Myrick *et al.* 2004). As the diamonds abrade the target surface they become blunt, reducing tool efficiency. Because the matrix is softer than the diamonds, the matrix wears away. This allows the blunt diamonds to fall out, exposing fresh, sharp diamonds for continued efficient abrasion. This resin was one of the most problematic parts for the NASA/Honeybee Robotics engineering team, and even on launch date issues persisted; specifically, that more diamonds were included than necessary for grinding in Mars gravity, which had the advantageous, if unexpected effect of reducing the resin wear rate by ~5 fold, allowing for more grinds than initially planned (Myrick *et al.* 2004).

Although the ingredients of the RAT resin are freely available (Myrick *et al.* 2004), the precise proportions used are not. A resin, based on open access information available from NASA and Honeybee Robotics literature (Myrick *et al.* 2004; Website 13), was developed in collaboration with the Buehler Centre for Excellence. The resin needed to balance sufficient shore hardness with a good wear rate during grinding operations in order to expose the cutting abrasive media (diamonds). Eastwind Diamond Abrasives supplied a 56 % nickel coated synthetic

Page | 95

diamond, as used on the RAT, at 120/140 mesh. The coating itself consists of 60 % carbon, 40 % nickel phosphide (Ni/P) and <1 % cobalt.

There are six main types of bonding used for industrial grinding.

- Oxychlorides
- Shellac
- Vitrified
- Silicate
- Rubber
- Resinoid

Each possesses specific properties advantageous to different types of surface and environmental conditions. This study is only concerned with the shock resistant and strong resinoid variety, which is particularly suitable for use on rough surfaces. All the ingredients of the RAT resin were carefully selected so as not to contaminate the target rock (Myrick *et al.* 2004).

The RAT uses a matrix bound together by phenolic resinoid. Phenolic is a reaction between phenol/carbolic, a white, crystalline, volatile aromatic organic acid (C₆H₆O) and formaldehyde/methanal (CH₂O). The phenolic is used to bind the other resin ingredients together (Myrick *et al.* 2004). For RAT grinding operations it is superior to other resin types such as epoxy, which uses monomers of bis-phenol A and epichlorohydrin to react into polymers for strength, or urethane/carbamate resins etc. Phenolic needs to be heated to high temperatures, pressure cured and set quickly. Phenolic has the advantage of being fire resistant, without additional additives and this is exceptionally valuable in the context of complex and expensive space operations. Phenolic is extremely resistant to degrading under high temperature and exposure to chemicals. This ability of phenolic to operate under high temperature is particularly important in a Mars rover setting, where no slurry or coolant can be used on the resin and target rock, and where the grind speed is 3000 rpm. These properties combine to make phenolic far more suitable

than epoxy alternatives. The RAT resin matrix also contains cryolite/trisodium hexafluoroaluminate, monoclinic crystal filler (Na_3AlF_6) that absorbs heat, invaluable in Mars rover settings. Cryolite is insoluble and unreactive, which helps minimise target contamination. Synthetic silicon carbide/carborundum (SiC) is then added to provide strength (Myrick *et al.* 2004).

The developed resin in this study used these same ingredients as used in the NASA RAT. Cryolite was purchased from the company Inoxia, silicon carbide with Duralum was gained from Washington Mills Ltd. in 240 (F240C6), 400 (F400C6) and 600 (F600C6) mesh varieties, and after experimentation, 400 mesh was selected for its intermediary properties, but if this resin were to be developed further in other studies, then experimentation with other mesh sizes might be of interest. The phenolic (phenocure) was supplied by Buehler. The RAT resin has a 28 % volume of diamond; however, the available literature does not state the proportions of the remainder components. It was decided to select 50 % phenocure and the remainder was equally divided between cryolite and silicon carbide/Duralum (Table 2.1).

Table 2.1. Composition of diamond resin used in this study.

Per batch	Weight (%)	Weight (grams)
Diamonds	28	2.35
Cryolite	11	0.92
Silica carbide / Duraluminv P-400	11	0.92
Phenocure	50	4.20
Total	100	8.39

The finished mock resin arrived from Buehler in 40 mm discs, 6 mm thick, which were cut using a diamond grinding wheel mounted on a cordless multispeed hand held Dremmel into 1.5 x 2.6 x 6.65 mm blocks to match the actual RAT paddle pads. Our created resin proved considerably harder than the diamond wheels, and numerous wheels were depleted just to fashion a few mock RAT pads.

On Mars, the RAT resin loses 0.5 to 0.64 mm of resin from its vertical depth per grind. A fresh pad has a 2.6 mm vertical depth; therefore ~4 to 5 grinds can be expected within the lifetime of a resin paddle. Figure 2.3.F is an example where the resin has become fully worn out and the RAT is grinding rock only on the metal stub, compared to the smooth resin grind of Figure 2.3.E.

The resin proportions used in this study are unlikely to be an exact match to the NASA RAT resin, which was researched and manufactured by a large team over a long-time. Failing to have a quantity of the actual RAT resin, a mock resin was the only option. Our ingredients approximate that of the RAT almost exactly, and the performance of this study's resin is hopefully a close approximation of the NASA RAT resin.

2.4.4 The mock RAT

To build an exact RAT, matching weight, size and performance was not deemed either practical or time well invested. The only aspects where equivalence matter for surface roughness analysis are power, weight on bit (WOB) via Z axis advancement, motor rpm, rotational dynamics and resin composition. Mechano was used to concept design a few rig housings, and after a few failures a 'box' model, open on two sides was deemed the most robust.

For the mock - RAT Z axis advancement, two NEMA 17 Hi-Torque 44 N cm⁻¹ 1.8° CNC stepper motors were used, instead of one, as on the NASA RAT. This was done because the mock - RAT rig was over four times larger than the NASA RAT, possessing considerably greater friction in the system. The two-motor configuration allowed a spatially balanced advancement towards the target rock,

unachievable with a single stepper motor. The z axis motors were mounted onto a 1.5 mm Zintec mild steel rig ~400 mm in height and ~100 mm width, held firmly together by 32 x 32 x 38 x 3 mm aluminium 90° angled corner braces (Fig. 2.14).

The two Z axis motors caused a synchronised rotation of two M8 threaded zinc plated steel bars, with an 8 mm CNC Delrin nut on each bar and a plastic 3D printed platform linking the two Delrin nuts. As the Z axis motors rotate the M8 threaded bars, the Delrin nuts which are fixed static to the platform and threaded into the M8 bars, act to lower the platform towards the target rock. The rotate and revolve motors are then attached to this platform. The Z axis advancement was further stabilised by 4 CNC router linear ball bearing sliders on 8 x 330 mm aluminium rods grade 6082 T6, collectively termed the Z rails (Fig. 2.14). These stabilisation rails, although valuable, increased the friction to an unacceptable level; therefore two aluminium CNC motor flexible shaft couplers, termed 'flexers' were mounted between the Z axis motor and the M8 threaded bar (Fig. 2.14) and this allowed for slight angle imperfections in the system and significantly reduced the friction to qualitatively acceptable levels.

The Z axis stepper motors themselves were programmed via an Arduino freeware code (C/C++ language), uploaded onto an Arduino Uno linked to an Itead two channel stepper motor drive shield expansion board. The Arduino code developed matched the Z axis advancement rate of the NASA RAT under ideal non-friction conditions, i.e. 0.05 mm per minute (full Arduino code can be found in appendix 1). The mock - RAT Z axis advancement was not inversely proportional to the revolve motor (closed looped), as in the NASA RAT. This NASA RAT closed looped system causes the RAT to cease advancement towards the rock target if the resistance becomes high enough to cause damage to the system. To compensate for this lack of a closed loop motor feedback system in the mock - RAT, the delay time in the code was manually varied in an ad hoc manner during grinding, depending on the rock type, to ensure advancement did not proceed too rapidly.

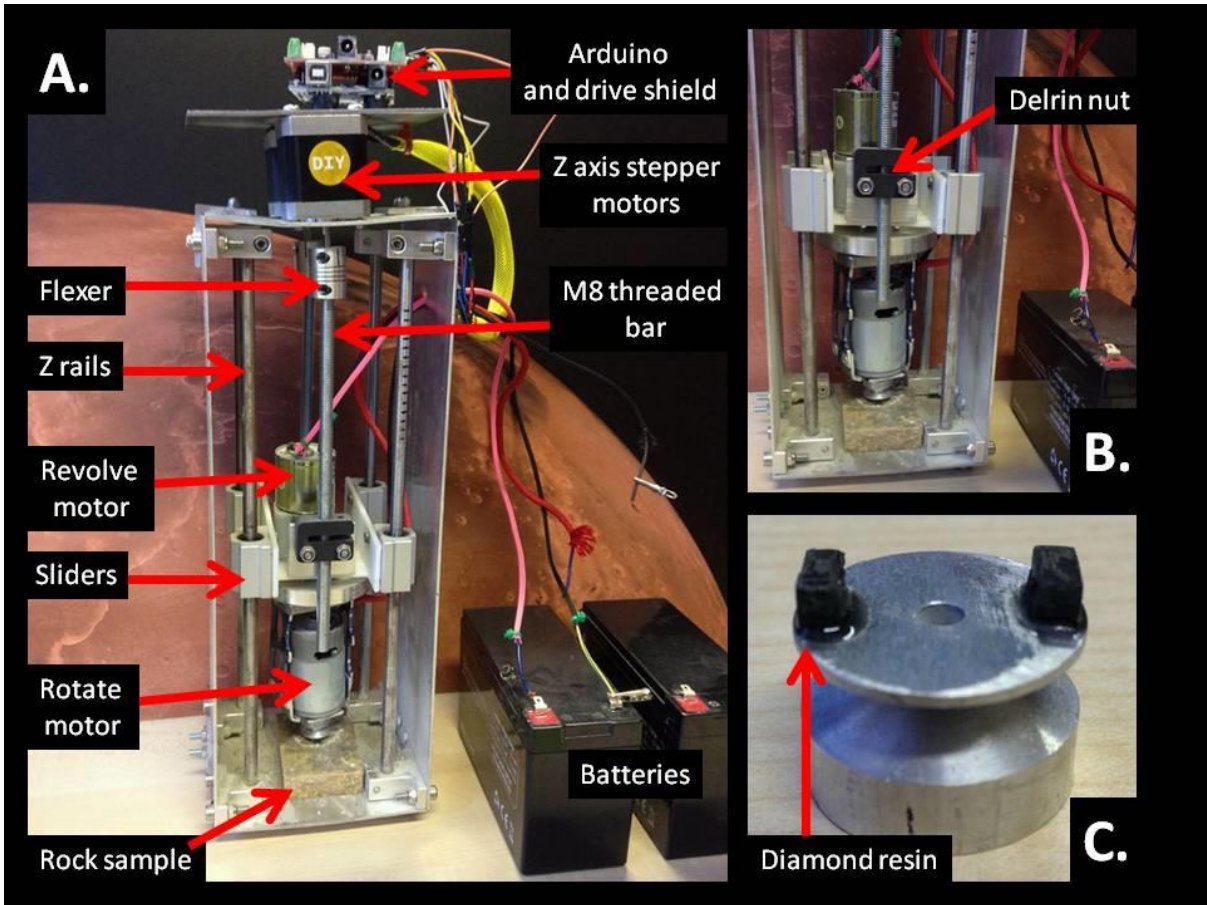


Figure 2.14. A. The mock RAT. B. Close up on the mock RAT platform. C. A mock RAT grinding wheel with two diamond resin tips.

2.4.5 Developing the Micro Optic Ultrasonic Exfoliator (MOUSE).

Considerable work was invested in developing the ultrasonic horn that could be compared against the RAT, with multiple failures occurring before a successful version was produced. The larger rig into which the developed horn would be mounted was already available, consisting of a standard 12 V DC power supply providing linear motion via a Faulhaber 2619S012SR flat ironless rotor DC 112:1 gearmotor, the rate of progress of which was recorded via a PS-C15M linear position 200 mm stroke potentiometer sensor. Ultrasonic vibration was provided to a 20 kHz L500 ultrasonic transducer piezoelectric stack, via a Sonic Systems P100 transducer driving unit connected to an Adafruit Industries 736 MC2065 slip ring for rotary electrical contact of the piezoelectric stack. The developed horns were attached to the transducer via an M10 thread in the base of the horn. A Kistler 9321B dynamometer used a Kistler 1631C connecting cable to connect a Kistler 5015A monitor for thrust force measurements. An adjustable free mass was attached to the rig via a pulley wheel to assess WOB (Fig. 2.15). The ultrasonic horn and tool tip rotates at a constant 14.66 rpm, powered by a 12V DC Faulhaber 2619S012SR 44 rpm motor using a 1:3 gear ratio.

The critical research lay in developing the appropriate shape of acoustic horn to channel the vibrations and in learning which mode and ultrasonic frequency to use to avoid wave propagation dissonance. Like the mock - RAT, the MOUSE was not attempting to be Mars rover flight ready regarding size and weight proportions. Only the characteristics of ultrasonic wave amplitude, power, rate of advancement, WOB, SR, thrust force and rock type were of interest in this study.

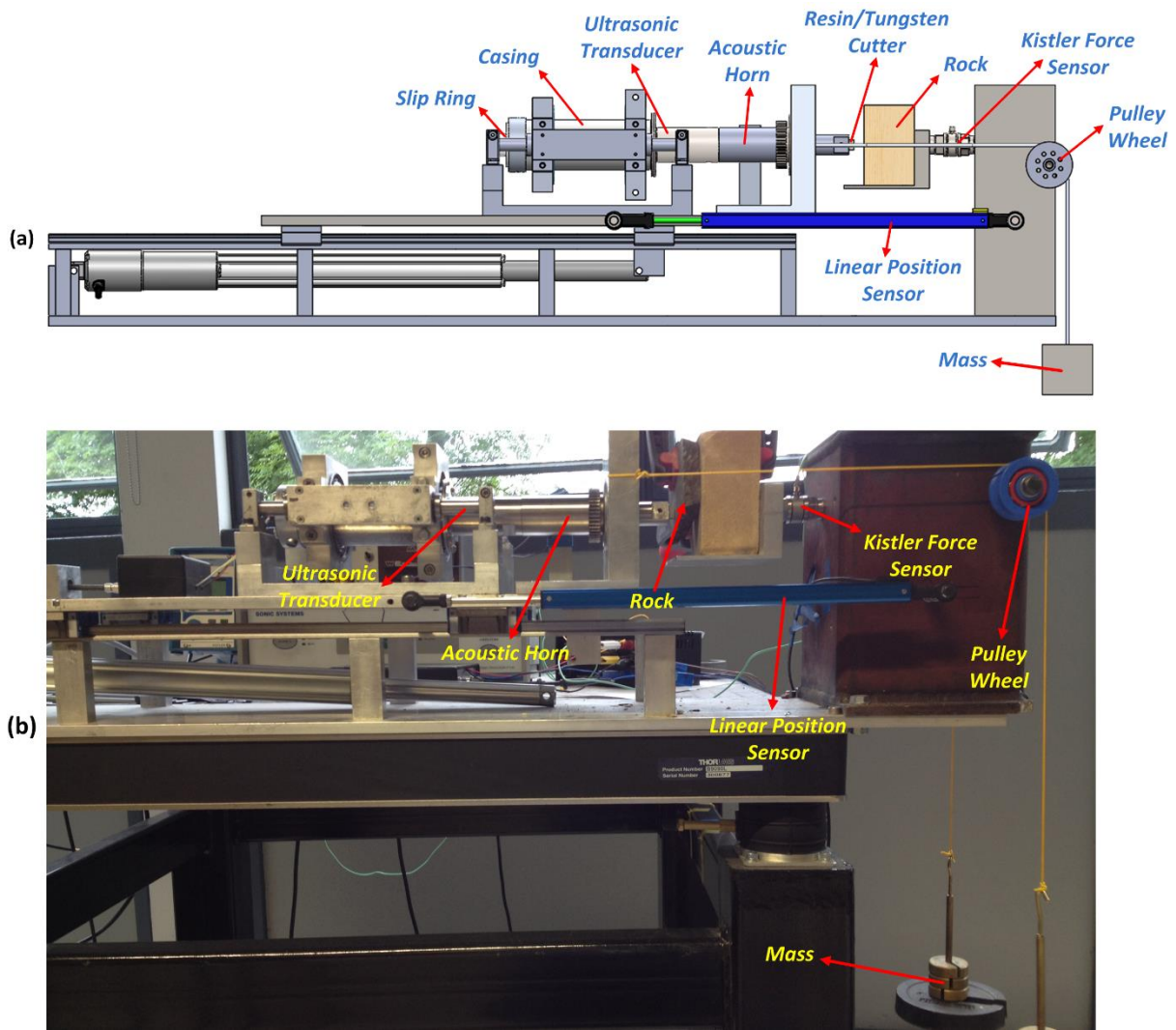


Figure 2.15. The ultrasonic rig supporting the MOUSE. **A.** Schematic. **B.** Actual rig. Adjustable free mass allows WOB variation. Linear position sensors monitor rate of penetration (ROP). Force and power are monitored and rock type can be varied. The acoustic horn and cutter material is where this study focused its research.

Numerous horns were numerically modelled using ABAQUS 6.14-2 Finite Element Analysis (FEA) software, which is a standard practice for designing ultrasonic acoustic horns for UAM (Seah *et al.* 1993; Amin *et al.* 1995; Amini *et al.* 2008). Horns were modelled with and without fluting, and varying the pitch, depth and number of flutes. Modal dynamic analysis was explored (Fig. 2.16), seeking a mode which caused the horn to resonate without too much stress and strain on the axis and move in a manner that directed the ultrasonic wave energy most

efficiently to the tool tip for abrasive action. Mode 6 was consistently the better performing, providing $f_{res} \sim 20\text{kHz}$ ($\sim 20,000$ wave cycles per second). The fluted designs did not model as well as the non-fluted ones and two non-fluted designs were selected for construction. The selected horns were constructed from titanium grade 5 Ti-6Al-4V alloy and operating at mode 6, $f_{res} 20.264\text{ kHz}$ (Fig. 2.17). One tool piece had an angled tool tip, which will be termed the ‘angled MOUSE’ and the other tool piece had a rectangular tool tip, which will be termed the ‘flat MOUSE’. The horns were of the stepped variety, with a 24 mm step, tapering for 7 mm in length midway on the horn piece and 67 mm from either end (Fig 2.17).

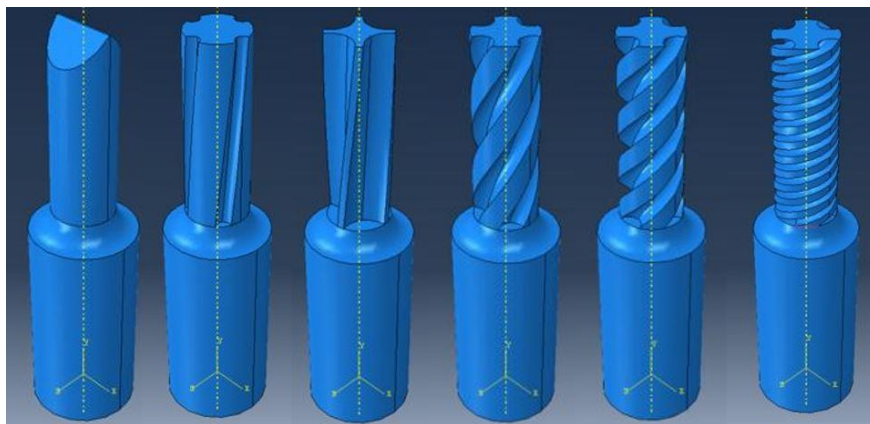


Figure 2.16. Varying flute depth and pitch via ABAQUS modal analysis software.

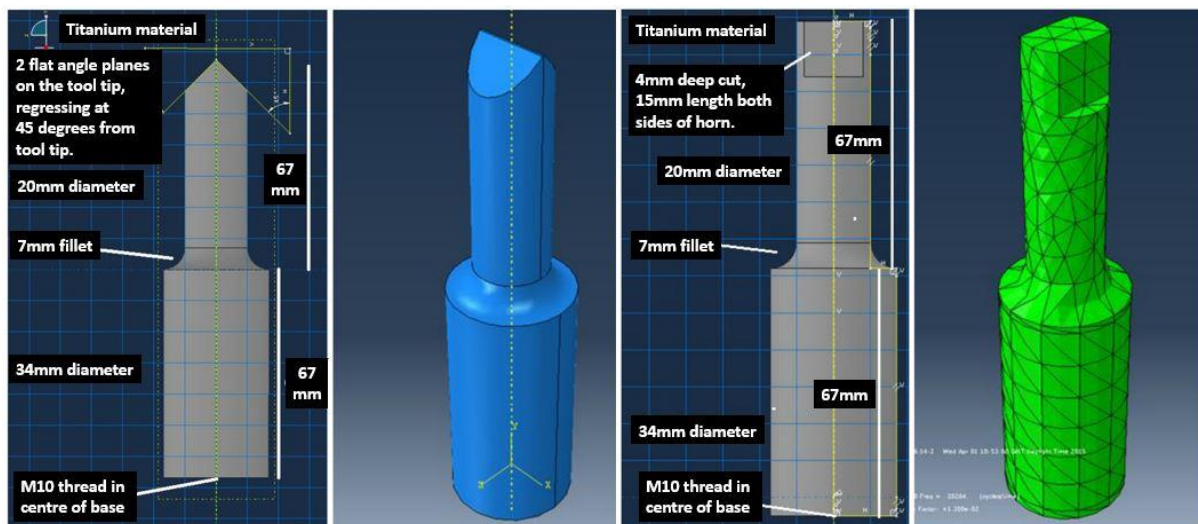


Figure 2.17. The two ultrasonic acoustic horns built from titanium. Only the rectangular tip one was ultimately used in the experiment. Termed ‘angled MOUSE’ and ‘flat MOUSE’.

Initial testing involved mounting the developed diamond resin onto one of the flat angles planes, bonded to the titanium tip by superglue and tested on rock. The result simply saw the superglue bond shear and fail. A second attempt replaced the superglue with an epoxy resin bond, which did not always shear, but instead transmitted the energy to the rock targets in a manner that shattered all the rock samples experimented upon in spectacular and violent fashion. This process of bond shear and rock failure was repeated on the flat 'MOUSE', although it was observed that vertical, rather than angled contact performed fractionally better.

To solve these issues, it was decided not to use any bonding, neither epoxy resin or glue, but instead to redesign the acoustic horn with a small trench slit in the tip 2 mm wide, 3 mm deep and 12 mm in length for the 'flat MOUSE' and 18 mm in length for the 'angled MOUSE', into which a slice of the developed diamond resin could be slotted securely (Fig. 2.18.A, 2.18.B). Although an improvement on the bonded attempts, during tests the diamond resin itself failed every time, although the tungsten carbide tips remained functional. This diamond resin failure is attributed to the resin not being held tightly enough within the trench, so when ultrasonically vibrated, the resin rattled at the microscopic (not visible) scale, causing a build-up of heat which manifested in the resin failure being ductile and soft against the target rock. To remove this rattle and heat build, two 5 mm threaded holes were centrally positioned 5 mm from the tool tip edge on both sides of the flat MOUSE, whilst a grub screw acted as a tightening force holding the resin securely in place. The trench slit was also deepened to 10 mm. This grub screw addition adequately solved the issue of rattle and heat build, but was only possible to employ on the 'flat MOUSE', and this was the only horn version used from this point onwards.

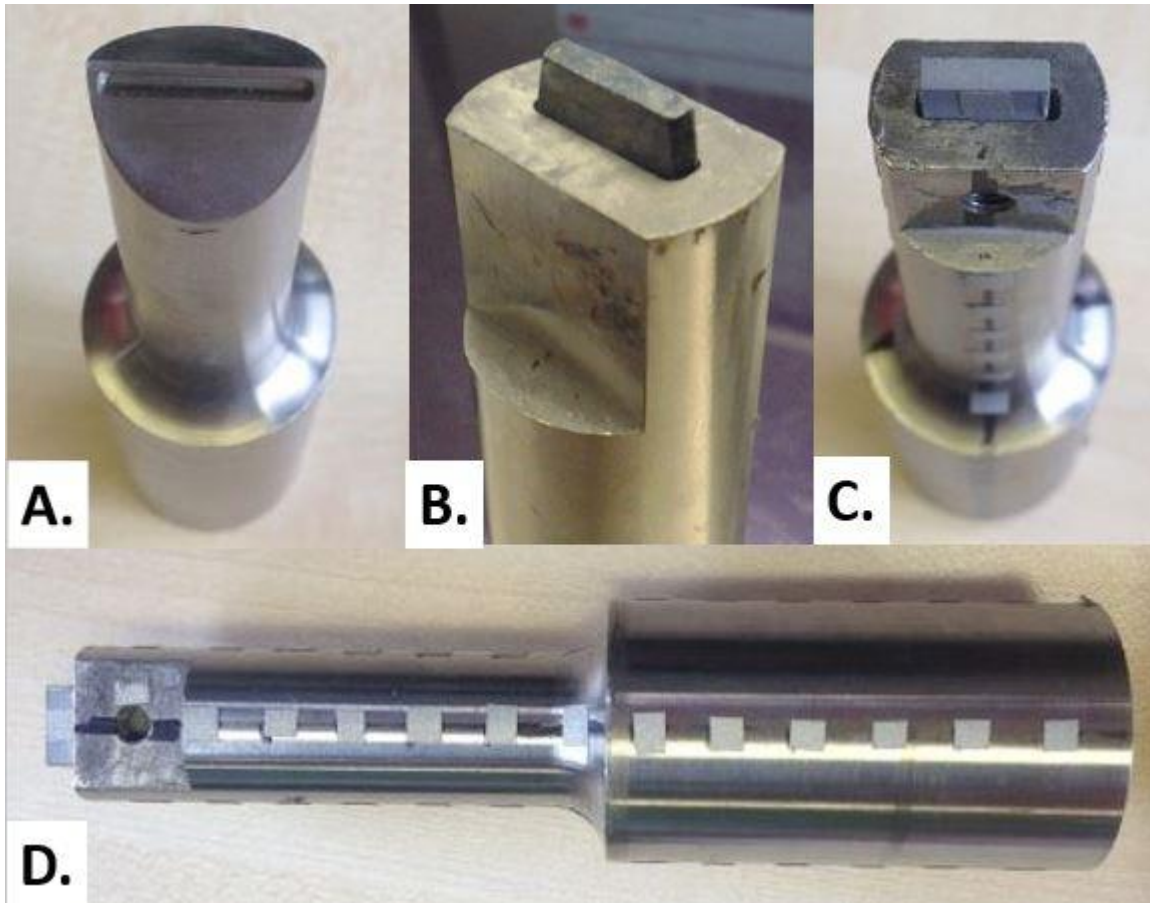


Figure 2.18. A. ‘Angled MOUSE’ and B. ‘flat’ MOUSE tool tips with a trench added in, 2 mm wide, 3 mm deep and 10 mm in length. This trench negated the need for any bonding substance fixing the diamond resin to the tool tip. C + D. Later additions included deepening the trench from the initial 3 mm to 10 mm and adding two M5 threaded holes to the ‘flat MOUSE’ horn tip, allowing grub screws to hold the resin tightly in place.

Despite the ‘flat MOUSE’ performing much better following the adjustments described above, the resin or the rock would still often fail after a few minutes of successful grinding. Most ultrasonic operations proceed using ~10 to 40 μm wave amplitudes. The definition of ultrasonic is based on cycles per second, not wave amplitude. Wave amplitude can be varied considerably whilst remaining at a fixed ultrasonic frequency. It was decided that the RAT resin was simply not suitable for such high amplitudes at any ultrasonic frequency. By lowering the wave amplitude to 5 μm or less but retaining an $f_{res} > 20$ kHz, successful, sustained grinding results

were achieved without significant wear of the diamond resin and without shattering the target rock samples. The resin and tungsten carbide tips were 15 mm x 10 mm x 2.8 mm thick, therefore 5 mm of tool tip protruded from the horn slot as an active cutting tip. A mixture between heat expansion and grub screws secured the material from wobble in the 3 mm wide slot.

In a perfect world, the movement of ultrasonic waves in a metal horn could be modelled and calculated by Newton's laws of motion, thermodynamics, equilibrium, conservation of energy and mass combined with Maxwell equations. The complexity of doing this, however, is virtually an impossible task, especially if a system is nonlinear or stochastic. Finite element analysis (FEA), which observes material stress and wave deflections, bypasses these complexity issues by dividing an object, in this case the horn, into highly simplified, discrete, non-overlapping geometric blocks called nodes, bound together by a hypothetical mesh. The coarser the mesh is, the simpler and faster the model calculations can be performed but the less accurate to real performance the model will be. Choosing between such tradeoffs between model size and validity to the physical task is an integral part of engineering. Each node can be modelled successfully to a simple uniformity, and the number of nodes in a system model can be user adjusted. Node placements should be positioned at points where the geometry or load changes (i.e. changing in places where the mathematics required to express a reality would need to change, for example changes in tool diameter). The nodes used in this analysis were cubic, despite the tool itself being cylindrical. This cubic modelling was done for model and data processing simplicity. The degree of freedom vector was displacement, and ultrasonics expressed as a harmonic vibratory mechanical force.

The term mode in this analysis does not refer to the longitudinal wave mode, although this is present, but to the resonant properties of the titanium horn. A mode is an object's combined properties of natural frequency (f_i) as Hz, damping ratio (ζ_i) as percent, and mode geometry (Takács & Rohal'-Ilkiv, 2012). High frequency modes such as ultrasonics are usually more complex than low frequency modes and require greater energy input. Object mass stiffness and

Page | 106

boundary conditions are also important in defining an object's mode. Any object will possess a specific natural resonating mode, or harmonic. This specific natural resonating mode will change if the object's shape or mass alters. FEA was combined with exploratory modal analysis (EMA) (Schwarz & Richardson, 1999), to discover the precise f_{res} required to cause the 'flat MOUSE' horn to resonate harmoniously at ultrasonic frequency. The FEA and EMA modelling describes how the ultrasonic wave energy progresses down the horn and where mass displacement is at a maximum and minimum. For maximum grinding efficiency on a target the peak energy displacement and horn stress should be focussed at the tool tip, with little to none elsewhere in the horn length.

To conduct FEA-EMA, the 'flat MOUSE' horn was vertically mounted to a small transducer connected to a power supply (Fig. 2.19.A). Attached to the horn were 108 small reflective tabs $\sim 3 \text{ mm}^2$ and evenly spaced into 4 lines of 27, spanning the base of the horn to the tool tip; the 4 lines of reflective tabs create the cubic shape of the model nodes. The horn was then excited to the specific frequencies of 19.2 kHz, 27.5 kHz, and 37 kHz (Fig. 2.20), each for 64 signal frames (~ 20 seconds). A Polytec CLV-3D non-contact laser vibrometer was fired at each individual reflective tab in turn, with the laser manually positioned as perpendicular to the reflective tab as was possible, with a stand-off distance of ~ 400 mm. The vibrometer simultaneously measured all three linear displacement velocities relative to the non-excited start position. A read-out box displayed the strength of contact between the reflective tab and the laser. Vibrational displacements were then converted into analogue readouts, with an adjustable number of count points, depending on resolution desired; this study modelled at 500 count points. Each reflective tab represents a corner point of a cubic node, the simplified (finite) method of modelling a complex reality. The 'flat MOUSE' FEA-EMA model comprised 26 cubic shaped nodes in total, the volume per cube varying along the tool length (Fig. 2.19.B).

The model vibratory displacement data is collected both as a frequency response function (FRF) (Fig. 2.19.C) and complex modal indicator function (CMIF) (Fig. 2.19.D). Input force and output acceleration of individual reflective tabs was

measured by the vibrometer and this data was converted to a frequency spectrum via a fast Fourier transform (FFT) algorithm that creates an input force spectrum and an output acceleration spectrum. FRF then divides the output spectrum by the input spectrum, after which a coherence function is used to ensure no undivided spectra exist that might produce error in the FRF spectrum. CMIF is an algorithm using Eigenvalue decomposition (ED) or singular value decomposition (SVD) and is an expansion theorem used to correctly identify the number of modal frequencies within a modelled point of an object (Allemang & Brown, 2006). CMIF is extracted from the FRF spectrum. For this study both an FRF and CMIF spectral graph was produced for each reflective tab on the ‘flat MOUSE’ horn. The resulting FEA-EMA data demonstrates where stress and displacement is located within the horn at varying wave frequencies (Fig. 2.20).

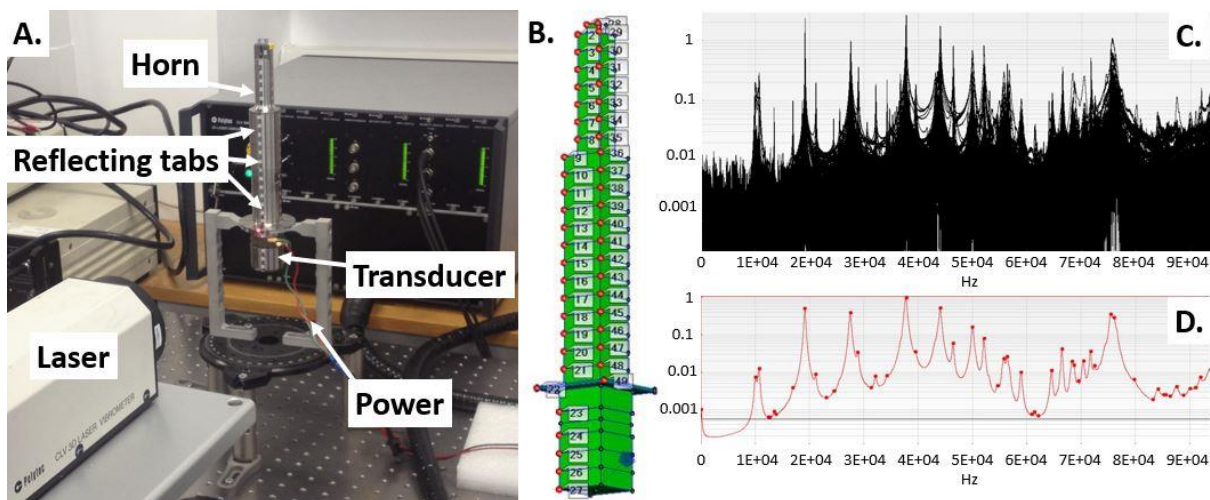


Figure 2.19. FEA-EMA set up and data collection example. **A.** FEA-EMA set up. The horn has 4 lines of reflective tabs (27 per line). Horn is attached to a transducer connected to a power supply. A laser is fired at each reflective tab in turn, ultrasonically excited for 64 signal frames (~20 seconds). **B.** The cylindrical horn simplified for modelling into a series of 26 connected cubic node blocks, the corner of each node block represents one of the reflective tabs. **C + D.** FRF and CMIF example data readouts show the relative displacement along the nodal points caused by the ultrasonic excitation.

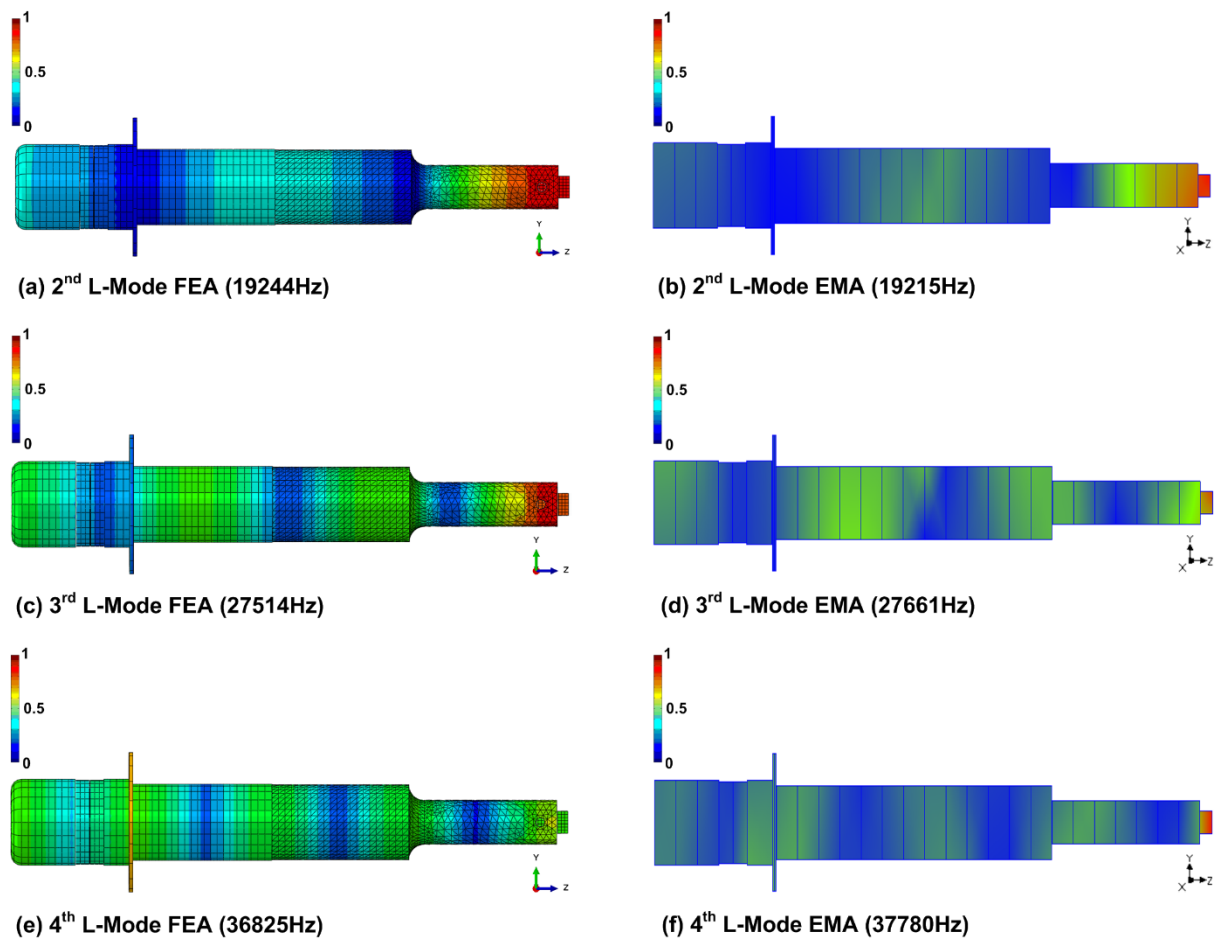


Figure 2.20. Modal finite element analysis (FEA) and exploratory modelling analysis (EMA) of the ‘flat MOUSE’, using four longitudinal wave modes under four increasingly high ultrasonic frequencies. The colours represent displacement (red = high displacement and dark blue = no displacement).

2.4.5 Experiment aim.

To determine whether ultrasonic assisted grinding performs better than common grinding on Mars analogue rock targets, assessing both a NASA rock abrasion tool type diamond resin grinding tip (RUG) and a tungsten carbide cutting tip (RUM).

Performance will be assessed on:

- A. Surface roughness (Ra and Rz) linking to key point 1
- B. Power consumption (Watts) linking to key point 2
- C. Tool tip wear rate (mm per hour) linking to key point 3
- D. Material removal rate (mm per hour) linking to key point 4

Variables used to explore performance will be:

- i. Weight on bit (N)
- ii. Wave amplitude (μm)
- iii. Rock type (Limestone, quartzite, basalt)
- iv. Cutting tip material (Diamond resin, tungsten carbide)

Fixed parameters:

- i. Time (600 seconds)
- ii. f_{res} (20.264 kHz)
- iii. Rig set up (Fig. 2.15)
- iv. Rotational speed 14.66 RPM

2.5 Methods.

2.5.1 The ultrasonic rig.

A robust comparative experiment is one that can quantitatively resolve which components exert influence over a complex system. Such an experiment is required to possess tightly constrained variables and, perhaps more importantly, identical fixed parameters. Without identical fixed parameters it becomes extremely difficult to ascertain whether results gained are due to the experimental variables or differences inherent in the fixed parameters.

Comparing the NASA RAT or the mock RAT performance directly against an ultrasonic rig (Fig. 2.16), would embody such comparative experiment flaws. Results might vary due to differences in rig torque, resin grind speed, variance in grinding surface area or the contact area of resin, and a multitude of other factors that can be identified but not quantitatively assessed. To address this issue, the mock - RAT was not used in the experiment, despite its functional success in grinding rock types in a manner qualitatively similar to the NASA RAT. Only the ultrasonic rig was used, thereby providing robust fixed parameters. Tool tips were switched between the developed mock-RAT resin and a hard wearing flat tungsten carbide tip. The experiment is not a rig-versus-rig comparison, but an experiment limited to demonstrating the performance difference between ultrasonic assisted grinding/machining versus common grinding.

2.5.2 Rock types.

Rock types were easily removed and replaced on the target platform, being held immovably in place during grinding operations via G-clamps. Three rock types were selected for testing (Table 2.2). The selection represents a compromise between having enough variety to explore performance in multiple geological settings whilst needing to keep experiment variables, hence data processing load, to a manageable level. The rocks selected were basalt, limestone and quartzite. Most of the Martian surface is basalt (Wyatt *et al.* 2004), therefore a Carboniferous (~300-360 Ma) 'Markle type' fine grained hawaiiite olivine basalt with porphyritic

feldspar from Campsie Glen, Glasgow, Scotland was selected (Caldwell & Young, 2011). The limestone was a fine grained, flat-cleaving, micritic, Jurassic (155 Ma Tithonian) limestone from the Konservat-Lagerstätte Solnhofen quarry, Bavaria, Germany (Barthel *et al.* 1994), selected for its soft, brittle, friable mechanical properties. This delicateness is particularly relevant considering the hunt for fragile Martian carbonates as a key to the loss of the early atmosphere. Finally, a very hard 500 Ma old Cambrian basal quartzite, from the Eriboll sandstone group, Loch Assynt, Scotland, was selected as the hardest rock to grind, being highly resistant to weathering and erosion and therefore a considerable test for any tool developed.

All three rock types possessed a very thin outer weathered and oxidised surface layer typically <0.5 mm (Fig. 2.21). This thin weathered layer allowed for a natural surface roughness to be tested upon while not being so physically degraded and heterogeneous so as to not allow the MOUSE to penetrate to the unaltered rock interior. Because all rock types possessed a similar thickness in the weathered and oxidised layer (Fig. 2.21) parity existed between the experiments.

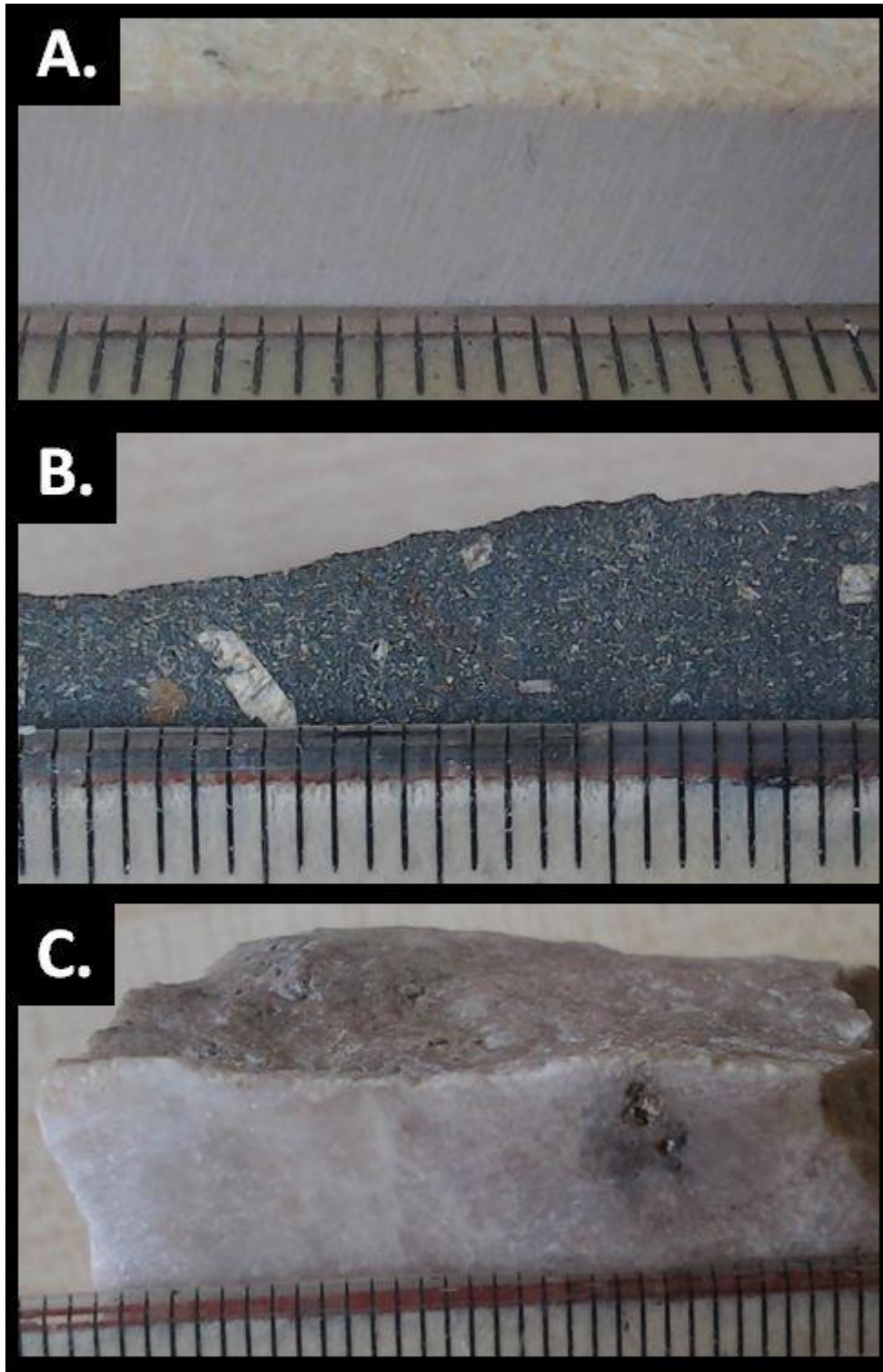


Figure 2.21. Images highlighting the initial surface roughness, the <math><0.5\text{ mm}</math> oxidised and weathered outer layers and unaltered interior of **A.** Limestone **B.** Basalt. **C.** Quartzite.

2.5.3 Weight on bit.

The rig (Fig. 2.14) uses a variable free hanging mass to drag it towards the target rock under a fixed WOB. Mass was added or subtracted from the hanging free mass (Fig. 2.14). Initial mass values of 2 N, 7 N, 12 N, 17 N, 22 N, 27 N, 32 N were assessed, but in consideration to the number of other variables and data management in the experiment, combined with the near negligible effect of the 2 N load on the target rock surface, it was decided to test only 12 N, 17 N, 22 N, 27 N, 32 N WOB (Table 2.2).

2.5.4 Wave amplitude.

Wave amplitude was explored by using 0.0 μm , 2.1 μm and 4.0 μm (Table 2.2). 0.0 μm is, obviously, no ultrasonics and represents rotary common grinding. Above 4 μm wave amplitude either the limestone or the diamond resin shattered, and although this itself is interesting and worth further exploration of the precise limits, there already existed a surfeit of variables under investigation.

2.5.5 Experiment design.

Table 2.2. Experiment variables. DR = Diamond resin. TC = Tungsten carbide.
Each WOB entry is a single experiment run of 10 minutes.

Rock Type	Cutting tool tip	Wave amplitude (μm)	WOB (N)	Rock Type	Wave amplitude (μm)	WOB (N)	Rock Type	Wave amplitude (μm)	WOB (N)
Limestone	DR	0.0	12	Quartzite	0.0	12	Basalt	0.0	12
			17			17			17
			22			22			22
			27			27			27
			32			32			32
	DR	2.1	12			12			12
			17			17			17
			22			22			22
			27			27			27
			32			32			32
	DR	4.0	12			12			12
			17			17			17
			22			22			22
			27			27			27
			32			32			32
TC	0.0	12	12	12					
		17	17	17					
		22	22	22					
		27	27	27					
		32	32	32					

TC	2.1	12	2.1	12	2.1	12
		17		17		17
		22		22		22
		27		27		27
		32		32		32
TC	4.0	12	4.0	12	4.0	12
		17		17		17
		22		22		22
		27		27		27
		32		32		32

2.5.6 Time.

The experiment required 90 grinds in total (Table 2.2). This large number of experiment runs was the governing logic in restricting each run time to 10 minutes (600 seconds). On initial tests 600 seconds was observed to be enough to penetrate the outer rock oxidation and weathering layers and produce a ground finish, but not long enough to penetrate to significant depth, usually <1 mm, but up to ~3 mm in soft limestone. Most importantly, it allowed a ground surface area in at least a partial sphere, on which surface roughness analysis could then be conducted. If these tests were to be repeated, or a variation thereof, selecting longer time frames of at least 30 minutes per grind would be recommended.

2.5.7 Surface roughness.

Two surface roughness values per grind were acquired; the average roughness (Ra) and the root mean square roughness (Rq). Ra is quantified by the total sum departure from the roughness profile mean divided by the scan length (Fig. 2.22) (equation 2.5):

$$R_a = \frac{1}{n} \sum_{i=1}^n |Y_i|$$

Equation 2.5

N = length of evaluation, Y_i = absolute value of profile deviation from the mean.

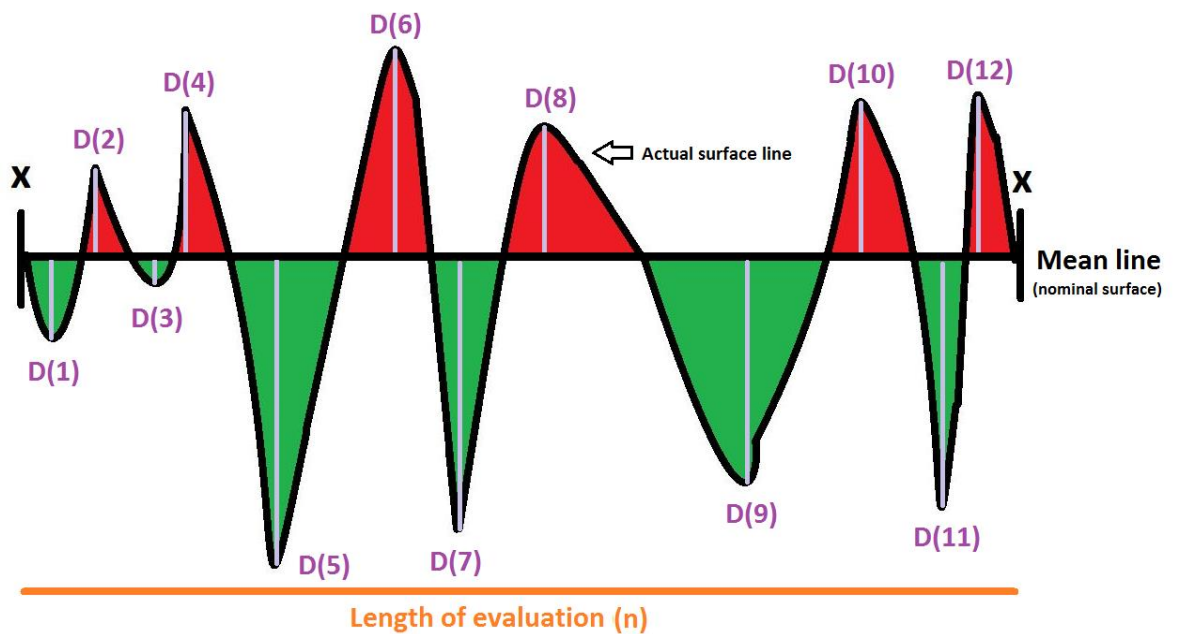


Figure 2.22. Calculation of R_a , $X - X$ = evaluation length, D = departure from mean.

There is nothing technically wrong with R_a as a roughness indicator; it used to be one of the most widely used methods of roughness calculation. Problems arise, however, when two very different surfaces possess the same departure values from the mean yet cannot be distinguished in the R_a value (Fig. 2.23); furthermore, R_a is not particularly effective at identifying extreme individual deviations, such as isolated anomalously deep notches; these R_a flaws amplify with evaluation length.

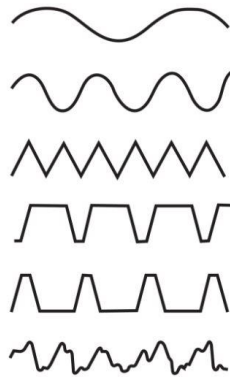


Figure 2.23. Differing surfaces which all have the same Ra value.

Rz is useful as a comparison surface roughness measurement to Ra. Rz can be calculated via equation 2.6:

$$R_q = \frac{1}{n} \sum_{i=1}^n |Y_i|^2$$

Equation 2.6

N = length of evaluation, Y_i = absolute value of profile deviation from the mean.

For Rz, the length of evaluation (n) is divided into zones (Fig. 2.24). Equation 2.6 is calculated for each zone using only the highest and lowest peaks, so for example D1 would be added to D4, ignoring D2 and D3 (Fig. 2.24). This peak selection is repeated for each zone, added together and then divided by the total number of zones evaluated, thus providing a single Rz value for each topographic line scan. Rz is a better measure than Ra, but for this project both will be calculated and compared. Ra is the most common roughness parameter used in the United States, Rz the most common roughness parameter in Europe.

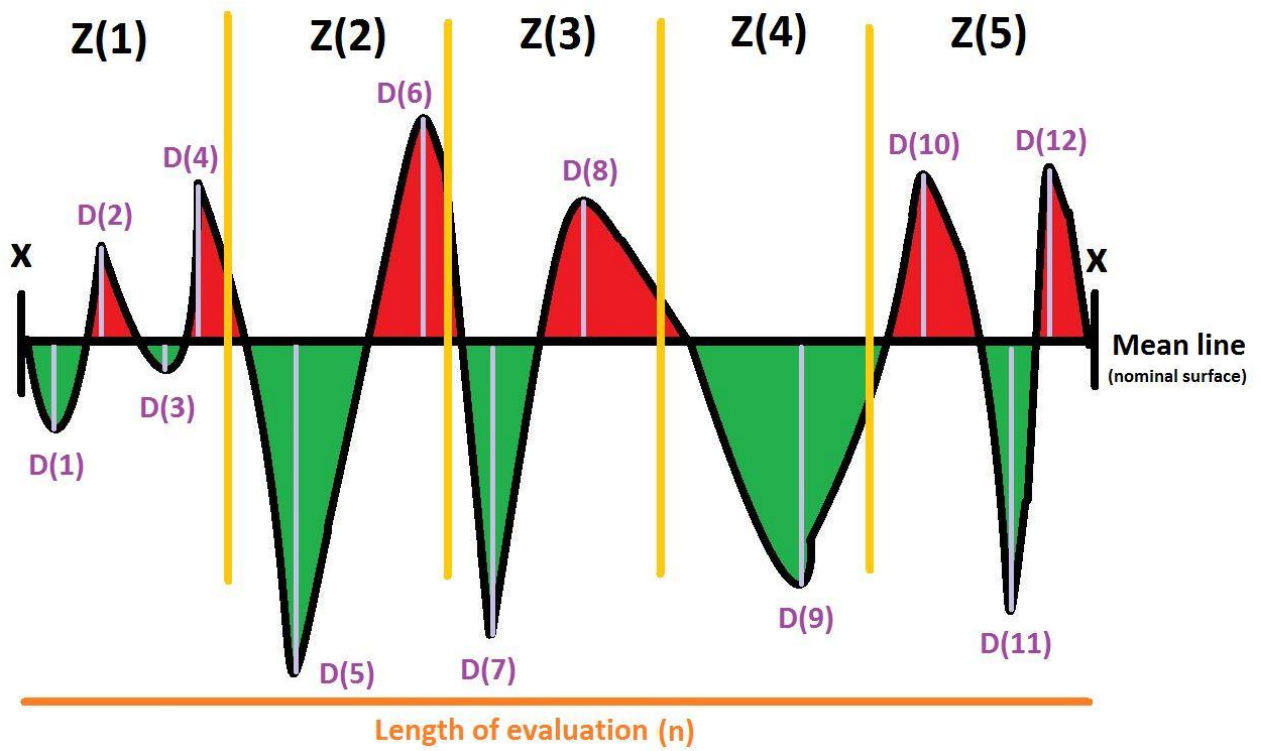


Figure 2.24. Calculation of Rz, X-X = evaluation length, D = departure from mean line, Z = zone division.

2.6 Results.

2.6.1 Surface roughness.

Initially, to calculate surface roughness, a Next Engine 3D laser scanner was used, which photographed and created a shaded relief image of the surface area, to which contour lines and colour could be added (Fig. 2.25.A - C). Cross sectional topographic profiles could be positioned along these images (Fig. 2.25.D).

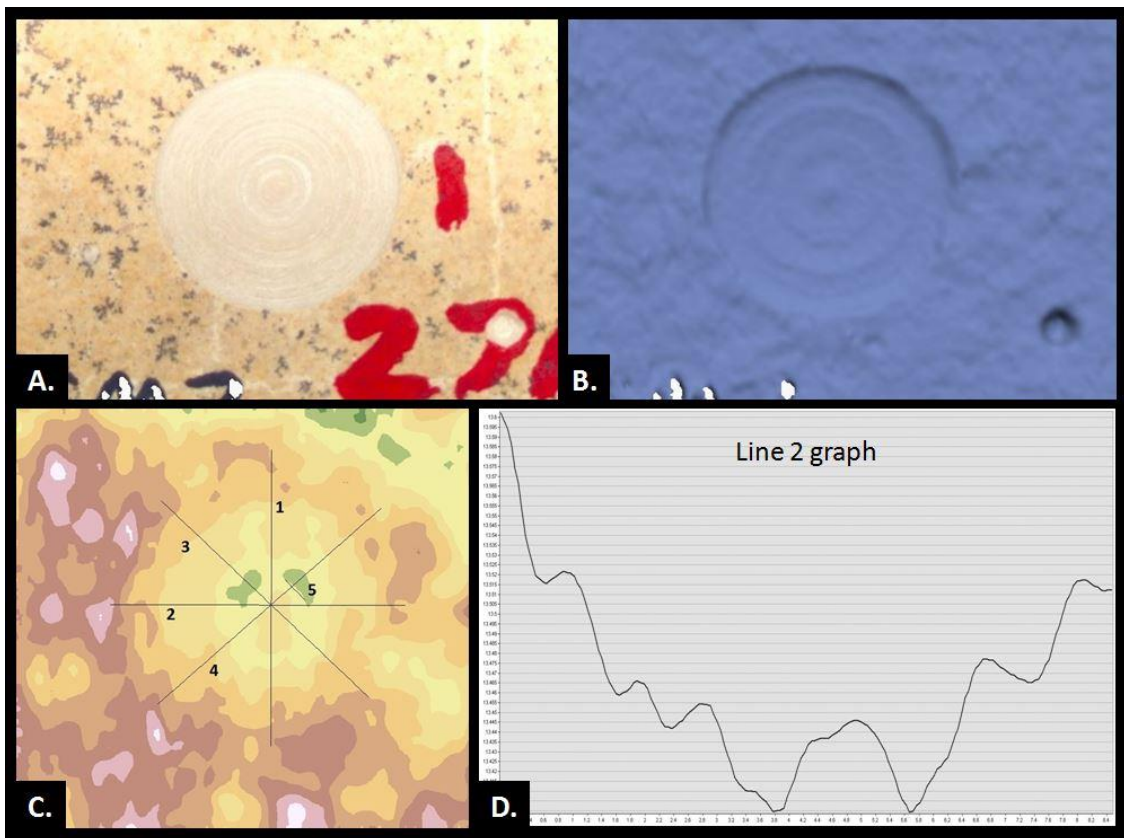


Figure 2.25. A. MOUSE grind on soft limestone. Grind is ~10 mm diameter. B. Shaded image of grind in A. C. Topography map of image in A. and B. showing location of cross section graphs. D. Cross section topography of line scan 2 from C. The axis values are on software specific values where the X axis is ~8 mm and the Y axis is ~1 mm).

This method of surface profiling was eventually rejected for the experiment for two reasons. Firstly, it was a highly time-consuming process, particularly extracting Ra and Rz values from multiple Excel graphs per rock sample grind. Secondly, due to potential Ra and Rz error arising from the need to manually position the rock sample in perpendicular alignment to the laser scanner (this was extremely difficult to achieve with exact precision). If the sample ended up being positioned at an angle this would distort the peaks and troughs of the measured topography profile (Fig. 2.26).

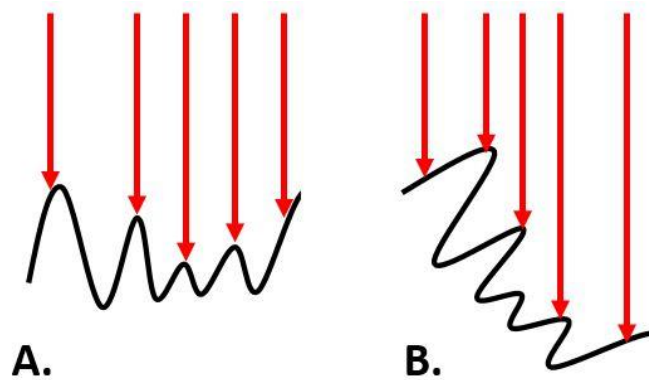


Figure 2.26. Illustrative example of how changing rock surface angle relative to a laser scanner could change the surface profile output and measured Ra and Rz values. **A.** Rock surface perpendicular to laser scanner. **B.** Rock surface at an angle to laser scanner.

However, these Next Engine laser scans and topographic profiles were qualitatively useful, even if not included quantitatively in the experiment. They revealed that nearly all grinds possessed a stepped profile, deepening towards the centre, with a small central upstanding peak (Fig. 2.25.D).

Surface roughness data was ultimately provided by a Mitutoyo SurfTest SJ-210 portable surface roughness tester with a stylus tip radius of 5 μm , and output in Ra and Rz. The stylus measured 1.6 mm per run, moving at 0.5 mm s^{-1} , at 0.8 λC (wavelength cut-off), and 300 $\lambda\text{C}/\lambda\text{S}$. λC is the point of overlap between the roughness profile and the waviness profile (Fig. 2.27). The difference between the

waviness and roughness profiles is analogous to a blanket draped over a mountain range (Fig. 2.28).

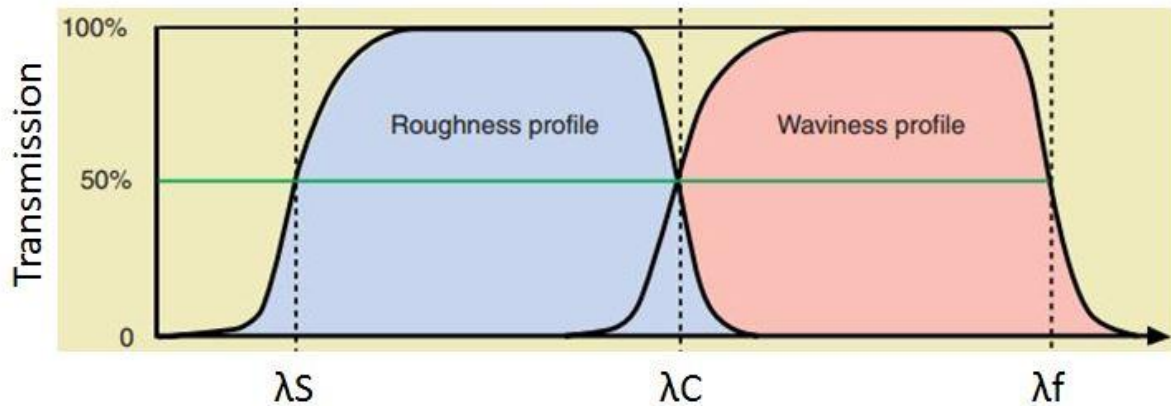


Figure 2.27. λ_C is calculated from the intersection of the roughness and waviness profiles. λ_S is the detection, noise and needle deformation limit of the stylus instrument tip, λ_C is the wave length cut off, λ_f is a filter limit of the maximum detection value. Transmission refers to the transmission of the wavelength to the measuring device. *Figure adapted from Inspection engineering (Website 15).*

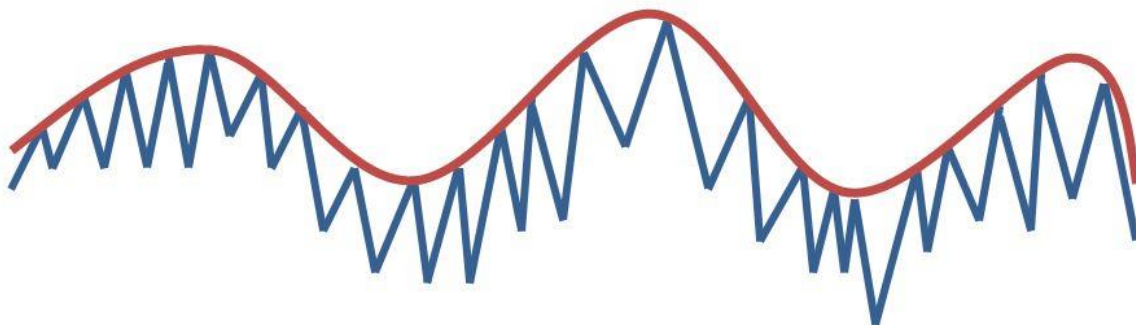


Figure 2.28. The difference between the roughness profile and the waviness profile. Blue line = surface roughness. Red line = waviness profile.

Ra and Rz measurements were conducted 5 times per grind sample for replication robustness. The reason for the short measuring length was that not all grinds had enough time to penetrate the rock sample enough to form a circle after 600 seconds, particularly on topographically rough or very hard starting rock. For accurate Ra and Rz values it was critical that only the post grind surface area was measured, with no overlap into the original unground rock. The 1.6 mm assessment length allowed precision and certainty for where measurements were taken,

providing confidence that the Ra and Rz values represented completed grind samples only. To counter the shortness of assessment length, the international norm of 5 Ra Rz replications per grind were recorded.

The shortness of length (1.6 mm) means that the Ra and Rz data falls short of the BS EN ISO1998 international standards for surface roughness measurement. These standards dictate that any evaluation length is 5 times that of λ_C . For example, an evaluation length of 4 mm would be required for 0.8 λ_C to conform to ISO1996 standards (Table 2.3). Using a λ_C of 0.25 would have allowed us to conform to the ISO standards by requiring only a 1.25 mm evaluation length. 0.25 λ_C was initially attempted, but provided unsatisfactory results (the machine was often unable to provide readout data for a λ_C of 0.25 over a 1.6 evaluation length). This study went with the more reliable 0.8 λ_C setting, but with the knowledge that an evaluation length of only 1.6 mm was insufficient to meet ISO standards.

Table 2.3. Roughness sampling length for the measurement of R parameters. The final two columns show the λ_c required for various evaluation lengths if ISO standards are to be met for periodically oscillating profiles. *Credit: (Website 15).*

Measuring condition: R-parameter ISO4288: '96							
Non-periodic profile				Periodic profile or RSm		Measuring Condition	
Ra, Rq, Rsk, Rku or RΔq		Rz, Rv, Rp, Rc, or Rt		RSm (mm)		Sampling length: $\ell_r = \text{CutOff } \lambda_c \text{ (mm)}$	Evaluation length $\ell_n \text{ (mm)} = 5 \times \ell_r$
Over>	Less≤	Over>	Less≤	Over>	Less≤		
0.006	0.02	0.025	0.1	0.013	0.04	0.08	0.4
0.02	0.1	0.1	0.5	0.04	0.13	0.25	1.25
0.1	2	0.5	10	0.13	0.4	0.8	4
2	10	10	50	0.4	1.3	2.5	12.5
10	80	50	200	1.3	4	8	40

A mean value of the 5 replications of Ra Rz measurements per grind was calculated and this mean value was the one used when plotting the results below. Following ISO1998 guidelines, surface roughness measurement lines were selected in a direction that corresponded with the maximum height variations of a grind

area, therefore in this study's case it was always a straight line radiating out from the central pivot point. Mean surface roughness, expressed as Ra (upper graphs) and Rz (lower graphs) for all three rock types, tool tip types, WOB and ultrasonic amplitude are presented in Figure 2.29.

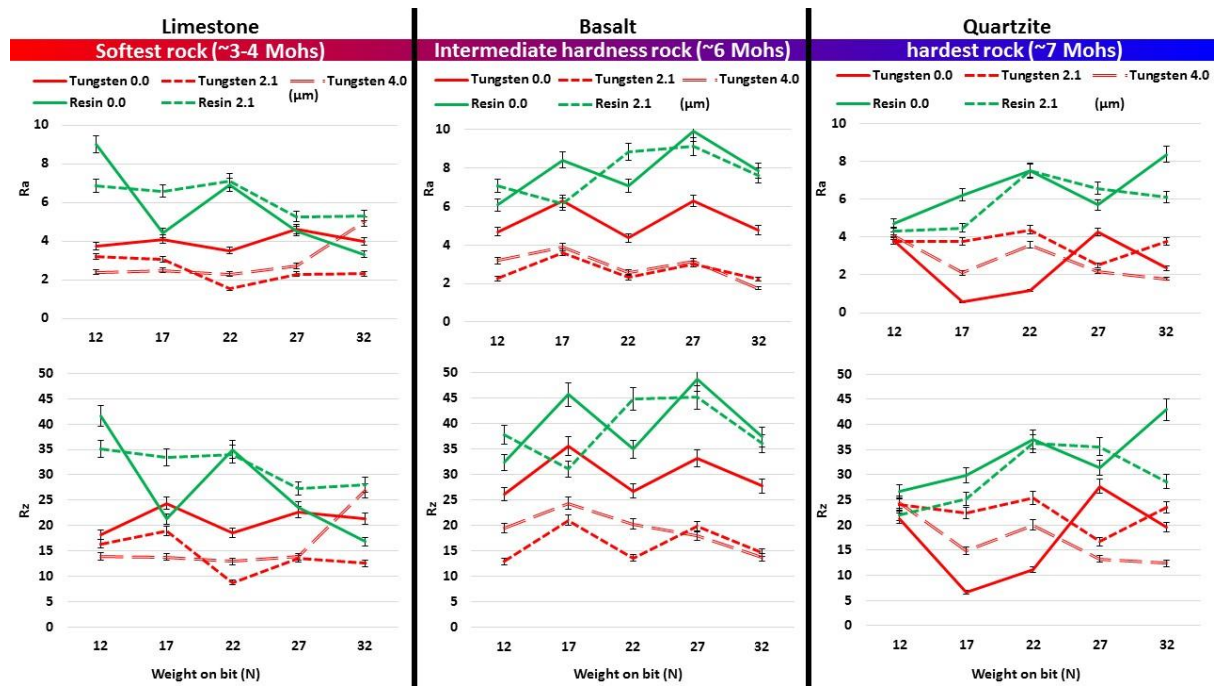


Figure 2.29. Ra and Rz surface roughness for limestone, basalt and quartzite target rocks, using both diamond resin (green) and tungsten carbide (red) tool tips under varying WOB, ultrasonic wave amplitudes and tool tip types. Ra and Rz are without units. Data error for all points is $\pm 5\%$ of measured value (machine error). The use of the Moh scale assumes calcite for limestone and quartz for quartzite and is a qualitative scale of relative hardness.

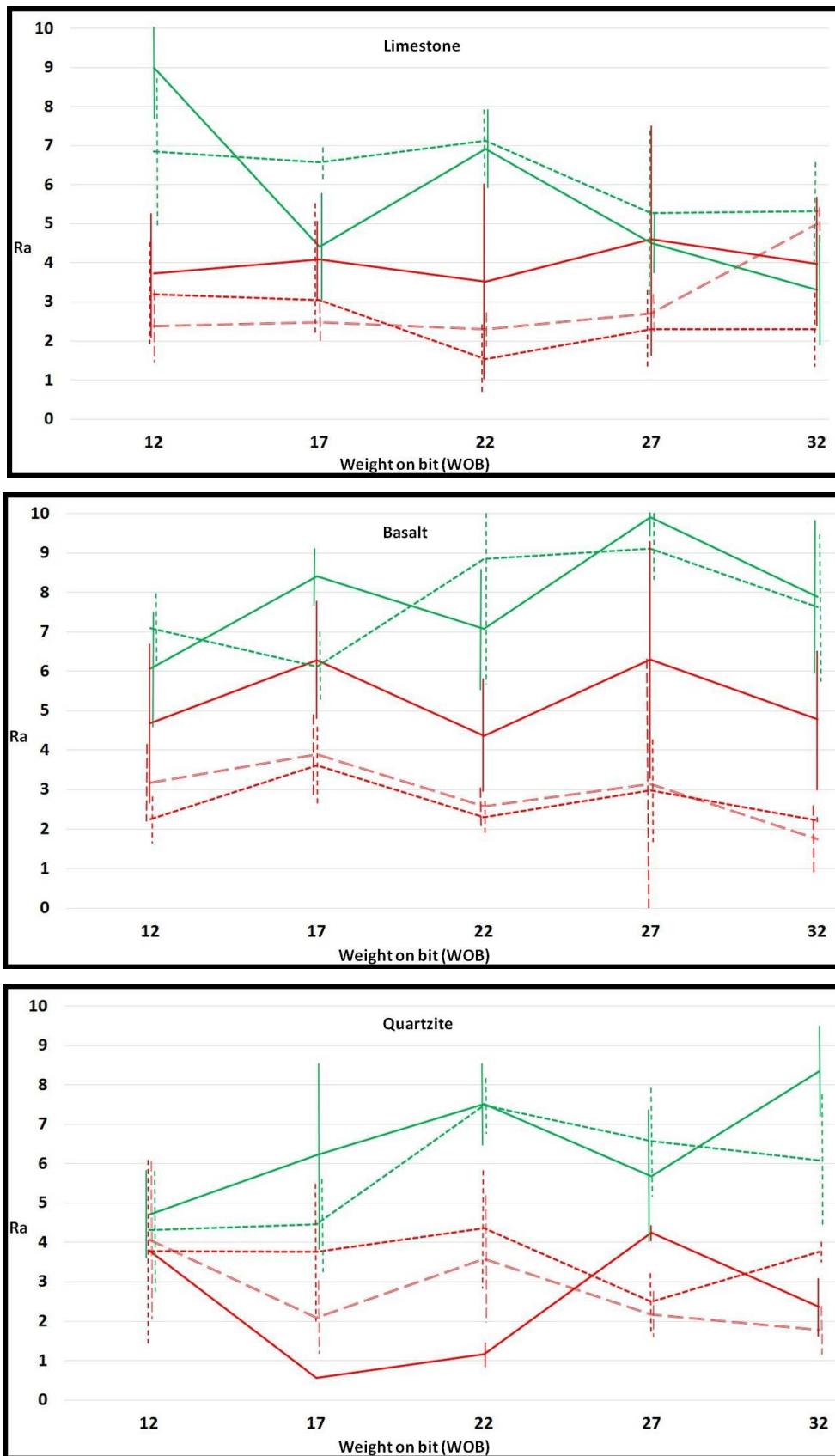


Figure 2.30. Post grind Ra on limestone, basalt and quartzite. Error is standard mean deviation of 5 Ra measurements.

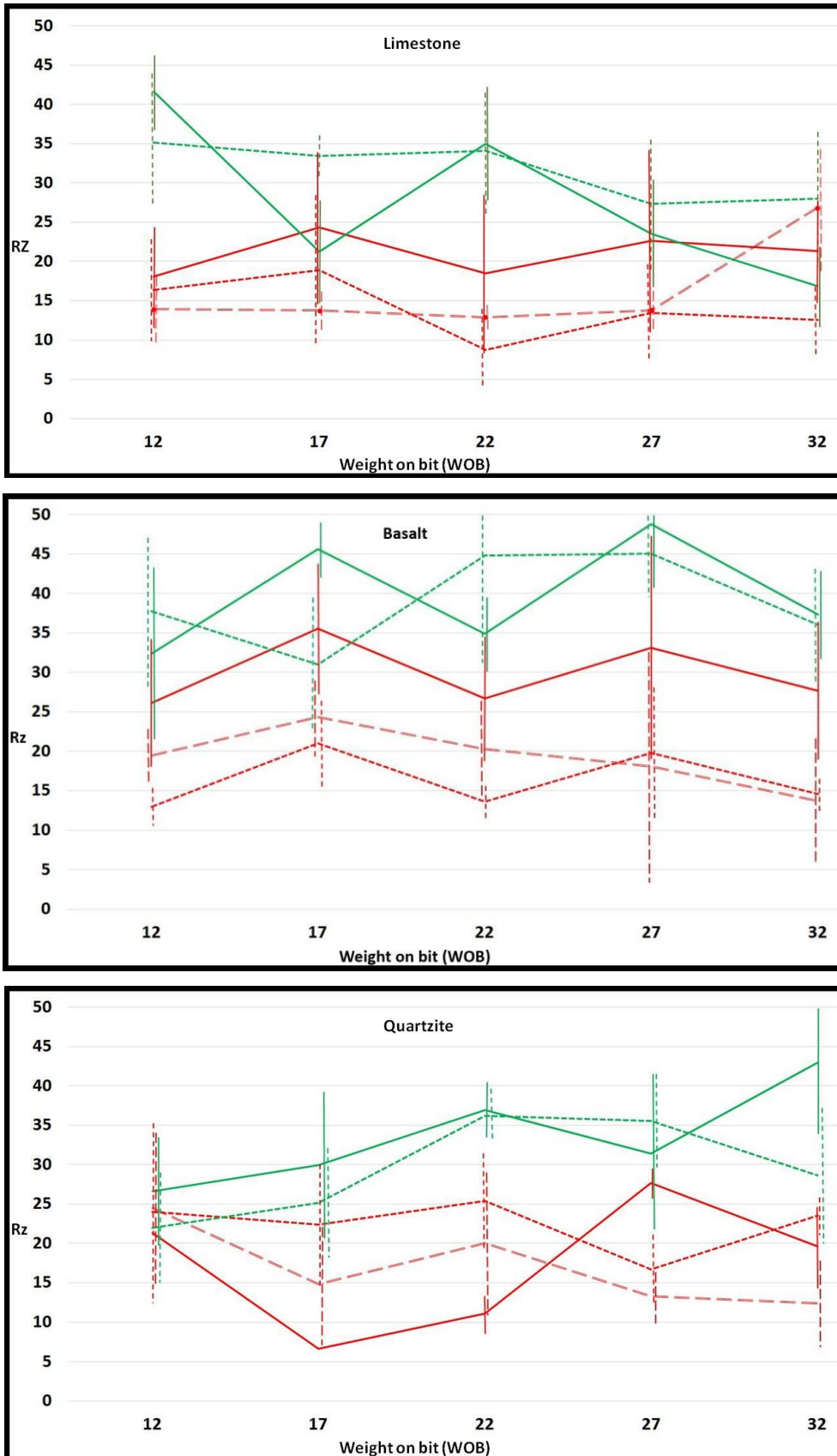


Figure 2.31. Post grind Rz on limestone, basalt and quartzite. Error is standard mean deviation of 5 Rz measurements.

A final method of viewing the surface roughness data is dividing the Ra value by the Rz value for each data point to create a roughness parameter ratio. The Ra data presented in Figure 2.29 has been divided by the Rz data in Figure 2.29, and the results presented in Figure 2.32.

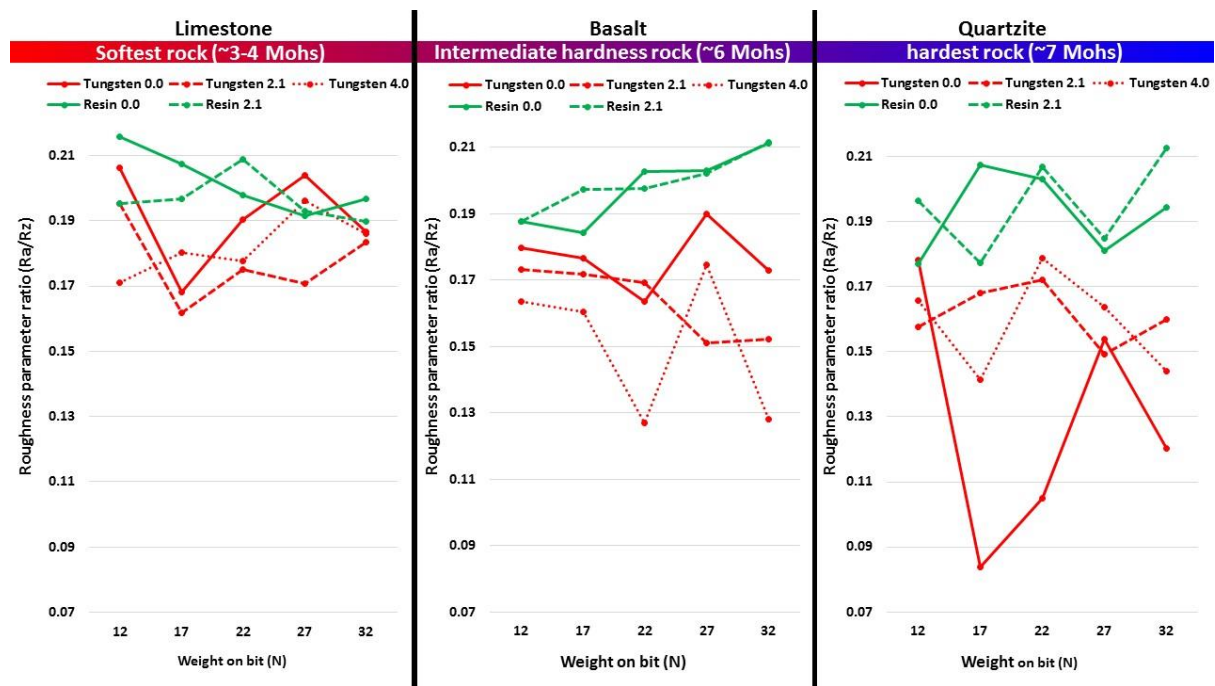


Figure 2.32. Roughness parameter ratio for limestone, basalt and quartzite target rocks, using both diamond resin (green) and tungsten carbide (red) tool tips under varying WOB, ultrasonic wave amplitudes and tool tip types. Ratios do not have error.

2.6.2 Power consumption.

Power consumption signal data was provided by a PC software oscilloscope P100 3-din control unit called Picoscope and is presented in Volts. The Volt readout was multiplied by 10 to provide a Watt output, based on a statement by the equipment manufacturer ($V \cdot 10 = W$). Each run lasted 10 minutes (600 seconds). X axis data was desired in two formats, both as a linear time series and as

increasing WOB. To construct the time series graphs a data point every 15 seconds was selected out of the raw data (Fig. 2.33 as an example for limestone).

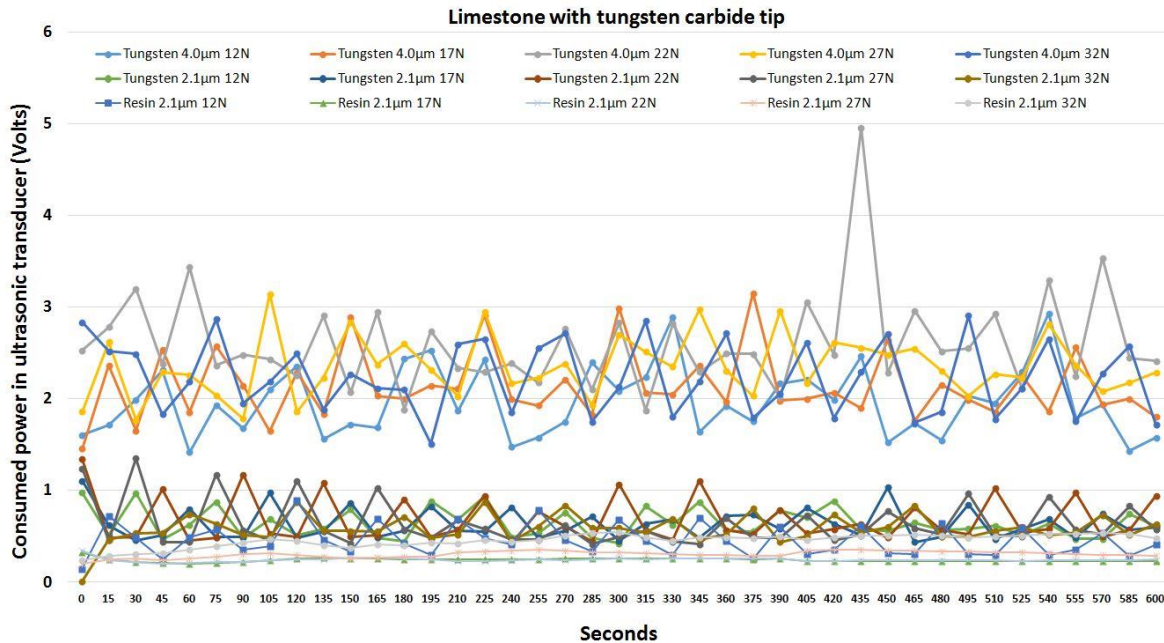


Figure 2.33. Example power consumption data in volts for limestone samples, using tungsten carbide (upper group) and diamond resin (lower group) tips at 2.1 μm and tungsten carbide tips only at 4.0 μm.

Mean trend lines were added and the raw data removed, leaving only the mean lines. Volts were then converted to Watts. Each rock type was given a single Y axis in Watts. On the left hand side of this Y axis is time; on the right hand side is increasing WOB. Each plotted data point is a mean value of the raw data (Fig. 2.34). This single Y axis, two X axis format was chosen to reduce clutter and bulk in what is a large collection of data sets.

Mean power consumption for all three rock types, tool tip types, WOB and ultrasonic amplitude are presented in Figure 2.34. On the limestone at 4.0 amplitude and high WOB, it can be observed that there exists a very steep increase of power consumption over time in the left hand X axis, with the data not continuing to 600 seconds and this corresponds to the rock samples shattering.

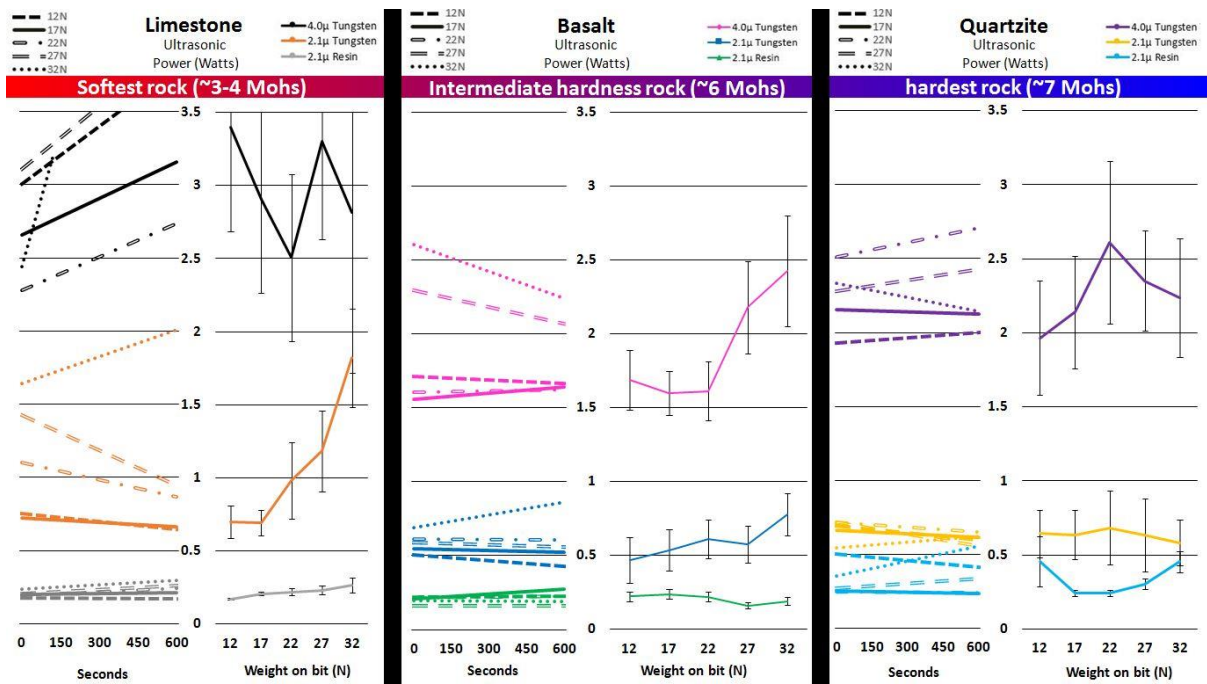


Figure 2.34. Power consumption in Watts for limestone, basalt and quartzite, using diamond resin and tungsten carbide tool tips under varying WOB and ultrasonic wave amplitudes. Y axis is Watts. Left X axis is time. Right X axis is WOB. All plotted data points are mean values of raw data replications. Error bars are standard mean deviation of the time series data.

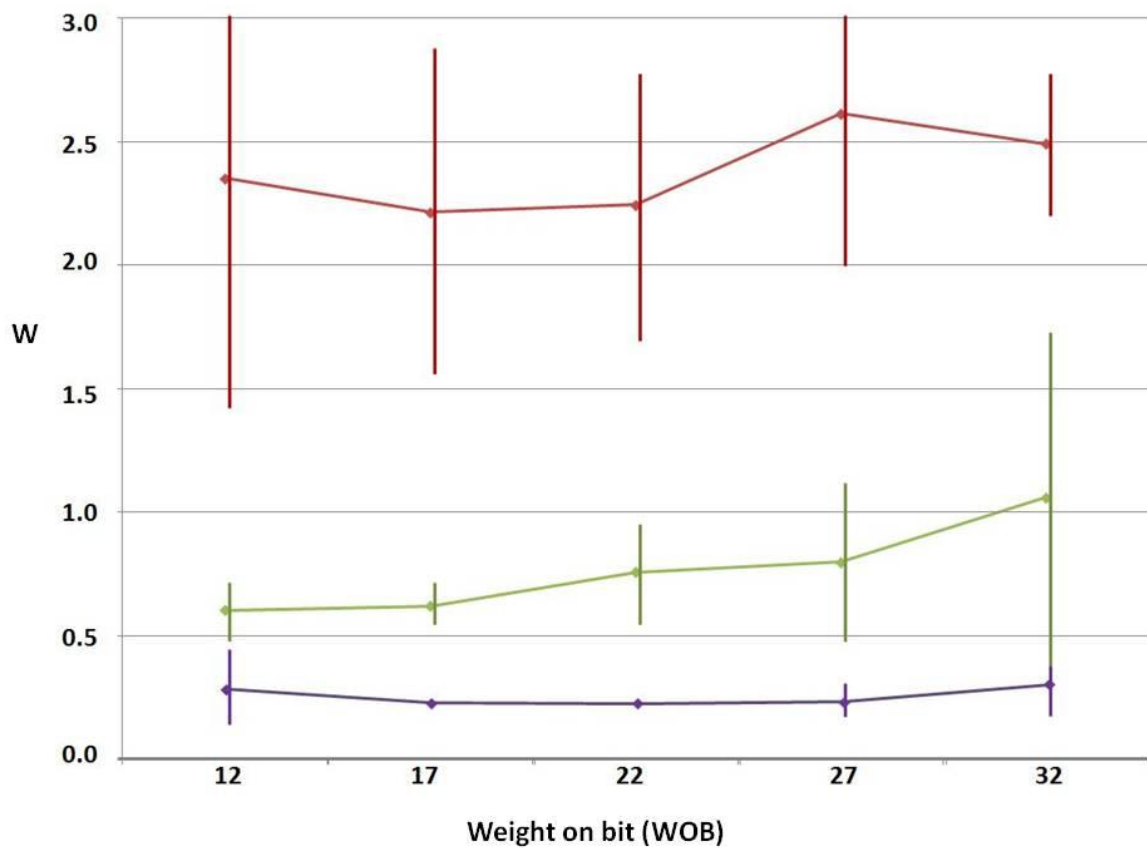


Figure 2.35. Each data point is the mean power consumption of all three rock types combined. Red is tungsten carbide tips at 4.0 μm, green is tungsten carbide tips at 2.1 μm, purple is diamond resin tips at 2.1 μm. Error bars indicate standard mean deviation over three rock type total mean values of raw data. Figure 2.35 is all the data expressed in Figure 2.34 combined into a single graph, ignoring rock type differentiation and change over time.

2.6.3 Thrust force.

Thrust force data were generated as Volts. To convert to Newtons, Volts were multiplied by 20 ($V \cdot 20 = N$), as the charge amplifier on the rig possessed a gain tuned to 20 N/V. As can be observed in an example of 3 WOB datasets (Fig. 2.36) there is a regular, although not identical oscillation of force through time during the experiment.

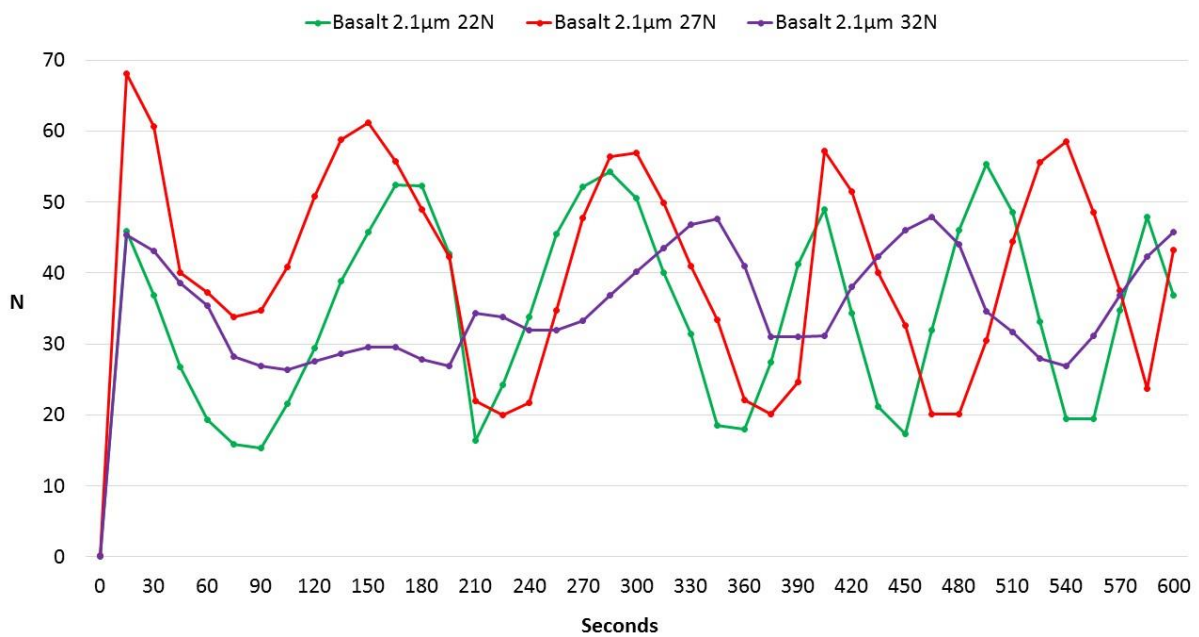


Figure 2.36. Example thrust force oscillations for three WOB data runs (22 N, 27 N, 32 N) on a basalt rock at 2.1 μm wave amplitude over 600 seconds. Force sensor absolute error is ± 0.1 N, which is too small to show given the scale on the Y axis.

This force oscillation is assumed to originate from the uneven surface dimensions of the rock samples (natural uncut, unpolished, rocks were used for testing). A peak in thrust force probably correlates with the tool tip rotating and being forced over a target rock topographic bump. Because the horn was rotating 360° in a fixed axis location and at a fixed speed, any topographic bumps would cause a regular force oscillation. On some samples the rock surface was so rough that there was not 100% contact across the tool tip and the rock surface.

An alternative explanation for regular force oscillation is a recurring wobble within the rig structure; possibly a mixture of both rig wobble and sample surface heterogeneity. If the force oscillation were caused by the rig, then such a rig oscillation might be expected exist as a repeating value in all samples. However, such repeating force oscillation values across samples is not the case (Fig. 2.37), perhaps confirming that it has more to do with inherent rock sample surface roughness. Interpretation of these oscillations will continue in the discussion.

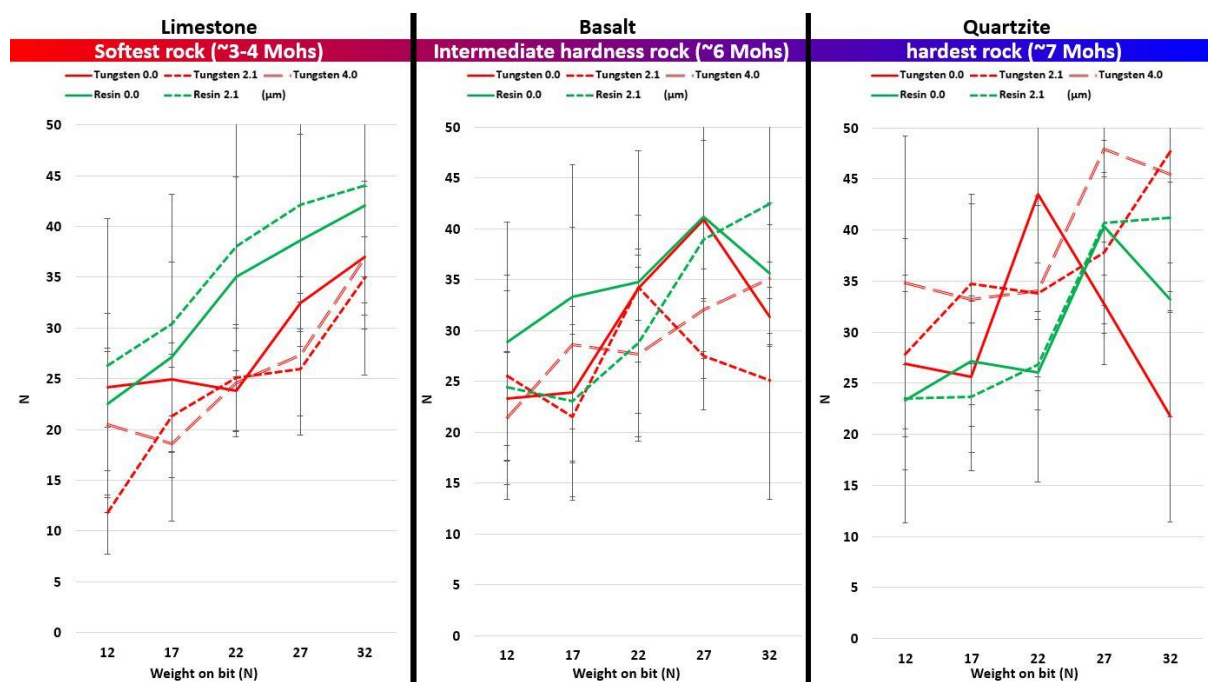


Figure 2.37. Thrust force (N) varying with WOB for limestone, basalt and quartzite, using both diamond resin and tungsten carbide tool tips under varying WOB and ultrasonic wave amplitudes. Each data point represents a mean of 40 data samples over a 600 second period. Force sensor absolute error is 0.1 N (not shown). Error bars are standard mean deviation of 40 measurements for each WOB run.

Figure 2.38 expresses the average value, in Newtons, of all the standard mean deviation error bars per data line in Figure 2.37 (i.e. combining weight on bit runs). Figure 2.38 is the deviation away from the mean thrust force by each rock type for each ultrasonic frequency. As such it does not express the *frequency* of the oscillations shown in Figure 2.36. Figure 2.38, however, highlights a distinct

set of patterns contained in the power data not obvious in the main data results plotted in Figure 2.36 or 2.37. The extent the thrust force deviates from the average has implications for rover tool performance consistency and power budgets.

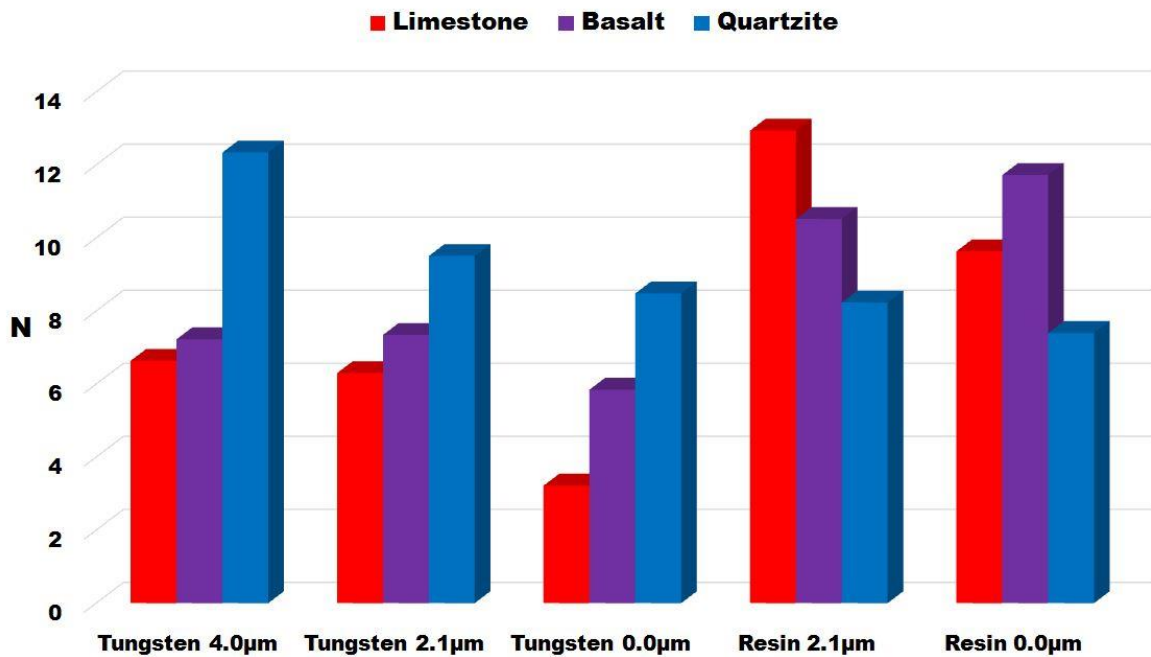


Figure 2.38. Thrust force oscillation (N) amplitude, expressed as standard mean deviation, for limestone, basalt and quartzite (increasing in hardness respectively), using either tungsten carbide or diamond resin cutting tips and various ultrasonic wave amplitudes.

Figure 2.37 expresses the mean thrust force of 40 data samples recorded evenly over 600 seconds for each WOB (with fewer data samples per mean for the limestone samples which shattered mid-run). One anomalous negative reading of -0.354N halfway through the limestone 4.0 12 N run was removed due to a negative Newton load being impossible and therefore attributed to machine error.

To confirm that using average force per run is a valid means of representing real rig dynamics, one would intuitively expect the hardest rock (quartzite) to demand the highest thrust force for penetration to proceed and the softest rock (limestone) to demand the lowest thrust force, with basalt as an intermediate

between the two extremes. The Newton mean for each rock type was calculated by using the sum means of all runs on each rock type, with quartzite possessing a mean thrust force of 33.4 N, basalt 30.5 N and limestone 29.4 N. These mean thrust force values for each rock type fit neatly with the logical predictions above, thereby validating the method of averaging force per run. Mean thrust force for all three rock types, tool tip types, WOB and ultrasonic amplitude are presented in Figure 2.37. The Kistler dynamometer has a detection limit of ≤ 0.02 N, a data hysteresis of $\leq 0.5\%$ full scale output (FSO), and a machine error of $\leq 0.5\%$ FSO. Error bars used for each data point in Figure 2.36 are the standard mean deviation values of the 40 measurements per WOB run (Fig. 2.37).

2.6.4 Material removal rate.

Rig position raw data were generated in Volts. The linear position sensor has a maximum stroke of 200 mm, measured by a linear potentiometer with a range between 0-12V. The Volt data was therefore multiplied by 200 then divided by 12 to convert to mm ($V \times 200 / 12 = \text{mm}$). Because the free mass (WOB) drags the rig towards the sample rock surface, it is assumed that any linear advancement (mm) translates to a directly proportional MRR (mm). Each data run was for 600 seconds. MRR data were processed by taking 40 position sensor data points, one every 15 seconds, ignoring the start position 0 second point (Fig 2.39.A). The mean trend line for each data run was created, the raw data removed to just leave the mean trend line. Then the start and end linear position for each mean trend run was identified and the mm difference between start and finish used as the MRR value (Fig. 2.39.B).

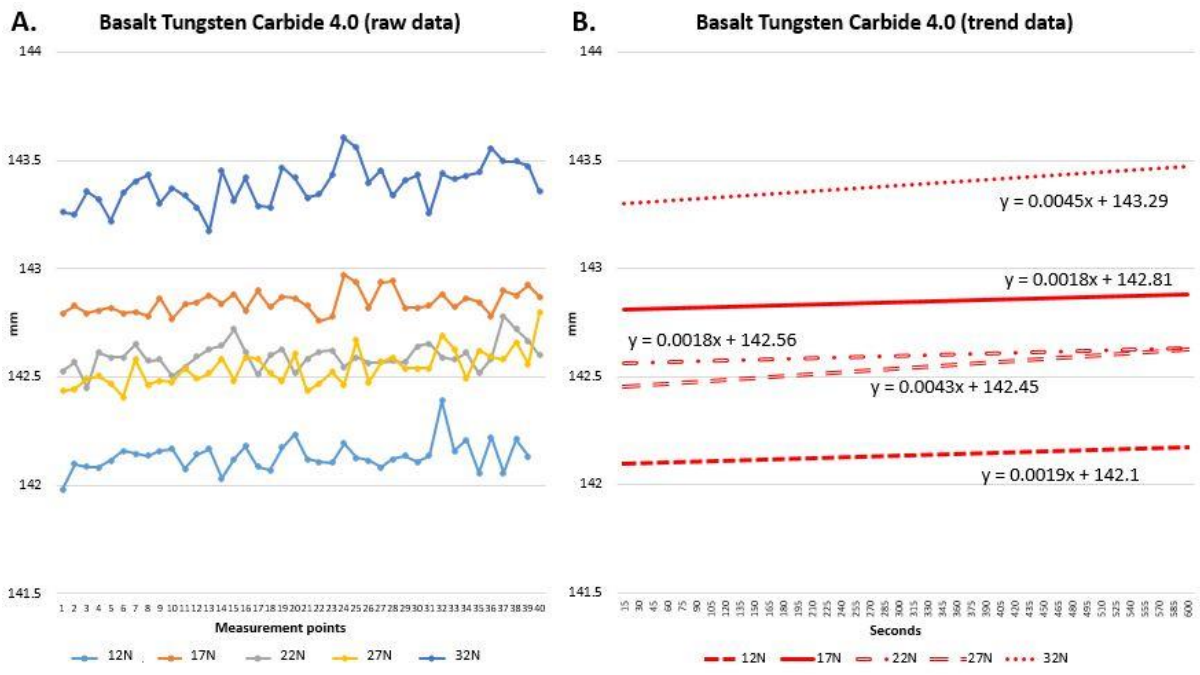


Figure 2.39. Example of data processing for linear advancement/MRR for a basalt target rock using a tungsten carbide tip at 4.0 μm. **A.** Raw data points of mm advancement collected once every 15 seconds, 40 in total over 585 seconds. The sensor range was 200 mm, and in these examples the run started ~142 mm along this sensor range. The absolute error on the linear potentiometer is ≤0.01 mm (error bars excluded as it is too small to show.). **B.** Mean trend lines of the data in A. with raw data removed, measurement points translated into seconds. An absolute error of ≤0.01 mm is maintained along the trend line.

The difference between start and end positions for each mean trend line was divided by the total time measured (585 seconds). This calculation provided a mm advancement per second, which was very low, ~0.00001 mm s⁻¹. To make this extremely low value more recognisable in human terms for tool performance discussions, the results were extrapolated up to mm per hour. MRR for all three rock types, tool tip types, WOB and ultrasonic amplitude are presented in Figure 2.40.

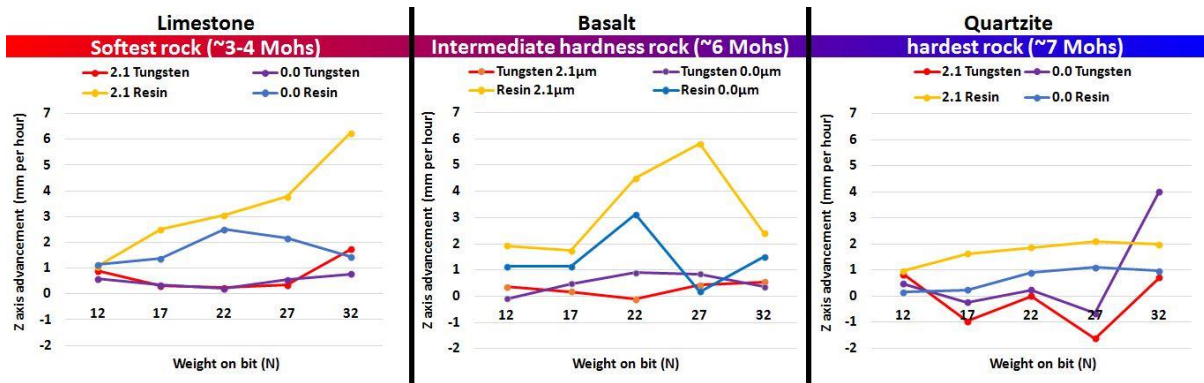


Figure 2.40. Material removal rate (MMR) in mm expressed as a function of Z axis advancement for limestone, quartzite and basalt target rocks, using both diamond resin and tungsten carbide tool tips under varying WOB (X axis) and ultrasonic wave amplitudes. Each data point is the difference between the start and end of the trend line for Z axis advancement, with an absolute machine error of ≤ 0.01 mm, excluded as it is too small to show. The graphs indicate that WOB generally makes little difference to MMR on tungsten tips, whereas increased WOB generally increases MMR on diamond resin when ultrasonically excited.

2.6.5 Error.

Error within all the result data can come from environmental conditions such as temperature, humidity etc. This error was kept to a minimum by maintaining the laboratory at a near constant temperature of $\sim 20^{\circ}\text{C}$ and humidity of $\sim 50\%$ via a thermostat. Experimental data does not include air friction, which although small, is not zero, and would provide an additional source of error which is assumed negligible.

Ra and Rz absolute machine error of the SurfTest SJ-210 is $\pm 5\%$ of measured value; this value was provided via the Mitutoyo manufacturer. There is a reference surface embedded in the drive unit of the SurfTest device which is contrasted against the target surface data.

A potentially high, variable, and unquantified, random error is the target material analyzed. This sample surface error has been minimised by using

qualitatively similar rock samples within each rock type (limestone, quartzite, basalt). Each rock type was collected from the same field site and the same rock exposure within that field site; therefore it might be expected to possess similar mechanical properties such as mineralogy, porosity, hardness etc. However, as any geologist can testify, such petrographic uniformity is rarely true in practice.

WOB error is not quantified, cast iron Newton loads were simply placed on a string running through a pulley and dragging the rig towards the rock target. However, there would be friction caused by the pulley, and certainly friction in the rig's linear runners, both of which would act to reduce WOB value. This error was minimised by daily cleaning of the pulley and runners, as well as checking that the rig would slide without manual assistance and contact the rock with only a 2 N load prior to experiment runs.

The force sensor apparatus has an absolute error of $\pm 0.1\text{N}$. The linear potentiometer has an absolute sensor error of $\leq 0.01\text{ mm}$ per raw data reading and this value was also applied to individual trend line positions. This study mostly uses machine error given by the equipment manufacturer or standard mean deviation. Sometimes the error bars have been excluded for clarity and cited in the graph description.

2.7 Discussion.

2.7.1 Surface roughness.

The stepped cross section topographic profile present in most samples (Fig. 2.25.D) is not surprising. The NASA RAT rotates 360° around two axes, the rotate 3000 rpm axis and the revolve 1 rpm axis, but as these are offset from each other, this provides an overlapping pattern, smoothing out any potential steps. If only one axis of rotation exists, such as on the ultrasonic rig, then the outside resin will travel further and therefore at a faster velocity than the central point, which will not be travelling at all, only pivoting on a fixed point (Fig. 2.41). This variation in resin velocity would cause differential grind rate, causing the centre of the grin not to wear down and thus limit Z axis progress (Myrick *et al.* 2004).

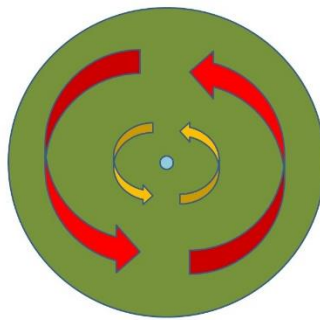


Figure 2.41. Rotation around a single fixed axis, where the outer section moves with the greatest speed (red), the inner section moves with lesser speed (yellow), and the absolute central point does not move (blue).

On diamond resin this faster outside section speed results in the outer resin eroding at a faster rate than the inner resin section, because it is traversing more ground. The outer section wears away to a point where it is no longer contacting the rock surface at all, only the slower moving, slower wearing inner section of resin is grinding. This outer resin non-contact continues until the slower inner section has also worn down and the outer section regains target contact. This speed and wear difference would create the observed V profile (Fig. 2.25.D). The small central peak is caused by the zero travel of the pivot point. The flaw of this

fixed one axis rotation was recognised by the NASA/Honeybee teams and this was the reason they created such a complex multiple motor two rotational axis RAT.

In an ideal set up the ultrasonic rig would also rotate around two axes, however, the engineering complexity and time limits of the project made this prohibitive. The stepped profile does not reduce the validity of the experiment though, as common grinding is being compared with ultrasonics under equal non-ideal conditions. As long as the mechanical movement remains identical, then the experiment remains a fair comparison between diamond resin and tungsten carbide, contrasting the effects of varying WOB and ultrasonic amplitude. What is interesting is that only the diamond resin possessed this stepped profile, and this is further validation of the resin erosion dynamic described above. The tungsten carbide tips did not erode at all over the 600 second grind time, there was no uneven wear and hence a more level grinding profile. This might be concluded as a functional advantage for using tungsten profile over diamond resin.

The patterns displayed by Ra and Rz closely match each other (Fig. 2.29, 2.30, 2.31), which is a positive validation that the measurements accurately reflect reality. One of the most prominent features is that the Ra and Rz values for diamond resin are consistently higher than for tungsten carbide, regardless of ultrasonic amplitude, this remains predominantly true even with the often uncomfortably large error bars for standard mean deviation. This higher Ra Rz for resin provides a very clear and strong case for the use of the hard-wearing tungsten carbide tips on rover grinding tools.

Tungsten carbide provides a superior surface finish compared to diamond resin as a general statement. When ultrasonics are not applied (0 μm) then the error in the standard deviation for most weight on bit runs make this statement one of low confidence; however, when ultrasonics are applied (2.1 μm or 4.0 μm) then even with error the ultrasonic grinding finish is significantly better for most weight on bit runs on all rock types, possibly except for low WOB values on quartzite. It is less clear whether there is any surface roughness advantage

between 2.1 μm or 4.0 μm ultrasonic wave amplitudes, particularly when error is considered.

Increasing WOB seems to make little difference to surface roughness. The Ra Rz data lines (Fig. 2.29, 2.30, 2.31) indicate that increased WOB correlates with increased surface roughness when using diamond resin tips on quartzite and basalt rock types, but increased WOB correlates with reduced roughness for limestone. Such differences possibly highlight the important influence that rock type exerts on grinding instrument results. Tungsten carbide tip grinds appear entirely unaffected by changes in WOB across all wave amplitudes. The Ra/Rz roughness parameter data supports the dynamics described above.

Similar to WOB dynamics, Ra Rz values and trends did not vary particularly between different rock types, again with the exception of limestone. The Ra/Rz roughness parameter supports this, with basalt and quartzite possessing very similar profiles, albeit with an anomalously smooth result for quartzite tungsten carbide without ultrasonics. This anomaly may be due to a smoother pre-grind surface on the quartzite rock sample in question. Limestone possesses a much more tightly grouped set of Ra Rz results, with a higher surface roughness on tungsten carbide runs compared with quartzite and basalt.

These results demonstrate that were a MOUSE to be developed and used in the field, it could operate successfully on a wide variety of Martian rocks, polishing to the same approximate standard and attaining a smoother finish than current diamond resin techniques.

Literature data suggest that surface roughness trends between ultrasonics and common grinding vary greatly and this variation is due to rotational speed, with <1000 rpm common grinding out performing ultrasonics for surface roughness, and >1000 rpm ultrasonics outperforming common grinding (Ning *et al.* 2016). The data from this experiment contradict such literature conclusions, where a low rpm of 14.66 saw ultrasonics out performing common grinding for surface roughness on

all rock types. It would be of considerable interest to conduct further experiments with rig rpm as a variable, assessing how changes in rpm affect Ra and Rz.

The often large error bars of standard mean deviation in Figures 2.30 and 2.31 are a result of only repeating the Ra Rz measurements 5 times per data point. This was a reflection of limited instrument time available and a large number of grinds to measure. Ideally at least 20 Ra Rz measurements should be done on any future tests and this would almost certainly reduce the error values. The Ra Rz with machine error (Fig. 2.29) and the Ra Rz ratio (Fig. 2.32) are included as they provide support for the conclusions drawn from Figures 2.30 and 2.31.

Summary of surface roughness results.

- Tungsten carbide tips consistently provide smoother surfaces than diamond resin tips with or without ultrasonics.
- Tungsten carbide tip surface roughness results appear unaffected by changes in WOB.
- Diamond resin tips and increased WOB, correlates with greater surface roughness on quartzite and basalt, but reduced surface roughness on limestone.
- Tungsten carbide tips used with ultrasonics produces a smoother surface than without ultrasonics.
- Tungsten carbide surface roughness results appear unaffected by changing wave amplitude (2.1 μm , 4.0 μm).

2.7.2 Power consumption.

Power consumption at 4.0 μm is \geq ~10 W higher compared to 2.1 μm wave amplitudes for tungsten carbide on all rock types. It would have been interesting to observe the power difference of diamond resin between 2.1 μm and 4.0 μm , however, the diamond resin disintegrated $>2.1 \mu\text{m}$. At 2.1 μm wave amplitude both tungsten and resin could be compared, with tungsten demanding ~0.5 W more power than the resin on all rock types. It may be stated, therefore, that tungsten carbide tips demand a slightly higher power consumption than diamond resin tips and this is true for all wave amplitudes and rock types.

Increasing WOB appears to make a negligible difference to power consumption when using diamond resin tool tips, certainly not on quartzite and basalt rock samples and only a slight increase in power consumption with increased WOB for limestone. Power consumption when using tungsten carbide tips appear to be more sensitive to WOB, with a general conclusion that increasing WOB correlates with increased power consumption. There are exceptions to this conclusion, as neither tungsten carbide at 4.0 μm on limestone, nor tungsten carbide at 2.1 μm on quartzite, showed much correlation between power and WOB. Tungsten carbide at 4.0 μm for basalt and tungsten carbide at 2.1 μm on limestone showed a particularly strong rise in power consumption above 22 N WOB.

The time series data demonstrates that the statement ‘increasing WOB on tungsten carbide tips increases power consumption’ becomes more complex over time. Many runs seem to show that as time progresses, power consumption lowers, and this would also correlate with penetration depth over time. This dynamic is not visible in the mean graphs, only the time series ones. It becomes more complex still, for there appears to be a pivotal WOB value, unique to each rock type and wave amplitude, where the trend shifts from power reducing over time to power increasing over time, and this trend shift correlates with increasing WOB. To provide a clear example, on tungsten carbide tips at 2.1 μm wave amplitude on basalt rock (Fig. 2.34), 12 to 27 N all display power consumption decreasing over time (left hand time series) until 32 N, when a pivot point is reached and power

consumption increases dramatically with time. The dynamic given in this example is also valid for both tungsten carbide at 2.1 μm on limestone and quartzite, with the change from decreasing power over time to increasing power over time occurring at 32 N.

At 4.0 μm a reverse trend occurs, with low WOB runs displaying an increase of power consumption over time, until a unique WOB pivot point is reached, after which there is a decrease of power consumption over time; except for limestone where all runs show increasing power consumption over time. An example is quartzite, tungsten carbide at 4.0 μm , where 12 N, 22 N and 27 N show increases of power consumption over time with a steeper trend line with higher WOB, until 32 N when the trend sharply reverses to a steep decrease of power over time. On basalt nearly all runs displayed decreasing power consumption with time, suggestive that the WOB tipping point may critically depend on the rock type; this suggestion is supported by the limestone showing increased power consumption with time for all runs and shattering samples. Diamond resin at 2.1 μm did not appear to show any such clear trends on any rock types. It is probable that both rock resistance and wave amplitude play a significant role in observed power dynamics, however, this experiment cannot quantitatively separate their individual contribution.

Reduced power consumption over time (depth of penetration) is expected intuitively, a rough initial grinding surface providing high friction correlating with high power consumption to overcome the friction. As time and depth progresses, the surface becomes smoother due to grinding action and there is less friction, hence less power consumption. This is a feasible explanation for the data runs displaying a reducing power draw over time. The pivoting shift to increasing power consumption over time may partially be a function of rock type. If a rock is comparatively coarse and granular, such as basalt compared to limestone, ground dust does not significantly fill the pore spaces and an increasing WOB shows decreasing power consumption over time. In limestone and quartzite, however, the increased WOB might hammer the ground dust, filling the smaller rock pores in the limestone, making the surface more cohesive, solid and difficult to penetrate,

Page | 143

thus requiring greater power consumption over time; up until a pivotal WOB is used that is forceful enough to overpower this dynamic, whereupon the trend shifts back to reduced power consumption with depth. This shift occurs at 32 N on quartzite, but does not occur at all with the limestone.

At 4.0 μm and high WOB (22 N, 27 N and 32 N) three of the limestone samples shattered before the 600 seconds had elapsed. This rock shattering is through no fault or error of the tool or rig, and perhaps is a clear conclusion that only low ultrasonic wave amplitudes and low WOB are appropriate for use on a Mars rover grinder, where many rock samples under investigation would be both delicate and potentially unable to be repeated, such as fragile carbonates.

Summary of power consumption results.

- Tungsten carbide tips consume more power than diamond resin tips on all rock types and wave amplitudes (Figures 2.34 and 2.35).
- Increased power consumption does not correlate with increased WOB when using diamond resin tips (Figure 2.34 and 2.35).
- At 2.1 μm tungsten carbide tips possess a WOB pivot point where decreasing power consumption with time shifts to increasing power consumption with time (Figure 2.34).
- At 4.0 μm even low WOB samples possess increasing power consumption with time, but higher WOB runs reach a pivot point and reverse to decreasing power consumption with time, or else the rock sample shatters.
- These changes in power consumption with time correlating with WOB and ultrasonic wave amplitude may be intricately associated with rock type and the filling of pore spaces and/or total force in the system.

2.7.3 Thrust force.

The initial oscillation in the thrust force (Fig. 2.36) is likely caused by slopes on the target rock surface causing a rise in thrust force every time a tool tip rotates up a slope. That the oscillations were not identical between samples and rock types, as might be expected were the oscillation attributable to a fault in the rig itself supports this interpretation.

The average of standard mean deviation (SMD) of thrust force (Fig. 2.38) reveals an interesting set of relationships, not obvious in the main data set (Fig. 2.37). When using tungsten carbide tips there is a uniform SMD increase from limestone, basalt to quartzite, and the magnitude of deviation increases as the ultrasonic wave amplitude is increased. When using resin SMD this trend reverses (with one basalt exception at 0.0 μm) and a uniform increase of deviation from quartzite, basalt to limestone takes place, the magnitude of deviation also increasing with increasing wave amplitude.

Quartzite was the hardest rock tested and tungsten carbide tips demonstrated a greatly higher thrust force variation on quartzite than diamond resin tips did. This higher thrust force variation on tungsten carbide is probably due to the tungsten and quartzite being very hard, neither one of abrading much, thus the thrust force rises and falls sharply over unyielding topographic bumps. On the other end of the spectrum, diamond resin is much softer than tungsten and can simply chip and erode its mass against the hard quartzite, thus possess a more stable thrust force over unyielding topographic bumps. This force dynamic reverses when hard quartzite is replaced by soft limestone. Limestone runs had much greater thrust force variation in the resin tip runs compared to the tungsten tip runs. Such a reversal of tool tip performance between rock types might be due to limestone abrading so swiftly against the hard tungsten that little thrust force variation occurs, yet the limestone was just about hard enough to resist the resin, thus demand more force. In conclusion, rock type almost certainly significantly affects thrust force consistency.

Summary of thrust force results.

- Rock type appears to be an important factor in controlling thrust force consistency, judged by standard mean deviation over 40 experimental runs.
 - Hard rock possesses greater thrust force instability than softer rocks when using tungsten carbide tips.
 - Softer rock possesses greater thrust force instability than hard rock when using diamond resin.
- Using and increasing ultrasonic wave amplitude correlates with an increase in thrust force variation with both resin and tungsten tips.

2.7.4 Material removal rate.

Little, if anything, should be concluded from the MRR data in this study. In the design phase there was uncertainty regarding what the penetration rates might be, particularly as the diamond resin was simply a best approximation of the NASA resin. The penetration depth over 600 seconds was far less than hoped for on all rock and tool tip types and wave amplitudes. Often by the end of a run only a partial circle had been ground due to initial rock surface heterogeneity. It is in soft, easily parted material that the deepest, swiftest, most effective penetrations take place. Limestone was the softest rock and also had the least initial surface roughness and it was with limestone that the deepest penetrations occurred, penetration being directly linked to MRR.

Because of this low MRR, the extrapolation (with concomitant error) required to discuss MRR at the mm per hour scale is deemed unacceptable. One might be tempted to state that MRR loosely correlates with higher WOB and that diamond resin possesses a higher MRR than tungsten carbide tips. However, this study refrains from such statements and concludes that the MRR data is too sparse to make such statements. The only statement to be made and lesson learned is that on future experiments, grind time per run must be increased to at least 30 minutes if MRR conclusions are to be drawn, preferably an hour per run.

2.8 Conclusions

The principal conclusion of the study is that the addition of ultrasonics correlate with a smoother surface finish and if applied to Mars rover operations would potentially allow clearer imaging of rock interiors, thereby advancing the Athena science goals of understanding the fate of water on Mars.

The data indicates that if ultrasonics is to be used on rover grinding operations, then diamond resin is not the best tool tip to use. Diamond resin produces a finish with a higher surface roughness than tungsten carbide, with or without ultrasonics applied, and possesses greater thrust force inconsistency. Using a tool tip such as tungsten carbide would dramatically reduce the tool tip wear rate (no wear at all was visually observed during testing, unlike the resin which sometimes disintegrated at 4.0 μm). The tungsten carbide consumed more power than diamond resin, increasing with higher ultrasonic amplitudes.

No particular surface finish advantage is apparent by using 4.0 μm over 2.1 μm ultrasonic wave amplitude. Therefore the lower, less destructive and power efficient 2.1 μm ultrasonic wave amplitude appears most appropriate for rover use.

WOB does not correlate with changes in surface roughness on any tool tip type. Higher WOB did correlate with higher power draw. High WOB on softer rock samples using 4.0 μm caused the samples to shatter. Any development of a rover tool should consider using low WOB and low μm ultrasonic amplitude to avoid damaging delicate geological structures of interest and reducing rover energy expenditure.

This study has demonstrated the potential advantage of using ultrasonics on rover tool grinding operations and also demonstrated the advantage of using tungsten carbide tips over diamond resin. If the project were to be continued and developed further, then the following points would be recommended:

- Scale down the ultrasonic rig to rover mountable dimensions and replace the heavy materials, such as steel, with light weight space ready alternatives such as aluminium, carbon fibre or ideally albernet.
- Explore the use of other hard tool tip materials, including pure synthetic diamond, comparing their performance with tungsten carbide.
- Increase the range of rock types tested and build a database of rock properties and tool responses.
- Explore a wider range of wave amplitudes, seeking an optimal performance wavelength (1.0 μm to 3.0 μm).
- Re-run the material removal rate measurements over the period of hours per run rather than minutes per run to gain a reliable MRR value per rock type.
- Increase the Ra Rz measurements per grind so as to reduce the error bars widths.
- Initiate discussions with space system engineers to collaborate on how to integrate such a tool into a rover operating system and build an operationally ready prototype.

2.9 Acknowledgements.

We are very grateful to the Buehler centre for excellence for assistance developing and producing the diamond resin. Surface roughness metrology was conducted at the Advanced Forming Research Centre at the University of Strathclyde. Adrienne MacArtney's PhD is fully funded by the UK Space Agency and delivered via the Science and Technology Facilities Council (STFC).

2.10 References.

- Agarwal S. (2015). On the mechanism and mechanics of material removal in ultrasonic machining. *International Journal of Machine Tools and Manufacture* 96:1-14.
- Allemang R.J., Brown D.L. (2006). A Complete Review of the Complex Mode Indicator Function (CMIF) with Applications. *University of Cincinnati Structural Dynamics Research Lab*. Available: http://www.sdrl.uc.edu/sdrl/referenceinfo/documents/papers/ISMA2006_CMIF.pdf.
- Amin S. G., Ahmed M. H. M., Youssef H. A. (1995). Computer-aided design of acoustic horns for ultrasonic using finite-element analysis. *Journal of Materials Processing Technology* 55:254-260.
- Amini S., Soleimanimehr H., Nategh M. J., Abudollah A., Sadeghi M. H. (2008). FEM analysis of ultrasonic-vibration-assisted turning and the vibratory tool. *Journal of Materials Processing Technology* 201:43-47.
- Barthel K. W., Swinburne N. H. M., Conway M. S. (1994). *Solnhofen: A study in Mesozoic palaeontology*. Cambridge: Cambridge University Press.
- Bartlett P. W., Basso B., Kusack A., Wilson J., Zacny K. (2005). New Rock Physical Properties Assessments From the Mars Exploration Rover Rock Abrasion Tool (RAT). *NASA Astrophysics Data System (ADS)*.
- Basa K. B. C., Gomez K. P. S., Navarro-Tanoco F. B., Co C. B. (2012). Design of a varying ultrasonic frequency amplifier. TENCON 2012 - 2012 IEEE Region 10 Conference. DOI: 10.1109/TENCON.2012.6412169.
- Brehl D. E., Dow T. A. (2008). Review of vibration-assisted machining. *Precision Engineering* 32(3):153-172.
- Caldwell W. G. E., Young G. M. (2011). Early Carboniferous minor intrusions of the Clyde Plateau: new data from the Cumbrae islands. *Earth and Environmental Science Transactions of the Royal Society of Edinburgh* 102:227-251.
- Chen H., Tang J., Zhou W. (2013). An experimental study of the effects of ultrasonic vibration on grinding surface roughness of C45 carbon steel. *International Journal Of Advanced Manufacturing Technology* 68(9-12):2095-2098.
- Eyding J., Wilkening W., Postert T. (2002). Brain perfusion and ultrasonic imaging techniques. *European Journal of Ultrasound* 16(1):91-104.
- Gorevan S. P., Myrick T., Davis k., Chau J. J., Bartlett P., Mukherjee S., Anderson R., Squyres S. W., Arvidson R. E., Madsen M. B., Bertelsen P., Goetz W., Binou C. S., Richter L. (2003).

Rock Abrasion Tool: Mars Exploration Rover mission. *Journal of Geophysical Research* 108:E12 8068.

Herkenhoff K. E., Squyres S. W., Bell J. F., Maki J. N., Arneson H. M., Bertelsen P., Brown D. I., Collins S. A., Dingizian A., Elliott S. T., Goetz W., Hagerott E. C., Hayes A. G., Johnson M. J., Kirk R. L., McLennan S., Morris R. V., Scherr L. M., Schwochert M. A., Shiraishi L. R., Smith G. H., Soderblom L. A., Sohl-Dickstein J. N., Wadsworth M. V. (2003). Athena Microscopic Imager investigation. *Journal of Geophysical Research: Planets* 108:E12.

Hoek E., Brown E. T. (1997). Practical estimates of rock mass strength. *International Journal of Rock Mechanics and Mining Sciences* 34(8):1165-1186.

Kalpakjian S. (2008). *Manufacturing Processes for Engineering Materials*. Upper Saddle River, NJ 07458: Pearson Education, Inc. 552-553. ISBN 0-13-227271-7.

Klingelhöfer G., Morris R. V., Bernhardt B., Rodionov D., De Souza P. A., Squyres S. W., Foh J., Kankleit E., Bonnes U., Gellert R., Schröder C., Linkin S., Evlanov E., Zubkov B., Prilutski O. (2003). Athena MIMOS II Mössbauer spectrometer investigation. *Journal of Geophysical Research: Planets* 108:E12.

Li Z., Fang F., Gong Hu., Zhang X. (2013). Review of diamond-cutting ferrous metals. *The International Journal of Advanced Manufacturing Technology* 68(5):1717-1731.

Li X. (2014). *Modelling and autoresonant control design of ultrasonic assisted drilling applications*. Thesis: University of Leicester.

Nad M. (2010). Ultrasonic horn design for ultrasonic machining technologies. *Applied and Computational Mechanics* 4:79-88.

Ning F. D., Cong W. L., Pei Z. J., Treadwell C. (2016). Rotary ultrasonic machining of CFRP: A comparison with grinding. *Ultrasonics* 66:125-132.

Manthey W., Kroemert N., Magori V. (1992). Ultrasonic transducers and transducer arrays for applications in air. *Measurement Science and Technology* 3:249-261.

Myrick T., Davis K., Wilson J. (2004). Rock Abrasion Tool. *Proceedings of the 37th Aerospace Mechanisms Symposium*. Available:
<http://www.esmats.eu/amspapers/pastpapers/pdfs/2004/myrick.pdf>

Rieder R., Gellert R., Brückner J., Klingelhöfer G., Dreibus G., Yen A., Squyres S. W. (2003). The new Athena alpha particle X-ray spectrometer for the Mars Exploration Rovers. *Journal of Geophysical Research: Planets* 108:E12.

Schwarz B. J., Richardson H. M. (1999). Experimental Modal Analysis. *Association of Asset Management Professionals*. Available:
<http://www.maintenance.org/fileSendAction/fcType/0/fcOid/399590942963653618/filePoi>

nter/399590942964787702/fodoid/399590942964787700/28-
_Experimental_Modal_Analysis.pdf.

Seah K. H. W., Wong Y. S., Lee L. C. (1993). Design of tool holders for ultrasonic machining using FEM. *Journal of Materials Processing Technology* 37:801-816.

Spier R. F. G. (1961). Ultrasonic Cleaning of Artifacts: A Preliminary Consideration. *American Antiquity* 26(3):410-414.

Squyres S., Arvidson R., Baumgartner E., Bell J., Christensen P., Gorevan S., Herkenhoff K., Klingelhofer G., Madsen M., Morris R., Rieder R., Romero R. (2003). Athena Mars rover science investigation. *Journal Of Geophysical Research-Planets* 108:E12.

Takács G., Rohal-Ilkiv B. (2012). Basics of Vibration Dynamics. In: Takács G., Rohal-Ilkiv B. *Model Predictive Vibration Control*. London: Springer. 25-64.

Teimouri R., Baseri H., Moharami R. (2015). Multi-responses optimization of ultrasonic machining process. *Journal of Intelligent Manufacturing* 26(4):745-753.

Thomason B. J., Bridges N. T., Cohen J., Hurowitz J. A., Lennon A., Paulsen G., Zacny K. (2013). Estimating rock compressive strength from rock abrasion tool (RAT) grinds. *Journal of Geophysical Research: Planets* 118:1233-1244.

Thomson B. J., Bridges N. T., Cohen J., Hurowitz J. A., Lennon A., Paulsen G., Zacny K. (2013). Estimating rock compressive strength from Rock Abrasion Tool (RAT) grinds. *Journal of Geophysical Research: Planets* 118(6):1233-1244.

Thomson B. J., Hurowitz J. A., Baker L. L., Bridges N. T., Lennon A. M., Paulsen G., Zacny K. (2014). The effects of weathering on the strength and chemistry of Columbia River Basalts and their implications for Mars Exploration Rover Rock Abrasion Tool (RAT) results. *Earth and Planetary Science Letters* 400:130(15).

Uchino K. (2010). Manufacturing Technologies for Piezoelectric Transducers. In: *Advanced Piezoelectric Materials - Science and Technology*: Woodhead Publishing.

Vig J.R. (1993). Military applications of high accuracy frequency standards and clocks. *IEEE Transactions on Ultrasonics, Ferroelectrics and Frequency Control* 40(5):522-527.

Wang Y., Lin B., Zhang X. (2014). Research on the system matching model in ultrasonic vibration-assisted grinding. *International Journal Of Advanced Manufacturing Technology* 70(1-4):449-458.

Website 1: Jet Propulsion Laboratory. (2011). *Photojournal*
<https://photojournal.jpl.nasa.gov/catalog/PIA13982>

- Website 2: Wikipedia. *File:MER Rock Abrasion Tool.JPG*
https://commons.wikimedia.org/wiki/File:MER_Rock_Abrasion_Tool.JPG
- Website 3: Jet Propulsion Laboratory. (2004). *Photojournal*
<https://photojournal.jpl.nasa.gov/catalog/PIA06792>
- Website 4: Jet Propulsion Laboratory. (2005). *Press Release Images: Spirit*. Available:
<https://mars.nasa.gov/mer/gallery/press/spirit/20050112a.html>
- Website 5: Jet Propulsion Laboratory. (2004) *Press Release Mars Exploration Rover Mission Status*. Available: <https://mars.nasa.gov/mer/newsroom/pressreleases/20040901a.html>
- Website 6: Universe Today. (2016). *Latest Panoramic View From Mars Rover*. Available:
<https://www.universetoday.com/96153/latest-panoramic-view-from-mars-rover/>
- Website 7: Jet Propulsion Laboratory. (2004). *Photojournal PIA05661: A Grind Well Done*. Available:
<https://photojournal.jpl.nasa.gov/catalog/PIA05661>
- Website 8: NASA. (2006). *Spirit and Opportunity Mars Exploration Rovers Looking for Changes in Soil over Time*. Available:
https://www.nasa.gov/mission_pages/mer/images/pia08455.html
- Website 9: NDT Resource Centre. *Introduction to Ultrasonic Testing*. Available: <https://www.nde-ed.org/EducationResources/CommunityCollege/Ultrasonics/Physics/wavepropagation.htm>
- Website 10: Science Learning Hub. *Earth Waves*. Available:
<https://www.sciencelearn.org.nz/images/353-earth-waves>
- Website 11: PI Piezo Technology. (2017). *Piezoceramic Components*. Available:
<https://www.piceramic.com/en/products/piezoceramic-components/>
- Website 12: NDT Resource Centre. (2017). *Piezoelectric Transducers*. Available: <https://www.nde-ed.org/EducationResources/CommunityCollege/Ultrasonics/EquipmentTrans/piezotransducers.htm>
- Website 13: Honeybee Robotics. (2015). *Rock Abrasion Tool*. Available:
<http://www.honeybeerobotics.com/portfolio/rock-abrasion-tool/>
- Website 14: Cornell University. (2005). *Rock Abrasion Tool (RAT)*. Available:
http://athena.cornell.edu/pdf/tb_rat.pdf
- Website 15: Inspection engineering. (2016). *Definition of Surface texture and Stylus instrument*. Available:
<http://www.inspectionengineering.com/Images/SurfaceFinishExplain.pdf>
- Wyatt M. B., McSween H. Y., Tanaka K. L., Head J. W. (2004). Global geologic context for rock types and surface alteration on Mars. *Geological Society of America* 32(8):654-648.

Xu W. Z., Zhang L. C. (2015). Ultrasonic vibration-assisted machining: principle, design and application. *Advances in Manufacturing* 3(3):173-192.

Chapter 3.

Terrestrial ophiolite zoned carbonates compared to ALH 84001 early Mars carbonates: Subsurface environments capable of supporting life.

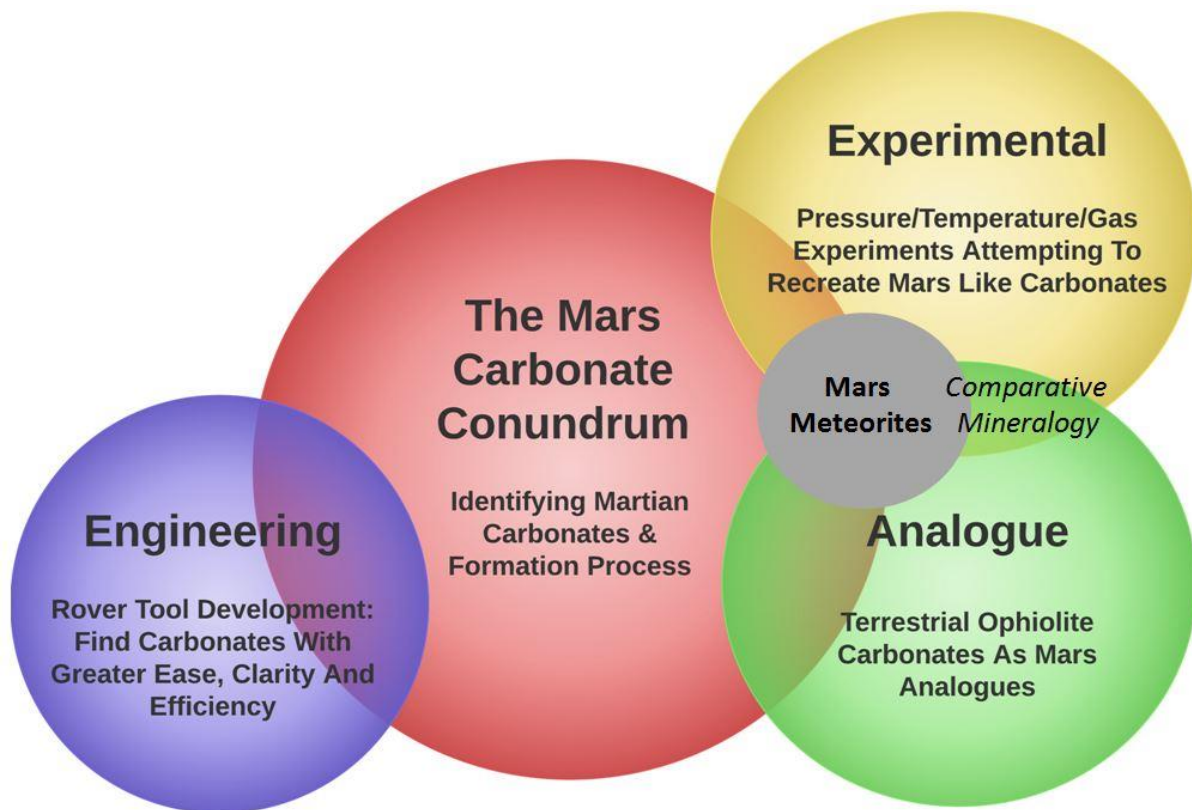


Figure 3.1. The carbonate conundrum that this PhD thesis seeks to address (red circle), along with the different spheres of research used to approach this question. These spheres of research correspond to the three main thesis chapters: engineering (chapter 2), analogues (chapter 3), and experimental (chapter 4). Overlapping circles indicate where chapter and research content overlap and support each other, allowing for comparative mineralogy.

Abstract.

The physical and chemical processes involved in the evolution and loss of the Mars atmosphere are varied and complex. This chapter begins with a summary and literature review of crust - atmosphere interaction processes on Mars. Beginning with surface geology and hydrology, particular attention is paid to carbonates and hydrous alteration products such as clays, and the role of sulphur. The ongoing debates around whether early Mars was warm and wet or cold and dry are discussed, and a theory of localised punctuated hyper carbonation is forwarded. A brief introduction to the Martian meteorites is also provided, with special focus on how their mineralogy can inform our understanding of Martian climate change. The literature review then expands to include terrestrial ophiolites, specifically the Leka ophiolite in Norway and the Semail ophiolite in the United Arab Emirates. Comparisons of geology and hydrology are made between ophiolites and Mars, and the relative formation environments for carbonates discussed.

The aim of the chapter is to compare carbonates found in Martian meteorites with those found in terrestrial ophiolites using light microscopy and scanning/transmission electron microscopy. ALH 84001 is a Martian meteorite representing early Mars, and Lafayette represents more recent Mars. Semail represents a dry but hot hydrological Mars geology analogue with abundant carbonates of all varieties; and Leka a wet but cold one analogue with no observed carbonates but extensive serpentinisation. Neither analogue is a perfect representative of early Mars. There are strong chemical and physical correlations between the early Mars carbonates in ALH 84001 and the Semail ophiolite carbonates; features in the Leka ophiolite and Lafayette correlate less well with each other, or with Semail and ALH 84001. Semail carbonates are known to zone into chemically distinct Mg or Ca - Mg carbonates depending on the hydrology of local aquifers, with distinctive water chemistry types. This study proposes that a similar division of chemically distinctive aquifers may be responsible for Mars carbonate zonations, with the higher Fe content in Mars carbonates caused by the higher Fe content in Martian olivine compared to Semail olivine.

Abbreviations

ALH	Allan Hills.
BSE	Back Scatter Electron.
CRISM	Compact Reconnaissance Imaging Spectrometer for Mars.
EDXS	Energy-Dispersive X-ray Spectroscopy.
EMPA	Electron probe micro-analyzer.
FIB	Focussed Ion Beam.
HiRISE	High Resolution Imaging Science Experiment.
LOC	Leka Ophiolite Complex.
Ma	Mega annum (a million years).
MGS	Mars Global Surveyor.
MOLA	Mars Orbiter Laser Altimeter.
MRO	Mars Reconnaissance Orbiter.
MSSS	Malin Space Science Systems.
SEM	Scanning Electron Microscope.
SMOW	Standard Mean Ocean Water.
SPLD	South Polar Layered Deposits.
TEM	Transmission Electron Microscope.
TES	Thermal Emission Spectrometer.

Chapter 3 contents.

	Page
3.1 A review of Mars geology and hydrology.	154 - 201
3.1.0 Introduction and objectives.	159 - 161
3.1.1 Geology.	162 - 164
3.1.2 Hydrology	164 - 174
3.1.2.1 Water on modern Mars.	164 - 167
3.1.2.2 Water on past Mars.	167 - 169
3.1.2.3 Warm and wet or cold and icy?	169 - 172
3.1.2.4 Punctuated hyper carbonation hypothesis.	172 - 174
3.1.3 Carbonates and clays.	174 - 178
3.1.4 Sulphur.	178 - 181
3.1.5 Atmosphere.	182 - 185
3.1.6 Martian meteorites.	186 - 201
3.1.6.1 Overview.	186 - 188
3.1.6.2 Verifying meteorite age and Martian origin.	189 - 191
3.1.6.3 ALH 84001: Carbonate formation on early Mars.	192 - 200
3.1.6.4 Lafayette: Carbonate formation on recent Mars.	201
3.2 A review of terrestrial ophiolites.	202 - 211
3.2.1 Introduction.	202 - 205
3.2.2 The Leka ophiolite, Norway.	206 - 209
3.2.3 The Semail ophiolite, Oman and United Arab Emirates.	210 - 211

3.3	Methods.	212 - 214
3.3.1	Quantitative SEM analysis methods.	212 - 214
3.3.2	TEM analysis methods.	214
3.4	Results.	215 - 234
3.4.1	Mars.	216 - 227
3.4.1.1	ALH 84001 results.	216 - 221
3.4.1.2	Lafayette results.	222 - 227
3.4.2	Terrestrial.	228 - 234
3.4.2.1	Leka ophiolite results.	228 - 229
3.4.2.2	Semail ophiolite results.	229 - 234
3.5	Discussion.	235 - 249
3.5.1	ALH 84001.	235 - 239
3.5.2	Lafayette.	240 - 242
3.5.3	Leka ophiolite.	242 - 244
3.5.4	Semail ophiolite.	245 - 249
3.6	Conclusions.	249 - 252
3.7	Acknowledgements.	252
3.8	References.	255 - 274

3.1 A history of Mars.

3.1.0 Introduction and objectives.

The atmosphere of a planet plays a profound role in determining surface environmental conditions such as temperature, pressure and the availability of water (Walker *et al.* 1981). Planetary atmospheres act as protective shields against solar radiation (Bouville & Lowder, 1988), and depending upon atmospheric composition and density, can nurture, poison or smother the possibility of life emerging and continuing to exist.

Yet atmospheres do not exist in physical isolation, they are intimately bound to the planet's rocky crust via chemical exchange (Clifford, 1993; Weisbrod *et al.* 2009) and supported by magnetic geodynamics deep within the planet's core (Dehant *et al.* 2007). Neither are atmospheres static and unchanging; they fluctuate and evolve through geological time. This atmospheric evolution is not always slow and it is certainly not linear.

Major events such as large meteorite impacts (Toon *et al.* 1996), or the shutting down of magnetospheres (Dehant *et al.* 2007) can rapidly alter a planet's atmosphere (Dehant *et al.* 2007). Chemical feedbacks and tipping points can also alter an atmosphere over geologically short time frames. This thesis explores the evolution of Mars' atmosphere, focussing on the relationship between the atmospheric reservoir and the mineral surface, specifically, the loss of atmospheric CO₂ via the formation of mineral carbonate.

The formation of mineral carbonate draws down atmospheric CO₂ and liquid water is consumed through intermediate mineral hydration reactions such as serpentinisation. Locating carbonates on Mars and understanding their formation process is critical to unravelling the planet's climate history and loss of the early atmosphere.

Satellite data (Calvin *et al.* 1994; Ehlmann *et al.* 2008), rover and lander discoveries (Mars Pathfinder Rover team, 1997; Boynton *et al.* 2009; Morris *et al.* 2010), and analysis of meteorites (Gooding *et al.* 1988; Treiman *et al.* 1993; McKay

et al. 1996; Scott *et al.* 1997; Valley *et al.* 1997; Vicenzi & Eiler, 1998) all provide uniquely specific insights into Martian carbonate mineral discoveries. Yet a wealth of lessons can also be drawn by comparing this Martian data with known and well analysed terrestrial carbonate forming environments. The terrestrial analogue maxim being:

‘If Martian and terrestrial mineralogy is chemically and physically similar then it may have formed in similar environments’

This maxim will never be 100 % accurate and Martian carbonates are unlikely to find their identical match on Earth. The two-planet’s gravity, magnetism, atmospheric composition and a range of other factors will never be of equal nature. However, such inequalities do not render the maxim without merit, and when visually and chemically similar carbonates and mineral alteration features to Mars are found on Earth (Fig. 2.1) they can prompt fresh ideas, validate existing ideas on formation environments, or constrain likely chemical processes at work.

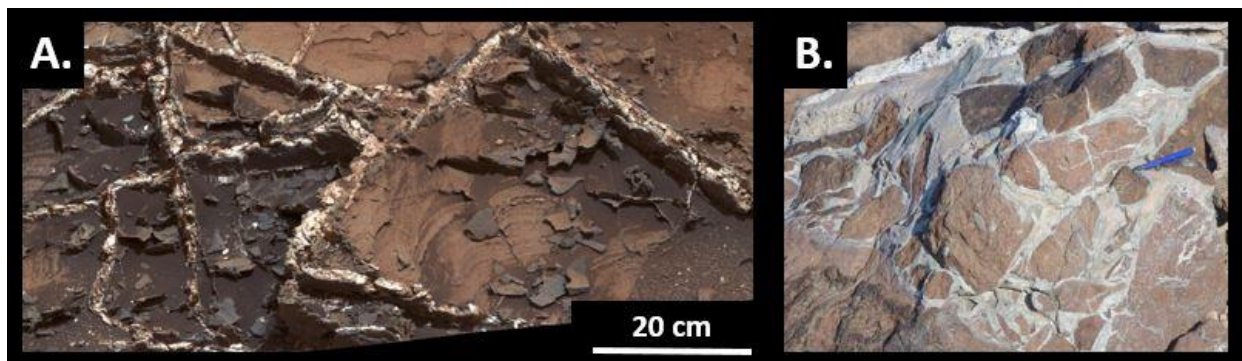


Figure 3.2. A. Curiosity rover Mastcam image from ‘Garden City’, lower Mt. Sharp, Mars, showing fluid alteration veins of calcium sulfate, cristobalite and quartz within a mudstone. *Credit: Nachon et al. (2017).* B. Dolomite carbonate in cracks within a listvenite outcrop at Wadi Mansah, Oman. *Credit: Falk, (2014).*

This study reviews Mars geology, hydrology and atmospheric evolution, focussing on carbonates, sulphur and CO₂ atmospheric drawdown. The study then presents specific carbonate examples in two Martian meteorites selected to represent early and more recent Mars. Terrestrial analogues of Martian carbonate are then sought in two ophiolites, the Norwegian Leka and United Arab Emirates Semail. Carbonates comparable to Mars are only discovered in the Semail samples and are analysed both quantitatively and qualitatively before being compared with carbonates in Martian meteorite ALH 84001. As with all comparative analysis, the lack of an exact match in the Semail carbonates, and the lack of any carbonates in the Leka samples, raises questions and hypothesis as to why there is not a match with Mars, and are therefore useful. Possible dynamics of water and CO₂ availability on early and recent Mars are suggested based on the results of this study, and what is known and observed in terrestrial ophiolite systems.

Objectives.

- 3. A.** Review Mars geology, specifically the interaction of water and CO₂ with the planet's crust through geological time, and evaluate a model of localised punctuated hyper carbonation.
- 3. B.** Analyse carbonates and other minerals in two Martian meteorites, ALH 84001 and Lafayette, representative of early and recent Mars, respectively. To present detailed analysis of glass replacement by carbonate in ALH 84001 and suggest models of formation for this glass - carbonate reaction.
- 3. C.** Analyse carbonates and hydrated minerals in terrestrial ophiolites, and contrast and compare them with the Martian meteorites of objective 3.B.
- 3. D.** To propose that early Mars carbonate zonation in ALH 84001 may be caused by ophiolite style type 1 - 4 type water aquifer flows.

3.1.1 Geology.

3. A. Review Mars' geology, specifically the interaction of water and CO₂ with the planet's crust through geological time, and to propose a model of localised punctuated hyper carbonation on Mars.

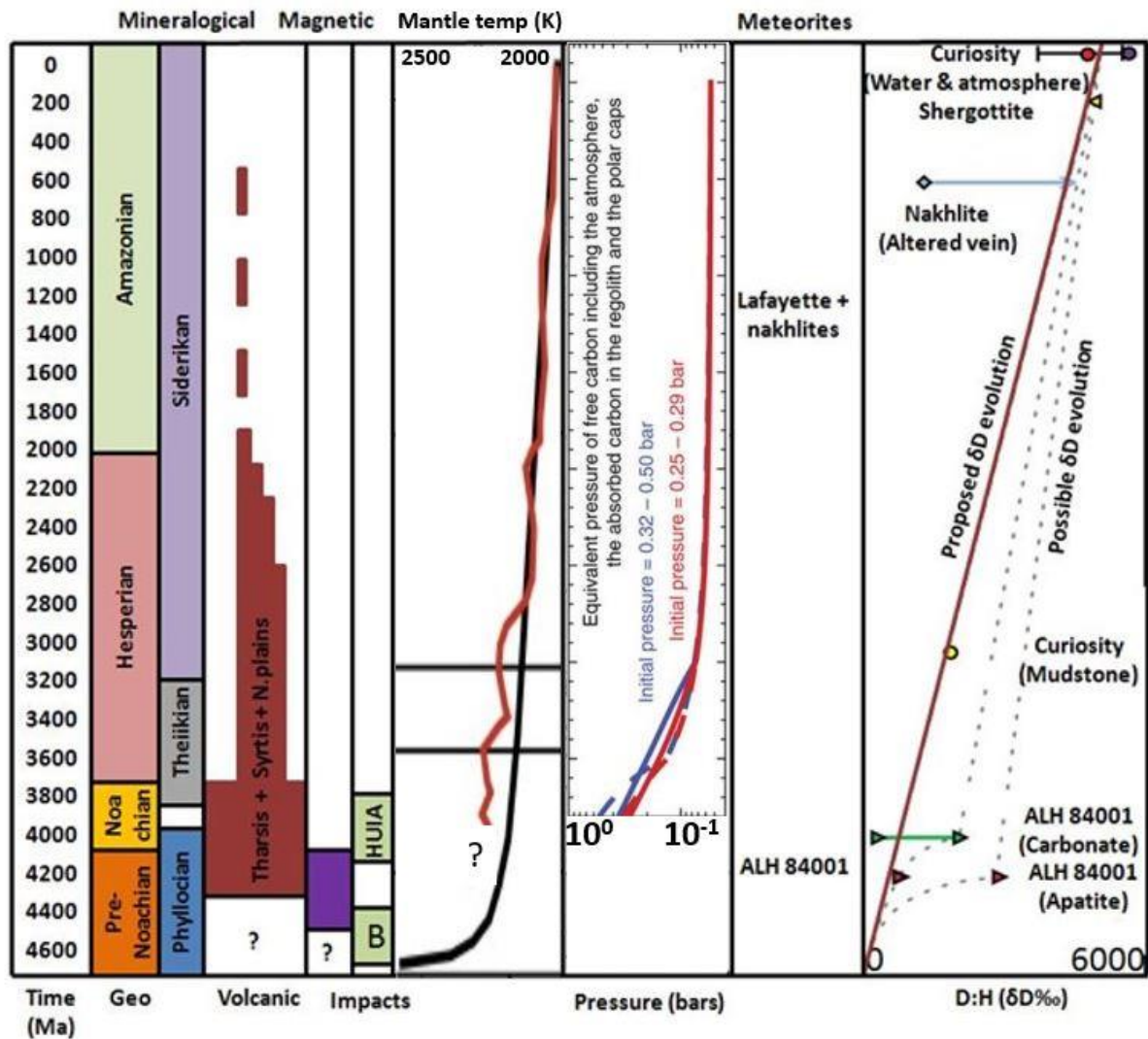


Figure 3.3. Geological, mineralogical, volcanic, magnetic, impact, temperature, pressure and D / H history of Mars. The meteorites presented in this study are also included for reference. Figure adapted from (Geological, mineralogical, volcanic, impact, magnetic: Ehlmann *et al.* 2011; temperature: Dohm *et al.* 2015; pressure: Hu *et al.* 2015; impacts: Bottke & Andrews-Hanna, 2017; D / H ratio: Hallis, 2017).

A basic understanding of Martian geology is required if the atmospheric and surface water evolution of the planet is to be seen in context. Following rapid planetary accretion (Harper *et al.* 1995), the Martian crust differentiated into a mantle and metallic core at ~4530 Ma ago (Borg & Connelly, 1999) based on Martian meteorite $^{87}\text{Rb} - ^{87}\text{Sr}$, $^{129}\text{I} - ^{129}\text{Xe}$, $^{146}\text{Sm} - ^{142}\text{Nd}$, $^{182}\text{Hf} - ^{182}\text{W}$, $^{187}\text{Re} - ^{187}\text{Os}$, $^{235}\text{U} - ^{207}\text{Pb}$ and $^{238}\text{U} - ^{206}\text{Pb}$ isotope work. Highly siderophile elements in Martian meteorite samples indicate a magma ocean was present, which allowed dense cumulate material to sink, and silicate partial melt to dominate the surface, forming a 20-30 km primary crust (Mezger *et al.* 2012). This silicate melt fractionated further as crustal solidification proceeded, with volatile elements being degassed into the atmosphere (Mezger *et al.* 2012).

The HiRISE and CRISM instruments have located primary crust (low fractionation) only in deeply exposed rocks within large impact craters, mostly in the central uplifts (Skok *et al.* 2011). These exposed basic melt products are thought to be composed of fayalite (Fe) rich olivine dunite, and high Fe enstatite orthopyroxenite (Skok *et al.* 2011).

Two schools of thought exist on the geology of the modern surface of Mars. The first divides the Martian surface into two types. An older, basaltic 'type 1' surface positioned in the Southern Highlands, which had most of its original ancient terrain reworked by the late heavy bombardment, and a younger, andesitic 'type 2' surface positioned in the Northern lowland plains (Mustard *et al.* 2005). This lithological interpretation of Mars' surface is based on mineral abundances from thermal emission spectrometer data via the Mars Global Surveyor (MGS). The second school of thought uses spectral data to suggest this andesitic 'type 2' signature may be a misinterpretation, and the composition is basaltic in both terrain types, but type 2 terrain has a thin alteration surface of silica producing the andesite spectral signature (Wyatt & McSween, 2002).

MGS MOLA (Mars Orbiter Laser Altimeter) data indicate a mantle average density of 600 kg m^{-3} and a current crustal depth of 32 km in the Northern lowlands and 58 km in the Southern highlands, with an average planetary crustal depth of 50 km (Neumann *et al.* 2004). Crustal thickness can vary greatly though, from ~3 km

in the Isidis basin to ~92 km in the Syria Planum region of Thaumasia (Zuber, 2001). Geochemical evidence from Martian meteorite Fe / Si values have estimated Martian crustal thicknesses of 100 - 250 km (Sohl & Spohn, 1997).

The geological history of Mars can be divided into four periods, the pre-Noachian, Noachian, Hesperian and Amazonian (Fig. 2.2). Little is known about the early pre-Noachian environment, but the Noachian is thought to be the apex of Mars' volcanic and aqueous activity with a steady decline through the Hesperian period (Ehlmann *et al.* 2011).

3.1.2 Hydrology on Mars.

3.1.2.1 Water on modern Mars.

The current surface of Mars is a cold, dry, barren desert swept by dust and sand. The modern average surface temperature on Mars is -63°C (Website 2), although it can fluctuate between -113°C and -33°C (Ditteon, 1982). These temperatures are too low to support surface liquid water unless it is highly saline (Richardson & Mischna, 2005). The water vapour pressure in the triple point of water is ~0.006 bar, which is below the current Martian surface pressure of ~0.007 to 0.008 bar (Rennó *et al.* 2009). This means that surface water would boil away and evaporate (Fig. 1.2). Therefore, both surface pressure and temperature conditions on modern Mars are unsuitable for the existence of liquid water. However, researchers have designed general circulation models to argue that the pressure and temperatures on Mars do fit the requirements for liquid water in five favourable regions, namely: the Hellas and Argyre impact basins and the plains of Amazonis, Arabia and Elysium between 0° and 30° (Haberle *et al.* 2001); though they concede that the waters are probably brine and only present for a very limited duration. That water exists on modern Mars in one form or another is supported by several lines of evidence:

- **Recurring slope lineae** are most likely small volume seasonal saline water flow just beneath the surface of solar warmed equator facing slopes, appearing in spring - summer and causing dark streaks on the Martian surface (Chevrier & Rivera-Valentin, 2012). Salt depresses the freezing point of water, and combinations of salts can possess lower eutectics than individual salts; landing sites on Mars have confirmed a complex mix of salts such as perchlorates and magnesium salts (Rennó *et al.* 2009). However, the ability of salt to lower the freezing temperature of water is limited by the reduced solubility of salt in low temperature liquids, with $-73\text{ }^{\circ}\text{C}$ being the lowest liquid water temperature likely on Mars based on the likely salts available (Rennó *et al.* 2009), although other researchers suggest a lower limit of $52\text{ }^{\circ}\text{C}$ (Primm *et al.* 2017). The slope lineae span 0.5 - 5 m and occur on slopes 25° to 40° at Southern latitudes of 48°S to 32°S during surface temperatures of exceeding $-23\text{ }^{\circ}\text{C}$ or 250 K (McEwen *et al.* 2011). Two models compete to answer why these recurring slope lineae occur. The first suggests that highly concentrated calcium and ferric chloride brines mixed with small volumes of water ice melt migrate downslope, evaporating as the summer season progresses (Kreslavsky & Head, 2009). The second non - aqueous model suggests a dry granular flow (Treiman & Louge, 2004). Other researchers have suggested recurring slope lineae may be dry granular flows, similar to the Martian sand dune flows observed in regions such as Eos Chasma (Dundas *et al.* 2017).
- **Water as subsurface ice** is present on Mars. Subsurface water ice has been predicted by thermal calculation modelling (Paige, 1992) and interpretation of observed geomorphic ground features such as quasi - relaxation of topography, lobate debris and compressional ridges associated with escarpments and viscous creep (Squyres & Carr, 1986). One potential discovery of this ground ice was at the Phoenix lander site, when oblate spheroids were splashed onto the lander's leg (Rennó *et al.* 2009). It is thought that a considerable amount of water ice may exist beneath the Martian regolith $\pm 30^{\circ}$ polewards (Squyres & Carr, 1986), protected from sublimation by regolith coverage (Rennó *et al.* 2009). This water reservoir,

predominantly in regolith pore space, is poorly quantified at present but may represent the largest on modern Mars, with mid latitude 30° to 60° N and S. Water volume estimates assuming a frozen soil depth of 1 to 10 m being 1.5 to 6 x 10⁴ km³ (Mustard *et al.* 2001). This amount of ice is equal to a planetary wide water depth of 0.1 to 0.4 m. Orbital obliquity (the angle between a planet's pole of rotation and ecliptic plane) on a 0.1 Ma timescale is thought to influence the formation or dissipation of such water soil reservoirs, with the current reservoir being depleted (Mustard *et al.* 2001). It has been hypothesized that obliquity cycles may have caused a major ice age on Mars 2.1 to 0.4 Ma ago which formed the bulk of the current soil ice deposits (Head *et al.* 2003). Gamma-Ray Spectrometer measurements from orbiting satellites suggest a reducing soil thickness in higher latitudes and a strong hydrogen signature supports the hypothesis of a large body of subsurface ice (Boynton *et al.* 2002).

- **Polar ice** on Mars exists in both North and South polar ice caps, which are stable over geological time frames. Originally it was thought that the North polar cap was dominated by water ice (Farmer *et al.* 1976) and the South polar cap by CO₂ ice (Sharp *et al.* 1971), however, utilising a suite of satellite instruments including altimetry and spectroscopy it is now understood that the Southern Polar cap consists of Layered Deposits (SPLD) of year-round water and CO₂ ice (Bibring *et al.* 2004), dust and sediment probably <10 % (Plaut *et al.* 2007). The sequence of layering depends on cyclical climatic shifts, and possibly astronomical cycles (Thomas *et al.* 1992), thus providing a potential climate data record. Analysis of these layered deposits has also prompted the idea of a recent astronomically caused ice age ~2.1 to 0.4 Ma ago extending the ice caps down to ~30° to 35° latitude and that modern Mars is in an interglacial period (Head *et al.* 2003). The estimated volume of CO₂ ice currently stored in the South pole increased by a factor of 30 following shallow radar soundings which indicated 9500 to 12500 km³ of CO₂ ice stored in the cap (Phillips *et al.* 2011). About 25 % of the current Martian atmospheric CO₂ budget condenses in the poles each winter, evaporating again in the summer although some

remains year round (Kieffer & Titus, 2001). This evaporation and condensation cycle makes the Mars South pole extremely dynamic, with ice sheets advancing and retreating annually, causing hypothesised physical phenomena such as high pressure CO₂ jets from the CO₂ slab ice (Kieffer *et al.* 2006). The polar caps do change diurnally as well as seasonally, with significant fluxes of energy migrating down to 70°N at night (Kieffer & Titus, 2001).

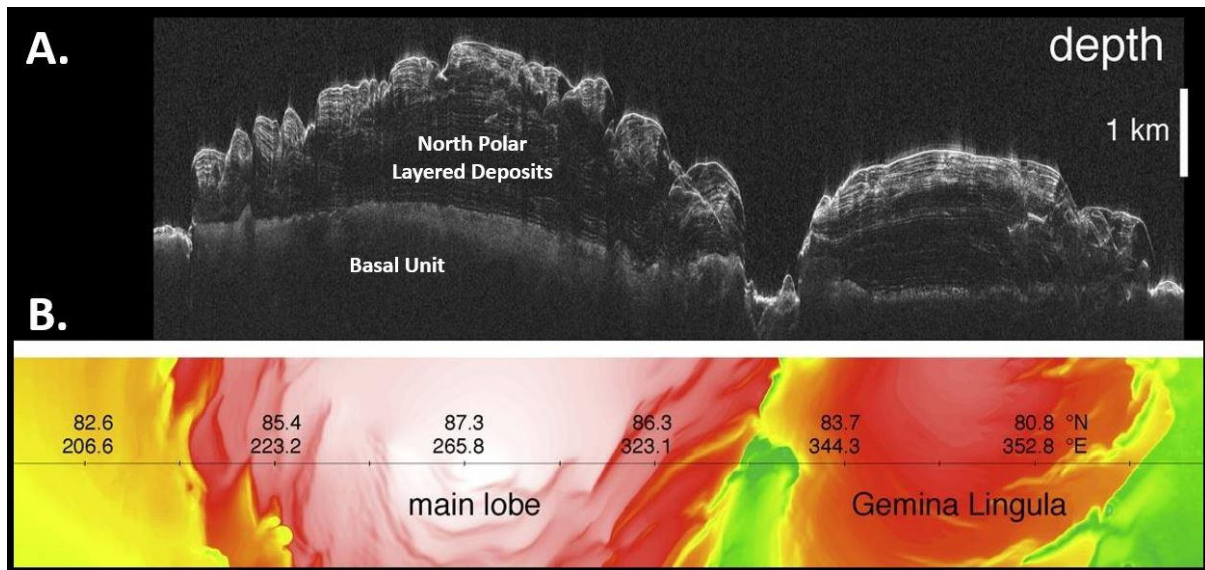


Figure 3.4. A. Layered ice deposits on the North pole of Mars imaged by shallow radar (SHARAD) on the Mars Reconnaissance Orbiter. B. Map showing the line of cross section in A, red and white = higher altitudes, yellow and green = lower altitudes. (Adapted from Website 3 and Putzig *et al.* 2009).

3.1.2.2 Water on past Mars.

The Martian surface displays numerous morphological features in its surface topography that are indicative of both water flow and large standing bodies of water in the Martian past (Showstack, 2012; Squyres & Kasting, 1994). The formation ages of these fluvial features are predominantly around the late Noachian to early Hesperian (Fig. 3.3), although occasionally they can be found in

Amazonian terrain (Seibert & Kargel, 2001). Past water flow on Mars can be supported by morphological/topographical evidence such as:

- **Polygons** in late Hesperian terrain in mid to high latitudes such as Utopia and Argyre Planitiae (Seibert & Kargel, 2001) provide evidence of glacial / tundra style melt water. Such polygonal features have their Earth analogue in glacial permafrost regions on Earth where they can form as both ice wedges (Brown, 1967) and sand wedges (Pewe, 1959), where ice or sand fills into surface cracks, freeze, expand and create polygonal structures. The polygons on Mars are most likely formed by ice (Seibert & Kargel, 2001).
- **Dendritic braided channels and valleys** such as in Valles Marineris region, dated ~3500 Ma (Quantin *et al.* 2004), are highly branched, possessing mature inner channels which indicate sustained water flow (Mangold *et al.* 2004). Atmospheric precipitation is considered the most likely candidate for the formation of these dendritic networks (Mangold *et al.* 2004).
- **Outflow channels** are long, wide, deep channels carved into the Martian landscape such as the Ares and Tiu Valles outflow channels found in Xanthe Terra (Nelson & Greeley, 1999). It is assumed that they were carved by significant bodies of rushing water.
- **Valleys, deltas (Achille & Hynek, 2010) and topographic features spanning thousands of kilometres suggestive of a deformed equipotential palaeo - shorelines (Perron *et al.* 2007; Head *et al.* 1999)** are all supportive evidence for an early ocean on Mars at ~ 3500 Ma (Achille & Hynek, 2010), where the modern lowland Northern plains now stand. Extensive glaciers and ice sheets of ice have also been suggested as part of the Northern plains history, based on physical characteristics analogous to terrestrial eskers, drumlins, moraines, tunnel channels and other glacial attributes (Kargel *et al.* 1995). Such glacial attributes may have contributed to other physical characteristics described above, such as glacial lake outburst flooding causing outflow channels, yet great uncertainty exists as to how such glaciation would fit with an early ocean and warm Mars models (Kargel *et al.* 1995).

Past water flow on Mars can also be supported by chemical and mineral evidence such as:

- **Spectral mapping from orbital satellites and telescope observations** show a range of minerals associated with aqueous alteration, the details of such research and mapping are covered in detail below (Fig. 3.9) under the carbonates section; carbonates being a mineral intimately associated with aqueous weathering.

3.1.2.3 Warm and wet or cold and icy?

The precise environmental conditions prevailing when water was relatively abundant in the Hesperian period remain unresolved. Was it warm and wet (Fig. 3.5.A., 3.6.C., Pollack *et al.* 1987; Craddock & Howard, 2002; Carter *et al.* 2015)? Or an icy world punctuated by episodic transient melting (Fig. 3.5.B., 3.6.A., 3.6.B., Halevy & Head, 2014)? In 3D climate models an unrealistic amount of solar or greenhouse gas warming is required to produce an ice free early ocean. However, in a cold and icy scenario, models predict snowfall in regions where morphological evidence suggests past water flow (Wordsworth *et al.* 2015).

Extensive mineralogical evidence exists for water and rock interaction on the Mars crust, as reviewed below. The most prevalent clays found are Mg - Fe smectites (Fig. 3.9.A), which do not require large volumes of water to form, and a low water to rock ratio under icy conditions is a reasonable smectite formation environment for smectite formation (Ehlmann, 2014). Researchers suggest abundant Mg - Fe smectites formed in subsurface closed system environments, with a low water to rock ratio, while the less abundant Al clays (Fig. 3.9.A) formed in open systems with higher water to rock ratio during episodic melting events (Ehlmann, 2014).

The morphological evidence presented, such as long dendritic braided channels may also have been formed by ice and snow melt rather than by rainfall

(Carr & Head, 2003). Many of the water-formed features are in mid latitudes, not polar, and it is suggested that mid latitude snowfall occurs from polar atmospheric transport and deposition (Christensen, 2003). A consensus is growing based on both morphological observation and model simulations that an icy cold early Mars appears more likely than a warm and wet one (Gaidos & Giles, 2003; Fastook *et al.* 2012; Head & Marchant, 2014; Wordsworth, 2016).

But opinion divides as to whether a cold and dry (3.6.A., Galofre & Jellinek, 2016) or a cold and wet (3.6.B., Fairén, 2010; Fastook *et al.* 2012, Fairén *et al.* 2017) early Mars is most plausible. The cold and wet model allows for sub glacial basal melting as a mechanism for forming minerals from aqueous activity (Fastook *et al.* 2012), with cold, saline and acidic liquid solutions created from acid weathering of basalt (Fairén, 2010). The relative scarcity of Noachian phyllosilicates is also consistent with glaciers and near freezing water temperatures (Fairén *et al.* 2011). Alternatively, a cold and dry early Mars may have been punctuated by volcanic or impact events causing short duration melting events (Halevy & Head, 2014). This scenario is consistent with other models that suggest a warm and wet Mars with ~0.5 to 1 bar of CO₂ during the late heavy bombardment, then a rapid transition to a cold, glacial Mars once the bombardment ended (Carr, 1999). Some researchers have even suggested that the valleys are neither water nor ice carved, but formed from gas supported density flow of CO₂ outgassed from the ice (Hoffman, 2000). Others have suggested a fluctuating cycle between models, and alternating oceans and ice sheets (Baker *et al.* 1991). The most recent studies based on the mineralogy of Gale crater mineralogy and using reactive transport models support the cold and dry model, with a Noachian CO₂ atmosphere of <1 bar (Bristow *et al.* 2017).

Other Research opposes the icy world model, advocating that the role of methane on early Mars has been underestimated and that even in an early atmosphere as low as 0.5 bar of CO₂ a couple of percent of CH₄ would raise surface temperatures by tens of degrees (Wordsworth *et al.* 2017), such methane may come from serpentinization reactions in the planet's basalt and peridotite crust.

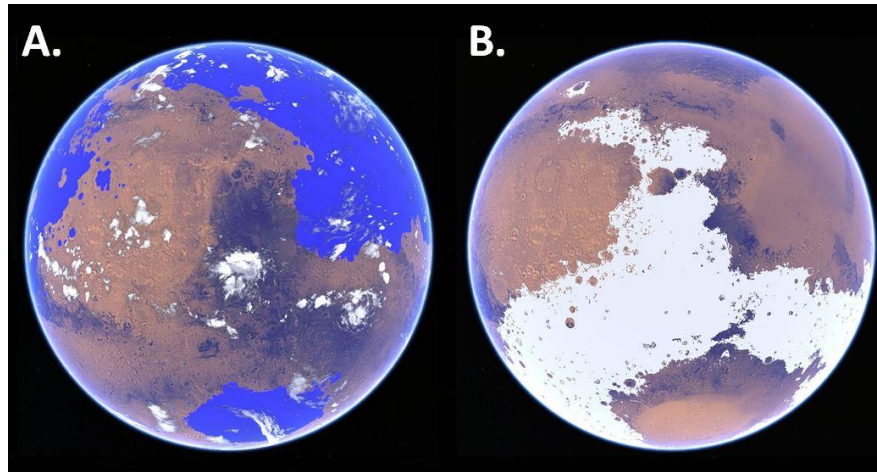


Figure 3.5. **A.** A warm and wet early Mars possessing a Northern ocean. **B.** A cold and icy early Mars dominated by glaciers and ice sheets (Website 1).

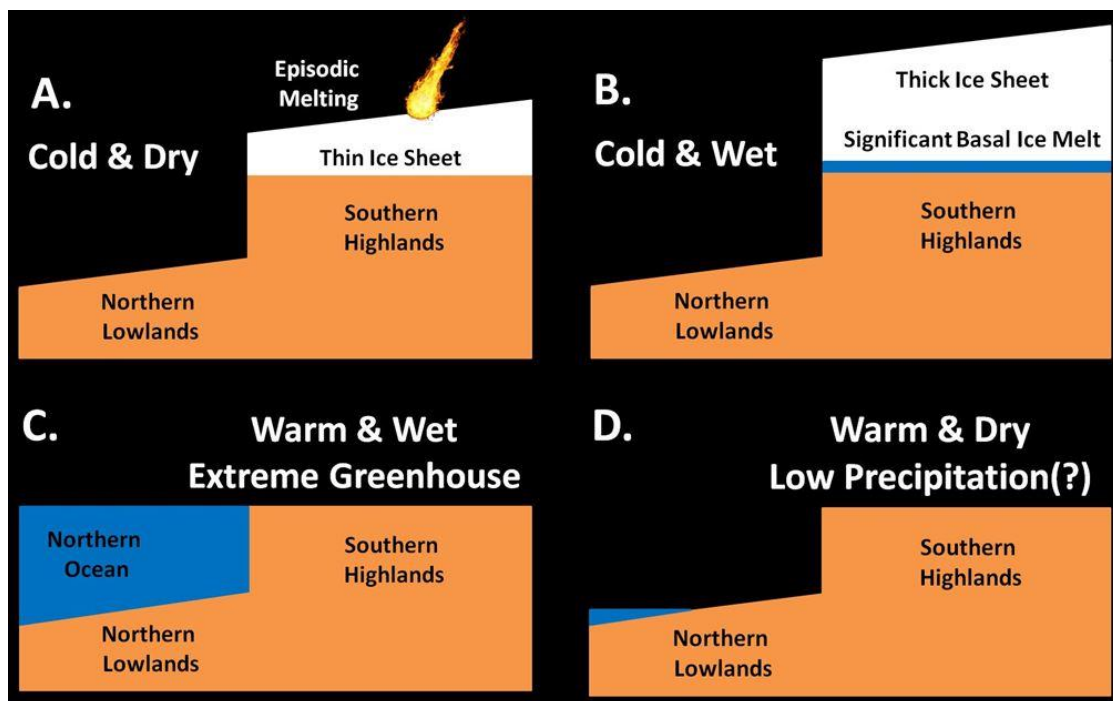


Figure 3.6. **A.** Cold and dry model of early Mars with thin ice sheets with little to no basal flow, no Northern Ocean or permanent surface water. Sporadic impacts and volcanism allow short term ice melt. **B.** Cold and wet model of early Mars, with a thick ice sheet, significant basal melt water, but still no Northern Ocean. **C.** Warm and wet model of early Mars, with no ice sheet and an extensive Northern Ocean. An extreme multiple bar greenhouse atmosphere is required for this model. **D.** Warm and dry model of early Mars, with no ice sheets or glaciations, but also with only minor permanent surface water. (Adapted from Wordsworth, 2016).

Estimates of the early Mars water inventory are ~24 m global equivalent water layer (GEL) in the late Noachian period, insufficient for a global ocean, and 64 m GEL at the end of the Hesperian (Carr & Head, 2015), compared to 34 m GEL on current Mars, mostly in the polar layered deposits. This favours a cold and icy model of early Mars. Such figures are surface unbounded water, and do not include deep subsurface reservoirs. One possible explanation for the low early surface water estimate is that impacts and volcanism created pathways for deep storage of water (Carr & Head, 2015).

3.1.2.4 Punctuated hyper carbonation hypothesis.

A hypothesis forwarded by this study (objective 3.A), applicable to all the models in figure 3.6, but especially relevant to the cold models, is the idea that aqueous alteration and mineral carbon sequestration was not a linear process, nor a geographically ubiquitous one. Sporadic impacts, particularly around the late heavy bombardment (4100 - 3800 Ma), which coincides with the Noachian period (4100 - 3700 Ma), as well as Tharsis volcanism (4100 - 3300 Ma) (Wise *et al.* 1979), would have produced localised areas of intense heat, as well as a range of exponentially cooling margin regions.

On Earth it has been demonstrated that mineral carbonation proceeds at a peak rate when the temperature is ~185°C (Keleman & Matter, 2008), and this temperature could certainly be created by volcanism and impact. At multi kilometre scale geoengineered mineral carbon sequestration (MCS) sites, such as the CarbFix project in Iceland (Matter *et al.* 2009; Matter *et al.* 2011), it has been demonstrated that MCS produces a positive feedback of runaway carbonation. Carbonation is exothermic (Matter & Keleman, 2009) and rocks are naturally heated at depth (to an extent that depends on the local geothermal gradient), at the Iceland site this depth is 1500 m (Alfredsson *et al.* 2013); as a result, the carbonation reaction can remain at a near optimal temperature subsurface. Further, incorporation of water into the crystal structures of precipitated minerals demands volumetric expansion, often >44% (Keleman *et al.* 2011), which causes

cracking (Keleman & Hirth, 2012) and exposure of fresh mineral surfaces for continued reaction (Keleman & Matter, 2008).

Mineral carbonation is rapid in Iceland, with 95% of the >170 tonnes of CO₂ injected becoming fully mineralised in ≤ 2 years (Sigfusson *et al.* 2015; Matter *et al.* 2016). Were such reactions to be scaled up to the size of entire volcanic regions over tens or hundreds of thousands of years, the potential for significant deep subsurface carbon sequestration becomes a serious prospect. Noachian strata generally occur at depth and are only revealed by craters (Grant *et al.* 2008; Milliken *et al.* 2010), or deeply cutting valleys, chasma and pits (Le Deit *et al.* 2012); Noachian lower units of clay and sulphates are overlain by sulphates and oxides (Milliken *et al.* 2010). If hyper carbonation occurred in the Noachian, and positive feedback of runaway carbonation happened in a CarbFix fashion, then these carbonates might be expected to be a full kilometre or so beneath the buried Noachian units, and thus potentially undiscovered. A hypothetical graph illustrating how localised hyper carbonation events might compare to regular models of carbonation is shown in figure 3.7.

However, assuming the aforementioned hydration reactions with subsequent fracturing and reduction in rock density, it should be possible to identify buried units of CarbFix style hyper carbonation via seismicity. The French Space Agency, CNES did plan on launching four Netlander surface stations to monitor global Mars seismicity (Marsal *et al.* 2002), which unfortunately was cancelled in 2003. Similarly, NASA planned the InSight lander mission to monitor Mars seismicity, due to launch in 2016 but placed on hold until 2018 (Banerdt *et al.* 2013; Zelenyi *et al.* 2015). ExoMars, due to land in 2020 will have a small seismic device on the lander part of the mission capable of monitoring horizontal base oscillations at 10^{-2} up to 10 Hz (Zelenyi *et al.* 2015), but clearly for the wider detection of localised, deep subsurface carbonates a significant future seismic mapping effort is required.

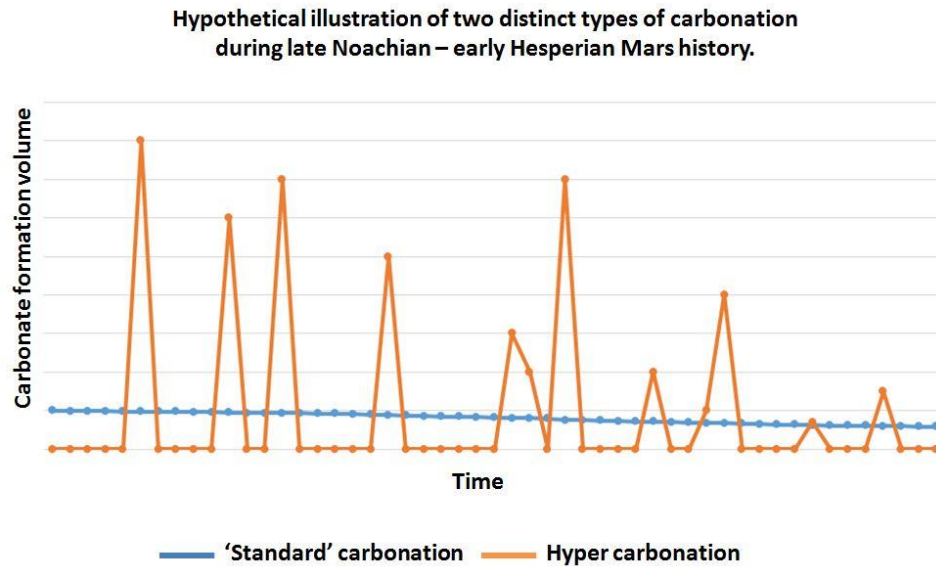


Figure 3.7. An illustrative graph of how volcanic or impact induced punctuated hyper carbonation volume/rates might compare with standard carbonation assumptions.

3.1.3 Carbonates, clays and other hydrated minerals.

Carbonates and clays have now been located in numerous localities on Mars, and via a wide variety of observational mechanisms.

- **Satellites and telescopes.** Spectral mapping from satellites such as the Thermal Emission Spectrometer (TES) on the Mars Global Surveyor (MGS) have located grey hematite, assumed to have formed under ambient or hydrothermal aqueous conditions and weathered from sulphate deposits, limited phyllosilicates were also located (Fig. 3.8. Bibring *et al.* 2006). No carbonates or clays were found by the MGS mission above the detection limit of ~10% (Christensen *et al.* 2001).

Mariner 6 / 7 located spectral signatures in the 2.28 and 5.4 μm range attributable to hydrous magnesium carbonates (Calvin *et al.* 1994).

Phyllosilicates have been discovered on Mars via CRISM and OMEGA orbital

spectral analysis in locations such as the Nili Fossae, Terra Tyrrhena, Libya Montes (Ehlmann *et al.* 2008), Marwth Vallis, Huygens crater and Syrtis Major region (Fig. 3.8. and 3.9, Niles *et al.* 2013), using a TES spectral index (Mustard *et al.* 2008; Michalski *et al.* 2010). In Nili Fossae, the CRISM/OMEGA data show an imprecise match for phyllosilicates, indicating phyllosilicates may be poorly crystalline, or part of a basalt glass matrix (Michalski *et al.* 2010), possibly part a low water-rock ratio style of mineral replacement. The Jezero Crater in the Nili Fossae is a strong candidate for future Mars missions and possesses Fe / Mg smectite and Mg carbonate sediment of Noachian - Hesperian boundary age (Goudge *et al.* 2017). Saponite, talc - saponite, smectites (nontronite), Fe rich mica (glaucosite), Fe and Mg serpentine, Mg Fe Ca-carbonate and Fe sulphide have been located in the Eridania region of the highlands, which some researchers propose to be hydrothermal deposits, and part of a vast Noachian lake or inland sea (Michalski *et al.* 2017).

Terrestrial telescopes at the Mauna Kea Observatory, Hawaii, have also detected carbonate spectral bands in the Syrtis Major region (Blaney & McCord, 1989).

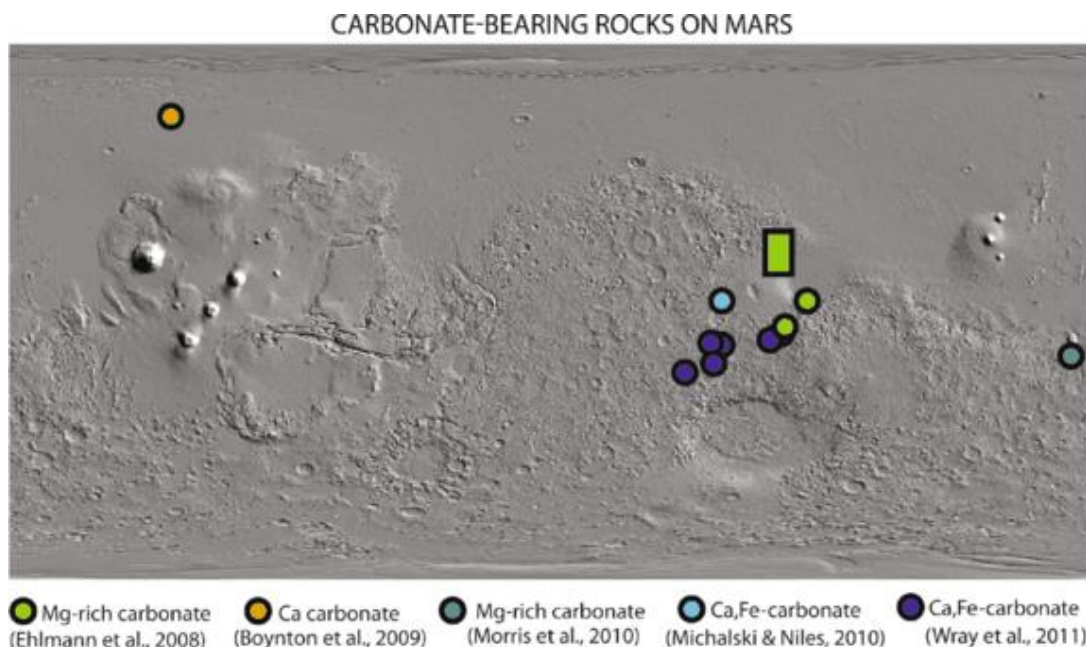


Figure 3.8. Map of carbonate bearing minerals identified on Mars superimposed over an MGS Mars Orbiter Laser Altimeter (MOLA) altitude map (Niles *et al.* 2013).

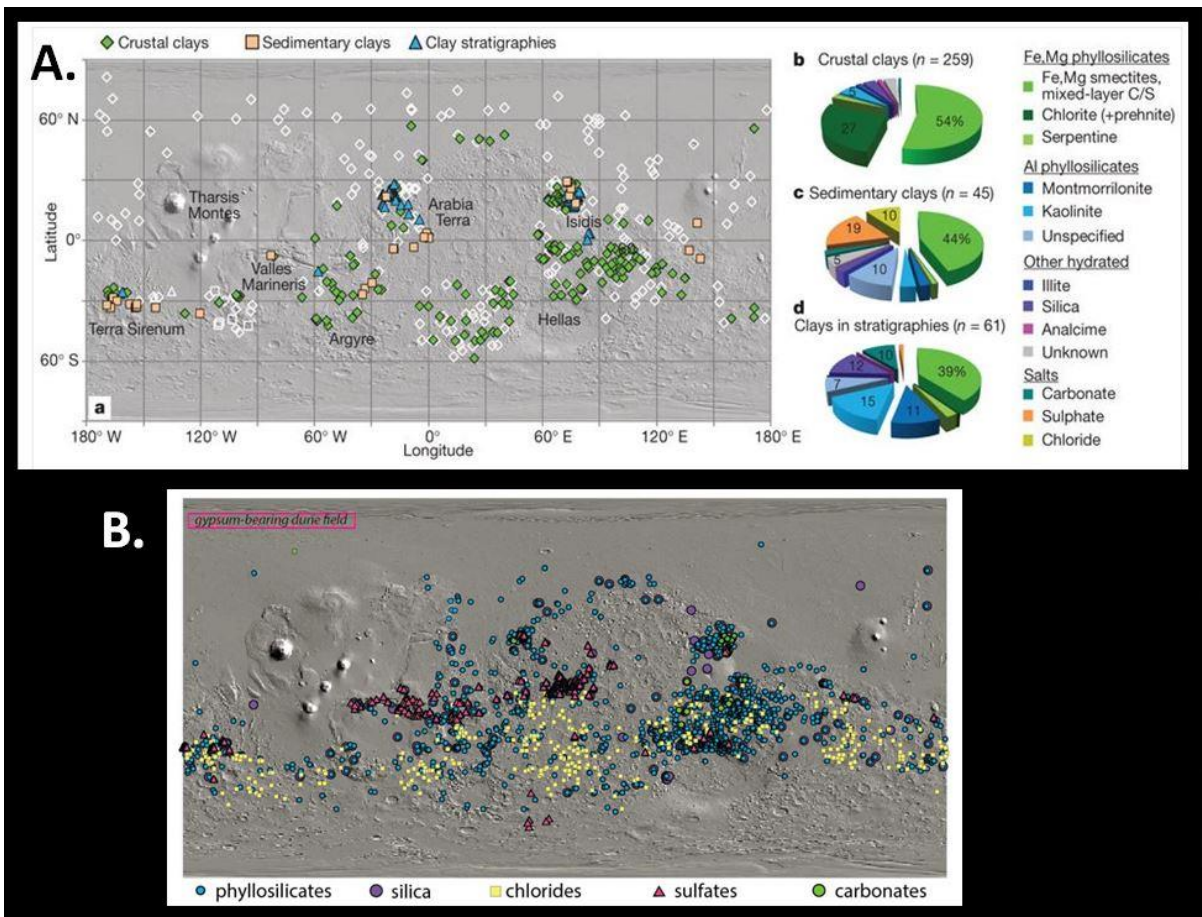
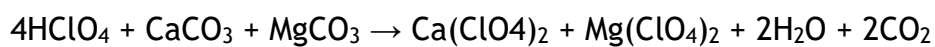


Figure 3.9. A. Target sites for CRISM search for clays and other hydrated minerals. Empty circles indicate no hydrated minerals found. % values = number of detections in target area, not areal extent (Ehlmann *et al.* 2011). **B.** Map of hydrous mineral discoveries (Ehlmann, 2014).

- Landers and rovers.** Landers and rovers have located carbonates at a number of sites on Mars. The Spirit rover found 16 to 34 wt. % carbonates at the Comanche outcrops in the Columbia Hills of Gusev Crater (Morris *et al.* 2010). The Comanche carbonates have been attributed to low temperature evaporation-precipitation conditions in a low water-rock ratio environment, with CO₂ rich fluid leaching metal cations from the parent tephra. The Phoenix lander found 3-6 wt. % calcite, dolomite and possible ankerite carbonate in soils samples in Green Valley, Vastitas Borealis (Northern plains), along with lower ~1% concentrations of magnesite and/or siderite (Boynton *et al.* 2009; Sutter *et al.* 2012). The Phoenix carbonates are

thought to be a mixture of “in-situ” pedogenic and wind deposited (Sutter *et al.* 2012). Perchlorate (ClO_4^-) was identified in the Phoenix soil at 0.6 wt. %, possibly forming from parent salts of calcium-perchlorate ($\text{Ca}(\text{ClO}_4)_2$) and magnesium-perchlorate ($\text{Mg}(\text{ClO}_4)_2$) in an arid environment. These Ca and Mg perchlorate phases have been experimentally demonstrated to be at the same ratio as Ca and Mg carbonates, and it may have been that perchloric acid (HClO_4) reacted with carbonate to produce these parent salts (Kounaves *et al.* 2014 and equation 3.0).



Equation 3.0

Finding and ideally dating carbonates and clays present on Mars is crucial if an accurate history of the planet’s hydrological and atmospheric past is to be constructed. This task can be difficult if, like on Earth, a significant amount of serpentinisation, clay and carbonate formation occurs beneath the ground and the mineral products are not visible from the surface unless exposed by impact.

Serpentines on Mars remain relatively rare, restricted to the Isidis basin (Noachian), mélange terrains such as Claritas Rise (Noachian pre - Tharsis) and Nili Fossae (Noachian), or at impact crater sites in the Southern Highlands (Ehlmann *et al.* 2010). Serpentine include a wide range of minerals, including antigorite, lizardite and chrysotile. A possible side product of serpentinisation is the formation of magnetite and this process is held responsible for magnetic anomalies associated with some of these serpentine regions such as the Claritas Rise (Ehlmann *et al.* 2010). That these sites are Noachian supports the hypothesis of a wetter early Mars and hence a denser atmosphere. It is surprising in many ways that serpentines are not more ubiquitous, explanations include that the serpentine may have existed then weathered to Fe or Mg smectite clays or the atmosphere was oxidising and cold enough to effectively skip the serpentine weathering phase and proceed directly to clay formation; alternatively most serpentine may remain

buried and as yet undiscovered or, perhaps most likely, that the parent rocks contained enough Si so as to form chlorite instead of serpentine (Ehlmann *et al.* 2010) as evidenced by surface observation (Fig. 3.9.B).

Clays are also found in the same locations as the serpentinites such as cratered Southern Highlands in much higher abundance to serpentinites, 65% compared to 5% (Ehlmann *et al.* 2010). Clays are also found in the Isidis basin.

3.1.4 Sulphur on Mars.

The role of sulphur in Martian history is important. Sulphur is acidic and will therefore dissolve carbonates, destroying records of past water and atmosphere. This section briefly examines the history of sulphur on Mars.

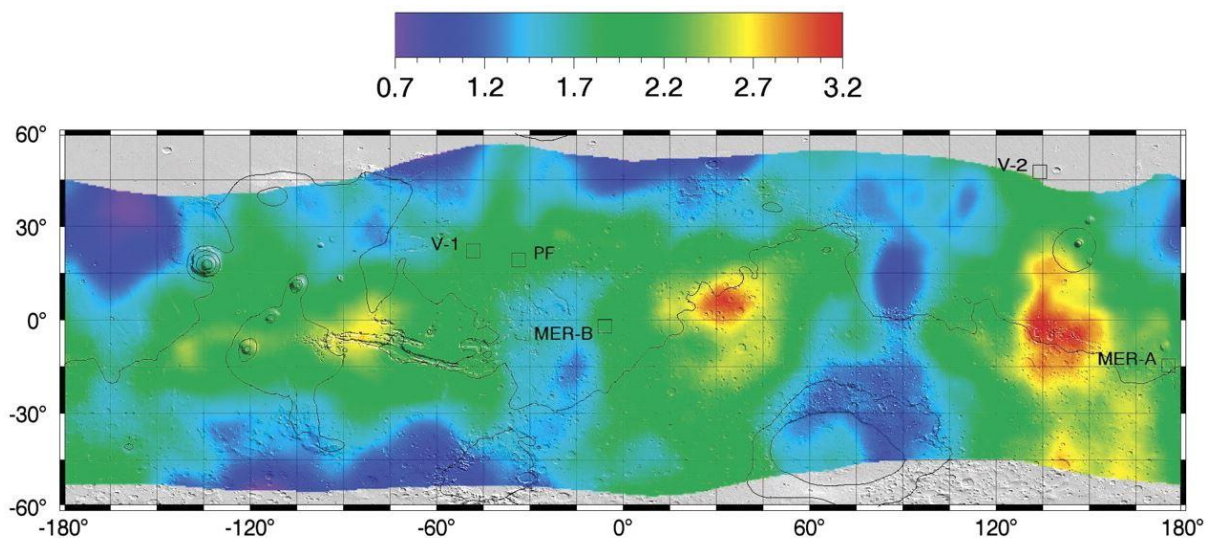


Figure 3.10 wt. % surface sulphur on Mars (King & McLennan, 2010).

Sulphur is extensively present in Mars' regolith (Fig. 2.9.B, Fig. 3.10). Modelled estimates indicate the Martian mantle has >3 to 4 times the amount of sulphur relative to Earth, with the Tharsis volcanic complex emitting 10 to 100 times the sulphur of terrestrial magmas (Gaillard & Scaillet, 2009). The Tharsis

complex is modelled to have emitted enough sulphur to deposit a 20 to 60 m thick layer of sulphate deposition on the Martian surface (Gaillard & Scaillet, 2009) and this calculation appears to be supported by observation. OMEGA Mars Express hyperspectral observations show hydrated and polyhydrated sulphates including kieserite and gypsum in a number of Martian terrains such as Valles Marineris, Margaritifer Sinus, and Terra Meridiani (Gendrin *et al.* 2005). Ca rich sulphate, probably gypsum, has been identified at the Martian North pole by OMEGA in the Olympia Planitia dunes, further evidencing the importance of mobile water on Mars (Langevin *et al.* 2005).

Sulphur affects the pH of brines, as well as altering local atmospheric humidity (Karunatillake *et al.* 2016) all of which influences the possibility of liquid water. Spectral mapping shows an association of H and S, with hydrated sulphur increasing in abundance towards the North pole and decreasing towards the South pole, possibly as a result of subsurface ice, circulation or insolation (Karunatillake *et al.* 2016). It is also proposed that water, not sulphur is the limiting component of the hydration state of salts on Mars (Karunatillake *et al.* 2016).

The discovery of jarosite and gypsum by the Mars rovers indicate a wet, oxidised and acidic environment during their formation, and in combination with the occurrence of only partially altered basalt suggest that fluid alteration never proceeded to completion, perhaps due to a loss of water from the environment (Elwood Madden *et al.* 2004).

Sulphur and halides are also present in the Martian meteorites (Gooding, 1992) and are discussed in more detail below. Sulphur isotopes in the meteorites suggest that the oxidised sulphur on the Martian surface probably has an atmospheric origin as volcanically degassed SO₂ and H₂S which became deposited via atmospheric photodecomposition, photooxidation and photodissociation (Fig. 3.11) (Farquhar *et al.* 2000).

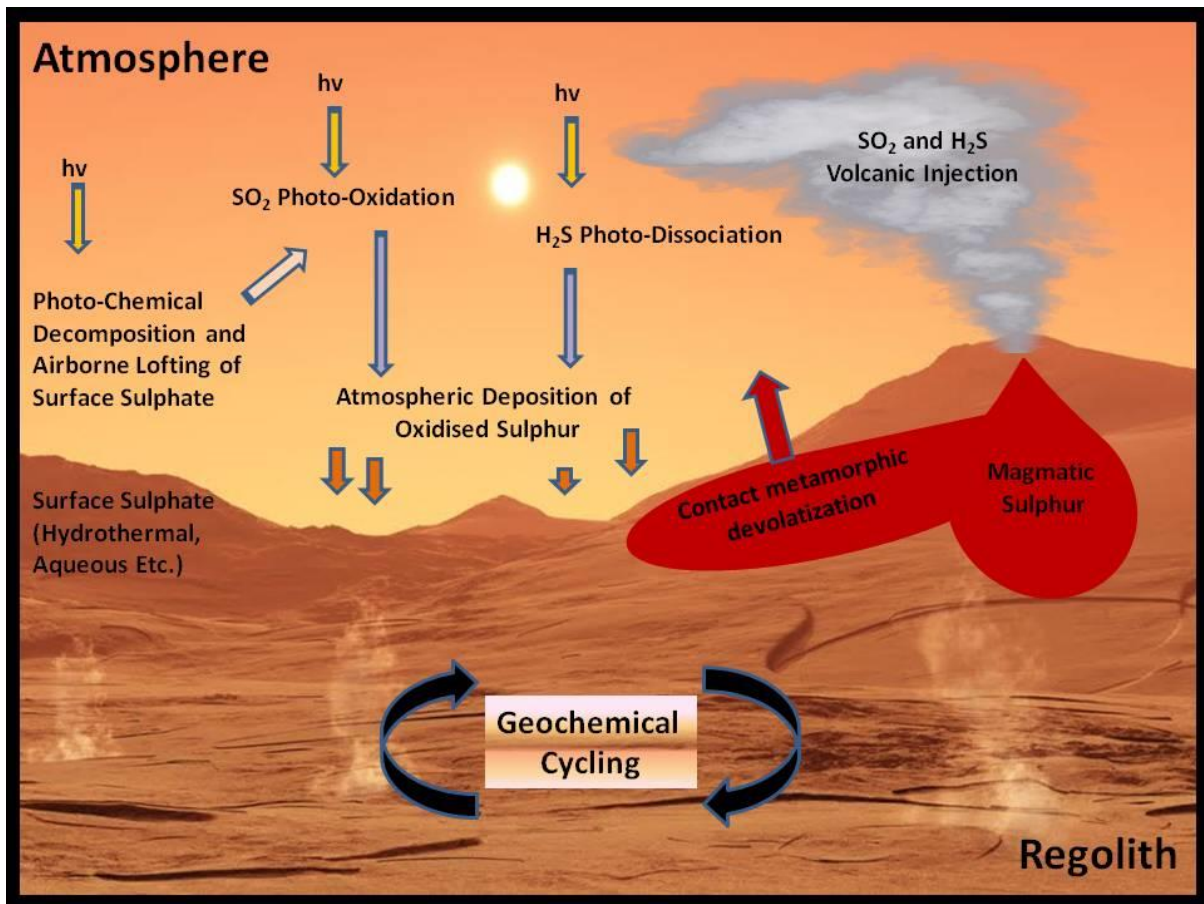
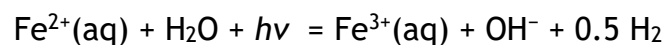


Figure 3.11 Sulphur cycle on Mars (adapted from Farquhar *et al.* 2000).

A simplified example of how the sulphur deposition shown in figure 3.7 proceeds is that atmospheric ferrous oxide (Fe^{2+}) reacts with water and ultraviolet light to produce ferric sulphate (Fe^{3+}), hydroxide and dihydrogen (equation 3.1):

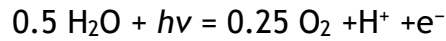


Equation 3.1

Other atmospheric reactions include water and electrons producing hydroxide and dihydrogen (equations 3.2), along with water and ultraviolet light creating dioxide, hydrogen and free electrons (equation 3.3):

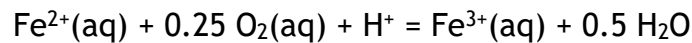


Equation 3.2



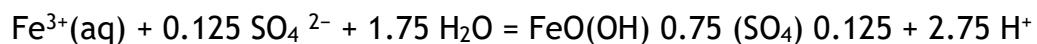
Equation 3.3

The products from equations 3.2 and 3.3 can then also react with airborne ferrous oxide (Fe^{2+}) to produce ferric sulphate (Fe^{3+}):



Equation 3.4

These ferric sulphates are then deposited onto the Martian regolith, creating acidic conditions that would dissolve exposed carbonates. An example of such atmospheric deposition of ferric sulphate (Fe^{3+}) is the formation of the mineral schwertmannite ($\text{FeO}(\text{OH})_{0.75}(\text{SO}_4)_{0.125}$), an iron-oxyhydroxysulfate:



Equation 3.5

It is thought that degassing of Tharsis volcanism may have been dominated by SO_2 rather than H_2S assuming ≥ 0.01 wt. % water and ≥ 0.08 wt. % carbon dioxide (Gaillard *et al.* 2013). This idea has led to the selection of SO_2 as a gas component in the experiment conducted in chapter 4. The importance of understanding the influence of sulphur on carbonate stability, aqueous and atmospheric chemistry, and secondary mineral formation when investigating the history of carbonates is paramount.

3.1.5 Atmosphere.

The history of surface water on Mars can also be explored by studying the atmosphere. Surface measurements from rover tools (Webster *et al.* 2013) and analysis of secondary mineral products in Martian meteorites (Hallis *et al.* 2012) provide a wealth of data on the processes of molecular atmospheric escape and the measurements of atmospheric isotope ratios, particularly of H, C, and O. The Curiosity rover Mars atmosphere isotope ratio findings are consistent with those from Martian meteorites (Mahaffy *et al.* 2013).

Hydrogen has one electron and one proton. Deuterium is an isotope of hydrogen with one electron, a proton and neutron; it is also referred to as 'heavy water' when combined with oxygen. Terrestrial water contains a well-known and characterised amount of deuterium. Standard Mean Ocean Water (SMOW) has a D / H ratio of 155.8×10^{-6} (De Wit *et al.*, 1980; Fisher, 2007), commonly expressed as δD 0‰. Because there is such a large reservoir of water on Earth, this SMOW value has probably remained unchanged for at least 4500 Ma (Donahue, 1995). This fixed terrestrial SMOW value can then be compared to extra-terrestrial bodies such as comets and Mars in order to answer questions such as whether terrestrial water originated from comets, or how similar the water history of Mars is compared to Earth. Because deuterium is heavier than hydrogen, it becomes preferentially left behind during evaporation processes, creating isotopic fractionation whereby meteoric precipitation and subsequent ice develops a negative amount of deuterium, up to δD -400‰ on Earth (Lécuyer *et al.* 1998). Rocks also isotopically fractionate and can possess up to δD -80‰ on Earth (Lécuyer *et al.* 1998).

The current atmosphere of Mars possesses δD +4200‰ (Bjoraker *et al.* 1989; Hallis *et al.* 2012). It is thought two Martian δD sources exist, one with high δD associated with surface water, and a low δD associated with primordial magmatic water (Chen *et al.* 2015). The reason for this high positive δD reservoir on Mars is due to atmospheric escape causing fractionation. The lighter hydrogen isotope will preferentially escape to space by a thermal mechanism called Jeans escape,

whereby particles exceeding an average speed particular to the gravity of the planetary body escape to space (equation 3.6).

$$\Phi_{\text{escape}} = \frac{n(z)V_0}{2\sqrt{\pi}} \left(\frac{V_{\text{esc}}^2}{V_0^2} + 1 \right) \exp\left(-\frac{V_{\text{esc}}^2}{V_0^2} \right)$$

Equation 3.6

Φ = Jeans escape, $n(z)$ = number density, V = velocity.

Jeans escape depends on many factors, including planetary size. Planetary bodies in the solar system have different escape velocities for the various elements (Fig. 3.12). Mars can be seen to retain H_2 and CO_2 but lose most other elements (Fig 3.12) and this is reflected in Martian atmospheric composition being dominated by CO_2 relative to Earth (Table 3.1).

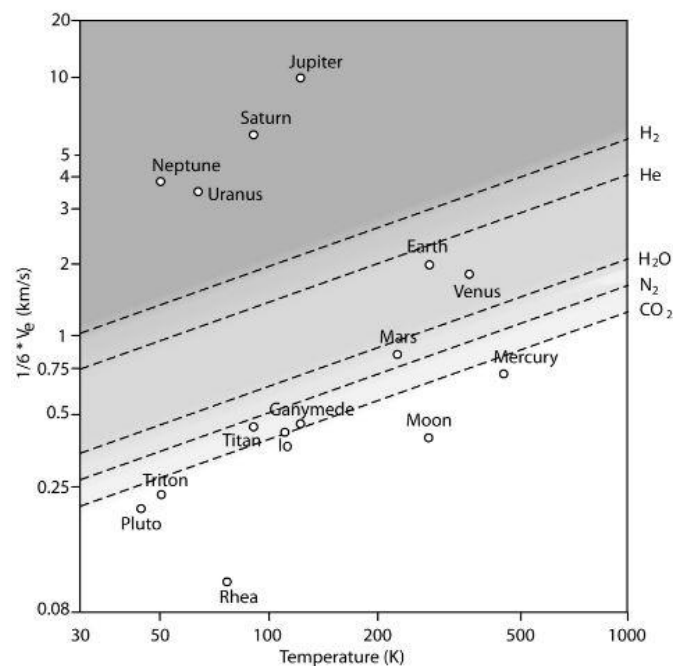
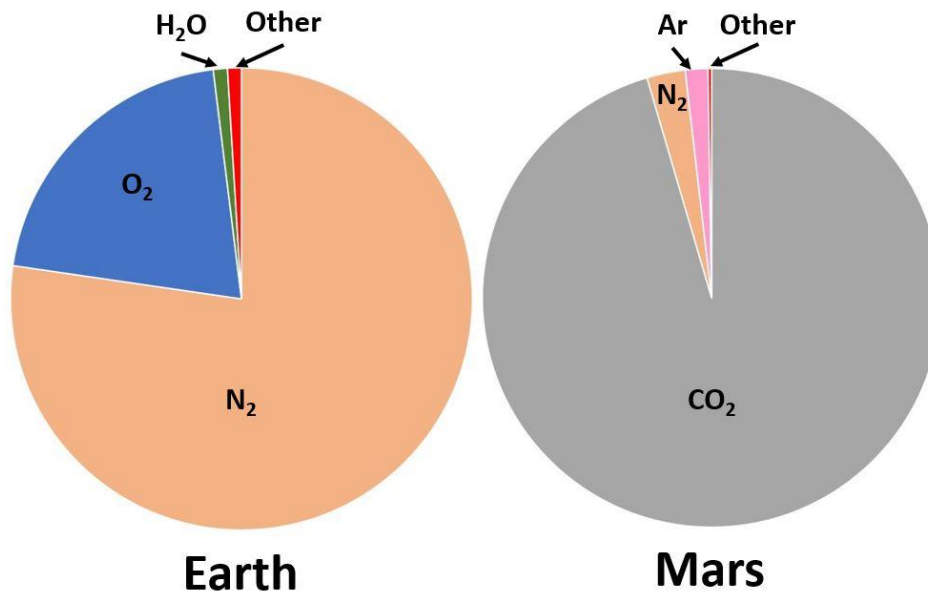


Figure 3.12. The one sixth escape speed required for elements and molecules to escape planetary bodies in the solar system based on surface temperature (Catling & Zahnle, 2009). If the mean thermal velocity of a gas exceeds one sixth of the planet’s escape velocity, then Jeans escape becomes considered a significant mechanism for that gas escaping a planet’s atmosphere.

Table 3.1. Atmospheric compositions of modern Earth and Mars (Website 4 for Earth, Website 5 for Mars). On Earth, other extremely minor components include sulphur dioxide, ammonia, hydrogen sulphide, dimethyl sulphide, tropospheric ozone, radicals, methylchloroform and carbon tetrachloride.



Earth surface atmospheric pressure = 1.014 bars Mars surface atmospheric pressure = 0.006 bars

Element	Earth % volume	Mars % volume	Earth ppm	Mars ppm
Nitrogen (N ₂)	78.09	2.7	780900	27000
Oxygen (O ₂)	20.95	0.13	209500	1300
Water vapour (H ₂ O)	~1% (variable)	0.021	~10000	210
Argon (Ar)	0.934	1.6	9340	16000
Carbon dioxide (CO ₂)	0.04	95.32	400	953200
Neon (Ne)	0.0018	0.00025	18.18	2.5
Helium (He)	0.000524	n/a	5.24	n/a
Methane (CH ₄)	0.00017	*	1.7	*
Krypton (Kr)	0.00014	0.00003	1.14	0.3
Hydrogen (H ₂)	0.000055	n/a	0.55	n/a
Carbon monoxide (CO)	*	0.08	*	800
HDO	*	0.000085	*	0.85
Xenon (Xe)	*	0.000008	*	0.08

*Extremely minor component. HDO = Hydrogen - Deuterium - Oxygen. ppm = Parts per million.

Non-thermal escape of atmospheric molecules can also occur on Mars, partly due to the collapse of the Martian dynamo ~4000 Ma (Arkani-Hamed & Olson, 2010). Non-thermal mechanisms include ion pickup, bulk plasma escape, dissociative recombination and photoelectron-induced ambipolar escape (Dubinin *et al.* 2011; Gacesa *et al.* 2012). Modelling and observation of current Mars hydrogen loss ($\text{H} + \text{H}_2$) to space via Jeans escape is $2.4 \times 10^8 \text{ cm}^{-2} \text{ s}^{-1}$ (Donahue, 1995) or $2.5 \times 10^8 \text{ cm}^{-2} \text{ s}^{-1}$ (Krasnopolsky, 1993).

The oxygen isotope ratio $^{18}\text{O} / ^{16}\text{O}$ ($\delta^{18}\text{O}$) can also be used to explore the history of water, with the abundance of $\delta^{18}\text{O}$ decreasing with increasing temperature, thus acting as a proxy for palaeothermometry (Webster *et al.* 2013), although $\delta^{18}\text{O}$ in Martian meteorites does not appear to fractionate leaving heavier isotopes behind, thus has not been used to evaluate atmospheric escape (Webster *et al.* 2013). $^{17}\text{O} / ^{16}\text{O}$, $^{13}\text{C} / ^{12}\text{C}$ ($\delta^{13}\text{C}$), $^{13}\text{C}^{18}\text{O} / ^{12}\text{C}^{16}\text{O}$ isotope ratios in CO_2 are also useful in understanding a planet's early atmosphere, with heavier isotopes remaining preferentially as atmosphere is lost to space. Gas, such as CO_2 , trapped in Martian meteorites can provide an accurate representation of Martian atmosphere development through time, with EETA 79001 providing one of the most reliable sources of true Martian atmosphere, with $\delta^{13}\text{C}$ of $36 \pm 10\text{‰}$ (Carr *et al.* 1985). Martian meteorites will be discussed in further detail below.

3.1.6 Meteorites.

3.1.6.1 Overview.

Nearly all the Martian meteorites can be categorised as either a shergottite, nakhlite or chassignite, collectively termed the SNC's. Meteorites provide a valuable petrologic record of the Martian past volcanism, hydrology and crust - atmosphere exchange; they can contain carbonates, sulphates and hydrated minerals.

- **Shergottites** are the largest group of Martian meteorites and can further be categorised as basaltic (with a sub group of olivine-phyric) or lherzolitic. They are named after the archetypal 4kg shergotty meteorite which fell in India in 1865. Most basaltic shergottites are dominated by augite, pigeonite pyroxene and relict plagioclase feldspar, while the lherzolites are dominated by olivine and orthopyroxene (Bridges, 2004). Shergottites can be partial cumulates, ultramafic cumulates and basalts, all usually not representative of the original melt source, which can confuse dating (Jones, 2015). Xenoliths have been found in EET 79001 (McSween & Jarosewich, 1983), complicating source identification. The shergottites are the only class of meteorite to have no good evidence for Martian aqueous alteration. Recent research on Dhofar 019 showed aqueous alteration rosettes with poorly ordered Mg-phyllsilicate and calcite, yet this was considered to come from terrestrial alteration (Hallis *et al.* 2017). However, the meteorite Tissint has offered mineral alteration evidence of subsurface Martian water, with δD values of 4600 ± 600 ‰, indicating alteration of the minerals by surface water ≤ 600 Ma ago (Chen *et al.* 2015).

Dating the shergottites has been problematic. It has been claimed $^{40}\text{Ar}/^{39}\text{Ar}$ age estimates are ~25% older than other dating methods such as Sm-Nd, with suggestions that ^{40}Ar has been added from other sources (Park *et al.* 2014). Early studies using U-Pb dating placed some shergottites as old

as 4000 Ma to 4500 Ma (Chen & Wasserburg, 1986), and more recently studies have placed the shergottite ages between 4100 Ma and 4300 Ma using Pb-Pb dating (Bouvier *et al.* 2005; Bouvier *et al.* 2008; Bouvier *et al.* 2009). Younger estimates ranged from 180 Ma using Sm-Nd (Jones, 1986). This difference in age depending on the chronometer used has been termed by others as the Shergottite age paradox (Nyquist *et al.* 1998). However, more recent research using Sm-Nd and Rb-Sr dating combined with REE partition coefficients indicate they have a relatively young age ≤ 600 Ma originating from a low water mantle source (Jones, 2015).

- **Nakhlites** are relatively young $\sim 1322 \pm 10$ Ma to 1416 ± 7 Ma (Cohen *et al.* 2017) olivine bearing clinopyroxenites that possess melt inclusions within olivine and augite (Sautter *et al.* 2012). Olivine zonation indicates they may have all originated from differing depths in the same magma sill or sills (Mikouchi *et al.* 2012), this is supported by $\delta^{13}\text{C}$ values (Grady *et al.* 2007). More recent studies indicate that multiple sills one atop the other are more likely than a single sill, based on augite zoning in NWA 5790 (Jambon *et al.* 2016), probably crystallising from at least four separate eruptive events spanning 93 ± 12 Ma (Cohen *et al.* 2017). Based on overlapping cosmogenic exposure ages of the Nakhlites it is thought that they ejected from Mars during a single impact event $\sim 10.7 \pm 0.8$ Ma ago (Cohen *et al.* 2017). Products of aqueous alteration such as hydrated silicates, iron oxide, iron oxyhydroxides, sulphates and chloride evaporates contained in the nakhlites make them of exceptional interest with respect to Martian mineral carbon sequestration dynamics (Lee *et al.* 2013).
- **Chassignites** are named from the archetype meteorite Chassigny, now with the addition of NWA2737. Chassignites share a remarkable number of similarities with the nakhlites with respect to age, petrography and cosmic ray exposure age. These similarities have led some researchers to conclude they may have a shared magmatic history (McCubbin *et al.* 2013), possibly originating at the same location on Mars. They are composed dominantly of olivine ($\sim 90\%$), and the rest is mostly pyroxene, plagioclase and chromite

(Bridges, 2004). Chassigny itself contains ~92% olivine and is a dunite (Fo₆₈), with shock features (Floran & Prinz, 1978). Chassignite has been variously dated at 1390 ± 3 Ma based on ¹⁴⁷Sm-¹⁴³Nd (Ozawa *et al.* 2009) to 1640 ± 7 based on ²⁰⁶Pb-²³⁵U (Ozawa *et al.* 2009; Ozawa *et al.* 2011). Ca-carbonate (CaCO₃), Mg-carbonate (magnesite and hydromagnesite), and Ca-sulphate (CaSO₄·2H₂O or CaSO₄·0.5H₂O) have been identified in Chassigny (Wentworth & Gooding, 1994). It was hypothesised that Martian soil components were incorporated into chassignite veins (Rao *et al.* 1999), although recent geochemical analysis dismisses this (Barrat *et al.* 2014).

- **Unique meteorites.** The Martian meteorites Alan Hills (ALH) 84001 and NWA 7034 / 7533 / 7455 (informally termed Black Beauty) fit outside of the SNC categorisations. Black beauty is thought to be a water altered polymict breccia ≤4400 Ma old (Agee, 2014; Beck *et al.* 2015; Wittmann *et al.* 2015), but will not be examined in this work. There is also NWA 8159, an augitic basalt from a depleted mantle source, dated ~ 2300 ± 500 Ma, which displays signs of aqueous alteration, including carbonate, although much of this may be terrestrial alteration (Hallis *et al.* 2016). ALH 84001, which is the oldest of the Martian meteorites at ~3900 +/- 40 Ma (Rb / Sr) and ~4004 +/- 100 Ma (Pb / Pb) (Borg *et al.* 1999) has here been studied in some detail.

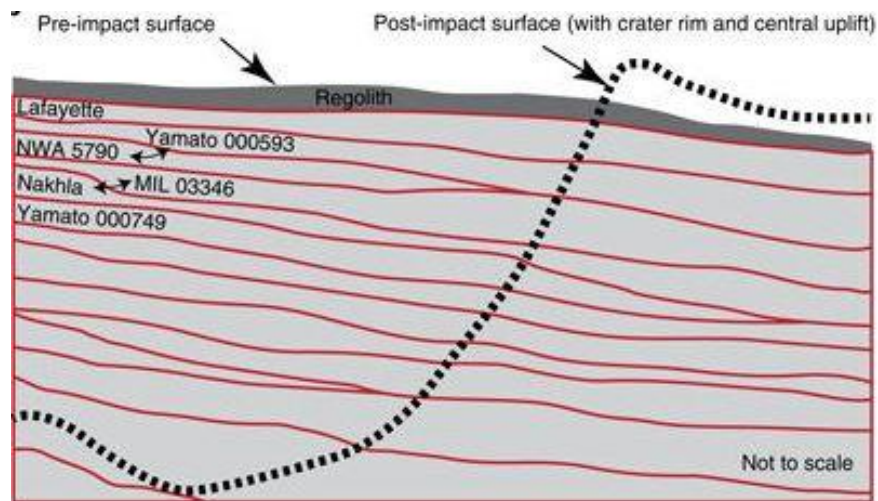


Figure 3.13. Sequence of burial depth in the proposed Nakhlite stack, based on $^{40}\text{Ar}/^{39}\text{Ar}$ age data (from Cohen *et al.* 2017). Also shown is a hypothetical outline of the crater from the impact that ejected all the Nakhrites in a single event $\sim 10.7 \pm 0.8$ Ma ago (Cohen *et al.* 2017).

3.1.6.2 Verifying meteorite age and Martian origin.

Numerous lines of evidence can potentially link a meteorite to a Martian origin and age. Martian meteorites are classed as achondrite based on their chemical composition and fractionation (McSween, 1985). Achondrites are defined as fractionated material not containing the chondrules of early solar system material that define chondrites. The two 1975 Viking missions analysed the atmospheric composition of Mars, which can be identically matched in gas inclusions within Martian meteorites (Pepin, 1985). Mars meteorites also have distinctive characteristics including:

- Fe oxide minerals such as magnetite, chromite etc.
- The Fe sulphide pyrrhotite instead of the troilite that occurs in most chondrites.
- Highly specific Fe : Mn ratio in pyroxene and olivine (Fig 3.14)(Irving, 2014).
- Distinct oxygen isotope compositions (Fig 3.15).
- Unique rare Earth element (REE) abundances such as lanthanum and gallium (Meyer, 2006).

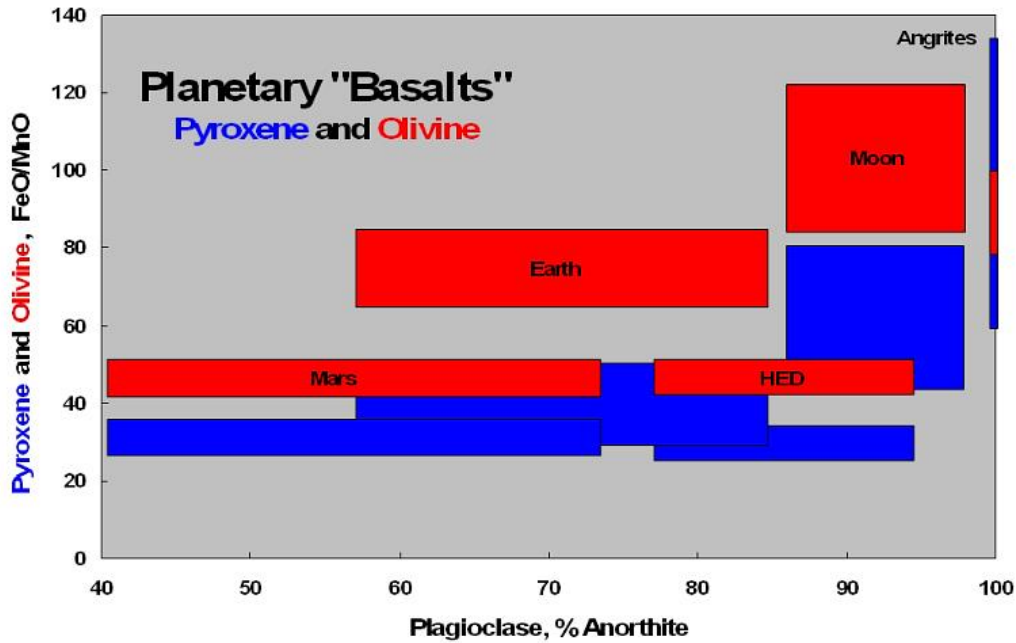


Figure 3.14. Fe / Mn ratio of basaltic minerals pyroxene and olivine vary between planets (Irving, 2014).

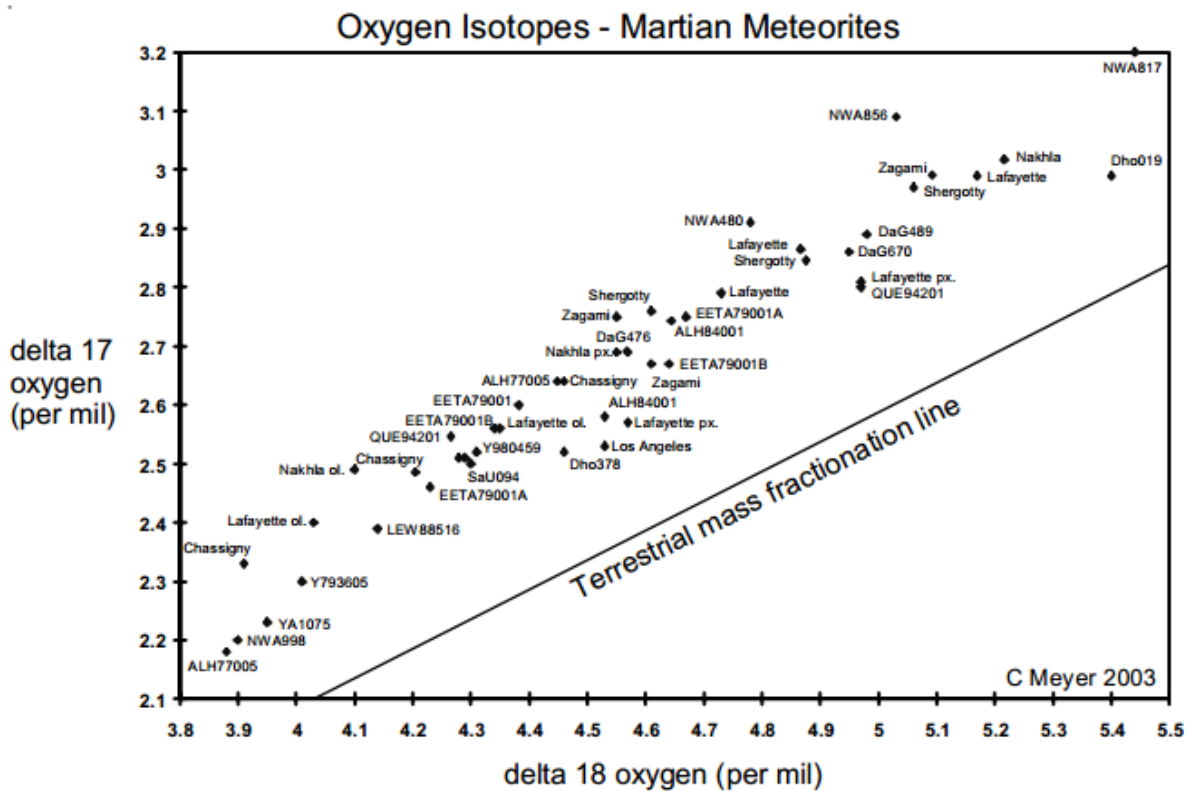


Figure 3.15. Oxygen isotope ratios of martian meteorites compared to terrestrial mass fractionation (Meyer, 2006).

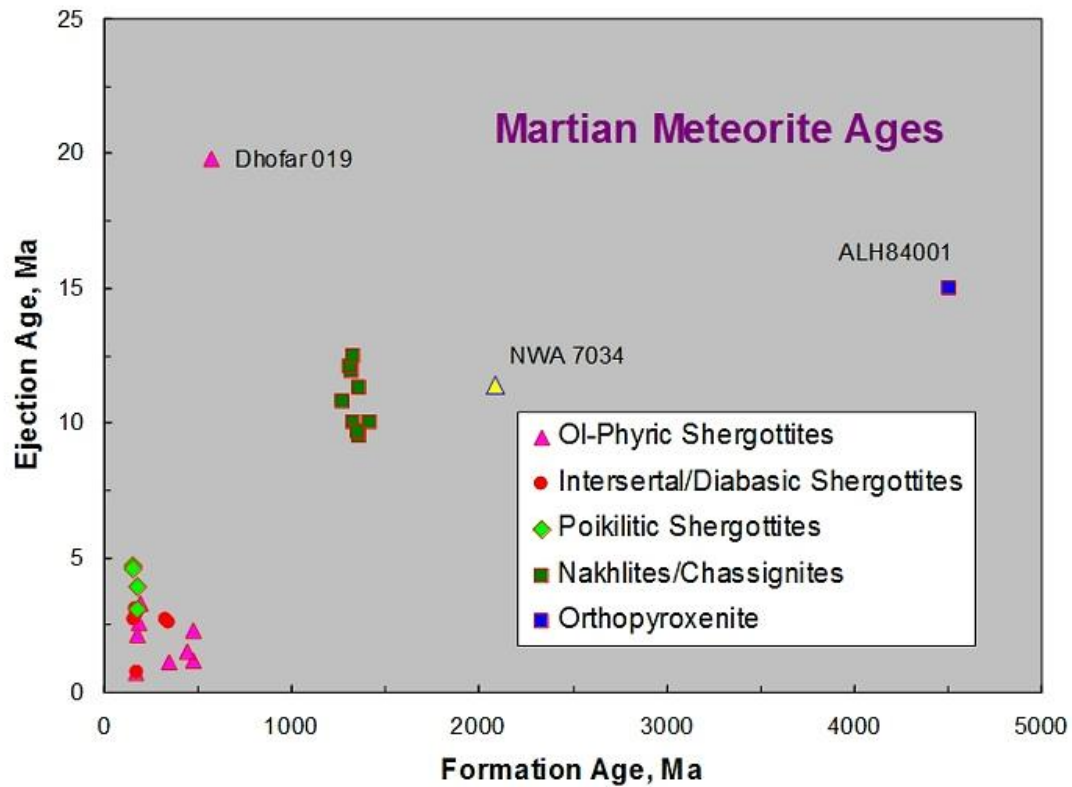


Figure 3.16. Ages of the Martian meteorites (Irving, 2014).

The ages of formation and ejection of the two samples used in this study can be seen in Figure 3.16, representing early Mars (ALH 84001) and more recent Mars (Lafayette). Martian meteorite ages (Fig 3.16) are determined by isotopic dating such as Rb / Sr, Pb / Pb (Borg *et al.* 1999), $^{147}\text{Sm}-^{143}\text{Nd}$, $^{206}\text{Pb}-^{235}\text{U}$ (Ozawa *et al.* 2009), $^{40}\text{Ar}/^{39}\text{Ar}$ etc. Determining ages is particularly problematic in older meteorites such as ALH 84001 where repeated shock resetting has occurred.

3.1.6.3 ALH 84001: Carbonate formation on early Mars.

Alan Hills (ALH) 84001 is unique among Martian meteorites, falling outside SNC categorization, and possessing a relatively high abundance (~1%) of heterogeneous carbonates (Fig. 3.17).

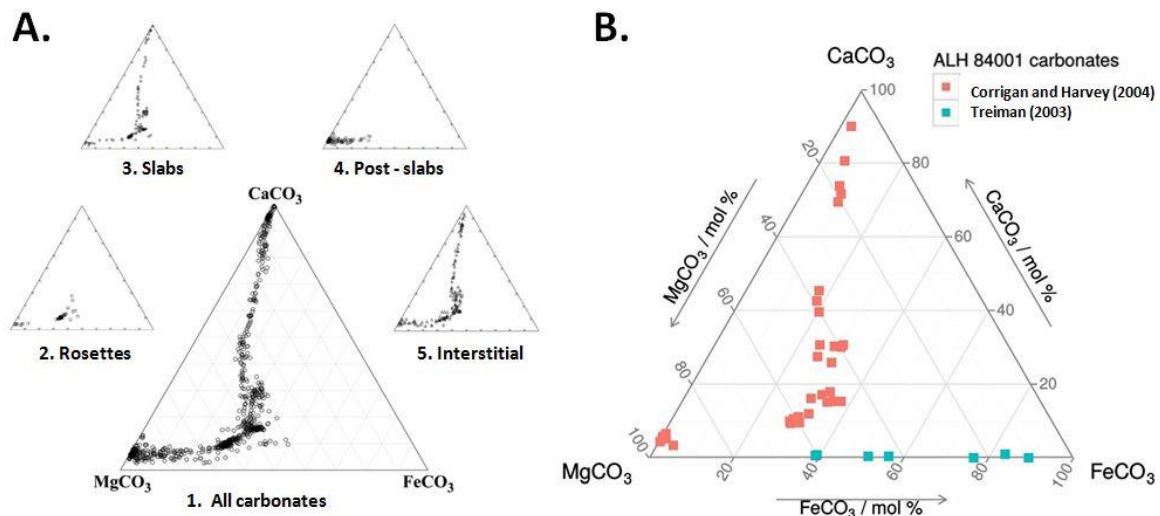


Figure 3.17. A. Chemical compositions of ALH 84001 carbonates. **1.** All carbonates. **2.** Rosettes. **3.** Slabs. **4.** Post - slabs. **5.** Interstitial. (Corrigan & Harvey, 2004). **B.** Chemical composition ternary of ‘all carbonate types’ in ALH 84001 (Daswani *et al.* 2016), contrasting the chemical findings between two different studies (Corrigan & Harvey, 2004; Treiman, 2003).

In addition to chemical variation, ALH 84001 carbonates divide into several physical structural types, described in figure 3.17.A.

This study reviews the major carbonate types observed in ALH 84001 and provides SEM and TEM analysis of two minor carbonate phases not described in figure 3.17 A. The two additional carbonates types presented are:

Carbonates in lines of glass weakness: Minor phase carbonates prevalent in lines of weakness within Al - Si rich glass, indicative of direct glass replacement.

Lamellae carbonates: Carbonates whose lamellar pattern precisely matches those in adjacent orthopyroxene grains, indicative of isomorphous carbonate replacement of orthopyroxene or a maskelynite glass intermediary.

ALH 84001 is a coarse grained cumulate orthopyroxenite that was found in Antarctica in 1984 and originally misclassified as a diogenite (from asteroid 4 Vesta), later reclassified in 1994 as Martian in origin (Mittlefehldt, 1994). Its crystallisation age is difficult to determine due to multiple shock events that wave reset isotopic ratios, though $\sim 4091 \pm 30$ Ma appears likely (Lapen *et al.* 2010). ALH 84001 consists of 96% orthopyroxene, 2% chromite, 1% plagioclase feldspar, 0.15% phosphate, with accessory augite, olivine, pyrite and carbonates (Nyquist *et al.* 2001). ALH 84001 has a high abundance of heterogeneously distributed carbonates relative to other Martian meteorites; some estimates place this abundance at $\sim 1\%$ (Romanek *et al.* 1994), while others suggest 0.46% (Dreibus *et al.* 1996). ALH 84001 does not contain the hydrated silicates that the nakhlite meteorites possess.

ALH 84001 carbonate formation age varies depending on the isotopic method used, with $\sim 3900 \pm 40$ Ma based on Rb / Sr, or $\sim 4004 \pm 100$ Ma based on Pb / Pb (Borg *et al.* 1999). Controversy enveloped ALH 84001 in 1996, when it was claimed that carbonate globules contained morphological evidence for magnetotactic bacterial structures analogous to the terrestrial *Magnetospirillum magnetotacticum* (McKay *et al.* 1996). It was suggested that these bacteria were responsible for both carbonate formation and the observed magnetite grains (McKay *et al.* 2003). A wide variety of robust abiotic carbonate formation theories have since been provided, for both the carbonate and magnetite formation. Principal ALH 84001 carbonate formation theories are:

Biogenic carbonate formation is based on ALH 84001 carbonates having $\delta^{13}\text{C}$ values of ≤ 42 ‰, similar to terrestrial biogenic carbonates. A polycyclic aromatic

hydrocarbon presence of >1 ppm also lends support to the biogenic model (McKay *et al.* 1996). Visual petrographic interpretation was heavily used in comparing the observed carbonates to terrestrial biological bacterial structures.

The impact metasomatism carbonate formation model is based on ALH 84001 phase relations of CaO - MgO - SiO₂ - H₂O using observation and calculation, C and O isotope analysis, combined with visual petrographic interpretation. These observations led to the conclusion that high temperature (>650 °C) impact induced reaction occurred between CO₂ saturated fluids and the mafic mineralogy resulting in carbonate formation (Harvey & McSween, 1996).

The impact melt carbonate formation is based on localised heterogeneity of K, Na, Ca in ALH 84001 glass which is indicative of non - stoichiometric open system formation (Scott *et al.* 1997). These element distributions led researchers to conclude that pre - existing carbonates and plagioclase were impact melted via localised crushing and redistribution, followed by rapid cooling within seconds (Scott *et al.* 1997).

The evaporation - precipitation carbonate formation model advocates that carbonates formed from low temperature (25 to 100 °C) brines within a closed system, and is based on ALH 84001 O isotope analysis and visual petrographic interpretation. The brine evaporates, precipitating as carbonate, occluding and cementing pore spaces (Romanek *et al.* 1994; Bridges *et al.* 2001).

The mineral / glass replacement model suggests carbonates replaced plagioclase glass in both clast and granular band settings, and that carbonate formation was later followed by shock micro offsetting (Treiman, 1995). This model is closely linked, but not identical to the impact melt model.

ALH 84001 was shocked to $\sim 32 \pm 1$ Gpa, a determination based on the presence of diaplectic glass and Raman spectroscopy studies (Fritz *et al.* 2005), although the inability to replicate these findings by experimental petrology has led to a higher estimate of 49 Gpa (Bell, 2007). This higher shock pressure is further

supported by vibrational spectroscopic studies on ALH 84001 plagioclase, indicating a shock pressure >50 Gpa (Cooney *et al.* 1999). Such high pressures potentially make melt glass a more appropriate term when discussing the majority of observed glass, rather than maskelynite, and the distinction is particularly important when discussing glass - carbonate reactions. Plagioclase melt glass is often misleadingly referred to as maskylenite in the ALH 84001 literature, and although both maskelynite and plagioclase melt glass are present in ALH 84001, the terms are often wrongly used rather interchangeably.

Diaplectic glass, thetomorphic glass and maskelynite: Synonyms for glass formed by shock at pressures of ~30 to 50 Gpa and temperatures beneath the plagioclase melting point. It is a solid-state transformation from original mineralogy to isotropic glass, usually preserving all pre-shock crystalline textures such as grain boundaries and twinning (Gary *et al.* 1973).

Melt glass: Shock pressures and temperatures above the plagioclase melting point, causing compositional disorder and quenching to glass; often possessing flow structure, vesiculation and loss of all pre-shock crystalline texture.

Enormous scope exists for an expanded analysis of glass in ALH 84001. Modelling and experimentation of terrestrial glass density, structural properties and pore space cavitations (thereby surface volume) have been conducted in considerably detail (Debenedetti *et al.* 2001). Similar research into ALH 84001 glass could provide valuable insight into the meteorite's thermal and aqueous history.

This study uses SEM and TEM to identify two carbonate types intimately associated with ALH 84001 glass. Because the formation of carbonate formation process is intrinsically linked to the availability of water, it follows that the extent to which minerals, and particularly glass, are replaced by carbonate is a useful indicator for the quantity of water available in the system at the time of formation; thus providing clues about planetary water on early Mars, and by inference, atmospheric density and temperature. This study's interpretation of its

carbonate findings lend support to a multiple shock, deformation and fracturing history forwarded by other researchers (Treiman, 1998):

Table 3.2. Approximate timeline of impacts (I), deformation (D), chemical events I, fracturing (Fr) and formation - melt mobilisation of carbonates and glass in ALH 84001. *Adapted from Treiman, (1998).*

Impacts	Deformation	Chemical	Fractures	Carbonates	Glass	Age (Ma)
	D0 Igneous cooling	C1 Cumulate from basalt melt				~4500
		C2 Sub solidus equilibration Aqueous alteration?				
I1	D1 Granular bands					~4000
I2	D2		Fr2	Rosettes	Feldspathic glass	~4000
		C3				
I3	D3		Fr3	Mobilisation	Mobilisation	~1400
I4	D4		Fr4 Ejection from Mars?			
I5	D5		Ejection from Mars			~15

The carbonates in ALH 84001 have been categorised in numerous ways, and the nomenclature can swiftly become bewilderingly convoluted and often contradictory. This study will use the categories provided by Corrigan & Harvey (2004), deeming their system particularly simple and distinct (Corrigan & Harvey, 2004) (Fig. 3.16.A). The principal carbonate types observed in the meteorite under this system are rosettes, slabs, post slabs and interstitial.

Rosettes (Fig. 3.18) are circular or partial semi - circular in shape, often concentrically chemically zoned in a Ca - Mg - Fe pattern (Corrigan & Harvey, 2004), manifesting as calcite (CaCO_3), dolomite - ankerite ($\text{CaMg}(\text{CO}_3)_2 - \text{I}(\text{CO}_3)_2$), magnesite - siderite ($\text{MgCO}_3 - \text{FeCO}_3$), although pure calcite is rare (Harvey & McSween, 1996). Metastable carbonates are also present, spanning compositions between these clear mineral divisions outlined above (Leshin *et al.* 1998). The rosettes formed at ~D2 in the ALH 84001 timeline (Table 3.2), ~4000 Ma ago, as a

result of the second major impact. In other literature the rosettes are termed globules or pancakes, varying between these terms depending on how three dimensional (globule) or two dimensional (pancake) the carbonate is (Treiman, 1995; Treiman, 1998). Both slab and rosette growth are thought to be kinetically rather than thermodynamically controlled (McKay & Lofgren, 1997; Corrigan & Harvey, 2004).

Although most research agrees that the rosettes formed by growth within an evolving fluid, much debate exists as to the precise temperature and composition of this fluid. Fluid temperature estimates vary, on the lower end 0 - 80°C is estimated based on $\delta^{18}\text{O}$ thermometry, whereby carbonate is dissolved using acid digestion technique, with different carbonate compositions dissolving at different rates in the acid, hence an evolving oxygen output over time (Romanek *et al.* 1994). $\Delta^{18}\text{O}$ was found to be much higher in the carbonate than the host rock (Romanek *et al.* 1994). This low temperature (high $\delta^{18}\text{O}$) carbonate, value has also been supported by ion microprobe analysis (Valley *et al.* 1997). Mid-range estimates predict a 40 - 250°C formation temperature, also based on $\delta^{18}\text{O}$ thermometry (Hutchins & Jakosky, 1997); upper estimates are up to ~650°C (Harvey & McSween, 1996) and assume impact induced metasomatic fluid flow.

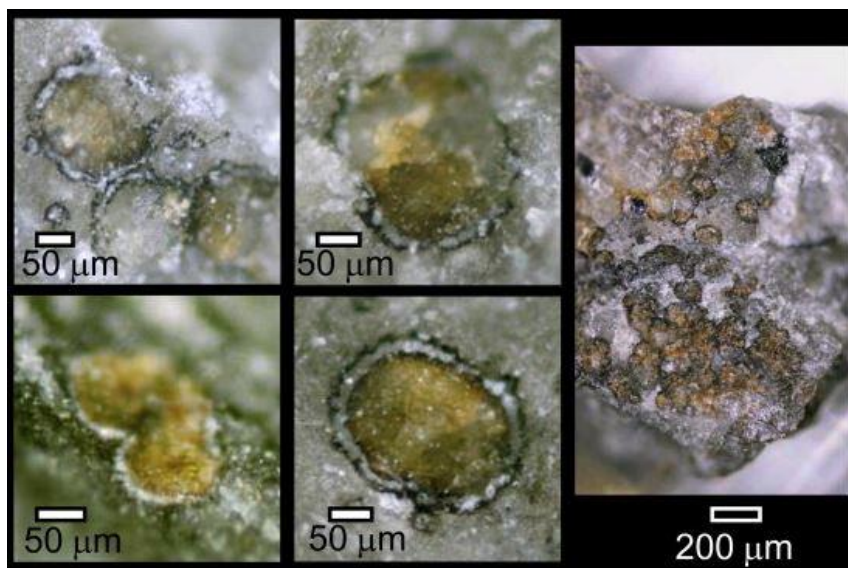


Figure 3.18. Optical microscope images of concentrically zoned rosette carbonates from ALH 84001 (Thomas-Keprta *et al.* 2009).

The outer rims of the rosettes are clearly different to the centre, observable even to the naked eye (Fig. 3.18). The rosette rims are composed of sometimes pure magnesite, or a magnesite and siderite mix. A clear element division can be observed between zones, most obvious in the variations of Ca and Mg (Fig 3.19). They are thought to have been caused by a chemical alteration event occurring after the initial kinetic growth stage (Corrigan & Harvey, 2004); the rims therefore probably formed ~C3 in the ALH 84001 timeline (Table 3.2).

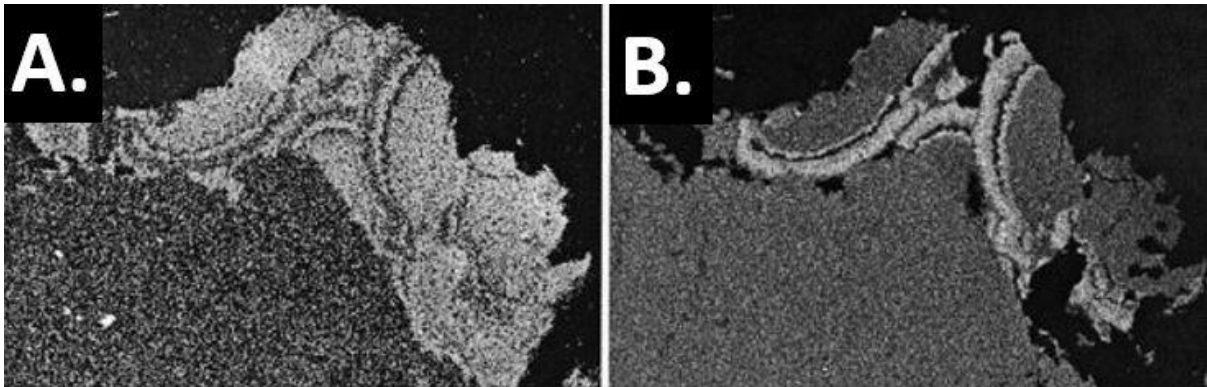


Figure 3.19. X-ray element distribution maps for ALH 84001 carbonates. **A.** Calcium. **B.** Magnesium. (Eiler *et al.* 2002).

Slab type carbonates.

Slab carbonates (Fig. 3.20) can also be zoned, usually with a more Ca rich nucleus that is often not observed in the rosettes (Corrigan & Harvey, 2004).

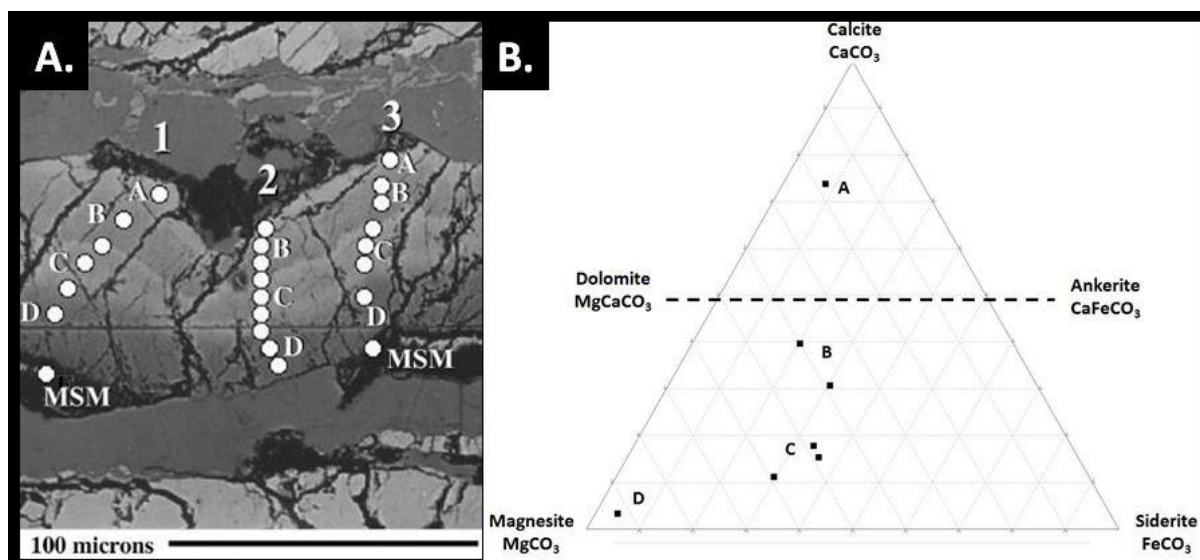


Figure 3.20. A. A ‘classic’ parallel chemically layered slab carbonate (Corrigan & Harvey, 2004). MSM = magnesite - siderite - magnesite layer. Black is feldspathic glass. Host rock walls are orthopyroxene. B. Carbonate chemistry ternary plot (atomic %) of data row 1 from A, letters correspond with approximate position of letters in A.

Both rosette and slab type carbonates possess the same chemical zonation pattern of Ca - Mg - Fe, described above. It has been forwarded that both rosettes and slabs likely formed via the same process, experiencing identical fluid chemistry and that it is local petrographic structure that dictates whether the carbonate grows as a rosette or slab (Leshin *et al.* 1998). Glass is observed to cross cut all carbonate zones (Eiler *et al.* 2002).

Whether these rosettes and slabs evolved in a deep closed system shut off from atmospheric O₂ and CO₂ recharge, or in a shallow open fluid flow system is also debated (Leshin *et al.* 1998; Halevy *et al.* 2011). Using the co variance of δ¹⁸O and δ¹³C Halevy *et al.* (2011) present a more nuanced chemical evolution of carbonates in ALH 84001 whereby lower δ¹⁸O correlates with increased Ca content (Fig. 3.21). The SMOW range was relatively narrow (5 - 30‰) between rosette core and rim indicating a similar formation temperature, probably ~ 18 ± 4 °C (Halevy *et al.* 2011). Crucially for the results of this thesis, Halevy *et al.* (2011) suggest the evolution of δ¹⁸O and Ca is due to carbonate formation in a shallow subsurface

aquifer. They hypothesise the water in this aquifer evaporated causing the $\delta^{18}\text{O}$ enrichment via fractionation. This thesis will advocate that a change in aquifer fluid, analogous to terrestrial ophiolite aquifer types, may account for such changes in both element composition and $\delta^{18}\text{O}$.

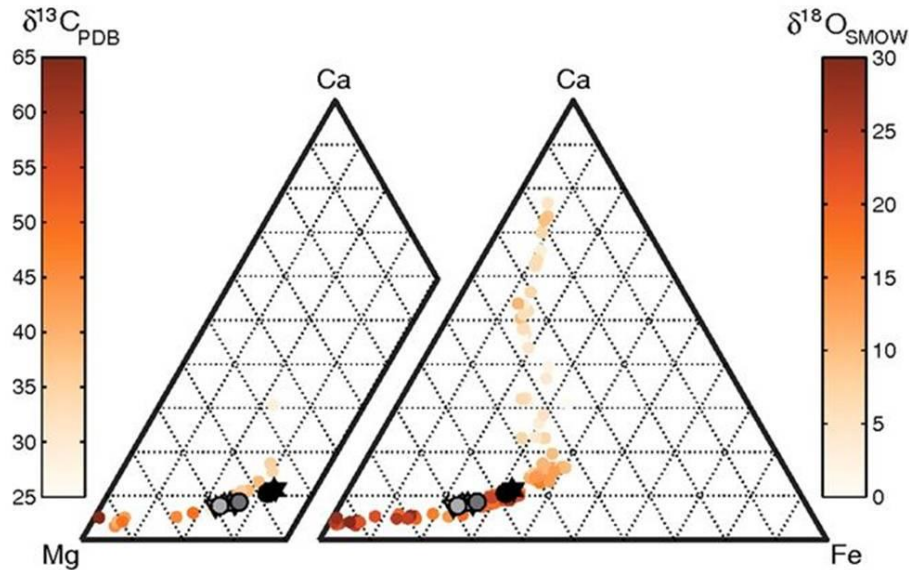


Figure 3.21.

Variations in $\delta^{18}\text{O}$ and $\delta^{13}\text{C}$ with observed carbonate composition (Halevy *et al.* 2011).

Corrigan and Harvey (2004) observe a “lack of any compositional changes associated with glass/carbonate contacts”; however, this thesis adds a further two carbonate types to their system which contradict this statement and indicate that melt glass has likely transformed into carbonate minerals.

3.1.6.4 Lafayette: Carbonate formation on recent Mars.

Lafayette is one of the nakhlite group of meteorites. Weighing 800g, it is compositionally similar to Nakhla and Govenador Valdares. It is a single stone possessing a fusion crusted cone like shape. Of all the Martian meteorites Lafayette possesses the most water (Karlsson *et al.* 1992) and the most secondary alteration products (Treiman *et al.* 1993). Its crystallisation age is 1322 ± 10 Ma using $^{40}\text{Ar} - ^{39}\text{Ar}$ techniques (Swindle & Olson, 2004), and was ejected from Mars 11 million years ago, based on cosmic ray exposure. Due to its near-pristine condition it is assumed it had a very short terrestrial residence time prior to curation (Nininger, 1935).

The mineralogy of Lafayette is dominantly zoned clinopyroxene (augite) with MgO rich cores (13.6 wt. %) and MgO poor rims (10.9 wt. %), with some orthopyroxene, plagioclase feldspar, Fe rich olivine and minor K-feldspar, Ti - Fe magnetite, chalcopyrite and marcasite, and the mesostasis is plagioclase / glass (Treiman, 2005). Alteration products comprising smectite clays, carbonates and Fe oxides occur in aqueously formed olivine veins (Swindle *et al.* 2000). These veins are interpreted to have predated the fusion crust, and thus formed on Mars (Treiman *et al.* 1993). At least some of this iddingsite has been K - Ar dated to 670 ± 91 Ma, and combined with an iddingsite Xe isotopic fingerprint distinct from terrestrial Xe, indicates that there must have been liquid water on Mars even as recently as this age (Swindle *et al.* 2000). The hydration of minerals may also have been affected by interaction with the Martian atmosphere by adsorption of atmospheric H₂O (Gilmour *et al.* 1999).

The principal focus of this study is on the early Mars aqueous history and the carbonate in ALH 84001. However, Lafayette has been analysed using SEM, specifically observing veins of alteration and carbonate formation. This work is predominantly qualitative SEM image analysis or X-ray mapping; the small amount of quantitative analysis is included in appendix 4. The purpose of including Lafayette is to provide comparative context to both ALH 84001 alteration, and as a more recent Mars comparison to the terrestrial ophiolite alteration.

3.2 A review of terrestrial ophiolites.

3.2.1 Introduction.

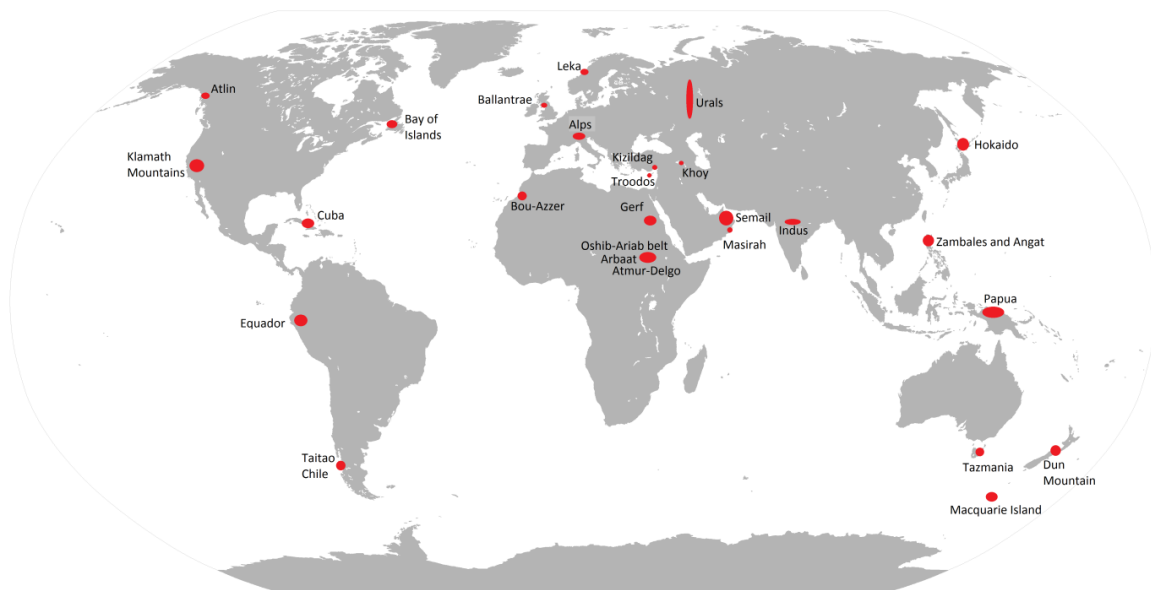


Figure 3.22. Principal terrestrial ophiolite regions. Area of red dot does not indicate size or importance.

Ophiolite is a term used when oceanic crust is obducted onto continental crust. Ophiolites occur worldwide (Fig. 3.22), and retain the same stratified petrology as the sea floor (Fig. 3.23); albeit deformed, weathered and chemically altered. Ophis is Greek for serpent or snake, and relates to the characteristic green colour in these landscapes, provided by the mineral olivine that is prevalent in basalt, gabbro and peridotite. The simplified and idealised structure of an ophiolite complex is illustrated in Figure 3.23.

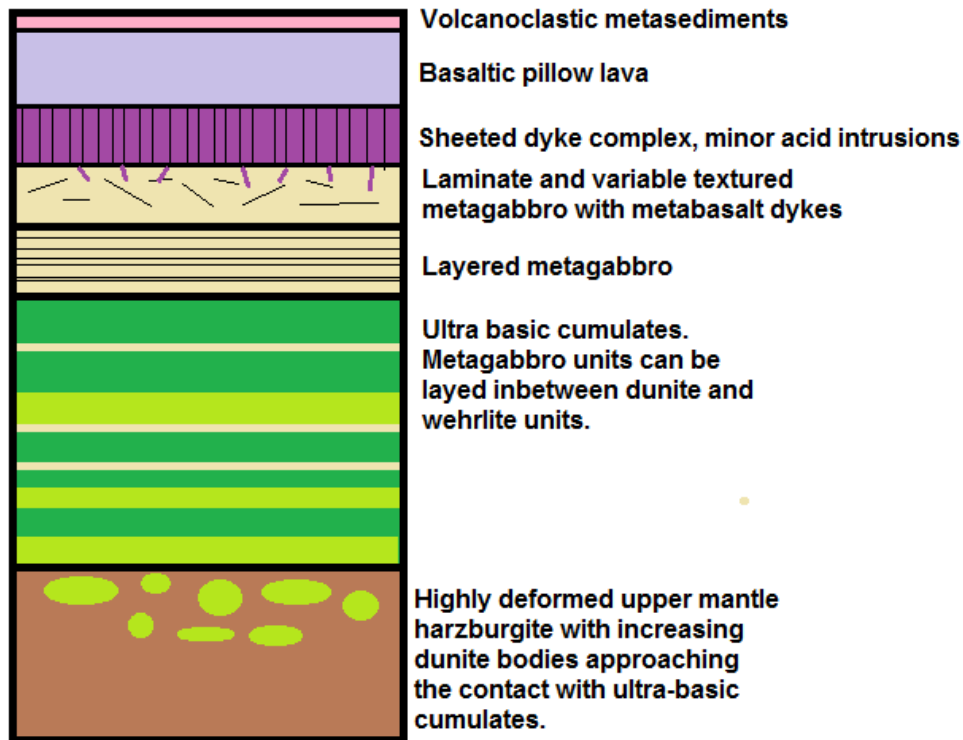


Figure 3.23. Illustration of the idealised sequence of mineralogy in an ophiolite complex. In reality, layers are often missing, partial or metamorphosed.

Ophiolites expose large volumes of basalt, gabbro and peridotite to weathering, hydration and potential carbonation. The minerals are strongly out of chemical equilibrium with the surrounding environment and are thus susceptible to rapid alteration, including carbonate formation with concomitant atmospheric CO₂ drawdown. Ophiolite basalt, gabbro and peridotite mineralogy is often used as a geological analogue for Mars in geological and astrobiological studies (Sadooni *et al.* 2010; Szponar *et al.* 2013); in part due to its high olivine content. For laboratory experiments San Carlos olivine, a mantle xenolith originating from a table plateaux (mesa) capped by basalt located immediately South West of San Carlos in North America, is the most commonly used Mars analogue olivine (Jain *et al.* 2006; Hausrath & Tschauer, 2013; McCollom, 2016).

There is a classic sequence of water chemistry with depth observed in many terrestrial ophiolites ranging from mildly acidic to ultra-alkaline, shown in Figure

3.24 (Barnes & O'Neil, 1969; Neal & Shand, 2002; Kelemen & Matter, 2008; Falk, 2014):

- Type 1.** Meteoritic water reacts with peridotite in shallow open aquifers forming magnesium bicarbonate waters Mg HCO_3 . Type 1 waters are CO_2 saturated. Magnesite or dolomite can precipitate.
- Type 2.** When type 1 waters percolate to a depth sufficient to become cut off from O_2 CO_2 recharge the waters become Na rich (137 to 178 mg l^{-1}) balanced by Cl-HCO_3 or $\text{SO}_4\text{-Cl}$ anions with low Mg. CO_2 under saturated. This is called type 2 water.
- Type 3.** These waters are hyperalkaline (pH 11.2 to 11.6) $\text{Na-Cl-SO}_4\text{-OH-CO}_3$ or $\text{Na-Ca-Cl-SO}_4\text{-OH}$ with low Mg. Type 3 waters are CO_2 under saturated and can extrude as hyperalkaline travertine springs, where Ca carbonates precipitate via both hydration-hydroxylation with surface waters and by reaction with atmospheric CO_2 (Leleu *et al.* 2016).
- Type 4.** These waters only occur in some ophiolites and contain high salts, representing a mixing with local sea waters. Type 4 waters are CO_2 undersaturated.

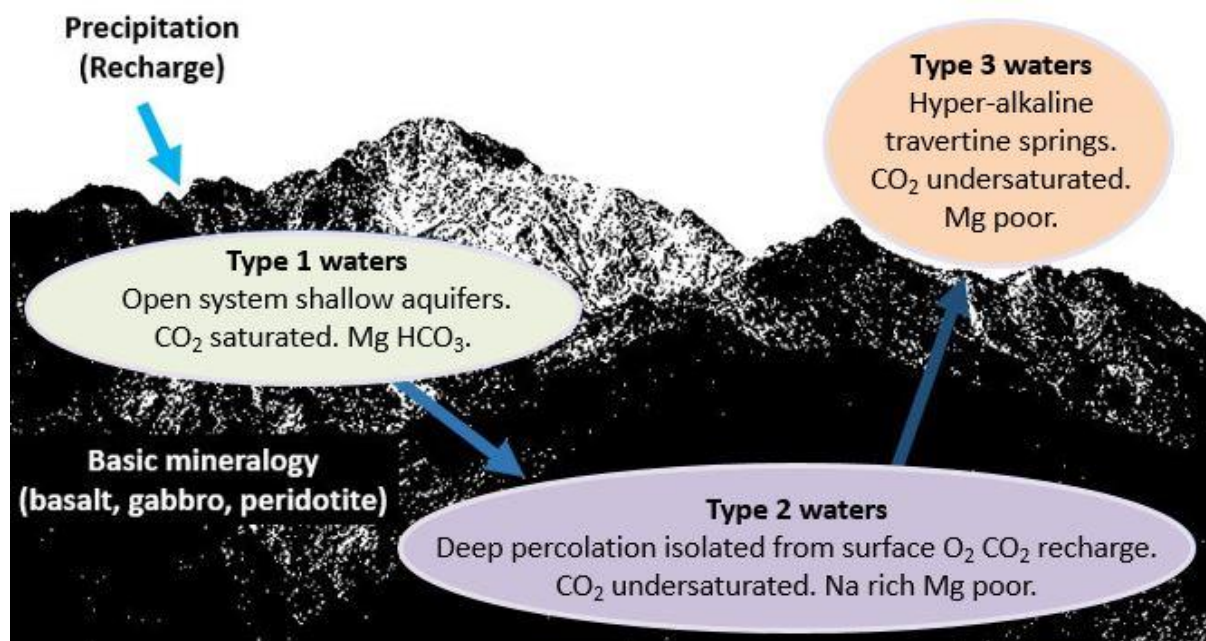


Figure 3.24. Illustration of ophiolite water types.

Some researchers simplify these waters into two types, merging types 1 and 2 together and discounting type 4 (Keleman & Matter, 2008). Neal & Shand, (2002) extend the water types to 5, and discuss the need for a more rigorous statistical framework of water types. This study uses the 4 water type division of Barnes & O'Neil, (1969). Weathering, serpentinisation and carbonation of terrestrial ophiolites produce a relatively steady release of abiotic methane and hydrogen gas with H₂ hydrogenating with CO₂ to produce CH₄ (Tsikouras *et al.* 2013; Falk, 2014; Etiope, 2017). Such abiotic methane releases are due to weathering of the mafic mineralogy and can occur in non - ophiolite mafic rock exposures such as igneous intrusions (Etiope *et al.* 2013). Low levels (10 ± 5 ppbv average) of methane release have also been observed in the modern Martian atmosphere (Formisano *et al.* 2004). Although some researchers suggest this may be due to subsurface life, and even go as far as estimating subsurface Martian biomass (Krasnopolsky *et al.* 2004), abiotic methane production similar to terrestrial ophiolite weathering appears more plausible (Oze & Sharma, 2005; Tsikouras *et al.* 2013). The potential for a deep subsurface microbial biosphere in the Semail ophiolite, however, remains an ongoing topic of research (Miller *et al.* 2016). The example of abiotic methane production via mafic mineral alteration and weathering clearly demonstrates that terrestrial ophiolites can offer insights into Martian crust-atmosphere processes.

It has been suggested that subaerial exposure of the ocean floor in the New Caledonian terrain of the South - West Pacific created a carbon sink $p\text{CO}_2 \sim 100$ ppmv during the Eocene (~35 Ma ago), which may have triggered the onset of the Antarctic glaciation (Reusch, 2011). The power of olivine weathering and alteration to transform whole planetary environments is perfectly feasible, both on Earth and Mars. This thesis investigates samples from two contrasting ophiolites, the Semail ophiolite from the United Arab Emirates which is rich in carbonate phases and the Leka ophiolite from Norway which is highly hydrated and serpentinised but relatively lacking in carbonates. The results are compared to Martian meteorites (Objective 3. C).

3.2.2 The Leka ophiolite, Norway.

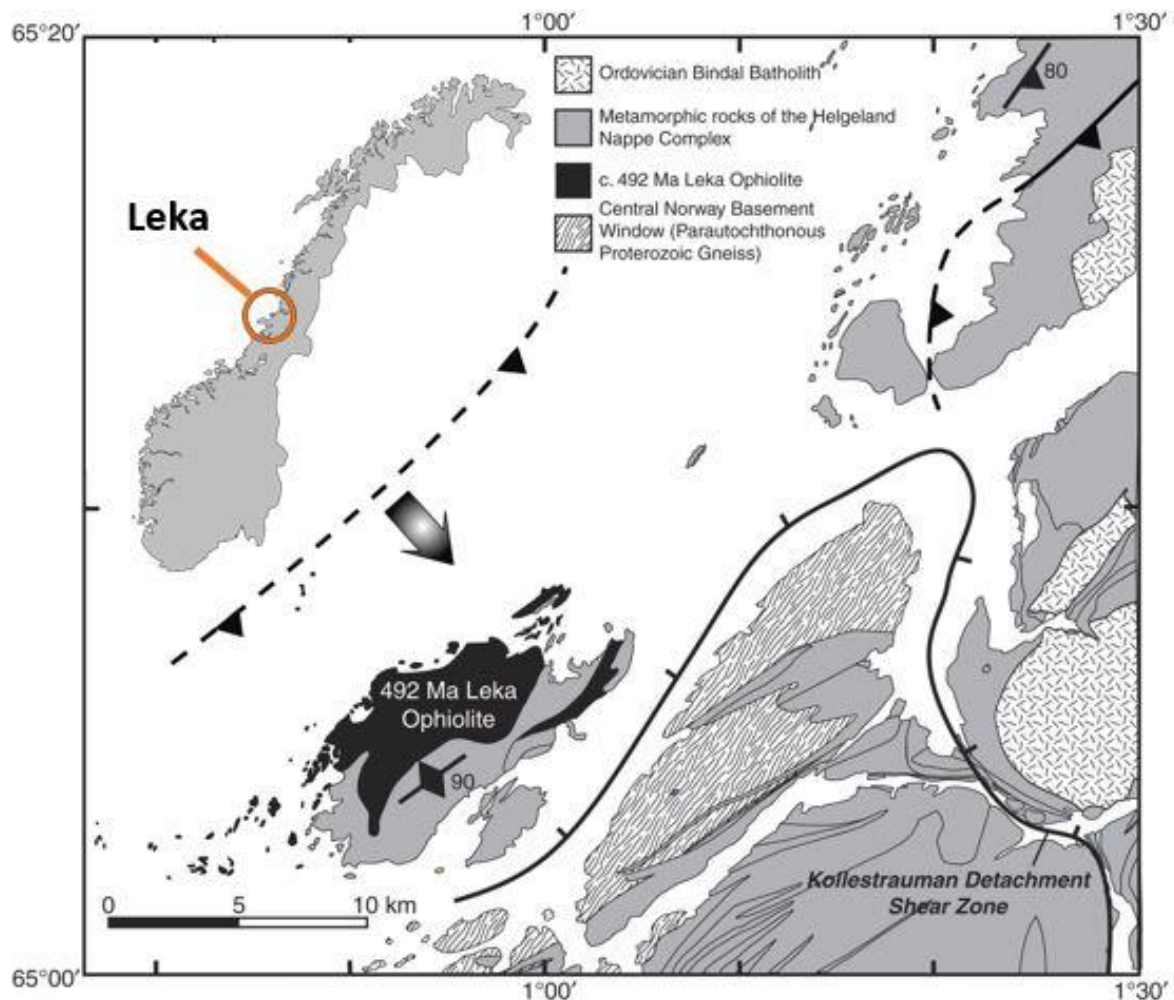


Figure 3.25. Location of the Leka ophiolite. Adapted from Barnes *et al.* (2009).

The island of Leka is situated at $\sim 65^{\circ} 04' 50''$ N $\sim 11^{\circ} 37' 11''$ S in the Norwegian Sea (Fig. 3.25). It is 90 km^2 and the only surface manifestation of the Leka Ophiolite Complex (LOC). The LOC retains all textbook ophiolite strata (Fig. 3.23), and its ultra-basic rocks are intensively serpentinised to various degrees (Iyer *et al.* 2008). The LOC formed in the late Cambrian Furongian epoch 497 ± 2 Ma ago, experiencing obduction onto the Baltic shield during the Caledonian orogeny and the closing of the North Lapetus Ocean in a suprasubduction setting; it forms the uppermost allochthon of the Scandinavian Caledonides and possesses a strong gravitational anomaly of 25 mGal (Titus *et al.* 2002). The Norwegian thrust

sheets are divided into the Parautochthon, Lower, Middle, Upper, and Uppermost Allochthons with numerous ophiolites preserved in the upper and uppermost (Milnes *et al.* 1996). The LOC is the most completely preserved ophiolite in the Scandinavian Caledonides, and is currently experiencing a post orogenic transtensional pull - apart, caused by tectonic relaxation (Plümpner *et al.* 2012).

High temperatures (>1000 °C) instigate crystal plastic deformation of sub-grain boundaries in mantle olivine, creating channels of weakness (Plümpner *et al.* 2012). Once the temperature lowers to <350 °C fluid can infiltrate these weaknesses at low water to rock ratios, forming high diffusivity pathways (Plümpner *et al.* 2012). This fluid infiltration coincides with a change in equilibration mechanisms, whereby diffusion dominates at high temperature and dissolution - precipitation dominates at lower temperatures; both mechanisms can be active at intermediate temperatures (Fig. 3.26).

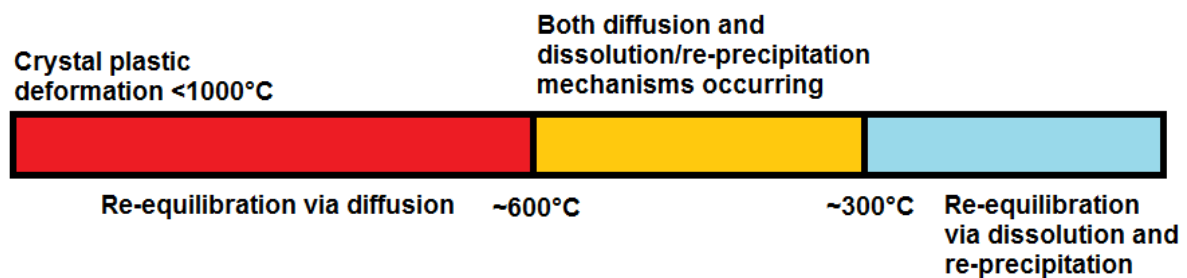


Figure 3.26. Illustrating the dominant equilibration mechanisms with temperature for olivine.

Leka peridotite olivine is extensively, and sometimes virtually entirely, serpentinised (Fig 3.28). Serpentine is a phyllosilicate composed of 1:1 tetrahedral to octahedral sheets, with polymorphs including chrysotile, lizardite and antigorite. Serpentes of identical crystal structure can thermally, mechanically and chemically behave differently depending on the parent rock genesis (Zulumyan *et al.* 2014).

This study conducted a sample collection expedition to Leka in February 2013 (Fig. 3.27; Fig. 3.28). 12 thin sections were made of a wide range of rock types throughout the ophiolite complex stratigraphy, including harzburgite (Fig. 3.28), lherzolite, wehrlite, dunite, gabbro, basalt, serpentinite, syenite and diorite. Light microscopy and SEM observations were concentrated on the peridotite samples with the assumption that the high volume of olivine contained in these rock types would make them probable candidates for carbonate formation.

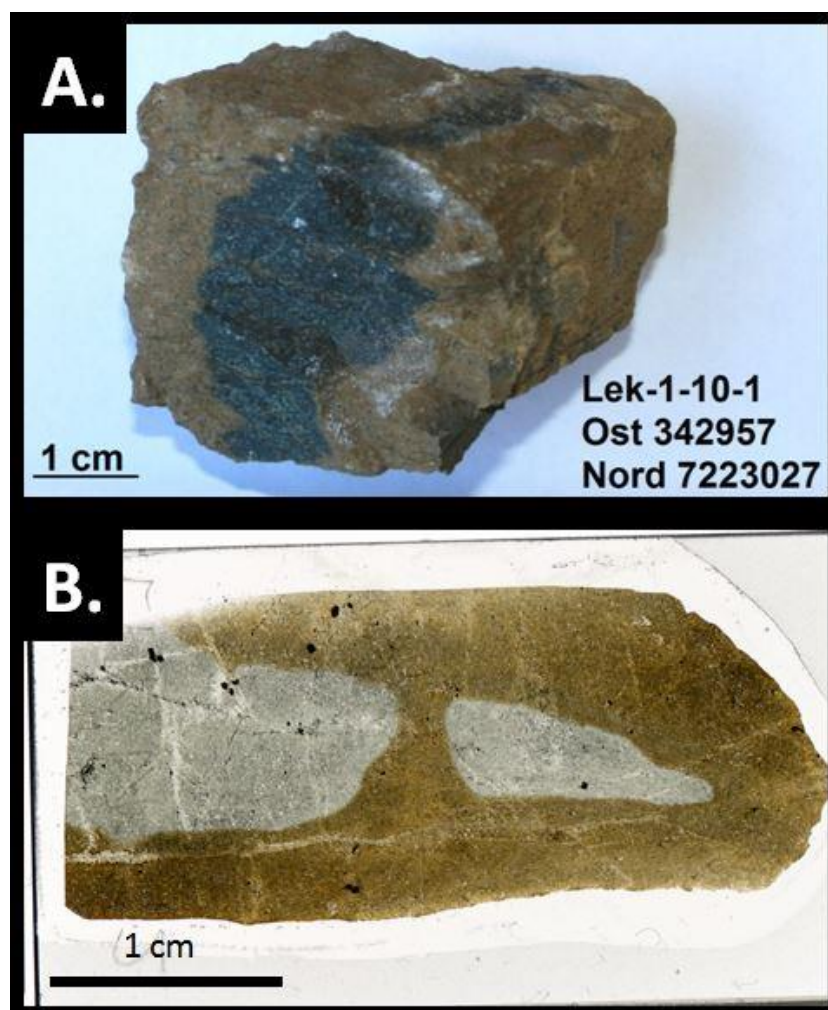
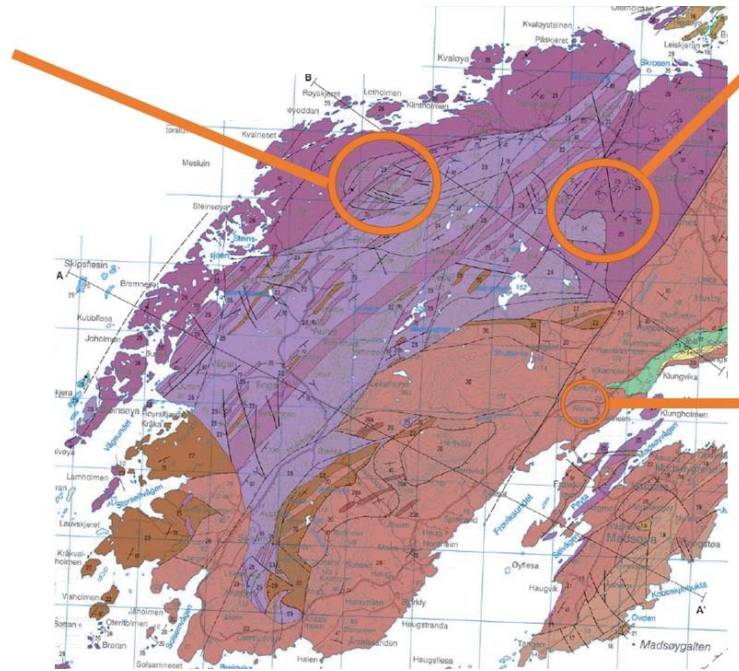


Figure 3.27. An example of the extensive peridotite harzburgite serpentinisation (brown outer rim is serpentine) of the Leka ophiolite. In other samples, this serpentinisation had proceeded to completion. **A.** Whole rock. **B.** Thin section.

Day 2:

- 23 – Light purple**
Clinopyroxenite
Wehrlite
Dunite
- 25 – Medium purple**
Serpentinite
Dunite
- 26 – Dark purple**
Harzburgite
Lherzolite



Day 1:

- 24 – Light purple**
Wehrlite
Dunite
- 25 – Medium purple**
Serpentinite
Dunite
- 26 – Dark purple**
Harzburgite
Lherzolite

Day 3:

- 20 – Red**
Gabbro

Figure 3.28. Geological map of Leka and the locations and rock types sampled during field work in February 2013. Sites highlight only those that later became thin sectioned samples.

No carbonates were found in any of the Leka samples collected. This is unfortunate, although not entirely a surprising result. Until recently the Leka ophiolite literature was dominated by serpentinisation research (Austrheim & Prestvik, 2008; Iyer *et al.* 2008), and only more recently have carbonates had been identified and reviewed (Bjerga *et al.* 2015). As carbonate formation was an integral part of the study, it was decided to extend the ophiolite research into the Semail ophiolite in the United Arab Emirates.

3.2.3 The Semail ophiolite, Oman and United Arab Emirates.

The Semail ophiolite in United Arab Emirates is the world's largest (Searle & Cox, 1999) with an areal extent 10 000 km². It extends ~600 km along North East Arabia where it meets the Gulf of Oman (Fig. 3.29) and is ~150km wide by ~5 to 10km thick. The ophiolite divides into 5 regions: The Arabian platform, the Huqf - Haushi uplift, the Oman mountains, the Masirah Ophiolite Uplift and the Gulf of Oman. The rocks formed in the Cretaceous, ~94 to 96 Ma ago, at a sea floor spreading ridge (Searle & Cox, 1999), however, regional magmatic origins are complex and multistage, with magma formation from seamounts, crustal uplift and continent - arc collision all being present (Alabaster *et al.* 1982). Obduction onto the continent was rapid at ~150 km Ma⁻¹ (Hacker *et al.* 1996). The ophiolite stratigraphy is remarkably well preserved (Searle & Cox, 1999), which is thought to be due to the young age of the sea floor (~1 to 2 Ma) at the time of obduction (Hacker *et al.* 1996; Boudier & Nicolas, 2007).

The Semail ophiolite has been used extensively as a geological Mars analogue, due to both its arid climate and basaltic - peridotite geology with subsequent serpentinisation, iron oxidation, and aqueous alterations (Rice & Mollard, 1994; Pinet *et al.* 2006; Clenet *et al.* 2013; Etiope *et al.* 2013; Etiope, 2015; Greenberger *et al.* 2015).

For this study a set of harzburgite and serpentine rock samples were provided by Dr Alicja M Lacinska of the British Geological Survey. The samples were from the United Arab Emirates; from a farm excavation near a town called Asimah, Universal Transverse Mercator coordinates: X 413679 and Y 2808846. Thin sections were made and qualitative and quantitative SEM analysis and light microscopy was conducted. Results were compared with Leka ophiolite and Martian meteorite alteration products (Objective 3. C).

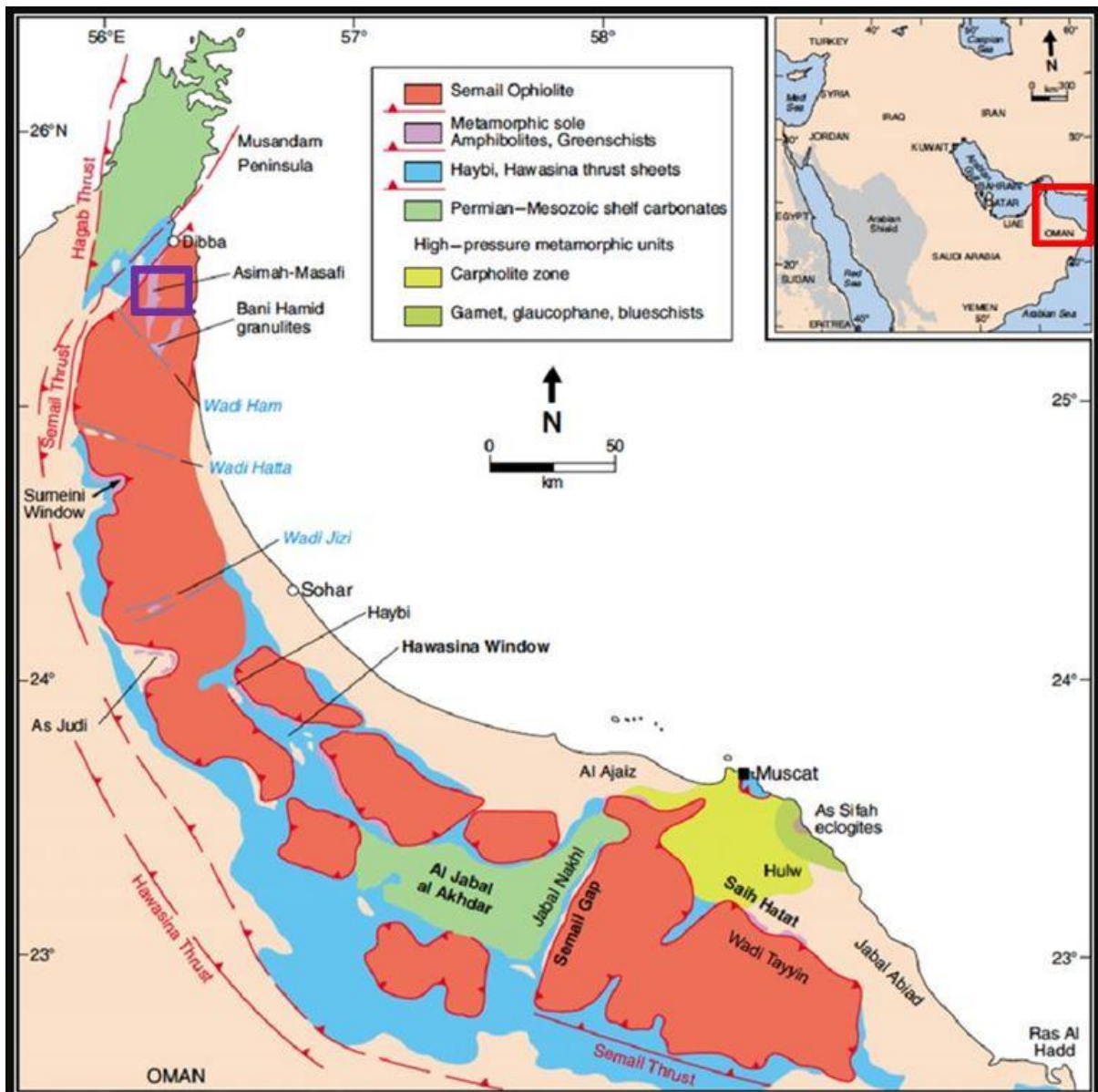


Figure 3.29. Map of the Semail ophiolite (red). Samples used in this study are serpentines and harzburgites from Asimah (purple box). Adapted from Cowan *et al.* (2014).

3.3 Methods.

3.3.1 Quantitative SEM analysis methods.

Quantitative X-Ray microanalysis was conducted using a Carl Zeiss Sigma VP SEM with Oxford Inca microanalysis software. Aluminium tape serves the dual purpose of securing the thin section onto the brass shuttle containing the mineral standards and allowing a conductive route for charge build up to dissipate from the thin section (Fig. 3.30). The brass shuttle was then placed in the SEM, pumped to a vacuum and the electron beam set at 80 μm aperture at 20 kV, and a probe current of 2.18 nA.

The cobalt standard was used to gain initial focus, bringing the sample to the analytical working distance of 8.5 mm from the electron gun. The track Z option was disabled at this point, and focus by raising or lowering the sample along the Z axis.

The beam current was measured by focussing a spot within a Faraday cup (Fig. 3.30). This beam current measurement was repeated every few hours to monitor stability, as variations in beam current alter the quantitative results; a typical measurement was 580 picoamperes (pA), and it took ~60 - 90 minutes for the beam current to stabilise. Individual standards (Table 3.3), were then measured using a live time of 60 seconds and a dead time of ~50 %, thus an acquisition time of 90 seconds. The standard used was changed in some cases to be compatible with the sample to be measured i.e. calcite was used as the Ca standard on carbonates whereas wollastonite was used for the Ca standard on silicates.

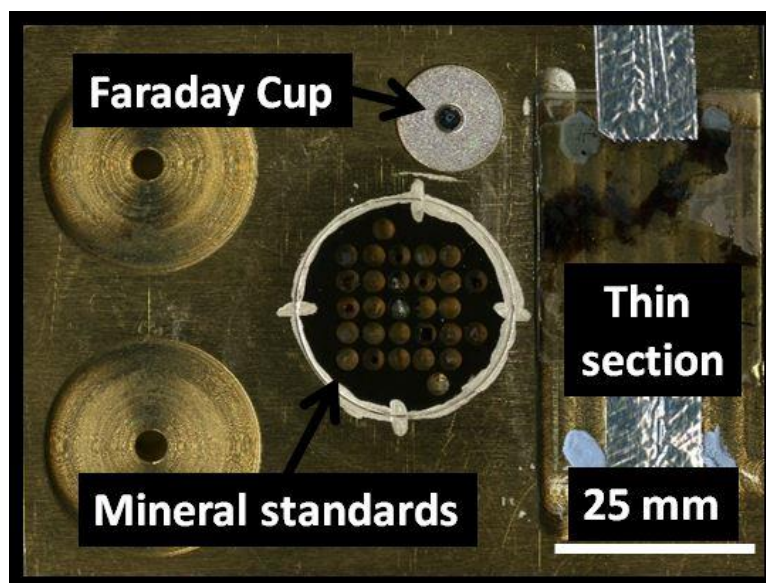


Figure 3.30. Mineral standards mounted onto the brass shuttle used for quantitative calibration.

Fixed List	Standard	Method	Detection Limit (wt. %)
Na	Jadeite	Raster	0.09
Mg	Periclase	Spot	0.05
Al	Jadeite	Raster	0.06
Si	Wollastonite	Spot	0.07
S	Pyrite	Spot	0.11
K	Orthoclase	Raster	0.10
Ca	Wollastonite	Spot	0.09
Ca	Calcite	Raster	0.10
Ti	Rutile	Spot	0.15
Cr	Chromite	Spot	0.20
Mn	Rhodonite	Spot	0.20
Fe	Heamatite	Spot	0.25
Fe	Garnet	Spot	0.22
Ni	Nickel	Spot	0.23
Cu	Copper	Spot	0.14
O	Calcite	Raster	0.71

Table 3.3. Elements measured for quantitative analysis, the standard mineral and method (spot or raster) used and lower detection limit to analyse the standards.

To calculate detection limits (Table 3.3), each standard was measured with a live time of 60 seconds. X-Ray intensity is determined by the number of pulses generated in the X-Ray detector, these pulses are caused by photons emitted from the sample. The number of counts per channel on the element peak of interest is recorded, as well as the number of counts in the background. The detection limit is then calculated via equation 3.5:

$$\text{Detection limit} = 3/m \sqrt{R_b/T_b}$$

Equation 3.5

Where m is counts per second per unit of concentration (cps/% or cps/ppm), R_b is the rate of background intensity (counts per second), T_b is the time on background (seconds). The denser the material measured, the higher the background count rate (R_b) will be, therefore the higher the detection limit. For example, chromite will have a higher background count than periclase, thus a higher, less precise detection limit.

3.3.2 TEM analysis methods.

This study used ALH 84001 polished thin section 173, on loan from the American museum of natural history. SEM X-ray element maps were used to identify examples of carbonates in contact with plagioclase glass. An FEI DuoMill focused ion beam (FIB) was used to cut electron-transparent foils across two plagioclase glass - carbonate interfaces. These foils were then studied using an FEI T20 TEM.

3.4 Results.

See appendix 4 for detailed quantitative mineral analysis. All samples discussed in this section are placed in epoxy resin, thin sectioned, and polished. Samples analysed by SEM were carbon coated.

Olivine is the key primary silicate involved in serpentinisation and carbonation reactions. Figure 3.31 demonstrates how San Carlos olivine and terrestrial ophiolite olivine, commonly used as Mars olivine analogues, may not be the best representatives, and that South African hortonolite is considerably more suitable due to its enriched Fe content.

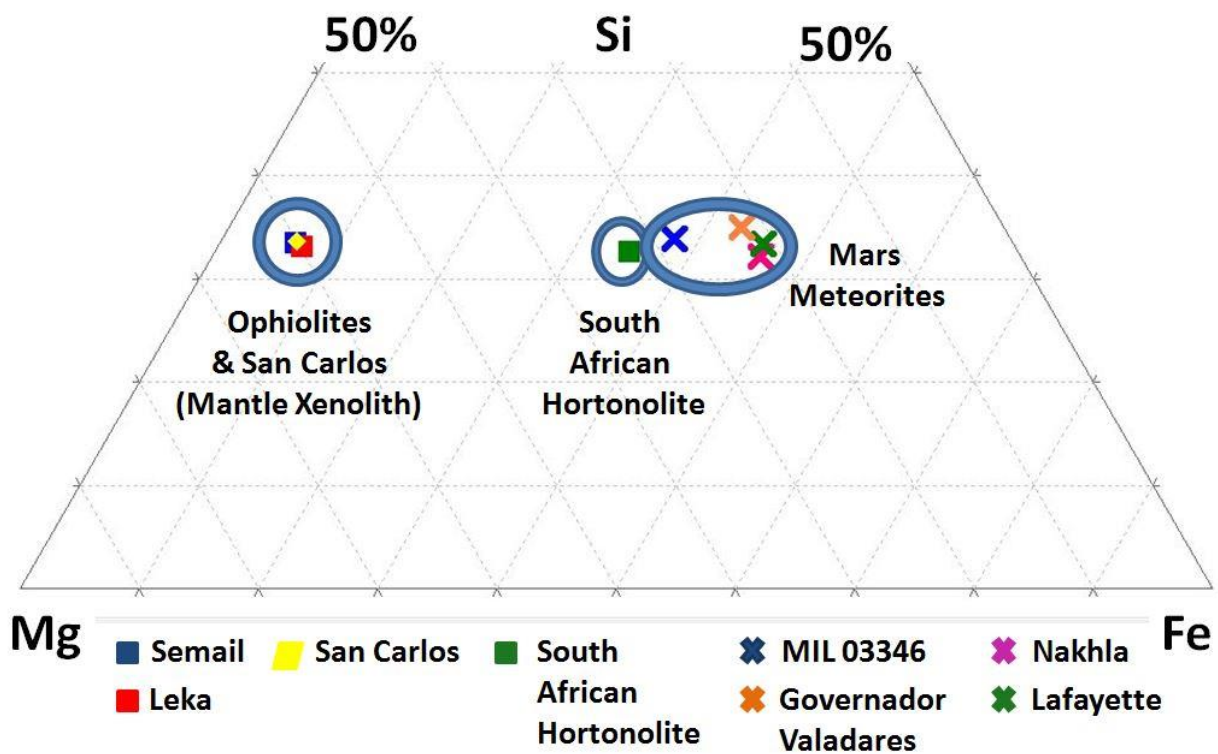


Figure 3.31. Ternary plot (atomic %) of olivine compositions for San Carlos olivine (Fournelle, 2009), terrestrial ophiolites (Semail and Leka), a selection of Martian meteorites (Bunch & Reid, 1975; Berkley *et al.* 1980; Lee *et al.* 2013; Day *et al.* 2006), and the South African hortonolite used in this study. Quantitative SEM analyses of the olivine for Leka, Semail and the South African hortonolite are in Appendix 4.

3.4.1 Mars.

3.4.1.1 ALH 84001 results.

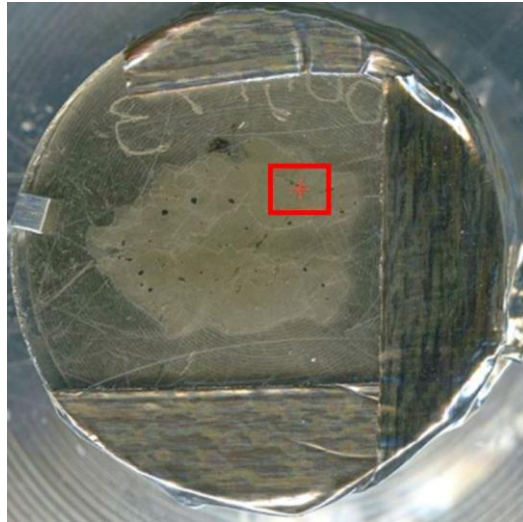


Figure 3.32. Thin section ALH 84001, sample 173, on loan from the American museum of natural history, used in this thesis to represent early Mars. The red square indicates the area of study. The glass slide is 25 mm in diameter.

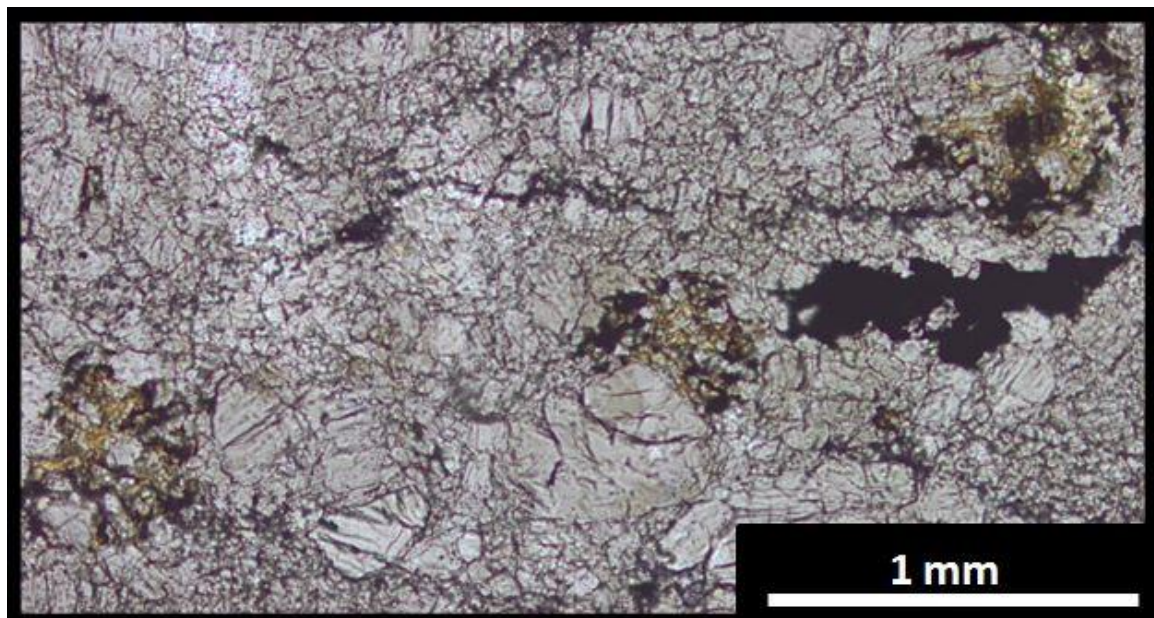


Figure 3.33. Transmitted light microscope image of the area of study area indicated in Fig. 3.32. Grey is mostly orthopyroxene. Carbonate is a gold colour. Black is chromite (large block), with some glass in the fractures.

A slice of ALH 84001, sample 173 (Fig. 3.32) was provided by the American museum of natural history, used in this thesis to represent early Mars. This sample was examined and imaged, locating key carbonate areas. These carbonates formed in globular, approximately spherical regions amidst a host mineralogy dominated by orthopyroxene and occasional chromite that was present in asymmetrical linear streaks (Fig. 3.33, 3.34). A region of well-defined carbonates was selected to be the key area of study (Fig. 3.34. A.). A section was selected with abundant chemically zoned carbonates as the prime area for detailed analysis (Fig. 3.34.B).

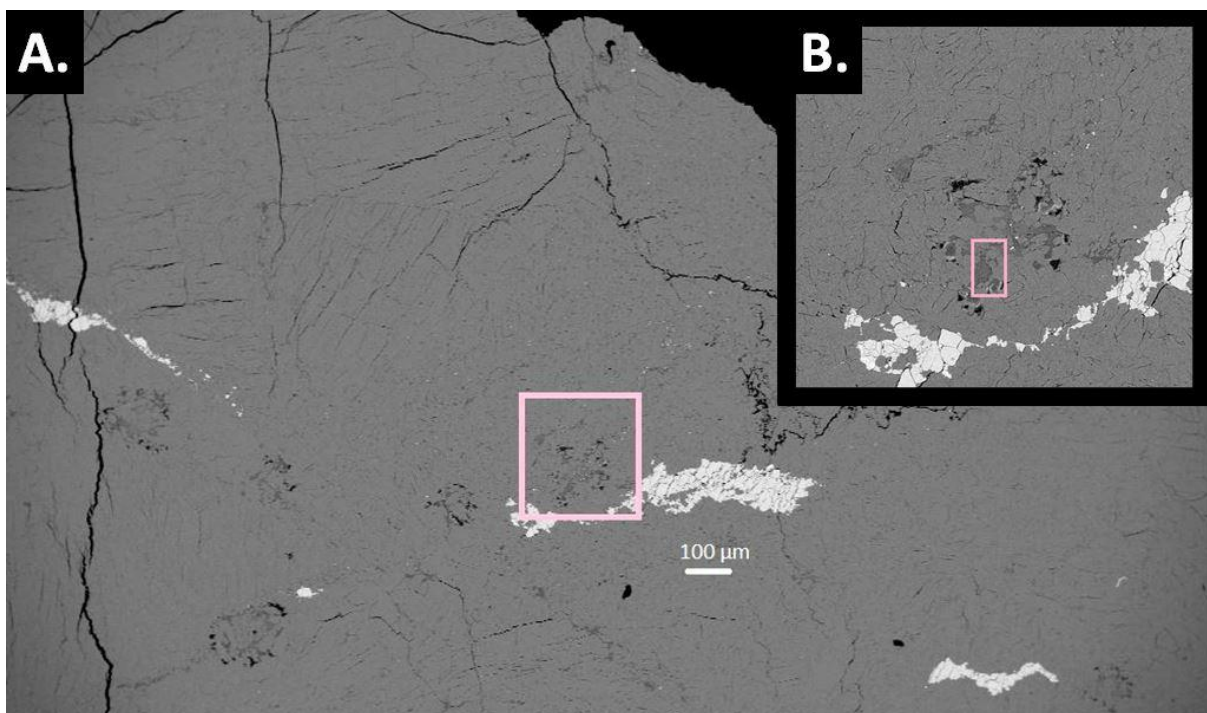


Figure 3.34. ALH 84001, 173. **A.** BSE SEM image of the area of study highlighted in Fig. 3.32. **B.** Higher magnification of the pink square highlighted in A.

X-Ray mapping of a prominent zoned carbonate within the selected region (Fig. 3.34.B) revealed Ca - Fe/S - Mg element zonation (Fig. 3.35). Two sites within the area shown in Figure 3.34.B were selected to extract FIB slices (Fig. 3.36) for TEM analysis (Fig. 3.37, Fig. 3.39), these FIB slices included carbonate, glass, orthopyroxene and iron oxide and chromite. Figure 3.38 shows the composition of the carbonates in the TEM analysis (Fig. 3.37).

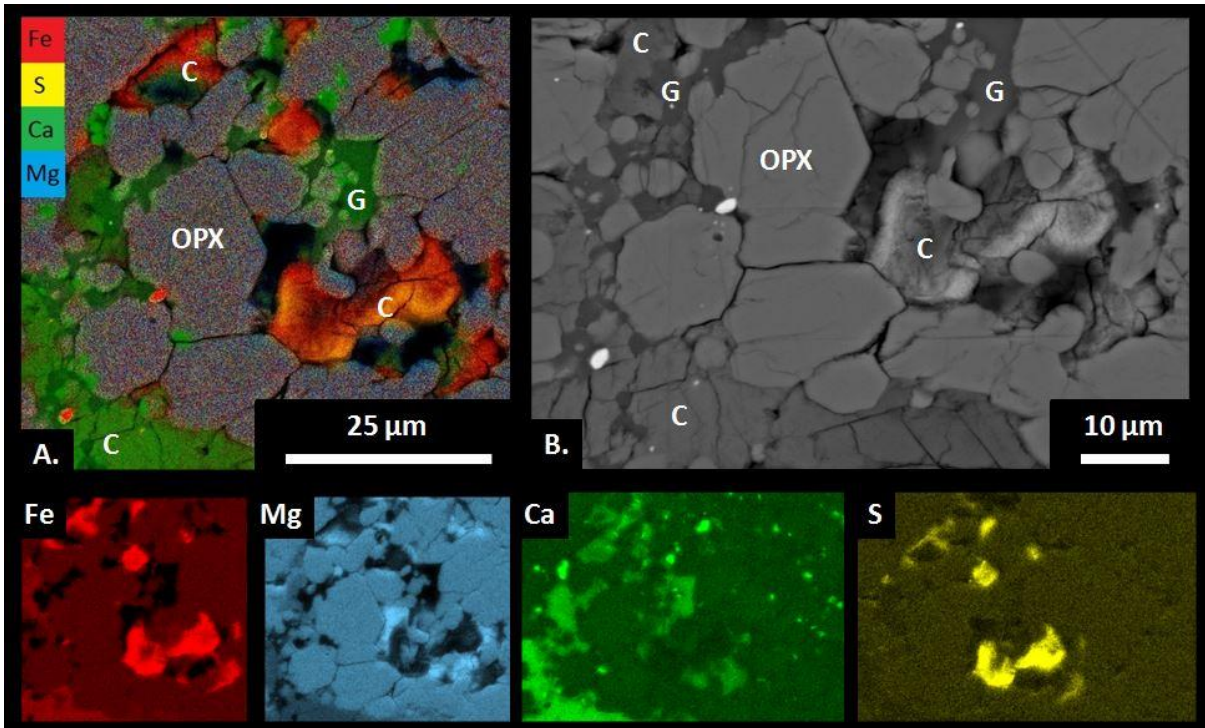


Figure 3.35. ALH 84001, 173. **A.** X-Ray map of a zoned and slab carbonate region surrounded by orthopyroxene. **B.** BSE image of A. Individual element maps of Fe, Mg, Ca and S are also shown. OPX = Orthopyroxene. C = Carbonate. G = Glass.

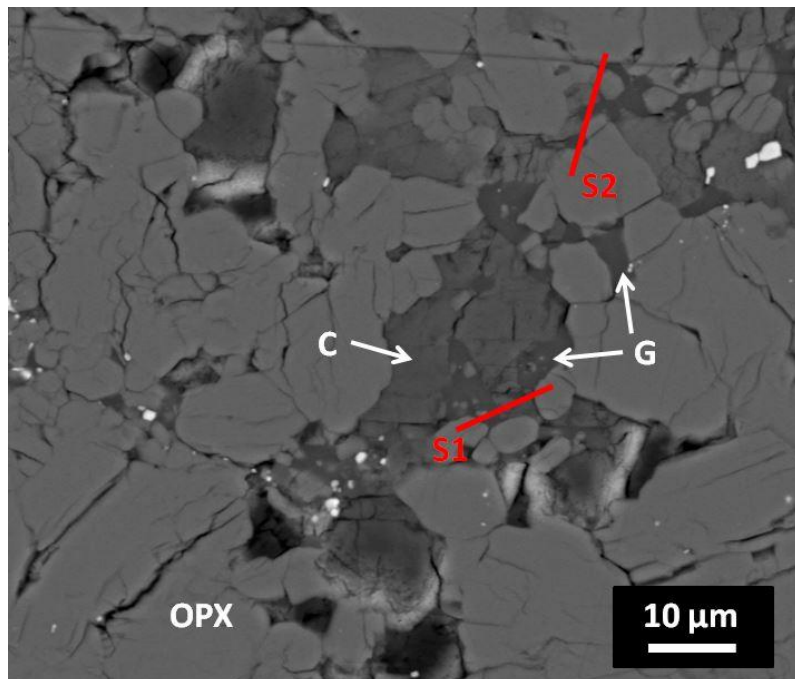


Figure 3.36. ALH 84001, 173. BSE SEM image correlating with the pink square in Fig. 3.33.B. S1 and S2 are the locations of the two FIB slices used for this study. OPX = Orthopyroxene. C = Carbonate. G = Glass.

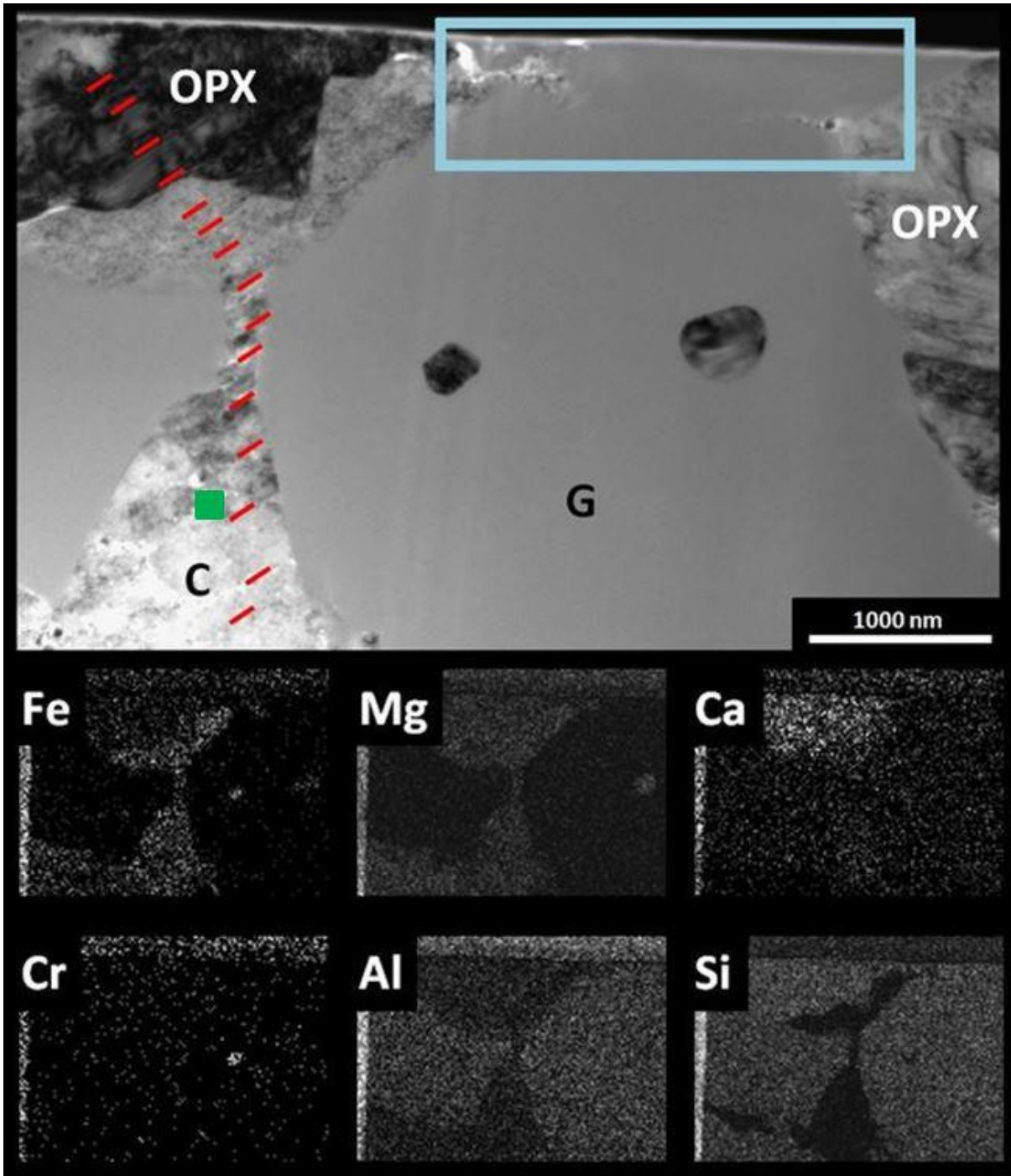


Figure 3.37. Bright-field TEM image of FIB slice S1 (Fig. 3.36) showing carbonates formed by distinctly different processes. Blue box highlights where carbonate replaced melt glass in a line of weakness. Red lines highlight lamellae of identical alignment in both the carbonate and orthopyroxene, indicating either isomorphous carbonate replacement of orthopyroxene directly, or replacement of a maskelynite intermediate phase. X-Ray element maps of Fe, Mg, Ca, Cr, Al, Si are also shown. OPX = Orthopyroxene. C = Carbonate. G = Glass.

Two types of carbonate were observed in the TEM FIB slice S1 (Fig. 3.37). One possesses diagonal, parallel lamellae whose orientation aligns with the lamellae of the orthopyroxene; the carbonate composition is shown in Figure 3.38. The second type of carbonate is granular in appearance and fills a fracture in the Si rich glass, highlighted by a blue rectangle in Figure 3.37.

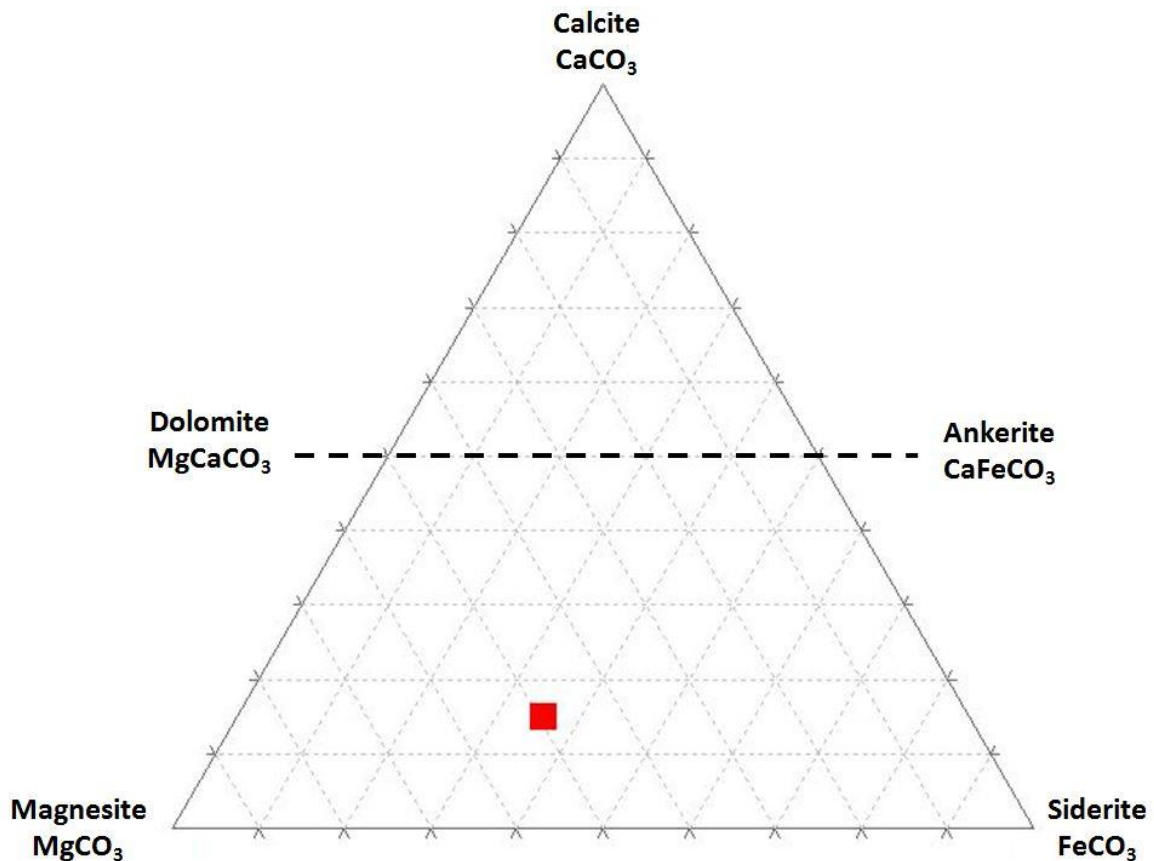


Figure 3.38. Ternary plot (atomic %) of carbonate in green square of Fig 3.37.

In the FIB slice S2 a granular carbonate can also be observed in veins cross cutting Si rich glass, as well as surrounding regions of glass and filling the space between glass and orthopyroxene host rock (Fig 3.39. B. C. D). A BSE SEM image (Fig. 3.39. A) demonstrates that this relationship of carbonate - glass - orthopyroxene interface occurs both on the nm and μm scale. BSE SEM images from within the region identified in Figure 3.34.B were acquired, some presenting clear carbonate element zonation (Fig. 3.40).

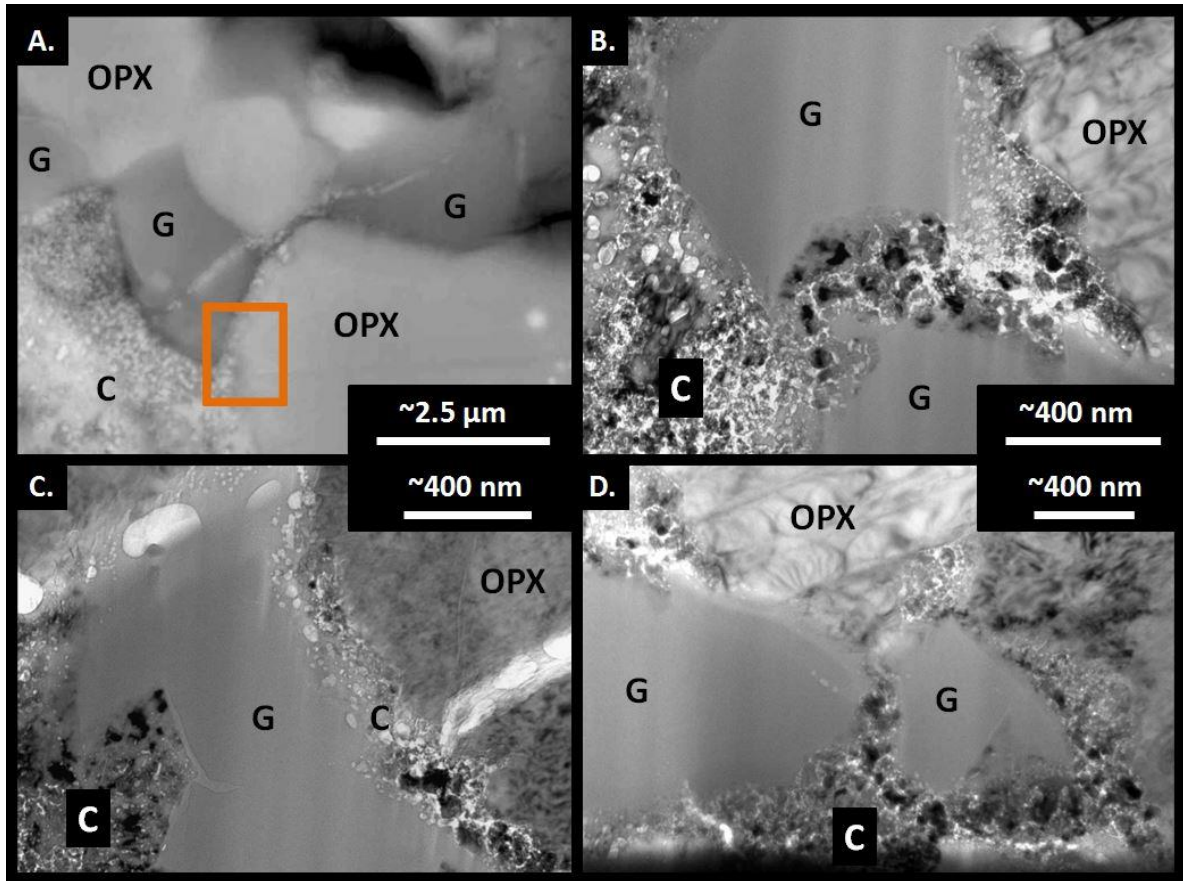


Figure 3.39. A. BSE SEM image of carbonate replacing melt glass, both along the glass - orthopyroxene boundary (orange square), and through a line of weakness in the glass. B – D. Bright - field TEM images of FIB slice S2 (Fig. 3.36), showing carbonates forming in lines of weakness in the glass, both around the glass edges and cross cutting the main body. OPX = Orthopyroxene. C = Carbonate. G = Glass.

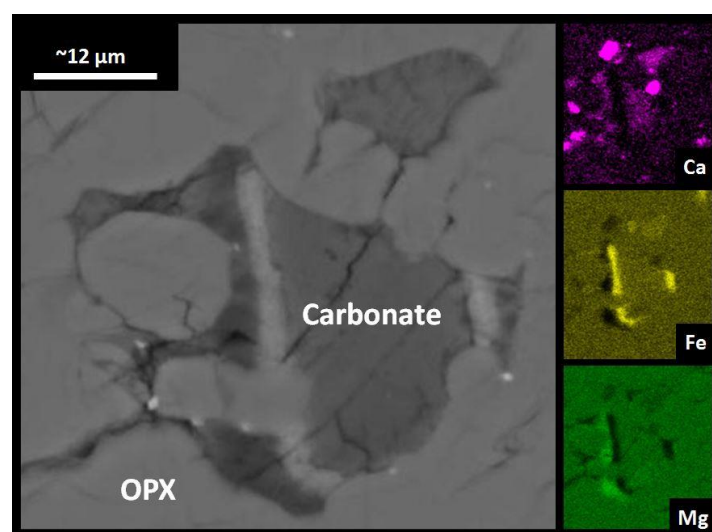


Figure 3.40. ALH 84001, 173. BSE SEM image of a zoned carbonate, with Individual AZTEC element maps of Fe, Mg, and Ca. OPX = Orthopyroxene.

3.4.1.2 Lafayette results.

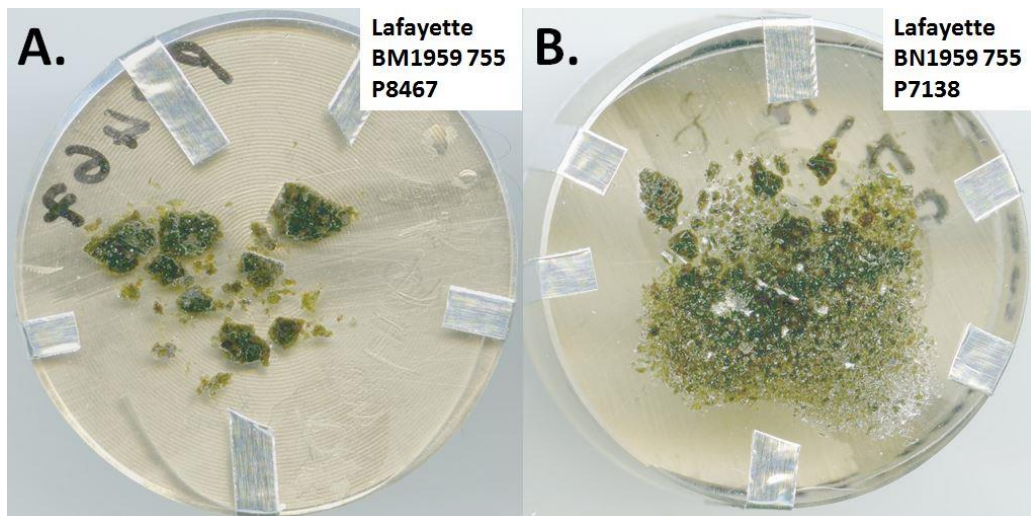


Figure 3.41. Lafayette meteorite samples used in this study. **A.** BM1959 755 P8467. **B.** BN1959 755 P7138. Each block is 25 mm in diameter.

Two samples of Lafayette, sample BM1959 755 P8467 (Fig. 3.41.A) and sample BN1959 755 P7138 (Fig. 3.41.B) was provided by the Natural History Museum, London, used in this thesis to represent more recent Mars. This sample was examined and imaged, searching for carbonates and other secondary minerals indicating aqueous alteration. Unlike the ALH 84001 sample, which was a single slice, the Lafayette samples are a collection of small fragments encased in epoxy resin. There was no observable difference in the composition or extent of secondary minerals based on grain size. Clays were more prevalent in Lafayette compared to ALH 84001, filling vein edges with phyllosilicates, with a vein centre of Si and Mg rich, near amorphous material. Host minerals were olivine (Fig. 4.42, Fig. 4.45, Fig. 4.47) or pyroxene (Fig. 3.43, Fig. 3.44). Occasionally, an Fe rich ‘bridge’ of phyllosilicate would cross the Si rich vein centre (Fig. 3.42).

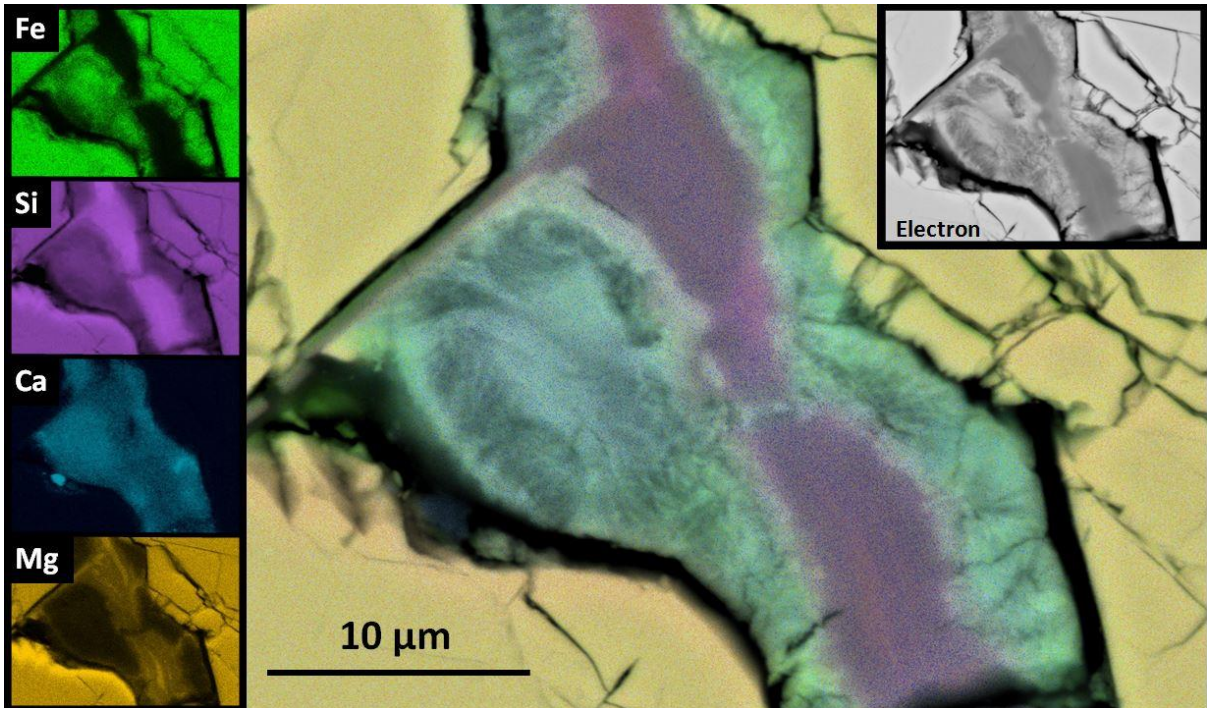


Figure 3.42. X-Ray map of an aqueous alteration vein within an olivine grain forming part of Lafayette sample BN1959 755 P7138. Individual AZTEC element EDXS maps of Fe, Si, Ca and Mg are also shown.

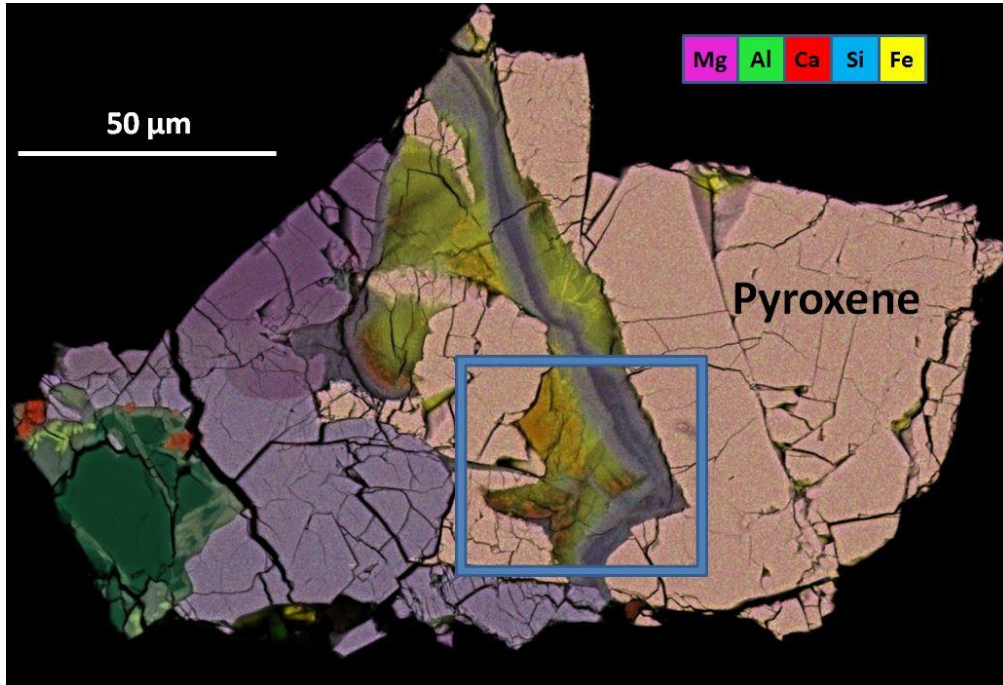


Figure 3.43. X-Ray map of a grain within sample BN1959 755 P7138, a prominent fracture within pyroxene bears hydrated minerals and carbonates. The area within the blue square is shown in Fig. 3.44.

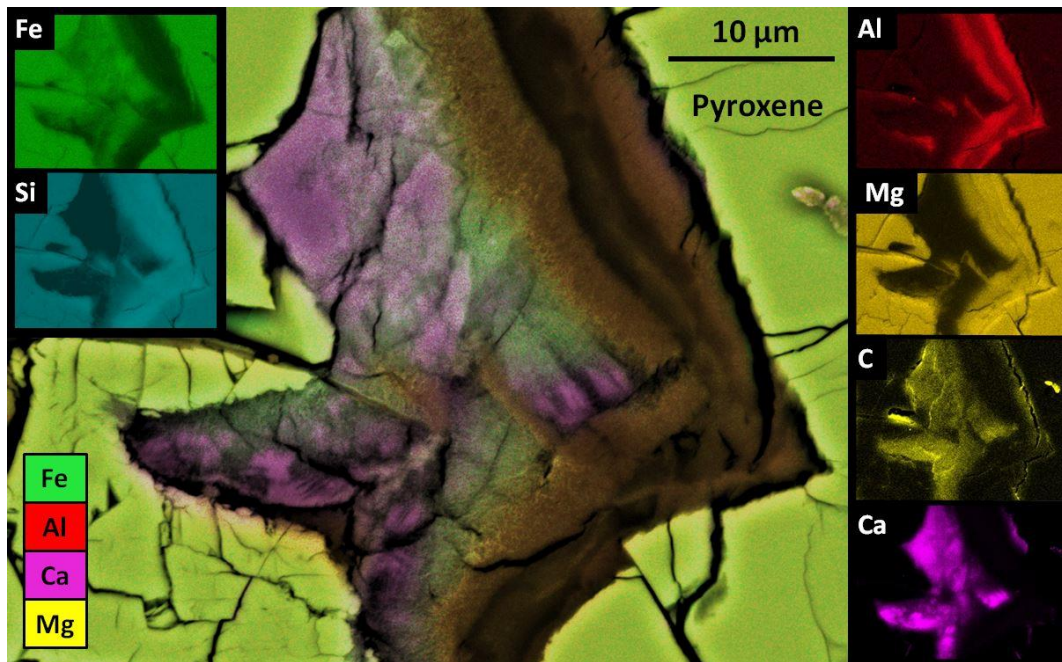


Figure 3.44. X-Ray map of the blue square in Fig. 4.43. Carbonate and hydrous minerals are surrounded by pyroxene. Individual AZTEC element EDXS maps of Fe, Si, Al, Mg, C and Ca are also shown.

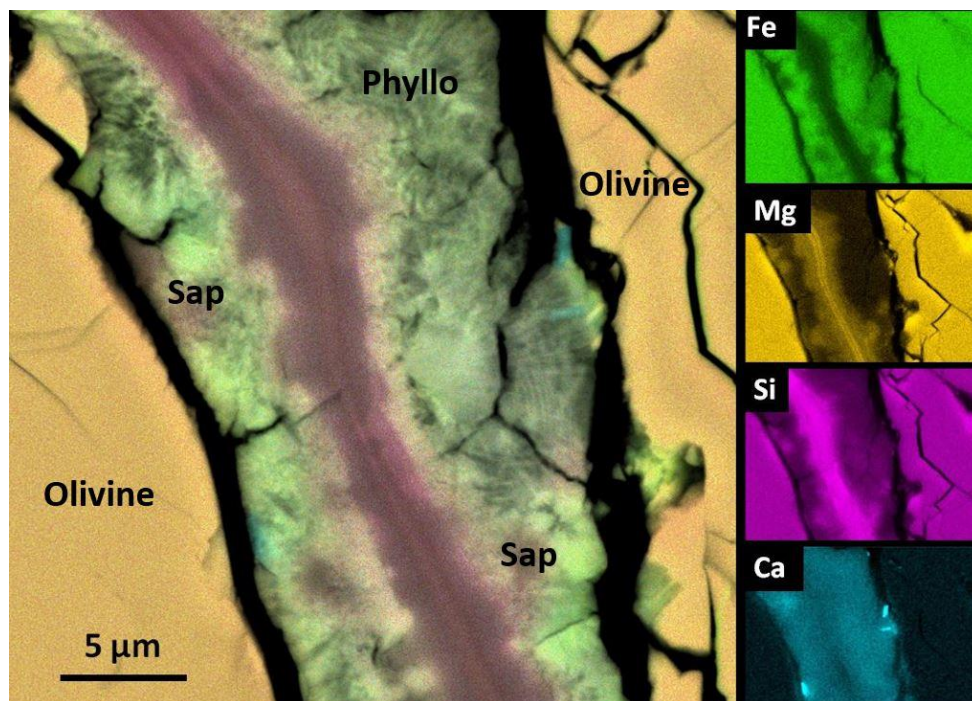


Figure 3.45. X-Ray map of an aqueously altered vein within an olivine grain forming part of Lafayette sample BN1959 755 P7138. Individual AZTEC element EDXS maps of Fe, Si, Ca and Mg are also shown. Sap = Saponite. Phyllo = Phyllosilicates.

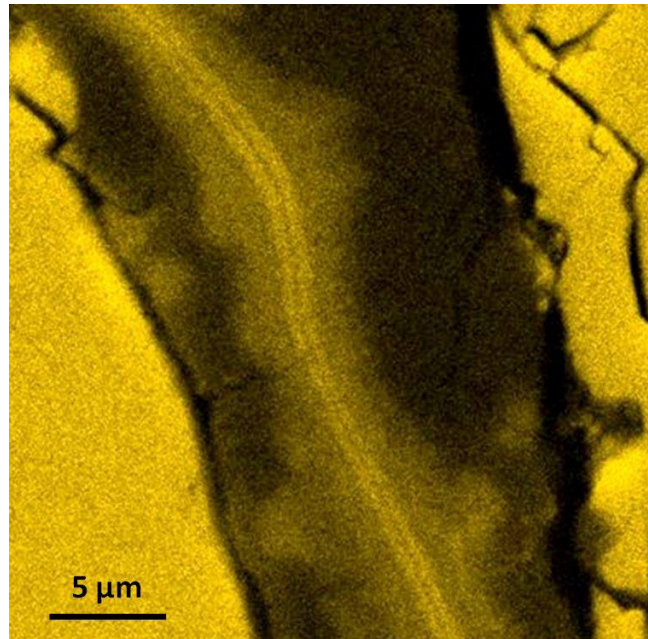


Figure 3.46. X-Ray micro-analysis map of Mg, as shown in Fig. 4.45. Enlarged to highlight the distinct axial band within the vein centre. See discussion.

The Si, Mg rich vein can be seen clearly in Figure 3.46, where a two very distinct Mg bands follow the vein centre in parallel, with a sub-micron gap in between that is filled with Si and appears to follow the line of what would have been the original mineral fracture. Immediately outside of the two distinct Mg bands then there is a lesser Mg signature for $\sim 5 \mu\text{m}$ which is where the clays dominate; some circular areas with high Mg exist in near random placements in the material (Fig 3.46). Some very high Ca grains $< 1 \mu\text{m}$ can be observed in some veins (Fig. 3.45), usually positioned at the vein wall. Carbonate was located both in pyroxene (Fig. 3.43) and olivine (Fig. 3.47) veins. The carbonate in Figure 3.47 was siderite and contained circular ‘flowers’ of saponite (Fig. 3.47.B, Fig. 3.48) which possessed an Fe core and rim.

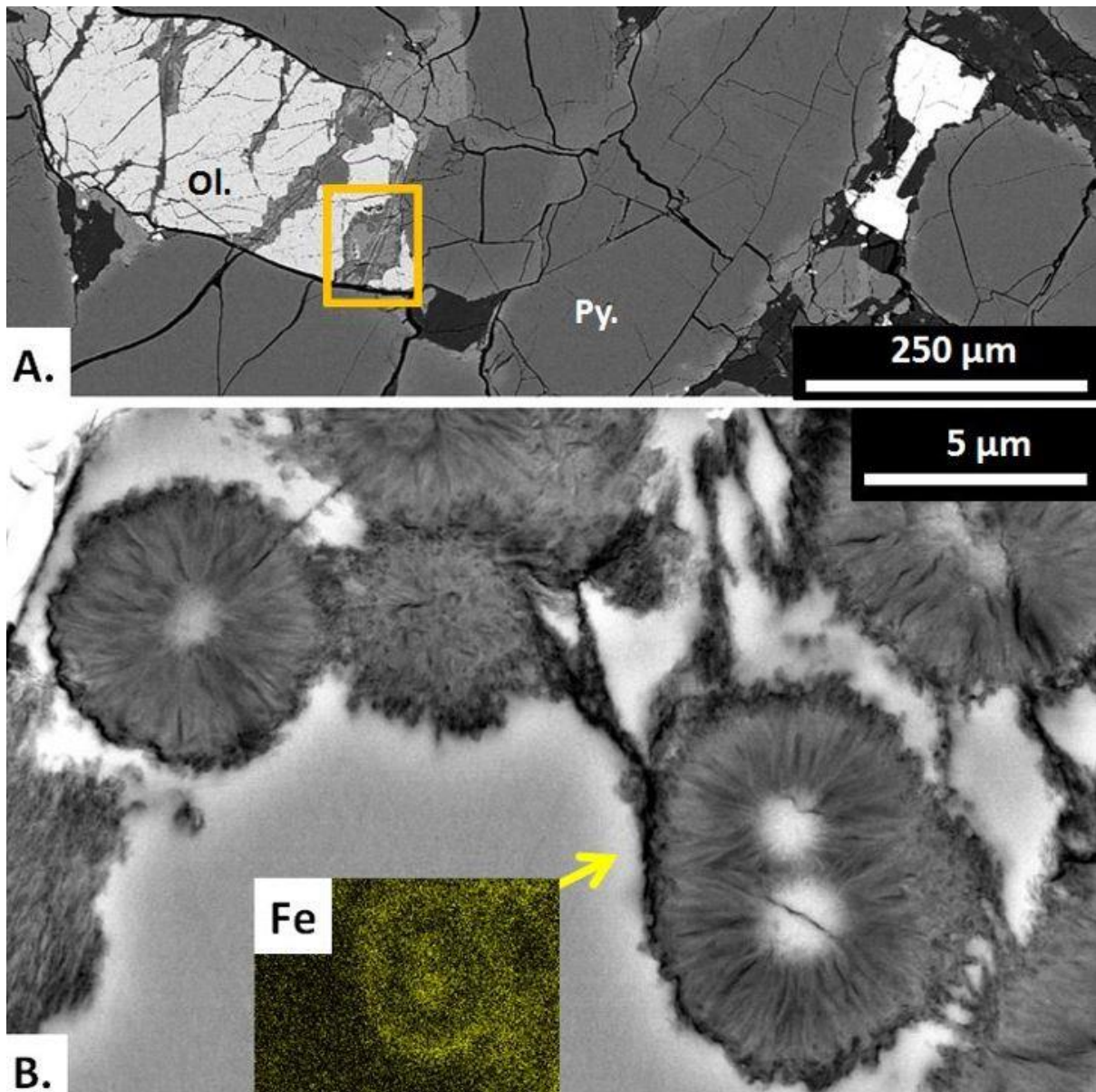


Figure 3.47. BSE SEM image of Lafayette BM1959 755 P8467. **A.** An olivine grain surrounded by pyroxene. **B.** Saponite ‘flowers’ with Fe rich cores surrounded by Ca Mn siderite within an olivine alteration vein (yellow square in A). X-Ray map for Fe of a single saponite flower is also shown. Ol. = Olivine. Py. = Pyroxene.

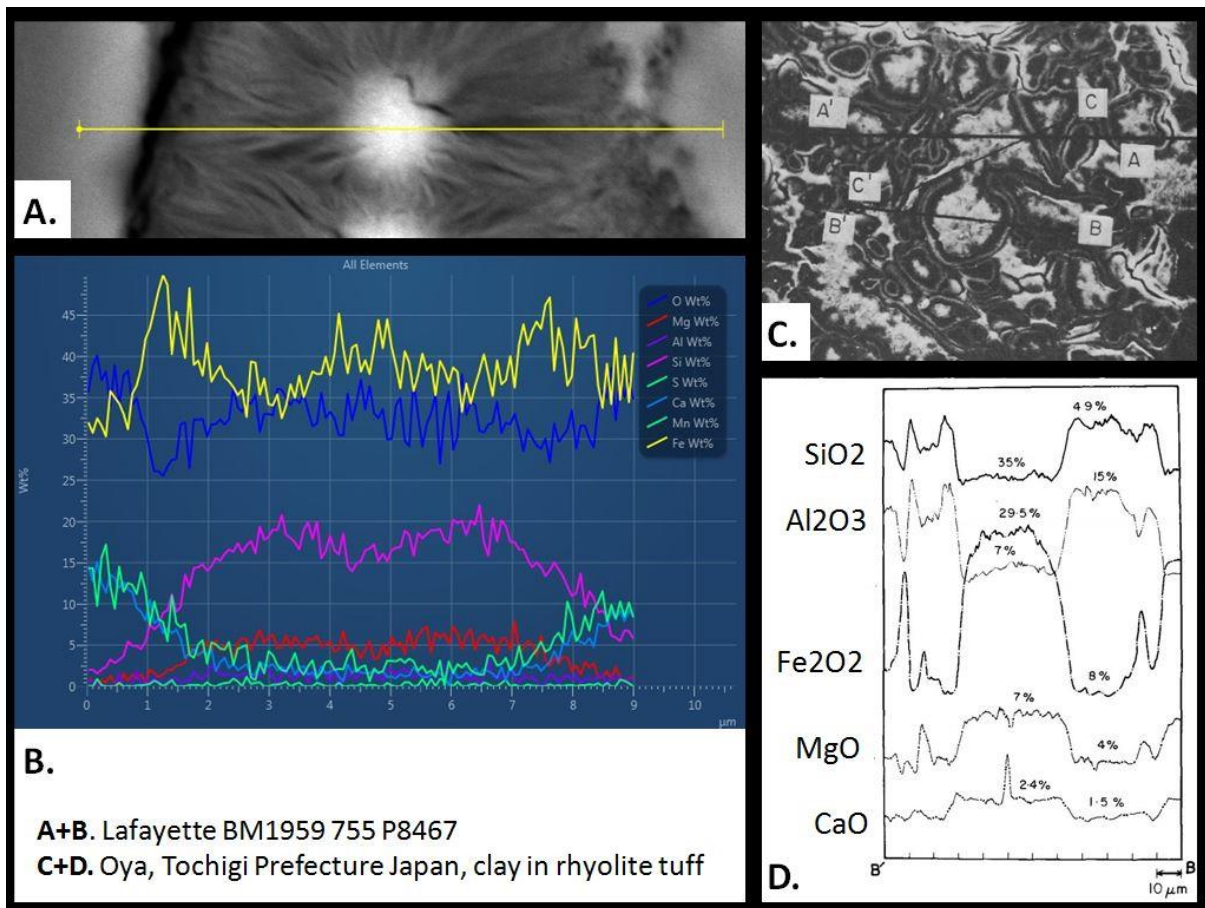


Figure 3.48. **A.** BSE SEM image of a saponite flower (Fig. 4.46.B) in Lafayette BM1959 755 P8467. **B.** AZTEC X-Ray line analyses of O, Mg, Al, Si, S, Ca, Mn, Fe along the yellow line show in A. **C.** Saponite clays within rhyolite tuff from Oya, Tochigi prefecture, Japan (Kohyama *et al.* 1973). **D.** EMPA analysis of SiO₂, Al₂O₃, Fe₂O₂, MgO, CaO along the B - B line in C (Kohyama *et al.* 1973).

A possible future analogue for the formation of these saponite ‘flowers’ was discovered in the literature surrounding rhyolite tuffs in Japan. Saponite clays within the Japanese rhyolite displayed remarkably similar cross section element distribution to the Martian Lafayette saponite flowers (Fig. 3.48), with high Fe in the centre and rims, and Si peaks on flanking either side of the Fe core. Mg element distribution peaked in correlation with the Fe in the Japan results, but correlated with the Si peaks of Lafayette in the results of this thesis (Fig 3.48). A future project might be to analyse and compare these structures and the surrounding locality in more detail.

3.4.2 Terrestrial.

3.4.2.1 Leka.

Results from Leka samples displayed fragmented remains of olivine grains that had been heavily altered and serpentinised (Fig. 3.49, Fig. 3.50). No carbonates were found in any samples. Whole rock field work samples often contained a white weathered rim (Fig. 3.49 inset), which did not survive thin section preparation, but did not react with hydrochloric acid. The rock rims were entirely serpentinised, and the fragmented olivine imaged in the figures comes from the less altered sample cores. With no carbonates located, the samples were not studied in extensive detail.

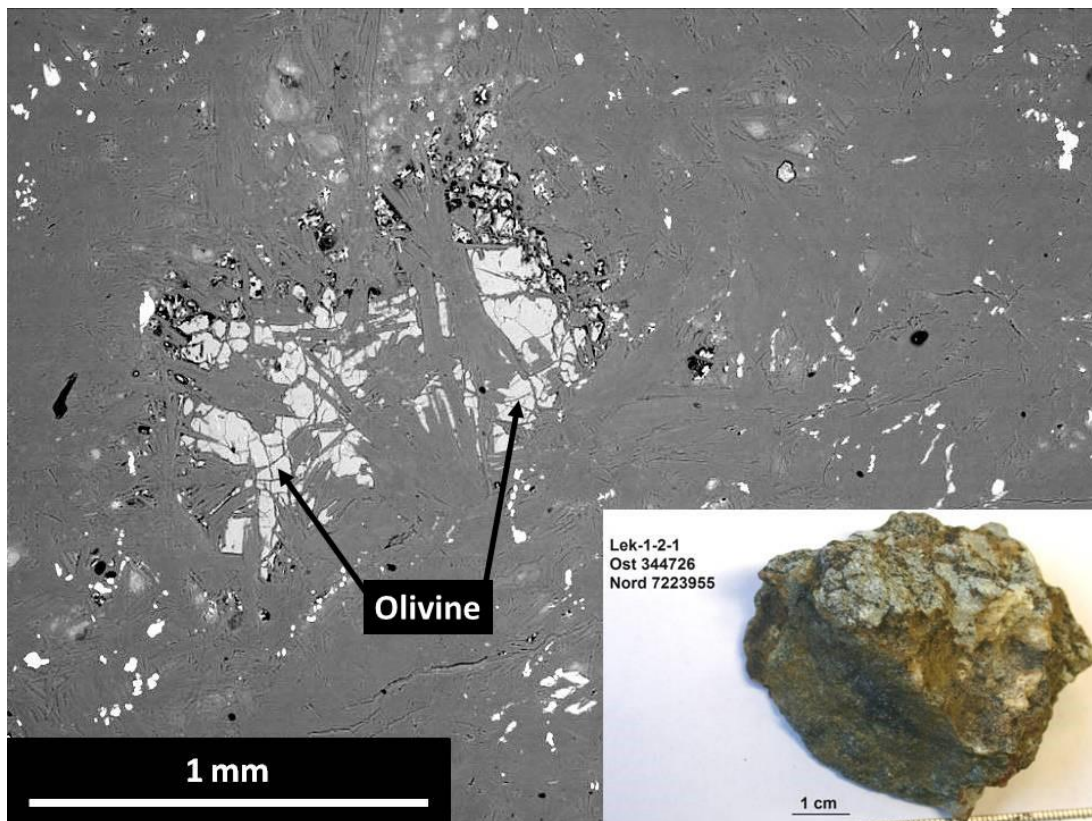


Figure 3.49. BSE SEM image showing the remains of an olivine grain within a heavily serpentinised matrix of what was originally a harzburgite - lherzolite.

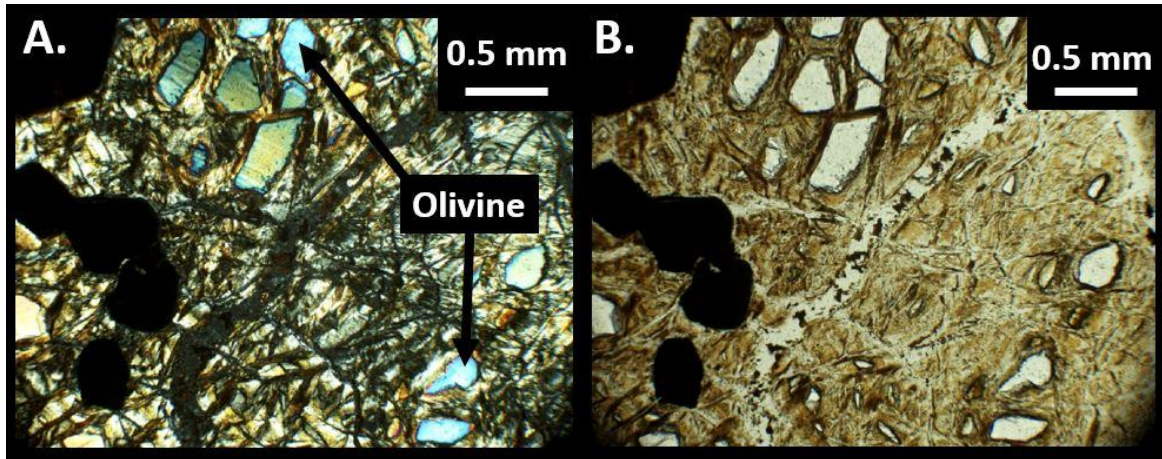


Figure 3.50. **A.** Transmitted light image between crossed polarisers. **B.** Plane polarised transmitted light image of remnant olivine in a serpentine matrix, of what was originally a harzburgite - lherzolite.

3.4.2.2 Semail ophiolite results.

Extensive, chemically zoned carbonates were located in all the Semail ophiolite samples. The carbonate composition of all carbonates was dolomite, with virtually no Fe (Fig. 3.51), as such they are notably different from the range of ALH 84001 carbonates, for which the zoned core and rim ALH 84001 carbonates are circled in Figure 3.51. The Semail element zonations fluctuated in Mg and Ca concentration, between 51 - 58 atomic % Ca (Fig. 3.51, Fig. 3.52, Fig. 3.53, Fig. 3.57). The compositional change between chemical zones was not linear, nor a consistently alternating oscillation (Fig. 3.52). On smaller rosettes it was common to observe only two compositional zones (Fig. 3.53).

On some rare, well-formed rosettes in Semail samples, the shape, structure, colour and zonations patterns were remarkably similar to the classic ALH 84001 rosettes (Fig. 3.54). The carbonate chemistry in Figure 3.54 is not identical to ALH 84001 as it lacks the Fe component, but the Mg abundant rims and core are prominent.

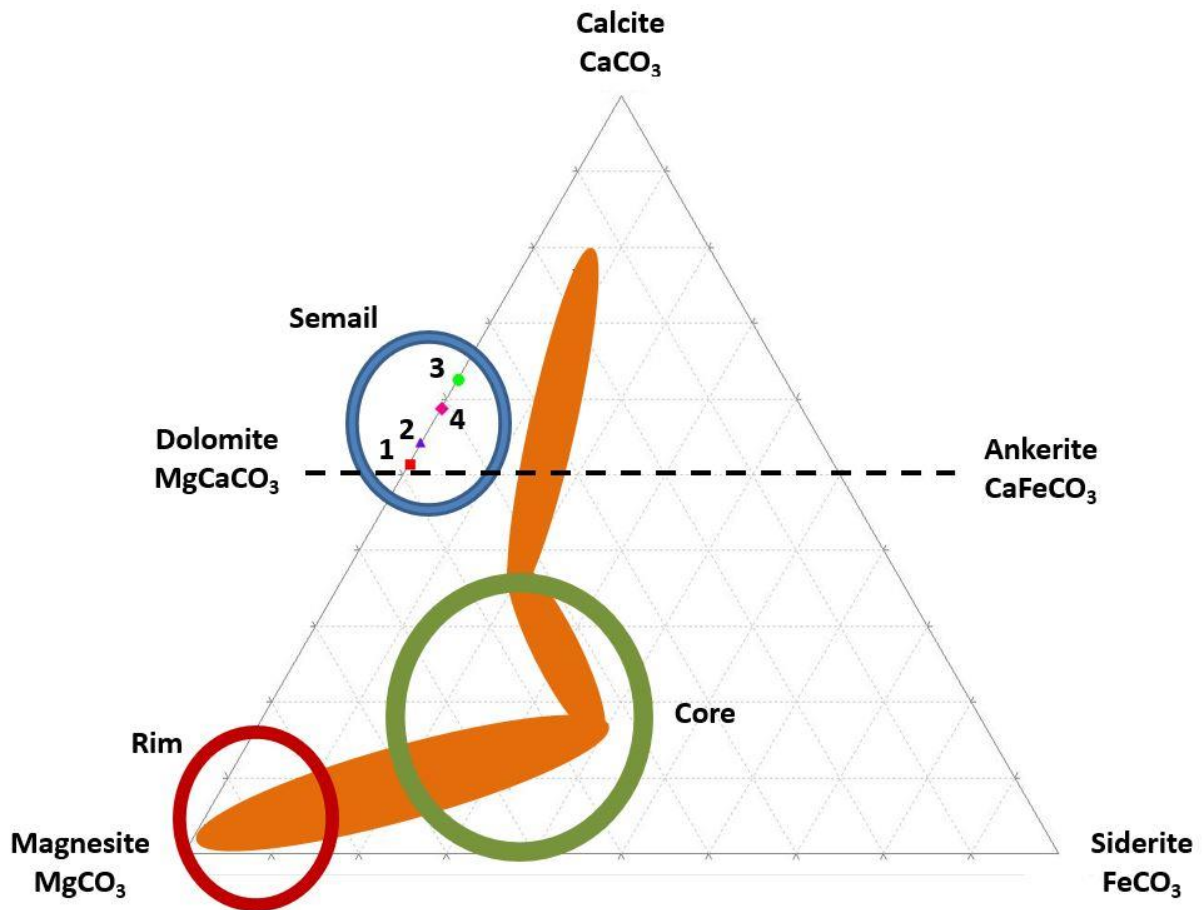


Figure 3.51. Carbonate compositional ternary plot (atomic %) comparing terrestrial Semail ophiolite carbonate rosette zonations (data in blue circle) with Martian ALH 84001 carbonate rosette zonations. **Semail:** Zones correlate to Fig. 3.52. Red square = Zone 1. Purple triangle = Zone 2. Green circle = Zone 3. See Appendix 4 for quantitative analysis. **ALH 84001:** Orange shape represents the broad data based on Eiler *et al.* (2002). The delineation of core (green circle) and rim (red circle) is based on Gleason *et al.* (1997). Pink square = Zone 4.

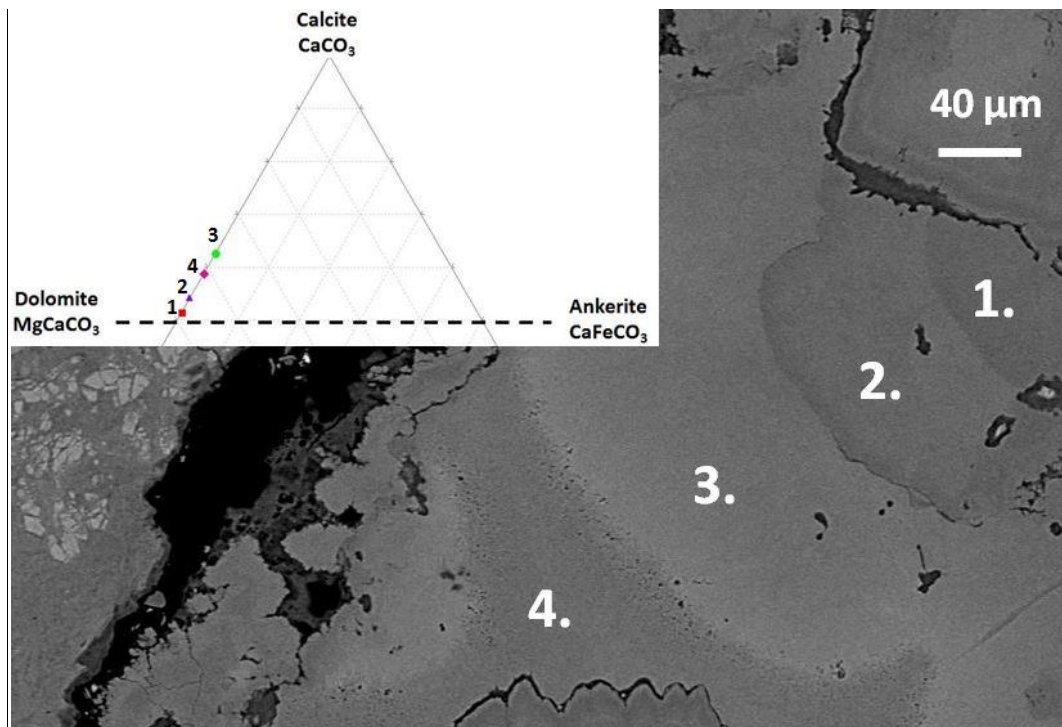


Figure 3.52. BSE SEM image of carbonate rosette zonation in SU 15 1, corresponding to Fig. 3.51. Inset: Ternary plot (atomic %) of zones.

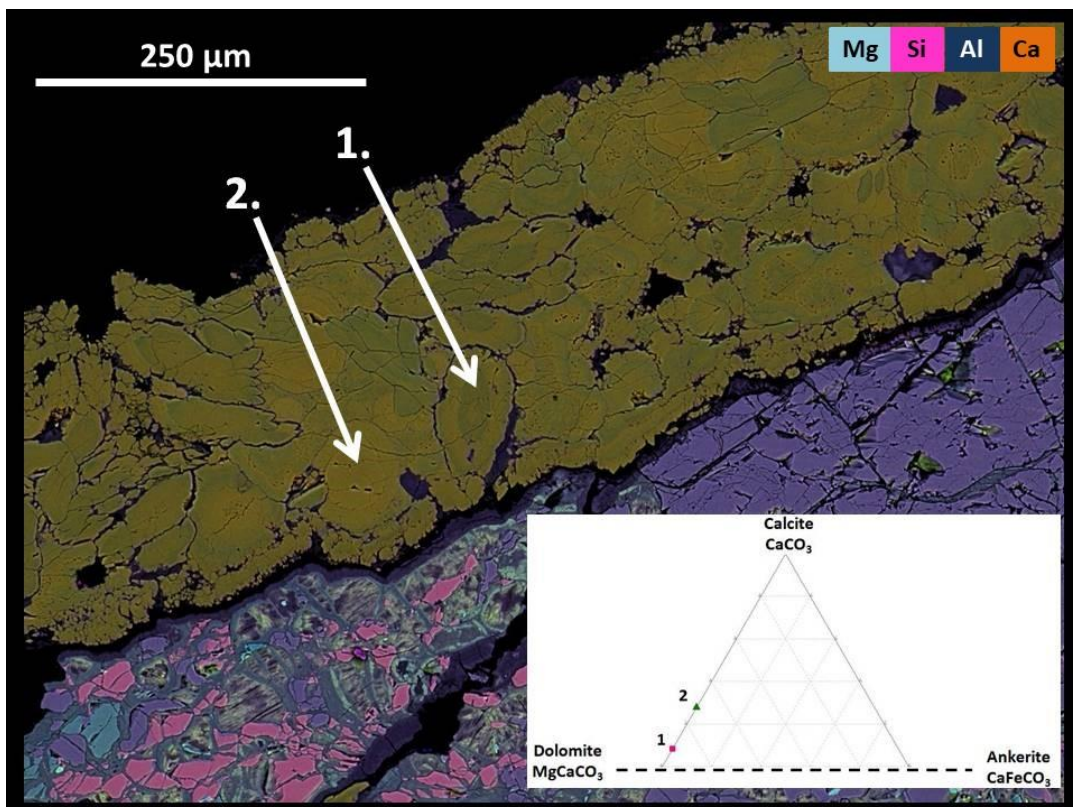


Figure 3.53. X-Ray map of Ca, Mg zonation in carbonate rosettes on the edge of Semail ophiolite sample SU 15 4. Inset: Ternary plot (atomic %) of locations. See Appendix 4 for quantitative analysis.

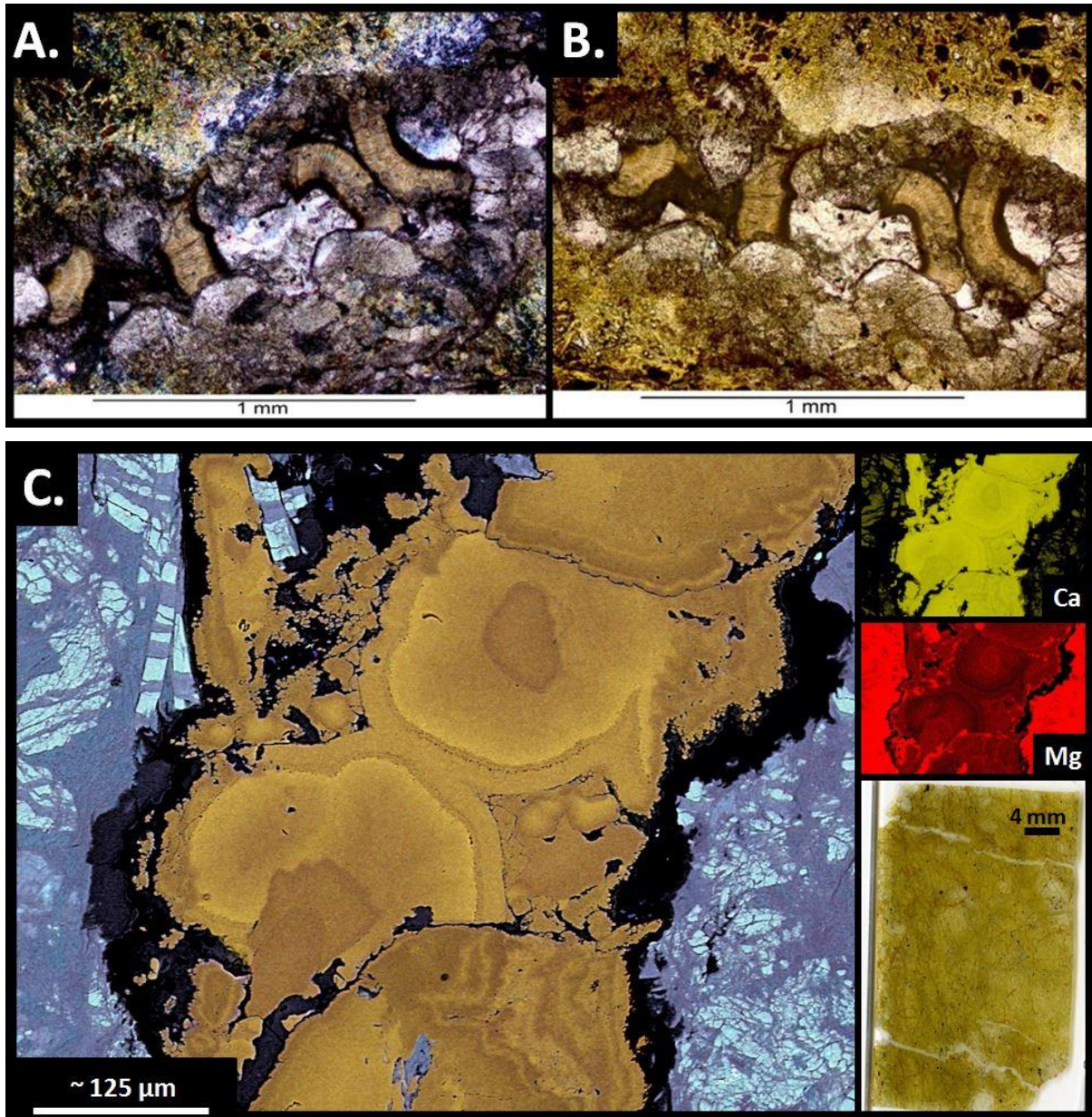


Figure 3.54. SU 15 1 carbonate rosettes. **A.** Transmitted light image between crossed polarisers. **B.** Plane polarised transmitted light image. **C.** X-Ray micro-analysis map of the carbonate rosette structure in A and B. Blue = Fe. Yellow = Ca. Green = Si. Red = Mg. Location of vein within the thin section shown in the inset. The altered host rock for the Semail samples are a mixture of serpentinite, tremolite, phyllosilicates with interspersed chromite - iron globules and rare pentlandite $(\text{Fe,Ni})_9\text{S}_8$. See Appendix 4 for quantitative analysis.

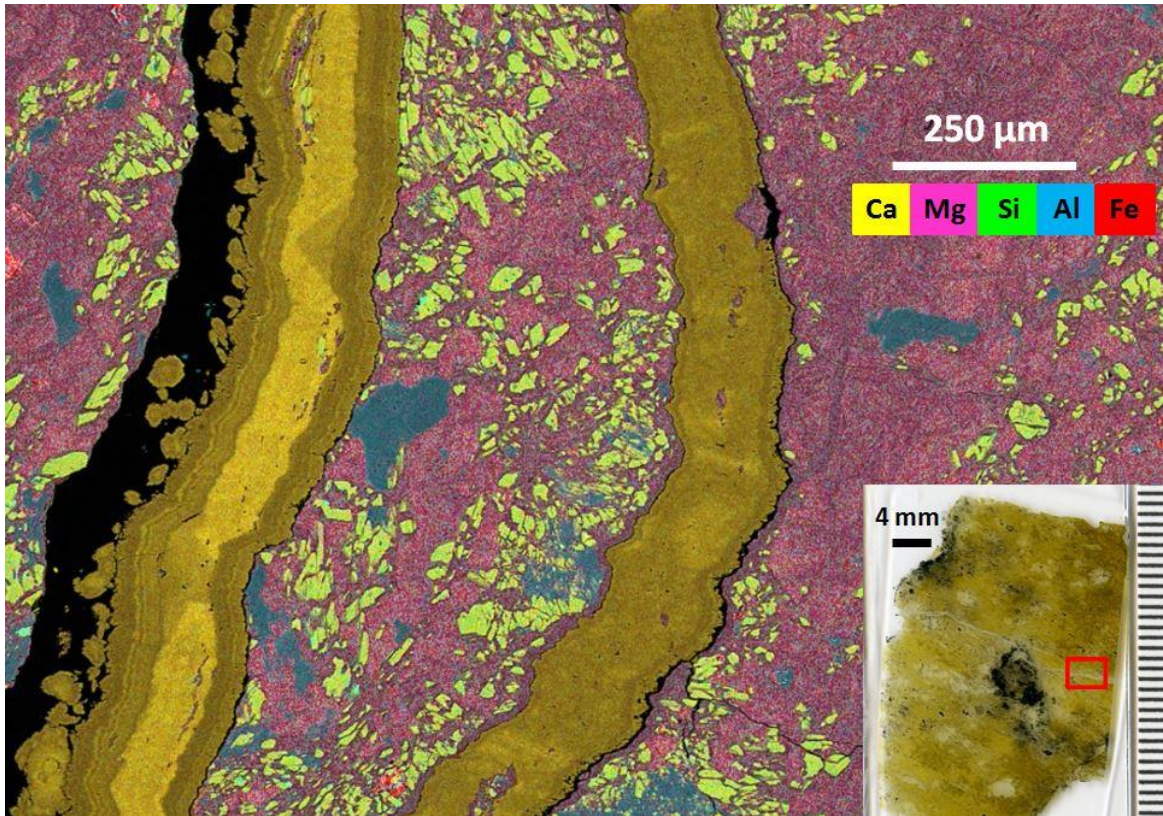


Figure 3.55. X-Ray map of parallel slab carbonate veins in SU 15 2.

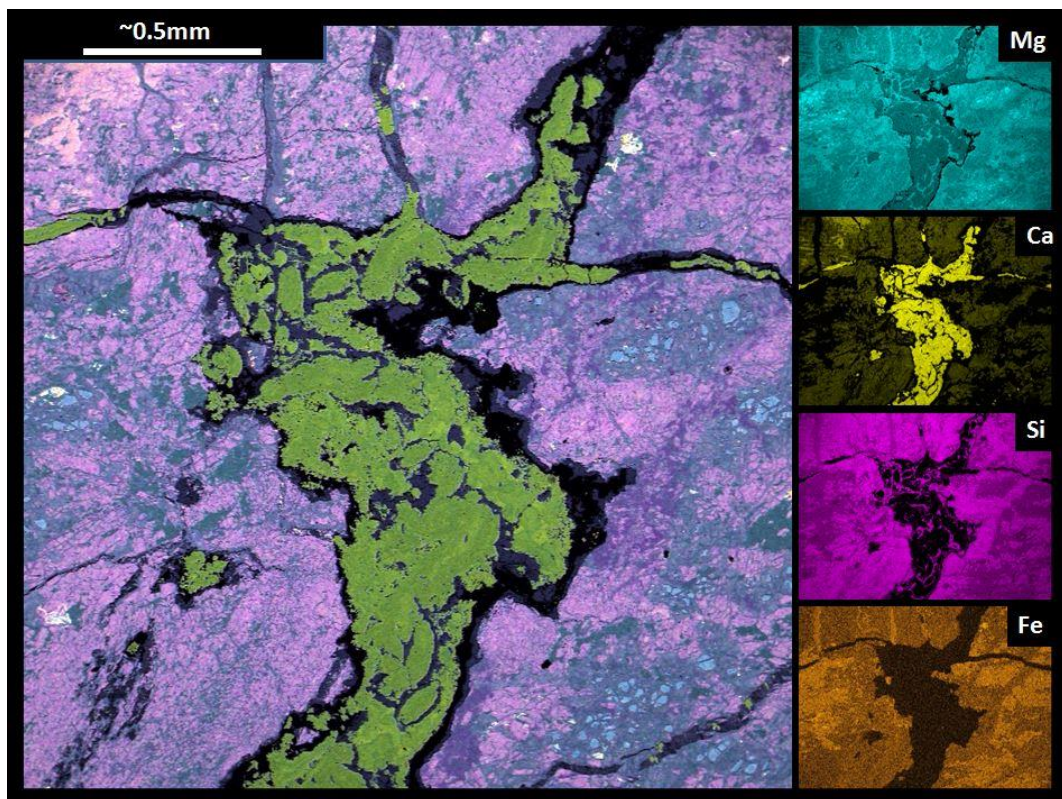


Figure 3.56. X-Ray map of a wide mixture of zoned and slab dolomite in sample SU 15 2. Mg, Ca, Si, Fe element maps are also shown.

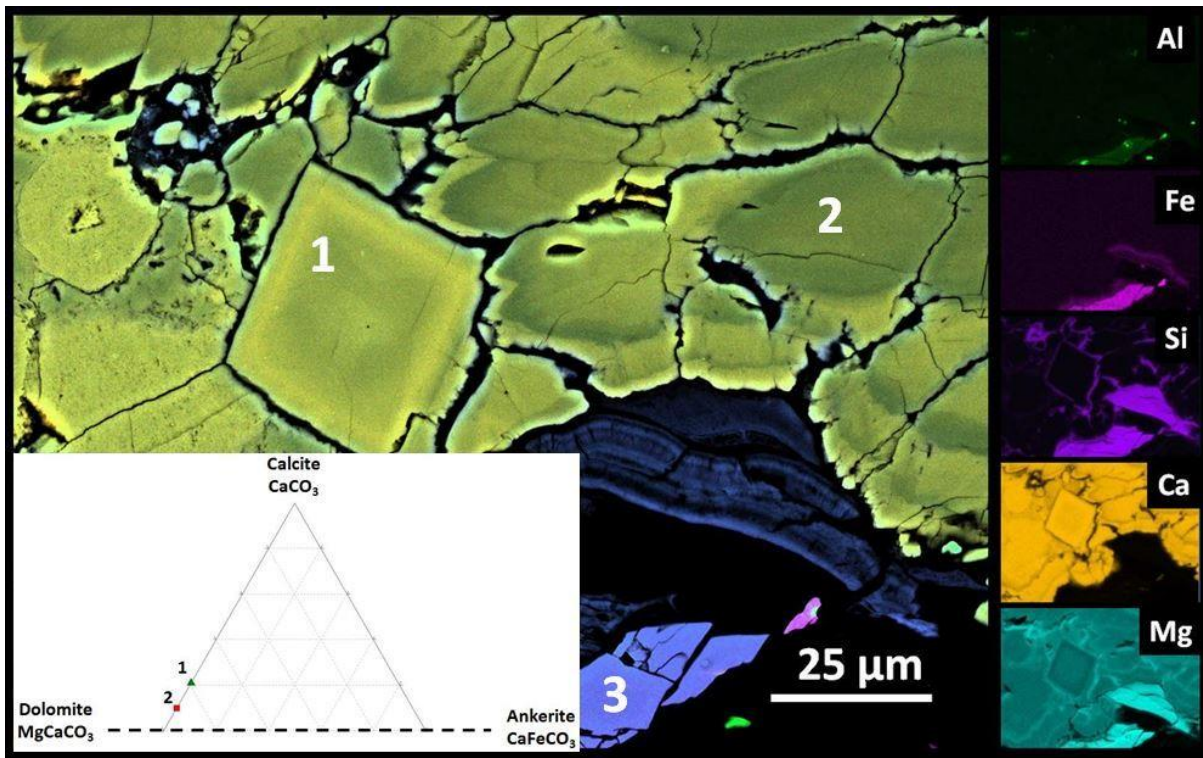


Figure 3.57. X-Ray map of UAE sample SU 15 4. Dolomitic carbonate displays Mg : Ca zonation and clear rhombohedral habit. Element distribution maps for Al, Fe, Si, Ca and Mg. Zone 3 is protoanthophyllite, an inosilicate common in metamorphosed ultramafic complex serpentinites. Inset: Ternary plot (atomic %) of locations. See Appendix 4 for quantitative analysis.

Two main categories of carbonate were identified, both dolomitic in composition. Concentrically zoned rosette carbonates (Fig. 3.52, Fig. 3.53, Fig. 3.54), and linear slab carbonates with oscillating chemical zonation (Fig. 3.55). A number of sites were a chaotic mixture of carbonate structures, not clearly rosette or slab (Fig. 3.56, Fig. 3.57). An almost perfect rhombohedral shaped carbonate can be observed in Figure 3.57, of dolomite composition (inset). Host minerals surrounding the carbonate veins included olivine fragments, serpentines, clays, chromite and iron globules.

3.5 Discussion.

Objective 3. B. Analyse carbonates and other minerals in two Martian meteorites, ALH 84001 and Lafayette, representative of early and recent Mars respectively. To present detailed analysis of glass replacement by carbonate in ALH 84001 and suggest models for this glass - carbonate reaction.

3.5.1 ALH 84001.

Carbonates and glass dominate the fracture and former pore spaces of ALH 84001, rather than clays and other hydrous minerals. The carbonate takes on numerous shapes and compositions, as introduced in section 3.1.6.3. The classic carbonate rosettes have been analysed and discussed at great depth by a wide variety of studies (Romanek *et al.* 1994; Treiman, 1995; Harvey & McSween, 1996; McKay *et al.* 1996; Scott *et al.* 1997; Bridges *et al.* 2001; Treiman, 2003; Corrigan & Harvey, 2004). This study does not seek to repeat their analysis and discussions, and instead contributes to the discussion of early Mars carbonates by providing detailed analysis of a minor carbonate phase little discussed in the literature, the alteration of melt glass into carbonate.

Glass and carbonate.

As discussed in 3.1.6.3. melt glass is not an interchangeable term with maskelynite. A melt glass is formed by minerals exceeding their melting point and flowing as a liquid, whereas maskelynite forms when a mineral is shocked to the point of solid state transform to glass, but the temperature remains beneath the mineral melting point, and the glass can retain original mineral features, such as lamellae. Such minor distinctions can provide useful constraints on the shock and thermal history experienced by this valuable sample of the early Mars environment.

Carbonates with diagonal lamellae (red lines) can be seen on FIB foil S1 (Fig. 3.36, Fig 3.37), in-between two regions of Si rich glass and beneath an orthopyroxene grain. The volume of lamellar-free carbonate filling the glass cracks (Fig. 3.37 blue box) is considerably less than the central lamellae-bearing carbonate. The carbonate is Mg - Fe rich, Ca poor (Fig. 3.38), and using semi-quantitative X-Ray analysis the composition of the lamellar carbonate changed little over ~1500 nm. The composition of this carbonate falls within the rosette 'core' region of carbonate compositions (green circle, Fig. 3.50), and zone C in the slab carbonate analysis (Fig. 3.20). The lamellae precisely and consistently align with the orthopyroxene lamellae (Fig. 3.37 red lines). Such a match implies the carbonate was not formed by cementing a pre-existing cavity, evaporation - precipitation, or any similar mechanism outlined in 3.1.6.3. Instead, the carbonate must have either isomorphously replaced the orthopyroxene, retaining the lamellar, or alternatively, high shock pressure could have transformed the orthopyroxene into maskelynite (not melt glass), which was later aqueously altered to carbonate. No fracturing or displacement of lamellae can be observed, indicative of a relatively stable, low energy history after the carbonate lamellae formed (i.e. no impacts).

A different type of carbonate, of lesser volume, and a more granular texture, occurs in a line of glass weakness (Fig. 3.37 blue box). Only a small amount of the glass has reacted, suggesting a low water to rock ratio at the time of carbonation, with all available water being fully consumed as the carbonate partially replaced the glass.

The two grains suspended in the centre of the glass (Fig. 3.37) are not of orthopyroxene composition, despite visual similarity. The right-hand grain is iron rich, and the left-hand grain chromium rich. These grains are important if melt entrained, for it allows the possibility that two types of glass formed adjacent to each other at different times. One glass type is a lamellae maskelynite glass which was later replaced by carbonate, as discussed above, with sufficient water available for significant carbonation. The second glass type being a melt glass entraining allochthonous mineral grains, with lines of weakness forming as the melt cooled, into which minor carbonate directly replaced the glass in an environment possessing insufficient water for the reaction to proceed significantly.

Glass is highly reactive, more so than orthopyroxene, and it is unlikely that if glass and orthopyroxene were both exposed to water that orthopyroxene would be isomorphously replaced at a faster rate than the glass. The lamellar patterns evidence a considerable volume of orthopyroxene replacement, but large amounts of unreacted glass remain. Three possible models exist to explain the evidence discussed above:

Melt glass model:

1. Primary orthopyroxene was partially isomorphously replaced by carbonate, from the grain edge inwards, until water ceased to be available.
2. There was an influx of melt glass, replete with allochthonous grains.
3. Carbonate replaced the melt glass in a line of weakness, but reaction ceased due to lack of water, leaving only minor carbonate and glass alteration.

Maskelynite model:

1. An impact converted orthopyroxene to maskelynite glass. All glass is maskelynite glass and did not visibly retain orthopyroxene lamellae.
2. Aqueous alteration caused partial carbonate replacement. The carbonate retains original orthopyroxene lamellae.

Maskelynite and melt glass model:

1. An impact converted orthopyroxene to maskelynite glass, retaining orthopyroxene lamellae.
2. High water abundance aqueously altered all maskelynite to carbonate, retaining lamellae.
3. A second impact of higher intensity introduced melt glass.
4. Lines of weakness in the melt glass formed during rapid cooling.
5. Low water abundance aqueously altered melt glass in lines of weakness, the reaction ceasing when all water was consumed water via hydration.

The maskelynite model is rejected, as the sharp contact between lamellar carbonate and glass is inconsistent with other images of glass - carbonate interface where carbonate has partially replaced glass (Fig. 3.39). These sharp contacts match the curves of the upper orthopyroxene grain in Fig. 3.37, consistent with melt glass filling an impact created cavity space post lamellae carbonate formation. The lamellar carbonates do not appear to be of the same texture to the glass weakness carbonates (Fig. 3.37 blue box). The melt glass model or the maskelynite and melt glass model are equally plausible and neither one can be dismissed based on the evidence available.

In FIB foil S2 (Fig. 3.36, Fig. 3.39.B.C.D) shows carbonate replacement of both glass and to a lesser extent, orthopyroxene, probably simultaneously. Carbonate replacement occurs both at the glass - orthopyroxene boundary and within lines of weakness in the glass, with no lamellae visible in any of the carbonate. That unreacted glass remains provides additional evidence for a low water to rock ratio.

Glass and carbonate summary.

Two types of carbonate were observed in association with glass. First, lamellar carbonates which are either a product of direct isomorphous replacement of orthopyroxene, or carbonate replacing a maskelynite glass; second, a minor carbonate phase replacing intruded melt glass, in a line of glass weakness. Carbonates in both FIB foils (Fig. 3.36, Fig. 3.37, Fig 3.39.B.C.D), expand outwards from fractures or glass - orthopyroxene boundaries, and this would be associated with fluid pathways. Where glass remains unaltered it is assumed carbonate formation ceased due to fluid depletion, indicating low water to rock ratios. It would be useful to date these carbonates, determining if the lamellae carbonates pre-date the glass altering carbonate (Fig. 3.37 blue box), and place their formation within the context of hypothesised ALH 84001 timelines such as Table 3.2.

Rosette carbonates.

ALH 84001 carbonate rosettes were analysed in this study (Fig. 3.35, Fig. 3.36, Fig 3.40), primarily to provide a comparison to zoned carbonates in terrestrial ophiolites. No new work is presented here, and so discussion here will be brief and continue in more depth in section 3.4.4. The main points for later discussion are:

- The carbonate zone possessing sulphur and iron (Fig 3.35).
- The distinct sharp sequence of Mg - Fe - Ca carbonate (Fig. 3.40).

Secondary sulphide minerals (pyrite, pyrrhotite, and greigite) have been located in the crush and fracture regions of ALH 84001 by previous researchers (Golden *et al.* 2001; Corrigan & Harvey, 2004). Grains of magnetite and iron sulphides can intergrow with the zoned carbonate, leading to hypothesis such as the biogenic carbonate model based on magnetite grains being similar in shape to bacteria (McKay *et al.* 1996). Some researchers have even experimentally reproduced the Fe - S zone replete with the wider Mg - Fe - Ca carbonate sequence (Golden *et al.* 2001), identifying the S as pyrrhotite and ascribing it to inorganic hydrothermal processes. The experimentally reproduced Fe phase is not pure pyrrhotite/pyrite but the co-precipitation of pyrrhotite/pyrite and siderite under reducing conditions, with magnetite grains forming due to the decomposition of siderite $>475^{\circ}\text{C}$ (Brearly, 1998; Golden *et al.* 2001).

The carbonate zonation has a number of differing explanations in the literature. Some argue it is due to changing temperatures within a hydrothermal system, causing partial growth and decomposition of carbonate phases into ankerite, siderite and magnesite (Golden *et al.* 2001). Others argue they form from distinct, discontinuous fluid interaction events, with fluids of very differing compositions (Corrigan & Harvey, 2001). It is this latter hypothesis that will be explored here by comparing the ALH 84001 carbonate zonation with the results from the Semail ophiolite carbonate rosettes (Fig. 3.52, Fig 3.53, Fig 3.54) and carbonate slabs (Fig 3.55).

3.5.2 Lafayette.

Two Lafayette samples (Fig. 3.41) were used for this study (BM1959755P8467 and BN1959755P7138), the former consisted of ~7 larger (>1 mm) shards and the latter of many smaller (<1 mm) grains. Both displayed similar evidence of aqueous alteration and formation of carbonates and hydrated minerals such as smectite clays. These hydrated secondary minerals were mostly in mineral grain veins. The dominant host mineral was orthopyroxene (Fig 3.43, Fig 3.44), although significant olivine was also present, forming the out of view fracture walls in Figure 3.48. It can be noted that alteration veins in orthopyroxene generally lack the signature wall edge serrations so characteristic of olivine vein alteration (compare Fig. 3.43 with Fig. 3.47.A). This lack of serrations in orthopyroxene supports the idea that the location of aqueous alteration in olivine is partially controlled by the grains crystallographic orientation.

The veins are composed of a complex mixture of alteration products, most of which do not appear to contain carbonates. Extensive phyllosilicates are present, and form a sizable portion of the vein volume. Vein centres are composed of silica (Fig 3.42); however, even within the mapped Si vein centre which is ~2 - 5 μm on average (3.45), there is a finer Si vein ~0.5 μm , bordered by an Mg signature for ~1 μm on either side, followed by a sharp boundary, after which only a weaker non - linear Mg signature is observed (Fig 3.46). This fine Si inner core has been variously identified as an amorphous 'gel' (Bridges & Schwenzer, 2012), or as a very finely crystalline Fe - Mg silicate (Lee *et al.* 2015).

Two disparate theories of alteration vein formation process have been published (Velbel, 2012), which will be investigated further in chapter 4. The first theory is that of isovolumetric replacement of primary silicates, which states alteration veins form via direct centripetal mineral replacement of primary silicate by secondary alteration minerals, propagating from an initial fracture of 1 - 2 μm (Lee *et al.* 2015). The second theory states that pre-existing fractures become cemented and filled by hydrothermal fluids precipitating secondary minerals (Changela & Bridges, 2010; Bridges & Schwenzer, 2012; Hicks *et al.* 2014).

This ~0.5 μm Si central trough is best explained by the isovolumetric replacement of primary silicates, and the line of central Si marks where an initial rock fracture existed, into which CO_2 fluids seeped forming the silicate vein, expanding outwards via a dissolution-precipitation front by initially forming presumably a serpentine (unobserved), followed by carbonate formation and finally Fe rich phyllosilicates, smectite and the distinctive saponite 'flowers' that can be observed replacing the carbonates (Fig. 3.47, Fig. 3.48). Some veins show only phyllosilicate between the central Si vein and the host rock wall (Fig. 3.45), whereas other veins clearly show Fe and / or Ca rich carbonates (Fig 3.44 and Fig. 3.47 respectively).

The Lafayette carbonates are usually referred to as siderite or Ca, Mn rich siderite (Bridges & Schwenzer, 2012; Lee *et al.* 2015), and qualitative SEM analysis in this study confirms a Ca Mn siderite in Figure 3.46. The saponite flowers that have replaced the siderite (Fig. 3.47.B) have Fe rich cores ~3 μm diameter and Fe rich rims, with Si being the next abundant element, and Si is inversely proportional to the Fe (Fig. 3.48.B). A potential Lafayette/Mars carbonate analogue is the clays in rhyolite tuff in Oya, Tochigi prefecture, Japan, which display almost identical size, shape and compositional patterns (Fig 3.48.C.D, Kohyama *et al.* 1973).

As with ALH 84001, the primary purpose of the Lafayette analysis is to provide a point of comparison to terrestrial ophiolite aqueous alteration and carbonate formation, and to provide a recent Mars comparison to the early Mars sample ALH 84001. The key points observed are:

- Considerably higher abundance of clays and other hydrated mineral phases compared to fractures and crush zones in ALH 84001.
- The absence of rosette carbonates, and the absence of chemically distinctive carbonate zonations.

Objective 3. C. Analyse carbonates and hydrated minerals in terrestrial ophiolites, and contrast and compare them with the Martian meteorites of objective B.

Objective 3. D. To propose that early Mars carbonate zonation in ALH 84001 may be caused by ophiolite style type 1 - 4 type water aquifer flows.

3.5.3 Leka ophiolite.

All Leka samples observed in this study were without carbonates. Samples were either heavily or entirely serpentinitised (Fig. 3.49, Fig 3.50), often with sharp reaction fronts with the unserpentinitised rock (Fig. 3.49, inset), and this finding agrees with other studies (Iyer *et al.* 2008; Plümper *et al.* 2012). The lack of carbonates in the samples studied here was unexpected, as the Leka ophiolite does possess them (Bjerga *et al.* 2015). Originally Leka was planned to be the only ophiolite studied, and the lack of carbonates prompted the Semail to become the prime focus, hence the cursory inclusion of Leka in the results section above; simply included to highlight the extensive serpentinitisation texture, and remnant olivine shards. Some samples possibly had a thin (<1 mm) coating of carbonate on the outer rock layer, but this layer did not survive thin section preparation, nor did the parts not used in thin section react with hydrochloric acid to any noticeable degree.

Qualitatively, the academic literature contains notably less carbonate observation and analysis in Leka compared with Semail ophiolite. Combined with this study's results it can be tentatively stated that Leka is less mineral carbonated than Semail. This conclusion raises some interesting questions, for Leka is both colder than Semail, and receives significantly more precipitation (Fig. 3.58.A.B. Fig. 3.59.A.B). Semail is drier and warmer than Leka, and possesses well-formed rosette carbonates. Leka is colder and wetter than Semail, and dominated by serpentines and clays, with minor carbonate. The Mars analogue is ambiguous.

Geological evidence indicates Noachian Mars/ALH 84001 conditions were probably wetter and warmer than recent Mars/Lafayette conditions (3.1.2). Yet ALH 84001 possesses diverse and well-formed carbonate rosettes and Lafayette does not, and is instead dominated by hydrated phyllosilicate alteration with minor carbonate and no rosettes. This result could suggest either:

- Temperature, rather than water to rock ratio, is the primary control of well-formed carbonate rosette growth.
- High water to rock ratio and through flow (aqueous cation removal) reduces carbonate growth.

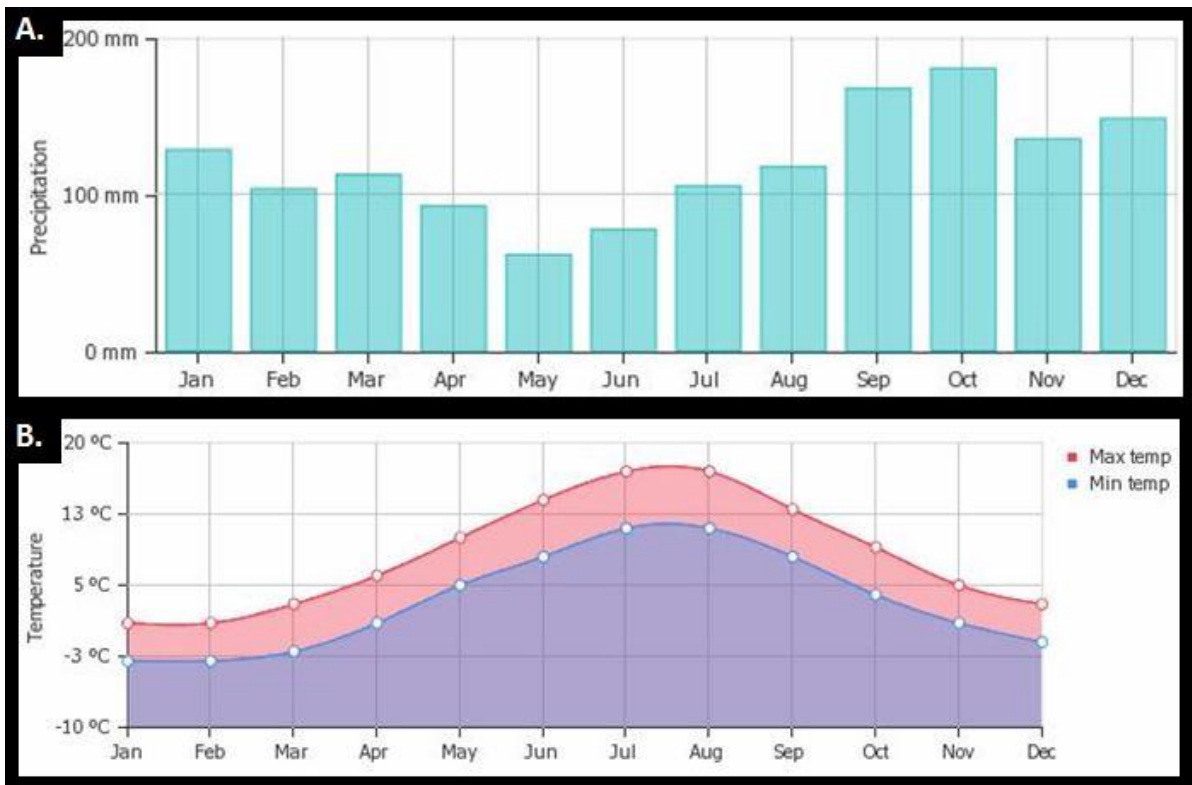


Figure 3.58. A. Average precipitation, including snow and hail for the Island of Leka, Norway. **B.** Average temperature for the Island of Leka, Norway (Website 6).

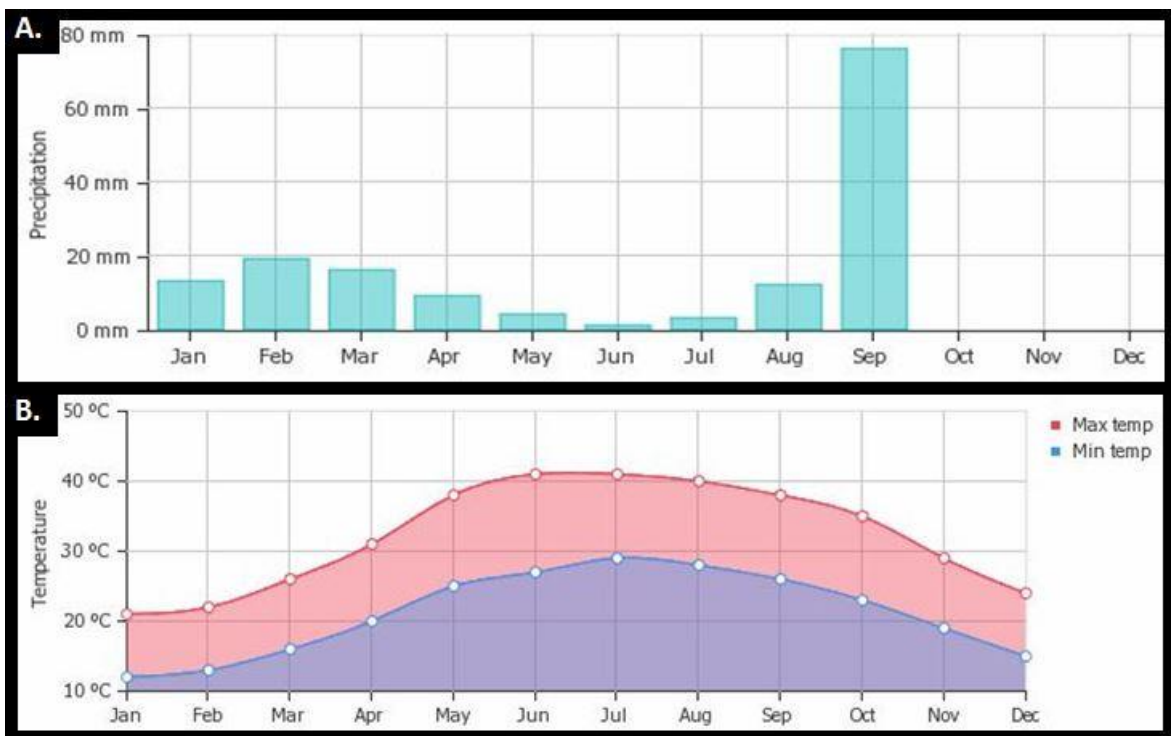


Figure 3.59. A. Average precipitation for Sohar (see Fig. 3.29) in the Semail ophiolite. **B.** Average temperature for Sohar, in the Semail ophiolite. (Website 7).

3.5.4 Semail ophiolite.

The Semail carbonates are remarkably similar in shape to those of ALH 84001. The Semail carbonate rosettes also possess distinct chemical zones that are similar, but not identical, to those in ALH 84001. There are no equivalent carbonates in Martian Lafayette or terrestrial Leka samples. One of the most notable differences between the Semail zoned carbonates and ALH4001 carbonates is that the Semail carbonates contain very little Fe. No siderite or ankerite was found in the Semail samples. Three possibilities might explain the lack of Fe in Semail carbonates:

- Primary unreacted olivine in Semail contains significantly less Fe than Martian meteorite samples (Fig. 3.31), with ALH 84001 olivine possessing Fo_{65} to Fo_{66} (Shearer *et al.* 1999) and Semail olivine possessing Fo_{90} to Fo_{92} (Hanghøj *et al.* 2010), Fo_{89} to Fo_{90} (this study Fig 3.31). This higher Fe content in ALH 84001 olivine could have created more Fe rich carbonates.
- The host rock containing the fractures in the Semail samples is highly aqueously altered, containing serpentinite, tremolite, phyllosilicates with interspersed chromite - iron globules and rare pentlandite $(Fe,Ni)_9S_8$. Very little unreacted olivine remains. See Appendix 4 for quantitative analysis. ALH 84001 carbonate veins are mostly surrounded by relatively unreacted orthopyroxene. This difference in fracture host mineralogy may partially explain the variations in carbonate Fe content, although specifically focussed mineral experiments would be required to prove this.
- The carbonates in both ALH 84001 and Semail may have been precipitated from allochthonous fluids whose composition was not affected by the host rock.

The rosette carbonates in Semail are very well formed and have filled large pre-existing fractures, as demonstrated by the following observations:

- The fractures retain open pore space (Fig. 3.34, Fig 3.56).
- This space is interspersed with isolated ‘perfectly formed’ rosette carbonates that do not appear to have ‘fell into’ the void space during thin section making, nor detached from a larger carbonate region during fracturing.
- The lack of dislocations (micro-fractures) within the carbonates.

The growth of these near perfectly formed, almost symmetrical, carbonate rosettes in Semail samples within wide pre-existing fractures provides good support for ALH 84001 researchers who state that the very similar zoned carbonate rosette growth (Fig. 3.18, Fig. 3.19) was kinetically controlled (McKay & Lofgren, 1997; Corrigan & Harvey, 2004). The rosettes formed where space was unrestricted, and slab or interstitial carbonate types formed where there was limited space for rosettes to develop. Kinetic carbonate growth in ALH 84001 is also supported by laboratory experiments (Golden *et al.* 2000). Kinetically controlled crystal growth refers to nucleation and outward growth from the nucleus of a new crystal from a supersaturated phase, with the growth attempted to equilibrate with the surrounding conditions (Heyer, 1966). This process would mean that individual rosettes would grow out from a single nucleation point developing a well-formed rosette until the growth meets either a vein wall, or another carbonate growth. Figure 3.54.C shows the most well-developed* carbonates from the Semail samples, where growth appears to have ceased just as two rosettes started to meet. In other less well-formed examples, numerous zoned carbonates can abut and vie for further growth space (Fig. 3.53. Fig 3.57), and this process usually results in deformed non-circular rosettes. Figure 3.56 shows a particularly wide fracture junction, where a messy conglomeration of carbonates have grown together, from numerous nucleation sites, and with little individual circular growth symmetry.

The Semail samples also display 'slab style' carbonates, where entire fracture veins are full of linear zoned carbonate, devoid of rosette structures (Fig. 3.55). These Semail slab carbonates are very similar to ALH 84001 slab carbonates (Fig. 3.20). If carbonate growth is kinetically controlled, the slabs fast growth from numerous nucleation sites. A proposal that could emerge from this is:

- Rosette carbonates grew slowly in fractures from a limited number of nucleation sites, perhaps due to low water to rock ratios i.e. a drained environment.
- Slab carbonates grew quickly in fractures from many nucleation sites, perhaps due to actively migrating water.

Semail carbonate zonations show a much tighter compositional grouping than the more chemically diverse ALH 84001 carbonate zonations (Fig. 3.51, Fig 3.53, Fig. 3.57). When Fe variation is accounted for, there remains significant Ca and Mg differences between zones in ALH 84001. However, even in the Semail samples, different carbonate zones have distinct Ca/Mg ratios (Fig. 3.52), and such variations can be explained by either:

- Chemical variation within a constant water flow.
- A chemically homogenous fluid, followed by an unspecified time gap and a new, chemically different fluid.

When a constant flow changes chemistry one would expect the contacts to be gradational. For water flows of different chemistry occurring at different time intervals one would expect sharp, clear contacts. Figure 3.52 and 3.54 (sample SU 15 1) has sharp boundaries to the Semail carbonate zones, whereas Figure 3.57 (sample SU 15 4) has graded transitions, implying that a constant chemically varying water source was available in SU 15 4 formation, but time separated water

flows occurred in SU 15 1. In Figure 3.55 a sharp contact can be observed in the left-hand fracture between the central Ca dominated carbonate portion of the vein and the rapidly alternating Ca - Mg dominated carbonate outer portion of the vein, whose alternations are much more graded, as is all the carbonate in the right-hand fracture. It is proposed that Mg - Ca alternating rich fluids percolated the fracture causing Mg - Ca alternating carbonates on the fracture walls, followed by an unspecified time gap, followed by a Ca rich flow forming the Ca carbonate in left hand vein centre. The open space in the left-hand fracture was caused by fracture widening post slab carbonate formation. After this vein widening event a few small rosette style carbonates formed in the open fracture space (Fig. 3.55).

In ALH 84001, sharp zone contacts can be seen in Fig. 3.40. Interestingly however, in Figure 3.35 a graded transition can be seen in the inner core, from a Ca dominated interior grading out with increasing Fe and S, to a sharp contact with an Mg carbonate zone. This may mean that two different water flows occurred, the first constant and changing slowly to become increasingly Fe and S rich, which then ceased, followed by a fresh influx of Mg rich water.

Regarding the sources of Ca and Mg rich Semail ophiolite waters, these most likely correlate with the classic ophiolite water types discussed in 3.2.1 (Fig 3.24. Barnes & O'Neil, 1969; Neal & Shand, 2002; Kelemen & Matter, 2008; Falk, 2014). Type 1 waters are Mg and CO₂ rich meteoritic water that reacts with olivine and can settle in shallow subsurface aquifers of magnesium bicarbonate water Mg HCO₃ signatures. When Mg rich type 1 waters react with olivine they can precipitate magnesite or Mg rich carbonate, and over time become Mg and CO₂ poor Na rich, unless replenished, and these are Type 2 waters. If type 2 waters flow to the surface and become CO₂ rich type 3 waters, then calcite can precipitate (Leleu *et al.* 2016).

Real systems are rarely textbook, and a wide variety of gradational water types and mid-type aquifers in chemical non-equilibrium may exist. If carbonates are forming in a type 2 or 3 environment and a precipitation event occurs, this can cause a type 1 aquifer to overflow into type 2 and 3 environments. Such water type aquifer overflows, linked to precipitation events is the mechanism proposed

for the formation of Semail carbonate zonations observed in this study. The Semail region receives relatively few precipitation events, yet the aquifers possess high storage capacity over long time periods, combined with a low/slow regional hydraulic conductivity permitting carbonate formation (Dewandel *et al.* 2005). There is no reason the water chemistry on early Mars should not be very similar, albeit comparatively enriched in Fe. If early Mars experienced limited precipitation, as in the Semail ophiolite, then shallow and deep subsurface aquifers of distinctive type 1 - 4 chemistry (section 3.2.1) is highly plausible. The overflowing of early Mars aquifers due to sporadic precipitation events or due to impact fracturing destroying the aquifer integrity becomes a plausible solution to carbonate zonation observed in ALH 84001.

3.6 Conclusions.

Following a review on Martian geology and geochemistry in relation to mineral carbonate formation (or lack thereof) and associated carbon sequestration, and an introduction to terrestrial ophiolites, this study goes on to make the following conclusions:

- **Punctuated hyper carbonation on Mars hypothesis.**
 - It is proposed that intense, highly geographically localised carbonation may have occurred in the early Martian subsurface (>500 m depth), with positive feedback ‘runaway’ carbonation taking place as observed in large terrestrial geoengineering sites such as CarbFix.
 - Regional impact heating or volcanic heating of waters to ~180°C can cause carbonation of olivine, which, combined with a positive geothermal gradient, and the exothermic nature of the carbonation reaction itself can sustain the temperature.

- Aqueous alteration of the host rock causes volumetric expansion, due to mineral hydration, with fractures developing that expose fresh mineral surfaces for continued alteration.
- Such hyper carbonation events would continue until heat, reactive primary mineral availability, or fluids became exhausted.
- Such hypothetical subsurface events would be identifiable via seismic investigation on Mars, and the density of hydrated alteration products would create a low signature.
- With a range of upcoming Mars missions capable of seismic investigations, such as InSight, this is a testable hypothesis.

- **Carbonate replacing glass in ALH 84001.**

- Clear evidence is provided, by SEM and TEM, of two differing carbonates in close association with Si rich glass in fractures within ALH 84001.
- The most plausible model of formation is maskelynite replacing orthopyroxene. Maskelynite is then replaced by carbonate. Melt glass intruded at a later date, with a final, low water to rock ratio carbonate replacement of the melt glass occurring in lines of weakness, ending when all water is consumed.
- What might initially appear an obscure investigation of a minor carbonate phase has relevance for wider questions on the availability of water on early Mars. Glass, whether maskelynite or melt glass, is highly reactive. If glass remains only partially aqueously altered by mineral carbonation then this finding testifies to a low water to rock ratio, and provides additional evidence when selecting probable early Mars models such as in Figure 3.6.
- The evidence presented in this study supports relatively dry models rather than wet ones.

- **Carbonate rosettes in ALH 84001.**

- Rosette carbonates in ALH 84001 were examined briefly. Ca - Fe - Mg patterns were identified, with S intimately associated with the Fe carbonate

phase (Fig. 3.35). Ca carbonate graded into Fe carbonate mixed with S (pyrite/pyrrhotite), but a sharp contact existed between Fe carbonate with S and Mg carbonates.

- **Carbonates in Lafayette.**

- No rosette type carbonates were identified in Lafayette.
- Alteration veins were located in olivine and orthopyroxene grains.
- A wide range of phyllosilicates dominate the alteration veins. Such phyllosilicates are absent from ALH 84001.
- Saponite 'flowers' were identified replacing Ca - Mn rich siderite, and a terrestrial analogue for such features was identified in rhyolite tuff from Oya, Tochigi prefecture, Japan.

- **The terrestrial Leka ophiolite.** No carbonates were identified, only intense, sometimes complete serpentinisation of peridotites.

- **Carbonates in the terrestrial Semail ophiolite.**

- Carbonates observed in the Semail samples included both rosette and slab types, similar in shape to those in ALH 84001.
- All Semail carbonates lacked Fe, probably due to an initially Fe poor primary olivine, or a loss of Fe during ensuing serpentinisation, or both.
- Dolomite carbonate rosette and slab zonations that were similar in shape to ALH 84001, albeit different in composition, varying from 51 - 58 atomic % Ca (Fig. 3.51. Fig. 3.52). It is proposed that rosette carbonates form in environments of slow growth, low density of nucleation sites (for example in drained but not dry pore spaces), whereas slab carbonates form in environments of rapid growth, high density of nucleation sites (for example in active water migration in fractures). These carbonate formation environment proposals would apply to both terrestrial Semail and ALH 84001. Interesting future work would be to design a specific laboratory mineral carbonate growth experiment to test this proposal.

- Some Semail carbonate zones have sharp contacts (sample SU 15 1), while others have graded contacts (sample SU 15 4). It is proposed that gradational contacts are due to chemical change through time in a single flow event, and that sharp contacts represent a gap of an unspecified time between flow events. This proposal could be tested experimentally, and if correct may add to the discussion regarding the formation environment and sequence of events surrounding the ALH 84001 carbonates, which possess similar graded and sharp carbonate contacts.
- It is proposed that variations in Mg and Ca carbonate may be due to the well known ophiolite water types, where an Mg rich shallow subsurface aquifer (type 1 water) overflows intermittently into deeper aquifers (type 2 waters), or mix with extrusive Ca waters (type 3 waters). The dolomite carbonates observed in this study do not neatly correlate with any classic ophiolite water type carbonate (i.e. type 1 magnesite and type 3 calcite), and so probably represent a transitional environment. Aquifer overflow may be due to infrequent precipitation events or aquifer faulting. Mars possesses a basaltic geology, similar in many respects to that of terrestrial ophiolites. It is entirely plausible that early Mars, with a more active surface hydrological cycle than present, could have possessed ophiolite water types which may have been responsible for forming distinct carbonate zones, such as observed in ALH 84001. As Mars became dryer over time, phyllosilicates began to be the dominate vein aqueous alteration type, as observed in Lafayette, with chemically uniform minor carbonates lacking in zonations.

3.7 Acknowledgements.

Semail ophiolite samples were kindly donated by Dr Alicja Lacinsk and Keith Bateman from the British Geological Survey. Thin section support was provided by John Gillece and SEM support from Peter Chung, both at the School of Geographical and Earth Sciences, University of Glasgow. Martian meteorite samples were kindly provided on loan by the Natural History Museum, London and the American Museum of Natural History.

3.8 References.

- Achille G. D., Hynek B. M. (2010). Ancient ocean on Mars supported by global distribution of deltas and valleys. *Nature Geoscience* 3:459-463.
- Agee C. (2014). Black beauty: A unique 4.4 Ga, water rich meteorite from Mars. *Elements* 10:168.
- Alabaster T., Pearce J. A., Malpas J. (1982). The volcanic stratigraphy and petrogenesis of the Oman ophiolite complex. *Contributions to Mineralogy and Petrology* 81(3):168-183.
- Alfredsson H. A., Oelkers E. H., Hardarsson B. S., Franzson H., Gunnlaugsson E., Gislason S. R. (2013). The geology and water chemistry of the Hellisheidi, SW-Iceland carbon storage site. *International Journal of Greenhouse Gas Control* 12:399-418.
- Arkani-Hamed J., Olson P. (2010). Giant impacts, core stratification, and failure of the Martian dynamo. *Journal of Geophysical Research* 114: E07012.
- Austrheim H., Prestvik T. (2008). Rodingitization and hydration of the oceanic lithosphere as developed in the Leka ophiolite, north-central Norway. *Lithos* 104(1-4):177-198.
- Baker V. R., Strom R. G., Gulick V. C., Kargel J. S., Komatsu G., Kale V. S. (1991). Ancient oceans, ice sheets and the hydrological cycle on Mars. *Nature* 352:589-594.
- Banerdt W. B., Smrekar S., Lognonné P., Spohn T., Asmar S. W., Banfield D., Boschi L., Christensen U., Dehant V., Folkner W., Giardini D., Goetze W., Golombek M., Grott M., Hudson T., Johnson C., Kargl G., Kobayashi N., Maki J., Mimoun D., Mocquet A., Morgan P., Panning M., Pike W. T., Tromp J., van Zoest T., Weber R., Wieczorek M. A., Garcia R., Hurst K. (2013). InSight: A Discovery Mission to Explore the Interior of Mars. *44th Lunar and Planetary Science Conference* 1719(1915).
- Barnes I., O'Neil J. R. (1969). The Relationship between Fluids in Some Fresh Alpine-Type Ultramafics and Possible Modern Serpentinization, Western United States. *Geological Society of America Bulletin* 80(10).
- Barnes C. G., Prestvik T., Li Y., McCulloch L., Yoshinobu A. S., Frost C. D. (2009). Growth and zoning of the Hortavær intrusive complex, a layered alkaline pluton in the Norwegian Caledonides. *Geosphere* 5(3):286-301.
- Barrat J., Jambon A., Ferrère L., Bollinger C., Langlade J., Liorzou C., Boudouma O., Fialin M. (2014). No Martian soil component in shergottite meteorites. *Geochimica Et Cosmochimica Acta* 125:23-33.
- Beck P., Pommerol A., Zanda B., Remusat L., Lorand J. P., Göpel C., Hewins R., Pont S., Lewing E., Quirico E., Schmitt B., Montes-Hernandez G., Garenne A., Bonal L., Proux O., Hazemann

- J. L., Chevrier V. F. (2015). A Noachian source region for the “Black Beauty” meteorite, and a source lithology for Mars surface hydrated dust? *Earth and Planetary Science Letters* 427(1):104-111.
- Bell M. (2007). Experimental shock decomposition of siderite and the origin of magnetite in Martian meteorite ALH 84001. *Meteoritics & Planetary Science* 42(6):935-949.
- Bibring J., Langevin Y., Poulet F., Gendrin A., Gondet B., Berthé M., Soufflot A., Drossart P., Combes M., Bellucci G., Moroz V., Mangold N., Schmitt B., OMEGA team. (2004). Perennial water ice identified in the south polar cap of Mars. *Nature* 428:627-630.
- Bibring J. P., Langevin Y., Mustard J. F., Poulet F., Arvidson R., Gendrin A., Gondet B., Mangold N., Pinet P., Forget F., the OMEGA team, Berthé M., Bibring J. P., Gendrin A., Gomez C., Gondet B., Jouglet D., Poulet F., Soufflot A., Vincendon M., Combes M., Drossart P., Encrenaz T., Fouchet T., Merchiorri R., Bellucci G., Altieri F., Formisano V., Capaccioni F., Ceroni P., Coradini A., Fonti S., Korabely O., Kottsov V., Ignatiev N., Moroz V., Titov D., Zasova L., Loiseau D., Mangold N., Pinet P., Douté S., Schmitt B., Sotin C., Hauber E., Hoffmann H., Jaumann R., Keller U., Arvidson R., Mustard J. F., Duxbury T., Forget F., Neukum G. (2006). Global Mineralogical and Aqueous Mars History Derived from OMEGA/Mars Express Data. *Science* 312(5772):400-404.
- Bjerga A., Konopásek J., Pedersen R. B. (2015). Talc-carbonate alteration of ultramafic rocks within the Leka Ophiolite Complex, Central Norway. *Lithos* 227:21-36.
- Bjoraker G. L., Mumma M. J., Larson H. P. (1989). Isotopic abundance ratios for hydrogen and oxygen in the martian atmosphere. *Bulletin of the American Astronomical Society* 21:991.
- Blaney D. L., McCord T. B. (1989). An observational search for carbonates on Mars. *Journal of Geophysical Research: Solid Earth* 94(B8):10159-10166.
- Borg L., Connelly J. Nyquist L. E., Shih C. Y., Wiesmann H., Reese Y. (1999). The Age of the Carbonates in Martian Meteorite ALH 84001. *Science* 286(5437):90-94.
- Bottke W. F., Andrews-Hanna J. C. (2017). A post-accretionary lull in large impacts on early Mars. *Nature Geoscience* 10:334-348.
- Boudier F., Nicolas A. (2007). Comment on “dating the geologic history of Oman’s Semail ophiolite: insights from U-Pb geochronology” by C. J. Warren, R. R. Parrish, D. J. Waters and M. P. Searle. *Contributions to Mineralogy and Petrology* 154(1):111-113.
- Bouvier A., Blichert-Toft J., Vervoort J. E., Albarède F. (2005). The age of SNC meteorites and the antiquity of the Martian surface. *Earth and Planetary Science Letters* 240:221-233.
- Bouvier A., Blichert-Toft J., Vervoort J. D., Gillet P., Albarède F. (2008). The case for old basaltic shergottites. *Earth and Planetary Science Letters* 266:105-124.

- Bouvier A., Blichert-Toft J., Albarède F. (2009). Martian meteorite chronology and the evolution of the interior of Mars. *Earth and Planetary Science Letters* 280:285-295.
- Bouville A., Lowder W. M. (1988). Human Population Exposure to Cosmic Radiation. *Radiation Protection Dosimetry* 24(1-4):293-299.
- Boynton W. V., Ming D. W., Kounaves S. P., Young S. M. M., Arvidson R. E., Hecht M. H., Hoffman J., Niles P. B., Hamara D. K., Quinn R. C., Smith P. H., Sutter B., Catling D. C., Morris R. V. (2009). Evidence for Calcium Carbonate at the Mars Phoenix Landing Site. *Science* 325(5936):61-64.
- Boynton W. V., Feldman W. C., Squyres S. W., Prettyman T. H., Brückner J., Evans L. G., Reedy R. C., Starr R., Arnold J. R., Drake D. M., Englert P. A. J., Metzger A. E., Mitrofanov I., Trombka J. I., d'Uston C., Wänke H., Gasnault O., Hamara D. K., Janes D. M., Marcialis R. L., Maurice S., Mikheeva I., Taylor G. J., Tokar R., Shinohara C. (2002). Distribution of Hydrogen in the Near Surface of Mars: Evidence for Subsurface Ice Deposits. *Science* 297(5578):81-85.
- Brearley A. J. (1998). Magnetite in ALH 84001: Product of the decomposition of ferroan carbonate (abstract #1451). *29th Lunar and Planetary Science Conference*. CD-ROM.
- Bridges J., Catling D., Saxton J., Swindle T., Lyon I., Grady M. (2001). Alteration assemblages in Martian meteorites: Implications for near-surface processes. *Space Science Reviews* 96(1-4):365-392.
- Bridges, J. (2004). *Martian meteorites*. Available: <http://www.nhm.ac.uk/research-curation/research/projects/martian-met/meteorites.html>.
- Bridges J. C., Schwenzer S. P. (2012). The nakhlite hydrothermal brine on Mars. *Earth and Planetary Science Letters* 359-360:117-123.
- Bristow T. F., Haberle R. M., Blake D. F., Des Marais D. J., Eigenbrode J. L., Fairén A. G., Grotzinger J. P., Stack K. M., Mischna M. A., Rampe E. B., Siebach K. L., Brad Sutter B., Vaniman D. T., Vasavada A. R. (2017). Low Hesperian PCO₂ constrained from in situ mineralogical analysis at Gale Crater, Mars. *Proceedings of the National Academy of Sciences* 114(9):2166-2170.
- Brown J. (1967). Tundra Soils Formed over Ice Wedges, Northern Alaska. *Soil Science Society of America Journal* 31(5):686-691.
- Calvin W. N., King T. V. V., Clark R. N. (1994). Hydrous carbonates on Mars?: Evidence from Mariner 6/7 infrared spectrometer and ground-based telescopic spectra. *Journal of Geophysical Research: Planets* 99(E7):14659-14675.

- Carr R. H., Grady M. M., Wright I. P., Pillinger C. T. (1985). Martian atmospheric carbon dioxide and weathering products in SNC meteorites. *Nature* 314, 248-250.
- Carr M. H. (1999). Retention of an atmosphere on early Mars. *Journal of Geophysical Research: Planets* 104(E9):21897-21909.
- Carr M. H., Head J. W. (2003). Basal melting of snow on early Mars: A possible origin of some valley networks. *Geophysical Research Letters* 30(20):2245.
- Carr M. H., Head J. W. (2015). Martian surface/near-surface water inventory: Sources, sinks, and changes with time. *Geophysical Research Letters* 42(3):726-732.
- Carter J., Loizeau D., Mangold N., Poulet F., Jean-Pierre Bibring J. P. (2015). Widespread surface weathering on early Mars: A case for a warmer and wetter climate. *Icarus* 248(1):373-382.
- Changela H. G., Bridges J. C. (2010). Alteration assemblages in the nakhlites: Variation with depth on Mars. *Meteoritics & Planetary Science* 45(12):1847-1867.
- Chen J. H., Wasserburg G. J. (1986). Formation ages and evolution of Shergotty and its parent planet from U-Th-Pb systematics. *Geochimica et Cosmochimica Acta* 50:955-968.
- Chen Y., Liu Y., Guan Y., Eiler J. M., Ma C., Rossman G. R., Taylor L. A. (2015). Evidence in Tissint for recent subsurface water on Mars. *Earth and Planetary Science Letters* 425:55-63.
- Chevrier V. F., Rivera-Valentin E. G. (2012). Formation of recurring slope lineae by liquid on present-day Mars. *Geophysical Research Letters* 39(21).
- Christensen P. R., Bandfield J. L., Hamilton V. E., Ruff S. W., Kieffer H. H., Titus T. N., Malin M. C., Morris R. V., Lane M. D., Clark R. L., Jakosky B. M., Mellon M. T., Pearl J. C., Conrath B. J., Smith M. D., Clancy R. T., Kuzmin R. O., Roush T., Mehall G. L., Gorelick N., Bender K., Murray K., Dason S., Greene E., Silverman S., Greenfield M. (2001). Mars Global Surveyor Thermal Emission Spectrometer experiment: Investigation description and surface science results. *Journal of Geophysical Research: Planets* 106(E10):23823-23871.
- Christensen P. R. (2003). Formation of recent Martian gullies through melting of extensive water-rich snow deposits. *Nature* 422:45-48.
- Clenet H., Pinet P., Ceuleneer G., Daydou Y., Heuripeau F., Rosemberg C., Bibring J. P., Bellucci G., Altieri F., Gondet B. (2013). A systematic mapping procedure based on the Modified Gaussian Model to characterize magmatic units from olivine/pyroxenes mixtures: Application to the Syrtis Major volcanic shield on Mars. *Journal of Geophysical Research: Planets* 118(8):1632-1655.
- Clifford S. M. (1993). A model for the hydrologic and climatic behaviour of water on Mars. *Journal of Geophysical Research: Planets* 98(E6):10973-11016.

- Cohen B. E., Mark D. F., Cassata W. S., Lee M. R., Tomkinson T., Smith C. L. (2017). Taking the pulse of Mars via dating of a plume-fed volcano. *Nature Communications* 8:640.
- Cooney T., Scott E., Krot A., Sharma S., Yamaguchi A. (1999). Vibrational spectroscopic study of minerals in the Martian meteorite ALH 84001. *American Mineralogist* 84(10):1569-1576.
- Corrigan C. M., Harvey R. P. (2004). Multi-generational carbonate assemblages in martian meteorite Allan Hills 84001: Implications for nucleation, growth, and alteration. *Meteoritics & Planetary Science* 39(1):17-30.
- Cowan R. J., Searle M. P., Waters D. (2014). Structure of the metamorphic sole to the Oman Ophiolite, Sumeini Window and Wadi Tayyin: Implications for ophiolite obduction processes. *Geological Society London Special Publications* 392(1).
- Craddock R. A., Howard A. D. (2002). The case for rainfall on a warm, wet early Mars. *Journal of Geophysical Research* 107(E11):21-1-21-36.
- Daswani M., Schwenzer S. P., Reed M. H., Wright I. P., Grady M. M. (2016). Alteration minerals, fluids, and gases on early Mars: Predictions from 1-D flow geochemical modeling of mineral assemblages in meteorite ALH 84001. *Meteoritics & Planetary Science* 51(11):2154-2174.
- Debenedetti P., Truskett T., Lewis C., Stillinger F. (2001). Theory of supercooled liquids and glasses: Energy landscape and statistical geometry perspectives. *Advances in Chemical Engineering* 28:21-79.
- Dehant V., Lammer H., Kulikov Y. N., Grießmeier J. M., Breuer D., Verhoeven O., Karatekin O., Van Hoolst T., Korablev O., Lognonné P. (2007). Planetary Magnetic Dynamo Effect on Atmospheric Protection of Early Earth and Mars. *Space Science Reviews* 129(1-3):279-300.
- Dewandel B., Lachassagne P., Boudier F., Al-Hattali S., Ladouche B., Pinault J. L., Al-Suleimani Z. (2005). A conceptual hydrogeological model of ophiolite hard-rock aquifers in Oman based on a multiscale and a multidisciplinary approach. *Hydrogeology Journal* 13(5-6):708-726.
- De Wit J. C., Van der Straaten C. M., Mook W. G. (1980). Determination of the absolute D/H ratio of V-SMOW and SLAP. *Geostandards Newsletter: The Journal of Geostandards and Geoanalysis* 4:33-36.
- Ditteon R. (1982). Daily temperature variations on Mars. *Journal of Geophysical Research* 87(B12):10,197-10,214.
- Donahue T. M. (1995). Evolution of water reservoirs on Mars from D/H ratios in the atmosphere and crust. *Nature* 375.
- Drake M. J., Swindle T. D., Owen T., Musselwhite D. S. (1994). Fractionated martian atmosphere in the nakhlites? *Meteoritics & Planetary Science* 29(6):854-859.

- Dreibus G., Burghelle A, Jochum K. L., Spettel B., Wlotzka F., Wänke H. (1994). Chemical and mineral composition of ALH 84001: A Martian orthopyroxenite. *Meteoritics* 29:461.
- Dubinini E., Fraenz M., Fedorov A., Lundin R., Edberg N., Duru F., Vaisberg O. (2011). Ion Energization and Escape on Mars and Venus. *Space Science Reviews* 162:173-211.
- Dundas C. M., McEwen A. S., Chojnacki M., Milazzo M. P., Byrne S., McElwaine J. N., Urso A. (2017). Granular flows at recurring slope lineae on Mars indicate a limited role for liquid water. *Nature Geoscience* 10:903-907.
- Ehlmann B. L., Mustard J. F., Murchie S. L., Poulet F., Bishop J. L., Brown A. J., Calvin W. M., Clark R. N., Des Marais D. J., Milliken R. E., Roach L. H., Roush T. L., Swayze G. A., Wray J. J. (2008). Orbital Identification of Carbonate-Bearing Rocks on Mars. *Science* 322(5909):1828-1832.
- Ehlmann B. L., Mustard J. F., Murchie S. L. (2010). Geologic setting of serpentine deposits on Mars. *Geophysical Research Letters* 37(L06201).
- Ehlmann B. L., Mustard J. F., Murchie S. L., Bibring J., Meunier A., Fraeman A. A., Langevin Y. (2011). Subsurface water and clay mineral formation during the early history of Mars. *Nature* 479:53-60.
- Ehlmann B. L. (2014). The first billion year - warm and wet Vs. cold and icy? *Eighth International Conference on Mars* 1245.
- Eiler J. M., Valley J. W., Graham C. M., Fournelle J. (2002). Two populations of carbonate in ALH84001: Geochemical evidence for discrimination and genesis. *Geochimica et Cosmochimica Acta* 66(7):1285-1303.
- Elwood Madden M. E., Bodnar R. J., Rimstidt J. D. (2004). Jarosite as an indicator of water-limited chemical weathering on Mars. *Nature* 431:821-823.
- Etiopio G., Ehlmann B. L., Schoelle M. (2013). Low temperature production and exhalation of methane from serpentinized rocks on Earth: A potential analog for methane production on Mars. *Icarus* 224(2):276-285.
- Etiopio G., Vance S., Christensen L. E., Marques J. M., Costa I. R. (2013). Methane in serpentinized ultramafic rocks in mainland Portugal. *Marine and Petroleum Geology* 45:12-16.
- Etiopio G. (2015). *Seepage in Serpentinized Peridotites and on Mars*. In: Etiopio G. Natural Gas Seepage. Switzerland: Springer 141-163.
- Etiopio G. (2017). Methane origin in the Samail ophiolite: Comment on "Modern water/rock reactions in Oman hyperalkaline peridotite aquifers and implications for microbial habitability" *Geochimica et Cosmochimica Acta* 197:467-470.

- Fairén A. G. (2010). A cold and wet Mars. *Icarus* 208(1):165-175.
- Fairén A. G., Davila A. F., Gago-Duport L., Haqq-Misra J. D., Gil C., McKay C. P., Kasting J. F. (2011). Cold glacial oceans would have inhibited phyllosilicate sedimentation on early Mars. *Nature Geoscience* 4:667-670.
- Fairén A. G., Mateo-Martí E., Gago-Duport L., Losa-Adams E., Chevrier V., Gil-Lozano C. (2017). Coeval formation of mineral sequences on a cold and wet early Mars. *Fourth Conference on Early Mars 2017* 2014:3037.
- Falk E. S. (2014). *Carbonation of Peridotite in The Oman Ophiolite*. PhD Thesis. Columbia University. <https://core.ac.uk/download/pdf/27298075.pdf>
- Farmer C. B., Davies D. W., Laporte D. D. (1976). Mars: Northern Summer Ice Cap—Water Vapor Observations from Viking 2. *Science* 194(4271):1339-1341.
- Farquhar J., Savarino J., Jackson T. L., Thiemens M. H. (2000). Evidence of atmospheric sulphur in the martian regolith from sulphur isotopes in meteorites. *Nature* 404:50-52.
- Fastook J. L., Head J. W., Marchant D. R., Forget F., Madeleine J. B. (2012). Early Mars climate near the Noachian-Hesperian boundary: Independent evidence for cold conditions from basal melting of the south polar ice sheet (Dorsa Argentea Formation) and implications for valley network formation. *Icarus* 219(1):25-40.
- Fisher D. A. (2007). Mars' water isotope (D/H) history in the strata of the North Polar Cap: Inferences about the water cycle. *Icarus* 187(2):430-441.
- Formisano V., Atreya S., Encrenaz T., Ignatiev N., Giuranna M. (2004). Detection of Methane in the Atmosphere of Mars. *Science* 306(5702):1758-1761.
- Floran R. J., Prinz M. (1978). The Chassigny meteorite: a cumulate dunite with hydrous amphibole-bearing melt inclusions. *Geochimica et Cosmochimica Acta* 42(8):1213-1219 and 1221-1229.
- Fritz J., Greshake A., Stöffler D. (2005). Micro-Raman spectroscopy of plagioclase and maskelynite in Martian meteorites: Evidence of progressive shock metamorphism. *Antarctic Meteorite Research* 18:96.
- Gacesa M., Zhang P., Kharchenko V. (2012). Non-thermal escape of molecular hydrogen from Mars. *Geophysical Research Letters* 39(10).
- Gaidos E., Giles M. (2003). Geological and geochemical legacy of a cold early Mars. *Journal of Geophysical Research Planets* 108(E6):9-1.
- Gaillard F., Scaillet B. (2009). The sulfur content of volcanic gases on Mars. *Earth and Planetary Science Letters* 279:34-43.

- Gaillard F., Michalski J., Berger G., McLennan S. M., Scaillet B. (2013). Geochemical reservoirs and timing of sulfur cycling on Mars. *Space Science Reviews* 174(1-4):251-300.
- Galofre G., Jellinek A. M. (2016). The Case for a Cold, Dry Early Mars from a Global Map of Valley Network Origin and Distribution. *47th Lunar and Planetary Science Conference* (2409).
- Gary M., McAfee R., Wolf C. L. (1973). *Glossary of geology*. Washington, D.C.: American Geological Institute. 443.
- Catling D. C., Zahnle K. J. (2009). The escape of planetary atmospheres. *Scientific American* 300:36-43.
- Gilmour J., Whitby J. A., Turner G. (1999). Martian atmospheric xenon contents of Nakhla mineral separates: Implications for the origin of elemental mass fractionation. *Earth and Planetary Science Letters* 166:139-148.
- Gleason J. D., Kring D. A., Dolores H. H., Boynton W. V. (1997). Petrography and bulk chemistry of Martian orthopyroxenite ALH84001: Implications for the origin of secondary carbonates. *Geochimica et Cosmochimica Acta* 61(16)3503-3512.
- Golden D. C., Ming D. W., Schwandt C. S., Morris R. V., Yang S. V., Lofgren G. E. (2000). An experimental study on kinetically-driven precipitation of calcium-magnesium-iron carbonates from solution: Implications for the low-temperature formation of carbonates in martian meteorite Allan Hills 84001. *Meteoritics & Planetary Science* 35:457-465.
- Golden D. C., Ming D. W., Lauer H. V., Socki R. A., Morris R. V., Lofgren G. E., McKay G. A. (2001). A simple inorganic process for formation of carbonates, magnetite, and sulfides in Martian meteorite ALH84001. *American Mineralogist* 86:370-375.
- Gooding J. G., Wentworth S. J., Zolensky M. E. (1988). Calcium carbonate and sulfate of possible extraterrestrial origin in EETA 79001 meteorite. *Geochimica et Cosmochimica Acta* 52:909-915.
- Gooding J. L. (1992). Soil mineralogy and chemistry on Mars: Possible clues from salts and clays in SNC meteorites. *Icarus* 99(1):28-41.
- Goudge T. A., Ehlmann B. L., Fassett C. I., Head J. W., Mustard J. F., Mangold N., Gupta S., Milliken R. E., Brown A. J. (2017). Jezero Crater, Mars, as a Compelling Site for Future In Situ Exploration. *48th Lunar and Planetary Science Conference* 20170002464.
- Grady M., Anand M., Gilmour M., Watson J., Wright I. (2007). Alteration of the Nakhlite lava pile: Was water on the surface, seeping down, or at depth, percolating up? Evidence (such as it is) from carbonates. (abstract #1826). *38th Lunar and Planetary Science Conference. CD-ROM*.

- Grant J. A., Irwin R. P., Grotzinger J. P., Milliken R. E., Tornabene L. L., McEwen A. S., Weitz C. M., Squyres S. W., Glotch T. D., Thomson B. J. (2008). HiRISE imaging of impact megabreccia and sub-meter aqueous strata in Holden Crater, Mars. *Geology* 36(3):195-198.
- Greenberger R. N., Mustard J. F., Cloutis E. A., Pratt L. M., Sauer P. E., Mann P., Turner K., Dyar M. D., Bish D. L. (2015). Serpentinization, iron oxidation, and aqueous conditions in an ophiolite: Implications for hydrogen production and habitability on Mars. *Earth and Planetary Science Letters* 416:21-34.
- Haberle R. M., McKay C. P., Schaeffer J., Cabrol N. A., Grin E. A., Zent A. P., Quinn R. (2001). On the possibility of liquid water on present Mars. *Journal of Geophysical Research* 106(E10):23317-23326.
- Hacker B. R., Mosenfelder J. L., Gnos E. (1996). Rapid emplacement of the Oman ophiolite: Thermal and geochronologic constraints. *Tectonics* 15(6):1230-1247.
- Halevy I., Fischer W. W., Eiler J. M. (2011). Carbonates in the Martian meteorite Allan Hills 84001 formed at 18 ± 4 °C in a near-surface aqueous environment. *Proceedings of the National Academy of Sciences* 108(41):16895-16899.
- Halevy I., Head J. W. (2014). Episodic warming of early Mars by punctuated volcanism. *Nature Geoscience* 7:865-868.
- Hallis L. J., Taylor G. J., Nagashima K., Huss G. R., Needham A. W., Grady M. M., Franchi I. A. (2012). Hydrogen isotope analyses of alteration phases in the nakhlite martian meteorites. *Geochimica et Cosmochimica Acta* 97:105-119.
- Hallis L. J. (2017). D/H ratios of the inner Solar System. *Philosophical Transactions of the Royal Society A: Mathematical Physical & Engineering Sciences* 375(2094).
- Hallis L. J., Kempainen L., Lee M. R., Taylor L. A. (2017). The origin of alteration “orangettes” in Dhofar 019: Implications for the age and aqueous history of the shergottites. *Meteoritics & Planetary Science* (early view).
- Hanghøj K., Kelemen P. B., Hassler D., Godard M. (2010). Composition and Genesis of Depleted Mantle Peridotites from the Wadi Tayin Massif, Oman Ophiolite; Major and Trace Element Geochemistry, and Os Isotope and PGE Systematics. *Journal of Petrology* (1-2):201-227.
- Harper C. L., Nyquist L. E., Bansal B., Wiesmann H., Shih C. Y. (1995). Rapid Accretion and Early Differentiation of Mars Indicated by $^{142}\text{Nd}/^{144}\text{Nd}$ in SNC Meteorites. *Science* 267:213-217.
- Hartogh P., Lellouch E., Crovisier J., Banaszkiwicz M., Bensch F., Bergin E. A., Billebaud F., Biver N., Blake G. A., Blecka M. I., Blommaert J., Bockelée-Morvan D., Cavalié T., Cernicharo J., Courtin R., Davis G., Decin L., Encrenaz P., Encrenaz T., González A., de Graauwo T., Hutsemékers D., Jarchow C., Jehin E., Kidger M., Küppers M., de Langeo A., Lara L. M., Lis

- D. C., Lorente R., Manfroid J., Medvedev A. S., Moreno R., Naylor D. A., Orton G., Portyankina G., Rengel M., Sagawa H., Sánchez-Portal M., Schieder R., Sidher S., Stam D., Swinyard B., Szutowicz S., Thomas N., Thornhill G., Vandenbussche B., Verdugo E., Waelkens C., Walker H. (2009). Water and related chemistry in the solar system. A guaranteed time key programme for Herschel. *Planetary and Space Science* 57(13):1596-1606.
- Harvey R., McSween H. (1996). A possible high-temperature origin for the carbonates in the Martian meteorite ALH 84001. *Nature* 382(6586):49-51.
- Hausrath E. M., Tschauer O. (2013). Natural Fumarolic Alteration of Fluorapatite, Olivine, and Basaltic Glass, and Implications for Habitable Environments on Mars. *Astrobiology* 13(11):1049-1064.
- Head J. W., Hiesinger H., Ivanov M. A., Kreslavsky M. A., Pratt S., Thomson B. J. (1999). Possible Ancient Oceans on Mars: Evidence from Mars Orbiter Laser Altimeter Data. *Science* 286(5447):2134-2137.
- Head J. W., Mustard J. F., Kreslavsky M. A., Milliken R. E., Marchant D. R. (2003). Recent ice ages on Mars. *Nature* 426:797-802.
- Head J. W., Marchant D. R. (2014). The climate history of early Mars: insights from the Antarctic McMurdo Dry Valleys hydrologic system. *Antarctic Science* 26(6):774-800.
- Heyer H. (1966). The Kinetics of Crystal Growth. *Angewandte Chemie International Edition* 5(1).
- Hicks L. J., Bridges J. C., Gurman S. J. (2014). Ferric saponite and serpentine in the nakhlite martian meteorites. *Geochimica et Cosmochimica Acta* 136(1):194-210.
- Hoffman N. (2000). White Mars: A New Model for Mars' Surface and Atmosphere Based on CO₂. *Icarus* 146(2):326-342.
- Hu R., Kass D. M., Ehlmann B. L., Yung Y. L. (2015). Tracing the fate of carbon and the atmospheric evolution of Mars. *Nature Communications* 6:10003.
- Hutchins K. S., Jakosky B. M. (1997). Carbonates in Martian meteorite ALH84001: A planetary perspective on formation temperature. *Geophysical Research Letters* 24(7):819-822.
- Irving T. (2014). *Martian meteorites*. Available: <http://www.imca.cc/mars/martian-meteorites.htm>. Last accessed 1st June 2014.
- Iyer K., Austrheim H., John T., Jamtveit B. (2008). Serpentinization of the oceanic lithosphere and some geochemical consequences: Constraints from the Leka Ophiolite Complex, Norway. *Chemical Geology* 249(1):66-90.

- Jain M., Andersen C. E., Botter-Jensen L., Murray A. S., Haack H., Bridges J. C. (2006). Luminescence dating on Mars: OSL characteristics of Martian analogue materials and GCR dosimetry. *Radiation Measurements* 41:755-76.
- Jones J. H. (1986). A discussion of isotopic systematics and mineral zoning in the shergottites: Evidence for a 180 m.y. igneous crystallization age. *Geochimica et Cosmochimica Acta* 50:969-977.
- Jones J. H. (2015). Various aspects of the petrogenesis of the Martian shergottite meteorites. *Meteoritics & Planetary Science* 50(4):674-690.
- Kargel J. S., Baker V. R., Begét J. E., Lockwood J. F., Péwé T. L., Shaw J. S., Strom R. G. (1995). Evidence of ancient continental glaciation in the Martian northern plains. *Journal of Geophysical Research: Planets* 100(E3):5351-5368.
- Karlsson H. R., Clayton R. N., Gibson E. K., Mayeda T. K. (1992). Water in SNC meteorites: Evidence for a Martian hydrosphere. *Science* 255:1409-1411.
- Karunatillake S., Wray J. J., Gasnault O., McLennan S. M., Rogers A. D., Squyres S. W., Boynton W. V., Skok J. R., Button N. E., Ojha L. (2016). The association of hydrogen with sulfur on Mars across latitudes, longitudes, and compositional extremes. *Journal of Geophysical Research: Planets* 121(7):1321-1341.
- Kelemen P. B., Matter J. (2008). In situ carbonation of peridotite for CO₂ storage. *Proceedings of the National Academy of Sciences* 105(45):17295-17300.
- Kelemen P., Matter J., Streit E., Rudge J., Curry W., Blusztajn J. (2011). Rates and Mechanisms of Mineral Carbonation in Peridotite: Natural Processes and Recipes for Enhanced, in situ CO₂ Capture and Storage. *Annual Review Of Earth And Planetary Sciences* 39:545-576.
- Kelemen P. B., Hirth G. (2012). Reaction-driven cracking during retrograde metamorphism: Olivine hydration and carbonation. *Earth and Planetary Science Letters* 345-348:81-89.
- Kieffer H. H., Titus T. N. (2001). TES Mapping of Mars' North Seasonal Cap. *Icarus* 154(1):162-180.
- Kieffer H. H., Christensen P. R., Titus T. N. (2006). CO₂ jets formed by sublimation beneath translucent slab ice in Mars' seasonal south polar ice cap. *Nature* 442:793-796.
- King P. L., McLennan S. M. (2010). Sulfur on Mars. *Elements* 6(2).
- Kohyama N., Shimoda S., Sudo T. (1973). Iron rich saponite (ferrous and ferric forms). *Clay and Clay Minerals* 21:229-237.
- Korochantseva E., Schwenzer S., Buikin A., Hopp J., Ott U., Trierloff M. (2011). ⁴⁰Ar-³⁹Ar and cosmic-ray exposure ages of nakhlites-Nakhlita, Lafayette, Governador Valadares-and Chassigny. *Meteoritics & Planetary Science* 46(9):1397-1417.

- Kounaves S. P., Chaniotakis N. A., Chevrier V. F., Carrier B. L., Folds K. E., Hansen V. M., McElhoney K. M., O'Neil G. D., Weber A. W. (2014). Identification of the Perchlorate Parent Salts at the Phoenix Mars Landing Site and Possible Implications. *Icarus* 232:226-231.
- Krasnopolsky V. A. (1993). Solar Cycle Variations of the Hydrogen Escape Rate and the CO Mixing Ratio on Mars. *Icarus* 101(1):33-41.
- Krasnopolsky V. A., Maillard J. P., Owen T. C. (2004). Detection of methane in the Martian atmosphere: evidence for life? *Icarus* 172(2):537-547.
- Kreslavsky M. A., Head J. W. (2009). Slope streaks on Mars: A new "wet" mechanism. *Icarus* 201(2):517-527.
- Langevin Y., Poulet F., Bibring J. P., Gondet B. (2005). Sulfates in the North Polar Region of Mars Detected by OMEGA/Mars Express. *Science* 307(5715):1584-1586.
- Lapen T., Righter M., Brandon A., Debaille V., Beard B., Shafer J., Peslier A. (2010). A Younger Age for ALH 84001 and Its Geochemical Link to Shergottite Sources in Mars. *Science* 328(5976):347-351.
- Lécuyer C., Gillet P., Robert F. (1998) The hydrogen isotope composition of seawater and the global water cycle. *Chemical Geology* 145:249-261.
- Le Deit L., Flahaut J., Quantin C., Hauber E., Mège D., Bourgeois O., Gurgurewicz J., Massé M., Jaumann R. (2012). Extensive surface pedogenic alteration of the Martian Noachian crust suggested by plateau phyllosilicates around Valles Marineris. *Journal of Geophysical Research: Planets* 117(E11).
- Lee M., Tomkinson T., Mark D., Stuart F., Smith C. (2013). Evidence for silicate dissolution on Mars from the Nakhla meteorite. *Meteoritics & Planetary Science* 48(2):224-240.
- Lee M. R., Tomkinson T., Hallis L. J., Mark D. F. (2015). Formation of iddingsite veins in the martian crust by centripetal replacement of olivine: Evidence from the nakhlite meteorite Lafayette. *Geochimica et Cosmochimica Acta* 154:49-65.
- Leleu T., Chavagnac V., Delacour A., Noiriél C., Ceuleneer G., Aretz M., Rommevaux C., Ventalon S. (2016). Travertines Associated With Hyperalkaline Springs: Evaluation As A Proxy For Paleoenvironmental Conditions And Sequestration of Atmospheric CO₂. *Journal of Sedimentary Research* 86(11):1328-1343.
- Leshin L. A., McKeegan K. D., Carpenter P. K., Harvey R. P. (1998). Oxygen Isotopic Constraints on the Genesis of Carbonates from Martian Meteorite ALH84001. *Geochimica et Cosmochimica Acta* 62(1):3-13.
- Mahaffy P. R., Webster C. R., Atreya S. K., Franz H., Wong M., Conrad P. G., Harpold D., Jones J. J., Leshin L. A., Manning H., Owen T., Pepin R. O., Squyres S., Trainer M., MSL Science

- Team. (2013). Abundance and Isotopic Composition of Gases in the Martian Atmosphere from the Curiosity Rover. *Science* 341(6143) :263-266.
- Mangold N., Quantin C., Ansan V., Delacourt C., Allemand P. (2004). Evidence for Precipitation on Mars from Dendritic Valleys in the Valles Marineris Area. *Science* 305(5680):78-81.
- Mars Pathfinder Rover team. (1997). Characterization of the Martian surface deposits by the Mars Pathfinder rover, Sojourner. *Science* 278:1765-1768.
- Marsall O., Venet M., Counil J. L., Ferri F., Harri A. M., Spohn T., Block J. (2002). The Netlander geophysical network on the surface of Mars: General mission description and technical design status. *Acta Astronautica* 51(1-9):379-386.
- Matter J. M., Broecker W. S., Stute M., Gislason S. R., Oelkers E. H., Stefánsson A., Wolff-Boenisch D., Gunnlaugsson E., Axelsson G., Björnsson G. (2009). Permanent Carbon Dioxide Storage into Basalt: The CarbFix Pilot Project, Iceland. *Energy Procedia* 1:3641-3646.
- Matter J. M., Broecker W. S., Gislason S. R., Gunnlaugsson E., Oelkers E. H., Stute M., Sigurdardóttir H., Stefansson A., Alfreðsson H. A., Aradóttir E. S., Axelsson G., Sigfússon B., Wolff-Boenisch D. (2011). The CarbFix Pilot Project - Storing Carbon Dioxide in Basalt. *Energy Procedia* 4:5579-5585.
- Matter J. M., Stute M., Snæbjörnsdóttir S. Ó., Oelkers E. H. Gislason S. R. Aradóttir E. S., Sigfusson B., Gunnarsson I., Sigurdardóttir H., Gunnlaugsson E., Axelsson G., Alfredsson H. A., Wolff-Boenisch D., Mesfin K., Fernandez De La Reguera T. D., Hall J., Dideriksen K., Broecker W. S. (2016). Rapid carbon mineralization for permanent disposal of anthropogenic carbon dioxide emissions. *Science* 352(6291):1312-4.
- McCollom T. M. (2016). Abiotic methane formation during experimental serpentinization of olivine. *Proceedings of the National Academy of Sciences* 113(49):13965-13970.
- McCubbin F., Elardo S., Shearer C., Smirnov A., Hauri E., Draper D. (2013). A petrogenetic model for the comagmatic origin of chassignites and nakhlites: Inferences from chlorine-rich minerals, petrology, and geochemistry. *Meteoritics & Planetary Science* 48(5):819-853.
- McEwen A. S., Ojha L., Dundas C. M., Mattson S. S., Byrne S., Wray J. J., Cull S. C., Murchie S. L., Thomas N., Gulick V. C. (2011). Seasonal Flows on Warm Martian Slopes. *Science* 333(6043):740-743.
- McKay D.S., Gibson E.K. Jr., Thomas-Keprta K.L., Vali H., Romanek C.S., Clemett S.J., Chillier X.D.F., Maechling C.R., Zare R.N. (1996). Search for past life on Mars: possible relic biogenic activity in Martian meteorite ALH 84001. *Science* 273:924-930.
- McKay G. A., Lofgren G. E. (1997). Carbonates in ALH84001 - Evidence for kinetically controlled growth. *Conference Paper, 28th Annual Lunar and Planetary Science Conference* 921.

- McKay C., Friedmann E., Frankel R., Bazylinski D. (2003). Magnetotactic bacteria on Earth and on Mars. *Astrobiology* 3(2):263-270.
- McSween H. Y., Jarosewich E. (1983). Petrogenesis of the Elephant Moraine A79001 meteorite: Multiple magma pulses on the shergottite parent body. *Geochimica et Cosmochimica Acta* 47:1501-1513.
- McSween H. Y. (1985). SNC meteorites: Clues to Martian petrologic evolution? *Reviews of Geophysics* 23(4):391-416.
- McSween H. Y., Harvey R. P. (1993). Outgassed Water on Mars: Constraints from Melt Inclusions in SNC Meteorites. *Science* 26;259(5103):1890-2.
- Meyer C. (2006). *Introduction to Martian Meteorites 2006*. Available: <http://curator.jsc.nasa.gov/antmet/mmc/Chap%20I.pdf>
- Mezger K., Debaille V., Kleine T. (2012). Core Formation and Mantle Differentiation on Mars. *Space Science Reviews* 174(1-4):27-48.
- Michalski J., Poulet F., Bibring J. P., Mangold N. (2010). Analysis of phyllosilicate deposits in the Nili Fossae region of Mars: Comparison of TES and OMEGA data. *Icarus* 206(1):269-289.
- Michalski J. R., Dobrea E. Z. N., Niles P. B., Cuadros J. (2017). Ancient hydrothermal seafloor deposits in Eridania basin on Mars. *Nature Communications* 8:15978.
- Mikouchi T., Makishima J., Kurihara T., Hoffmann V., Miyamoto M. (2012). *Relative burial of nakhlites revisited*. Available: <http://www.lpi.usra.edu/meetings/lpsc2012/pdf/2363.pdf>
- Miller H. M., Matter J. M., Kelemen P., Ellison E. T., Conrad M. E., Fierer N., Ruchala T., Tominaga M., Templeton A. S. (2016). Modern water/rock reactions in Oman hyperalkaline peridotite aquifers and implications for microbial habitability. *Geochimica et Cosmochimica Acta* 179:217-241.
- Milliken R. E., Grotzinger J. P., Thomson B. J. (2010). Paleoclimate of Mars as captured by the stratigraphic record in Gale Crater. *Geophysical Research Letters: Planets* 37(4).
- Milnes A., Wennberg O., Skaar O., Koestler A. (1996). Contraction, extension and timing in the South Norwegian Caledonides: the Sognefjord transect. *Special Publication- Geological Society Of London* 121:123-148.
- Mittlefehldt D. (1994). ALH 84001, A cumulate orthopyroxenite member of the Martian meteorite clan. *Meteoritics* 29(2):214-221.
- Morris R. V., Ruff S. W., Gellert R., Ming D. W., Arvidson R. E., Clark B. C., Golden D. C., Siebach K., Klingelhöfer G., Schröder C., Fleischer I., Yen A. S., Squyres S. W. (2010). Identification of Carbonate-Rich Outcrops on Mars by the Spirit Rover. *Science* 329(5990):421-424.

- Mustard J. F., Cooper D. C., Rifkin M. K. (2001). Evidence for recent climate change on Mars from the identification of youthful near-surface ground ice. *Nature* 412:411-414.
- Mustard J. F., Poulet F., Gendrin A., Bibring J. P., Langevin Y., Gondet B., Mangold N., Bellucci G., Altieri F. (2005). Olivine and Pyroxene Diversity in the Crust of Mars. *Science* 307(5715):1594-1597.
- Mustard J. F., Murchie S. L., Pelkey S. M., Ehlmann B. L., Milliken R. E., Grant J. A., Bibring J. P., Poulet F., Bishop J., Dobra E. N., Roach L., Seelos F., Arvidson R. E., Wiseman S., Green R., Hash C., Humm D., Malaret E., McGovern J. A., Seelos K., Clancy T., Clark R., Marais D. D., Izenberg N., Knudson A., Langevin Y., Martin T., McGuire P., Morris R., Robinson M., Roush T., Smith M., Swayze G., Taylor H., Titus T., Wolff M. (2008). Hydrated silicate minerals on Mars observed by the Mars Reconnaissance Orbiter CRISM instrument. *Nature* 454:305-309.
- Nachon M., Mangold N., Forni O., Kah L. C., Cousin A., Wiens R. C., Anderson R., Blaney D., Blank J. G., Calef F., Clegg S. M., Fabre C., Fisk M. R., Gasnault O., Grotzinger J. P., Kronyak R., Lanza N. L., Lasue J., Le Deit L., Le Mouélic S., Maurice S., Meslin P. Y., Oehler D. Z., Payré V., Rapin W., Schröder S., Stack K., Sumner D. (2017). Chemistry of diagenetic features analyzed by ChemCam at Pahrump Hills, Gale crater, Mars. *Icarus* 281(1):121-136.
- Neal C., Shand P. (2002). Spring and surface water quality of the Cyprus ophiolites. *Hydrology and Earth System Sciences* 6(5):797-817.
- Nelson D. M., Greeley R. (1999). Geology of Xanthe Terra outflow channels and the Mars Pathfinder landing site. *Journal of Geophysical Research: Planets* 104(E4):8653-8669.
- Neumann G., Zuber M., Wieczorek M., McGovern P., Lemoine F., Smith D. (2004). Crustal structure of Mars from gravity and topography. *Journal Of Geophysical Research-Planets* 109:E8.
- Niles P. B., Catling D. C., Berger G., Chassefière E., Ehlmann B. L., Michalski J. R., Morris R., Ruff S. W., Sutter B. (2013). Geochemistry of Carbonates on Mars: Implications for Climate History and Nature of Aqueous Environments. *Space Science Reviews* 174(1-4):301-328.
- Nininger H. H. (1935). The Lafayette meteorite. *Popular Astronomy* 43:404.
- Nyquist L., Borg L., Shih C. (1998). The Shergottite age paradox and the relative probabilities for Martian meteorites of differing ages. *Journal Of Geophysical Research: Planets* 103(E13):31445-31455.
- Nyquist L., Bogard D., Shih C., Greshake A., Stoffler D., Eugster O. (2001). Ages and geologic histories of Martian meteorites. *Space Science Reviews* 96(1-4):105-164.
- Owen T., Maillard J. P., De Bergh C., Lutz B. L. (1988). Deuterium on Mars: The abundance of HDO and the value of D/H. *Science* 240.4860:1767.

- Ozawa S., Ireland T., El Goresy A., E. Ohtani E. (2009). U-Pb dating of baddeleyite in Shergotty, Zagami and NWA 2737: implications for crystallization and impact ages of Martian meteorites. *Meteoritics & Planetary Science* 44 (Suppl.):A163.
- Ozawa S. (2011). *Impact events in the solar system inferred from shocked meteorites*. Ph. D. thesis, 1-109, Tohoku University.
- Oze C., Sharma M. (2005). Have olivine, will gas: Serpentinization and the abiogenic production of methane on Mars. *Geophysical Research Letters* 32(10):L10203.
- Paige D. A. (1992). The thermal stability of near surface ground ice on Mars. *Nature* 43.
- Park J., Bogard D., Nyquist L., Herzog G. (2014). Issues in dating young rocks from another planet: Martian Shergottites. *Special Publication- Geological Society Of London* 378:297-316.
- Pepin R. (1985). Meteorites: evidence of Martian origin. *Nature* 317:473-475.
- Perron J. T., Mitrovica J. X., Manga M., Matsuyama I., Richards M. A. (2007). Evidence for an ancient martian ocean in the topography of deformed shorelines. *Nature* 447:840-843.
- Pewe T. L. (1959). Sand-wedge polygons (tesselations) in the McMurdo Sound region, Antarctica; a progress report. *American Journal of Science* 257(8):545-552.
- Phillips R. J., Davis B. J., Tanaka K. L., Byrne S., Mellon M. T., Putzig N. E., Haberle R. M., Kahre M. A., Campbell B. A., Carter L. M., Smith I. B., Holt J. W., Smrekar S. E., Nunes D. C., Plaut J. J., Egan A. F., Titus T. N., Seu R. (2011). Massive CO₂ Ice Deposits Sequestered in the South Polar Layered Deposits of Mars. *Science* 332(6031):838-841.
- Pinet P. C., Clenet H., Rosemberg C., Ceuleneer G., Heuripeau F., Harris E., Daydou Y., Baratoux D., Chevrel S. C., Launeau P., Combes J. P., Le Mouélic S., Sotin C. (2006). Mantle rock surface mineralogy mapping in arid environment from imaging spectroscopy: The case of the Maqsd peridotitic massif in Oman and implications for the spectroscopic study of exposed mafic units on Mars. *37th Lunar and Planetary Science Conference* 1346.
- Plaut J. J., Picardi G., Safaeinili A., Ivanov A. B., Milkovich S. M., Cicchetti A., Kofman W., Mouginit J., Farrell W. M., Phillips R. J., Clifford S. M., Frigeri A., Orosei R., Federico C., Williams I. P., Gurnett D. A., Nielsen E., Hagfors T., Heggy E., Stofan E. R., Plettemeier D., Thomas R. Watters T. R., Leuschen C. J., Edenhofer P. (2007). Subsurface Radar Sounding of the South Polar Layered Deposits of Mars. *Science* 316(5821):92-95.
- Plümper O., Piazzolo S., Austrheim H. (2012). Olivine Pseudomorphs after Serpentinized Orthopyroxene Record Transient Oceanic Lithospheric Mantle Dehydration (Leka Ophiolite Complex, Norway). *Journal Of Petrology* 53(9):1943-1968.
- Pollack J. B., Kasting J. F., Richardson S. M., Poliakov K. (1987). The case for a wet, warm climate on early Mars. *Icarus* 71(2):203-224.

- Primm K. M., Gough R. V., Chevrier V. F., Tolbert M. A. (2017). Freezing of perchlorate and chloride brines under Mars-relevant conditions. *Geochimica et Cosmochimica Acta* 212:211-220.
- Putzig N. E., Phillips R. J., Campbell B. A., Holt J. W., Plaut J. J., Carter L. M., Egan A. F., Bernardini F., Safaeinili A., Seu R. (2009). Subsurface structure of Planum Boreum from Mars Reconnaissance Orbiter Shallow Radar soundings. *Icarus* 204(2):443-457.
- Quantin C., Allemand P., Mangold N., Delacourt C. (2004). Ages of Valles Marineris (Mars) landslides and implications for canyon history. *Icarus* 172(2):555-572.
- Rao M., Borg L., McKay D., Wentworth S. (1999). Martian soil component in impact glasses in a Martian meteorite. *Geophysical Research Letters* 26:3265-3268.
- Rennó N. O., Bos B. J., Catling D., Clark B. C., Drube L., Fisher D., Goetz W., Hviid S. F., Keller H. U., Kok J. F., Kounaves S. P., Leer K., Lemmon M., Madsen M. B., Markiewicz W. J., Marshall J., McKay C., Mehta M., Smith M., Zorzano M. P., Smith P. H., Stoker C., Young S. M. M. (2009). Possible physical and thermodynamical evidence for liquid water at the Phoenix landing site. *Journal of Geophysical Research: Planets* 114(E1).
- Reusch D. N. (2011). New Caledonian carbon sinks at the onset of Antarctic glaciation. *Geology* 39(9):807-810.
- Rice J. W., Mollard J. D. (1994). Analogs and interpretations for the Martian thumbprint terrain and sinuous ridges. *25th Lunar and Planetary Science Conference* 1127.
- Richardson M. I., Mischna M. A. (2005). Long-term evolution of transient liquid water on Mars. *Journal of Geophysical Research* 110(E03003).
- Romanek C., Grady M., Wright I., Mittlefehldt D., Socki R., Pillinger C., Gibson E. (1994). Record of fluid-rock interactions on Mars from the meteorite ALH 84001. *Nature* 372(6507):655-657.
- Sadooni F. N., Howari F., H. G. M. Edwards., El-Saiy A. (2010). Lithology, mineral assemblages and microbial fingerprints of the evaporite-carbonate sediments of the coastal sabkha of Abu Dhabi and their extraterrestrial implications. *International Journal of Astrobiology* 9(3):147-156.
- Sautter V., Toplis M., Lorand J., Macri M. (2012). Melt inclusions in augite from the nakhlite meteorites: A reassessment of nakhlite parental melt and implications for petrogenesis. *Meteoritics & Planetary Science* 47(3):330-344.
- Scott E., Yamaguchi A., Krot A. (1997). Petrological evidence for shock melting of carbonates in the Martian meteorite ALH 84001. *Nature* 387(6631):377-379.
- Searle M., Cox J. (1999). Tectonic setting, origin, and obduction of the Oman ophiolite. *Geological Society of America Bulletin* 111(1):104-122.

- Seibert N. M., Kargel J. S. (2001). Small scale Martian polygonal terrain: Implications for liquid surface water. *Geophysical Research Letters* 28(5):899-902.
- Sharp R. P., Murray B. C., Leighton R. B., Soderblom L. A., Cutts J. A. (1971) The surface of Mars 4. South polar cap. *Journal of Geophysical Research* 76(2):357-368.
- Shearer C. K., Leshin L. A., Adcock C. T. (1999). Olivine in Martian meteorite Allan Hills 84001: Evidence for a high-temperature origin and implications for signs of life. *Meteoritics & Planetary Science* 34:331-339.
- Showstack, R. (2012). Evidence suggests water once flowed vigorously on Mars. *Eos, Transactions American Geophysical Union* 93(41):402-403.
- Sigfusson B., Gislason S. R., Matter J. M., Stute M., Gunnlaugsson E., Gunnarsson I., Aradottir E. S., Sigurdardottir H., Mesfin K., Alfredsson H. A., Wolff-Boenisch D., Arnarsson M. T., Oelkers E. H. (2015). Solving the carbon-dioxide buoyancy challenge: The design and field testing of a dissolved CO₂ injection system. *International Journal of Greenhouse Gas Control* 37:213-219.
- Skok J. R., Mustard J. F., Tornabene L. L., Murchie S. L. (2011). Composition of the Primary Crust of Mars: Observations of Deeply Excavated Crater Central Peaks. *American Geophysical Union Fall Meeting 2011 (#P11A-1583)*.
- Sohl F., Spohn T. (1997). The interior structure of Mars: Implications from SNC meteorites. *Journal Of Geophysical Research-Planets* 102(E1):1613-1635.
- Squyres S. W., Carr M. H. (1986). Geomorphic evidence for the distribution of ground ice on Mars. *Science* 231(4735):249-252.
- Squyres S. W., Kasting J. F. (1994). Early Mars: how warm and how wet? *Science* 265:744-749.
- Sutter B., Boynton W. V., Ming D. W., Niles P. B., Morris R. V., Golden D. C., Lauer H. V., Fellows C., Hamara D. K., Mertzman S. A. (2012). The detection of carbonate in the martian soil at the Phoenix Landing site: A laboratory investigation and comparison with the Thermal and Evolved Gas Analyzer (TEGA) data. *Icarus* 218(1):290-296.
- Swindle T. D., Treiman A. H., Lindstrom D. J., Burkland M. K., Cohen B. A., Grier J. A., Li B., Olsen E. K. (2000). Noble gases in iddingsite from the Lafayette meteorite: Evidence for liquid water on Mars in the last few hundred million years. *Meteoritics & Planetary Science* 35(1):107-115.
- Swindle T., Olson E. (2004). Ar-40-Ar-39 studies of whole rock nakhlites: Evidence for the timing of formation and aqueous alteration on Mars. *Meteoritics & Planetary Science* 39(5):755-766.

- Szponar N., Brazelton W. J., Schrenk M. O., Bower D. M., Steele A., Morrill P. L. (2013). Geochemistry of a continental site of serpentinization, the Tablelands Ophiolite, Gros Morne National Park: A Mars analogue. *Icarus* 224(2):286-296.
- Taylor L. A., Nazarov M. A., Shearer C. K., McSween H. Y. Jr., Cahill J., Neal C. R., Ivanova M. A., Barsukova L. D., Lentz R. C., Clayton R. N., Mayeda T. K. (2002). Martian meteorite Dhofar 019: A new shergottite. *Meteoritics & Planetary Science* 37:1107-1128.
- Thomas-Keprta K. L., Clemett S. J., McKay D. S., Gibson E. K., Wentworth S. J. (2009). Origins of magnetite nanocrystals in Martian meteorite ALH84001. *Geochimica et Cosmochimica Acta* 73(21):6631-6677.
- Thomas P., Squyres S., Herkenhoff K., Howard A., Murray B. (1992). Polar deposits of Mars. *The Smithsonian/NASA Astrophysics Data System: Mars A93-27852 09-91:767-795*.
- Titus S., Fossen H., Pedersen R., Vigneresse J., Tikoff B. (2002). Pull-apart formation and strike-slip partitioning in an obliquely divergent setting, Leka Ophiolite, Norway. *Tectonophysics* 354(1-2):101-119.
- Toon O. B., Zahnle K., Morrison D., Turco R., Covey C. (1997). Environmental perturbations caused by the impacts of asteroids and comets. *Reviews of Geophysics* 35(1):41-78.
- Treiman A. H., Barrett R. A., Gooding J. L. (1993). Preterrestrial aqueous alteration of the Lafayette (SNC) meteorite. *Meteoritics & Planetary Science* 28(1):86-97.
- Treiman A. (1995). A petrographic history of Martian meteorite ALH 84001 - 2 shocks and an ancient age. *Meteoritics* 30(3):294-302.
- Treiman A. H. (1998). The history of Allan Hills 84001 revised: Multiple shock events. *Meteoritics & Planetary Science* 33(4):753-764.
- Treiman A. H. (2003). Submicron magnetite grains and carbon compounds in Martian meteorite ALH 84001: Inorganic, abiotic formation by shock and thermal metamorphism. *Astrobiology* 3:369-392.
- Treiman A. H., Louge M. Y. (2004). Martian Slope Streaks and Gullies: Origins as Dry Granular Flows. *35th Lunar and Planetary Science Conference* 1323.
- Treiman A. (2005). The Nakhlite meteorites: Augite-rich igneous rocks from Mars. *Chemie der Erde* 65:203-270.
- Tsikouras B., Etiope G., Ifandi E., Kordella S., Papatheodorou G., Hatzipanagiotou K. (2013). Petrological implications for the production of methane and hydrogen in hyperalkaline springs from the Othrys ophiolite, Greece. *Proceedings of the 13th International Congress, Chania. Bulletin of the Geological Society of Greece* XLVII:1-449.

- Valley J. W., Eiler J. M., Graham C. M., Gibson E. K., Romanek C. S., Stolper E. M. (1997). Low temperature carbonate concretions in the Martian meteorite ALH84001: Evidence from stable isotopes and mineralogy. *Science* 275:1633-1638.
- Velbel M. A. (2012). Aqueous alteration in Martian meteorites: Comparing mineral relations in igneous-rock weathering of Martian meteorites and in the sedimentary cycle of Mars. *Sedimentary geology of Mars edited by Grotzinger J. and Milliken R. Society for Sedimentary Geology Special Publication* 102:97-117.
- Vicenzi E. P., Eiler J. (1998). Oxygen-isotopic composition and high-resolution secondary ion mass spectrometry imaging of Martian carbonate in Lafayette meteorite. *Meteoritics & Planetary Science* 33(S4):A159-A160.
- Walker J. C. G., Hays P. B., Kasting J. F. (1981). A negative feedback mechanism for the long-term stabilization of Earth's surface temperature. *Journal of Geophysical Research: Oceans* 86(C10):9776-9782.
- Watson L. L., Hutcheon I. D., Epstein S., Stolper E. M. (1994). Water on Mars: clues from deuterium/hydrogen and water contents of hydrous phases in SNC meteorites. *Science* 265(5168):86-90.
- Webster C. R., Mahaffy P. R., Flesch G. J., Niles P. B., Jones J. H., Leshin L. A., Atreya S. K., Stern J. C., Christensen L. E., Owen T. Franz H., Pepin R. O., Steele A., MSL Science Team. (2013). Isotope Ratios of H, C, and O in CO₂ and H₂O of the Martian Atmosphere. *Science* 341:260-263.
- Website 1. O'Hanlon L. (2015). *Unveiling the ancient climate of Mars*. Available: <https://news.harvard.edu/gazette/story/2015/06/unveiling-the-ancient-climate-of-mars/>
- Website 2. NASA. (2017). *Mars Facts*. Available: <https://mars.nasa.gov/allaboutmars/facts/#?c=inspace&s=distance>
- Website 3. NASA. (2018). *Recent Climate Change*. Available: <https://mepag.jpl.nasa.gov/topten.cfm?topten=4>
- Website 4. NASA. (2016). *Earth Fact Sheet*. <https://nssdc.gsfc.nasa.gov/planetary/factsheet/earthfact.html>
- Website 5. NASA. (2016). *Mars Fact Sheet*. <https://nssdc.gsfc.nasa.gov/planetary/factsheet/marsfact.html>
- Website 6. World Weather & Climate Information. (2017). *Climate: Average Monthly Weather in Leka, Norway*. <https://weather-and-climate.com/average-monthly-Rainfall-Temperature-Sunshine,Leka,Norway>

- Website 7. World Weather & Climate Information. (2017). *Climate: Average Monthly Weather in Sohar, Oman*. <https://weather-and-climate.com/average-monthly-Rainfall-Temperature-Sunshine,sohar,Oman>
- Weisbrod N., Dragila M. I., Nachshon U., Pillersdorf M. (2009). Falling through the cracks: The role of fractures in Earth-atmosphere gas exchange. *Geophysical Research Letters* 36(2).
- Wentworth S. J., Gooding J. L. (1994). Carbonates and sulfates in the Chassigny meteorite: Further evidence for aqueous chemistry on the SNC parent planet. *Meteoritics & Planetary Science* 29(6):860-863.
- Werner S., Ody A., Poulet F. (2014). The source crater of Martian shergottite meteorites. *Science* 343(6177):1343-1346.
- Wise D. U., Golombek M. P., McGill G. E. (1979). Tharsis province of Mars: Geologic sequence, geometry, and a deformation mechanism. *Icarus* 38(3):456-472.
- Wittmann A., Korotev R. L., Jolliff B. L., Irving A. J., Moser D. E., Barker I., Rumble D. (2015). Petrography and composition of Martian regolith breccia meteorite Northwest Africa 7475. *Meteoritics and Planetary Science* 50(2):326-352.
- Wordsworth R. D. (2016). The Climate of Early Mars. *Annual Review of Earth & Planetary Sciences* 44:1-31.
- Wordsworth R. D., Kerber L., Pierrehumbert R. T., Forget F., Head J. W. (2015). Comparison of “warm and wet” and “cold and icy” scenarios for early Mars in a 3-D climate model. *Journal of Geophysical Research: Planets* 120(6):1201-1219.
- Wordsworth R., Kalugina Y., Lokshtanov S., Vigasin A., Ehlmann B., Head J., Sanders C., Wang H. (2017). Transient reducing greenhouse warming on early Mars. *Geophysical Research Letters* 44(2):665-671.
- Wray J. J., Murchie S. L., Ehlmann B. L., Milliken R. E., Seelos K. D., Noe Dobrea E. Z., Mustard J. F., Squyres S. W. (2011). Evidence for regional deeply buried carbonate-bearing rocks on Mars. *Lunar and Planetary Science Conference Abstracts* 42:2635.
- Wyatt M., McSween H. (2002). Spectral evidence for weathered basalt as an alternative to andesite in the northern lowlands of Mars. *Nature* 417(6886):263.
- Yung Y. L., Wen J. S., Allen M., Pierce K. K., Paulson S., Pinto J. P. H. (1987). HDO in the Martian Atmosphere: Implications for the Abundance of Crustal Water. *Bulletin of the American Astronomical Society* 19:818.
- Zelenyi L. M., Korablev O. I., Rodionov D. S., Novikov B. S., Marchenkov K. I., Andreev O. N., Larionov E. V. (2015). Scientific Objectives of the Scientific Equipment of the Landing Platform of the ExoMars 2018 Mission. *Solar System Research* 49(7):509-517.

Zuber M. T. (2001). The crust and mantle of Mars. *Nature* 412:220-227.

Zulumyan N., Mirgorodski A., Isahakyan A., Beglaryan H. (2014). The mechanism of decomposition of serpentines from peridotites on heating. *Journal of Thermal Analysis & Calorimetry* 115(2):1003-1012.

Chapter 4

Experimental reproduction of Martian type carbonates and clays.

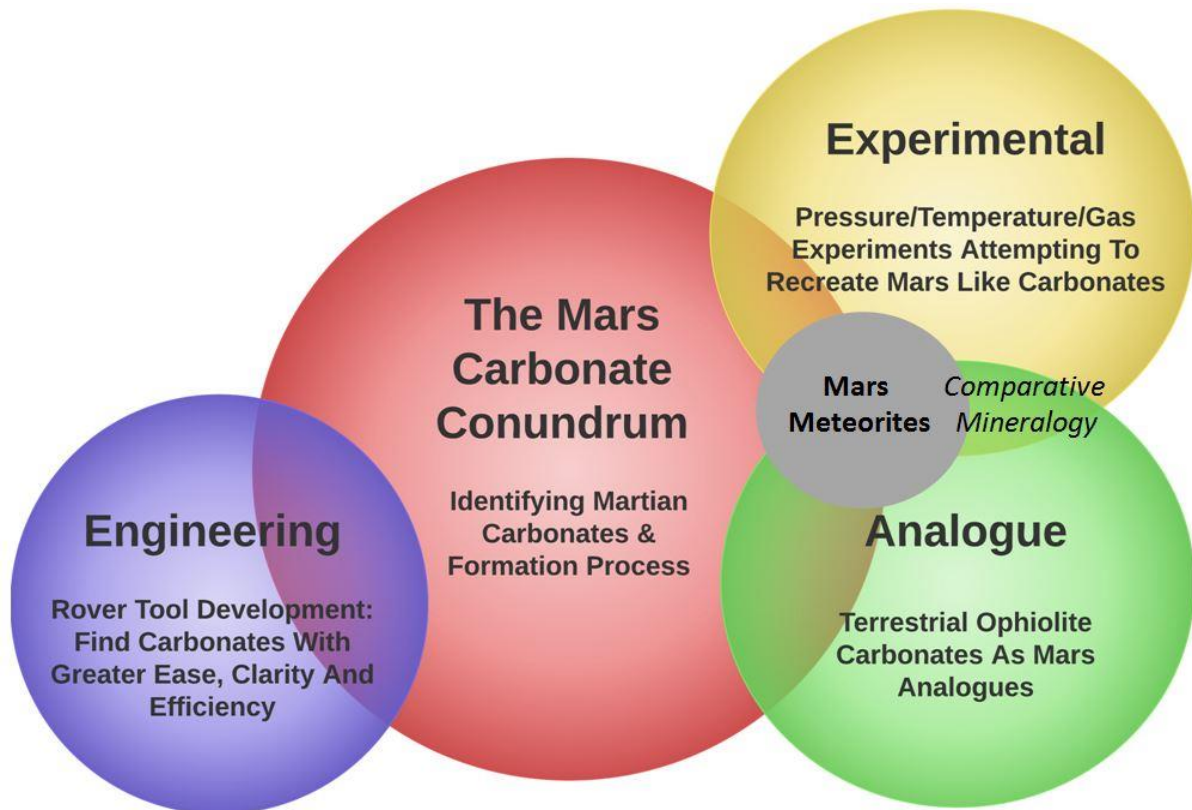


Figure 4.1. The carbonate conundrum that this PhD thesis seeks to address (red circle), along with the different spheres of research used to approach this question. These spheres of research correspond to the three main thesis chapters: engineering (chapter 2), analogues (chapter 3), and experimental (chapter 4). Overlapping circles indicate where chapter and research content overlap and support each other, allowing for comparative mineralogy.

Chapter 4 contents.

	Page.
4.1 Introduction.	280 - 304
4.1.1 Overview.	280 - 284
4.1.2 Geochemistry of silicate mineral alteration.	285 - 290
4.1.3 Isovolumetric replacement versus pore space precipitation.	290 - 293
4.1.4 The role of controlled mineral experiments.	293 - 295
4.1.5 Large scale experiments: The CARBFIX project.	296- 297
4.1.6 Terrestrial mineral carbon sequestration experiments.	298 - 299
4.1.7 Martian mineral carbon sequestration experiments.	299 - 302
4.1.8 Can Mars mineralogy inform terrestrial climate research?	303 - 304
4.2 Experiment objectives.	305
4.3 Methods.	306 - 332
4.3.1 Overview.	306
4.3.2 Experimental fixed parameters.	307
4.3.3 Experimental variables.	308 - 319
4.3.4 Quantitative SEM analysis methods.	320 - 322
4.3.5 Experiment sampling procedure.	323 - 328
4.3.6 IC/ICPMS and colorimetric data.	329
4.3.7 Experiment CO ₂ and SO ₂ solubility.	329 - 332

4.4	Results.	333 - 360
4.4.1	pH.	333 - 339
4.4.2	Fluid chemistry.	340 - 345
4.4.3	Saturation indices.	345 - 349
4.4.4	Mineral surface alterations.	350 - 360
4.5	Discussion.	361 - 376
4.5.1	pH.	361 - 363
4.5.2	Mineral pyrrhotite dissolution and Fe mobility.	363 – 366
4.5.3	Smectite, kaolinite and other clays.	367
4.5.4	Si mobility.	367 - 368
4.5.5	Total cation, total anion and Ca mobility.	368
4.5.6	Lack of carbonate formation.	369 - 370
4.5.7	Olivine dissolution, and Martian model implications.	370 - 373
4.5.8	Discussion summary.	374 - 376
4.6	Conclusion.	376 - 377
4.7	Acknowledgements.	377
4.8	References.	378 - 389

Abbreviations

BGS	British Geological Survey.
BSE	Back Scattered Electrons.
CCS	Carbon Capture and Storage.
EDXS	Energy-dispersive X-Ray spectroscopy.
Fa	Fayalite.
FIB	Focussed Ion Beam.
Fo	Forsterite.
IC	Ion Chromatography
ICPMS	Inductively Coupled Plasma Mass Spectrometry.
LNLL	Lawrence Livermore National Laboratory.
MCS	Mineral Carbon Sequestration.
NIRS	Near Infrared Spectroscopy.
PCF	Poynting Correction Factor.
PHREEQC	pH-REdox-Equilibrium (a geochemical modelling program).
SHE	Standard Hydrogen Electrode.
TEM	Transmission Electron Microscope.
UV	UltraViolet (radiation).

4.1 Introduction.

4.1.1 Overview.

This study seeks to replicate alteration processes and products that are recorded by Martian meteorites within a Mars analogue laboratory environment. The effects of differing initial atmospheric and mineral compositions will be explored, specifically the comparison of CO₂ with SO₂ and basalt versus CO₂ and olivine.

The geological evidence for atmospheric mineral carbon sequestration (MCS) on Mars, and hence partial loss of the early Martian atmosphere, has been obtained using rovers and landers (Boynton *et al.* 2009; Morris *et al.* 2010; Sutter *et al.* 2012), satellite observations (Calvin *et al.* 1994) and Martian meteorites that have landed on Earth (Wadhwa, 2004). These meteorites contain aqueous alteration products in veins and pore spaces that include carbonate, clay and serpentine (Bridges *et al.* 2001; Halevy *et al.* 2011). As an approximate average, these altered minerals comprise ~1 wt. % of Martian meteorite samples (Bridges *et al.* 2001). Veins of alteration products in the Nakhilites are typically ~5-10 µm across and are most prominent in olivine, where phyllosilicates and/or siderite are present (Fig. 4.2), often with a ferric 'amorphous silica gel' in the centre of the vein (Changela & Bridges, 2010; Hicks *et al.* 2014). Most researchers argue this vein centre contains finely crystalline smectite and not amorphous silica (Gooding, 1992; Lee *et al.* 2013).

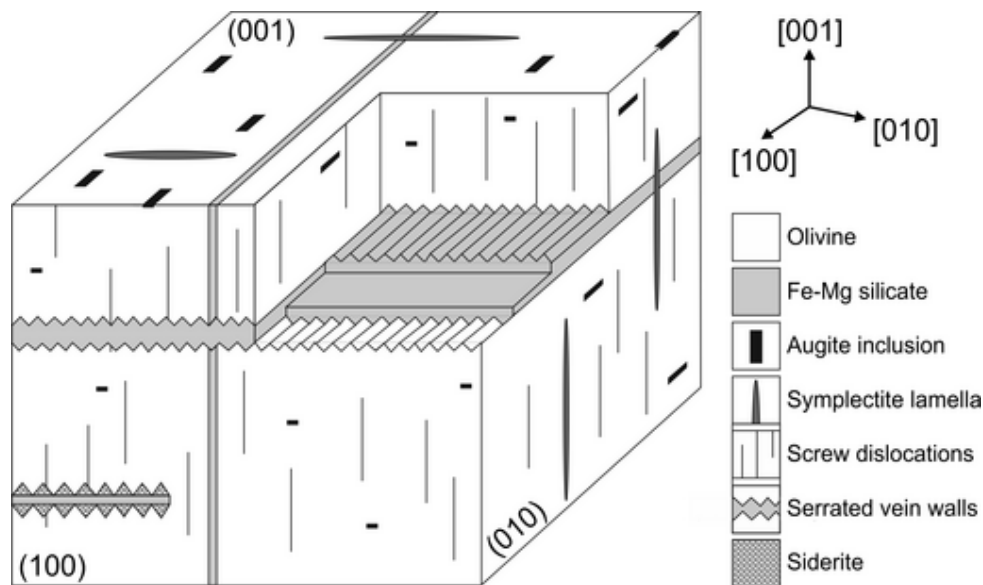


Figure 4.2. Illustration of alteration veins within an olivine grain in the Nakhla Martian meteorite (Lee *et al.* 2013). The key points are the serrated nature of alteration veins, the potential for siderite in the serrations, and the Fe - Mg silicate in the veins.

The formation mechanisms, sequence of alteration and environmental conditions under which these alteration veins, including carbonates, formed remain poorly constrained, and competing theories exist (Lee *et al.* 2015; Hicks *et al.* 2014). An important technique for investigating how MCS and aqueous alteration may have proceeded on early Mars is via controlled laboratory experiments that seek to replicate the crustal and atmospheric conditions to varying degrees of complexity (Booth *et al.* 1982; Mukhin *et al.* 1996; Moore & Bullock, 1999; Baker *et al.* 2000; Tosca *et al.* 2004; Hausrath & Brantley, 2010; Golden *et al.* 2012; Dehouck *et al.* 2013; Schwensen *et al.* 2017).

Often, these laboratory Mars analogue experiments represent the early Martian crust using only olivine (Dehouck *et al.* 2013), and nearly always the type used is terrestrial San Carlos olivine (Hausrath & Brantley, 2010; Golden *et al.* 2012; Dehouck *et al.* 2013). San Carlos is also almost always used for laboratory experiments on terrestrial MCS (Malvoisin *et al.* 2012; Lafay *et al.* 2012). San Carlos olivine is a mantle xenolith originating from a table plateaux (mesa) capped

by basalt located immediately South West of San Carlos in North America. In its gem form olivine is called peridot. San Carlos olivine is easily commercially available and has become the default standard (USNM 111312/444) used for olivine in most laboratories (Fournelle, 2009). An advantage of diverse experiments all using San Carlos olivine is that it becomes simpler to directly compare results across experiments, however, there are drawbacks to transferring this logic to Martian analogue experiments.

The forsterite content of San Carlos is $Fo\ 91.1 \pm 0.3$ and $Fo\ 89.2 \pm 0.2$ which is considerably less than Martian olivine (Fournelle, 2009 and Fig. 4.3). This study seeks to use a variety of mineral compositions and Mars crustal analogues, including olivine, pyrrhotite, pyrite, chalcopyrite and glass rich Icelandic basalt to investigate whether complex mineral assemblages allow a more accurate representation of Martian aqueous alteration. The olivine used is South African hortonolite with a fayalite composition much closer to that of Martian olivine, the selection based on the premise that:

If the experimental primary mineralogy represents Martian minerals more accurately then the secondary alteration minerals may also be a more accurate representation of Martian alteration.

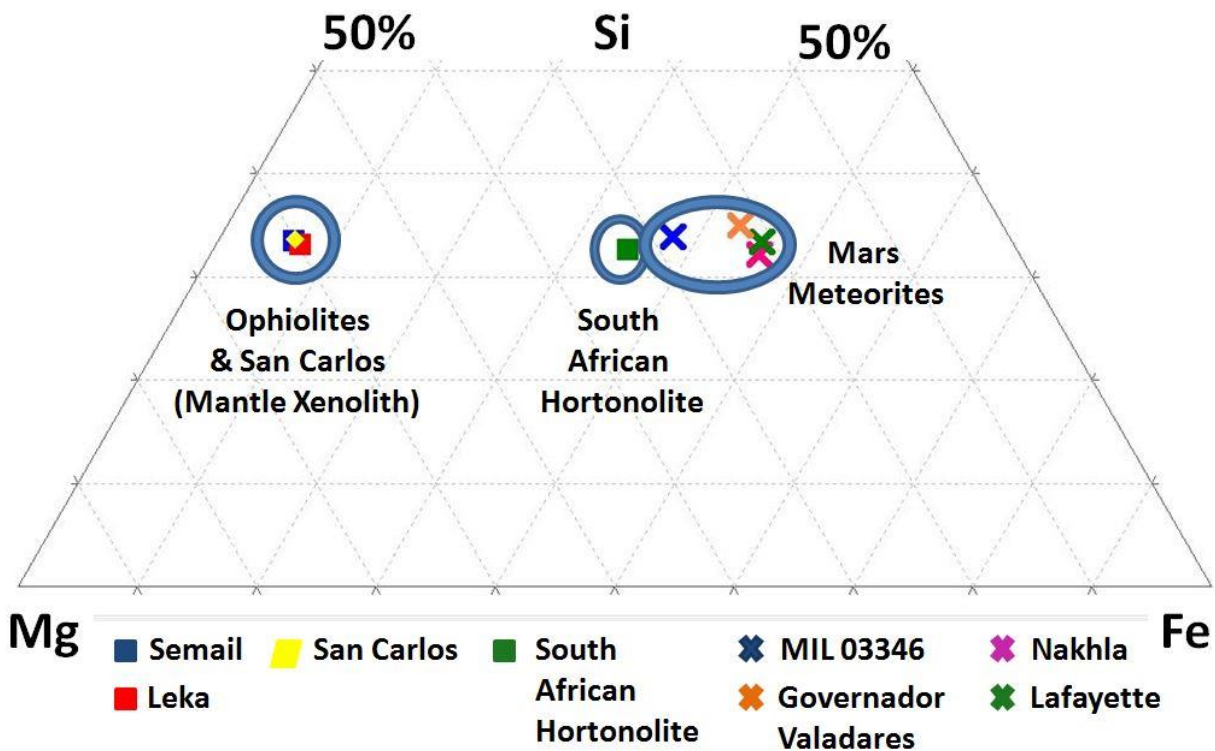


Figure 4.3. Ternary plot (atomic %) of olivine compositions for San Carlos olivine (Fournelle, 2009), terrestrial ophiolites (Oman and Leka), a selection of Martian meteorites (Bunch & Reid, 1975; Berkley *et al.* 1980; Lee *et al.* 2013; Day *et al.* 2006), and the South African hortonolite used in this study. Quantitative SEM analysis of the olivine for Leka, Semail and the South African hortonolite can be found in Appendix 4.

Another common feature in laboratory Martian mineral experiments is using pure CO₂ gas to represent the atmosphere of early Mars (Baker *et al.* 2000; Schwenser *et al.* 2017). The principal disadvantage of such simplified early Mars atmosphere analogues is disregarding the role of sulphur in mineral dissolution and evolving fluid chemistry. Sulphur decreases fluid pH and aids silicate mineral dissolution. A significant proportion of the early Martian atmosphere may have contained SO₂ from mantle outgassing from extensive early planetary volcanism (Halevy *et al.* 2007; King & McLennan, 2010; Tian *et al.* 2010). The abundance of sulphur on early Mars is evidenced by surface mineralogy such as the sulphate-rich Meridiani sediments (Bullock & Moore, 2007).

This study investigates the mineralogical changes that occur minerals at set conditions are exposed to pure CO₂ or CO₂ - SO₂ mixed atmospheres. However, unlike Mars, this experiment's dark sealed chambers will prevent photo-dissociation of SO₂ into H₂SO₄. This study also investigates the effects on water mediated mineral alteration of olivine and basalt by adding mineral sulphur (pyrite, chalcopyrite, pyrrhotite).

Overview summary.

- Replacement mechanisms, sequence of alteration and environmental conditions of MCS on early Mars are poorly constrained.
- Fe rich hortonolite is a chemically more accurate Mars olivine analogue than San Carlos olivine.
- This study uses both the 'simple Mars crust' analogue of pure olivine, and a 'complex Mars crust' analogue of glass rich basalt.
- This study uses both pure CO₂ and a CO₂ - SO₂ mix as comparative analogues for an early Mars atmosphere and observes differing effects on mineralogy.
- This study investigates how the inclusion of mineral sulphur (pyrite, chalcopyrite, pyrrhotite) affects MCS on the 'complex Mars crust' analogue.

4.1.2 Geochemistry of silicate mineral alteration.

As basalt reacts with CO₂ rich fluids, porosity and permeability will initially increase due to the formation of fractures (Keleman & Hirth, 2012). Fracturing is caused by mineral hydration and related volumetric expansion. Decreased porosity then occurs, as secondary minerals fill available pore space (Neuhoff *et al.* 1999). Basaltic parent minerals such as olivine, pyroxene, plagioclase etc. form secondary minerals like chalcedony, kaolinite, allophone, imogolite, Al and Fe oxyhydroxides, zeolites and Ca - Mg - Fe carbonates such as dolomite, ankerite and calcite. If sulphur is present in the reacted fluid, perhaps in the form of H₂S or S₂⁻, then sulphides and sulphates can also precipitate. The degree of basalt reaction dictates which secondary minerals form (Fig. 4.4 and 4.5). Secondary mineral formation type can depend greatly upon initial fluid acidity and solute content, water to rock ratio, and only suggestive models are presented here.

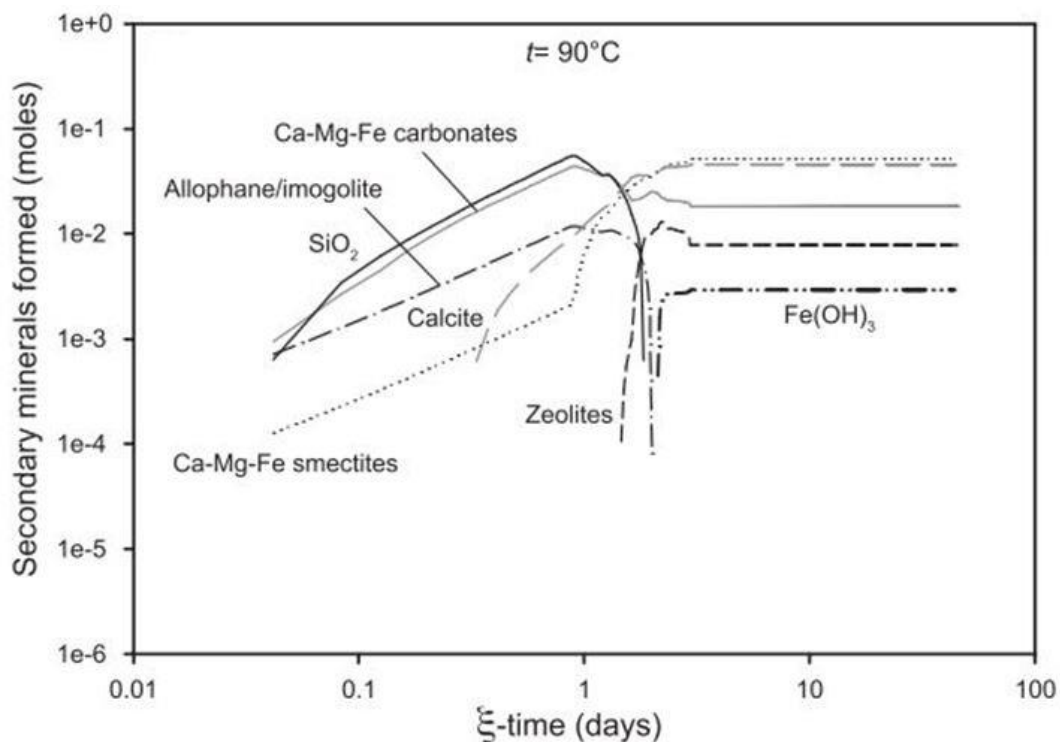


Figure 4.4. PHREEQC geochemical model of secondary mineral formation sequence at 90°C and 2 bars, using basalt in 200 ml of water (Gysi & Stefánsson, 2011). A close approximation of this study's conditions.



Figure 4.5. Highly simplified sulphur precipitation sequence for pyrite progressively aqueously reacting (based on Hunger & Benning, 2007). Pyrite formation and dissolution remains poorly understood and this is highly simplistic.

In basaltic terrains such as Iceland, where precipitation is close to oceanic ratios of Na/Cl, K/Cl, Mg/Cl, and Sr/Cl and with pH 5.4 (Gislason *et al.* 1994). Springs can form travertines, potentially possessing hyperalkaline pH (>12) and are Ca rich, Mg poor (Chavagnac *et al.* 2013). Travertines springs are common in ophiolites around the world (Fig. 4.6), for example the Gros Morne park in Canada (Szponar *et al.* 2013), the Othrys ophiolite in Greece (Tsikouras *et al.* 2013), California (Blank *et al.* 2009), and the desert of Oman (Olsson *et al.* 2014). Terrestrial analogues for Mars commonly use ophiolites (Blank *et al.* 2009), travertine springs (Szponar *et al.* 2013) and basaltic terrains such as Iceland (Allen *et al.* 1981; Bishop *et al.* 2002).

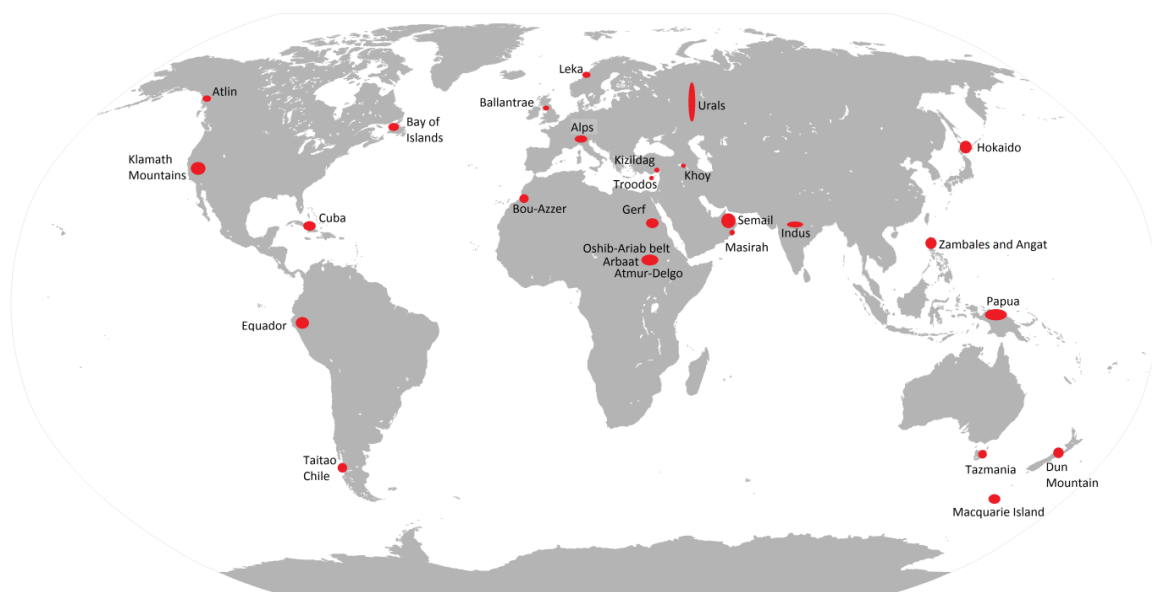


Figure 4.6. Principal terrestrial ophiolite regions. Size of red dot does not indicate size or importance.

This change of water chemistry in Iceland from relatively acidic initial water (pH 5.4) to alkaline travertine is due to the fluid's subsurface reaction with the basalt. A common relative sequence of element mobility during aqueous alteration of basalts is $SO_4 > F > Na > K \gg Ca > SiO_2 > Mg > PO_4 > Sr \gg Mn > Al > Fe > Ti$ (Gislason *et al.* 1994). The chemical alteration path of basalt is therefore a process of increasing Al and loss of (aqueous mobility of) Ca, Na, K, Fe and Mg (Fig. 4.7), SiO_2 ().

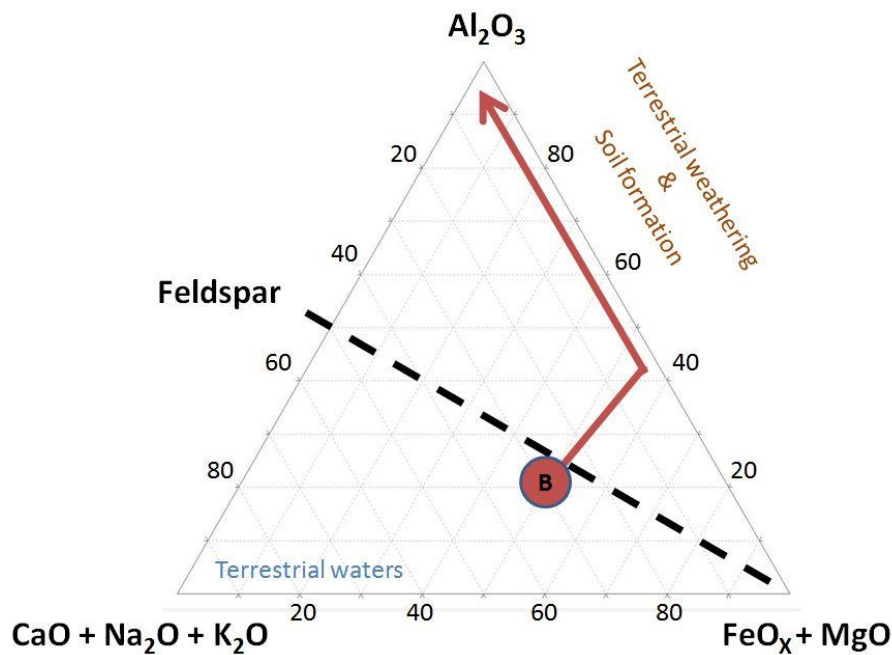


Figure 4.7. Ternary diagram (atomic %) showing approximate chemical evolution trends of terrestrial silicate rocks during weathering. Basalt (B). Granodiorite (G). Based on (Hurowitz *et al.* 2006).

However, due to the diversity of secondary mineral possibilities combined with non-conservative behaviour of elements during alteration reactions it is extremely difficult to assess the rate of chemical alteration (and carbon drawdown) simply by correlation with the volumetric quantity of secondary products observable (White & Buss, 2013). This difficulty is relevant to Martian research, where density estimates of the early Mars atmosphere are correlated with carbonate volumes in soils and meteorites (Jakosky *et al.* 1994). Mars is

predominantly basaltic and thus shares many geological parallels with terrestrial ophiolites (Blank *et al.* 2009).

Thus, caution is required when suggesting rates of early Mars atmosphere loss based on interpretations of secondary mineral products in meteorites and *in situ* rocks. With Mars particularly, the role of volcanic sulphur converting via photodecomposition from SO₂ to H₂SO₄ with subsequent acidification of Martian waters and dissolution/inhibition of secondary carbonate minerals is critical to the interpretation of field mineralogy findings (Fairén *et al.* 2004; Bullock & Moore, 2007). Many critics who dismiss the idea of a dense multiple bar early Mars atmosphere on the basis of ‘missing carbonates’ (Edwards & Ehlmann, 2015; Hu *et al.* 2015) may be underestimating the importance of both the non-conservative nature of secondary minerals and the role of sulphur in the geochemical history of Mars. This study seeks to examine in detail the role of sulphur in the dissolution of primary minerals, and the difference in secondary mineral precipitation when sulphur is included in alteration systems.

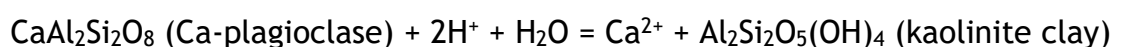
How basic primary minerals can aqueously alter to form secondary minerals.

Forsterite and pyroxene can aqueously alter to serpentine via equation 4.1:



Equation 4.1

Plagioclase can aqueously alter to kaolinite via equation 4.2:

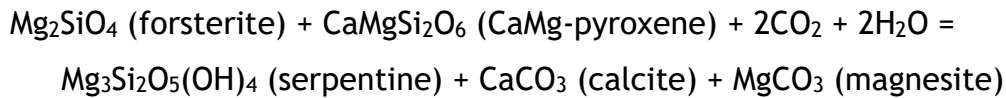


Equation 4.2

CO₂ can combine with water to aqueously alter forsterite and pyroxene to carbonates, silica polymorphs and serpentine via equations 4.3 and 4.4:



Equation 4.3



Equation 4.4

The variety of such equations is nearly endless in complex natural systems and the equations above are merely a few simple examples used to demonstrate potential reaction pathways for primary silicates to alter into secondary products.

Younger silicate rocks weather at a faster rate than older ones, particularly when <8 Ma old (Gislason *et al.* 1994), hence the age of the primary rocks should be a key factor when discussing potential aqueous alteration rates. There is also a known, but poorly understood, discrepancy between weathering rates in real geological sites and weathering in the laboratory (White & Brantley, 2003). This discrepancy has been shown to be 2 to 4 fold in magnitude (Schnoor, 1990; Brantley, 1992; White *et al.* 1996), and is most likely due to the over simplification of natural complex systems in the laboratory. This problem of needing to simplify intensely complex and long reaction length systems into something manageable within an experimental or grant timeline is an ongoing conundrum and a compromise for all geochemists.

High temperature - pressure reactions proceed faster than low temperature - low pressure reactions (albeit temperature exerts a greater influence over reaction speeds than pressure; pressure dominantly affecting gas solubility and speciation). Using temperature and pressure to increase primary silicate reaction rates can be achieved in industrial/terrestrial MCS scenarios by injecting at depth

and using the planet's geothermal gradient; in theory it can also be used to represent planetary rock reaction processes over millions of years in the laboratory. The problem is in demonstrating high temperature - pressure validity as analogues for real geological lower temperature systems. One method of validation is to compare low temperature-pressure experimental results with the early time series data of the high temperature-pressure experiments. Data from geochemical models such as PHREEQC, large scale experiments such as CarbFix, and natural analogues such as ophiolites can also all provide result validation to high temperature-pressure mineral carbon sequestration experiment data.

For all types of laboratory mineral experiments an important factor is the state of alteration of the mineral substrates prior to experiment. A detailed pre-experiment evaluation is essential in order to distinguish what is pre and post experiment alteration and therefore quantify extents and rates of alteration caused by the experiment itself.

4.1.3 Isovolumetric replacement versus pore space precipitation.

The formation process of Mars olivine alteration veins, specifically those observed in Martian meteorites, and the environmental conditions prevailing during the alteration process are poorly understood. Two disparate theories of alteration vein formation process are prevalent in the literature (Velbel, 2012). One suggests significant fracture pore space was available pre-alteration, which then became filled in by carbonates (Changela & Bridges, 2010; Bridges & Schwenger, 2012; Hicks *et al.* 2014); the other advocates outward silicate replacement from hairline fractures (Lee *et al.* 2015).

The mineral evidence comes from the meteorite Lafayette, which formed $\sim 1322 \pm 10$ Ma ago (Swindle & Olson, 2004), and the alteration veins are dated $\sim 670 \pm 91$ Ma ago (Swindle *et al.* 2000). This meteorite represents relatively modern Mars. Early Mars can be represented by ALH 84001, dated $\sim 4091 \pm 30$ Ma (Lapen *et al.* 2010). ALH 84001 contains distinct well formed rosette shaped

carbonates (McKay *et al.* 1996). It has been recognised that growth of these rosette style carbonates depends on available pore space (Corrigan & Harvey, 2004). Thus, carbonate structure and formation processes on recent Mars have implications for early Mars: no rosettes are found in Lafayette, so if mineral replacement from micro-fractures is proven, this is consistent with the availability of pore space controlling carbonate growth kinetics. If infilling of pre-existing pore space is proven to be the carbonate formation mechanism in Lafayette, then other explanations in addition to the availability of pore space would be required to explain the lack of rosette type carbonates on modern Mars. The question also has implications for subsurface water storage capacity throughout Mars' history. Further implications exist for how subsurface terrestrial MCS might proceed, for if silicate replacement and significant carbonate formation from initial micro-fractures can be demonstrated then storage capacity of MCS wells would need significant revision (Bradshaw *et al.* 2007).

Isovolumetric replacement of primary silicates is the first theory (Fig. 4.8), which states alteration veins formed via direct centripetal mineral replacement of primary olivine silicate by secondary alteration minerals, propagating from an initial fracture of 1 - 2 μm (Lee *et al.* 2015). Fe - Mg silicates became cemented in this 1 - 2 μm fracture, followed by interface coupled dissolution - precipitation expanding the vein width, possibly with additional CO_2 rich fluids pulsing in, producing siderite, which then become replaced by fibrous saponite (Lee *et al.* 2015). The jagged serrated nature of the veins and the angle at which they form and advance being crystallographic controlled.

Key point: *Secondary minerals in this mechanism first form in the vein centre and progress outwards via mineral replacement.*

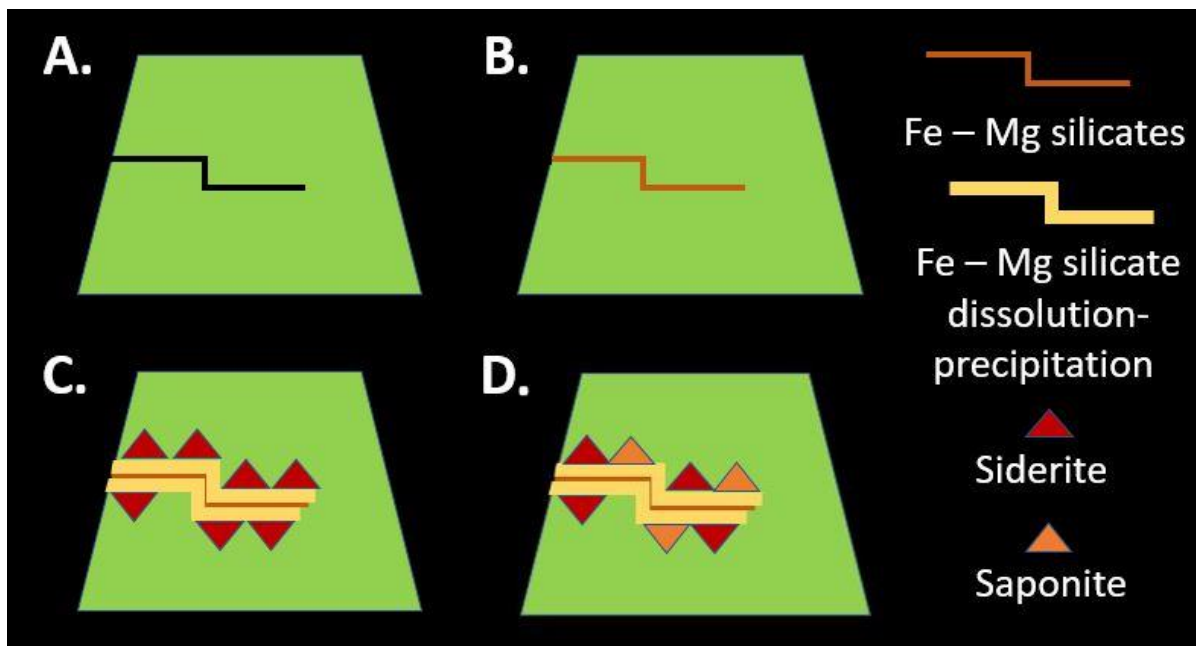


Figure 4.8. Simplified illustration of the isovolumetric mineral replacement sequence in Martian meteorite olivine. *Adapted from Tomkinson et al. 2013.*

The second theory states that pre-existing fractures become cemented and filled by hydrothermal fluids precipitating secondary minerals (Changela & Bridges, 2010; Bridges & Schwenzer, 2012; Hicks *et al.* 2014). This theory merges an additional option that the fracture may have been dissolved prior to cementation (Velbel, 2012). This theory does not invoke any vein widening dissolution - precipitation kinetics (Fig. 4.9).

Key point: *Secondary minerals in this mechanism first form in the vein edges and progress inwards via mineral precipitation.*

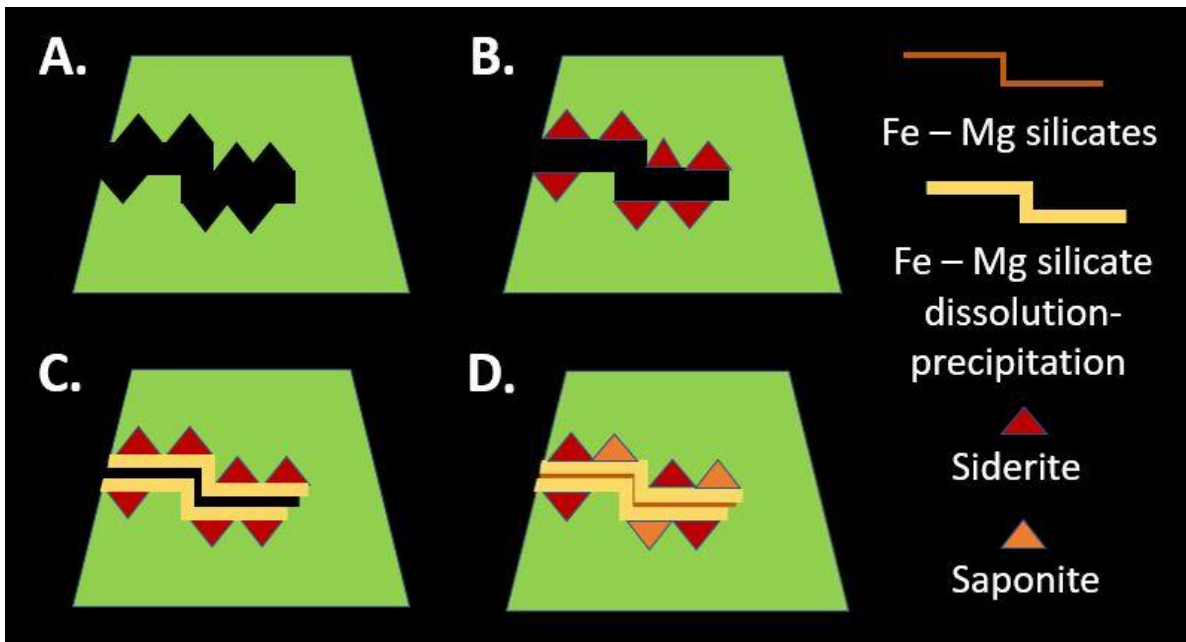


Figure 4.9. Simplified illustration of pore space precipitation in Martian meteorite olivine.

This study, by use of controlled mineral experiments seeks to investigate which of these mechanisms is the better candidate for Martian olivine dissolution.

4.1.4 The role of controlled mineral experiments.

The exact conditions of MCS in Martian samples is poorly constrained, quantified and understood. This is where study of terrestrial analogues and laboratory experimentation can assist in developing and testing hypotheses around the loss of the early Mars atmosphere. Further, MCS provides a research overlap between Mars planetary research and terrestrial climate change, with concomitant advances in terrestrial geo-engineering. The word analogue is selected as the experiments are conducted in controlled laboratory environments with precisely defined variables, and their aim is to represent isolated aspects of holistic planetary rock dynamics, i.e. they intentionally lack the complexity of real planet geochemical systems and through reduction seek to understand real planet geochemical principles.

Each individual experiment can usually only focus on a small targeted aspect of the large-scale process of MSC, but en masse, the diverse range of MCS laboratory experiments provide invaluable data to validate and test theoretical modelling and field work observations, whether on Mars or Earth. This study extends a lively literature of laboratory pressure-temperature-gas-mineralogy experiments (Table 4.1) seeking to understand how MCS can alter entire planetary systems.

Table 4.1. A short selection of literature demonstrating the range of laboratory experiments into MCS, the key parameters used and the similarity between Martian and terrestrial experimental variables of gas, mineral and fluid phases. Ol = Olivine. Bas = Basalt. Py = Pyroxene. Pl = Plagioclase. Carb = Carbonate. Sul = Sulphate. 1 = Adeoye *et al.* (2017). 2 = Giammar *et al.* 2005. 3 = Chen & Brantley (2000). 4 = Gysi & Stefansson (2012). 5 = Haug *et al.* (2011). 6 = Qafoku *et al.* (2014). 7 = Schaef *et al.* (2014). 8 = Sissmann *et al.* (2014). 9 = Luce *et al.* (1972). 10 = Lafay *et al.* (2012). 11 = Malvoisin *et al.* (2012). 12 = Wells *et al.* (2017). 13 = Hausrath & Brantley (2010). 14 = Golden *et al.* (2012). 15 = Baker *et al.* (2000). 16 = Dehouck *et al.* (2013). 17 = Tosca *et al.* (2004). 18 = Schwenser *et al.* (2017). 19 = Moore & Bullock (1999). 20 = Booth *et al.* (1982). 21 = Mukhin *et al.* (1996).

Reference	Target	Time (Days)	Temperature (°C)	Aqueous Phase	Gas Phase	Mineral Phase	Pressure (Bars)
1	T	42	45/100	H ₂ O + NaCl	CO ₂	Bas	100
2	T	1/7/10/14	30/95	H ₂ O + MgCl ₂ + NaHCO ₃	CO ₂	Ol	1/100
2	T	1/7/10/14/26	30/95	H ₂ O	CO ₂	Ol	1/100
3	T	0.4 (5 hours)	65	HCl + H ₂ O	Air	Ol	1
4	T	125	75 to 250	H ₂ O	CO ₂	Bas	10/25
5	T	1	185	HCl + H ₂ O	CO ₂	Ol	115
6	T	124	35/50/80	H ₂ O	CO ₂	Ol	91.19
7	T	48/98	90	H ₂ O	CO ₂ + SO ₂ + O ₂	Bas	100
8	T	45	150	H ₂ O	CO ₂	Ol or Bas	280
9	T	0.66 to 4.16	25	H ₂ O + HNO ₃ /KOH	Air	Ol	1
10	T	1 to 90	150/200	NaOH	Air	Ol	5/16
11	T	8.3 to 500	250/270/300/350	H ₂ O + NaCl	Air	Ol	500
12	T	1 to 28	150	H ₂ O	CO ₂	Bas	100
13	M	56	34/22/6/-9	H ₂ O/CaCl ₂ + NaCl + H ₂ O	N ₂ /Na-Ca-Cl/air	Ol or Bas	1
14	M	10 to 12	80	H ₂ SO ₄	Air	Ol/Fe Carb or Bas	1
15	M	4 to 7	23/75	H ₂ O	CO ₂	Bas	1 to 2
16	M	90	45	H ₂ O	CO ₂ /H ₂ O ₂ /air	Ol	1.5
17	M	14	25	H ₂ O + HCl + H ₂ SO ₄	Air	Bas	1
18	M	4 to 7	23/75/200/400	H ₂ O + CO ₂	CO ₂ /H ₂ O + CO ₂	Bas	1/2/500/1000
19	M	30/90/270	35	H ₂ O	Modern Mars mix	Ol/Py/Pl/Bas	Unstated
20	M	2	25 to -94	H ₂ O	H ₂ O + O ₂ + SO ₂ + CO ₂	Ol or Bas	0.025 (SO ₂)/0.1 (CO ₂)
21	M	0.5	Room to 200	-	Degassed	Ca/Mg carb + Mg sul	Vac (1.3 x 10 ⁻¹¹)

Although these experiments can be categorised in several ways, this study divides the experiments into either Earth or Mars analogues, and conducted at either low ($\leq 180^{\circ}\text{C}$) or high ($\geq 180^{\circ}\text{C}$) temperature. Low temperature Mars analogue experiments are the most relevant to mimicking the loss of an early Martian atmosphere, and the experiment presented in this study belongs to this category. However, terrestrial analogues and high temperature experiments also provide a wealth of data pertinent to Mars carbonation questions.

As the technology advances experiments investigating the industrial and environmental applications of MCS are moving beyond the controlled laboratory environment and are entering larger, less controlled, multi-km scale tests, where a vast number of natural variables influence the results. The highest profile terrestrial experiment of this genre is the CarbFix project (Matter *et al.* 2009), located at the Hellisheidi Geothermal Power Station in Southern Iceland. CarbFix is managed by Reykjavik Energy, the University of Iceland, Columbia University and Centre National de la Recherche Scientifique (France). This chapter will focus on the smaller laboratory scale experiments, but due to its enormous influence on the development of the research field, the CarbFix project will be briefly outlined. The author visited the CarbFix project in July 2015 to discuss the past and future research with on-site staff, and tour the facility.

4.1.5 Large scale experiments: The CARBFIX project.



Figure 4.10. The Hellisheidi Geothermal Power Station CarbFix facility in Southern Iceland. *Credit: Orkuveita Reykjavíkur (Website 1).*

The CarbFix project (Fig. 4.10) began in 2007 in the Western Hengill central volcano and fissure swarm, Iceland, injecting geothermal heated water which had been artificially saturated with CO₂ into an olivine tholeiite basaltic terrain at a rate of 0.5 to 0.7 kg/s⁻¹ (Alfredsson *et al.* 2013; Matter *et al.* 2009). The target rock consists of olivine (Fo₉₀ to Fo₈₀), plagioclase (An₉₀₋₃₀), pyroxene (augite), magnetite, ilmenite, chromium spinel and glass (Alfredsson *et al.* 2013; Jakobsson *et al.* 1997). The injected water was mixed with an addition of pure CO₂ equilibrated to 25 bar and another addition of CO₂-H₂S-H₂ equilibrated to 14 bar at a ratio 75:24.2:0.8 (Alfredsson *et al.* 2013). The reason for adding hydrogen sulphide and dihydrogen was to raise the overall acidity of the injected solution, because olivine rich basaltic rocks release cations at a higher rate if the pH is low. The final equilibrated injection solution has a CO₂ concentration of 0.8 to 0.42 mol kg⁻¹ and a pH of 3.7 - 4.0 (Alfredsson *et al.* 2013).

The project drilled a number of holes 550 m to 800 m in depth (Aradóttir *et al.* 2015), and the injection site has a geothermal gradient of 80 °C/km and an overlying impermeable cap rock of glassy basaltic hyaloclastites (Alfredsson *et al.* 2013). Basalt rocks are rich in divalent cations (Mg^{2+} , Fe^{2+} , Ca^{2+}) and the CarbFix target rock has 6 mol Kg^{-1} of cations potentially available for reaction (Alfredsson *et al.* 2013). Ambient water in the target rocks was ~30 - 60 °C at 300 - 800 m depth and 180 °C at 1500 m depth, with pH 8.4 to 9.8, hence relatively alkaline; the injected fluid mix was at ~25 °C (Alfredsson *et al.* 2013). Tracer fluids were added into the main injection waters to observe for both leaks in the cap rock and transport fate of the injection fluid. 1 m³ water was injected with 50 kg of fluorescent Na dye, and 1 m³ water injected with ~14 g sulphur hexafluoride SF₆ (Matter *et al.* 2009). The project site has a natural groundwater through flow rate of 25 m yr⁻¹ (Alfredsson *et al.* 2013). No leakage has yet been discovered.

CarbFix has so far been a groundbreaking success, with 95% of the >170 tonnes of CO₂ injected becoming fully mineralised as calcite in ≤ 2 years (Sigfusson *et al.* 2015; Matter *et al.* 2016), demonstrating that industrial scale MCS can be effective in human, as well as geological, time scales. The demonstration that CarbFix provides for such rapid carbon sequestration also has implications for the loss of Mars' atmosphere, albeit via natural MSC. CarbFix also demonstrates an ideal progression from theoretical calculation and modelling, through to small scale laboratory experiment into industrial large scale physical application. Much of the literature around geo-engineered MCS is dominated by the CarbFix project (Alfredsson *et al.* 2011; Aradóttir *et al.* 2011; Gislason *et al.* 2010; Gislason & Oelkers, 2014; Johnsson, 2011; Matter *et al.* 2009; Matter *et al.* 2011).

The CARBIX project has now evolved to incorporate the SulFix project. The SulFix project injects hydrogen sulphide into the same rock formation, but rather than inject at the CARBIFIX depth of 550 - 800 m to aid in primary mineral dissolution, H₂S is instead injected ~1350 m (Aradóttir *et al.* 2015), where the pressure and temperature is more conducive to sulphide mineral stability and thus long term storage (Juliussón *et al.* 2015; Ragnarsson, 2015).

4.1.6 Terrestrial mineral carbon sequestration experiments.

Following the CarbFix experiments in Iceland, a great number of laboratory experiments have been conducted, often using simple components such as water, CO₂ gas, basaltic glass or ultramafic rocks, as these react most rapidly. For example, experiments at 40 °C for 260 days have produced poorly crystalline carbonates and clays of Ca-Mg-Fe composition, along with Fe-hydroxides and oxy-hydroxides (Gysi & Stefánsson, 2012). Other researchers have found that using diluted amounts of CO₂ (18.2 % in a gas stream) reacted with serpentine can sometimes be more efficient in producing Mg - rich secondary minerals than when using 100 % CO₂ (Pasquier *et al.* 2014); it would be interesting to apply such diluted CO₂ gas stream experiments to Martian - specific settings and compare the results with pure CO₂. Certainly, a majority of terrestrial MCS experiments only use pure CO₂ as the gas component (Giammar *et al.* 2005; Haug *et al.* 2011; Qafoku *et al.* 2014; Sissmann *et al.* 2014; Wells *et al.* 2017). Although pure CO₂ gas in a laboratory experiment could be argued a valid analogue for an industrial MCS, it has serious defects as an early Mars analogue, lacking in elements representing volcanic sulphur. Comparing fluid chemistry and mineral alteration changes between a system using pure CO₂, and one using CO₂ and SO₂, and was thus selected as a variable for this study.

Perhaps most importantly for this study, some terrestrial experiments demonstrate that carbonation occurs up to 40 times more efficiently in olivine rich basalt compared with pure olivine (Sissmann *et al.* 2014). This result means that pure olivine carbonation experiment results are highly conservative compared to field injection results. This leads to the concept pursued in this study of having one of the experiment variables being the comparison of olivine alteration with that of basalt alteration. Even with pure olivine experiments, it has been noted that the limiting factor in the reaction between olivine and water is usually the precipitation rate of carbonates, not the dissolution rate of olivine (Haug *et al.* 2011).

Many of these low temperature laboratory experiments have been used to support and advance other large scale semi-industrial 'CARBFIX like' sites, such as the Wallula project in the Columbia river basalts, USA (Sissmann *et al.* 2014; Adeoye *et al.* 2017; Wells *et al.* 2017), or the Sleipner project in Norway (Hermanruda *et al.* 2009).

4.1.7 Martian mineral carbon sequestration experiments.

Laboratory experiments have sought to discover which variables may be important for weathering and mineral alteration on Mars (Table 3.1). These experiments typically investigate variables such as temperature, ionic strength, and oxygen concentration using olivine and basalt substrates, both with and without CaCl₂ and NaCl brine (Hausrath & Brantley, 2010). It has been found that Si release is significantly slower in brines than deionized water (Hausrath & Brantley, 2010). This Si relationship to brine becomes relevant because researchers find that olivine dissolution and alteration can be slowed by up to ~2 orders of magnitude by the formation of a ~≤ 40 nm thick silica layer on the reaction surface olivine grain (Daval *et al.* 2011). Furthermore, in order to invoke liquid water on the Martian surface many researchers proposed brine solutions (Bridges *et al.* 2012). Laboratory simulations of brine under Mars conditions, 0°C to -26.0°C, have found that it evaporates a factor of 30 times slower than pure liquid water. Hence, brine extends the stability of water on Mars via reducing both the temperature of evaporation *and* evaporation rate (Sears & Chittenden, 2005). This finding supports an extensive research area stating that high ionic strengths help to make liquids stable in Martian environments (Brass, 1980; Knauth *et al.* 2002; Altheide *et al.* 2009). Brine was considered and rejected for inclusion in this study in order to avoid overcomplicating an experiment already replete with variables.

Observations of the occurrence of jarosite, Ca- Mg- sulphates and siderite at the surface of Mars, and in Martian meteorites, has led to a number of laboratory experiments seeking to recreate the conditions under which these minerals formed. The experiments used olivine, siderite and basalt in through flow reactors

at 80 °C and monitored leachate chemistry (Golden *et al.* 2012). The result of these experiments, using H₂SO₄, was an abundance of amorphous silica and slightly dissolved but relatively unreacted olivine substrate (Golden *et al.* 2012). It is worth noting however that when SO₂ dissolves in water it initially forms a weak acid (HSO₃), and not the stronger sulphuric acid (H₂SO₄), and this may unduly drive the experimental results of Golden *et al.* (2012). The authors cite the importance of the use of sulphur in the experiment in order to achieve more robust Martian analogue conditions, and this comment influenced the design of the experiments undertaken here. A through flow reactor for this study would have been ideal as it is a more robust replication of percolating hydrothermal fluids, but was unavailable for the budget and amount of variables chosen for investigation. Thus this study uses closed system batch reactors.

The importance of sulphur in Martian experiments has been recognised by other studies that used volcanic hydrothermal laboratory analogues to investigate acid - sulphate weathering of basalt rocks (Marcucci & Hynek, 2014). Sulphuric acid solutions were used at temperatures ranging from 65 - 200 °C at various fluid to rock ratios (1:1, 4:1, 10:1) for 60 days. The relative abundance of elements in the fluid was Al > Mg > Fe > Na > Ca > Si > Mn (Marcucci & Hynek, 2014). Secondary minerals formed from the experiment included Ca, Mg, Al, Fe sulphates, anhydrite, kieserite, hexahydrite, pentahydrite, alunogen, voltaite, rhomboclase, natroalunite, Fe oxide, amorphous silica 'gel', ferroxahydrite, starkeyite, and gypsum. They found that these alteration minerals were produced under all experimental conditions and that only volume and grain size changed. Interestingly they note that the amorphous Si 'gel' increased with greater water to rock ratio (Marcucci & Hynek, 2014). Other experiments conducted on acid - sulphate weathering with basalt found Mg, Fe, Ca, and Al sulphate alteration products along with ferric oxides and the ubiquitous amorphous Si (Tosca *et al.* 2004).

Laboratory experiments have specifically attempted to replicate secondary mineral veins in Martian meteorites and precipitation of carbonates and clays. They have used water and CO₂ at high water to rock ratio (1:1) and low temperatures (23 and 75 °C), and low water to rock ratios (1:10) at high temperatures (200 and 400 °C) (Baker *et al.* 2000). These experiments showed that

even after only 7 days, some alteration can occur, notably the mobility of Si, although the authors were unsure whether this manifested as opal, quartz or hydrated silica (Baker *et al.* 2000). Perhaps surprisingly, all of their experiments produced carbonate, sometimes including magnesite, siderite and ankerite on experiment runs of between 4 to 7 days. The results of such experiments prompted confidence that if such carbonates could be formed within 7 days, then a longer experiment of 120 days under similar low temperature, high water to rock ratio, should produce extensive secondary minerals representative of Martian meteorites. However, many of the Mars analogue experiments that have successfully produced carbonate used mineral powders (Dehouck *et al.* 2013). Such powders may be a questionable analogue for the observations on the subsurface Mars crust, and were not selected for this experiment. Individual mineral reaction kinetics become indistinguishable, and the physical relationship between primary and secondary minerals becomes meaningless; further, the powders can form skins on the surface water of experiment chambers and / or clog fluid extraction filters.

Some experiments that ran for 3 months produced virtually no carbonate (~0.05 wt. %), poorly crystalline smectite clay in limited abundance (<1 wt. %), and significant hydrated silica (up to 4 wt. %), which the authors suggest may have limited further alteration (Dehouck *et al.* 2013). The smectite was generally found as a thin 'cotton-like' film surrounding the edge of the olivine grains. The magnesite they measured may have been an artefact, and nesquehonite ($\text{Mg}(\text{HCO}_3)(\text{OH})\cdot 2(\text{H}_2\text{O})$) may have converted to magnesite during gravimetric analysis (Dehouck *et al.* 2013).

A range of laboratory mineral experiments have focussed on decomposition of carbonates by UV radiation, as opposed to carbonate formation. These studies found that CO_2 release from photodecomposition of carbonate exceeded atmospheric CO_2 removal potential from the solar wind, even if carbonate abundance was low (Mukhin *et al.* 1996). Photodecomposition of surface carbonate to sustain a CO_2 rich atmosphere, which was then slowly stripped away by the solar wind, is one possible solution to the carbonate conundrum (Mukhin *et al.* 1996).

The composition and nature of Martian brines is poorly understood, and is important to constrain if pore space precipitation of secondary minerals via hydrothermal veins is considered a valid theory. It is also important with respect to understanding the formation of evaporite deposits that have been discovered on Mars' surface, for example the Burns formation on the Meridiani Planum (McLennan *et al.* 2005; Andrews-Hanna *et al.* 2010). Such extensive playa evaporate deposits may have formed by evaporation of brine (Moore & Bullock, 1999). Relatively long (1 year) laboratory experiments have been conducted by NASA AMES with deoxygenated water combined with a range of minerals including olivine, pyrite, augite and anorthoclase (Moore & Bullock, 1999). They found that even after a year of the minerals being immersed in the deoxygenated water, the fluid composition was considerably more dilute than natural terrestrial brines (Moore & Bullock, 1999). Ca^{2+} , Mg^{2+} , Na^+ and Al^{3+} were the dominant cations released, all of which rose ~3 orders of magnitude over 6 months and then started declining, except for Mg^{2+} , which peaked after 100 days then declined. Anions (SO_4^{2-} , SO_3^- , NO_2^- , CO_3^{2-} , Cl^- , F^-) showed a similar trend of rising to a peak after 6 months and then declining (Moore & Bullock, 1999). Experiments such as these provide a valuable background of mineral and fluid data to compare experiment results from the present study. Anhydrite (CaCO_4), barite (BaSO_4) and gibbsite ($\text{Al}(\text{OH})_3$) were thought to have precipitated based on PHREEQC saturation modelling (Moore & Bullock, 1999). The long duration of this experiment, the use of mineral sulphur (pyrite) and the application of saturation modelling using PHREEQC all influenced the formation of the design of experiments undertaken here.

More recent experiments conducted at the aqueous simulation facility at NASA AMES using water at 35 °C over 9 months with a modern Mars atmosphere composition, and mineral suits representative of the nakhlite meteorite have produced carbonates alongside amorphous and crystalline clays (Schwenser *et al.* 2017). Whereas recent experiments with H_2SO_4 (sulphuric acid; see comment above about H_2SO_4 potentially unduly driving the reaction compared to HSO_3), and Mars analogue basalt have produced only hematite, anhydrite, antroalunite, and also dissolved olivine (Peretyazhko *et al.* 2017 *In Press*).

4.1.8 Can Mars mineralogy inform terrestrial climate research?

Space sector research on the loss of carbon from the atmosphere of early Mars, particularly the MCS aspect of this atmosphere loss, can provide significant collaborative crossover with terrestrial CCS and climate change research (Schulte *et al.* 2006; Schrenk *et al.* 2013; Tomkinson *et al.* 2013). The following are just a few examples of the transferable research benefits:

- Large scale projects vital to advancing terrestrial MCS technology, such as CarbFix, rely on building a thermodynamic and kinetic database of gas - fluid - mineral reactions under a range of conditions that are often similar to Martian experiments (Website 1). The greater detail and wider data range that such databases possess, the more useful they are to the project. The CarbFix project's thermodynamic database has only 36 mineral reactions described, and the researchers found that many other terrestrial databases lacked the full range of mineral reaction data needed to model the system they were attempting to implement. CarbFix primarily used the EQ3/6 V7.2b database, but found Al-hydroxy complexes particularly lacking; SUPCRT92 was used for computing solubility constants where experimental data were insufficient (Website 1). 110 minerals were included in the CarbFix kinetic database, however, they also found the kinetic experimental data lacking, and relied on PHREEQC modelling to fill the empirical data gaps. Controlled laboratory experiments of Martian MCS processes, which often involve the same minerals, fluids and gases as their terrestrial counterparts, can add valuable empirical data into these terrestrial MCS databases and thus help advance terrestrial MCS projects.
- Critical areas of ongoing terrestrial MCS investigation include CO₂/brine multiphase migration (Wang *et al.* 2015) on the pore scale (Chen & Zhang, 2010; Bandara *et al.* 2011), core sample scale (Perrin *et al.* 2009; Gunde *et al.* 2010; Perrin *et al.* 2011), and large project scale (Ghomian *et al.* 2008; Yamamoto *et al.* 2009; Doughty, 2010; Chasset *et al.* 2011). Researchers in this field specifically state that quantitative empirical knowledge of MCS

kinetics is in short supply, and that more research on mineral surface alteration processes, precipitation controls and reaction pathways are desperately needed (Wang et al. 2015). Laboratory experiments focussing on producing early Mars analogues could provide a host of valuable data to these terrestrial MCS research areas.

Our advancing knowledge of the mechanisms, chemistry and quantification of the loss of the early Mars atmosphere via MCS will directly translate to an improved understanding of terrestrial MCS, and aid in the human effort to slow down the negative consequences of global climate change.

4.2 Experiment objectives.

1. To recreate the environmental conditions under which carbonates formed on early Mars (~4000 Ma ago).
2. To observe the effects on mineral alteration and fluid chemistry when sulphur (either as a gas or mineral) is added into a traditional CO₂ Mars analogue system.
3. To test whether Mars meteorite olivine alteration sequences form by isovolumetric replacement of primary minerals or via dissolution and precipitation of secondary minerals into fractures and pore spaces.
4. To assess whether South African hortonolite is a more suitable Martian olivine analogue than San Carlos olivine.

The specific focus of the experiments is on understanding conditions of carbonate and sulphate formation, and mineral dissolution. Objectives 1 - 4 will be addressed by:

- A. Selecting experiment gas compositions analogous to the early Mars atmosphere and observing changes in mineralogy and water chemistry caused by gas variation (minerals were water saturated).

Gas compositions: - Pure CO₂.

- Pure CO₂ with a 50 ml SO₂ injection.

- B. Selecting experiment gas compositions analogous to the early Mars crust and observing changes in water chemistry caused by mineral variation.

Mineral substrates: - Olivine (Mg,Fe²⁺)₂SiO₄ (Fo ~50%).

- Basalt (Glass & olivine rich).

- Basalt (Glass & olivine rich) with pyrrhotite.

4.3 Methods.

4.3.1 Overview.

These experiments investigate a large number of variables. In order to keep data quantity to a manageable level, a closed system batch reaction chamber experiment was selected. A series of 8 titanium - lined pressure chambers were used to explore the reactions of basalt, olivine and basalt mixed with pyrrhotite (selected to introduce mineral sulphur) when saturated with water. A constant 2 bar gas pressure was used with N₂ (control), CO₂ and CO₂ with SO₂ combinations of gas in the chamber head space. This study assumes the gas will chemically equilibrate with the water. The gas pressure was monitored daily and topped up (N₂ or CO₂ respectively) as required to maintain 2 bar pressure as equilibration and reaction proceeded.

The experiment monitors the chemical evolution of the water in the chambers via staggered fluid extraction, followed by IC/ICPMS analysis. PHREEQC geochemical modelling software was used to correct the IC/ICPMS data, due to the IC/ICPMS data being obtained at laboratory room temperature (20°C) and atmospheric pressure, and not the experiment temperature of 80°C and 2 bar. In addition, IC/ICPMS fluid data was combined with PHREEQC to model the saturation state of important elements. Minerals used in the experiments were characterised by SEM both before the experiments had started, and after completion. Observed changes in mineralogy and mineral surface textures were related to fluid chemistry and modelled saturation indices.

4.3.2 Experimental fixed parameters.

Temperature (°C):	80
Pressure (bar):	2
Water to Rock ratio (W:R):	All minerals were fully immersed in 200 ml demineralised H ₂ O. This H ₂ O was neither topped up nor volumetrically measured once the experiment began. Five 15 ml samples were extracted throughout the experiment for ICPMS analysis, so that changes in fluid chemistry could be tracked. H ₂ O chemistry and volume is expected to fluctuate as mineral reactions progress.
Time (days):	120

4.3.3 Experimental variables.

Gas composition and initial mineralogy are the two experimental variables. Three different batches of minerals were used: basalt, basalt with pyrrhotite and olivine (Fig. 4.11 and 4.12). Inert nitrogen was used as the gas in three chambers (one for each mineral batch type), providing a control to determine what reactions were due to the gas/fluid being out of equilibrium with the mineral assemblage.

Gas variables are CO₂ alone and CO₂ with SO₂ (Fig. 4.11 and 4.12). A practical limitation of this experiment design was the number of chambers available. Eight was the maximum allowable; therefore, not every mineralogy could be paired with every gas regime (basalt with pyrrhotite is not assessed in a CO₂ with SO₂ chamber for example). The choices of experimental variability are a compromise between:

- Requiring control samples to make the experiment scientifically robust.
- Requiring a useful level of mineral diversity to assess how mineral composition affects carbonate formation.
- Requiring a useful level of gas diversity to assess how gas composition affects carbonate formation, and the role of SO₂ in this process.

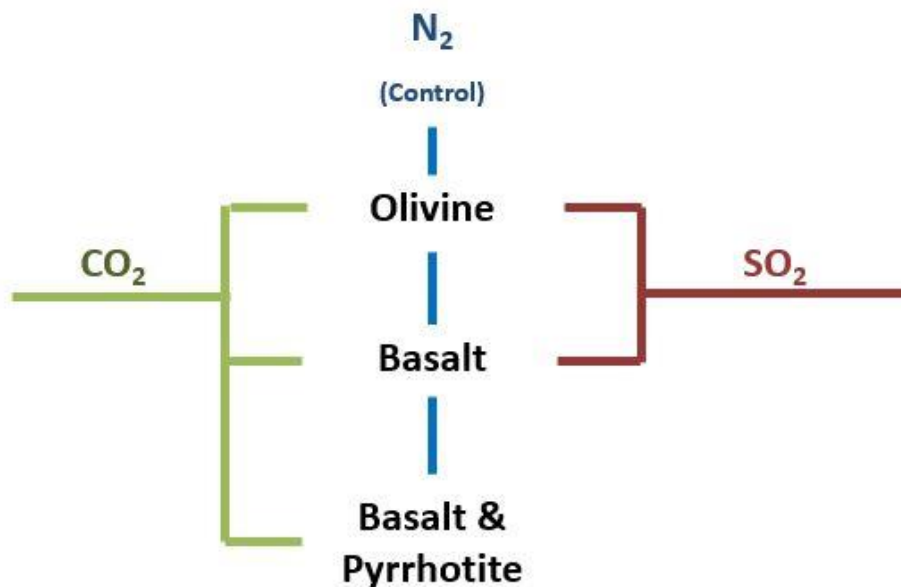


Figure 4.11. Network diagram of how the gas and mineral experiment variables interconnect.

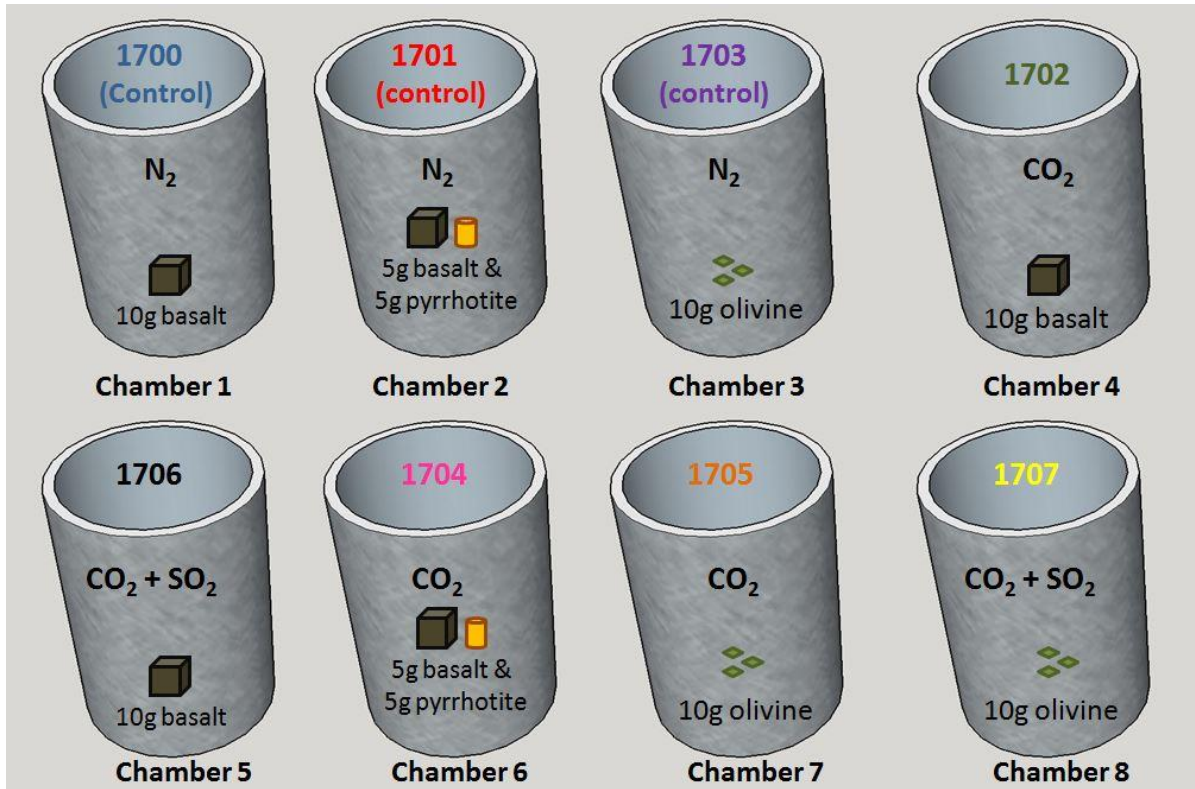


Figure 4.12. Gas and mineral variables for the eight experimental chambers, with approximate weight (g) of minerals used. The 4 digit numbering starting 170X is based on the number etched on the metal experiment chambers for health and safety chamber identification, and is unfortunately not in an intuitive order. The colour coding of chamber numbers presented here remains consistent throughout the chapter.

Reactants:

Whole rock pahoehoe / helluhraun post - glacial basalt was used from Hvaleyrarhraun, SW of Hafnarfjörður, Iceland. The sample possesses ~20 % vesicle (Schopka *et al.* 2006), and ~10 wt. % glass (some palagonite) and ~10 - 20 wt. % olivine (Hunterian communication), along with augite, plagioclase phenocrysts and a range of Ti - Fe oxides (Fig. 4.13, Fig. 4.14). Thin section TS7545 was provided on loan from the Hunterian museum for petrographic characterisation (Fig. 4.13).

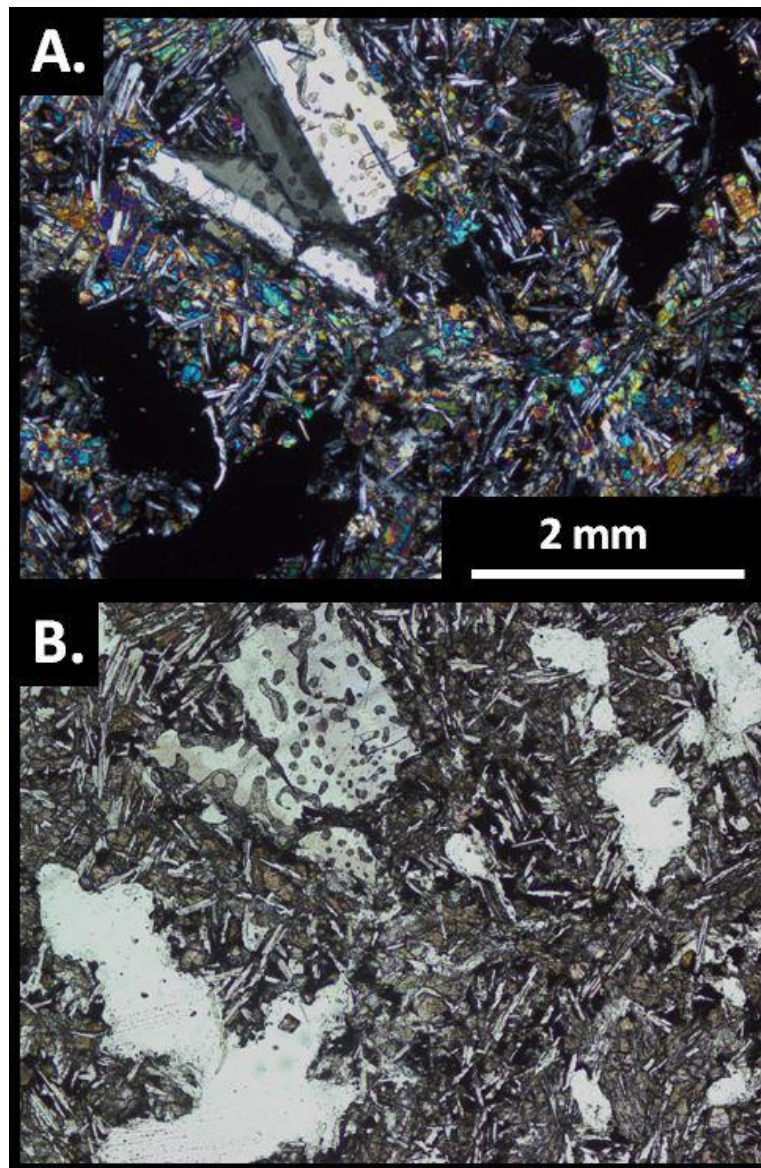


Figure 4.13. **A.** Transmitted polarized light and **B.** Transmitted plain light image of basalt thin section TS7545. Note heterogeneous vesicle distribution and relatively high glass content (black patches in B).

Using quantitative X-Ray microanalysis the dominant minerals were identified as augite (pyroxene), andesine (plagioclase), olivine, Ti- Fe- oxide (pseudobrookite) and glass (see Appendix 4 for details). The glass contains ~0.26 - 0.37 wt. % H₂O (Schopka *et al.* 2006).

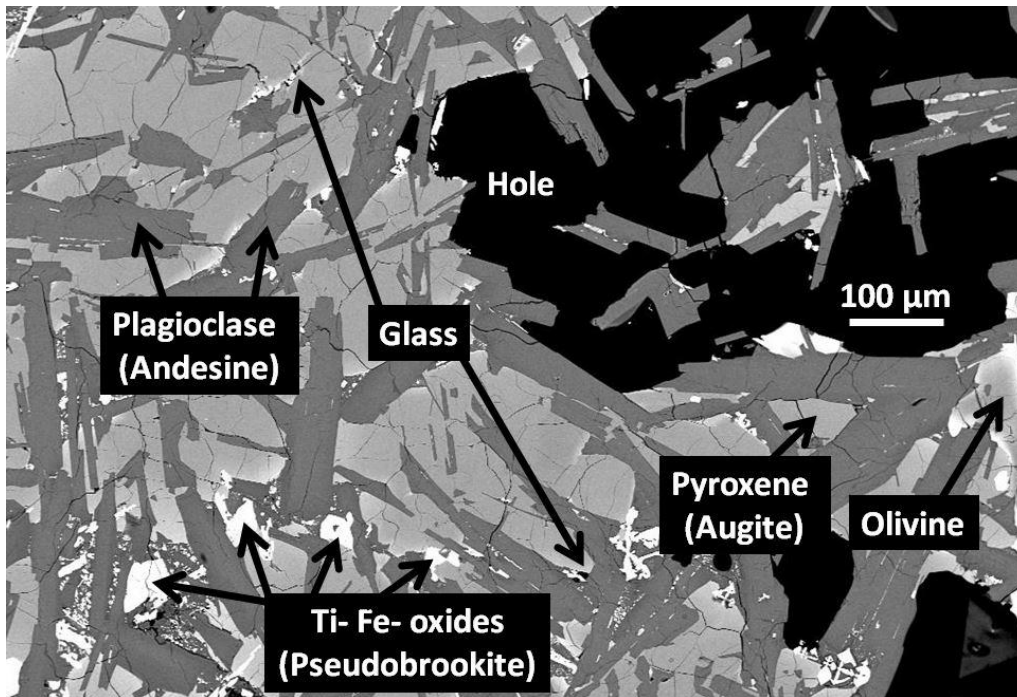


Figure 4.14. BSE SEM image of pre - experiment Icelandic basalt. See SEM quantitative data appendix for individual mineral analysis.

Semi quantitative X-Ray microanalysis of ~300 μm^2 areas, combining all minerals, provided the following compositions (Table 4.2), and these values were compared with another Icelandic basalt analysis (Shorttle & Maclennan, 2011):

	Area 1	Area 2	Area 3	Area 4	Average	Average normalised	Example Iceland Basalt
SiO ₂	44.30	44.30	44.94	45.80	44.83	46.38	48.70
Al ₂ O ₃	20.22	20.03	19.66	19.66	19.89	20.58	14.90
CaO	13.58	13.86	13.72	13.86	13.76	14.23	12.90
FeO	10.58	9.80	9.68	10.32	10.09	10.44	9.20
Na ₂ O	3.24	3.11	3.24	3.24	3.21	3.32	1.70
MgO	3.15	3.32	3.49	3.49	3.36	3.48	11.80
TiO ₂	1.34	1.34	1.34	1.34	1.34	1.38	0.69
K ₂ O	0.24	0.24	0.24	0.00	0.18	0.19	0.04
Total	96.65	96.00	96.29	97.69	96.66	100.00	99.93

Table 4.2. X-Ray semi-quantitative microanalysis (wt. %) of ~300 µm² areas of pre-experiment Icelandic basalt. Example basalt for comparison from Shorttle & Maclennan, 2011.

The analysis in Table 4.2 show that the basalt used in this experiment has low MgO and elevated CaO and Al₂O₃ compared to other Icelandic basalt. The analysis was conducted in order to provide a uniform bulk chemical reference point for which the evolving experiment fluid chemistry results and post experiment mineralogy can be compared.

Pyrrhotite used was from sample GLAHM 134475, provided on loan from the Hunterian museum for partially destructive purposes (Fig. 4.15). A dominantly pyrrhotite mineral was chosen over pyrite for this experiment as pyrrhotite oxidises and alters considerably faster than pyrite; ~20 - 100 times faster under atmospheric conditions (Nicholson & Scharer, 1994). However, the pyrrhotite selected contains impurities including chalcopyrite, pyrite and calcium carbonate, detailed below. The sample is massive, strongly magnetic and from the SW corner of the working quarry in Shierglas, Blair Atholl, Tayside, Scotland (NN882 639). The pyrrhotite formed *in situ* as part of a limestone and dark schist formation of the Appin group, Dalradian supergroup.

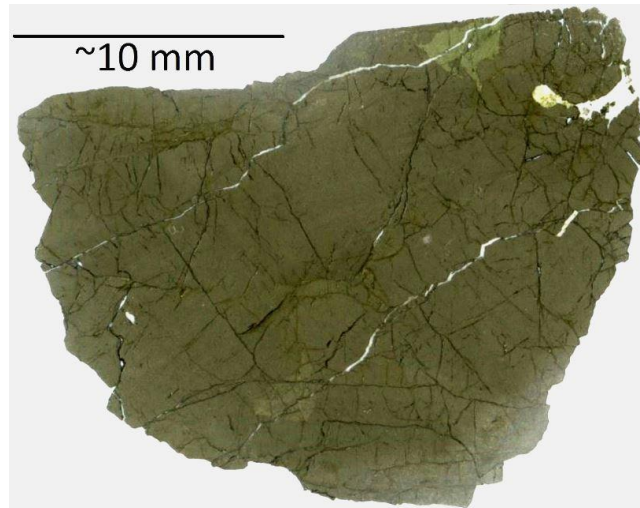


Figure. 4.15. Photograph of the pre-experiment pyrrhotite sample in thin section. Even with the naked eye, differences in colour shade can be observed within the sample. This shade variation is due to differences in concentrations of iron, sulphur and copper composition. The sample divides into three types, type 1 (dominant) is a pyrrhotite, type 2 is a chalcopyrite and type 3 is a pyrite (Fig. 4.16, 4.17 and 4.18). Calcite was also present pre-experiment. For the sake of brevity, the term pyrrhotite will be used for all three types of sulphide for the rest of the chapter. Quantitative SEM analysis of all three sulphides and the calcite is available in Appendix 4.

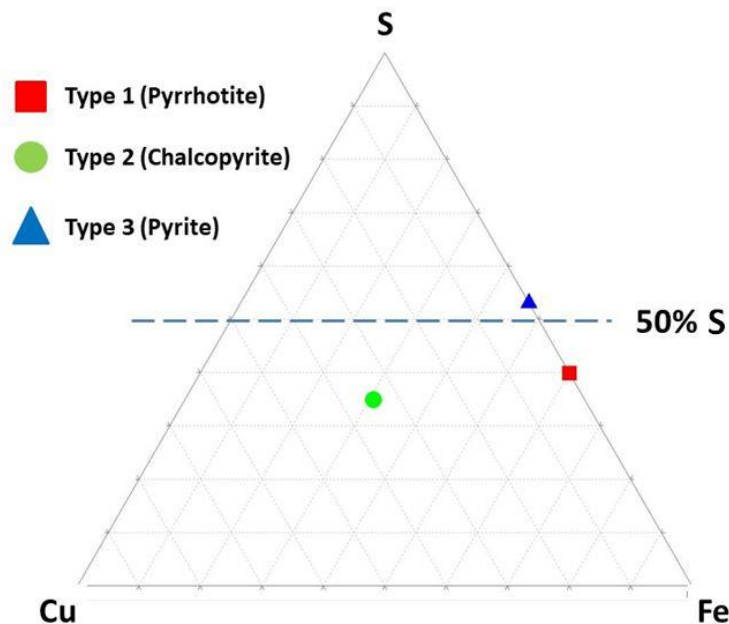


Figure 4.16. Ternary plot (atomic %) of the three types of sulphide present in the pre-experiment 'pyrrhotite' sample.

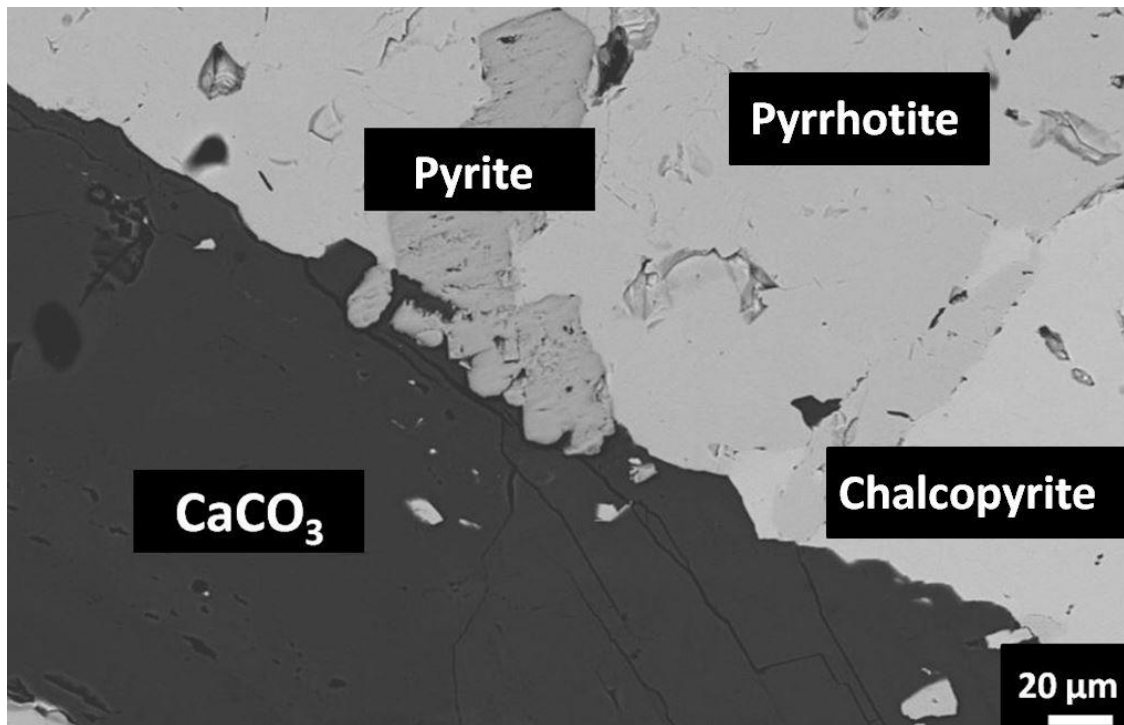


Figure 4.17. BSE SEM image of sample GLAHM 134475, pre-experiment.

The calcium carbonate impurity is the one of principal concern considering the aim of these experiments is to mimic an early Martian environment and assess carbon drawdown and mineral carbonate formation. The impurity was determined as CaCO_3 via quantitative SEM analysis (appendix 3) and occurred as veins within the pyrrhotite (Fig. 4.18).

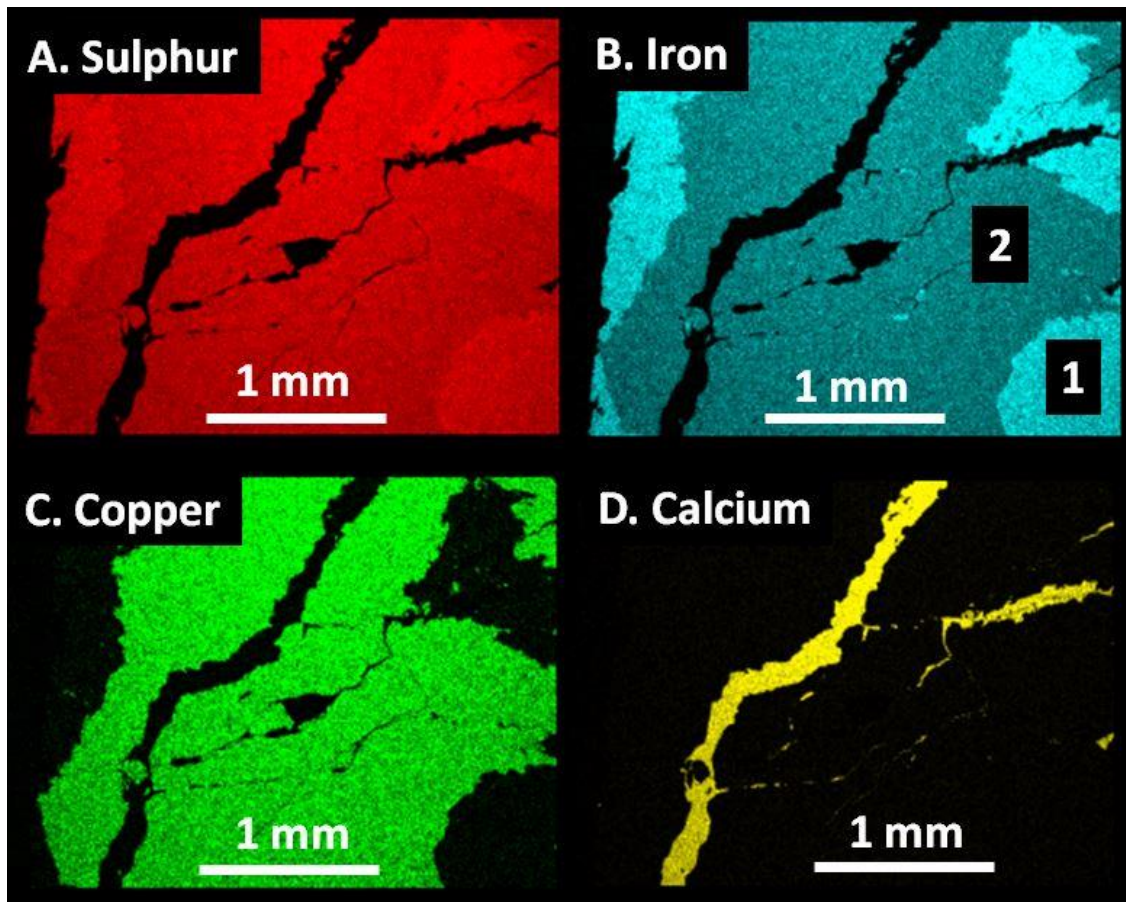


Figure 4.18. Energy-dispersive X-Ray maps of GLAHM 134475. **A – C.** Highlight the variations in S, Cu, Fe in type 1 (pyrrhotite) and type 2 (chalcopyrite). **D.** Ca distribution, displaying the CaCO_3 impurities streaking the fractures in the sample. Carbon and oxygen are not shown as they show the same distribution as Ca.

To remove the CaCO_3 impurity the pyrrhotite was crushed and sieved through an 80 mesh (~175 micron) grating, then immersed in a 10% hydrochloric acid solution for 24 hours. The sample was then cleaned with pure deionised water repeatedly until solution pH became neutral (i.e. HCl removed). The sample was then dried for 12 hours under a heat lamp. This method successfully removed the CaCO_3 , confirmed by SEM, without damaging the other minerals. A test was conducted using hydrofluoric acid, which although very successful in dissolving the calcite, also severely degraded the structure of the other minerals present, and was thus discarded as a method.

Olivine was extracted from sample GLAHM 111337 (Fig. 4.19), a coarse grained magnesian fayalite (hortonolite) dunite from the Onverwacht Mine, Lydenburg, Eastern Bushveld Complex, Mpumalanga Province, South Africa. It is part of the Onverwacht platiniferous sub vertical cylindrical pipe cutting the Rustenburg layered cumulate suite in the Proterozoic Bushveld igneous complex (Gruenewaldt, 1979).

The Bushveld complex rests on the ~3000 Ma old Kaapval craton which developed into a series of tension induced basins that later filled with volcanic and sedimentary depositional supergroups, of which the Transvaal is one (Gruenewaldt, 1979). This sedimentary infilling was punctuated by mafic plutonism with dyke and sill intrusions. The ~600 km wide Bushveld complex was one such mafic intrusion occurring after sedimentation of the Transvaal basin and during a period the basin was experiencing compression (Gruenewaldt, 1979). The Bushveld is mafic layered cumulates from which cross cutting pipes have extruded.

These pipes contain olivine, predominately of hortonolite composition with Fe rich clinopyroxenite and minor ilmenite, Ti magnetite and metal sulphides such as pyrrhotite (Viljoen & Scoon, 1985; Maier *et al.* 2012). The pipes are highly fractionated which provides the high Fe content, high specific gravity and dark colour (Viljoen & Scoon, 1985). The Onverwacht pipe is rimmed by harzburgite grading into pyroxenite and layered norites and anorthosites, however, the sample used for this experiment was the central dunite of the pipe; wehrlite pegmatites are also present in this central core but not included in the samples. The Bushveld complex is the world's largest reserve of platinum, chromium, Ni - sulfide and vanadium (Gruenewaldt, 1979). Olivine content is around Fo₅₀ and therefore provides an Fe - rich analogue for Mars olivine (Fig. 4.3).

The whole rock sample was crushed using a Retsch B2A rock crusher before single olivine grains picked out using sterilised tweezers in an attempt to reduce (as much as possible) the mica and Ti / Fe / Cr oxide impurities present (Fig. 4.19 and 4.20). Although impurities would undoubtedly remain, it was decided that this sample was appropriate to use for the experiments as its Fe content is representative of Mars (Fig. 4.3). Hortonolite thin section TSSA38 (Fig. 4.19) was

loaned from the Hunterian museum. A pre-experiment thin section was made from the uncrushed sample material.



Figure 4.19. Photograph of hortonolite dunite thin section TSSA38, part of sample GLAHM 111337, prior to being picked for olivine. Note the hydrobiotite mica (light brown) and Ti/Fe/Cr oxide (black), often ilmenite, which are the principal impurities. Full quantitative SEM analysis data for olivine and all principal impurities is available in Appendix 4.

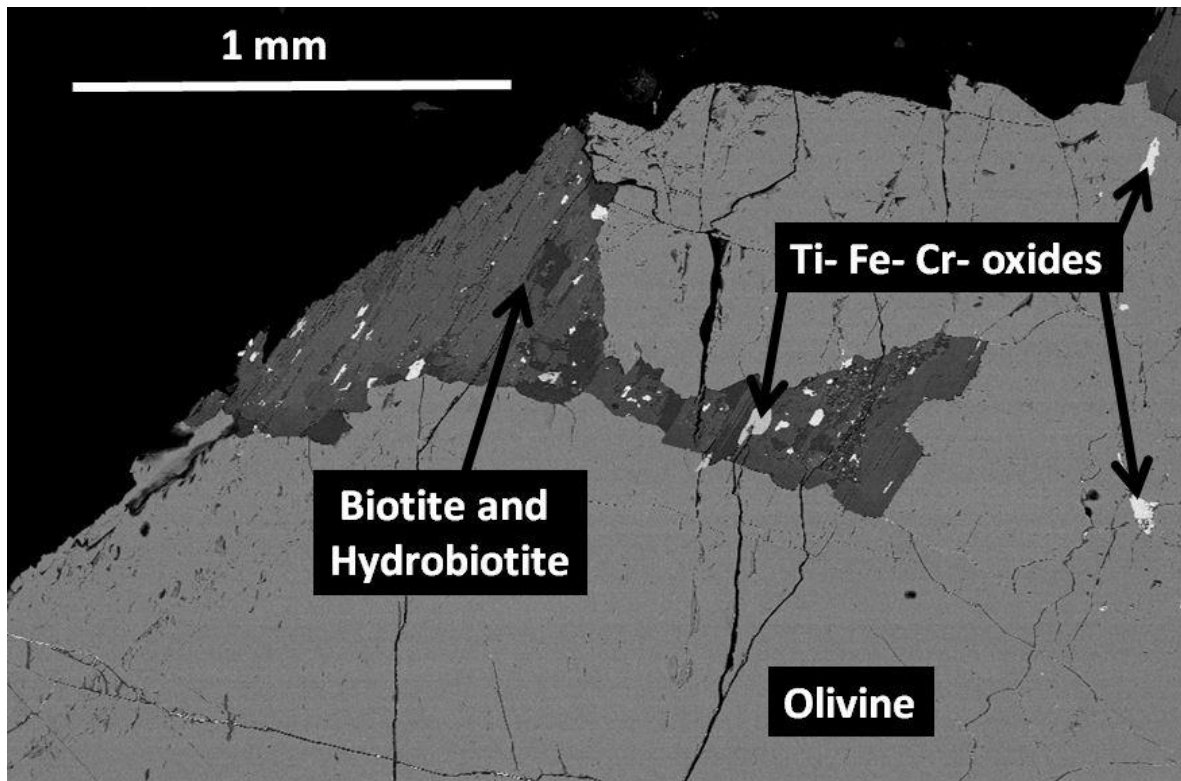


Figure 4.20. BSE SEM image of the pre-experiment uncrushed hortonolite, dominated by olivine, with biotite impurities that were later picked out as much as possible; the majority of the biotite was quantitatively analysed as aqueously altered hydrobiotite. Ti- Fe- oxides are ilmenite from quantitative analysis. From the literature it is known Cr oxide, spinel, Ni sulphide, platinum and vanadium is also present in the impurities (Viljoen & Scoon, 1985; Scoon & Mitchell, 2004; Maier *et al.* 2012), although they were not analysed in this study.

The LECO Corporation chemically analysed prepared powders (<175 micron) of the pre-experiment rock samples using a LECO SC-632 Carbon and Sulphur Determinator, quantifying whole rock carbon and sulphur concentrations (Table 4.3). Spectral analysis was at 1450°C with measurement times of 120-360 seconds per sulphur measurement and 60-360 seconds per carbon measurement. The main use of these measurements was to establish whole rock sulphur concentrations in the pyrrhotite sample; olivine and basalt results are shown to demonstrate their lack of sulphur contribution.

LECO analysis				
Basalt	Run 1	Run 2	Run 3	Average
Carbon (wt%)	0.075	0.082	0.075	0.078
Sulphur (wt%)	0.008	0.008	0.007	0.008
Mass analysed (g)	0.206	0.202	0.203	0.204
<175 micron size				
Pyrrhotite	Run 1	Run 1	Run 3	Average
Carbon (wt%)	0.017	0.016	0.018	0.017
Sulphur (wt%)	39.077	39.506	39.384	39.322
Mass analysed (g)	0.101	0.107	0.104	0.104
<175 micron size				
Olivine	Run 1	Run 2	Run 3	Average
Carbon (wt%)	0.041	0.038	0.038	0.039
Sulphur (wt%)	0.004	0.008	0.009	0.007
Mass analysed (g)	0.211	0.204	0.203	0.206
<175 micron size				

Table 4.3. LECO Corporation SC-632 analysis results for carbon and sulphur in pre-experiment rock samples.

Approximate average density of mineral reactants used:

Olivine density will vary greatly based on Fe composition.

Basalt 2.4 - 3.1 g cm³ / 2.75 g cm³ average (www.engineeringtoolbox.com)

Olivine 3.27 - 3.37 g cm³ / 3.32 g cm³ average (www.webmineral.com)

Pyrrhotite 4.58 - 4.65 g cm³ / 4.62 g cm³ average (www.mindat.org)

Chamber	Olivine (g)	Olivine (cm ³)	Basalt (g)	Basalt (cm ³)	Pyrrhotite (g)	Pyrrhotite (cm ³)	Total (g)	Total (cm ³)
1			10.014	1.8			10.014	1.8
2			5.004	0.9	5.023	0.5	10.026	1.4
3	10.039	1.5					10.039	1.5
4			10.038	1.8			10.038	1.8
5			10.033	1.8			10.033	1.8
6			5.037	0.9	5.037	0.5	10.074	1.4
7	10.001	1.5					10.001	1.5
8	10.016	1.5					10.016	1.5

Table 4.4. Substrate sample weights (g) and approximate volume (cm³) based on average density per g in each experiment chamber.

4.3.4 Quantitative SEM analysis methods.

Quantitative X-Ray microanalysis was conducted using a Carl Zeiss Sigma VP with Oxford Inca microanalysis software. Aluminium tape serves the dual purpose of securing the thin section onto the brass shuttle containing the mineral standards and allowing a conductive route for charge build up to dissipate from the thin section (Fig. 4.21). The brass shuttle was then placed in the SEM, pumped to a vacuum and the electron beam set at 80 μm aperture at 20 kV, and a probe current of 2.18 nA.

The cobalt standard was used to gain initial focus, bringing the sample to the analytical working distance of 8.5 mm from the electron gun. The track Z option was disabled at this point, and the manual focus fixed in place by use of tape, therefore focus control becomes a function of raising or lowering the sample along the Z axis.

The beam current was measured by focussing a spot within a Faraday cup (Fig. 4.21). This beam current measurement was repeated every few hours to monitor stability, as variations in beam current alter the quantitative results; a typical measurement was 580 picoamperes (pA), and it took ~60 - 90 minutes for the beam current to stabilise. Individual standards (Table 4.5), were then measured using a live time of 60 seconds and a dead time of ~50 %, thus an acquisition time of 90 seconds. The standard used was changed in some cases to be compatible with the sample to be measured i.e. calcite was used as the Ca standard on carbonates whereas wollastonite was used for the Ca standard on silicates.



Figure 4.21. Mineral standards mounted onto the brass shuttle used for quantitative calibration.

Fixed List	Standard	Method	Detection Limit (wt. %)
Na	Jadeite	Raster	0.09
Mg	Periclase	Spot	0.05
Al	Jadeite	Raster	0.06
Si	Wollastonite	Spot	0.07
S	Pyrite	Spot	0.11
K	Orthoclase	Raster	0.10
Ca	Wollastonite	Spot	0.09
Ca	Calcite	Spot	0.10
Ti	Rutile	Spot	0.15
Cr	Chromite	Spot	0.20
Mn	Rhodonite	Spot	0.20
Fe	Heamatite	Spot	0.25
Fe	Garnet	Spot	0.22
Ni	Nickel	Spot	0.23
Cu	Copper	Spot	0.14
O	Calcite	Raster	0.71

Table 4.5. Elements measured for quantitative analysis, the standard mineral and analysis method (spot or raster) used, and the element detection limit.

To calculate detection limits (Table 4.5), each standard was measured with a live time of 60 seconds. X-Ray intensity is determined by the number of pulses generated in the X-Ray detector, these pulses are caused by photons emitted from the sample. The number of counts per channel on the element peak of interest is recorded, as well as the number of counts in the background. The detection limit is then calculated via equation 4.5:

$$\text{Detection limit} = 3/m \sqrt{R_b/T_b}$$

Equation 4.5

Where m is counts per second per unit of concentration (cps/% or cps/ppm), R_b is the rate of background intensity (counts per second), T_b is the time on background (seconds). The denser the material measured, the higher the background count rate (R_b) will be, therefore the higher the detection limit. For example, chromite will have a higher background count than periclase, thus a higher, less precise detection limit.

4.3.5 Experimental sampling procedure.

1. The experimental vessels are constructed out of stainless steel (316 grade). They possess titanium inner lining, a working volumetric capacity of 450 ml and a 65 mm internal diameter. Oxidised Ti (TiO) is inert and does not react or interfere chemically with the experiment, and is therefore used as the containing vessel. All experiment vessels were specifically treated to become oxidised. Each vessel rig consists of a Ti lid (Fig. 4.22.A), a stainless steel retaining ring and the main Ti pressure casing (Fig. 4.22.B), a fluid sample tube, pressure lines, two valves and one filter (Fig. 4.22.C). All were thoroughly cleaned with 18 mΩ two stage demineralised water, and air dried, prior to the experiment commencing.



Figure 22. Components of a pressure vessel after being washed in demineralised water prior to experiment commencement. **A.** Chamber screw lids. **B.** Chamber vessels. **C.** Fluid sampling tubes, valves, filters, and the SO₂ ‘bomb’.

2. The lid for each vessel was then ‘threaded and screwed’ with the two sample tubes, one for gas inflow and the other for fluid sampling (Fig. 4.23.A). A four part filter was then attached to the sampling tube to prevent substrate particles being sucked into the fluid to be analysed (Fig. 4.24.A and B).
3. Mineral substrates were placed in the vessel and 200 ml of 18 mΩ two stage demineralised water added. The two stages of demineralisation used were reverse osmosis - filtering and ultraviolet radiation to sterilise the water.
4. Two ‘O’ rings are placed on the inner lid, then the lid was hammered into the top of the container, and the pressure cap screwed over both the lid and container.
5. Stainless steel valves with Ti needles are then screwed onto the sampling tubes (Fig. 4.23.A).
6. The N₂ and CO₂ vessels (1700, 1701, 1702, 1703, 1704, 1705 of Fig. 4.12) were pressurised to 1 bar, checked for leaks, pressurised to 1.5 bar, checked for leaks, then locked off at 2 bar. The ovens were started and set at 80 °C while the chambers were between 1 and 1.5 bar and left for 1 hour to allow for thermal expansion of gas inside the chambers before the final pressure raise to 2 bar. Any leaks were found using ‘Snoop’ (commercially available soapy water), and sealed by tightening the connectors. It is worth noting that when talking about pressure, this study is describing pressure *above atmospheric pressure*. Hence, 1 bar, 1.5 or 2 bar described above equals 2 bar, 2.5 bar or 3 bar total pressure.
7. The CO₂ with SO₂ chambers (1706, 1707) were isolated on separate gas lines and in a separate oven. A 47.5 ml (50 ml including valves) SO₂ ‘bomb’ with a valve on each end (Fig. 4.26.A) was flushed out and filled to 1 bar with ultra pure SO₂ (Fig. 4.26. B), then attached into the chamber gas line outside the oven (Fig. 4.26.C). The gas line from the bomb to the CO₂ canister was then pressurised to 1 bar, the bomb valve opened to release the SO₂ into the vessel, and then the other valve opened to flush CO₂ into the vessel until 1.6 bar was reached. The vessels were then checked for

leaks, heated to 80 °C for an hour to allow for thermal expansion, before finally being taken to 2 bar and sealed. Throughout this process a pressure gradient was maintained, ensuring all 50 ml of SO₂ was entirely pushed into the chamber. This gradient allows confidence in the later modelling of gas quantities.

The chambers were then placed in a Binder FED115 oven, on top of a HANNA magnetic stirrer base (for moving a magnetic plastic coated 'flea'), and the gas valve screwed into the appropriate gas pipeline (Fig. 4.23.A and B). 12ml fluid samples were extracted for IC/ICPMS fluid analysis at 10, 24, 51, 80 and 120 days using the sampling valves (Fig. 4.23.A). For each set of batch experiments, fluid samples were treated in the same way. This involved degassing a sample of aqueous fluid straight into a polythene syringe. After sampling, each of the reacted fluids was split into several sub-samples:

≈ 1 ml was taken for immediate analysis of pH.

≈ 1 ml was taken for immediate analysis of Eh.

≈ 1 ml was taken for analysis of carbonate/bicarbonate by titration against a known volume of known strength sulphuric acid.

The remaining fluid sample was filtered using a 0.2 µm 'Anotop'® nylon syringe filter. 5 ml of this sample was placed into a polystyrene tube and acidified with 1% v/v (0.05 ml) of concentrated 'High Purity Analytical' grade nitric acid. This solution was analysed subsequently for major and trace cations by inductively coupled plasma mass spectrometry (ICP-MS). A further 1 ml aliquot of the filtered sample was taken and placed in a polyethylene tube for analysis of anions by ion chromatography (IC). This sample was diluted to 4 ml to minimise the potential for mineral precipitation. Exactly 2.7 ml of the filtered sample was taken into a polystyrene tube, 0.3 ml of 2,2'-dipyridyl solution was added. This sample was used for the colorimetric determination of reduced iron.

The pH and Eh measurements were made as soon as possible after sampling, on cooled and depressurised samples, at laboratory temperature ($\approx 20^{\circ}\text{C}$), using an Orion VERSA STAR pH / Eh meter calibrated using NBS traceable buffers, and ZoBell's solution. All fluid samples were stored in a fridge (below 5°C) prior to analysis.

The experiment worked successfully from a practical and mechanical point of view; which is often not the case with these types of gas - fluid - mineral pressure experiments (British Geological Survey personal communication). One chamber, olivine $\text{CO}_2 + \text{SO}_2$ (1707) did leak some fluid, and dropped beneath the fluid extraction filter (Fig. 4.25), resulting in no ICPMS fluid extraction on day 80. This leaked chamber fluid was topped up for the remaining experiment period, and this problem needs consideration when interpreting the data for this specific sample.

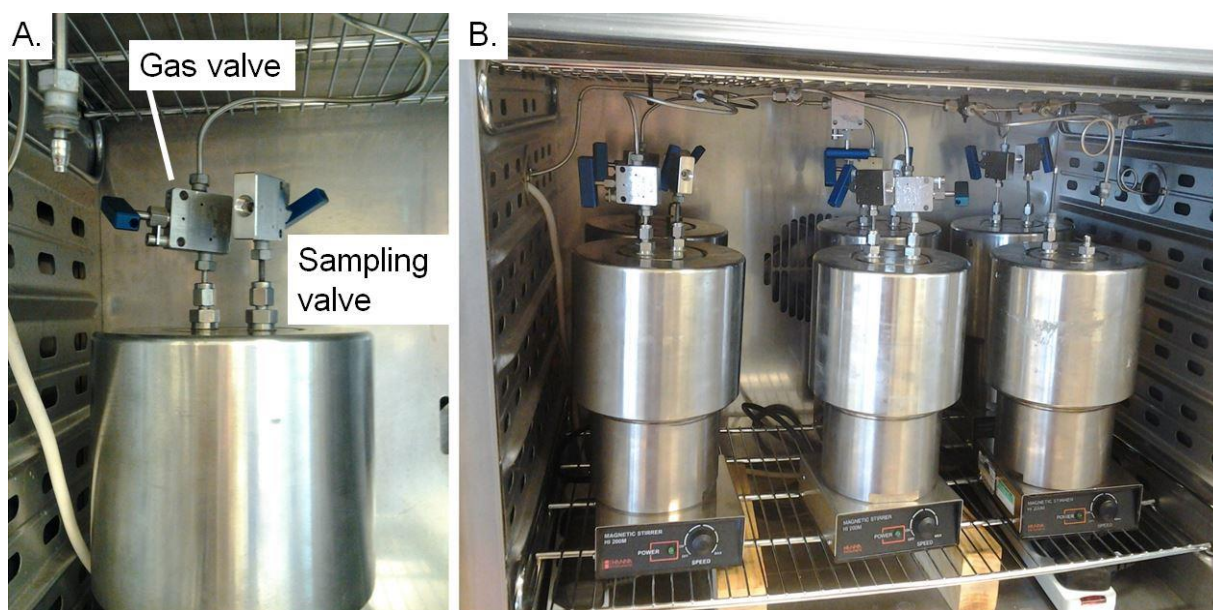


Figure 4.23. Pressure vessel rigs attached to gas pipelines, mounted on HANNA magnetic stirrer bases within a Binder FED115 oven set to 80°C .

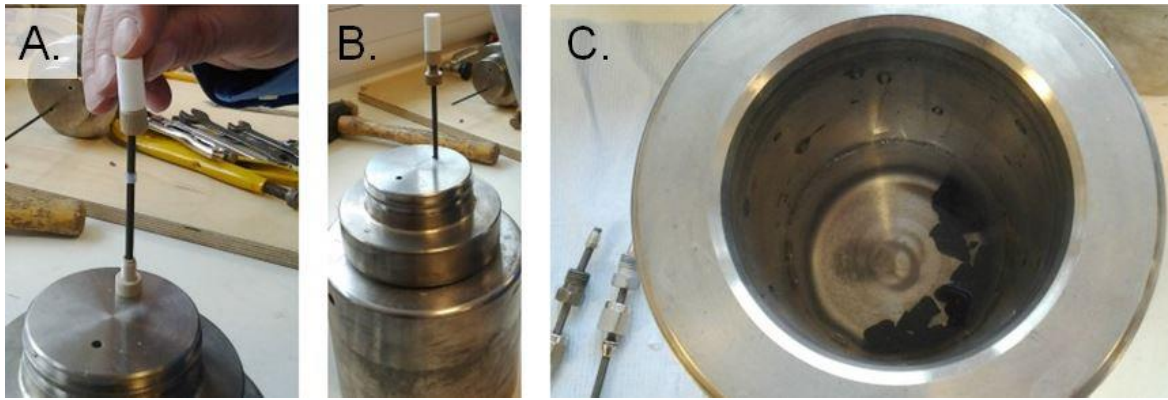


Figure 4.24. A. Attaching the filter to the fluid sampling tube. B. The chamber lid with fluid sampling tube and filter. C. 200 ml of demineralised water immersing the rock substrate inside the chamber.

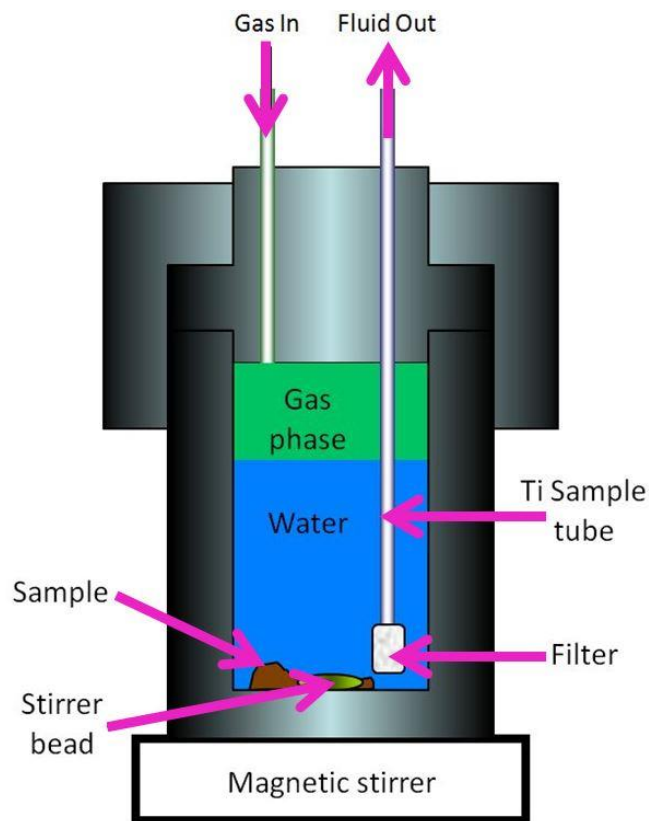


Figure 4.25. Experiment chamber setup.

The experimental setup for each vessel (Fig. 4.25) provides ~5 mm gap between the filter and vessel base. A ‘flea’ or magnetic stirrer bead is inserted

into each vessel and a timer set to magnetically activate the stirrer once every two minutes throughout the duration of the experiment.



Figure 4.26. A. The SO₂ 'bomb'. B. Filling the 'bomb' with ultra pure SO₂. C. The 'bomb' attached to the CO₂ gas line external to the oven.

The CO₂ used in this study was sourced from high purity (99.99%) liquid CO₂ (Air Products, 4.5 Grade). The N₂ used in this study was obtained from BOC Gases and classified as 'oxygen free' (99.998% pure). SO₂ high purity gas used in this study was supplied by Air Liquide UK Ltd. O₂ (99.99%) in a cylinder with a pressure of 3.3 bar. It was added directly to the experiments using a 50 ml Swagelok double-ended pressure vessel.

4.3.6 IC/ICPMS and colorimetric data.

Raw data obtained by IC (for anion analysis), ICPMS (for cation analysis) and colorimetry (for reduced Fe analysis) is not included here, due to its volume, and is instead included in appendix 5. Considerable manual processing of IC/ICPMS data was required because the 48 fluid samples used for IC/ICPMS analysis were acquired at lab pressure and temperature, not at the experimental conditions of 80 °C. This procedure affects the pH results of the IC/ICPMS, and therefore PHREEQC was used to geochemically model the results back to an 80 °C temperature.

4.3.7 Experiment CO₂ and SO₂ solubility.

CO₂ solubility in pure water at 80 °C and 2 bar is not as clearly understood as might be expected. Values can vary depending on whether the system is open or closed, and the method of measurement used, along with experimental uncertainty. This study has adopted the values and calculations presented in a study that combined ~100 experimental investigations into CO₂ - water solubility (Carroll *et al.* 1991). The solubility of a phase can be calculated using Henry's law:

"At a constant temperature, the amount of a given gas that dissolves in a given type and volume of liquid is directly proportional to the partial pressure of that gas in equilibrium with that liquid."

This statement creates a value termed Henry solubility (H), that can be expressed in a variety of forms, such as concentration solubility (H^{cp}), dimensionless solubility (H^{cc}), and the aqueous phase mixing concentration solubility (H^{cp}). The model used by Carroll *et al.* (1991) is an extension of previous

work on hydrogen sulphide solubility (Carroll and Mather, 1989) and is based on the premise that CO₂ possesses a similar solubility magnitude as H₂S (Carroll and Mather, 1989). It assumes that activity coefficients of solute and solvent are in unity, and have a negligible Poynting correction factor (PCF). PCF is an exponent used in calculating fugacity. Carroll et al. (1991) used equation 4.6 to calculate CO₂ solubility using Henry's law:

$$\ln(H_{21}/\text{MPa}) = -6.8346 + 1.2817 \times 10^4 / T - 3.7668 \times 10^6 / T^2 + 2.997 \times 10^8 / T^3$$

Equation 4.6

H₂₁ = Henry's constant, T = temperature (K)

The calculated CO₂ solubility in water at 80°C and 2 bar is 2.065 x 10⁻⁵ mol/L (0.0463 mol %) total pressure, or 2.065 x 10⁻⁵ mol/L (0.0463 mol %) partial pressure; table 4.6:

Temperature (°C)	Pressure (bars)				
	1.01	2.00	5.00	7.50	10.00
80	0.567	1.592	4.684	7.226	9.724
80	1.053	2.065	5.121		

Table 4.6. CO₂ solubility (mol/L x 10⁻⁵) in water at 80°C and 2 bar. Blue is total pressure, orange is partial pressure. *Adapted from Carroll et al. (1991).*

The 1.592 x 10⁻⁵ mol/L (0.0357 mol %) CO₂ solubility value would apply for all chambers where CO₂ is the only gas (1700, 1701, 1702, 1703, 1704, 1705). The 2.065 x 10⁻⁵ mol/L (0.0463 mol %) CO₂ solubility value would apply for all chambers where CO₂ is a partial pressure with SO₂ (1706 and 1707). CO₂ solubility and the reaction from CO₂ into HCO₃⁻ and H₂CO₃ is kinetically slow, with the

majority of CO₂ remaining as solvated molecular CO₂. CO₂ will favour particular phases dependent on pH (Fig. 4.27):

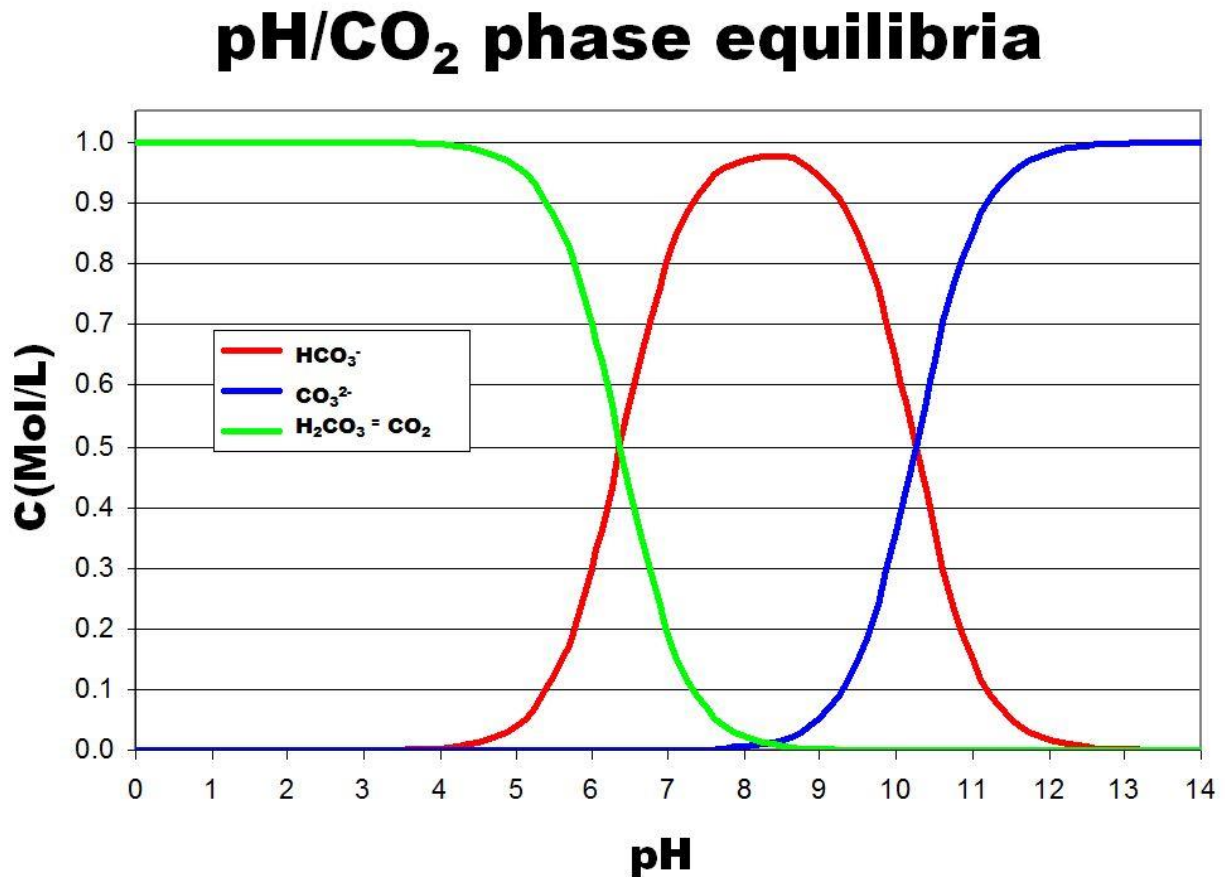


Figure 4.27. CO₂ - pH phase equilibria. *Adapted (Website 2).*

SO₂ solubility in water has been extensively studied. It is extremely soluble in water, although solubility decreases with increasing temperature (Hudson, 1925; Campbell & Maass, 1930; Rabe & Harris, 1963; Goldberg & Parker, 1985). The SO₂ dissolution process is exothermic via equation 4.7:



Equation 4.7

Solubility of SO₂ in water

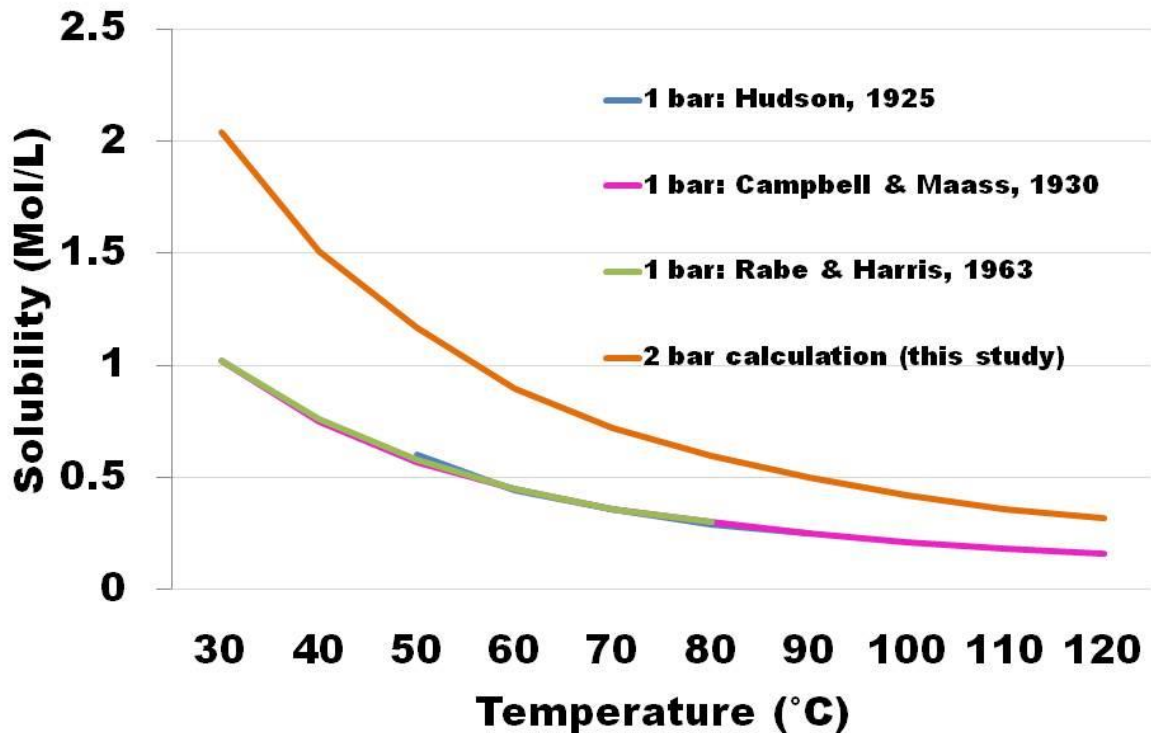


Figure 4.28. Solubility of SO₂ in water, calculated from Goldberg & Parker (1985).

SO₂ solubility in water at 2 bar pressure, 80 °C is calculated to be 0.59 mol/L (Fig. 4.28), based on averaging multiple research data (Hudson, 1925; Campbell & Maass, 1930; Rabe & Harris, 1963), converting to mol/L and adjusting it to 2 bar based on Goldberg & Parker (1985).

4.4 Results.

4.4.1 pH.

The change in pH with temperature is called the solution temperature coefficient (pH/°C). For example, if a solution has a temperature coefficient of -0.035 [pH/°C], the pH decreases 0.035 units for every 1°C increase in temperature. Usually the temperature coefficient must be determined empirically.

pH (*pondus hydrogenii or potential of hydrogen*) is usually measured on a *logarithmic scale* between 0 to 14. Although pH is often described as the *concentration* of hydrogen ions (H⁺) in solution, for experimental solutions (such as in this study) pH is the measurement of the *activity*, rather than the concentration, of H⁺ in a solution, therefore expressed on a *thermodynamic scale* of 0 to 14 defined by equation 4.8:

$$\text{pH} = -\log a \{\text{H}^+\}$$

Equation 4.8

Where $a \{\text{H}^+\}$ is the activity of the hydrogen ions. Due to the difficulty in measuring activity directly, however, the International Union of Pure and Applied Chemistry (IUPAC) and the National Bureau of Standards (NBS) uses standards in the calculation, and defines pH by equation 4.9:

$$\text{pH} = (F(E - E_{\text{standard}}) / RT \ln 10) + \text{pH}_{\text{standard}}$$

Equation 4.9

Where R is the ideal gas constant (R = 8.3145 J/mol·K)

F is Faraday's constant (F = 96 485.33289 C/mol)

T is absolute temperature in Kelvin (K)

E is the electromotive force (see below)

As shown in equations 4.8 and 4.9, the pH of a solution depends upon (and is meaningless without) the sample temperature at the point of pH measurement. Therefore, when comparing pH values between samples, the samples must either be at the same temperature, or else the pH values converted using a solution temperature compensation to the usual reference temperature of 25°. Most modern pH measurements use an inbuilt automatic temperature compensation (ATC) by use of the Nernst equation (see below) when providing readings.

Unfortunately, this experiment did not have automated correction available; and raw pH data was acquired at a laboratory temperature of 20°C (Fig. 4.29). Therefore, manual corrections have been calculated to correct the pH values to the experiment sample temperature of 80°C. An understanding of the Nernst equation, which in turn relies on the Gibbs free energy equation and the electromotive force equation, is therefore pertinent and described in equations 4.10 to 4.14.

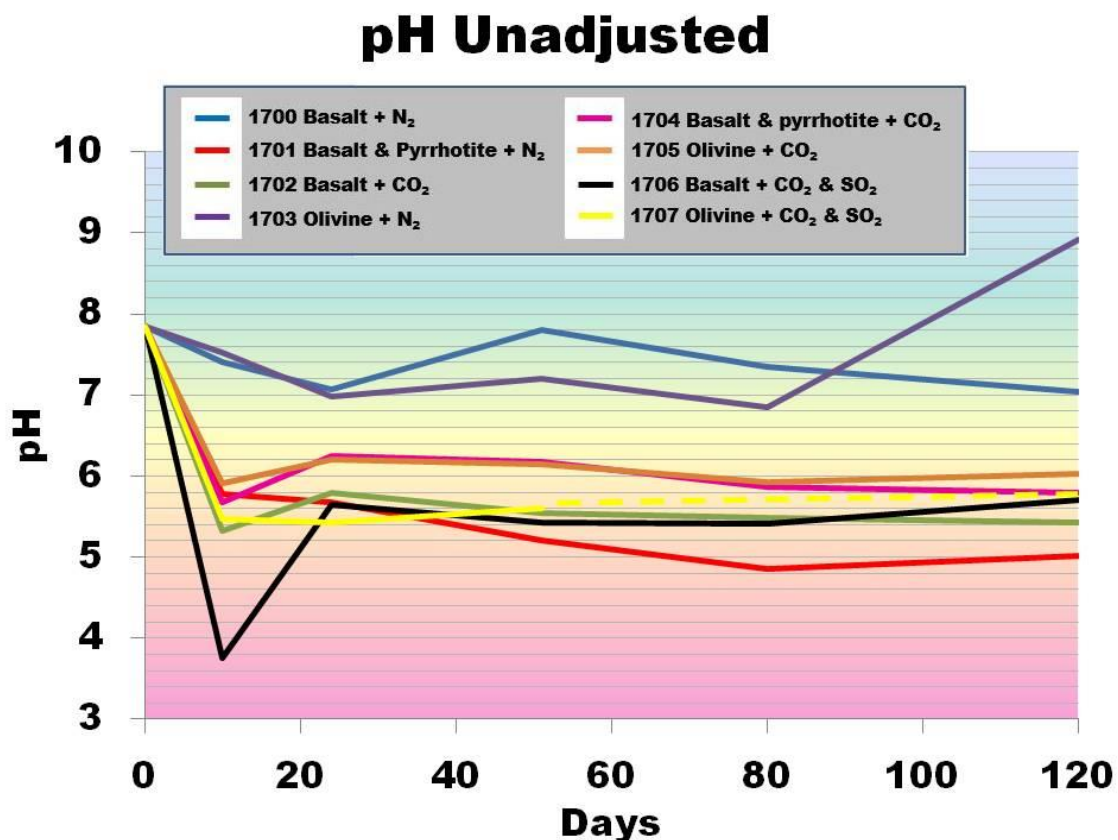


Figure 4.29. Experiment results for chamber fluid pH evolution over 120 days at 20°C, prior to PHREEQC geochemical model adjustment.

The movement of charged particles, for example H^+ , creates a potential energy difference, the maximum of which is called the electromotive force (E), with the maximum electric work (W) attainable defined by equation 4.10:

$$W = q \Delta E$$

Equation 4.10

Where q is charge Coulomb (C)

ΔE is the potential electromotive force in Volt (J/C)

The negative value of W , above, is called the Gibbs free energy (ΔG), described by equation 4.11:

$$\Delta G = -W$$

Equation 4.11

Or, as equation 4.7 illustrated, and expressed in equation 4.12:

$$\Delta G = - q \Delta E$$

Equation 4.12

As shown in equation 4.9, each mole of electrons has a charge equal to the Faraday constant (F), therefore, during a redox reaction which will employ a fixed number of reactants and products, the number (n) of electrons used in such a reaction will be correlated with the amount of charge (q) as described by equation 4.13:

$$q = n F$$

Equation 4.13

Exchanging this into equation 4.12 provides the Gibbs free energy equation described by equation 4.14:

$$\Delta G = - n F \Delta E$$

Equation 4.14

Under standard conditions it can be described by equation 4.15:

$$\Delta G^\circ = - n F \Delta E^\circ$$

Equation 4.15

Combining elements of the above equations allows us to calculate the correct pH value for a given temperature by using the Nernst equation described in equation 4.16:

$$E = E^\circ - (RT/n F) \ln Q$$

Equation 4.16

Where E° = standard electrochemical cell potential (voltage)

R = ideal gas constant

T = temperature

n = moles of electrons

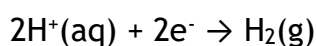
F = Faraday constant = 96,485 C mol⁻¹

Q = mass-action expression (approximated by the equilibrium expression)

For an ideal electrode at 80°C the Nernst slope is 70.07 mV/pH.

Before beginning the pH conversions, a further calculation was required, as the BGS supplied the oxidation/reduction (redox) potential values in E_h (oxidation potential) and E_h standard hydrogen electrode (SHE), whereas PHREEQC (the geochemical modelling package used to calculate the pH adjustments) requires pE

(reduction potential) values. E_h and pE effectively say the same thing about a system but from different perspectives. The temperature used in these calculations was 20°C, and the E_h (SHE) value was used in the calculation rather than E_h . E_h (SHE) is a standard reference of 0.0 mV half cell potential. The half cell for hydrogen is described by equation 4.17:



Equation 4.17

Silver chloride or saturated calomel (SCE) were not available for the experiment, but may have provided a more reliable pH value. E_h can be determined from pE via equation 4.18, and pE from E_h via equation 4.19:

$$E_h \text{ (mV)} = (2.303RT/F) \cdot pE$$

Equation 4.18

$$pE = E_h \text{ (mV)} \cdot F / 2.303RT$$

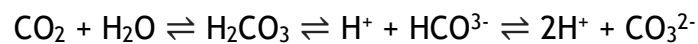
Equation 4.19

Once measured E_h was converted into pE for all fluid extraction samples, pH was modelled using PHREEQC.3, initially using the PHREEQC.dat database by applying the SOLUTION function to input individual elements (Ca, Mg, Na, K, P, S, Si, Ba, Sr, Mn, NO_2^- , NO_3^- , Fe, B, Li, Al, Cu, Zn, Cd, Pb) with the fixed system parameters of temperature at 20°C, density of 1 and water mass of 0.2 litres.

The initial conversion models gave pH changes of ~0.4 of a pH unit at 80°C than at 20°C. Although small changes in temperature can slightly affect pH, a change this large implied the PHREEQC default database was at fault. The database was changed to LNLL database, which allows many more individual elements, all of which had been measured in the experiment (Ag, Al, As, B, Ba, Br^- , Ca, Cd, Ce, Cl^- , Co, Cr, Cs, Cu, Dy, Er, Eu, Fe^{2+} , Fe^{3+} , Ga, Gd, HCO_3^- , Hf, Ho, Page | 337

HPO₄⁻², K, La, Li, Lu, Mg, Mn, Mo, Na, Nd, Ni, NO⁻², NO⁻³, Pb, Pr, Rb, Sb, Se, Si, Sm, Sn, Sr, Tb, Th, Ti, Tl, Tm, U, V, W, Y, Yb, Zn, Zr, S). The change of database provided a pH adjustment for temperature small enough to the original to be deemed a good approximation of the actual fluid system (Fig. 4.30).

PHREEQC.3 requires a number of selections to be made in any database. For the models used in this analysis it was decided to select total S values, which negates SO₄⁻² as an individual input, but accounting for the S within SO₄⁻². The same rationale applied in selecting total P, and not including HPO₄⁻² as an individual input, and total Fe, rather than Fe²⁺ and Fe³⁺ individually. Total inorganic carbon (TIC) was entered simply as C; TIC includes carbon dioxide, carbonic acids, bicarbonate and carbonate concentrations. The TIC values are calculated as a function of pH via equation 4.20:



Equation 4.20

Where the value of an element or molecule was below the ICPMS detection limit, the lower detection limit value was entered. This inevitably introduces an unavoidable minor error to the model, yet this was chosen because many important minor elements beneath the ICPMS limit will be present in the fluid. The negative aspect of applying this rule to the model is that elements such as S in the N₂ basalt control are unlikely to be at the detection limit of 4 mg l⁻¹, further, the lower detection limit is different for the various elements, which can further introduce an artificial bias to the application. Nonetheless, the inclusion of the elements beneath the IC/ICPMS detection is deemed important enough to take the action described above.

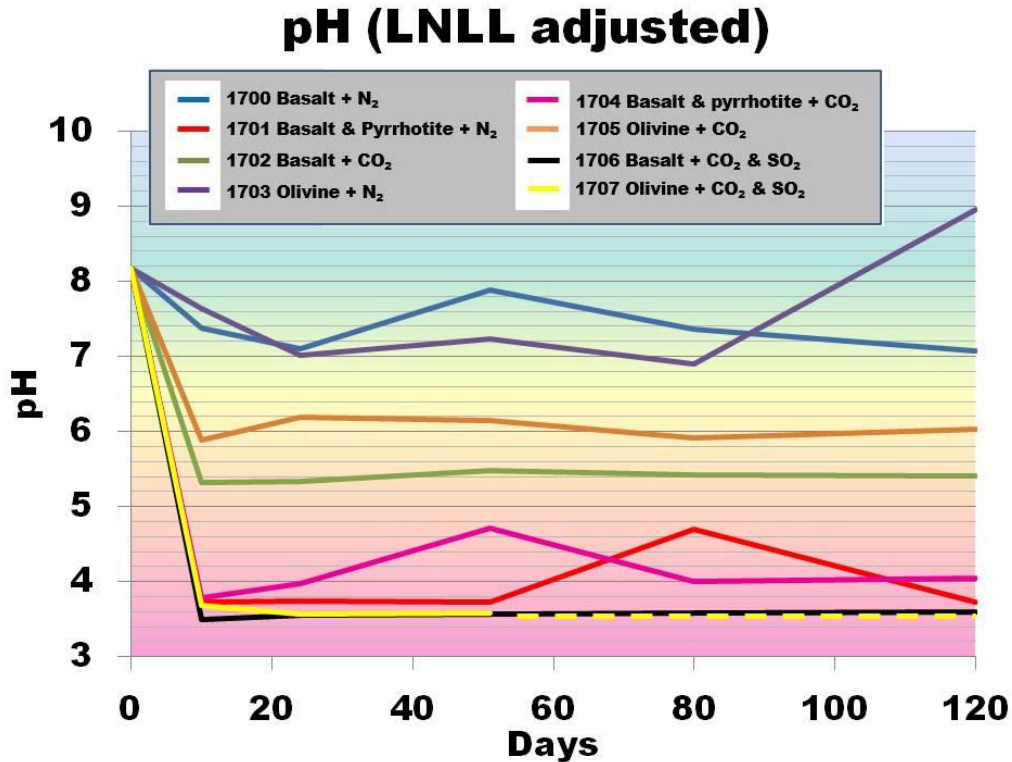


Figure 4.30. Experiment results for chamber fluid pH evolution over time at 80 °C, adjusted using PHREEQC.3 geochemical modelling.

Summary of pH results.

- pH values stay largely stable for individual chambers after 10 days, with the exception of **1703** after 80 days.
- Basalt with N₂, and olivine with N₂ (**1700**, **1703**), possess the most neutral pH ~7.5 and change little from the initial pH of the demineralised water.
- Basalt with CO₂, and olivine with CO₂ (**1702**, **1705**), display stable pH ~5.5 to 6 respectively.
- Chambers containing pyrrhotite (**1701**, **1704**) initially drop to pH ~3.5 followed by a rise to pH ~4.8 before returning to ~3.5. These 3.5 to 4.8 to 3.5 steps occur over ~51 days for both samples. The CO₂ containing chamber (**1704**) initiates this pH step change ~40 days before the N₂ (**1701**).
- Chambers with SO₂ gas (**1706**, **1707**) have the lowest pH of ~3.5.

4.4.2 Fluid chemistry.



Figure 4.31. The colour key used consistently throughout this study and as applied for the fluid chemistry graphs.

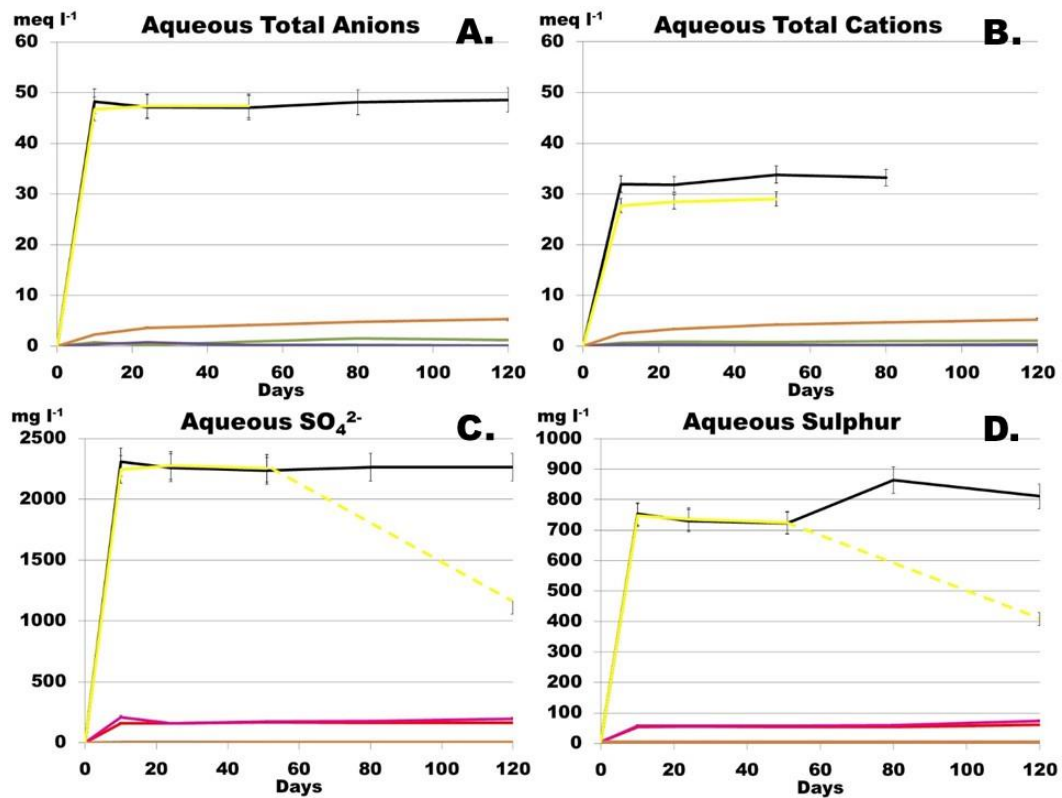


Figure 4.32. IC (for anions), ICPMS (for cations), colorimetric (for reduced Fe), titration (for bicarbonate) fluid chemistry results for all experiment chambers (continued....)

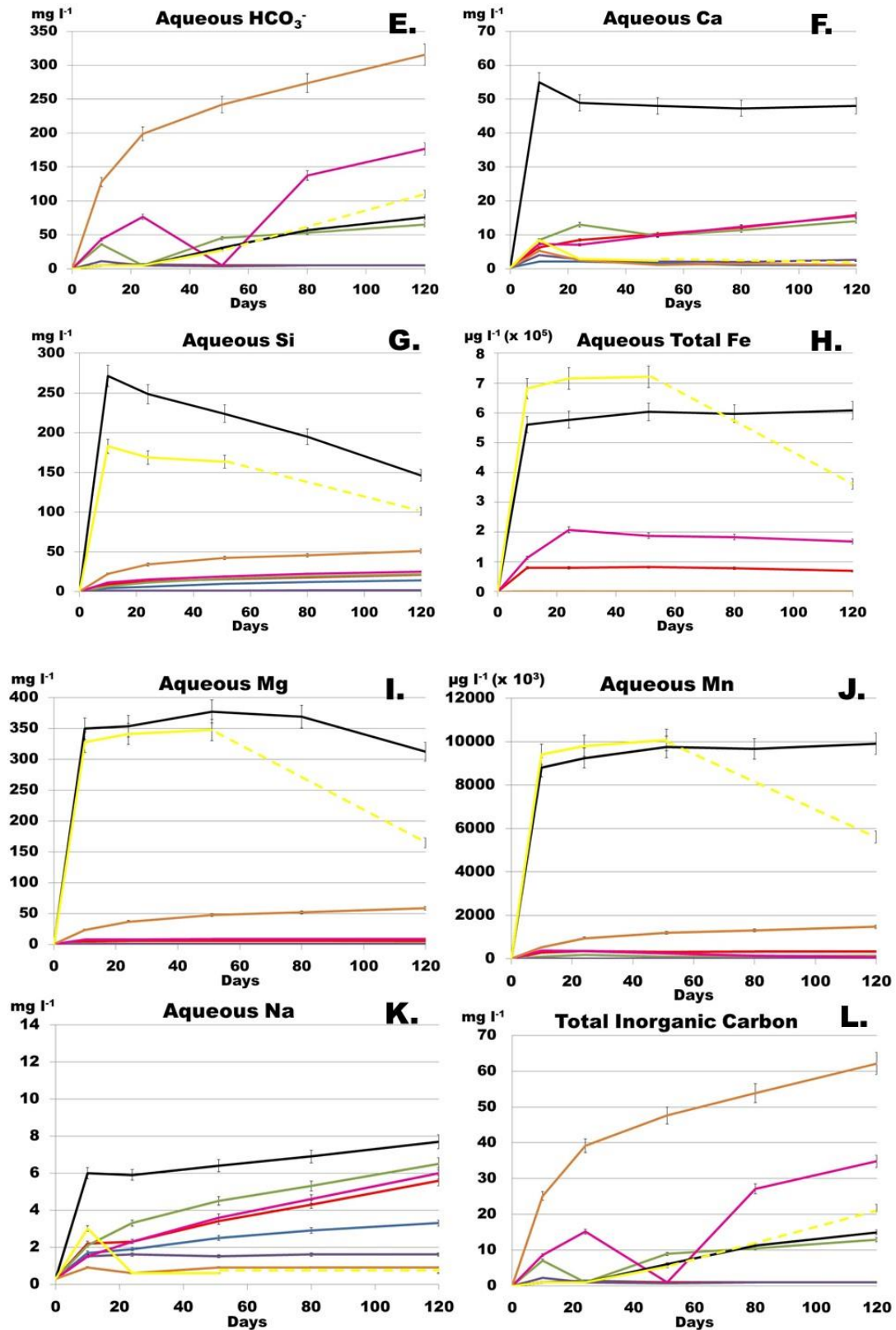


Figure 4.32 (continued). IC (for anions), ICPMS (for cations), colorimetric (for reduced Fe), titration (for bicarbonate) fluid chemistry results for all experiment chambers

Summary of fluid chemistry results.

- **Anion and cation release (Fig. 4.32.A. and 4.32.B).**
 - Basalt with CO₂ (1706), and SO₂, and olivine with CO₂ and SO₂ (1707), release the highest concentrations of anions and cations to the fluid by a significant margin (~48 and ~30 meq l⁻¹ respectively).
 - Basalt with CO₂ (1702), and olivine with CO₂ (1705), release low concentrations of anions and cations (~1 and ~5 meq l⁻¹ respectively).
 - Samples in chambers with either pyrrhotite and/or N₂ release virtually no anions or cations into the fluid.
 - Sulphur in gas form (SO₂) is highly correlated with mineral cation and anion release. Sulphur in mineral form (pyrrhotite) is not correlated with cation and anion release.
- **SO₄²⁻ and sulphur (Fig. 4.32.C. and 4.32.D).**
 - Basalt with CO₂ and SO₂ (1706), or olivine with CO₂ and SO₂ (1707), release by far the most SO₄²⁻ and S into the fluid (~2250 and ~750 mg l⁻¹ respectively). After 51 days S rises to ~850, then declines to ~800 mg l⁻¹ for 1706 (with basalt), whereas a sharp decline occurs to ~400 mg l⁻¹ for 1707 (with olivine). This dynamic is mirrored for SO₄²⁻ after 51 days, with SO₄²⁻ in 1707 (with olivine) dropping to ~1200 mg l⁻¹ although without any SO₄²⁻ change in 1706 (with basalt).
 - Basalt and pyrrhotite with N₂ (1700), and basalt and pyrrhotite with CO₂ (1704), peak at ~200 mg l⁻¹ for SO₄²⁻, and ~70 mg l⁻¹ for S, the remain fairly constant throughout the experiment.
 - Samples in chambers without either pyrrhotite or SO₂ in them contain negligible aqueous SO₄²⁻ and S.
 - Including SO₂ in the experiments correlates with increased fluid sulphur far more than including pyrrhotite does.

- **Bicarbonate (HCO_3^-) and Ca (Fig. 4.32.E).**

- Olivine with CO_2 (1705), provides the largest release of HCO_3^- by a significant amount, with a negative exponential curve reaching $\sim 320 \text{ mg l}^{-1}$ by 120 days.
- Basalt and pyrrhotite with CO_2 (1704) also display a consistent increase in aqueous bicarbonate, reaching $\sim 180 \text{ mg l}^{-1}$ by 120 days, possibly with a reaction (or data error) occurring at ~ 51 days.
- Basalt with CO_2 (1702), basalt with CO_2 and SO_2 (1706) and olivine with CO_2 and SO_2 (1707), all shared approximately similar dynamics of a slow and steady increase of aqueous bicarbonate beginning ~ 24 days in and reaching $\sim 60\text{-}110 \text{ mg l}^{-1}$ by 120 days.
- All chambers with N_2 released negligible bicarbonate (1700, 1701, 1703).

- **Ca (Fig. 4.32.F).**

- Basalt with CO_2 and SO_2 (1706) released the most aqueous Ca by a significant amount, stabilising $\sim 50 \text{ mg l}^{-1}$ after ~ 24 days.
- All other chambers have a slight spike in Ca $\sim 8 \text{ mg l}^{-1}$ after 10 days, then all chambers with only CO_2 i.e. basalt and pyrrhotite with N_2 (1701), basalt with CO_2 (1702), basalt and pyrrhotite with CO_2 (1704), increase in aqueous Ca, reaching $\sim 15 \text{ mg l}^{-1}$ by 120 days. In comparison, all other chambers decrease and remain negligible i.e. basalt with N_2 (1700), olivine with N_2 (1703), olivine with CO_2 (1705), olivine with CO_2 and SO_2 (1707).

- **Si, Fe, Mg, Mn (Fig. 4.32.G, 4.32.H, 4.32.I, 4.32.J).**
 - Basalt with CO₂ and SO₂ (1706), and olivine with CO₂ and SO₂ (1707), release the most aqueous elements by a significant amount. The graphs for Si, Fe, Mg, Mn, all show the same proportional trends between the chambers, despite differing Y axis scales.
 - Olivine with CO₂ (1705) is the next, after 1706 and 1707, in order of aqueous element abundance for Si, Mg, Mn, although ~5 - 8 times less than (1706) (1707) levels.
 - For Fe abundance, chambers with pyrrhotite (1701, 1704) show ~1 and 2 μg l⁻¹ respectively after ~24 days, compared to ~6 μg l⁻¹ for 1706 and ~7 μg l⁻¹ for 1707 (although this declines rapidly after 51 days).
 - All other chambers displayed low to negligible aqueous abundance in these elements.

- **Na (Fig. 4.32.K).**
 - The basalt bearing chambers (1700, 1701, 1702, 1704, 1706) display a higher concentration of Na in solution than the olivine bearing chambers.
 - Basalt with CO₂ and SO₂ (1706) liberates greater concentrations of Na than basalt with only CO₂ (1702), and both are greater than when N₂ is used.
 - Chambers with pyrrhotite do not appear to correlate with increased abundance of Na in solution, whereas chambers with SO₂ show some correlation.

- **Inorganic carbon (Fig. 4.32.L).**

- Olivine with CO₂ (**1705**) displays the highest aqueous inorganic carbon abundance, peaking on a negative exponential curve ~62 mg l⁻¹ after 120 days.
- Basalt and pyrrhotite with CO₂ (**1704**) displays a lesser negative exponential rise throughout the experiment (compared to **1705**) peaking at ~35 mg l⁻¹ after 120 days, although with a major drop followed by recovery at 51 days, which may be either a mineral reaction or a data error.
- Basalt with CO₂ and SO₂ (**1706**), olivine with CO₂ and SO₂ (**1707**), basalt with CO₂ (**1702**), all display similar slow increases to ~15 - 20 mg l⁻¹ after 120 days.
- All chambers with N₂ (**1700**, **1701**, **1703**) display negligible aqueous organic carbon throughout.

4.4.3 Saturation indices.









	1700 Basalt + N₂		1704 Basalt & pyrrhotite + CO₂
	1701 Basalt & Pyrrhotite + N₂		1705 Olivine + CO₂
	1702 Basalt + CO₂		1706 Basalt + CO₂ & SO₂
	1703 Olivine + N₂		1707 Olivine + CO₂ & SO₂

Figure 4.33. The colour key used consistently throughout this study and as applied for the saturation indices data (Fig. 4.34).

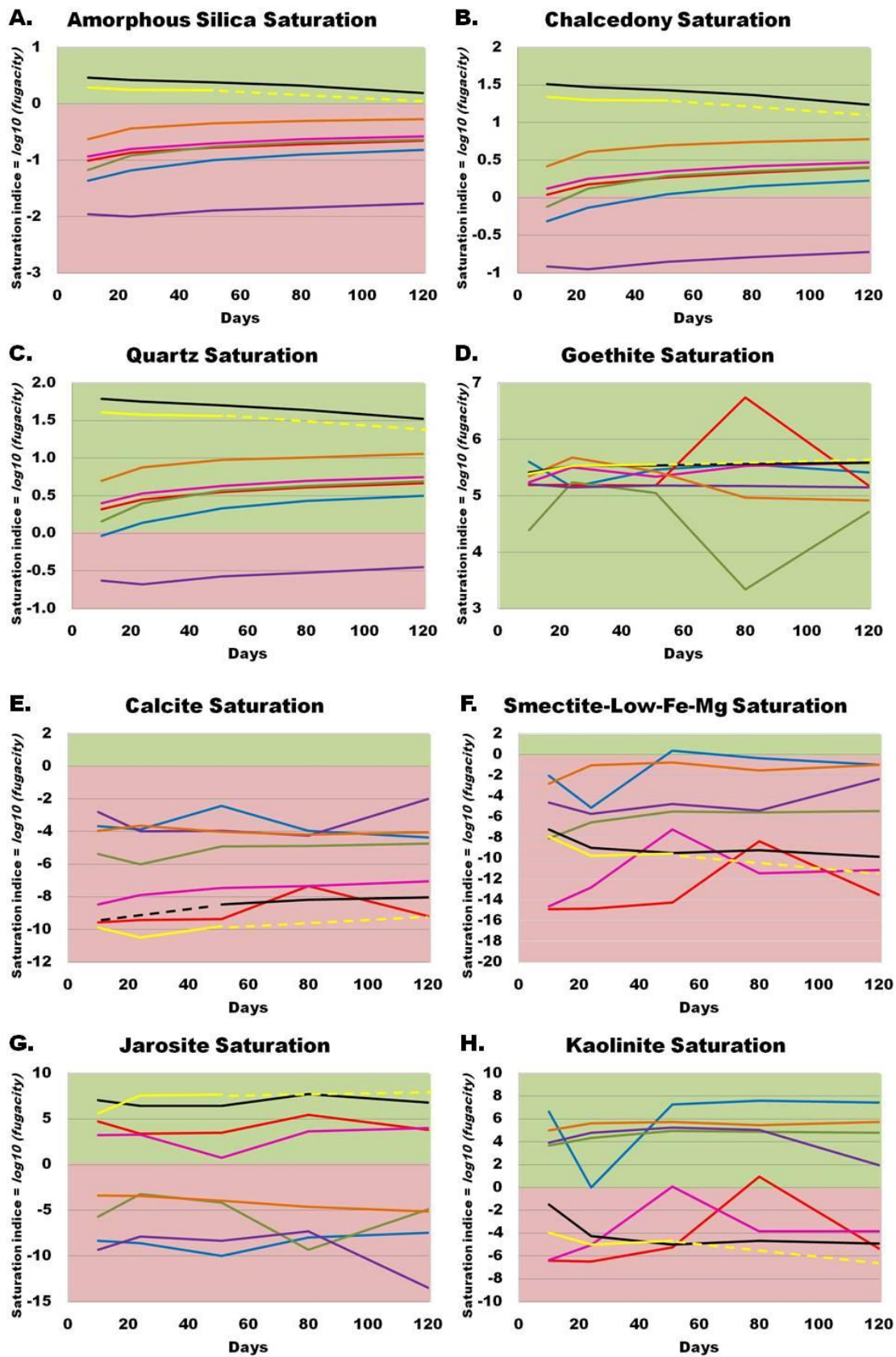


Figure 4.34. Saturation indices PHREEQC modelled from IC/ICPMS data. Pink = Undersaturated. Green = Super-saturated.

Saturation indices were calculated via PHREEQC modelling, the same models compiled for adjusting experiment Ph/temperature results. A separate PHREEQC model was run for each chamber, at each ICPMS fluid extraction point (39 instead of 40 extractions/models in total due to one failed extraction).

It is important to note that just because a mineral is modelled to be oversaturated by PHREEQC, it does not mean it is precipitating in the chamber. PHREEQC modelling produces a long list of all possible minerals that could potentially precipitate based the starting water element concentrations. This long potential mineral list varies depending on the PHREEQC database chosen.

For this experiment the LNLL database was selected primarily because it keeps the pH modelling error to a minimum, compared to the .dat database, as discussed in 4.5.1. The Lawrence Livermore National Laboratory (LLNL) database was originally compiled for EQ3/6nr as part of the USA program for radioactive waste disposal and was then adopted by Geochemist's Workbench and PHREEQC due to its comprehensive nature. LNLL version 3.3.3 was used in this study. On minerals such as nontronite, montmorillonite and saponite, the LNLL database displayed Ca, Cs, K, Mg, and Na varieties for montmorillonite, and Ca, Cs, H, K, Mg, and Na varieties for nontronite and saponite. Only Ca varieties were selected to be graphed, as all varieties (apart from Cs) displayed extremely similar saturation values throughout the models. Both high and low Fe - Mg smectite varieties were modelled as they displayed notably different values, although only low Fe - Mg smectite saturation is included in figure 4.34.

The eight minerals plotted in the graphs were selected from the longer possible list due to them being the most reasonable and likely to be precipitated in a serpentinisation and carbonate precipitation environment such as this one. Consideration of the minerals to be selected for graphing was also based on whether the mineral was commonly cited in the literature (Martian or terrestrial) on carbonation and CO₂ drawdown. A more expanded version of the mineral saturation data that was explored can be found in Appendix 6.

Important minerals in the serpentinisation and carbonation process that have not been shown in this chapter but are contained in the Appendix 6 include

brucite and saponite. These minerals were consistently undersaturated between -4 to -14 and -2 to -27 \log_{10} fugacity (f) respectively throughout the experiments and thus not thought to have precipitated at all. One exception here is olivine with N₂ (1703), which increases sharply in saturation with respect to both brucite and saponite between 80 to 120 days. Saponite may precipitate by 120 days for 1703. Hematite was only included in the appendix as the results were similar in pattern as for goethite, although hematite \log_{10} f averaged ~11 to 12 instead of 5 to 6 as for goethite. Gypsum is in the appendix but assumed to have not precipitated, remaining beneath -1 \log_{10} f for all chambers. Magnesite and dolomite are also only in the appendix as they matched calcite data so closely it was unneeded repetition to include them all in the chapter data, hence only calcite is included. Quartz is left in the appendix as, although it was modelled to precipitate, it models almost identically to chalcedony which seemed the more likely silica precipitant. High Fe - Mg smectite is only in the appendix, with all chambers plotting beneath saturation, although possessing a similar pattern as low Mg - Fe smectite, shown in this chapter, which modelled potential precipitation for basalt with N₂ (1700) at 51 days. Finally, montmorillonite ((Na,Ca)_{0,3}(Al,Mg)₂Si₄O₁₀(OH)₂•n(H₂O)) is also only in the appendix as it plotted in a very similar way to kaolinite (Al₂Si₂O₅(OH)₄), which is unsurprising, as they are relatively similar phyllosilicate clays.

For each experiment chamber there was also a control IC/ICPMS reading and a saturation model based on standard 18 mΩ two stage demineralised water chemistry.

Summary of saturation indices.

- Goethite (and hematite in appendix 6) remain oversaturated in all chambers by 10 and 5 $\log_{10} f$ respectively, throughout the experiment.
- Jarosite is above saturation for both chambers containing pyrrhotite (1701, 1704) and for chambers with SO_2 as a gas component (1706, 1707).
- Saponite is only above saturation fleetingly for olivine with N_2 (1703).
- Carbonates (calcite, magnesite, dolomite) all remain beneath the saturation point by at least $-2 \log_{10} f$ for all chambers throughout the experiment. Siderite (in appendix 6) remains beneath saturation, between -4 and $-14 \log_{10} f$.
- Amorphous silica can precipitate in chambers containing SO_2 as a gas component (1706, 1707) on a declining trend, but remains beneath saturation for all others, albeit on rising saturation values.
- Chalcedony has a similar pattern to amorphous silica but with higher saturation values. Chambers containing SO_2 as a gas component (1706, 1707) are the most oversaturated ~ 1.5 declining over time to $\sim 1 \log_{10} f$. Most other chambers are also saturated with respect to chalcedony, with rising data curves. Chambers with N_2 display the least saturation.
- Kaolinite (and monmorillonite in appendix 6) display a very clear dynamic where chambers with either SO_2 or pyrrhotite (1701, 1704, 1706, 1707) remain beneath saturation whereas all other chambers are above saturation. Smectite is not modelled to be oversaturated, apart from fleetingly for basalt with N_2 (1700) at 51 days.

4.4.4 Mineral surface alterations.

See appendix 4 for detailed quantitative mineral analysis. All samples discussed in this section are post experiment, placed in epoxy resin, thin sectioned, and polished. Samples analysed by SEM were carbon coated, while Raman samples were not.

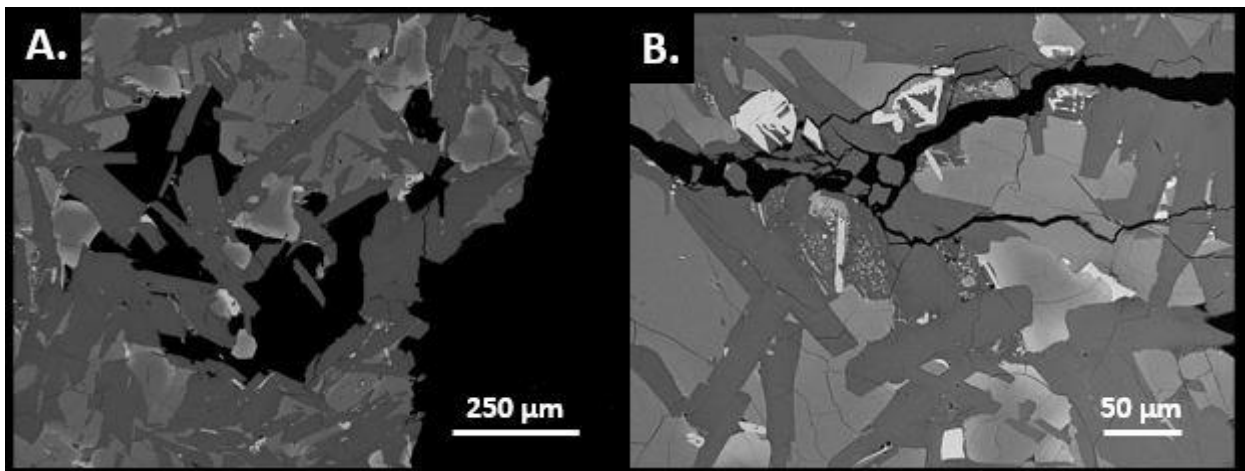


Figure 4.35. SEM BSE images of basalt after 120 days of reaction with N₂ (1700). Neither primary mineral dissolution or secondary mineral precipitation was observed either on

A. rock sample edges and cavities or

B. rock fractures. Bright white minerals are metal oxides/pseudobrookite, medium grey minerals are pyroxene (augite) and dark grey minerals are plagioclase (andesine).

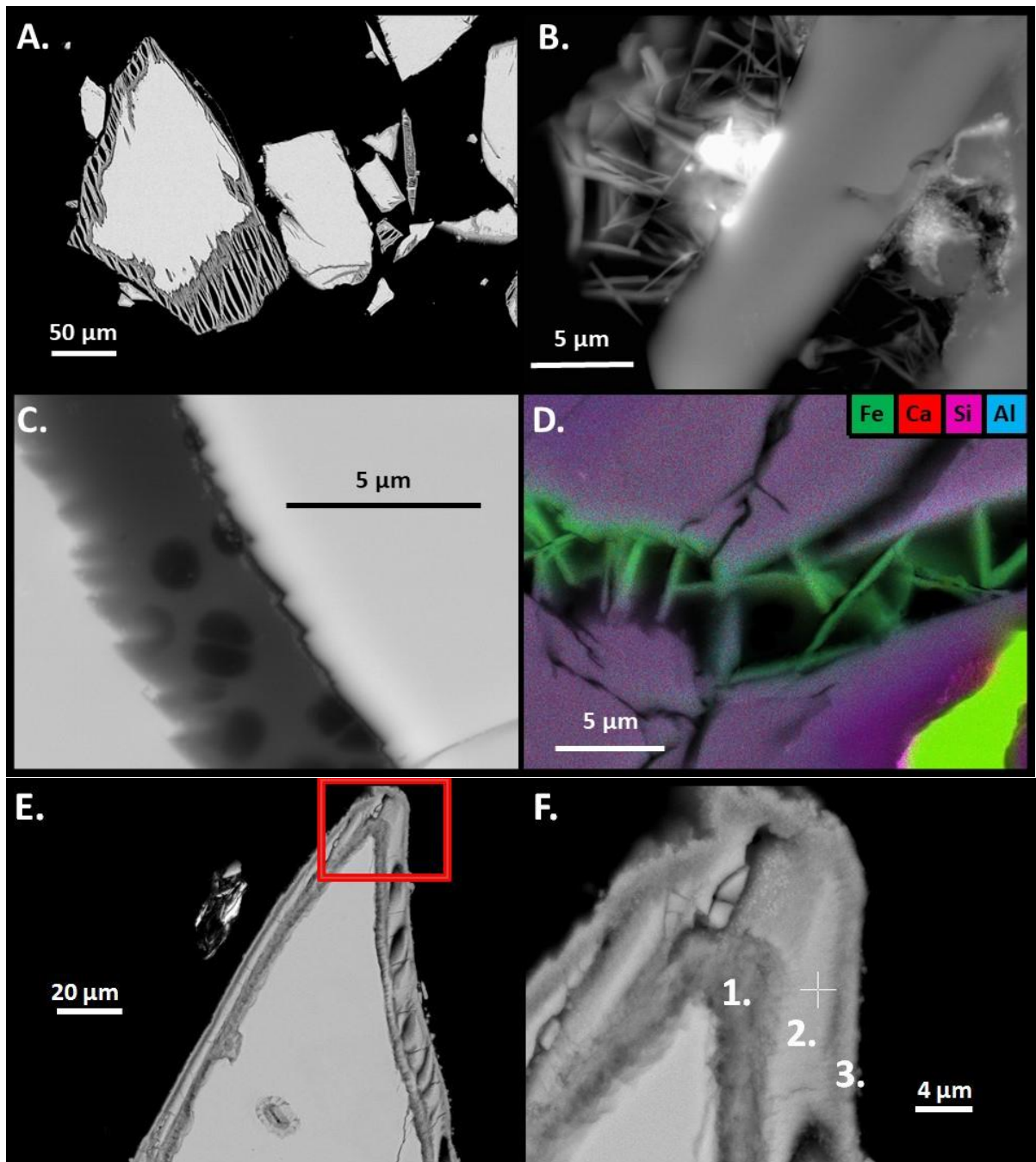


Figure 4.36. Basalt and pyrrhotite with N₂ (1701) after 120 days of reaction.

A. Type 1 pyrrhotite displaying an alteration rim where iron has leached from the edges leaving a sulphur dominated, low Fe mineral rim. **B.** Acicular iron rich secondary mineral product too small to analyse on the SEM attached to a grain of Bytownite plagioclase. Semi quantitatively the light grain is nearly all iron and probably hematite. **C.** Fracture within olivine displaying serrated edges that all have the same angle of serration. **D.** The iron rich flakes similar to those in B. filling a mineral fracture. **E.** An alteration rim on a grain of pyrrhotite. The

alteration is less advanced than in A. Alteration can also be observed in the central portion of the grain, following a diagonal line of weakness. **F.** Magnified view of the red square in E. Three distinct bands of alteration can be observed, two of which were identified in Raman analysis (Fig. 4.40. Fig. 4.41).

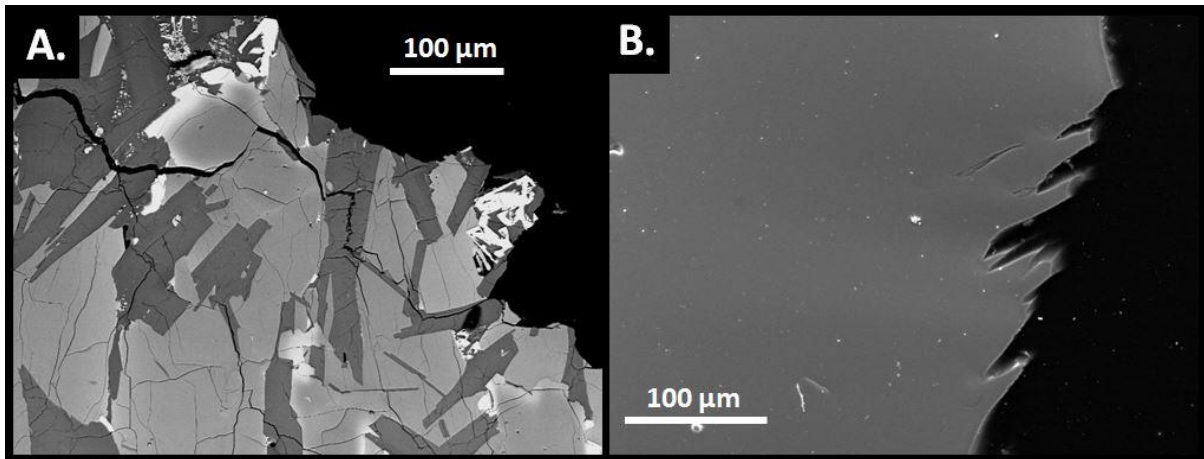


Figure 4.37. Basalt after 120 days of reaction with CO₂ (1702).

A. BSE SEM image of an unaltered post-experiment basalt.

B. SE SEM image of plagioclase (bytownite) displaying grain boundary dissolution but no secondary mineral precipitation.

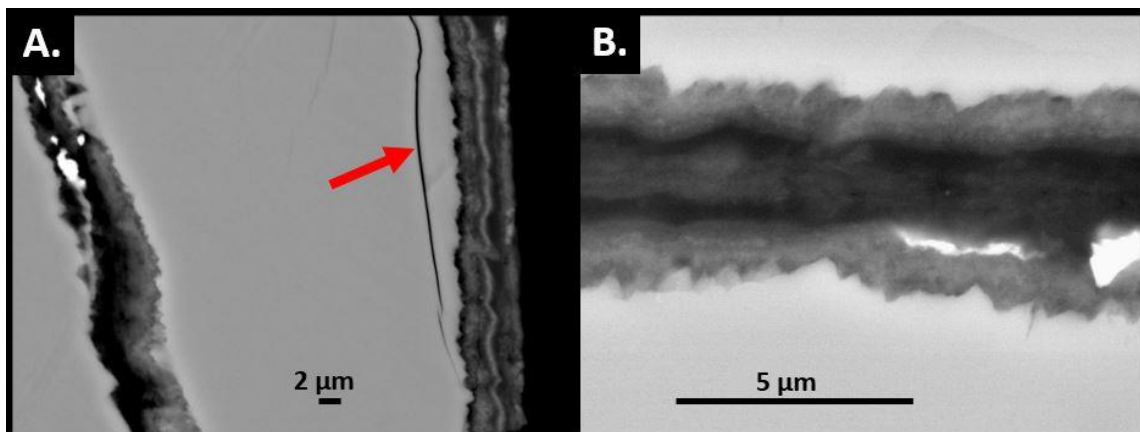


Figure 4.38. BSE SEM images of olivine with N₂ (1703) after 120 days of reaction.

A. Pre-experiment alteration on the outer edge of an olivine grain. This is half of an alteration vein which are usually semi-symmetrical in alteration deposit pattern and must have sheared from being a line of weakness. Note the lack of alteration in the smaller fresh fracture (red arrow). **B.** Semi-symmetrical pre-experiment alteration in an olivine fracture.

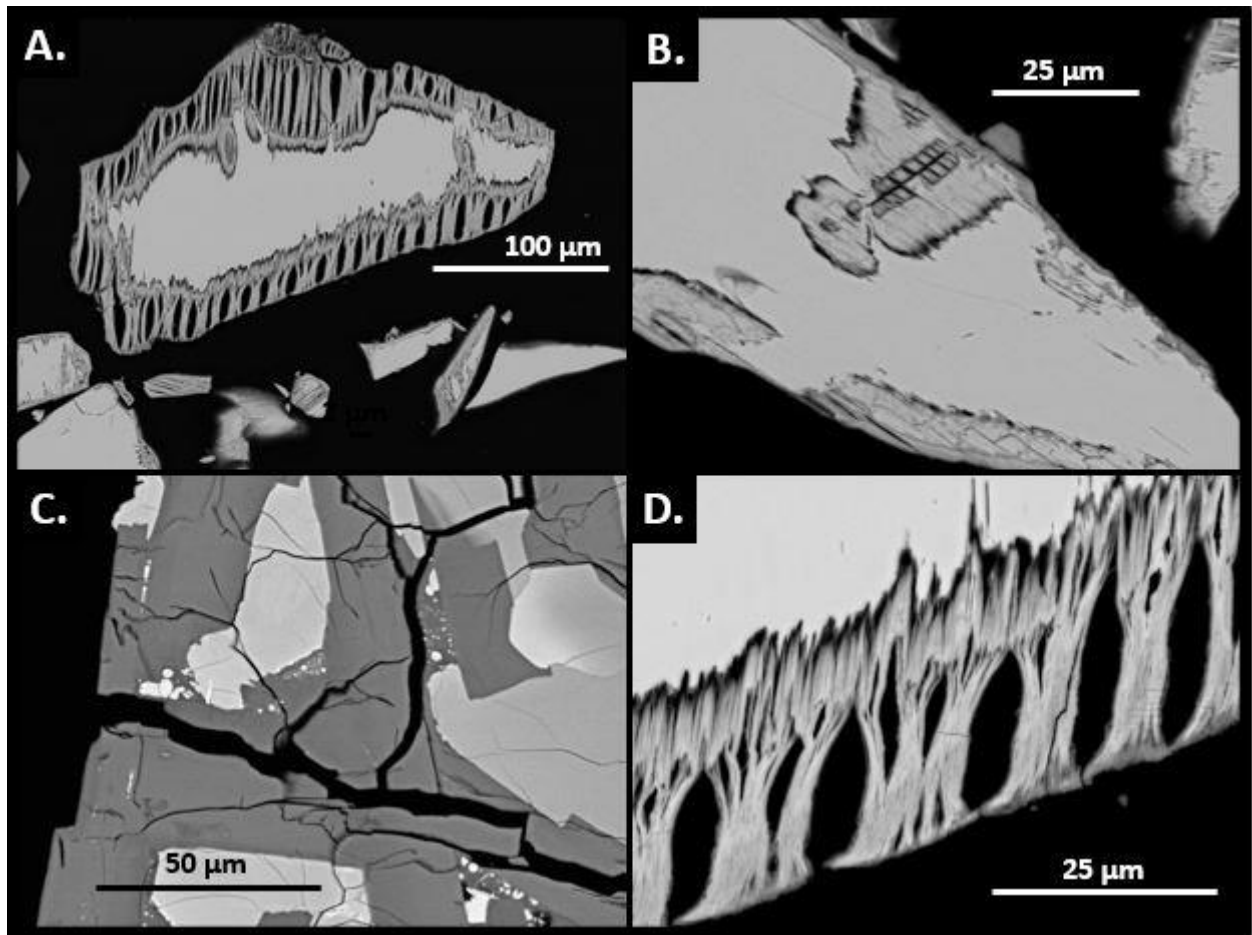


Figure 4.39. BSE SEM images of basalt and pyrrhotite after 120 days of reaction with CO₂ (1704).

A. A grain of pyrrhotite displaying a well-developed alteration rim.

B. Early stages of the same alteration observed in A. This pyrrhotite alteration can be observed in many stages of progression in the numerous grains studied, and the alteration beginning to divide the grain in B. can proceed along the line of weakness until the grain is divided.

C. Fractured and unaltered basalt.

D. Type 1 pyrrhotite (see appendix 4) displaying an alteration rim where iron has leached from the edges leaving a sulphur dominated mineral (Fig. 40, Fig. 41).

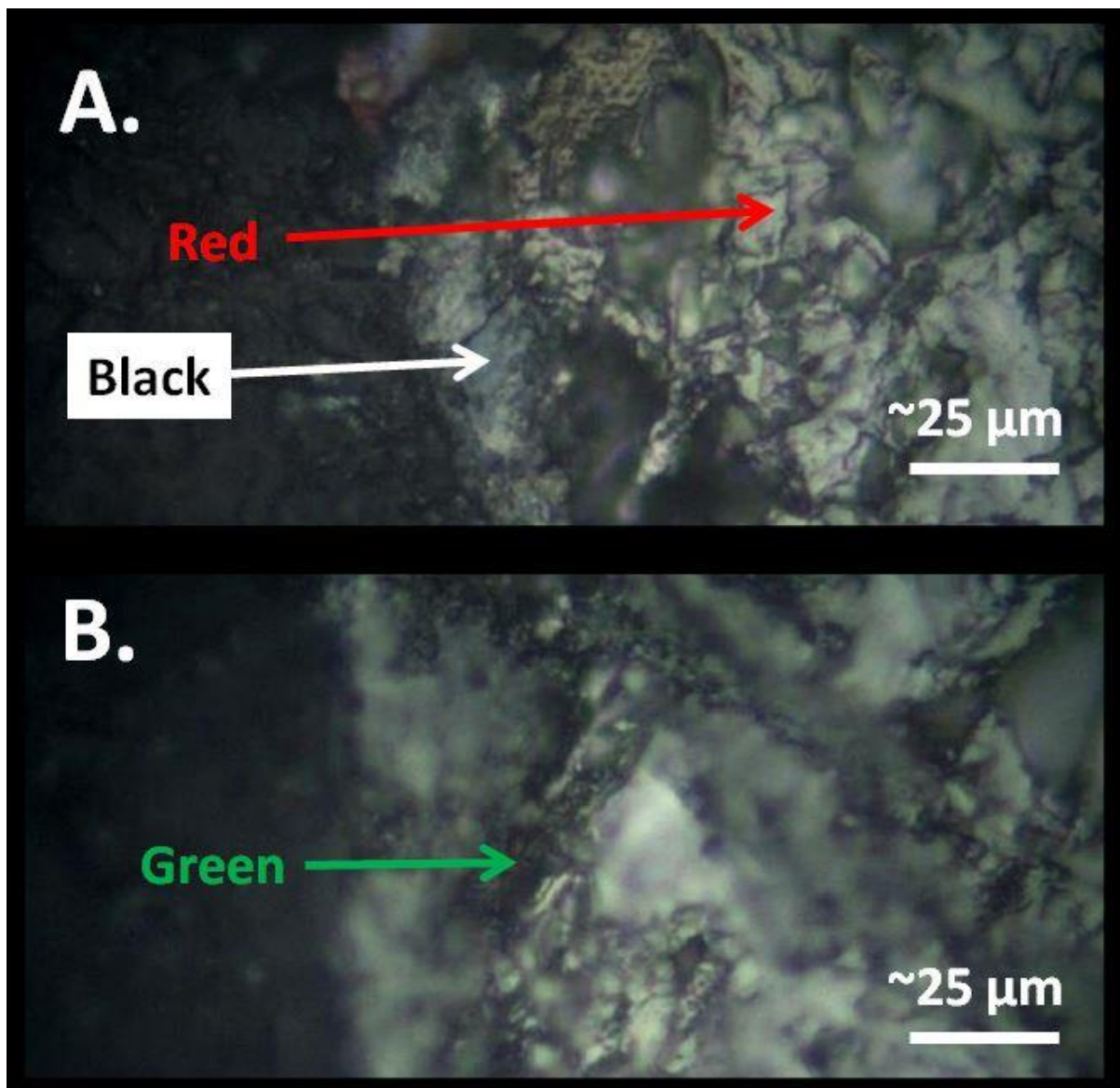


Figure 4.40. Pyrrhotite grain from 1704 with alteration rim under Raman light microscopy. **A.** Locations of the red and black spectra displayed in Figure 41. **B.** Locations of the green spectra displayed in Figure 41.

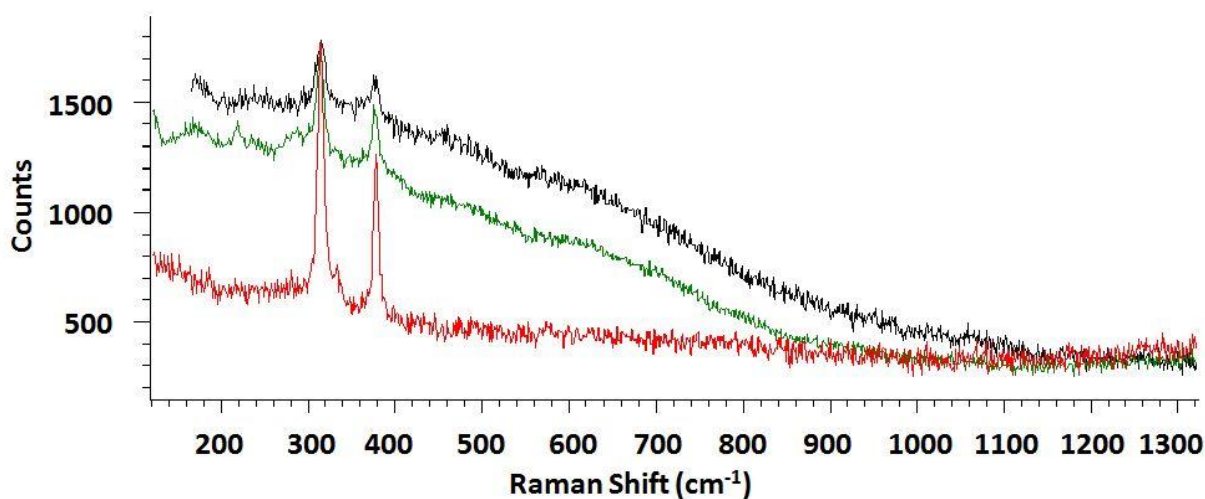


Figure 41. Raman spectroscopy with the red, green and black spectra correlating with the positions in figure 40. Exposure time 1 second, laser power 1 %, 10 accumulations per spectra, 785 nm edge laser, 1200 l/mm (633/780) static grating.

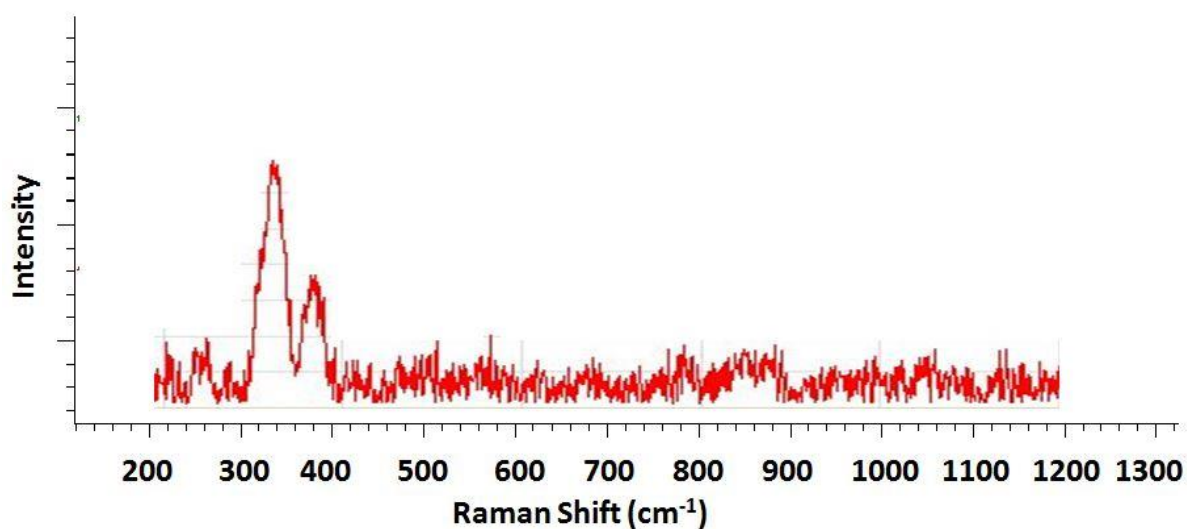


Figure 42. Ideal unoriented Raman spectra for pyrrhotite using a 780 grating, from the RRUFF database, ID R060440.

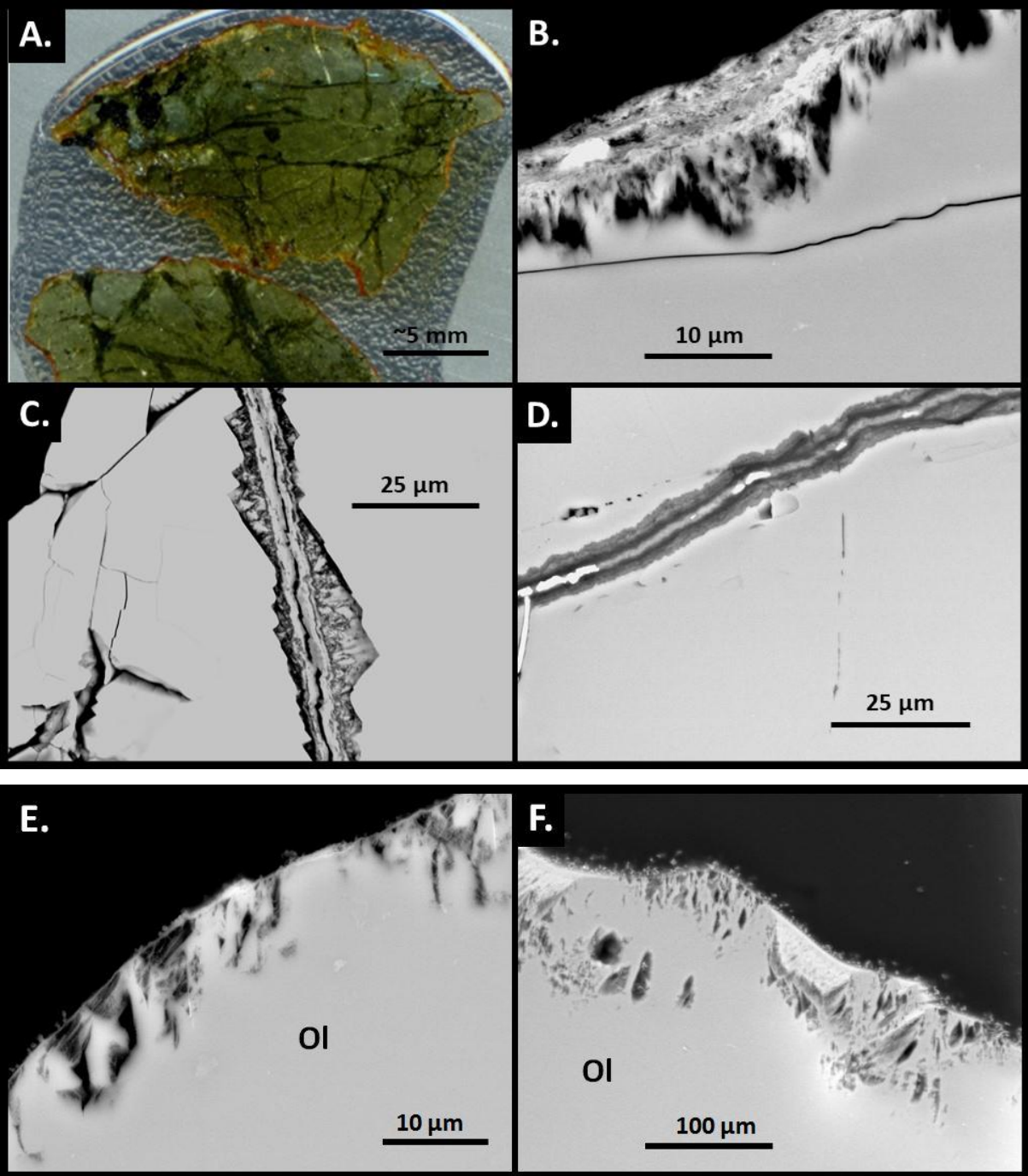


Figure 4.43. Olivine after 120 days of reaction with CO₂ (1705).

A. Post experiment thin section displaying an orange iron oxide rim visible to the naked eye.

B. BSE SEM image of the iron oxide rim on an olivine grain that also shows dissolution on its edge.

C. BSE SEM image of pre-experiment alteration in an olivine fracture, predominately phyllosilicate/kaolinite.

D. BSE SEM image of pre-experiment alteration in an olivine fracture, showing phyllosilicates but also clumps of pure iron oxide (white), see Quantitative SEM appendix, it is probably a wustite where some Fe²⁺ has become Fe³⁺.

E. F. BSE SEM images of initial (E.) and more advanced (F.) grain edge dissolution and Fe deposition.

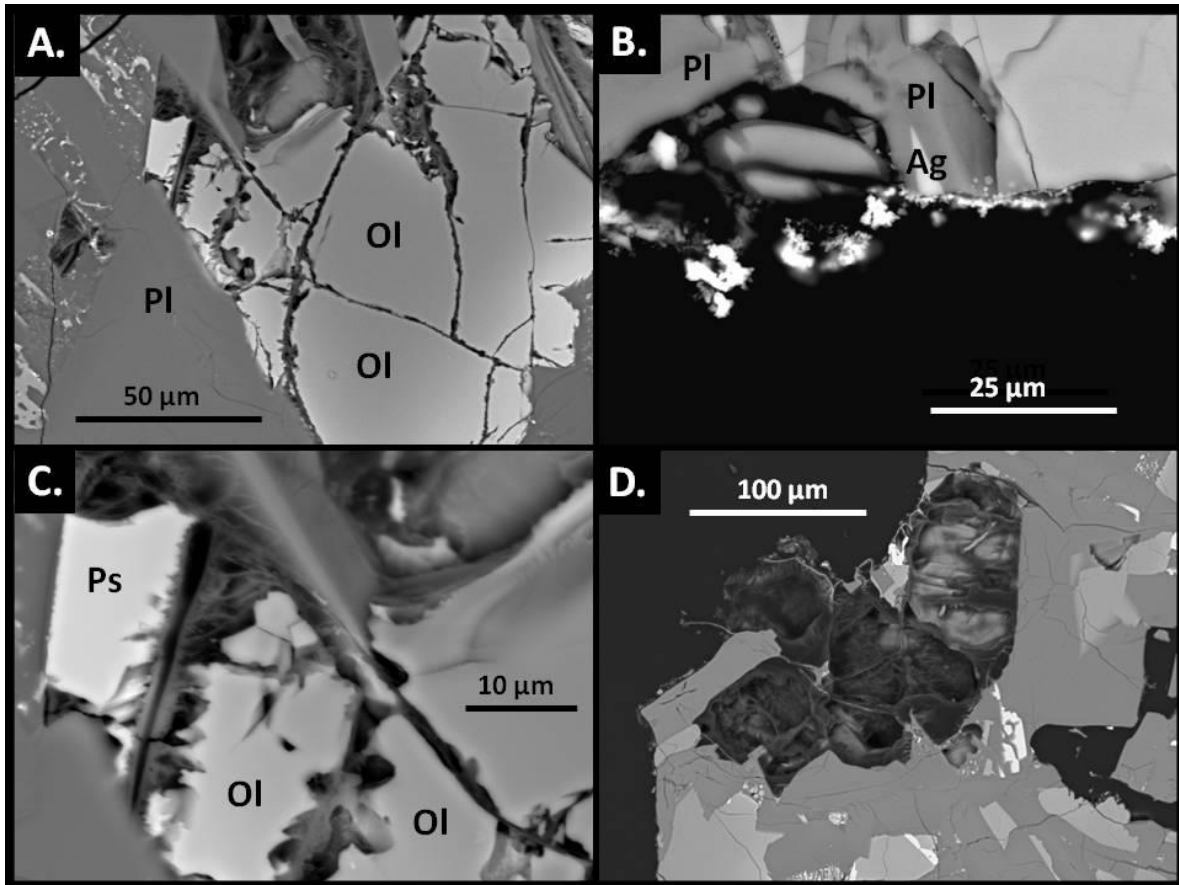


Figure 4.44. Basalt with CO₂ and SO₂ (1706) after 120 days of reaction. Ol = Olivine. Pl = Plagioclase Ag = Augite Ps = pseudobrookite.

A. Olivine showing serrated dissolution within fractures.

B. Altered chalcopyrite crystals very close to valleriite precipitating on the edge of a basalt surface.

C. Serrated dissolution in an olivine grain. Note how olivine reacts much more than the adjacent pseudobrookite.

D. A relic mineral grain, probably olivine, that has either dissolved fully, or fell out during the experiment and thin section preparing process. Note that the former Si-Fe dominated fractures that were filled with secondary mineral precipitant remain.

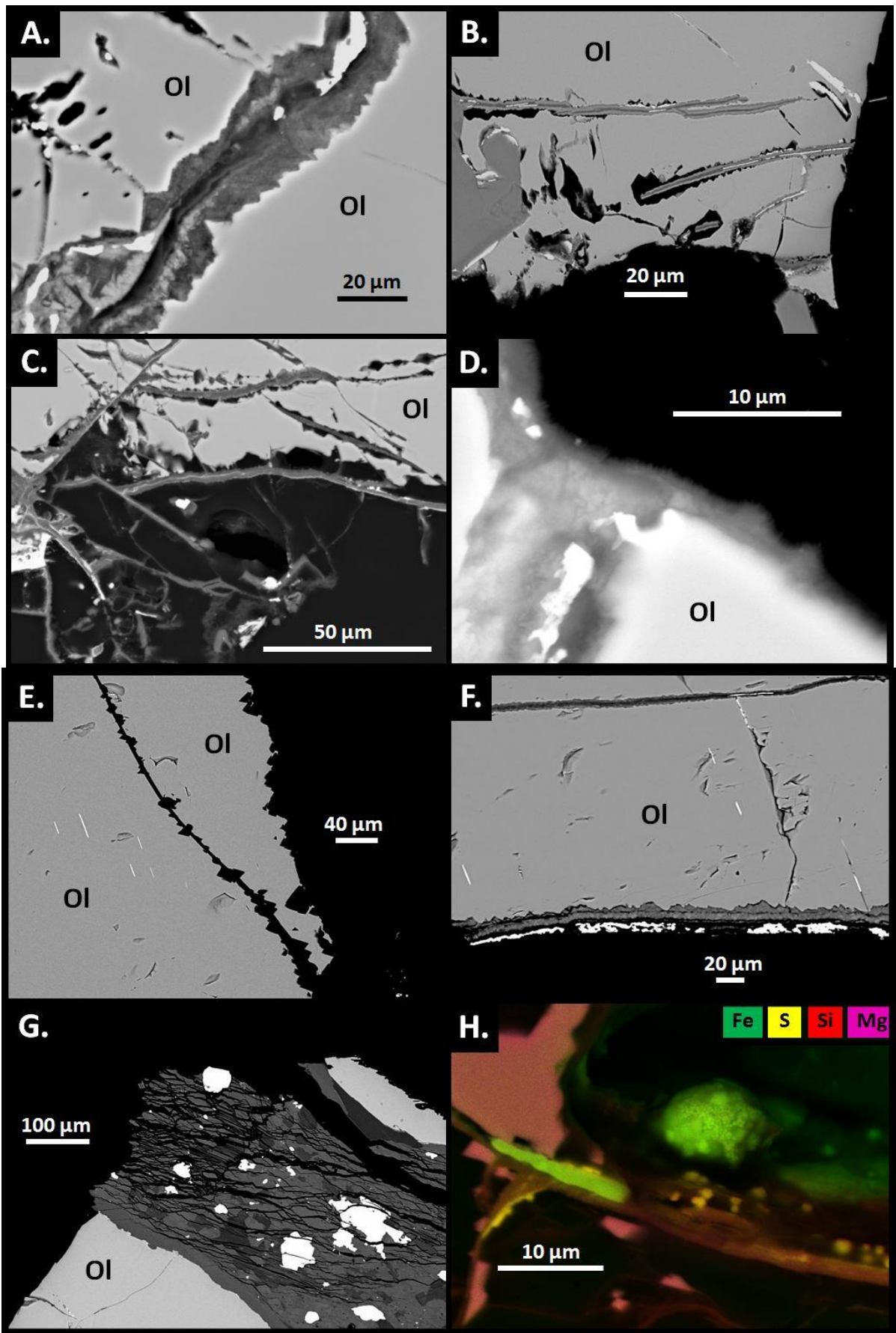


Figure 4.45. Olivine with CO₂ and SO₂ (1707) after 120 days of reaction.

A. A pre-experiment alteration vein in an olivine grain, above which is some dissolution holes that formed during the experiment.

B. An olivine grain showing a complex mixture of pre-experiment alteration veins which have widened via olivine dissolution during the experiment whilst leaving the Si, Fe rich pre-experiment alteration vein intact.

C. As for B. except olivine dissolution has proceeded to completion in parts, leaving only a webbed network of pre-existing alteration veins.

D. A pre-experiment alteration vein surrounded by intact olivine, however a 1 - 2 µm serrated film of Fe- Mg- silicate has been deposited on the grain edge has occurred, possibly during the experiment, very similar to the pre-experiment alteration. Alternatively, this is all pre-experiment and is where two alteration veins met, the site shattered during experiment preparation and the experiment slightly dissolved the silicate vein edge.

E. Serrated fracture in an olivine vein that has begun the process of dissolution creating serrations but lack any secondary mineral precipitation. The grain edge also shows dissolution.

F. Pre-experiment alteration on the edge of an olivine grain.

G. A pre-experiment impurity in the olivine sample. The bright white is ilmenite and the darker mineral hydrobiotite (see appendix 3).

H. EDXS mapping displaying Fe oxides (green) and precipitated sulphides (yellow) attached to a remnant pre-experiment alteration vein where the surrounding olivine has been dissolved. See appendix 3 for detailed mineral analysis.

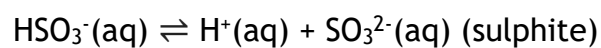
4.5 Discussion

4.5.1 pH

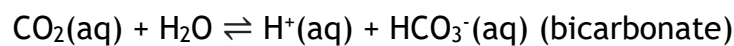
Experiment chambers that included SO₂ (1706, 1707) experienced a rapid and sustained drop in pH, from ~8 to ~3.6. This increase in H⁺ would have occurred via equations 4.21 and 4.22 for the SO₂ reactions (Goldberg & Parker, 1985), and 4.23 and 4.24 for the CO₂ reactions (Tarbuck & Richmond, 2006):



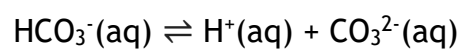
Equation 4.21



Equation 4.22

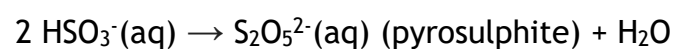


Equation 4.23



Equation 4.24

Further fluid reaction could include equation 4.25 (Goldberg & Parker, 1985):



Equation 4.25

CO₂ and SO₂ are clathrates when dissolved in water, and despite equations 4.21 and 4.22 bearing resemblance to 4.23 and 4.24, the molecular clathrate geometry and relative reaction rates are extremely disparate; SO₂ has a 1st order reaction rate constant of $3.4 \times 10^6 \text{ s}^{-1}$ and CO₂ is 0.14 s^{-1} (Tarbuck & Richmond, 2006). Thus, SO₂ is significantly more reactive than CO₂ by itself, and certainly more than N₂. This reactivity difference is observed in fluid chemistry, saturation state and mineral alteration observations in this experiment, with SO₂ in the chambers (1706, 1707) consistently showing amplified reaction trends across the data sets compared to other chambers.

For the control N₂ chambers, pH remained at ~ 7.5 throughout the experiment, which demonstrates the extremely slow kinetics of minerals changing the pH of a neutral solution without gaseous influence. The exception for this was the chamber where pyrrhotite was a mineral component (1701) which behaved similar to the SO₂ chambers lowering to pH 3.5, followed by a rise to 4.8 at 50 days and then down to pH 4, over a 70 day period.

Chambers containing CO₂ (1702, 1705) fall from pH 8 and remain ~5.8, except for the chamber where pyrrhotite was a mineral component (1704), which displayed the same pattern as the control (1701), except the reaction was ~30 days later at 80 days. The inclusion of SO₂ gas increases and sustains SO₄²⁻ (sulphate) level to ~2250 mg l⁻¹ in both basalt and olivine, though olivine reduces to ~1100 Mg l⁻¹ after 51 days. Pyrrhotite samples retain a steady ~200 mg l⁻¹ SO₄²⁻ content, and all other samples have negligible levels. Clearly, pyrrhotite is a slower, more moderate, method of introducing of SO₄²⁻ into a system compared to SO₂ gas. SO₂ gas combined with CO₂ and basalt is the most reactive at releasing SO₄²⁻, and thus the more accurate analogue of early Mars weathering.

The inclusion of CO₂ (without SO₂) is the dominant control on HCO₃⁻, with olivine having the highest values, followed by basalt & pyrrhotite followed by basalt. Samples with CO₂ and SO₂ increase in HCO₃⁻ after 24 days. pH exerts a major control over all aspects of these results and will be referred to many times in this discussion. To be able to focus on the mineral reactions occurring in the

pyrrhotite bearing chambers (1701, 1704), which create these pH changes, a short discussion on the nature of pyrrhotite dissolution is required.

4.5.2 Mineral pyrrhotite dissolution.

Pyrrhotite (Fe_7S_8) is a polytype of pyrite (FeS_2). Pyrrhotite is an iron monosulphide that can be either monoclinic or hexagonal, and this crystal structure can control dissolution kinetics and secondary mineral formation (Harries *et al.* 2013). Hexagonal pyrrhotite has been shown to dissolve faster when conditions are <2.5 pH, whereas at >2.5 pH monoclinic pyrrhotite dissolves quicker (Harries *et al.* 2013). The Shierglas pyrrhotite used in this experiment is hexagonal. None of the experiment chambers dropped beneath 2.5 pH at any point during the 120 day experiment, so dissolution rates should have been relatively moderate. Pyrrhotite reacted and oxidised rapidly in comparison to the other basaltic minerals present in the chamber, and this pattern has been found in other studies observing Martian sulphide oxidation to secondary Fe (hydr)oxides or Fe^{2+} sulphates such as melanterite (King & McSween, 2005). Jarosite at the Meridiani Planum, Mars, may have formed via similar processes, although the pH during formation of Meridiani Planum jarosite is estimated as <4 (Zolotov & Shock, 2005).

Modelling of fluid saturation chemistry shows that jarosite is oversaturated for both pyrrhotite bearing 1701, 1704 chambers and also for SO_2 bearing chambers 1706, 1707 (Fig. 4.34.G), and under saturated for all others. One implication from this is that the oxidation of mineral sulphides, and presence of SO_2 gas, played an essential role in forming Martian jarosite, and should not be neglected in any Mars analogue experiment.

Reaction textures for pyrrhotite grains were similar for both chambers (1701, 1704). The cores of the larger grains remained chemically identical to the pre-experiment values, while a linear inner reaction front, followed by a series of parallel spindle legs, then an outer reaction layer consumed the grain edges (Fig. 4.36 & 4.39). In many instances, alteration continued to completion and only small

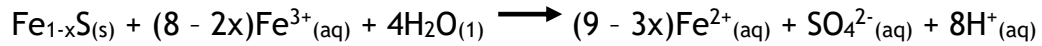
entirely altered fragments remained. The observed degree of alteration places the reaction at ~6 on the Sulphide Alteration Index developed by Blowes & Jambor (1990), shown in Table 4.7.

Numerical Scale	Degree of Alteration of Sulphides
0 - 1	Only a few grains of pyrrhotite are weakly altered along rims and fractures; >95% of the grains have sharp, fresh margins.
2 - 6	At scale 6 the pyrrhotite grains have broad alteration rims, but the cores of numerous grains are preserved; gradation to scale 2 is marked by the appearance of narrower alteration rims and a predominance of unaltered grains.
7 - 8	At scale 7 the vestiges of strongly altered pyrrhotite are abundant, or at least a degree of preservation; at scale 8 there is trace amounts of pyrrhotite.
9 - 10	Pyrrhotite and pyrite obliterated; only traces of sulfide, typically chalcopyrite are present.

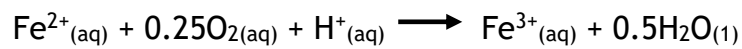
Table 4.7. The degrees of alteration of sulphides, adapted from Blowes & Jambor (1990).

Mechanisms of pyrrhotite dissolution are complex, but are essentially a series of oxidation and hydration reactions; similar to those affecting silicate minerals experiencing serpentinisation. Sulphur leaches out and a range of ferrihydrites form; alternatively, iron can leach leaving iron deficient sulphides and sulphates, and even elemental sulphur (Buckley & Woods, 1985).

The initial oxygen available in the chamber heads would allow dissolved oxygen into the fluid, hence become an oxidising agent and dissolve sulphides (i.e. pyrrhotite) and lower fluid pH via the release of H⁺ ions. Fe³⁺ can be an intermediary in the reactions in equations 4.26 and 4.27 (Harries *et al.* 2013):



Equation 4.26



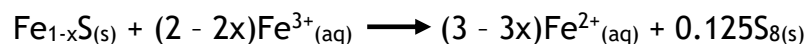
Equation 4.27

However, when pH is >2.5, as was the case in all chambers throughout this experiment, then ferric hydroxides and oxyhydroxides can compete with equation 4.26 via equation 4.28 (Harries *et al.* 2013):



Equation 4.28

During the change from sulphide to sulphate, elemental sulphur can be precipitated via equation 4.29:



Equation 4.29

The altered rims on pyrrhotite grains in chambers **1701** and **1704** have a higher S content than the cores indicating iron has been leached leaving an iron

deficient oxidised sulphate. This alteration product could be identified by making a focussed ion beam (FIB) slice of the altered pyrrhotite rim and analysing it on the nm scale using transmission electron microscopy (TEM). Quantitative SEM analysis yielded ~40 wt. % Fe, ~40 wt. % S and ~20 wt. % O. Webmineral.com gave the best match to these weightings as coyoteite ($\text{NaFe}_3\text{S}_5 \cdot 2\text{H}_2\text{O}$), however, this can be dismissed due to the complete lack of Na (coyoteite should possess ~6 wt. % Na). The Raman spectroscopy conducted (Fig. 40, Fig. 41) initially destroyed the sample, and a low power laser was required. The Raman results still show a pyrrhotite signature (Fig. 42), but less crystalline. This finding is consistent with other studies of sulphide oxidation, which commonly find pyrrhotite alters at the rim into complex, sometimes amorphous (non-crystalline), sulphide oxidation species (Website 3). This rim is sometimes referred to as the non-stoichiometric non-equilibrium layer, or the metal deficient layer (Mikhlin *et al.* 1998).

Iron rich flakes, ~5 μm long and <0.5 μm in width, flocculate encrust on the basalt grain edges and in open basalt fractures, which are otherwise devoid of alteration products. These iron rich flakes are only observed in chambers containing pyrrhotite (1701, 1704), and are therefore likely to be a secondary mineral precipitating from the reacted pyrrhotite, possibly hematite, rather than a product of altered basalt. Hematite was modelled to be able to precipitate in all chambers, see Appendix 6.

SO_2 is the dominant control on fluid Fe content (Fig. 4.32.H), with olivine (1707) releasing more Fe than basalt (1706). 1707 had a major decline in Fe after 51 days, presumably at the point where iron deposits form on grain edges (Fig. 4.44.B, 4.45.H). This Fe drop in the chamber containing olivine with CO_2 and SO_2 is correlated with a drop in total S at the same time, suggestive of FeS deposition. Pyrrhotite (1701, 1704), also liberates Fe (Fig. 4.32.H), although many times less than SO_2 .

4.5.3 Smectite, kaolinite and other clays.

Smectites and other clays, like carbonate, are favoured in pH environments >neutral (Peretyazhko *et al.* 2017 *In Press*). On Mars, considerably more clay than carbonate deposits have been found, and it has been hypothesised that this disparity is due to a sulphuric environment that allowed precipitation of clays, but inhibited carbonate deposition (Peretyazhko *et al.* 2017 *In Press*). The deposition of Fe - rich phases and sulphates, and lack of carbonates observed in this experiment, is similar to the Martian observations, albeit the sulphur deposition observed in 1707 (Fig. 4.45.H) was on a scale too small for quantitative SEM analysis.

4.5.4 Si mobility.

SO₂ is the principal influence controlling Si release into the fluid, with basalt containing chambers releasing the most Si (peaking at ~275 mg l⁻¹), presumably as silicic acid considering the relatively low pH. Interestingly the Si release peaks at 10 days when SO₂ is present, then steadily declines over the rest of the experiment; for all non SO₂ bearing chambers Si release steadily increases through the experiment, with olivine and CO₂ showing a slightly higher release rate.

The Mars Reconnaissance Orbiter Compact Reconnaissance Imaging Spectrometer for Mars (CRISM) instrument has detected opaline silica and H₂O⁻ and SiOH⁻ bearing phases in association with hydrated Fe sulphates, including H₃O⁻ bearing jarosite (Milliken *et al.* 2008). Jarosite and siliciclastic deposits in the Meridiani Planum on Mars indicate an acidic, sulphur rich, aqueous environment that can precipitate silica phases (Golden *et al.* 2012).

With Si release being the highest in SO₂ chambers, and with SO₂ playing an important role in Martian surface geology, causing the formation of surface sulphates, it is reasonable that that the Si release patterns in chambers 1706 and 1707 might be similar in nature to those that occurred on Mars during the

formation of opaline silica in association with surface sulphates under an SO₂ rich atmosphere and in the presence of surface waters. Were the experiments to proceed for longer, the precipitation of opaline silica would be anticipated.

4.5.5 Total cation, total anion and Ca mobility.

Cation, anion and Ca mobility patterns divided into two clear groups, with basalt samples (whether combined with pyrrhotite or not) steadily releasing more Ca over time than those with olivine (Fig. 4.32). Pure olivine chambers released a spike of Ca over the first 24 days then little after, ~2 mg l⁻¹. Basalt with CO₂ and SO₂ was ~4 times higher in its release of Ca, again spiking over the first 24 days then remaining steady at ~48 mg l⁻¹. As Ca is essential in the formation of calcite, these results clearly show that using basalt with a CO₂ and SO₂ mixed atmosphere will release significantly more Ca, thus potentially more carbonate formation, than olivine in a CO₂ atmosphere. Olivine doesn't have Ca in its chemical formula, and so the Ca observed in olivine chambers would be due to mineral impurities. The basalt possessed ~13 wt. % CaO pre-experiment (Table 4.2) in minerals such as plagioclase and pyroxene.

Chamber fluids containing SO₂ (1706, 1707) had a cation and anion increase. CO₂ (particularly with olivine) also releases cations and anions, but considerably less than SO₂ and over a longer time frame. The inclusion of SO₂ increases overall system reactivity significantly. Previous studies on olivine dissolution in low pH solutions have stated that initially total Ca Mg Fe cation release accompanying dissolution is dominant over Si dissolution, but then after a short time Ca Mg Fe cations and Si dissolve at equal rates (Pokrovsky & Schott, 2000; Rosso & Rimstidt). This study finds that after an initial rapid increase in aqueous total cations and Si over 10 days (~30 meq l⁻¹ and ~180 mg l⁻¹ respectively for 1707), that Si declines steadily, whereas total cations remain approximately stable. This may be due to the precipitation of Si. On removing the samples from the chambers 1705, 1706, 1707 possessed coatings of whitish slime that did not survive the thin section making process, and this was probably precipitated Si.

4.5.6 Lack of carbonate formation.

PHREEQC modelling predicted that no carbonates would have precipitated from the fluid in any chamber (Appendix 6), and this is supported by SEM analysis of post experiment samples. The saturation models show an interesting feature in that over the 120 day duration all chambers with SO₂ or pyrrhotite (1701, 1704, 1706, 1707) are grouped at $\sim 7-10 \log_{10} f$ for calcite, and show a slow increase ($\sim 1 \log_{10} f$) towards the saturation point. Had the experiment been conducted over a longer duration these chambers might be expected to precipitate carbonate from the fluid, if a linear increase in saturation is assumed. All chambers without SO₂ or pyrrhotite, although grouping closer to the saturation point ($\sim 2-7 \log_{10} f$ for calcite), do not show any trend of increasing saturation throughout the experiment.

The other carbonates (dolomite, magnesite) show similar trends to those described above, albeit at slightly different saturation values. For this experiment calcite would be the more probable candidate for carbonate precipitation, as at lower depths <800 m and 25 - 90°C models predict calcite the most likely mineral carbonate to form, while magnesite is far more likely and indeed the only mineral carbonate to form at higher pressures and >250°C (Aradóttir *et al.* 2015).

Other studies have modelled that as little as 1 μmolar of H₂SO₄ precludes carbonate formation, which corresponds to a pH of 6.2 or less (Bullock & Moore, 2007). Basalt and olivine with N₂ (chambers 1700 and 1703) are the only chambers with the pH to precipitate carbonates using this model, but their high pH corresponds with a near zero amount of aqueous cations (Fig. 4.32.B) including Ca (Fig. 4.32.F), making carbonate deposition impossible. Olivine with CO₂ and SO₂ 1705 hovers around the pH 6 mark throughout the experiment, and is probably the best candidate for carbonate precipitation (Fig. 4.30). 1705 possessed the highest amount of aqueous bicarbonate HCO₃⁻, peaking $\sim 320 \text{ mg l}^{-1}$ after 120 days (Fig. 4.32.E and equation 4.23), yet relatively low aqueous cations peaking $\sim 5 \text{ meq l}^{-1}$, and it was the closest chamber to precipitating magnesite (appendix 4), and the

closest reasonable chamber to precipitating calcite (Fig. 4.34.E); but remaining beneath the carbonate saturation point.

Mars had significant sulphur in both mineral and gas form in its early history (Gaillard *et al.* 2013), and its modern surface possesses massive sulphate deposits but no massive carbonate deposits (Bullock & Moore, 2007). These experiment results clearly demonstrate the importance of sulphur (whether in mineral or gaseous form) inhibiting carbonate formation in MSC. Some Martian MCS laboratory experiments do not use sulphur and have pure CO₂ as the analogue for an early Mars atmosphere (Booth & Kieffer, 1978; Baker *et al.* 2000; Dehouck *et al.* 2013; Garenne *et al.* 2013; Schwenser *et al.* 2017) and thus present a questionable analogue for Mars dynamics.

Other potential reasons for the lack of carbonate formed in the experiments of this chapter may be the water to rock ratio used. By either reducing the water volume down from 200 ml, or increasing the rock volume per chamber, increased reaction would be expected. Reducing water volume is not ideal however, as IC/ICPMS extraction samples were regularly taken, thus increasing rock sample amount would be a good idea were the experiment to be repeated.

The results of this study support the conclusions of other researchers who found the limiting factor in MCS is usually the precipitation rate of Mg- and Fe-carbonates, not the dissolution rate of olivine (Haug *et al.* 2011).

4.5.7 Olivine dissolution and Martian model implications.

Olivine dissolution is one of the principal mineral reactions observed in this experiment. Increased olivine dissolution is negatively correlated with declining pH, as observed in other experiments and is referred to as proton promoted dissolution (Pokrovsky & Schott, 2000; Rosso & Rimstidt, 2000; Liu *et al.* 2006). Dissolution occurs at grain boundaries, reducing grain size, and also within grains, widening veins. Dissolution depth below grain surfaces varies from <1 µm for olivine with N₂ (1703), to ~100 µm for olivine with CO₂ and SO₂ (1707). Dissolution

depth within fractures is generally much less than grain edges, ~1 - 5 μm for olivine grains as part of basalt with CO_2 and SO_2 (1706) and the same for olivine with CO_2 and SO_2 (1707).

Olivine dissolution textures in all chambers display a serrated profile which deepens as the reaction proceeds (Fig. 4.38.D, 4.43.C, 4.44.C, 4.45.E). This same dynamic has been observed by other researchers (Tomkinson *et al.* 2013) who concluded the alteration veins are controlled by, and run parallel to, the olivine crystallographic (001)_{Ol} plane, and that the serrations correspond in angle to the (102)/(111)_{Ol} plane (Tomkinson *et al.* 2013). There is no reason to doubt that the same process controls the observed serrated nature of the dissolved olivine grains in this experiment.

Dissolution is notably less intense in chambers without SO_2 , highlighting the important role gaseous sulphur plays in planetary mineral dynamics, and why it should be included in early Mars mineral analogue experiments. Olivine with only CO_2 (1705) displays ~10 μm grain edge dissolution, whereas olivine with CO_2 and SO_2 (1707) displays ~100 μm grain edge dissolution.

Whether the system is olivine with CO_2 , or olivine with CO_2 and SO_2 , both display significant olivine dissolution and fracture widening. However, olivine with only CO_2 (1705) has ~10 μm of Fe oxide deposition on the grain edges, whereas olivine with CO_2 and SO_2 (1707) and olivine grains as part of basalt with CO_2 and SO_2 (1706), lack any significant mineral deposition at grain edges and along widened fractures. 1707 does display minor Fe (~10 μm clumps) and S (<1 μm particles) deposition, but this appears limited to grain edges and on the pre-experiment veins that survive the dissolution of enclosing olivine.

This difference in olivine dissolution/mineral deposition between chambers with and without SO_2 has implications for the isovolumetric replacement versus pore space precipitation question. Chambers with SO_2 (1706, 1707) can only support a pore space precipitation model as the veins are clearly shown to widen via olivine dissolution and not via isovolumetric dissolution-precipitation; pore space precipitation then may or may not occur were the experiment continued, but either way, isovolumetric replacement can be discounted where the system is

CO₂ and SO₂. Where the chamber is pure CO₂ (1705), and a rim of Fe oxide has been deposited, it is unknown whether dissolution happened first, followed by Fe oxide precipitation, supporting the pore space precipitation model, or whether the Fe oxide is part of an early stage isovolumetric mineral replacement sequence. Further investigation would be required to arrive at a conclusion on this, perhaps by multiple experiment chambers with identical mineral and gas regimes, but the experiment being halted at different stages for each chamber and the mineral alteration examined. From the petrographic hints observed, and from logical expectation, it seems the olivine dissolves first, followed by Fe precipitation. The IC - ICPMS data does not support this interpretation though, with a gradual increase of aqueous Si throughout the experiment, reaching 50 Mg l⁻¹ after 120 days, which would be the olivine dissolving and serrating (Fig. 4.32), but virtually no aqueous Fe observed throughout the experiment for 1705. This lack of aqueous Fe may imply that Fe did not dissolve and precipitate, but instead was insoluble and remained as an Fe rim once all other olivine elements had dissolved.

The early Mars atmosphere almost certainly possessed an SO₂ component (Tian *et al.* 2010; Gaillard *et al.* 2013), and hence chambers 1706 and 1707 are nominally better analogues. Results from these chambers supporting the pore space precipitation model of Martian meteorite vein evolution. However, in a sub-environment of the Martian regolith not influenced by SO₂, and instead dominated by CO₂ rich fluids containing little to no sulphur, an isovolumetric dissolution-precipitation process may potentially be valid. An alternative option is that this experiment lacks environmental variables and time duration to represent the fluid/pressure/temperature/gas conditions experienced by the Martian alteration veins, and hence these results are not a suitable analogue.

Although not directly relevant to the experimental part of this study, observations of mineral veins in the Martian meteorite Lafayette, clearly shows at least some isovolumetric direct mineral replacement, which cannot be accounted for by mineral dissolution followed by pore space precipitation (Fig. 4.46, red arrows). Therefore, on Mars it is likely a combination of primary mineral dissolution followed by mineral pore space precipitation and isovolumetric mineral

replacement occurred. This experiment, however, can only offer evidence supporting pore space precipitation.

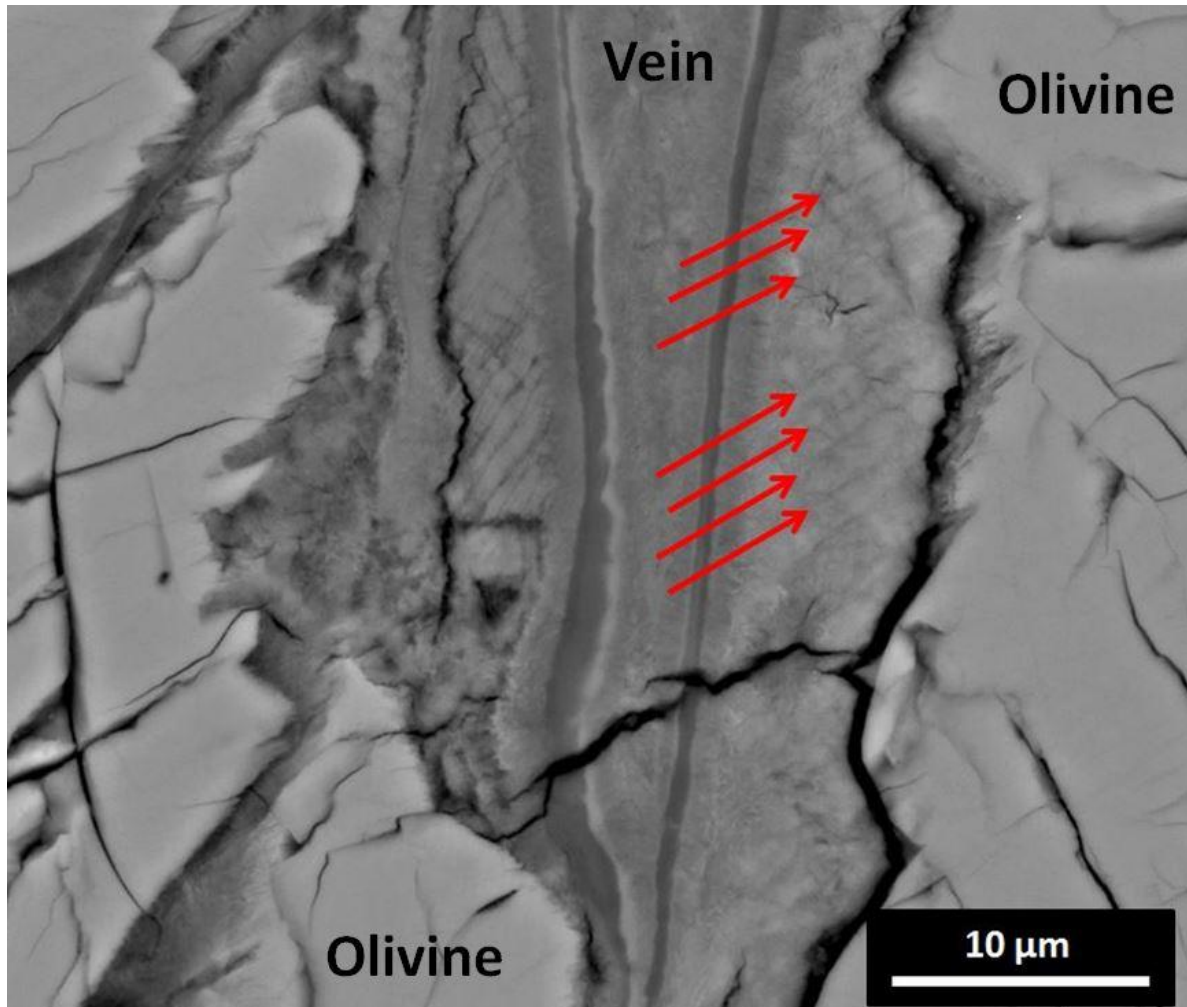


Figure 4.43. BSE SEM image of complex and extensive mineral vein alteration in olivine from the Martian meteorite Lafayette. Red arrows point to linear striations within the secondary minerals that appear to align with crystallographic controlled primary olivine mineral serrations. This can only be explained by isovolumetric mineral replacement.

4.5.8 Discussion Summary.

- **No carbonate precipitates.** In all chambers, no carbonates are modelled to have precipitated, nor were any observed. Precipitation of carbonates is the limiting factor in MCS rather than the dissolution of olivine.
- **Sulphur increases the carbonate saturation state over time.** All chambers containing sulphur as either pyrrhotite or SO₂ show a slow trend towards carbonate saturation. Chambers lacking sulphur do not show this trend in solution chemistry.
- **Calcite would be the first carbonate expected to precipitate (with basalts), Mg carbonate or siderite (with olivine).**
- **Experiment duration an important variable.** Running the experiment over a 360 day period instead of 120 days would be an interesting exercise to see whether carbonates eventually precipitate, as well as observing the extent to which sulphur leads to the dissolution of the olivine.
- **Mineral alteration and fluid chemistry changes** are influenced more by chamber gas composition than by initial mineralogy composition.
- **Release of ions** from the reactant minerals is enhanced significantly by SO₂, and much less so by pyrrhotite.
- Both SO₂ and pyrrhotite greatly reduces solution pH.
- SO₂ with olivine releases high concentrations of Fe, then after 51 days precipitates Fe and S.
- **Pore space precipitation model** of Martian meteorite alteration vein formation is strongly supported by results from chamber (1707) olivine dissolution with CO₂ and SO₂, whereas olivine dissolution with only CO₂ (1705) remains less conclusive.

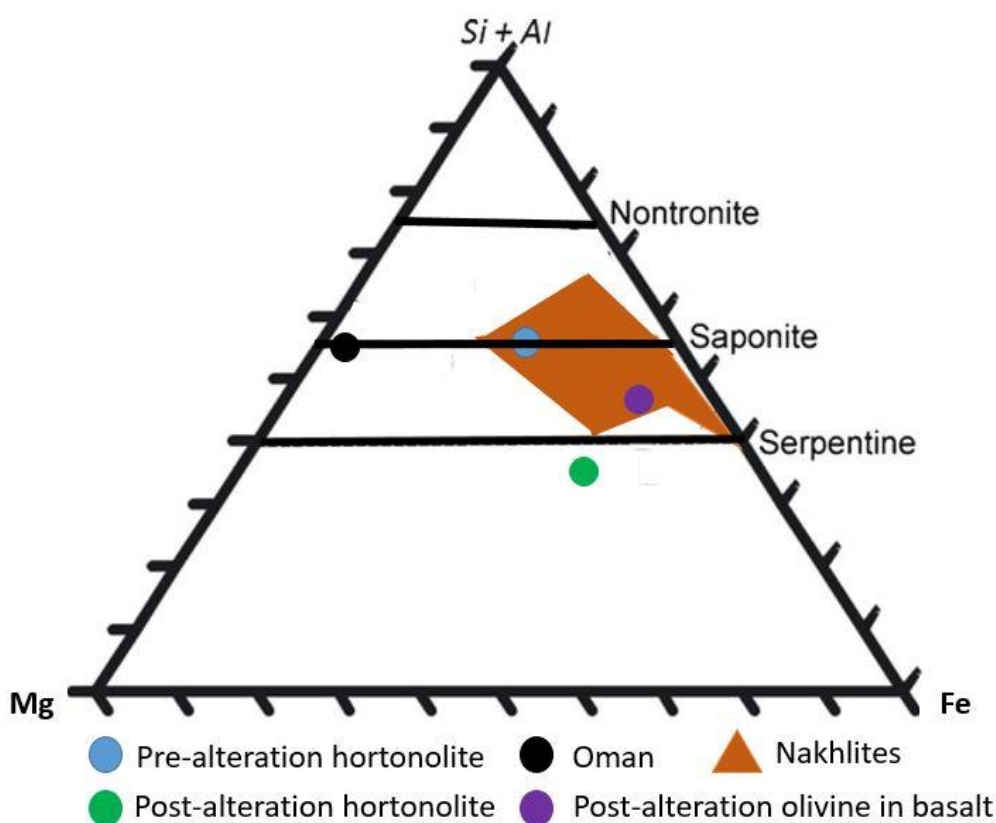


Figure 4.44. Normalised quantitative analysis of phyllosilicates showing how closely samples used as Mars analogues in chapters 3 and 4 match those of Nakhlite Martian meteorites. Nakhlite data covers that provided by Changela and Bridges (2011). Oman ophiolite data from sample SU 15 1 (chapter 3). Icelandic basalt from chamber 1706 (chapter 4). Hortonolite data from chamber 1707 (chapter 4).

The aim of chapter 4 was to form carbonates under conditions representative of early Mars. Unfortunately with no carbonates forming within the experiment chambers, a comparison of phyllosilicate data between experiment samples, Mars meteorites and terrestrial ophiolites may serve as an alternative. Figure 4.44 is a normalised plot of quantitative SEM phyllosilicate data acquired from chapters 3 and 4. It can be seen that the experiment samples selected for chapter 4 significantly correlate with the Nakhla meteorite phyllosilicates, mostly Fe rich saponite and serpentine (Changela and Bridges, 2011). This correlation suggests South African hortonolite and Icelandic basalt are better terrestrial

analogues of Mars than the ophiolites more commonly cited in the literature as ideal Mars analogues (Greenberger *et al.* 2015). The reason for this better correlation is almost certainly the higher Fe content in pre-experiment South African hortonolite olivine (Fig. 4.3), and this Fe content in the olivine translates to high Fe in the post reaction phyllosilicates (Fig. 4.44).

4.6 Conclusions.

This study demonstrates the importance of using more than pure CO₂ gas when attempting to reproduce an early Martian atmosphere for mineral alteration experiments. The inclusion of SO₂ gas into the experiments drastically alters primary mineral dissolution rates, fluid chemistry/element saturation and formation/inhibition of alteration products.

Although in principal using an olivine primary mineral that is geochemically closer to Martian olivine is sensible, i.e. South African hortonolite, it is only effective if the material is extremely pure and/or extremely well characterised pre-experiment. South African hortonolite has enormous potential to become a superior olivine analogue for Mars than San Carlos, due to its higher iron content, however, more extensive mineral characterization and standardisation is required.

The lack of carbonates produced by this study, despite water saturated mineral surfaces and 2 bar atmospheric conditions indicate that in order to produce Mars like carbonates the experiment would need to be conducted over a considerably longer time period, or the temperature - pressure - mineral volume increased. However, doing so potentially reduces accurate pressure and temperature representation of an early Mars environment.

The results indicate that carbonates can take a considerable time to form, even in high water to rock ratio and physically conducive environments, casting doubt on the hypothesis that Mars mineral alteration occurred in short, sporadic, localised melting with low water to rock ratio on a cold icy early Mars (Weiss & Head, 2015; Wordsworth *et al.* 2015). No explanation is forthcoming as to why no

carbonates formed in this experiment, yet have been observed in other experiments using similar conditions in as little as 7 days (Baker *et al.* 2000). Some of the experiments in the literature that have successfully produced Mars analogue carbonates used rock powders (Dehouck *et al.* 2013), rather than whole rock samples as used in this study. Perhaps using powder, hence higher reactive surface area, would have influenced results.

On the question of whether Martian olivine alteration minerals form via isovolumetric replacement or pore space precipitation into open fractures, this experiment supports the pore space precipitation mechanism; whereby olivine fractures are widened replete with crystallographic controlled serrated edges via dissolution (observed in this experiment), then secondary minerals precipitate into these serrated open fractures (unobserved in this experiment).

Extensive dissolution, yet little secondary mineral precipitation, defines this experiment. Minor precipitation of iron and sulphur is observed on the edges of dissolved olivine grains (Fig. 4.43.B, 4.44.B, 4.45.H), but a layered mineral replacement sequence of secondary minerals analogous to Martian meteorite alteration veins such as Lafayette was absent. This outcome either means that Mars alteration minerals, such as those in the Martian meteorites, precipitated into pre-existing fractures and pores, or, that the conditions of this experiment do not sufficiently represent early Mars conditions.

4.7 Acknowledgements.

I am extremely grateful to Keith Bateman and Dr Chris Rochelle from the British Geological survey for equipment provision, laboratory space, ICPMS processing and extensive technical advice. Gratitude is also extended to John Faithful from the Hunterian museum, Glasgow, for supplying the pyrrhotite and hortonolite. Further, appreciation to Peter Chung, from the school of geographical and Earth sciences, University of Glasgow, for scanning electron microscope support. Adrienne MacArtney's PhD is fully funded by the UK Space Agency and delivered via the Science and Technology Facilities Council (STFC).

4.8 References.

- Adeoye J. T., Menefee A. H., Xiong W., Wells R. K., Skemer P., Giammar D. E., Ellis B. R. (2017). Effect of transport limitations and fluid properties on reaction products in fractures of unaltered and serpentinized basalt exposed to high PCO₂ fluids. *International Journal of Greenhouse Gas Control* Volume 63:310-320.
- Alfredsson H. A., Wolff-Boenisch D., Stefánsson A. (2011). CO₂ sequestration in basaltic rocks in Iceland: Development of a piston-type downhole sampler for CO₂ rich fluids and tracers. *Energy Procedia* 4:3510-3517.
- Alfredsson H. A., Oelkers E. H., Hardarsson B. S., Franzson H., Gunnlaugsson E., Gislason S. R. (2013). The geology and water chemistry of the Hellisheidi, SW-Iceland carbon storage site. *International Journal of Greenhouse Gas Control* 12:399-418.
- Allen C. C., Gooding J. L., Jercinovic M., Keil K. (1981). Altered basaltic glass: A terrestrial analog to the soil of Mars. *Icarus* 45(2):347-369.
- Altheide T., Chevrier V., Nicholson C., Denson J. (2009). Experimental investigation of the stability and evaporation of sulfate and chloride brines on Mars. *Earth and Planetary Science Letters* 282(1-4):69-78.
- Andrews-Hanna J. C., Zuber M. T., Arvidson R. E., Wiseman S. M. (2010). Early Mars hydrology: Meridiani playa deposits and the sedimentary record of Arabia Terra. *Journal of Geophysical Research: Planets* 115(E6).
- Aradóttir E. S. P., Sigurdardóttir H., Sigfússon B., Gunnlaugsson E. (2011). CarbFix: a CCS pilot project imitating and accelerating natural CO₂ sequestration. *Greenhouse Gases* 1(2):105-118.
- Aradóttir E. S. P., Gunnarsson I., Sigfússon B., Gunnarsson G., Júlíusson B. M., Gunnlaugsson E., Sigurdardóttir H., Arnarson M. T., Sonnenthal E. (2015). Toward Cleaner Geothermal Energy Utilization: Capturing and Sequestering CO₂ and H₂S Emissions from Geothermal Power Plants. *Transport in Porous Media* 108(1):61-84.
- Baker L. L., Agenbroad D. J., Wood S. A. (2000). Experimental hydrothermal alteration of a martian analog basalt: Implications for martian meteorites. *Meteoritics & Planetary Science* 35(1):31-38.
- Bandara U. C., Tartakovsky A. M., Palmer B. J. (2011). Pore-scale study of capillary trapping mechanism during CO₂ injection in geological formations. *International Journal of Green Gas Control* 5:1566-1577.

- Berkley J. L., Keil K., Prinz M. (1980). Comparative petrology and origin of Governador Valadares and other nakhlites. *Lunar and Planetary Science Conference, 11th, Houston, Texas. Pergamon Press, New York* 2(A82-22296 09-91):1089-1102.
- Bishop J. L., Schiffman P., Southard R. (2002). Geochemical and mineralogical analyses of palagonitic tuffs and altered rinds of pillow basalts in Iceland and applications to Mars. *Geological Society, London, Special Publications* 202:371-392.
- Blank J. G., Green S. J., Blake D., Valley J. W., Kita N. T., Treiman A., Dobson P. F. (2009). An alkaline spring system within the Del Puerto Ophiolite (California, USA): A Mars analog site. *Planetary and Space Science* 57(5-6):533-540.
- Blowes D.W., Jambor J.L. (1990). The Pore-water Geochemistry and the Mineralogy of the Vadose Zone of Sulfide Tailings, Waite Amulet, Quebec, Canada. *Applied Geochemistry* 5:327-346.
- Booth M. C., Kieffer H. H. (1978). Carbonate formation in Mars like environments. *Journal of Geophysical Research: Solid Earth* 83(B4):1809-1815.
- Booth M. C., Gibson E. K., Kotra R. (1982). Chemical Weathering on Mars: Interactions of Sulfur Dioxide with Olivine and Olivine Tholeiite in Simulated Martian Environments. *Lunar and Planetary Science* XIII:55-56.
- Boynton W. V., Ming D. W., Kounaves S. P., Young S. M. M., Arvidson R. E., Hecht M. H., Hoffman J., Niles P. B., Hamara D. K., Quinn R. C., Smith P. H., Sutter B., Catling D. C., Morris R. V. (2009). Evidence for Calcium Carbonate at the Mars Phoenix Landing Site. *Science* 325(5936):61-64.
- Bradshaw J., Bachu S., Bonijoly D., Burruss R., Holloway S., Christensen N. P., Mathiassen O. M. (2007). CO₂ storage capacity estimation: Issues and development of standards. *International Journal of Greenhouse Gas Control* 1(1):62-68.
- Brantley S. L. (1992). Kinetics of dissolution and precipitation—experimental and field results. *Water-Rock Interaction* 7:465-469.
- Brass G. W. (1980). Stability of brines on Mars. *Icarus* 42(1):20-28.
- Bridges J. C., Catling D. C., Saxton J. M., Swindle T. D., Lyon I. C., Grady M. M. (2001). Alteration Assemblages in Martian Meteorites: Implications for Near-Surface Processes. In: Kallenbach R., Geiss J., Hartmann W.K. (eds) *Chronology and Evolution of Mars*. Space Sciences Series of ISSI, 12. Springer, Dordrecht.
- Bridges J. C., Schwenger S. P. (2012). The nakhlite hydrothermal brine on Mars. *Earth and Planetary Science Letters* 359-360:117-123.
- Buckley A. N., Woods R. (1985). X-Ray photoelectron spectroscopy of oxidised pyrrhotite surfaces. *Applications of Surface Science* 20(4):472-480.

- Bullock M. A., Moore J. M. (2007). Atmospheric conditions on early Mars and the missing layered carbonates. *Geophysical Research Letters* 34:L19201.
- Bunch T. E., Reid A. M. (1975). The Nakhilites Part I: Petrography and mineral chemistry. *Meteoritics & Planetary Science* 10(4):303-315.
- Calvin W. N., King T. V. V., Clark R. N. (1994). Hydrous carbonates on Mars?: Evidence from Mariner 6/7 infrared spectrometer and ground-based telescopic spectra. *Journal of Geophysical Research: Planets* 99(E7):14659-14675.
- Campbell W. B., Maass O. (1930). Equilibria in sulphur dioxide solutions. *Canadian Journal of Research* 2(1):42-64.
- Carroll J. J., Skupsky J. D., Mather A. E. (1991). The solubility of carbon dioxide in water at low pressure. *Journal of Physical and Chemical Data (Reprints)* 20:6.
- Changela H. G., Bridges J. C. (2011). Alteration assemblages in the nakhilites: Variation with depth on Mars. *Meteoritics & Planetary Science* 45(12):1847-1867.
- Chasset C., Jarsjö J., Erlström M., Cvetkovic V., Destouni G. (2011). Scenario simulations of CO₂ injection feasibility, plume migration and storage in a saline aquifer, Scania, Sweden. *International Journal of Green Gas Control* 5:1303-1318.
- Chavagnac V., Monnin C., Ceuleneer G., Boulart C., Hoareau G. (2013). Characterization of hyperalkaline fluids produced by low-temperature serpentinization of mantle peridotites in the Oman and Ligurian ophiolites. *Geochemistry, Geophysics, Geosystems* 14(7):2496-2522.
- Chen Y., Brantley S. L. (2000). Dissolution of forsteritic olivine at 65 °C and 2 < pH < 5. *Chemical Geology* 165(3-4):267-281.
- Chen C., Zhang D. (2010). Pore-scale simulation of density-driven convection in fractured porous media during geological CO₂ sequestration. *Water Resources Research* 46:W11527.
- Gooding J. L. (1992). Soil mineralogy and chemistry on Mars: Possible clues from salts and clays in SNC meteorites. *Icarus* 99(1):28-41.
- Daval D., Sissmann O., Menguy N., Saldi G. D., Guyot F., Martinez I., Corvisier J., Garcia B., Machouk I., Knauss K. G., Hellmann R. (2011). Influence of amorphous silica layer formation on the dissolution rate of olivine at 90 °C and elevated pCO₂. *Chemical Geology* 284(1-2):193-209.
- Day J. M. D., Taylor L. A., Floss C., McSween H. Y. (2006). Petrology and chemistry of MIL 03346 and its significance in understanding the petrogenesis of nakhilites on Mars. *Meteoritics & Planetary Science* 41(4):581-606.

- Dehouck E., Gaudin A., Mangold N., Lajaunie L., Dauzeres A., Le Menn E. (2013). Weathering of olivine under CO₂ atmosphere: A Martian perspective. *44th Lunar and Planetary Science Conference 2017*.
- Doughty C. (2010). Investigation of CO₂ plume behavior for a largescale pilot test of geologic carbon storage in a saline formation. *Transport in Porous Media* 82:49-76.
- Edwards C. S., Ehlmann B. L. (2015). Carbon sequestration on Mars. *Geology* 43(10):863-866.
- Fairen A. G., Fernandez-Remolar D., Dohm J. M., Baker V. R., Amils R. (2004). Inhibition of carbonate synthesis in acidic oceans on early Mars. *Nature* 431.7007: 423-6.
- Fournelle J. (2009). Notes on Some Crystals of San Carlos Olivine and EPMA Standards. *American Geophysical Union, Fall Meeting 2009 abstract #V31E-2009*.
- Gaillard F., Michalski J., Berger G., McLennan S. M., Scaillet B. (2013). Geochemical reservoirs and timing of sulfur cycling on Mars. *Space Science Reviews* 174:251-300.
- Garenne A., Montes-Hernandez G., Beck P., Schmitt B., Brissaud O., Pommerol A. (2013). Gas-solid carbonation as a possible source of carbonates in cold planetary environments. *Planetary and Space Science* 76:28-41.
- Ghomian Y., Pope G. A., Sepehrnoori K. (2008). Reservoir simulation of CO₂ sequestration pilot in Frio Brine formation, USA Gulf Coast. *Energy* 33:1055-1067.
- Giammar D. E., Bruant R. G., Peters C. A. (2005). Forsterite dissolution and magnesite precipitation at conditions relevant for deep saline aquifer storage and sequestration of carbon dioxide. *Chemical Geology* 217(3-4):257-276.
- Gislason S. R., Arnorsson S., Armannsson H. (1994). Present chemical weathering of basalt in Iceland. *Mineralogical Magazine* 58(A):333.
- Gislason S. R., Wolff-Boenisch D., Stefansson A., Oelkers E. H., Gunnlaugsson E., Sigurdardottir H., Sigfusson B., Broecker W. S., Matter J. M., Stute M., Axelsson G., Fridriksson T. (2010). Mineral sequestration of carbon dioxide in basalt: A pre-injection overview of the CarbFix project. *International Journal of Greenhouse Gas Control* 4:537-545.
- Gislason S. R., Oelkers E. H. (2014). Carbon Storage in Basalt. *Science* 344(6182):373-374.
- Golden D. C., Ming D. W., Hausrath E. M., Morris R. V., Niles P. B., Achilles C. N., Ross D. K., Cooper B. L., Gonzalez C. P., Mertzman S. A. (2012). Dissolution of olivine, siderite, and basalt at 80 °C in 0.1 M H₂SO₄ in a flow through process: Insights into acidic weathering on Mars. *43rd Lunar and Planetary Science Conference* 2521.
- Goldberg R. N., Parker V. B. (1985). Thermodynamics of Solution of SO₂(g) in Water and of Aqueous Sulfur Dioxide Solutions. *Journal of Research of the National Bureau of Standards* 90(5).

- Greenberger R. N., Mustard J. F., Cloutis E. A., Pratt L. M., Sauer P. E., Mann P., Turner K., Dyar M. D., Bish D. L. (2015). Serpentinization, iron oxidation, and aqueous conditions in an ophiolite: Implications for hydrogen production and habitability on Mars. *Earth and Planetary Science Letters* 416:21-34.
- Gruenewaldt G. (1979). A review of some recent concepts of the Bushveld complex, with particular reference to sulphide mineralization. *Canadian Mineralogist* 17:233-256.
- Gunde A. C., Bera B., Mitra S. K. (2010). Investigation of water and CO₂ (carbon dioxide) flooding using micro-CT (microcomputed tomography) images of Berea sandstone core using finite element simulations. *Energy* 35:5209-5216.
- Gysi, A. P., Stefánsson A. (2011). CO₂-water-basalt interaction. Numerical simulation of low temperature CO₂ sequestration into basalts. *Geochimica et Cosmochimica Acta* 75:4728-4751.
- Gysi, A. P., Stefánsson A. (2012). CO₂-water-basalt interaction. Low temperature experiments and implications for CO₂ sequestration into basalts. *Geochimica et Cosmochimica Acta* 81:129-152.
- Halevy I, Zuber M. T., Schrag D. P. (2007). A Sulfur Dioxide Climate Feedback on Early Mars. *Science* 318(5858):1903-1907.
- Halevy I., Fischer W. W., Eiler J. M. (2011). Carbonates in the Martian meteorite Allan Hills 84001 formed at 18 ± 4 °C in a near-surface aqueous environment. *Proceedings of the National Academy of Sciences* 108(41):16895-16899.
- Hallis L. J., Simpson S., Mark D., Lee M. R. (2016). Martian alteration in unique meteorite NWA 8159. *79th Annual Meeting of the Meteoritical Society* 6442
- Harries D., Pollok K., Langenhorst F. (2013). Oxidative dissolution of 4C- and NC-pyrrhotite: Intrinsic reactivity differences, pH dependence, and the effect of anisotropy. *Geochimica et Cosmochimica Acta* 102(1):23-44.
- Haug T. A., Munz I. A., Kleiv R. A. (2011). Importance of dissolution and precipitation kinetics for mineral carbonation. *Energy Procedia* 4:5029-5036.
- Hausrath E. M., Brantley S. L. (2010). Basalt and olivine dissolution under cold, salty, and acidic conditions: What can we learn about recent aqueous weathering on Mars? *Journal of Geophysical Research: Planets* 115(E12).
- Hausrath E. M., Tschauer O. (2013). Natural Fumarolic Alteration of Fluorapatite, Olivine, and Basaltic Glass, and Implications for Habitable Environments on Mars. *Astrobiology* 13(11):1049-1064.

- Hermanrud C., Andresen T., Eiken O., Hansen H., Janbu A., Lippard J., Bolås H. N., Simmenes T. H., Teige G. M. G., Østmo S. (2009). Storage of CO₂ in saline aquifers - lessons learned from 10 years of injection into the Utsira Formation in the Sleipner area. *Energy Procedia* 1:1997-2004.
- Hicks L. J., Bridges J. C., Gurman S. J. (2014). Ferric saponite and serpentine in the nakhlite martian meteorites. *Geochimica et Cosmochimica Acta* 136(1):194-210.
- Hu R., Kass D. M., Ehlmann B. L., Yung Y. L. (2015). Tracing the fate of carbon and the atmospheric evolution of Mars. *Nature Communications* 6:10003.
- Hudson J. C. (1925). The solubility of sulphur dioxide. *Journal of the Chemical Society* 1332.
- Hunger S., Benning L. G. (2007). Greigite: a true intermediate on the polysulfide pathway to pyrite. *Geochemical Transactions* 8(1).
- Hurowitz J. A., McLennan S. M., Tosca N. J., Arvidson R. E., Michalski J. R., Ming D. W., Schröder C., Squyres S. W. (2006). In situ and experimental evidence for acidic weathering of rocks and soils on Mars. *Journal of Geophysical Research: Planets* 111:(E2).
- Jakobsson S. P., Jónsson J., Shido F. (1977). Petrology of the Western Reykjanes Peninsula, Iceland. *Journal of Petrology* 19:669-705.
- Jakosky B. M., Pepin R. O., Johnson R. E., Fox J. L. (1994). Mars Atmospheric Loss and Isotopic Fractionation by Solar-Wind-Induced Sputtering and Photochemical Escape. *Icarus* 111(2):271-288.
- Johnsson F. (2011). Perspectives on CO₂ capture and storage. *Greenhouse Gases* 1(2):119-133.
- Juliusson B. M., Gunnarsson I., Matthiasdottir K. V., Markusson S. H., Bjarnason B., Sveinsson O. G., Gislason T., Thorsteinsson H. H. (2015). Tackling the Challenge of H₂S Emissions. *Proceedings World Geothermal Congress 2015*.
- Keleman P. B., Hirth G. (2012). Reaction-driven cracking during retrograde metamorphism: Olivine hydration and carbonation. *Earth and Planetary Science Letters* 345-348:81-89.
- King P. L., McSween H. Y. (2005). Effects of H₂O, pH, and oxidation state on the stability of Fe minerals on Mars. *Journal of Geophysical Research: Planets* 110(E12).
- King P. L., McLennan S. M. (2010). Sulfur on Mars. *Elements* 6 (2).
- Knauth L. P., Burt D. M. (2002). Eutectic brines on Mars: Origin and possible relation to young seepage features. *Icarus* 158(1):267-271.
- Lafay R., Montes-Hernandez G., Janots E., Chiriac R., Findling N., Toche F. (2012). Mineral replacement rate of olivine by chrysotile and brucite under high alkaline conditions. *Journal of Crystal Growth* 347(1):62-72.

- Lapen T., Righter M., Brandon A., Debaille V., Beard B., Shafer J., Peslier A. (2010). A Younger Age for ALH 84001 and Its Geochemical Link to Shergottite Sources in Mars. *Science* 328(5976):347-351.
- Lee M. R., Tomkinson T., Mark D. F., Stuart F. M., Smith C. L. (2013). Evidence for silicate dissolution on Mars from the Nakhla meteorite. *Meteoritics & Planetary Sciences* 48(2):224-240.
- Lee M. R., Tomkinson T., Hallis L. J., Mark D. F. (2015). Formation of iddingsite veins in the martian crust by centripetal replacement of olivine: Evidence from the nakhlite meteorite Lafayette. *Geochimica et Cosmochimica Acta* 154:49-65.
- Liu Y., Olsen A. A., Rimstidt J. D. (2006). Mechanism for the dissolution of olivine series minerals in acidic dissolution. *American Mineralogist* 91:455-458.
- Luce R. W., Bartlett R. W., Parks G. A. (1972). Dissolution kinetics of magnesium silicates. *Geochimica et Cosmochimica Acta* 36(1):35-50.
- Maier W. D., Barnes S. J., Groves D. I. (2012). The Bushveld Complex, South Africa: formation of platinum-palladium, chrome- and vanadium-rich layers via hydrodynamic sorting of a mobilized cumulate slurry in a large, relatively slowly cooling, subsiding magma chamber. *Miner Deposita* 48(1).
- Malvoisin B., Brunet F., Carlut J., Rouméjon S., Cannat M. (2012). Serpentinization of oceanic peridotites: 2. Kinetics and processes of San Carlos olivine hydrothermal alteration. *Journal of Geophysical Research: Solid Earth* 117:B4.
- Marcucci E. C., Hynek B. M. (2014). Laboratory simulations of acid-sulfate weathering under volcanic hydrothermal conditions: Implications for early Mars. *Journal of Geophysical Research: Planets* 119(3):679-703.
- Matter J. M., Broecker W. S., Stute M., Gislason S. R., Oelkers E. H., Stefánsson A., Wolff-Boenisch D., Gunnlaugsson E., Axelsson G., Björnsson G. (2009). Permanent Carbon Dioxide Storage into Basalt: The CarbFix Pilot Project, Iceland. *Energy Procedia* 1:3641-3646.
- Matter J. M., Broecker W. S., Gislason S. R., Gunnlaugsson E., Oelkers E. H., Stute M., Sigurdardóttir H., Stefansson A., Alfreðsson H. A., Aradóttir E. S., Axelsson G., Sigfússon B., Wolff-Boenisch D. (2011). The CarbFix Pilot Project - Storing Carbon Dioxide in Basalt. *Energy Procedia* 4:5579-5585
- Matter J. M., Stute M., Snæbjörnsdóttir S. Ó., Oelkers E. H. Gislason S. R. Aradóttir E. S., Sigfusson B., Gunnarsson I., Sigurdardóttir H., Gunnlaugsson E., Axelsson G., Alfredsson H. A., Wolff-Boenisch D., Mesfin K., Fernandez De La Reguera T. D., Hall J., Dideriksen K., Broecker W. S. (2016). Rapid carbon mineralization for permanent disposal of anthropogenic carbon dioxide emissions. *Science* 352(6291):1312-4.

- McKay D.S., Gibson E.K. Jr., Thomas-Keppta K.L., Vali H., Romanek C.S., Clemett S.J., Chillier X.D.F., Maechling C.R., Zare R.N. (1996). Search for past life on Mars: possible relic biogenic activity in Martian meteorite ALH 84001. *Science* 273:924-930.
- McLennan S. M., Bell J. F., Calvin W. M., Christensen P. R., Clarke B. C., de Souza P. A., Farmer J., Farrand W. H., Fike D. A., Gellert R., Ghosh A., Glotch T. D., Grotzinger J. P., Hahn B., Herkenhoff K. E., Hurowitz J. A., Johnson J. R., Johnson S. S., Yen A. (2005). Provenance and diagenesis of the evaporite-bearing Burns formation, Meridiani Planum, Mars. *Earth and Planetary Science Letters* 240(1):95-121.
- Mikhlin Y. L., Tomashevich Y. V., Pashkov G. L., Okotrub A. V., Asanov I. P., Mazalov L. N. (1998). Electronic structure of the non-equilibrium iron-deficient layer of hexagonal pyrrhotite. *Applied Surface Science* 125:73-84.
- Milliken R. E., Swayze G. A., Arvidson R. E., Bishop J. L., Clark R. N., Ehlmann B. L., Green R. O., Grotzinger J. P., Morris R. V., Murchie S. L., Mustard J. F., Weitz C. (2008). Opaline silica in young deposits on Mars. *Geology* 36(11):847-850.
- Moore J. M., Bullock M. A. (1999). Experimental studies of Mars-analog brines. *Journal of Geophysical Research: Planets* 104(E9):21925-21934.
- Morris R. V., Ruff S. W., Gellert R., Ming D. W., Arvidson R. E., Clark B. C., Golden D. C., Siebach K., Klingelhöfer G., Schröder C., Fleischer I., Yen A. S., Squyres S. W. (2010). Identification of Carbonate-Rich Outcrops on Mars by the Spirit Rover. *Science* 329(5990):421-424.
- Mukhin L. M., Koscheev A. P., Dikov Yu P., Huth J., Wanke H. (1996). Experimental simulations of the photodecomposition of carbonates and sulphates on Mars. *Nature* 379.6561:141-3.
- Neuhoff P. S., Fridriksson T., Arnorsson S., Bird D. K. (1999). Porosity evolution and mineral paragenesis during low-grade metamorphism of basaltic lavas at Teigarhorn, eastern Iceland. *American Journal of Science* 299:467-501.
- Pasquier L. C., Mercier G., Blais J. F., Cecchi E., Kentish S. (2014). Reaction Mechanism for the Aqueous-Phase Mineral Carbonation of Heat-Activated Serpentine at Low Temperatures and Pressures in Flue Gas Conditions. *Environmental Science and Technology Letters* 48(9):5163-5170.
- Peretyazhko T. S., Niles P. B., Sutter B., Morris R. V., Agresti D. G., Lea L., Ming D. W. (2017). Smectite formation in the presence of sulfuric acid: Implications for acidic smectite formation on early Mars. *Geochimica et Cosmochimica Acta* (In Press).
- Perrin J. C., Krause M., Kuo C. W., Miljkovic L., Charoba E., Benson S. M. (2009). Core-scale experimental study of relative permeability properties of CO₂ and brine in reservoir rocks. *Energy Procedia* 1:3515-3522.

- Perrin J. C., Falta R. W., Krevor S., Zuo L., Ellison K., Benson S. M. (2011). Laboratory experiments on core-scale behaviour of CO₂ exolved from CO₂-saturated brine. *Energy Procedia* 4:3210-3215.
- Povrovsky O. S., Schott J. (2000). Forsterite surface composition in aqueous solutions: A combined potentiometric, electrokinetic, and spectroscopic approach. *Geochimica et Cosmochimica Acta* 64:3299-3312.
- Olsson J., Stipp S. L. S., Gislason S. R. (2014). Element scavenging by recently formed travertine deposits in the alkaline springs from the Oman Semail Ophiolite. *Mineralogical Magazine: Journal of Mineral Science* 78(6).
- Quafoku O., Hu J., Hess N. J., Hu M. Y., Ilton E. S., Feng J., Arey B. W., Felmy A. R. (2014). Formation of submicron magnesite during reaction of natural forsterite in H₂O saturated supercritical CO₂. *Geochimica et Cosmochimica Acta* 134:197-209.
- Rabe A. E., Harris J. F. (1963). Vapor Liquid Equilibrium Data for the Binary System Sulfur Dioxide and Water. *Journal of Chemical Engineering Data* 8(3):333-336.
- Ragnarsson Á. (2015). Geothermal Development in Iceland 2010-2014. *Proceedings World Geothermal Congress 2015*.
- Rosso J. J., Rimstidt J. D. (2000). A high resolution study of forsterite dissolution rates. *Geochimica et Cosmochimica Acta* 64:797-811.
- Schaefer H. T., Horner J. A., Owen A. T., Thompson C. J., Loring J. S., McGrail B. P. (2014). Mineralization of Basalts in the CO₂-H₂O-SO₂-O₂ System. *Environmental Science & Technology Letters* 48(9):5298-5305.
- Schnoor J. L. (1990). Kinetics of chemical weathering: a comparison of laboratory and field rates. *Aquatic Chemical Kinetics*. Wiley, New York 475-504.
- Schopka H. H., Gudmundsson M. T., Tuffen H. (2006). The formation of Helgafell, southwest Iceland, a monogenetic subglacial hyaloclastite ridge: Sedimentology, hydrology and volcano-ice interaction. *Journal of Volcanology and Geothermal Research* 152(3-4):359-377.
- Schrenk M. O., Brazelton W. J., Lang S. Q. (2013). Serpentinization, Carbon, and Deep Life. *Reviews in Mineralogy & Geochemistry* 75:575-606.
- Schulte M., Blake D., Hoehler T., McCollom T. (2006). Serpentinization and Its Implications for Life on the Early Earth and Mars. *Astrobiology* 6(2):364-376.
- Schwensler S. P., Bridges J. C., Miller M. A., Hicks L. J., Ott U., Filiberto J., Chavez C., Smith H., Treiman A. H., Kelley S. P., Moore J. M., Swindle T. D., Bullock M. A. (2017). Diagenesis on Mars: insights into noble gas pathways and newly formed mineral assemblages from long term experiments. *48th Lunar and Planetary Science Conference XLVIII* 1344.

- Scoon R. N., Mitchell A. A. (2004). Petrogenesis of Discordant Magnesian Dunite Pipes from the Central Sector of the Eastern Bushveld Complex with Emphasis on the Winnaarshoek Pipe and Disruption of the Merensky Reef. *Economic Geology* 99(3):517-541.
- Sears D. W. G., Chittenden J. D. (2005). On laboratory simulation and the temperature dependence of the evaporation rate of brine on Mars. *Geophysical Research Letters: Planets* 32(23).
- Shorttle O., Maclennan J. (2011). Compositional trends of Icelandic basalts: Implications for short-length scale lithological heterogeneity in mantle plumes. *Geochemistry, Geophysics, Geosystems* 12(11).
- Sigfusson B., Gislason S. R., Matter J. M., Stute M., Gunnlaugsson E., Gunnarsson I., Aradottir E. S., Sigurdardottir H., Mesfin K., Alfredsson H. A., Wolff-Boenisch D., Arnarsson M. T., Oelkers E. H. (2015). Solving the carbon-dioxide buoyancy challenge: The design and field testing of a dissolved CO₂ injection system. *International Journal of Greenhouse Gas Control* 37:213-219.
- Sissmann O., Brunet F., Martinez I., Guyot F., Verlaquet A., Piquier Y., Daval D. (2014). Enhanced Olivine Carbonation within a Basalt as Compared to Single-Phase Experiments: Reevaluating the Potential of CO₂ Mineral Sequestration. *Environmental Science and Technology Letters* 48(10):5512-5519.
- Sutter B., Boynton W. V., Ming D. W., Niles P. B., Morris R. V., Golden D. C., Lauer H. V., Fellows C., Hamara D. K., Mertzman S. A. (2012). The detection of carbonate in the martian soil at the Phoenix Landing site: A laboratory investigation and comparison with the Thermal and Evolved Gas Analyzer (TEGA) data. *Icarus* 218(1):290-296.
- Swindle T. D., Treiman A. H., Lindstrom D. J., Burkland M. K., Cohen B. A., Grier J. A., Li B., Olsen E. K. (2000). Noble gases in iddingsite from the Lafayette meteorite: Evidence for liquid water on Mars in the last few hundred million years. *Meteoritics & Planetary Science* 35(1):107-115.
- Swindle T., Olson E. (2004). Ar-40-Ar-39 studies of whole rock nakhlites: Evidence for the timing of formation and aqueous alteration on Mars. *Meteoritics & Planetary Science* 39(5):755-766.
- Szponar N., Brazelton W. J., Schrenk M. O., Bower D. M., Steele A., Morrill P. L. (2013). Geochemistry of a continental site of serpentinization, the Tablelands ophiolite, Gros Morne National Park: A Mars analogue. *Icarus* 224(2):286-296.
- Tar buck T. L., Richmond G. L. (2006). Adsorption and reaction of CO₂ and SO₂ at a water surface. *Journal of the American Chemical Society* 128:3256-3267.
- Tian F., Claire M. W., Haqq-Misra J. D., Smith M., Crisp D. C., Catling D., Zahnle K., Kasting J. F. (2010). Photochemical and climate consequences of sulfur outgassing on early Mars. *Earth and Planetary Science Letters* 295(3-4):412-418.

- Tosca N. J., McLennan S. M., Lindsley D. H., Schoonen M. A. A. (2004). Acid-sulfate weathering of synthetic Martian basalt: The acid fog model revisited. *Journal of Geophysical Research: Planets* 109(E5).
- Tsikouras B., Etiope G., Ifandi E., Kordella S., Papatheodorou G., Hatzipanagiotou K. (2013). Petrological implications for the production of methane and hydrogen in hyperalkaline springs from the Othrys ophiolite, Greece. *Proceedings of the 13th International Congress, Chania. Bulletin of the Geological Society of Greece* XLVII:1-449.
- Tomkinson T., Lee M. R., Mark D. F., Smith C. L. (2013). Sequestration of Martian CO₂ by mineral carbonation. *Nature Communications* 4:2662.
- Tosca N. J., McLennan S. M., Lindsley D. H., Schoonen M. A. A. (2004). Acid-sulfate weathering of synthetic Martian basalt: The acid fog model revisited. *Journal of Geophysical Research: Planets* 109(E5).
- Velbel M. A. (2012). Aqueous alteration in Martian meteorites: Comparing mineral relations in igneous-rock weathering of Martian meteorites and in the sedimentary cycle of Mars. *Sedimentary geology of Mars edited by Grotzinger J. and Milliken R. Society for Sedimentary Geology Special Publication* 102:97-117.
- Viljoen M. J., Scoon R. N. (1985). The distribution and main geologic features of discordant bodies of iron-rich ultramafic pegmatite in the Bushveld Complex. *Economic Geology* 80(4):1109-1128.
- Wadhwa M. (2004). Treasure hunting to the ends of the earth. *Science* 303:5654.
- Wang D., Dong B., Breen S., Zhao M., Qiao J., Liu Y., Zhang Y., Song Y. (2015). Review: Approaches to research on CO₂/brine two-phase migration in saline aquifers. *Hydrogeology Journal* 23:1-18.
- Website 1. Orkuveita Reykjavíkur. (2017). *CarbFix Project*. Available: <https://www.or.is/english/carbfix-project/about-carbfix-0>
- Website 2. AES. (2017). *CO₂ dosing system*. Available: <http://www.aesarabia.com/co2-dosing-system/>
- Website 3. Shaw S., Mills C. (2017). *Petrology and Mineralogy in ARD Prediction*. Available: <http://technology.infomine.com/enviromine/ard/Mineralogy/Petrology%20and%20Mineralogy.htm>
- Weiss D. K., Head J. W. (2015). Crater degradation in the Noachian highlands of Mars: Assessing the hypothesis of regional snow and ice deposits on a cold and icy early Mars. *Planetary and Space Science* 117:401-420.

- Wells R. K., Xiong W., Giammar D., Skemer P. (2017). Dissolution and surface roughening of Columbia River flood basalt at geologic carbon sequestration conditions. *Chemical Geology* 467:100-109.
- White A. F., Blum A. E., Schulz M. S., Bullen T. D., Harden J. W., Peterson M. L. (1996). Chemical weathering of a soil chronosequence on granitic alluvium: 1. Reaction rates based on changes in soil mineralogy. *Geochimica et Cosmochimica Acta* 60:2533-2550.
- White A. F., Brantley S. L. (2003). The effect of time on the weathering of silicate minerals: why do weathering rates differ in the laboratory and field? *Chemical Geology* 202(3-4)479-506.
- White A. F., Buss H. L. (2013). Natural Weathering Rates of Silicate Minerals. In: Holland H. D., Turekian K. K. *Treatise on Geochemistry*: Elsevier Science Ltd. 115-155.
- Wordsworth R. D., Kerber L., Pierrehumbert R. T., Forget F., Head J. W. (2015). Comparison of “warm and wet” and “cold and icy” scenarios for early Mars in a 3-D climate model. *Journal of Geophysical Research: Planets* 120(6):1201-1219.
- Yamamoto H., Zhang K., Karasaki K., Marui A., Uehara H., Nishikawa N. (2009). Large-scale numerical simulation of CO₂ geologic storage and its impact on regional groundwater flow: a hypothetical case study at Tokyo Bay, Japan. *Energy Procedia* 1:1871-1878.
- Zolotov M. Y., Shock E. L. (2005). Formation of jarosite-bearing deposits through aqueous oxidation of pyrite at Meridiani Planum, Mars. *Geophysical Research Letters* 32:L21203.

Chapter 5

Conclusions.

5.1 Thesis conclusions.

The aim of this work was to investigate the role of interactions between the Martian crust and hydrosphere in the loss of the early Mars atmosphere, specifically the process of mineral carbon sequestration. The work provides a bridge between the disciplines of applied engineering, geology and experimental geochemistry. The engineering element aimed to improve our ability to locate carbonates on the Martian surface. The geological aspect compared Martian meteorites to terrestrial ophiolite analogues, observing aqueous alteration and carbon sequestration. The geochemical experiments sought to replicate the processes of rock-water interaction and carbon sequestration in the laboratory, thus constraining their formation conditions and environments.

5.1.1 Engineering (Chapter 2).

The applied engineering sought to improve the Mars rover rock abrasion tool (RAT) by applying ultrasonics to enhance the surface smoothness capability, reduce power consumption, lower tool tip wear rate and increase material removal rate. The new tool developed is called the Micro Optic UltraSonic Exfoliator (MOUSE). Smoother rock grind surfaces allow clearer imaging of minerals and rock microstructures. By improving rover tool capabilities, it will become easier to discover and identify carbonate phases at the Martian surface, potentially giving new insights to assist in resolving questions around the loss of Mars' early atmosphere via mineral carbon sequestration. A lower power consumption on grinding operations will allow a rover to operate over a wider range of conditions, and for a longer period. With regards to grinding operations on current Mars rovers the diamond resin wears down relatively quickly, and a hard-wearing alternative would mean a longer tool life and greater science return per payload.

This work contrasted diamond resin against tungsten carbide tips, both with and without ultrasonics. Both tip types were used on soft limestone, basalt and quartzite under a range of weight on bit loads (12-32 N). Increasing material removal rate would reduce grind time, allowing for greater time for the rover to

travel, or to deploy other instruments, thus increasing data yield per mission. The summary of the results from the engineering experiments were as follows:

Surface roughness. The principal conclusion of the study is that ultrasonics makes for a smoother surface finish on all rock types and under all weight on bit variations when using a tungsten carbide tool tip. The addition of ultrasonics to a tungsten carbide tip reduced surface roughness by ~4 Ra. No Ra difference occurred when ultrasonics were applied to diamond resin. Tungsten carbide produces a smoother surface than diamond resin, diamond resin tips produced a finish that was >5 Ra and tungsten carbide tips produced a finish that was <5 Ra. Increased weight on bit made no difference to surface roughness, but consumed more power.

Power consumption. Power consumption is considerably higher when operating at 4.0 μm (wavelength) compare to 2.1 μm , but without improvement in surface smoothness. Tungsten carbide tips consumed more power than diamond resin tips. High weight on bit on softer rock samples using 4.0 μm caused the samples to shatter.

Tool tip wear rate. No observable wear occurred throughout the experiments on the tungsten carbide tips. The diamond resin tips showed minor wear on grinding without ultrasonics, but degraded significantly when ultrasonics were applied.

Material removal rate. Ultrasonic assisted grinding could potentially penetrate rock at a faster rate than the common rotary grinding techniques that the Mars rovers currently employ. However, this aspect was not sufficiently demonstrated owing to the limited timescale of the experiments.

To summarise, the addition of ultrasonics improves rock grind surface smoothness significantly, and tungsten carbide is a superior tool tip to diamond resin when ultrasonics are applied, producing a smoother surface with a more stable thrust force. The smoother surface finish comes at a moderate power increase compared to traditional diamond resin rotary methods, yet has the

advantage of a much longer tool tip life. These results, and the prototype tool that was developed represent a valuable new contribution to Mars rover engineering research and applied ultrasonics. As ultrasonics are currently not used on the Mars rovers, results from this thesis make a strong case for rover redesign. Space Glasgow is continuing to conduct extensive research in the Mars rover applications of ultrasonics, for drilling, polishing and rock sample return missions (Feeny *et al.* 2017; Firstbrook *et al.* 2017; Li *et al.* 2017 and others).

5.1.2 Mars analogues (Chapter 3).

The aim of this part of the study was to compare carbonates that occur in Martian meteorites with those in the Semail (United Arab Emirates and Oman) and Leka (Norway) ophiolites. The two meteorites selected for study were ALH 84001 to represent early Mars (~4 Ga), and Lafayette to represent more recent Mars (~1 Ga). Semail is a dry and hot Mars analogue, with abundant carbonates of diverse varieties. Leka is a wet and cold Mars analogue that lacks carbonates but displays extensive serpentinisation.

There are strong chemical and physical similarities between the early Mars carbonates in ALH 84001 and the Oman ophiolite carbonates. Semail carbonates have a strong zoning that comprises Mg or Ca - Mg bands, depending on the characteristics of local aqueous solutions, with distinctive water types that differ in chemical composition between shallow and deep aquifers. This study proposes that a similar division of chemically distinctive aquifers may be responsible for Mars carbonate zonations, with the higher Fe content in Mars carbonates caused by the higher Fe content of Martian olivine compared to Semail olivine. The principal conclusions of the analogue work are as follows:

- **Punctuated hyper carbonation on Mars hypothesis.**
 - It is proposed that intense, geographically localised carbonation may have occurred in the subsurface (>500 m depth) of early Mars, with positive

feedback 'runaway' carbonation taking place as observed in large terrestrial geoengineering sites such as CarbFix.

- Regional impact or volcanic heating of groundwater to ~180°C can cause carbonation of olivine. The high temperatures can be sustained at locations with a high and positive geothermal gradient (i.e., temperature increasing sharply with depth) and by the carbonation reaction itself, which is exothermic.
 - Aqueous alteration of the Martian crust causes a volume increase, due to mineral hydration, with fractures developing to expose fresh mineral surfaces for continued alteration.
 - Such hyper carbonation events would continue until one or more of heat, reactive primary mineral availability, and fluids became exhausted.
 - Such hypothetical subsurface events would be identifiable via seismic investigation on Mars and by other geophysical signatures such as anomalies in rock density created by the hydrated alteration products.
 - With a range of upcoming Mars missions capable of seismic investigations, such as InSight, this is a testable hypothesis.
- **Carbonate replacing glass in ALH 84001.**
 - Clear evidence is provided, by SEM and TEM imaging and microanalysis, of two different generations of fracture-filling carbonate within ALH 84001 that are in close association with Si rich glass.
 - The most plausible model of formation is maskelynite replacing orthopyroxene, then the maskelynite itself is then replaced by carbonate. Melt glass intruded at a later date, with a final, low water to rock ratio carbonate replacement of the melt glass occurring in lines of glass weakness, ending when all water was consumed.
 - What might initially appear an obscure investigation of a minor carbonate phase has relevance for wider questions on the availability of water on early Mars. Glass, whether maskelynite or melt glass, is highly reactive. If glass remains only partially aqueously altered by mineral carbonation then this limited reaction testifies to low water to rock ratios, and provides

additional evidence when selecting probable early Mars models such as in Figure 3.6.

- The evidence presented in this study supports relatively dry rather than wet models for early Mars.

- **Carbonate rosettes in ALH 84001.**
 - Rosette carbonates in ALH 84001 were examined. Ca - Fe - Mg zoning patterns were identified, with S intimately associated with the Fe carbonate phase. Ca carbonate graded into Fe carbonate mixed with S (pyrite/pyrrhotite), but there was a sharp contact between Fe carbonate and carbonates containing S and Mg.

- **Carbonates in Lafayette.**
 - No rosette type carbonates were identified in Lafayette.
 - Veins of alteration products were located in olivine and orthopyroxene grains.
 - A wide range of phyllosilicates dominate the veins, in stark contrast to ALH 84001.
 - Saponite 'flowers' were identified replacing Ca - Mn rich siderite, and a terrestrial analogue for such features was identified in rhyolite tuff from Oya, Tochigi prefecture, Japan.

The terrestrial Leka ophiolite. No carbonates were identified, only intense, sometimes complete serpentinisation of peridotites. This concurs with the academic literature which contains notably less carbonate observation and analysis in Leka compared with Semail ophiolite. Combined with this study's results it can be tentatively stated that Leka is less mineral carbonated than Semail. Leka is wet and cold. Semail dry and hot. This result could suggest either:

- Temperature, rather than water to rock ratio, is the primary control of well-formed carbonate rosette growth.

- High water to rock ratio and through flow (aqueous cation removal) reduces carbonate growth.

- **Carbonates in the Semail ophiolite.**
 - Carbonates observed in the Semail samples included both rosette and slab types, similar to those in ALH 84001.
 - All Semail carbonates lacked Fe, probably due to an initially Fe poor primary olivine, loss of Fe during ensuing serpentinisation, or both.
 - Dolomite carbonate rosette and slab zonations that were similar in shape to ALH 84001, albeit different in composition, varied between 51 - 58 atomic % Ca. It is proposed that rosette carbonates form in environments of slow growth, low density of nucleation sites (for example in drained but not dry pore spaces), whereas slab carbonates form in environments of rapid growth, high density of nucleation sites (for example where water is actively migrating through fractures). These conclusions about the determinants of carbonate formation would apply to both Earth (Semail) and Mars (ALH 84001). Interesting future work would be to design a specific laboratory mineral carbonate growth experiment to test this hypothesis.
 - Some Semail carbonate zones have sharp contacts, while others have graded contacts. It is proposed that gradational contacts are due to chemical change through time during a single crystal growth event, and that sharp contacts represent a gap of an unspecified time between events. This proposal could be tested experimentally, and if correct may add to our understanding of the formation environment and sequence of events surrounding the ALH 84001 carbonates, which possess similar graded and sharp carbonate contacts.
 - It is proposed that changes in Mg and Ca abundance in carbonates may be due to the well-known ophiolite water types, where an Mg rich shallow subsurface aquifer (type 1 water) overflows intermittently into deeper aquifers (type 2 waters), or mix with extrusive Ca waters (type 3 waters). The dolomite carbonates observed in this study do not neatly correlate with

any classic ophiolite water type carbonate (i.e. type 1 magnesite and type 3 calcite), and so probably represent a transitional environment. Aquifer overflow may be due to infrequent precipitation events or aquifer faulting. Mars possesses a basaltic geology, similar in many respects to that of terrestrial ophiolites. It is entirely plausible that early Mars, with a more active surface hydrological cycle than present, could have possessed ophiolite water types which may have been responsible for forming distinct carbonate zones, such as observed in ALH 84001. As water became scarcer on Mars and more CO₂ left the atmosphere, phyllosilicates began to be the dominant alteration product, as observed in Lafayette, with chemically uniform minor carbonates lacking in zonation.

5.1.3 Experimental (Chapter 4).

The geochemical experiments sought to replicate alteration processes and products that are recorded by Martian meteorites and within a Mars analogue laboratory environment. The effects of differing initial atmospheric and mineral compositions were explored at 2 bar pressure, comparing the effect of differing primary silicate starting materials (olivine versus basalt), and investigating the influence of sulphur (SO₂ and pyrrhotite) on the mineral alteration process. The key gases compared were CO₂ versus a CO₂ and SO₂ mixture. Results and key findings of these experiments are as follows:

- **No carbonate precipitates.** In all chambers, no carbonates were modelled to have precipitated, nor were any observed. Thus, precipitation of carbonates is the limiting factor in MCS rather than the dissolution of olivine to liberate Mg and Fe to solution.
- **Sulphur increases the carbonate saturation state over time.** All chambers containing sulphur as either pyrrhotite or SO₂ show a slow trend towards carbonate saturation. Chambers lacking sulphur do not show this trend in solution chemistry.

- **Calcite would be the first carbonate expected to precipitate on reaction with basalts, whereas Mg carbonate or siderite would precipitate from olivine.**
- **Experiment duration is an important variable.** Running the experiment over a 360 day period instead of 120 days would be an interesting exercise to see whether carbonates eventually precipitate, as well as observing the extent to which sulphur catalyses the dissolution of the olivine.
- **The nature of mineral alteration, and changes in fluid chemistry,** are influenced more by chamber gas composition than by initial mineralogy.
- **Release of ions** from the reactant minerals is enhanced significantly by SO₂ gas, and much less so by including pyrrhotite as a reactant.
- The presence of both SO₂ and pyrrhotite greatly reduces solution pH.
- SO₂ reacting with olivine releases high concentrations of Fe, then after 51 days precipitates Fe and S.
- **The pore space precipitation model** for formation of veins of alteration products in Martian meteorites is strongly supported by chambers containing olivine with CO₂ and SO₂, and olivine with only CO₂.

This study demonstrates the importance of using more than pure CO₂ gas when attempting to reproduce an early Martian atmosphere for mineral alteration experiments. The inclusion of sulphur in some form is important, and addition of SO₂ gas into the experiments drastically increases dissolution rates of primary minerals, fluid chemistry/element saturation and formation/inhibition of alteration products.

South African hortonolite has enormous potential to become a superior olivine analogue for Mars than San Carlos, due to its higher iron content. However, more extensive mineral characterization and standardisation is required prior to it being adopted more widely.

The results indicate that carbonates can take a considerable time to form (>120 days), even in high water to rock ratio and physically conducive environments (2 bar and 80°C), casting doubt that Mars mineral alteration occurred in short, sporadic, localised melting with low water to rock ratio on a cold icy early Mars.

5.2 Future work.

5.2.1 Engineering.

Further development of the MOUSE should focus on using low WOB and low μm ultrasonic amplitude in order to avoid damaging delicate geological structures of interest and reduce rover energy expenditure.

- Scale down the ultrasonic rig to rover mountable dimensions and replace the heavy materials, such as steel, with light weight space-ready alternatives such as aluminium, carbon fibre or ideally albernet.
- Explore the use of other hard tool tip materials, including pure synthetic diamond, comparing their performance with tungsten carbide.
- Increase the range of rock types tested and build a database of rock properties and tool responses.
- Explore a wider range of wave amplitudes, seeking an optimal performance wavelength (1.0 μm to 3.0 μm).
- Re-run the material removal rate measurements over the period of hours per run rather than minutes per run to gain a reliable material removal rate value per rock type.
- Increase the Ra Rz measurements per grind so as to reduce experimental uncertainties.
- Change the rotation pattern away from a simple 360 revolve, possibly adopting the rotate and revolve dual motion action of the RAT, which would increase grind uniformity, at the expense of increasing power consumption and weight (an additional motor would be required).

- Initiate discussions with space system engineers to collaborate on how to integrate such a tool into a rover operating system and build an operationally ready prototype. Perhaps attempt to merge it with a corer/drill tool as part of a future Mars sample return mission.

The MOUSE concept has generated significant external interest for future work, specifically:

- i. Heriot Watt University, St Andrews University are attempting to gain funds, with the British Geological Survey and Space Glasgow as supporting partners, to use the MOUSE in a terrestrial borehole setting. A team at Heriot Watt is working to miniaturise a fourier transform infrared spectroscopy (FTIR) instrument to ~ 150 mm length. This FTIR would descend down the borehole in a shell and analyse rock mineralogy, however, to be effective in a borehole environment, it must first penetrate past the immediate borehole rock contact, which is often highly contaminated and altered. In order to achieve this penetration the MOUSE would also be miniaturised to <150 mm and work in conjunction with the FTIR, ultrasonically grinding away to reach the unaltered rock interior prior to FTIR analysis. If funding is successful this project would begin in September 2019.
- ii. A 5 year fellowship proposal has been submitted to the astronaut training centre (EAC) at the European Space Agency, to miniaturise the MOUSE and mount it on drones. Drones may become the future of robotic planetary exploration. This drone-MOUSE combination would then be tested on a variety of terrestrial Mars analogue environments.

5.2.2 Analogue.

To further the Mars meteorite - terrestrial ophiolite analogue work, the first step would be to gain a more extensive library of ophiolite carbonate samples. A field season in the United Arab Emirates would allow detailed collection and logging of sample locations, with the aim to gather a range of carbonated

peridotite from all known aquifer type regions. Part of these samples could be made into thin sections for microscope observation and quantitative mineral analysis, allowing for greater confidence that carbonate element type is correlating with aquifer type.

To test the proposal that rosette carbonate structures grow slowly in open pore spaces with low water to rock ratio, hence low nucleation site availability, and that slab carbonates dominate in high water to rock ratio, high nucleation site and grow more rapidly, a laboratory experiment could be conducted. Ideally the experiment would span at least a year, and take place in a chamber where pressure and temperature could remain constant and reflect the subsurface ophiolite environment at conditions that are representative of shallow and deep aquifers. A basalt and/or peridotite substrate from the Semail could be used, and ideally both closed chambers and through flow reactors used, to investigate the impact of fluid percolation.

Regarding the punctuated hyper carbonation hypothesis, apart from waiting for seismic equipment to reach Mars and measure upper crust density profiles, a number of other investigative routes could be pursued. Notably, in Leka, the hydrated peridotite creates distinctive approximately rectangular fractured surface features reminiscent of baked bread, on a range of scales (Jamtveit *et al.* 2007; Iyer *et al.* 2008). A search of Martian surface data for similar features on both macro and micro scales may prove fruitful.

The section on punctuated hypercarbonation on Mars has attracted the attention of NASA, and the McKay fellowship may be offered in late 2018 in order to either investigate:

- i. The punctuated hyper carbonation. This concept might be advanced by scrutinising image data of Mars in where regions of past volcanism, impacts and glaciation have occurred and comparing the features with those of ophiolite and geo-engineered CARBFIX style regions on Earth. Carbonation at depth may be found via low gravity anomalies (carbonate being less dense than basalt), expansion fracturing and associated mound formations. This information might then be used to identify potential landing sites for

seismic exploration on Mars, carbonate regions having a differing seismic signal to basaltic regions.

- ii. Zonation of carbonates via overflow events of subsurface aquifers with individually distinct chemistry, and the idea that individual zonations may be linked to single precipitation events. A range of potential laboratory Mars simulation settings are under consideration with large masses of substrate (basalt or peridotite) simulating the Martian crust and aquifers that periodically overflow under early Mars pressure, temperature and gas conditions. Full details are still in progress.

5.2.3 Experimental.

The lack of carbonates produced by this study, despite water saturated mineral surfaces and 2 bar atmospheric conditions indicate that in order to produce Mars like carbonates the experiment would need to be conducted over a considerably longer time period, or the temperature - pressure - mineral volume increased. However, doing so potentially reduces accurate pressure and temperature representation of an early Mars environment. Another aspect that could be improved upon is characterising South African hortonolite to the same level as the well characterised San Carlos olivine. SEM and TEM combined with replicate bulk chemical analysis (XRF, ICP or wet chemical techniques) would highlight any regional subtypes and variations in impurities. Hortonolite might then become the standard used in Martian mineral experiments, possessing as it does, a more accurate iron content relative to Mars compared with San Carlos olivine.

Further geochemical experiment work using mineral carbon sequestration and olivine could also pursue the terrestrial climate change line of enquiry. Considerable research interest exists for adding olivine and basalt to agricultural soil as part of an effort to draw down anthropogenic CO₂, termed advanced weathering (Schuiling & Krijgsman, 2006, Edwards *et al.* 2017). It has also been proposed to add olivine to coastal marine environments for the same purpose (Montserrat *et al.* 2017). It would be interesting to conduct similar types of batch experiments as undertaken in this work, varying mineralogy, but keeping

temperature and pressure fixed. The additional variables of water content/salinity could be included. IC/ICPMS and quantitative SEM analysis could observe mineral changes and aqueous element mobility. For a marine environment, the releases of Si and Ca from basalt and olivine are a limiting nutrient for micro fauna, and observing element flux on population life cycles would be important for aquatic food chains. For agriculture, the key aspect to observe might be the pH fluxes during alteration reactions that might affect crops.

All of these experiment suggestions demonstrate how Mars crust research can inform and potentially collaborate with terrestrial climate change research communities with respect to mineral carbon sequestration.

Another line of investigation that would be interesting to pursue would be to repeat a similar set of experiments, removing the number of substrate variables to only basalt or peridotite, but increasing the gas variables to include methane, with and without SO₂. Observing if methane reacts to produce CO₂, and if so at what rate and the influence of these reactions on carbonate formation. Such experiments would significantly aid discussions of crust - atmosphere coupling of early Mars.

The introduction to this thesis stated the central goal was to investigate the Mars carbonate conundrum, whereby evidence exists for great volumes of water on early Mars. Liquid surface water requires a much denser atmosphere than modern Mars possesses, probably predominantly composed of CO₂. Such significant volumes of CO₂ and water in the presence of basalt should have produced vast concentrations of carbonate minerals, yet little carbonate has been discovered thus far. Determining how much CO₂ was stored as carbonate minerals, locating these carbonates on the Martian surface, determining the species of carbonate and the precise formation processes involved all constitute elements of the Mars carbonate conundrum and are the focus of this thesis.

The engineering (chapter 2) and the successful development of the MOUSE contributes to the task of locating carbonates on Mars' surface, by providing a more efficient grinding tool and smoother grind surfaces. The comparative analysis of ophiolites as Martian geology analogues (chapter 3), replete with analysis of ALH

84001 and Lafayette, contributed to identifying carbonate species on Mars and their formation processes. A minor carbonate phase replacing Si rich melt glass was identified in ALH 84001. The hypothesis of punctuated hyper carbonation is presented as a potential solution to the missing carbonates on Mars. The hypothesis of distinct Martian aquifer water types reminiscent of ophiolite aquifer water types is suggested as potential answer to explain carbonate zoning in ALH 84001. The geochemistry experiment (chapter 4) sought to create conditions suitable for carbonate formation representative of Mars, thereby aiding in quantification of environmental conditions on early Mars. Although the experiment did not produce carbonates, it showed the effect of sulphur on olivine dissolution and supports vein widening as an important factor in the process of silicate alteration, which would provide increased pore space for carbonate formation and affect the mineral carbon storage capacity of the Martian crust.

Collaboration between engineers, field geologists and experimental chemists has the potential to considerably advance our knowledge of Mars, with many lessons learned about the fate of the Mars atmosphere also being highly applicable to questions about the short to medium term fate of Earth's atmosphere. The emergence of highly cross disciplinary thesis provides bridges for such research community symbiosis.

5.3 References.

- Edwards D. P., Lim F., James R. H., Pearce C. R., Scholes J., Freckleton R. P., Beerling D. J. (2017). Climate change mitigation: potential benefits and pitfalls of enhanced rock weathering in tropical agriculture. *Biology Letters* 13(4).
- Feeney A., Sikaneta S., Harkness P., Lucas M. (2017). Ultrasonic compaction of granular geological materials. *Ultrasonics* 76:136-144.
- Firstbrook D., Worrall K., Timoney R., Suñol F., Gao Y., Harkness P. (2017). An experimental study of ultrasonic vibration and the penetration of granular material. *Proceedings of the Royal Society of London Series A: Mathematical, Physical and Engineering Sciences* 473(2198):20160673.
- Iyer K., Jamtveit B., Mathiesen J., Malthe-Sørensen A., Feder J. (2008). Reaction-assisted hierarchical fracturing during serpentinisation. *Earth and Planetary Science Letters* 267(3-4):503-516.
- Jamtveit B., Iyer K., Royne A., Malthe-Sørensen A., Mathiesen J., Feder J. (2007). Stress generation and hierarchical fracturing in reactive systems. *American Geophysical Union Fall Meeting 2007 abstract #T14A-05*.
- Li X., Harkness P., Worrall K., Timoney R., Lucas M. (2017). A parametric study for the design of an optimized ultrasonic-percussive planetary drill tool. *IEEE Transactions on Ultrasonics, Ferroelectrics, and Frequency Control* 64(3):577-589.
- Montserrat F., Renforth P., Hartmann J., Leermakers M., Knops P., Meysman F. J. R. (2017). Olivine Dissolution in Seawater: Implications for CO₂ Sequestration through Enhanced Weathering in Coastal Environments. *Environmental Science & Technology Letters* 51(7):3960-3972.
- Schuiling R. D., Krijgsman P. (2006). Enhanced Weathering: An Effective and Cheap Tool to Sequester CO₂. *Climatic Change* 74(1-3):349-354.

Appendix 1.

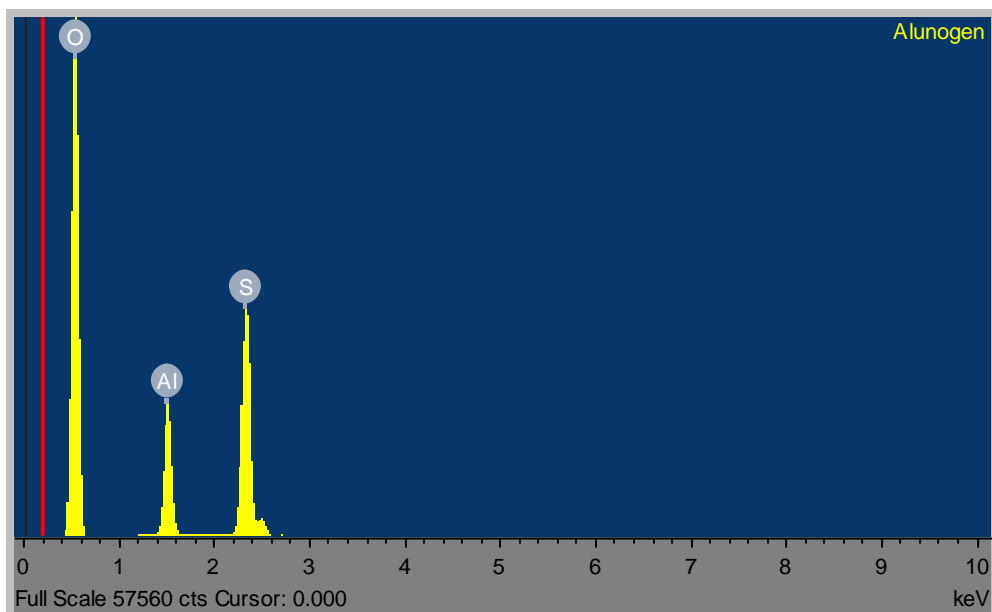
Spectral and mineral data for carbonates, clays and weathered minerals of particular relevance to mineral carbonation.

Alunogen (Jarosite variation)

Dana class 29.08.06.01 (29) Hydrated Acid and Sulfates

Chemical Formula:	$\text{Al}_2(\text{SO}_4)_3 \cdot 17(\text{H}_2\text{O})$		
Composition:	Molecular Weight =	648.41 gm	
	Aluminum	8.32 % Al	15.72 % Al_2O_3
	Hydrogen	5.29 % H	47.23 % H_2O
	Sulfur	14.84 % S	37.04 % SO_3
	Oxygen	71.56 % O	
		100.00 %	100.00 % = TOTAL OXIDE

Empirical Formula: $\text{Al}_2(\text{SO}_4)_3 \cdot 17(\text{H}_2\text{O})$

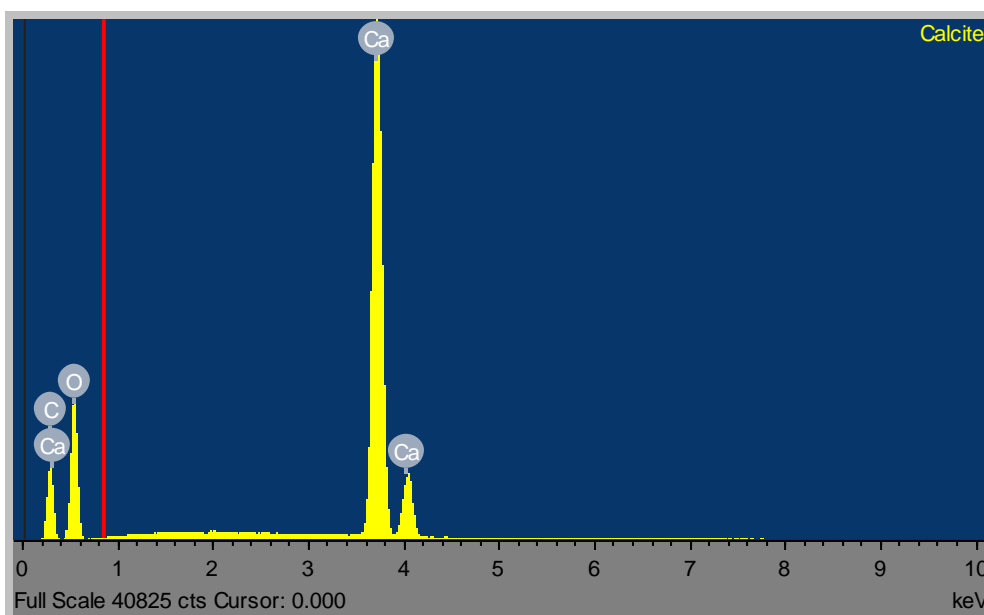


Synonym:	Aluminum Sulfate, Doughtyite, ICSD 4292, Keramohalite, PDF 26-1010
Cleavage:	{010} Perfect, {100} Very Good, {313} Distinct
Color:	White, Yellowish white, Reddish white, Yellowish white.
Density:	1.65 - 1.78, Average = 1.71
Diaphaneity:	Transparent
Fracture:	Sub Conchoidal - Fractures developed in brittle materials characterized by semi-curving surfaces.
Habit:	Acicular - Occurs as needle-like crystals.
Habit:	Encrustations - Forms crust-like aggregates on matrix.
Habit:	Fibrous - Crystals made up of fibers.
Hardness:	1.5-2 - Talc-Gypsum
Luminescence:	Non-fluorescent.
Luster:	Vitreous - Pearly
Streak:	white
Axial Ratios:	a:b:c = 0.2751:1:0.2247
Cell Dimensions:	a = 7.42, b = 26.97, c = 6.062, Z = 2; alpha = 89.95°, beta = 97.566°, gamma = 91.888° V = 1,201.90 Den(Calc) = 1.79
Crystal System:	Triclinic - Pinacoidal H-M Symbol (1) Space Group: P1
X Ray Diffraction:	By Intensity(I/I ₀): 4.49(1), 4.33(0.8), 4.39(0.8), 13.5(0.6), 3.68(0.5), 3.9(0.5), 3.02(0.4),

Calcite

Dana class 14.01.01.01 (14) Anhydrous Carbonates

Chemical Formula:	CaCO ₃		
Composition:	Molecular Weight =	100.09 gm	
	Calcium	40.04 % Ca	56.03 % CaO
	Carbon	12.00 % C	43.97 % CO ₂
	Oxygen	47.96 % O	
		100.00 %	100.00 % = TOTAL OXIDE
Empirical Formula:	(CO ₃)		



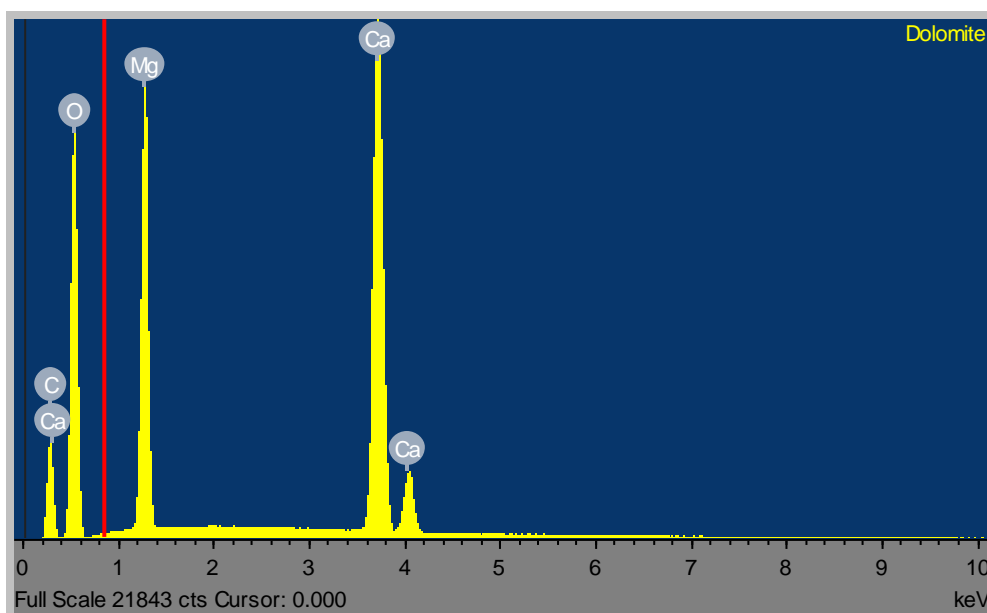
Synonym:	Glendonite – pseudomorph, ICSD 73446, Manganocalcite – variety, Nicols, PDF 5-586, Parakutnohorite - intermediate composition between calcite and rhodochrosite, Travertine.
Cleavage:	{1011} Perfect, {1011} Perfect, {1011} Perfect
Color:	Colorless, White, Pink, Yellow, Brown.
Density:	2.71
Diaphaneity:	Transparent to translucent to opaque
Fracture:	Brittle - Conchoidal - Very brittle fracturing to small, conchoidal fragments.
Habit:	Crystalline - Coarse - Occurs as well-formed coarse sized crystals.
Habit:	Massive - Uniformly indistinguishable crystals forming large masses.
Habit:	Stalactitic - Shaped like pendant columns as stalactites or stalagmites.
Hardness:	3 - Calcite
Luminescence:	Fluorescent and phosphorescent, Short UV=yellow, blue, red green, Long UV=yellow, blue, red green.
Luster:	Vitreous (Glassy)
Streak:	white
Axial Ratios:	a:c = 1:3.41992
Cell Dimensions:	a = 4.989, c = 17.062, Z = 6; V = 367.78 Den(Calc)= 2.71
Crystal System:	Trigonal - Hexagonal ScalenohedralH-M Symbol (3 2/m) Space Group: R 3c
X Ray Diffraction:	By Intensity(I/I ₀): 3.035(1), 2.095(0.18), 2.285(0.18),

Dolomite

Dana class 14.02.01.01 (14) Anhydrous Carbonates

Chemical Formula:	CaMg(CO ₃) ₂		
Composition:	Molecular Weight =	184.40 gm	
	Calcium	21.73 % Ca	30.41 % CaO
	Magnesium	13.18 % Mg	21.86 % MgO
	Carbon	13.03 % C	47.73 % CO ₂
	Oxygen	52.06 % O	
		100.00 %	100.00 % = TOTAL OXIDE

Empirical Formula: CaMg(CO₃)₂



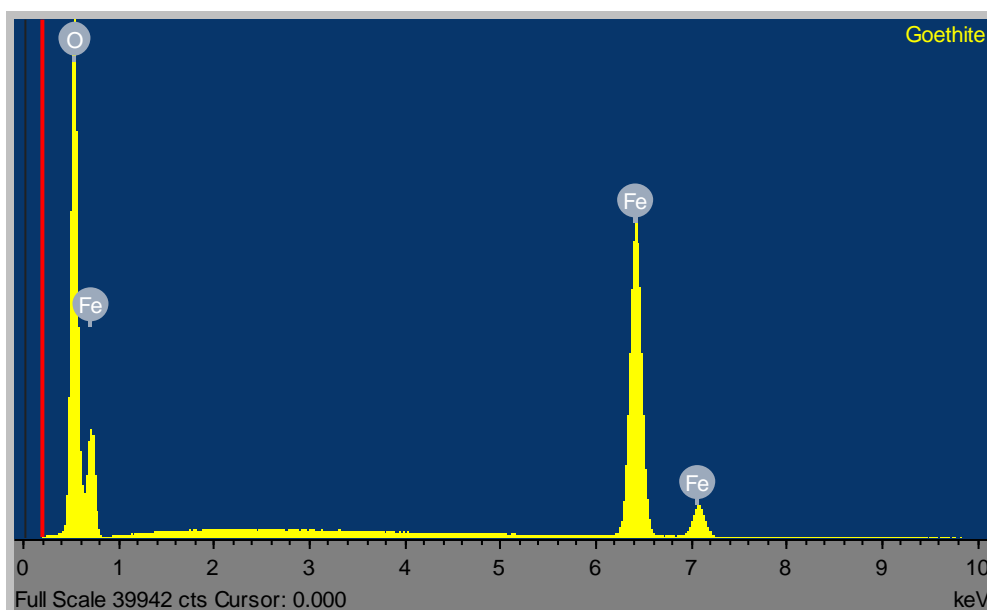
Synonym:	ICSD 31336, PDF 36-426
Cleavage:	{1011} Perfect, {1011} Perfect, {1011} Perfect
Color:	White, Gray, Reddish white, Brownish white, Gray.
Density:	2.8 - 2.9, Average = 2.84
Diaphaneity:	Transparent to translucent
Fracture:	Brittle - Conchoidal - Very brittle fracturing to small, conchoidal fragments.
Habit:	Blocky - Rhombohedral - Crystal shape resembles rhombohedrons.
Habit:	Crystalline - Coarse - Occurs as well-formed coarse sized crystals.
Habit:	Massive - Uniformly indistinguishable crystals forming large masses.
Hardness:	3.5-4 - Copper Penny-Fluorite
Luminescence:	Non-fluorescent
Luster:	Vitreous (Glassy)
Streak:	white
Axial Ratios:	a:c = 1:3.29409
Cell Dimensions:	a = 4.842, c = 15.95, Z = 3; V = 323.85 Den(Calc)= 2.84
Crystal System:	Trigonal - RhombohedralH-M Symbol (3) Space Group: R 3
X Ray Diffraction:	By Intensity(I/I ₀): 2.883(1), 1.785(0.6), 2.191(0.5),

Goethite

Dana class 06.01.01.02 (06) Hydroxides and Oxides Containing Hydroxyl

Chemical Formula:	$\text{Fe}^{3+}\text{O}(\text{OH})$		
Composition:	Molecular Weight =	88.85 gm	
	Iron	62.85 % Fe	89.86 % Fe_2O_3
	Hydrogen	1.13 % H	10.14 % H_2O
	Oxygen	36.01 % O	
		100.00 %	100.00 % = TOTAL OXIDE

Empirical Formula: $\text{Fe}^{3+}\text{O}(\text{OH})$



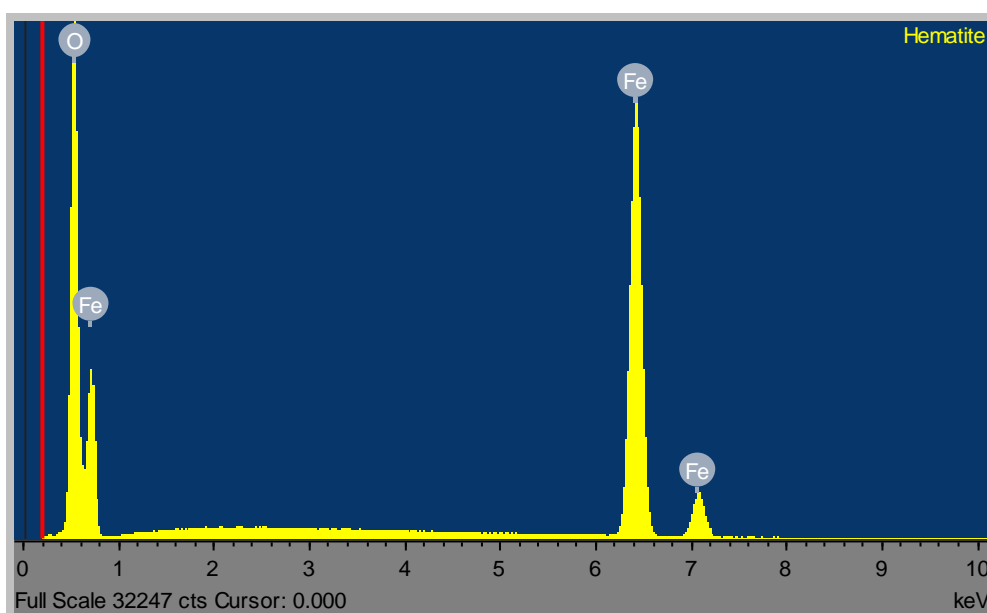
Synonym:	Acicular iron ore, ICSD 28247, Limonite, Needle ironstone, PDF 29-713
Cleavage:	{010} Perfect, {100} Distinct
Color:	Brown, Reddish brown, Yellowish brown, Brownish yellow, Ocher yellow.
Density:	3.3 - 4.3, Average = 3.8
Diaphaneity:	Subtranslucent to opaque
Fracture:	Hackly - Jagged, torn surfaces, (e.g. fractured metals).
Habit:	Acicular - Occurs as needle-like crystals.
Habit:	Radial - Crystals radiate from a center without stellar forms (e.g. stibnite)
Habit:	Reniform - "Kidney like" in shape (e.g.. hematite).
Hardness:	5-5.5 - Apatite-Knife Blade
Luminescence:	Non-fluorescent.
Luster:	Adamantine - Silky
Streak:	yellowish brown
Axial Ratios:	a:b:c=0.4615:1:0.3034
Cell Dimensions:	a = 4.596, b = 9.957, c = 3.021, Z = 4; V = 138.25 Den(Calc)= 4.27
Crystal System:	Orthorhombic - DipyramidalH-M Symbol (2/m 2/m 2/m) Space Group: Pbnm
X Ray Diffraction:	By Intensity(I/I ₀): 4.18(1), 2.69(0.3), 2.452(0.25),

Hematite

Dana class 04.03.01.02 (04) Simple Oxides

Chemical Formula:	Fe ₂ O ₃		
Composition:	Molecular Weight =	159.69 gm	
	Iron	69.94 % Fe	100.00 % Fe ₂ O ₃
	Oxygen	30.06 % O	
		100.00 %	100.00 % = TOTAL OXIDE

Empirical Formula: Fe³⁺₂O₃



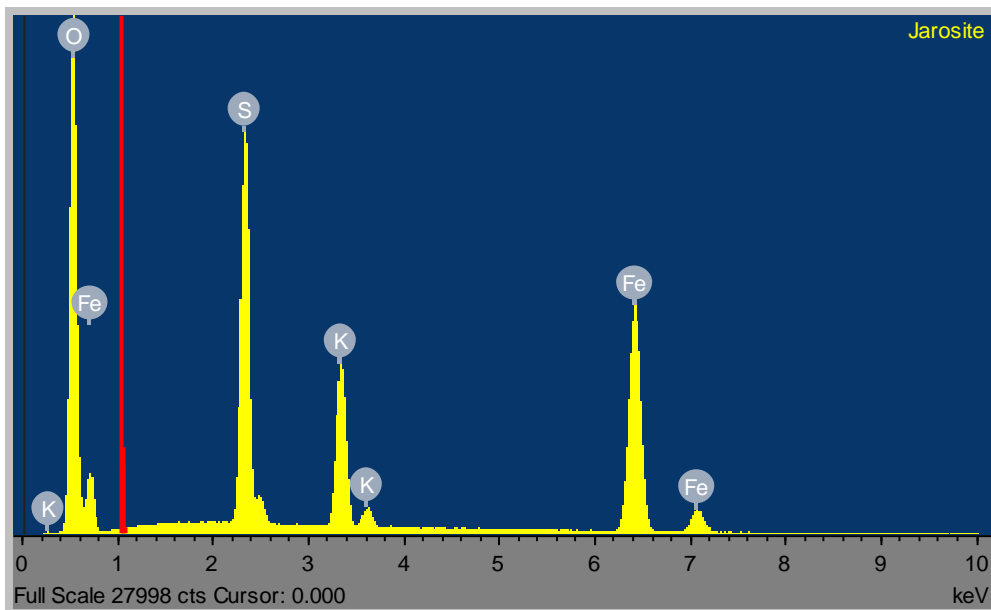
Synonym:	ICSD 64599, Kidney Ore, Martite, PDF 33-664, Specularite
Cleavage:	None
Color:	Reddish gray, Black, Blackish red.
Density:	5.3
Diaphaneity:	Subtranslucent to opaque
Fracture:	Conchoidal - Fractures developed in brittle materials characterized by smoothly curving surfaces, (e.g. quartz).
Habit:	Blocky - Crystal shape tends to be equant (e.g. feldspars).
Habit:	Earthy - Dull, clay-like texture with no visible crystalline affinities.
Habit:	Tabular - Form dimensions are thin in one direction.
Hardness:	6.5 - Pyrite
Luminescence:	Non-fluorescent.
Luster:	Metallic
Magnetism:	Magnetic after heating
Streak:	reddish brown
Axial Ratios:	a:c = 1:2.73009
Cell Dimensions:	a = 5.0317, c = 13.737, Z = 6; V = 301.20 Den(Calc)= 5.28
Crystal System:	Trigonal - Hexagonal ScalenohedralH-M Symbol (3 2/m) Space Group: R 3c
X Ray Diffraction:	By Intensity(I/I ₀): 2.69(1), 1.69(0.6), 2.51(0.5),

Jarosite

Dana class 30.02.05.01 (30) Anhydrous Sulfates Containing Hydroxyl or Halogen

Chemical Formula:	$KFe^{3+}_3(SO_4)_2(OH)_6$		
Composition:	Molecular Weight =	500.81 gm	
	Potassium	7.81 % K	9.40 % K_2O
	Iron	33.45 % Fe	47.83 % Fe_2O_3
	Hydrogen	1.21 % H	10.79 % H_2O
	Sulfur	12.81 % S	31.97 % SO_3
	Oxygen	44.73 % O	
		100.00 %	100.00 % = TOTAL OXIDE

Empirical Formula: $KFe^{3+}_3(SO_4)_2(OH)_6$



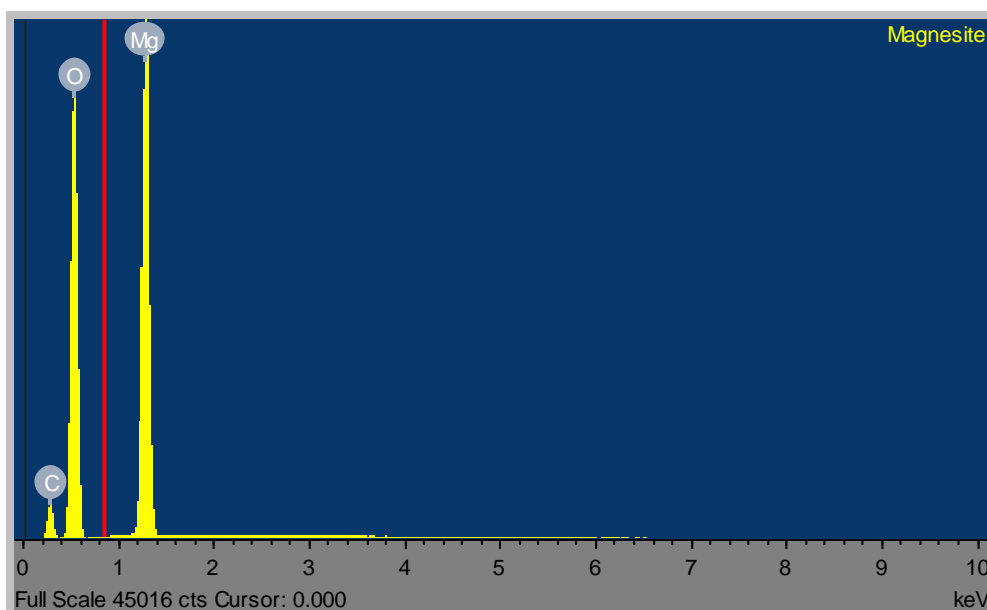
Synonym:	ICSD 12107, PDF 36-427, Utahite
Cleavage:	{0001} Distinct
Color:	Brown, Yellow, Yellow brown, Light yellow.
Density:	2.9 - 3.3, Average = 3.09
Diaphaneity:	Translucent
Fracture:	Uneven - Flat surfaces (not cleavage) fractured in an uneven pattern.
Habit:	Crystalline - Fine - Occurs as well-formed fine sized crystals.
Habit:	Fibrous - Crystals made up of fibers.
Habit:	Massive - Uniformly indistinguishable crystals forming large masses.
Hardness:	2.5-3.5 - Finger Nail-Copper Penny
Luminescence:	Non-fluorescent.
Luster:	Vitreous (Glassy)
Streak:	yellow
Axial Ratios:	a:c = 1:2.36199
Cell Dimensions:	a = 7.21, c = 17.03, Z = 3; V = 766.68 Den(Calc)= 3.25
Crystal System:	Trigonal - PyramidalH-M Symbol (3) Space Group: R 3
X Ray Diffraction:	By Intensity(I/I ₀): 3.08(1), 3.11(0.6), 2.292(0.5),

Magnesite

Dana class 14.01.01.02 (14) Anhydrous Carbonates

Chemical Formula:	MgCO ₃		
Composition:	Molecular Weight =	84.31 gm	
	Magnesium	28.83 % Mg	47.80 % MgO
	Carbon	14.25 % C	52.20 % CO ₂
	Oxygen	56.93 % O	
		100.00 %	100.00 % = TOTAL OXIDE

Empirical Formula: Mg(CO₃)



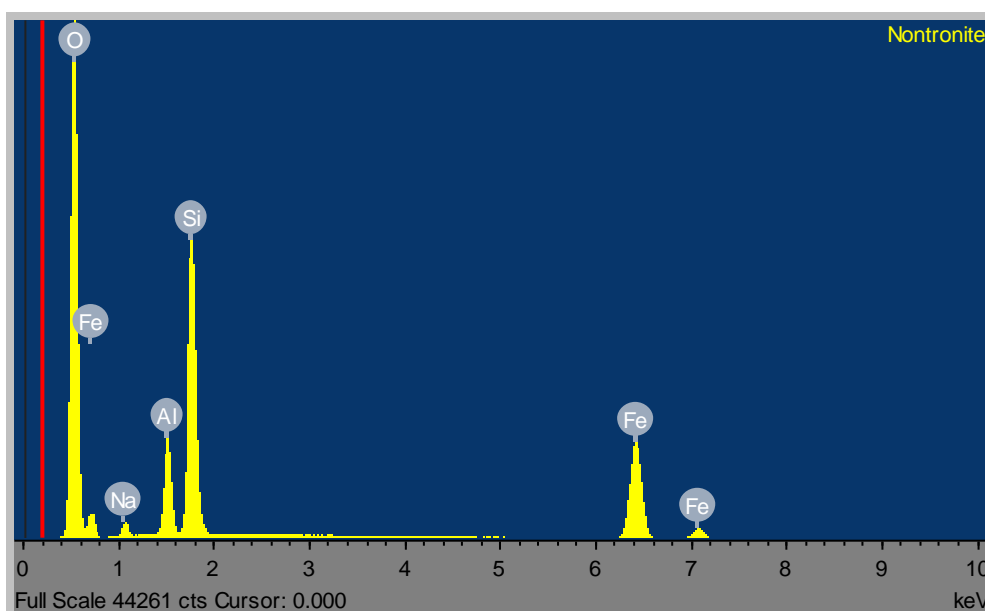
Synonym:	Bitter spar, Hoshiite - Ni-bearing magnesite, ICSD 80870, PDF 8-479
Cleavage:	{1011} Perfect, {1011} Perfect, {1011} Perfect
Color:	Colorless, White, Grayish white, Yellowish white, Brownish white.
Density:	3
Diaphaneity:	Transparent to translucent to opaque
Fracture:	Brittle - Conchoidal - Very brittle fracturing to small, conchoidal fragments.
Habit:	Earthy - Dull, clay-like texture with no visible crystalline affinities.
Habit:	Massive - Fibrous - Distinctly fibrous fine-grained forms.
Habit:	Massive - Granular - Common texture observed in granite/igneous rock.
Hardness:	4 - Fluorite
Luminescence:	Fluorescent, Short UV=blue white, Long UV=bright blue white.
Luster:	Vitreous (Glassy)
Streak:	white
Axial Ratios:	a:c = 1:3.27001
Cell Dimensions:	a = 4.633, c = 15.15, Z = 6; V = 281.62 Den(Calc)= 2.98
Crystal System:	Trigonal - Hexagonal ScalenohedralH-M Symbol (3 2/m) Space Group: R 3c
X Ray Diffraction:	By Intensity(I/I ₀): 2.742(1), 2.102(0.45), 1.7(0.35),

Nontronite

Dana class 71.03.01a.03 (71) Phyllosilicate Sheets of Six-Membered Rings

Chemical Formula:	$\text{Na}_{0.3}\text{Fe}^{3+}_2(\text{Si},\text{Al})_4\text{O}_{10}(\text{OH})_2 \cdot n(\text{H}_2\text{O})$		
Composition:	Molecular Weight =	495.90 gm	
	Sodium	1.39 % Na	1.87 % Na_2O
	Aluminum	5.44 % Al	10.28 % Al_2O_3
	Iron	22.52 % Fe	32.20 % Fe_2O_3
	Silicon	16.99 % Si	36.35 % SiO_2
	Hydrogen	2.03 % H	18.16 % H_2O
	Oxygen	51.62 % O	
		100.00 %	98.87 % = TOTAL OXIDE

Empirical Formula: $\text{Na}_{0.3}\text{Fe}^{3+}_2\text{Si}_3\text{AlO}_{10}(\text{OH})_2 \cdot 4(\text{H}_2\text{O})$



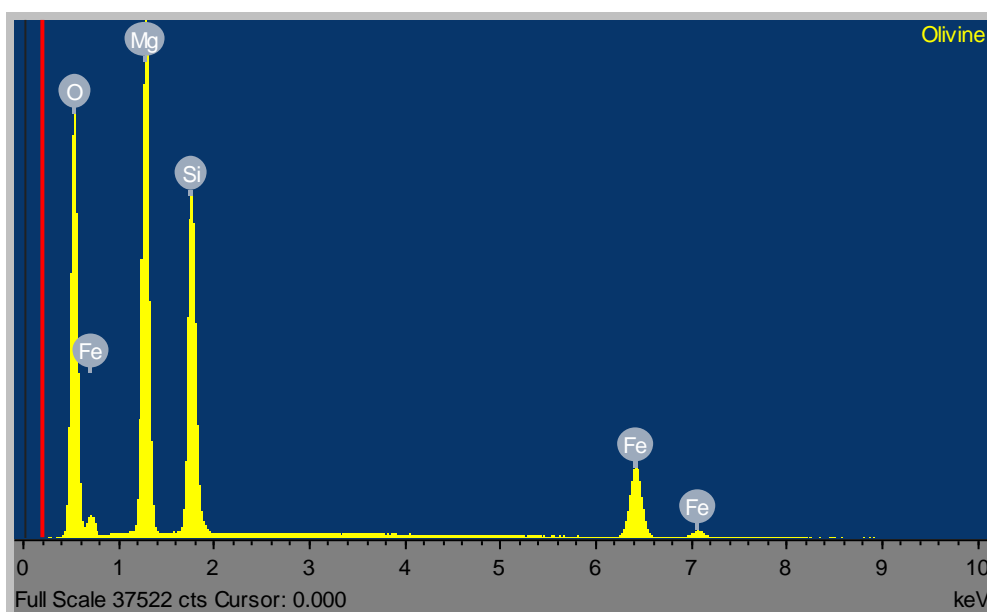
Synonym:	Chloropal, ICSD 86916
Cleavage:	{001} Perfect
Color:	Greenish yellow, Brownish green, Olive green.
Density:	2.3
Diaphaneity:	Subopaque
Fracture:	Earthy - Dull, clay-like fractures with no visible crystalline affinities.
Habit:	Earthy - Dull, clay-like texture with no visible crystalline affinities.
Hardness:	1.5-2 - Talc-Gypsum
Luminescence:	Non-fluorescent.
Luster:	Earthy (Dull)
Streak:	white
Axial Ratios:	a:b:c = 0.574:1:1.6739
Cell Dimensions:	a = 5.23, b = 9.11, c = 15.25, Z = 2; beta = 96° V = 722.61 Den(Calc) = 2.28
Crystal System:	Monoclinic - Prismatic H-M Symbol (2/m) Space Group: C 2/m
X Ray Diffraction:	By Intensity(I/I ₀): 1.52(1), 4.56(1), 15.4(1),

Olivine

Dana class 51.03.01.00 (51) Nesosilicate Insular SiO4 Groups Only

Chemical Formula:	(Mg,Fe) ₂ SiO ₄		
Composition:	Molecular Weight =	153.31 gm	
	Magnesium	25.37 % Mg	42.06 % MgO
	Iron	14.57 % Fe	18.75 % FeO
	Silicon	18.32 % Si	39.19 % SiO ₂
	Oxygen	41.74 % O	
		<hr/>	<hr/>
		100.00 %	100.00 % = TOTAL OXIDE

Empirical Formula: Mg_{1.6}Fe_{0.4}(SiO₄)



Synonym:	Calcio-olivine - calcium-dominant member of the olivine group Chrysolite - light yellowish green Peridot
Cleavage:	{001} Good, {010} Distinct
Color:	Yellowish green, Olive green, Greenish black, Reddish brown.
Density:	3.27 - 3.37, Average = 3.32
Diaphaneity:	Transparent to translucent
Fracture:	Brittle - Conchoidal - Very brittle fracturing to small, conchoidal fragments.
Habit:	Massive - Granular - Common texture observed in granite/igneous rock.
Hardness:	6.5-7 - Pyrite-Quartz
Luminescence:	Non-fluorescent.
Luster:	Vitreous (Glassy)
Streak:	white
Axial Ratios:	a:b:c=0.4663:1:0.6146
Cell Dimensions:	a = 4.78, b = 10.25, c = 6.3, Z = 4; V = 308.67 Den(Calc)= 3.30
Crystal System:	Orthorhombic - DipyramidalH-M Symbol (2/m 2/m 2/m) Space Group: Pbnm

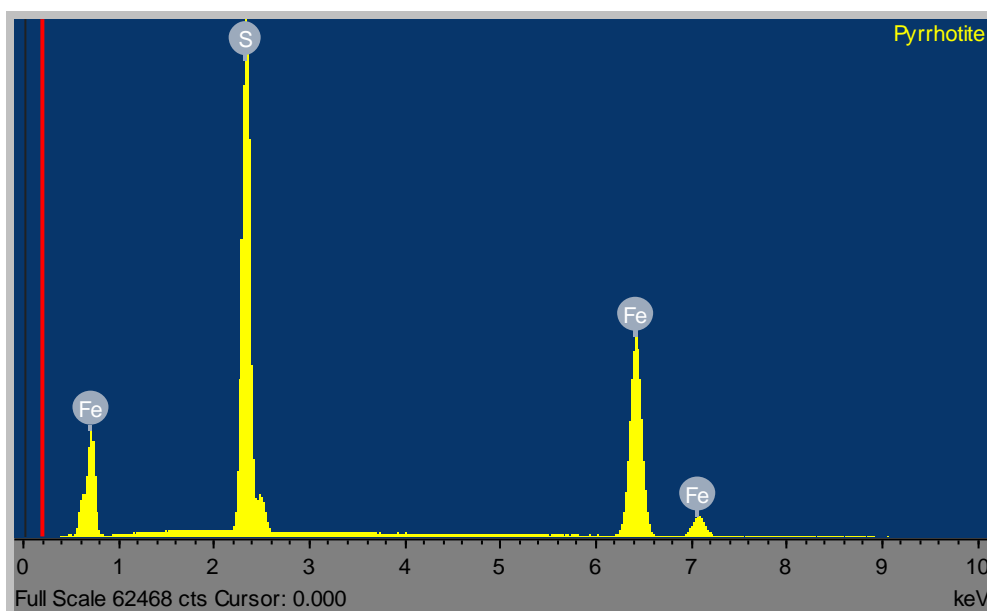
Pyrrhotite

Dana class 02.08.10.01 (02) Sulfides - Including Selenides and Tellurides

Chemical Formula: $\text{Fe}_{(1-x)}\text{S}$ ($x=0-0.17$)
Composition: Molecular Weight = 85.12 gm
Iron 62.33 % Fe
Sulfur 37.67 % S

100.00 %

Empirical Formula: $\text{Fe}^{2+}_{0.95}\text{S}$



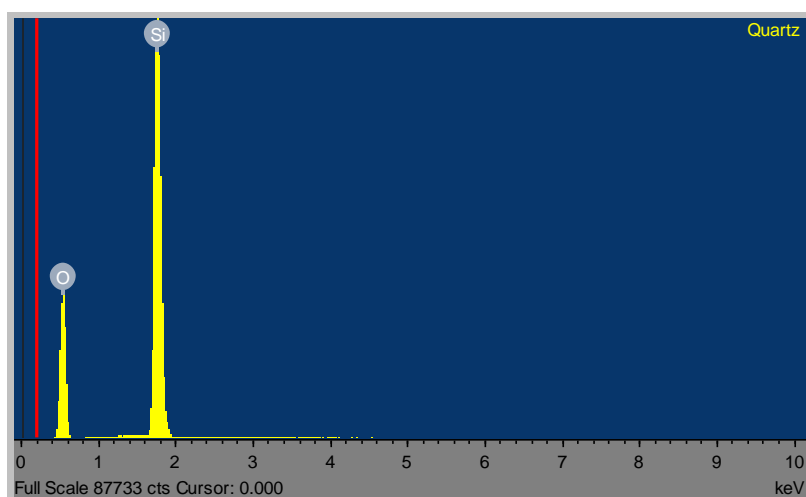
Synonym: Magnetic pyrites
Cleavage: {0001} Imperfect, {1120} Imperfect
Color: Bronze, Bronze red, Dark brown.
Density: 4.58 - 4.65, Average = 4.61
Diaphaneity: Opaque
Fracture: Uneven - Flat surfaces (not cleavage) fractured in an uneven pattern.
Habit: Massive - Granular - Common texture observed in granite/igneous rock.
Habit: Platy - Sheet forms (e.g. micas).
Habit: Tabular - Form dimensions are thin in one direction.
Hardness: 3.5-4 - Copper Penny-Fluorite
Luminescence: Non-fluorescent.
Luster: Metallic
Magnetism: Naturally strong
Streak: gray black
Axial Ratios: a:b:c=1.8647:1:1.7299
Cell Dimensions: a = 12.811, b = 6.87, c = 11.885, Z = 26; beta = 117.3° V = 929.51 Den(Calc)= 3.95
Crystal System: Monoclinic - PrismaticH-M Symbol (2/m) Space Group: A2/a
X Ray Diffraction: By Intensity(I/I₀): 2.057(1), 2.635(0.9), 2.966(0.9),

Quartz

Dana class 75.01.03.01 (75) Tectosilicate Si Tetrahedral Frameworks

Chemical Formula:	SiO ₂		
Composition:	Molecular Weight =	60.08 gm	
	Silicon	46.74 % Si	100.00 % SiO ₂
	Oxygen	53.26 % O	
		100.00 %	100.00 % = TOTAL OXIDE

Empirical Formula: (SiO₂)



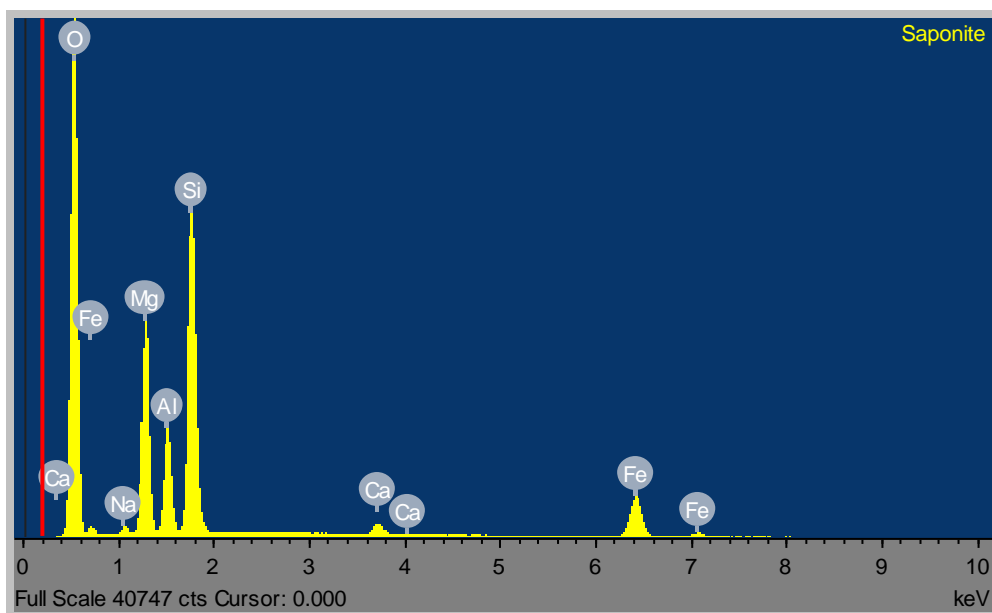
Synonym:	Agate - banded variety of chalcedony, Amethyst – purple, Aventurine - feebly translucent chalcedony, Carnelian - flesh red chalcedony, Cat's Eye – chatoyant, Chalcedony - microcrystalline quartz, Chert - cryptocrystalline quartz, Chrysoprase - apple green chalcedony, Citrine – yellow, Flint - microcrystalline quartz, Hornstone – flint, Jasper - red or brown chalcedony, Moss Agate - variety of chalcedony, Plasma - green chalcedony, Prase - leek green chalcedony, Rock Crystal, Rose Quartz - rose colored, Sapphire Quartz - blue colored, Sapphire Quartz - blue colored, Smoky Quartz - brown to black, Tiger Eye - pseudomorph of asbestos
Cleavage:	{0110} Indistinct
Color:	Brown, Colorless, Violet, Gray, Yellow.
Density:	2.6 - 2.65, Average = 2.62
Diaphaneity:	Transparent
Fracture:	Conchoidal - Fractures developed in brittle materials characterized by smoothly curving surfaces, (e.g. quartz).
Habit:	Crystalline - Coarse - Occurs as well-formed coarse sized crystals.
Habit:	Crystalline - Fine - Occurs as well-formed fine sized crystals.
Habit:	Druse – Cavity crystal growth resulting in numerous crystal tipped surfaces.
Hardness:	7 - Quartz
Luminescence:	Fluorescent and Triboluminescent, Short UV=yellow-orange, Long UV=yellow-orange.
Luster:	Vitreous (Glassy)
Streak:	white
Axial Ratios:	a:c = 1:1.10013
Cell Dimensions:	a = 4.9133, c = 5.4053, Z = 3; V = 113.00 Den(Calc)= 2.65
Crystal System:	Trigonal - TrapezohedralH-M Symbol (3 2) Space Group: P 3121,P 3221
X Ray Diffraction:	By Intensity(I/I ₀): 3.342(1), 4.257(0.22), 1.8179(0.14),

Saponite

Dana class 71.03.01b.02 (71) Phyllosilicate Sheets of Six-Membered Rings

Chemical Formula:	$(Ca/2,Na)_{0.3}(Mg,Fe^{2+})_3(Si,Al)_4O_{10}(OH)_2 \cdot 4(H_2O)$		
Composition:	Molecular Weight =	480.19 gm	
	Sodium	0.48 % Na	0.65 % Na ₂ O
	Calcium	0.83 % Ca	1.17 % CaO
	Magnesium	11.39 % Mg	18.89 % MgO
	Aluminum	5.62 % Al	10.62 % Al ₂ O ₃
	Iron	8.72 % Fe	11.22 % FeO
	Silicon	17.55 % Si	37.54 % SiO ₂
	Hydrogen	2.10 % H	18.76 % H ₂ O
	Oxygen	53.31 % O	
		100.00 %	98.83 % = TOTAL OXIDE

Empirical Formula: $Ca_{0.1}Na_{0.1}Mg_{2.25}Fe^{2+}_{0.75}Si_3AlO_{10}(OH)_2 \cdot 4(H_2O)$

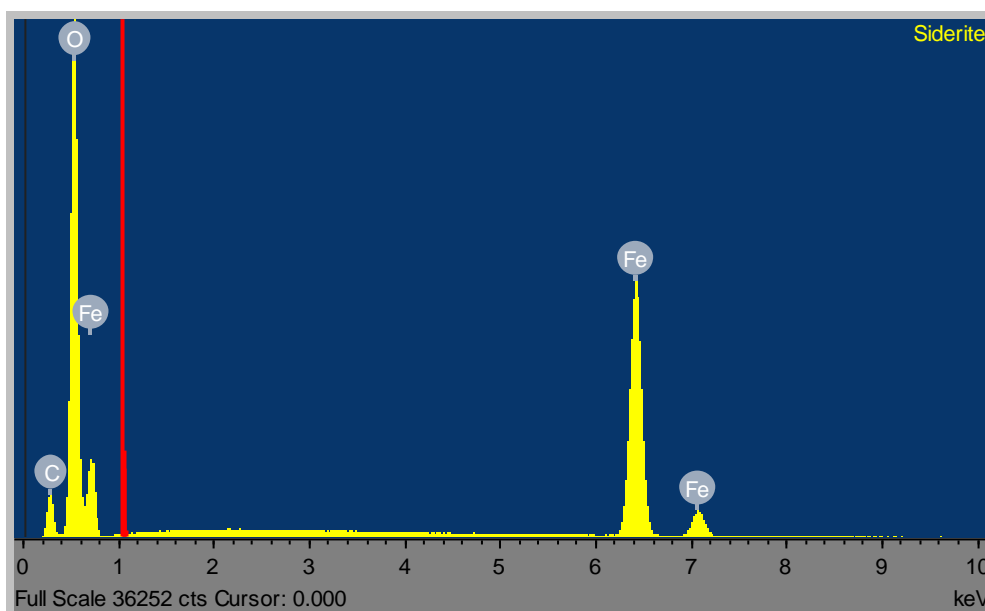


Synonym:	Griffithite-Ferroan, Piotine, Sobotkite - Al bearing
Cleavage:	{001} Perfect
Color:	White, Yellowish white, Greenish white, Reddish white, Bluish white.
Density:	2.3
Diaphaneity:	Subtranslucent to opaque
Fracture:	Earthy - Dull, clay-like fractures with no visible crystalline affinities.
Habit:	Granular - Generally occurs as anhedral to subhedral crystals in matrix.
Habit:	Massive - Uniformly indistinguishable crystals forming large masses.
Hardness:	1.5-2 - Talc-Gypsum
Luminescence:	Non-fluorescent.
Luster:	Earthy (Dull)
Streak:	white
Axial Ratios:	a:b:c=0.5786:1:1.3537
Cell Dimensions:	a = 5.3, b = 9.16, c = 12.4, Z = 2; beta = 96.5° V = 598.13 Den(Calc)= 2.67
Crystal System:	Monoclinic - PrismaticH-M Symbol (2/m) Space Group: C 2/m
X Ray Diffraction:	By Intensity(I/I ₀): 12.3(1), 1.53(0.7), 3.1(0.5),

Siderite

Dana class 14.01.01.03 (14) Anhydrous Carbonates

Chemical Formula:	Fe ²⁺ CO ₃		
Composition:	Molecular Weight =	115.86 gm	
	Iron	48.20 % Fe	62.01 % FeO
	Carbon	10.37 % C	37.99 % CO ₂
	Oxygen	41.43 % O	
		100.00 %	100.00 % = TOTAL OXIDE
Empirical Formula:	Fe ²⁺ (CO ₃)		



Synonym:	Chalybite, ICSD 100678, Iron spar, PDF 29-696, Spathose iron
Cleavage:	{1011} Perfect, {1011} Perfect, {1011} Perfect
Color:	Yellowish brown, Brown, Gray, Yellowish gray, Greenish gray.
Density:	3.96
Diaphaneity:	Translucent to subtranslucent
Fracture:	Brittle - Conchoidal - Very brittle fracturing to small, conchoidal fragments.
Habit:	Botryoidal - "Grape-like" rounded forms (e.g.. malachite).
Habit:	Massive - Uniformly indistinguishable crystals forming large masses.
Habit:	Tabular - Form dimensions are thin in one direction.
Hardness:	3.5 - Copper Penny
Luminescence:	Non-fluorescent.
Luster:	Vitreous (Glassy)
Streak:	white
Axial Ratios:	a:c = 1:3.27542
Cell Dimensions:	a = 4.72, c = 15.46, Z = 6; V = 298.28 Den(Calc)= 3.87
Crystal System:	Trigonal - Hexagonal ScalenohedralH-M Symbol (3 2/m) Space Group: R 3c
X Ray Diffraction:	By Intensity(I/I ₀): 2.79(1), 1.734(0.8), 3.59(0.6),

Appendix 2.

Rock abrasion tool stepper motor Arduino code from chapter 2.

```
// set pin numbers:
const int a1 = 1;
const int a2 = 2;
const int b1 = 3;
const int b2 = 4;

void setup() {
  // initialize pins
  pinMode(a1, OUTPUT);
  pinMode(a2, OUTPUT);
  pinMode(b1, OUTPUT);
  pinMode(b2, OUTPUT);

  digitalWrite(a1, LOW);
  digitalWrite(a2, LOW);
  digitalWrite(b1, LOW);
  digitalWrite(b2, LOW);
}

void loop(){
  step1();
  delay(50);
  step2();
  delay(50);
  step3();
  delay(50);
  step4();

  delay(50);
}

void step1 (){
  digitalWrite(a1, HIGH);
  digitalWrite(a2, LOW);
  digitalWrite(b1, LOW);
  digitalWrite(b2, LOW);
}

void step2 (){
  digitalWrite(a1, LOW);
  digitalWrite(a2, LOW);
  digitalWrite(b1, HIGH);
  digitalWrite(b2, LOW);
}

void step3 (){
  digitalWrite(a1, LOW);
  digitalWrite(a2, HIGH);
  digitalWrite(b1, LOW);
  digitalWrite(b2, LOW);
}

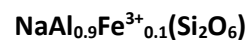
void step4 (){
  digitalWrite(a1, LOW);
  digitalWrite(a2, LOW);
  digitalWrite(b1, LOW);
  digitalWrite(b2, HIGH);
}
```

Appendix 3.

Scanning Electron Microscope Standards used for chapters 3 and 4.

Fixed list	Standard		Method
Na	Jadeite	(Table 1)	Raster
Mg	Periclase	(Table 2)	Spot
Al	Jadeite	(Table 1)	Raster
Si	Wollastonite	(Table 3)	Spot
S	Pyrite	(Table 4)	Spot
K	Orthoclase (K-feldspar)	(Table 5)	Raster
Ca	Wollastonite or calcite	(Table 3 or 6)	Spot
Ti	Rutile	(Table 7)	Spot
Cr	Chromite	(Table 8)	Spot
Mn	Rhodonite	(Table 9)	Spot
Fe	Heamatite or garnet/alamandine	(Table 10 or 11)	Spot
Cu	Copper	(Table 12)	Spot
O	Calcite	(Table 6)	Raster

Peridotite (table 13) and diopside (table 14) standards were also measured as they were occasionally used to test accuracy of calibration.

Table 1. Group analysis of jadeite standard

Blank = beneath detection limit. SMD = standard mean deviation. – Not tested.

	1	2	3	4	5	6	7	8	9	10	Mean	SMD	True
Na ₂ O	15.04	15.15	15.26	15.35	15.26	14.99	15.10	15.06	15.03	15.50	15.17	0.17	15.21
MgO	0.20		0.12	0.17	0.23	0.15	0.23	0.22	0.27	0.12	0.19	0.05	0.10
Al ₂ O ₃	25.10	25.17	25.38	25.15	24.77	25.15	25.21	25.17	25.08	24.98	25.12	0.16	25.18
SiO ₂	59.15	58.45	59.17	59.11	58.83	58.62	58.68	59.02	59.56	58.57	58.92	0.35	59.44
SO ₃													
K ₂ O													
CaO	0.20	0.13			0.18	0.14	0.20	0.15	0.31	0.14	0.18	0.06	0.06
TiO ₂					0.27	0.27					0.27	0.00	
Cr ₂ O ₃													
MnO													
FeO													0.13
NiO													
CuO						0.20					0.20		
Total	99.69	98.89	99.93	99.78	99.55	99.52	99.42	99.62	100.24	99.31	99.59		100.12

Numbers of ions based on 40

Na	1.213	1.231	1.226	1.236	1.233	1.213	1.221	1.215	1.206	1.254	1.750	0.014
Mg	0.006		0.004	0.005	0.007	0.005	0.007	0.007	0.008	0.004	0.006	0.002
Al	0.615	0.622	0.620	0.615	0.608	0.619	0.620	0.617	0.612	0.614	0.616	0.004
Si	1.230	1.225	1.227	1.227	1.226	1.223	1.224	1.228	1.232	1.222	1.226	0.003
S												
K												
Ca	0.004	0.003			0.004	0.003	0.004	0.003	0.007	0.003	0.004	0.001
Ti					0.004	0.004					0.004	0.000
Cr												
Mn												
Fe												
Ni												
Cu						0.003					0.003	
Total	3.069	3.080	3.077	3.083	3.082	3.070	3.077	3.071	3.065	3.098	3.077	

Table 2. Group analysis of periclase standard

MgO

Blank = beneath detection limit. SMD = standard mean deviation. – Not tested.

	1	2	3	4	5	6	7	8	9	10	Mean	SMD	True
Na ₂ O	0.12	0.24	0.20	0.34	0.20	0.27		0.12	0.23	0.30	0.22	0.07	
MgO	100.26	100.13	99.76	99.84	99.56	100.32	99.96	100.08	99.35	100.52	99.98	0.36	100.30
Al ₂ O ₃		0.11									0.11		
SiO ₂		0.19	0.24	0.30	0.28	0.28		0.26	0.24	0.32	0.26	0.04	
SO ₃													
K ₂ O													
CaO													
TiO ₂													
Cr ₂ O ₃													
MnO													
FeO													
NiO													
CuO													
Total	100.38	100.67	#####	100.48	100.04	100.87	99.96	100.45	99.81	101.14	100.40		100.30

Numbers of ions based on 10

Na	0.003	0.006	0.005	0.009	0.005	0.007		0.003	0.006	0.008	0.006	0.002	
Mg	0.998	0.993	0.994	0.992	0.994	0.993	1.000	0.995	0.994	0.992	0.994	0.003	
Al		0.001									0.001		
Si		0.001	0.002	0.002	0.002	0.002		0.002	0.002	0.002	0.002	0.000	
S													
K													
Ca													
Ti													
Cr													
Mn													
Fe													
Ni													
Cu													
Total	1.002	1.001	1.001	1.002	1.001	1.002	1.000	1.000	1.001	1.002	1.001		

Table 3. Group analysis of wollastonite standard

CaSiO₃

Blank = beneath detection limit. SMD = standard mean deviation. – Not tested.

	1	2	3	4	5	6	7	8	9	10	Mean	SMD	True
Na ₂ O													0.01
MgO			0.08										0.02
Al ₂ O ₃													
SiO ₂	51.19	51.41	51.09	51.47	51.24	51.34	51.19	51.51	51.32	51.30	51.31	0.13	51.31
SO ₃													
K ₂ O													
CaO	47.60	47.85	47.53	47.74	47.57	47.29	47.74	47.71	47.99	47.82	47.69	0.20	47.80
TiO ₂													0.02
Cr ₂ O ₃	0.64				0.58				0.64		0.62	0.03	
MnO	0.36	0.37	0.30	0.43	0.52	0.54	0.44	0.39	0.34	0.46	0.41	0.08	0.63
FeO													0.19
NiO													
CuO			0.18										
Total	99.80	99.63	99.17	99.64	99.91	99.18	99.37	99.61	100.29	99.59	99.62		99.98

Numbers of ions based on 30

Na													
Mg			0.002										
Al													
Si	0.994	0.999	0.998	1.000	0.994	1.001	0.998	1.000	0.993	0.998	0.998	0.003	
S													
K													
Ca	0.991	0.996	0.995	0.994	0.989	0.988	0.997	0.993	0.995	0.997	0.993	0.003	
Ti													
Cr	0.010				0.009				0.010		0.010	0.001	
Mn	0.006	0.006	0.005	0.007	0.008	0.009	0.007	0.006	0.005	0.008	0.007	0.001	
Fe													
Ni													
Cu			0.003										
Total	2.001	2.001	2.002	2.000	2.001	1.999	2.002	2.000	2.002	2.002	2.001		

Table 4. Group analysis of pyrite standard**Fe²⁺S₂**

Blank = beneath detection limit. SMD = standard mean deviation. – Not tested. Values are wt. %.

	1	2	3	4	5	6	7	8	9	10	Mean	SMD	True
Na													
Mg													
Al													
Si													
S	53.43	53.85	53.52	54.04	53.92	53.22	54.29	53.26	53.15	53.92	53.66	0.39	53.45
K													
Ca													
Ti													
Cr													
Mn													
Fe	46.56	47.30	46.57	46.60	47.01	46.22	46.92	46.73	47.15	46.52	46.76	0.33	46.55
Ni													
Cu													
Totals	99.99	101.15	100.09	100.64	100.93	99.44	101.21	99.99	100.30	100.44	100.42		100.00

Table 5. Group analysis of orthoclase (K-feldspar) standard

KAlSi₃O₈

Blank = beneath detection limit. SMD = standard mean deviation. – Not tested.

	1	2	3	4	5	6	7	8	9	10	Mean	SMD	True
Na ₂ O	1.59	2.43	2.28	1.62	1.78	2.67	1.73	1.56	1.43	1.19	1.83	0.47	1.36
MgO			0.08		0.08						0.08	0.00	
Al ₂ O ₃	18.56	18.35	18.61	18.43	18.52	18.41	18.63	18.48	18.52	18.52	18.50		18.55
SiO ₂	64.84	65.08	64.65	64.59	64.69	64.44	64.22	64.54	64.74	65.06	64.68	0.26	65.13
SO ₃													
K ₂ O	14.63	13.74	14.28	14.58	14.48	13.90	14.44	14.66	14.63	15.15	14.45	0.40	14.70
CaO													0.01
TiO ₂	0.43		0.40	0.35		0.62			0.45		0.45	0.10	
Cr ₂ O ₃													
MnO													
FeO													0.03
NiO													
CuO										0.24	0.24		
Total	100.06	99.59	100.31	99.56	99.55	100.03	99.02	99.24	99.77	100.15	99.73		99.78
Numbers of ions based on 8O													
Na	0.281	0.428	0.400	0.287	0.316	0.469	0.308	0.279	0.253	0.210	0.323	0.082	
Mg			0.006		0.006						0.006	0.000	
Al	0.997	0.983	0.995	0.994	0.998	0.984	1.010	1.001	0.998	0.998	0.996		
Si	2.955	2.957	2.931	2.957	2.959	2.923	2.954	2.965	2.959	2.974	2.953	0.015	
S													
K	0.851	0.797	0.826	0.852	0.845	0.804	0.847	0.859	0.853	0.884	0.842	0.026	
Ca													
Ti	0.015		0.014	0.012		0.021			0.015		0.015	0.003	
Cr													
Mn													
Fe													
Ni													
Cu										0.008	0.008		
Total	5.098	5.164	5.171	5.103	5.122	5.201	5.119	5.103	5.079	5.074	5.123		

Table 6. Analysis of calcite standard**CaCO₃**

Blank = beneath detection limit. SMD = standard mean deviation. – Not tested.

	1	2	3	4	5	Mean	SMD	True
FeCO ₃								
MnCO ₃								
MgCO ₃								
CaCO ₃	98.11	100.33	98.58	99.71	99.26	99.20	0.88	99.98
Total	98.11	100.33	98.58	99.71	99.26	99.20		99.98

Numbers of ions based on 60

Fe								
Mn								
Mg								
Ca	6.000	6.000	6.000	6.000	6.000	6.000	0.000	
Total	6.000	6.000	6.000	6.000	6.000	6.000		

Table 7. Group analysis of rutile standard

TiO₂

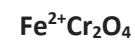
Blank = beneath detection limit. SMD = standard mean deviation. – Not tested.

	1	2	3	4	5	6	7	8	9	10	Mean	SMD	True
Na ₂ O													
MgO													
Al ₂ O ₃													
SiO ₂													
SO ₃													
K ₂ O													
CaO													
TiO ₂	100.86	100.88	100.93	101.34	100.88	101.64	100.78	101.23	100.16	101.08	100.98	0.39	100.00
Cr ₂ O ₃													
MnO													
FeO													
NiO													
CuO													
Total	100.86	100.88	100.93	101.34	100.88	101.64	100.78	101.23	100.16	101.08	100.98		100.00

Numbers of ions based on 2O

Na													
Mg													
Al													
Si													
S													
K													
Ca													
Ti	1.000	1.000	1.000	1.000	1.000	1.000	1.000	1.000	1.000	1.000	1.000	0.000	
Cr													
Mn													
Fe													
Ni													
Cu													
Total	1.000	1.000	1.000	1.000	1.000	1.000	1.000	1.000	1.000	1.000	1.000		

Table 8. Group analysis of chromite standard



Blank = beneath detection limit. SMD = standard mean deviation. – Not tested.

	1	2	3	4	5	6	7	8	9	10	Mean	SMD	True
Na ₂ O		0.16		0.12	0.15		0.18				0.15	0.02	
MgO													
Al ₂ O ₃													
SiO ₂													
SO ₃													
K ₂ O													
CaO													
TiO ₂													
Cr ₂ O ₃	99.60	98.93	99.73	99.89	99.45	99.47	99.31	98.85	99.82	99.66	99.47	0.35	100.03
MnO													
FeO													
NiO													
CuO													
Total	99.60	99.09	99.73	100.01	99.60	99.47	99.48	98.85	99.82	99.66	99.53		100.03

Numbers of ions based on 30

Na		0.016		0.012	0.015		0.017				0.015	0.002	
Mg													
Al													
Si													
S													
K													
Ca													
Ti													
Cr	2.000	1.995	2.000	1.996	1.995	2.000	1.994	2.000	2.000	2.000	1.998	0.003	
Mn													
Fe													
Ni													
Cu													
Total	2.000	2.011	2.000	2.008	2.010	2.000	2.012	2.000	2.000	2.000	2.004		

Table 9. Group analysis of rhodonite standard



Blank = beneath detection limit. SMD = standard mean deviation. – Not tested.

	1	2	3	4	5	6	7	8	9	10	Mean	SMD	True
Na ₂ O	0.24	0.32			0.32	0.24	0.30	0.27	0.32		0.29	0.04	
MgO	1.74	1.77	1.81	1.84	1.77	1.81	1.79	1.81	1.72	1.84	1.79	0.04	1.86
Al ₂ O ₃					0.23								
SiO ₂	47.15	47.21	47.00	47.00	47.06	47.00	47.19	46.89	47.32	47.06	47.09	0.13	47.42
SO ₃													
K ₂ O													
CaO	7.22	7.22	7.22	7.28	7.22	7.14	7.26	7.23	7.32	7.19	7.23	0.05	7.15
TiO ₂													
Cr ₂ O ₃													
MnO	42.26	42.52	42.20	42.51	42.30	42.40	42.39	42.30	42.24	42.42	42.35	0.11	42.51
FeO	1.36	1.21	1.22	1.13	1.22	1.34	1.33	1.11	1.14	1.26	1.23	0.09	1.02
NiO													
CuO													
Total	99.98	100.26	99.45	99.76	100.13	99.93	100.26	99.61	100.07	99.77	99.92		99.96

Numbers of ions based on 30

Na	0.010	0.013			0.013	0.010	0.012	0.011	0.013		0.012	0.002	
Mg	0.055	0.056	0.057	0.058	0.056	0.057	0.056	0.057	0.054	0.058	0.057	0.001	
Al					0.006								
Si	0.998	0.996	0.999	0.997	0.994	0.996	0.996	0.996	0.999	0.997	0.997	0.002	
S													
K													
Ca	0.164	0.163	0.164	0.165	0.163	0.162	0.164	0.165	0.166	0.163	0.164	0.001	
Ti													
Cr													
Mn	0.757	0.760	0.759	0.763	0.757	0.761	0.758	0.761	0.755	0.761	0.759	0.003	
Fe	0.024	0.021	0.022	0.020	0.022	0.024	0.023	0.020	0.020	0.022	0.022	0.002	
Ni													
Cu													
Total	2.007	2.010	2.001	2.003	2.010	2.009	2.010	2.010	2.008	2.003	2.007		

Table 10. Group analysis of hematite standard

Fe³⁺₂O₃

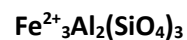
Blank = beneath detection limit. SMD = standard mean deviation. – Not tested.

	1	2	3	4	5	6	7	8	9	10	Mean	SMD	True
Na ₂ O													
MgO													
Al ₂ O ₃													
SiO ₂													
SO ₃													
K ₂ O													
CaO													
TiO ₂													
Cr ₂ O ₃													
MnO													
FeO	87.88	89.00	88.47	88.66	88.37	88.03	88.65	89.13	88.24	88.54	88.50	0.39	100.01
NiO													
CuO													
Total	87.88	89.00	88.47	88.66	88.37	88.03	88.65	89.13	88.24	88.54	88.50		100.01

Numbers of ions based on 30

Na													
Mg													
Al													
Si													
S													
K													
Ca													
Ti													
Cr													
Mn													
Fe	3.000	3.000	3.000	3.000	3.000	3.000	3.000	3.000	3.000	3.000	3.000	0.000	
Ni													
Cu													
Total	3.000	3.000	3.000	3.000	3.000	3.000	3.000	3.000	3.000	3.000	3.000		

Table 11. Group analysis of almandine (garnet) standard



Blank = beneath detection limit. SMD = standard mean deviation. – Not tested

	1	2	3	4	5	6	7	8	9	10	Mean	SMD	True
Na ₂ O													
MgO	2.34	2.45	2.42	2.40	2.37	2.45	2.45	2.44	2.49	2.49	2.43	0.05	2.35
Al ₂ O ₃	20.94	20.81	20.81	20.84	20.75	20.28	20.71	20.64	20.83	20.75	20.73	0.18	21.01
SiO ₂	37.03	37.16	36.82	36.88	36.84	36.84	37.03	36.58	37.01	36.73	36.89	0.17	37.17
SO ₃													
K ₂ O													
CaO	3.85	4.04	4.16	4.06	3.65	3.83	3.95	3.97	3.92	3.99	3.94	0.14	3.94
TiO ₂		0.67	0.42	0.57	0.40				0.27		0.46	0.16	0.07
Cr ₂ O ₃													0.02
MnO			0.36	0.46	0.61	0.37	0.59	0.45			0.48	0.11	0.20
FeO	35.20	34.58	34.77	34.62	35.12	34.95	34.86	34.71	34.76	34.79	34.84	0.20	35.13
NiO													
CuO				0.18	0.30				0.18		0.22	0.07	
Total	99.35	99.71	99.75	100.01	100.04	98.73	99.60	98.79	99.44	98.74	99.42		99.89

Numbers of ions based on 240

Na													
Mg	0.565	0.589	0.583	0.578	0.571	0.598	0.592	0.594	0.600	0.605	0.587	0.013	
Al	3.998	3.949	3.963	3.960	3.952	3.906	3.952	3.972	3.971	3.987	3.961	0.025	
Si	6.000	5.985	5.951	5.946	5.953	6.021	5.996	5.975	5.988	5.988	5.980	0.024	
S													
K													
Ca	0.668	0.698	0.720	0.701	0.632	0.671	0.685	0.695	0.679	0.697	0.685	0.024	
Ti		0.081	0.051	0.069	0.049				0.032		0.056	0.019	
Cr													
Mn			0.049	0.063	0.083	0.052	0.081	0.063			0.065	0.014	
Fe	4.770	4.658	4.700	4.667	4.746	4.778	4.721	4.741	4.703	4.743	4.723	0.040	
Ni													
Cu				0.021	0.037				0.021		0.026	0.009	
Total	16.001	15.960	16.017	16.005	16.023	16.026	16.028	16.039	15.995	16.019	16.011		

Table 12. Group analysis of copper standard

Cu

Blank = beneath detection limit. SMD = standard mean deviation. – Not tested.

	1	2	3	4	5	6	7	8	9	10	Mean	SMD
Na												
Mg												
Al												
Si												
S												
K												
Ca												
Ti												
Cr												
Mn												
Fe												
Ni												
Cu	99.38	99.37	100.36	98.42	98.89	98.71	100.3	100.19	100.26	100.96	99.68	0.80
Total	99.38	99.37	100.36	98.42	98.89	98.71	100.3	100.19	100.26	100.96	99.68	

Table 13. Group analysis of peridotite standard

Mg₂SiO₄

Blank = beneath detection limit. SMD = standard mean deviation.

	1	2	3	4	5	6	7	8	9	10	Mean	SMD	True
Na ₂ O	0.27			0.30	0.27	0.27	0.24	0.46	0.30		0.30	0.07	
MgO	53.15	52.40	52.68	52.70	52.58	52.60	52.48	52.77	52.48	52.37	52.62	0.23	52.66
Al ₂ O ₃		0.23											
SiO ₂	41.20	41.29	41.40	41.48	41.55	41.40	41.20	41.46	41.20	41.27	41.34	0.13	41.84
SO ₃													
K ₂ O													
CaO													0.01
TiO ₂													0.01
Cr ₂ O ₃													
MnO													0.15
FeO	5.39	5.22	5.38	5.29	5.35	5.36	5.27	5.31	5.24	5.36	5.32	0.06	4.44
NiO													0.20
CuO													
Total	100.01	99.14	99.46	99.76	99.75	99.63	99.20	100.00	99.22	99.00	99.52		99.31

Numbers of ions based on 40

Na	0.013			0.014	0.013	0.013	0.011	0.021	0.014		0.014	0.003	
Mg	1.905	1.888	1.894	1.890	1.886	1.890	1.893	1.890	1.893	1.892	1.892	0.005	
Al		0.006											
Si	0.990	0.998	0.999	0.998	1.000	0.998	0.997	0.996	0.997	1.000	0.997	0.003	
S													
K													
Ca													
Ti													
Cr													
Mn													
Fe	0.108	0.106	0.108	0.106	0.108	0.108	0.107	0.107	0.106	0.109	0.107	0.001	
Ni													
Cu													
Total	3.016	2.999	3.001	3.009	3.007	3.009	3.009	3.014	3.010	3.000	3.007		

Table 14. Group analysis of diopside standard



Blank = beneath detection limit. SMD = standard mean deviation. – Not tested.

	1	2	3	4	5	6	7	8	9	10	Mean	SMD	True
Na ₂ O	0.24	0.38	0.30	0.32	0.35		0.38	0.32	0.24	0.38	0.32	0.05	0.07
MgO	17.94	17.99	17.94	17.98	18.06	18.14	17.94	17.91	17.96	17.86	17.97	0.08	17.98
Al ₂ O ₃				0.26			0.30	0.23		0.26	0.26	0.03	0.06
SiO ₂	54.87	55.02	54.79	54.98	55.04	55.09	55.02	54.96	55.02	54.94	54.97	0.09	55.36
SO ₃													
K ₂ O													
CaO	25.75	25.80	25.75	25.86	25.90	25.84	25.97	25.80	25.77	25.98	25.84	0.09	25.72
TiO ₂													0.05
Cr ₂ O ₃													
MnO													0.09
FeO	0.76	0.82	0.78	0.71	0.85	0.76	0.68	0.73	0.71	0.76	0.76	0.05	0.90
NiO													
CuO													
Total	99.56	100.02	99.56	100.11	100.20	99.83	100.30	99.95	99.71	100.18	99.94		100.23

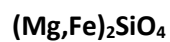
Numbers of ions based on 6O

Na	0.017	0.027	0.021	0.023	0.025		0.026	0.023	0.017	0.026	0.023	0.004
Mg	0.973	0.972	0.974	0.970	0.974	0.980	0.966	0.967	0.972	0.963	0.971	0.005
Al				0.011			0.013	0.010		0.011	0.011	0.001
Si	1.996	1.994	1.994	1.989	1.992	1.997	1.988	1.991	1.998	1.988	1.993	0.004
S												
K												
Ca	1.003	1.002	1.004	1.002	1.004	1.004	1.005	1.002	1.003	1.007	1.004	0.002
Ti												
Cr												
Mn												
Fe	0.023	0.025	0.024	0.021	0.026	0.023	0.021	0.022	0.021	0.023	0.023	0.002
Ni												
Cu												
Total	4.013	4.019	4.016	4.016	4.020	4.003	4.019	4.015	4.011	4.020	4.015	

Appendix 4.

Quantitative SEM data from chapters 3 and 4.

sTable 3.1. From figure 3.31. Analysis of Semail olivine (sample SU 15 1).



Blank = beneath detection limit. SMD = standard mean deviation.

	1	2	3	4	5	Mean	SMD
Na ₂ O					0.3		
MgO	48.9	49.3	48.6	49.2	49.2	49.0	0.3
Al ₂ O ₃			0.3		0.3	0.3	0.0
SiO ₂	40.5	40.7	40.7	40.8	40.8	40.7	0.1
SO ₃							
K ₂ O							
CaO							
TiO ₂							
Cr ₂ O ₃							
MnO							
FeO	9.2	9.1	9.1	9.2	9.5	9.2	0.2
NiO							
CuO							
Total	98.6	99.2	98.6	99.2	100.1	99.1	

Numbers of ions based on 40

Na					0.015		
Mg	1.806	1.809	1.790	1.802	1.792	1.800	0.008
Al			0.008		0.008	0.008	0.000
Si	1.002	1.002	1.006	1.004	0.997	1.002	0.003
S							
K							
Ca							
Ti							
Cr							
Mn							
Fe	0.190	0.188	0.187	0.190	0.195	0.190	0.003
Ni							
Cu							
Total	2.998	2.998	2.990	2.996	3.007	2.998	

Table 3.2. From figure 3.31. Group analysis of South African pre-experiment olivine-hortonolite.

(Mg,Fe)₂SiO₄

Blank = beneath detection limit. SMD = standard mean deviation.

	1	2	3	Mean	SMD
Na ₂ O	0.2		0.3	0.3	0.0
MgO	22.3	22.5	22.6	22.4	0.2
Al ₂ O ₃	0.3	0.2	0.2	0.2	0.0
SiO ₂	34.1	34.2	34.0	34.1	0.1
SO ₃					
K ₂ O					
CaO					
TiO ₂					
Cr ₂ O ₃					
MnO	0.5	0.6	0.5	0.5	0.0
FeO	42.4	42.6	42.8	42.6	0.2
NiO					
CuO					
Total	99.8	100.1	100.3	100.1	

Numbers of ions based on 40

Na	0.014		0.015	0.014	0.001
Mg	0.962	0.969	0.972	0.967	0.005
Al	0.009	0.008	0.008	0.008	0.001
Si	0.989	0.988	0.981	0.986	0.004
S					
K					
Ca					
Ti					
Cr					
Mn	0.013	0.014	0.013	0.013	0.001
Fe	1.027	1.029	1.033	1.030	0.003
Ni					
Cu					
Total	3.013	3.008	3.022	3.014	

Table 3.3. From figure 3.31. Group analysis of Leka olivine (sample LEK2).

(Mg,Fe)₂SiO₄

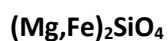
Blank = beneath detection limit. SMD = standard mean deviation.

	1	2	3	Mean	SMD
Na ₂ O					
MgO	49.3	49.5	49.3	49.4	0.1
Al ₂ O ₃			0.2		
SiO ₂	40.4	40.6	40.6	40.5	0.1
SO ₃					
K ₂ O					
CaO		0.1	0.1	0.1	0.0
TiO ₂					
Cr ₂ O ₃					
MnO					
FeO	9.3	9.2	9.2	9.3	0.0
NiO			0.4		
CuO					
Total	99.0	99.5	100.0	99.5	

Numbers of ions based on 4O

Na					
Mg	1.814	1.810	1.802	1.809	0.006
Al			0.007		
Si	0.997	0.998	0.995	0.997	0.002
S					
K					
Ca		0.004	0.003	0.002	0.000
Ti					
Cr					
Mn					
Fe	0.192	0.190	0.189	0.190	0.001
Ni			0.006		
Cu					
Total	3.003	3.002	3.002	3.002	

Table 3.4. From figure 3.31. Group analysis of Leka olivine (sample LEK192T2).

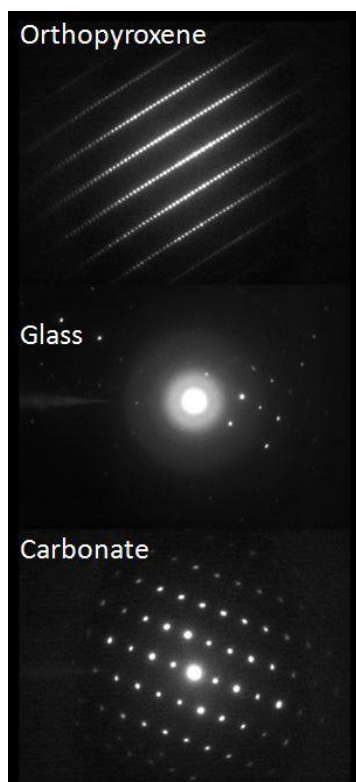


Blank = beneath detection limit. SMD = standard mean deviation.

	1	2	3	4	5	Mean	SMD
Na ₂ O		0.3					
MgO	48.6	48.7	47.5	47.3	48.5	48.1	0.6
Al ₂ O ₃							
SiO ₂	40.1	39.7	39.6	40.1	39.6	39.8	0.3
SO ₃							
K ₂ O							
CaO							
TiO ₂							
Cr ₂ O ₃							
MnO			0.3				
FeO	10.3	10.3	11.1	11.2	10.4	10.6	0.4
NiO							
CuO							
Total	99.0	99.0	98.4	98.6	98.5	98.7	

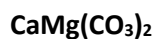
Numbers of ions based on 40

Na		0.016					
Mg	1.797	1.803	1.776	1.762	1.806	1.789	0.019
Al							
Si	0.995	0.988	0.993	1.002	0.988	0.993	0.006
S							
K							
Ca							
Ti							
Cr							
Mn			0.006				
Fe	0.213	0.213	0.232	0.234	0.218	0.222	0.010
Ni							
Cu							
Total	3.005	3.020	3.007	2.998	3.012	3.008	



Bragg diffraction patterns from TEM analysis from figure 3.36.

Table 3.5. From figure 3.51. Group analysis of Semail carbonate (SU 15 1) zone 1.



Blank = beneath detection limit. SMD = standard mean deviation.

	1	2	3	Mean	SMD
FeCO_3					
MnCO_3					
MgCO_3	48.3	49.1	47.7	48.4	0.7
CaCO_3	50.9	50.7	52.2	51.3	0.8
Total	99.2	99.8	100.0	99.7	

Numbers of ions based on 60

Fe					
Mn					
Mg	2.119	2.139	2.082	2.113	0.029
Ca	1.881	1.861	1.918	1.887	0.029
Total	4.000	4.000	4.000	4.000	

Table 3.6. From figure 3.51. Group analysis of Semail carbonate (SU 15 1) zone 2.

CaMg(CO₃)₂

Blank = beneath detection limit. SMD = standard mean deviation.

	1	2	3	Mean	SMD
FeCO ₃					
MnCO ₃					
MgCO ₃	45.4	45.7	46.0	45.7	0.3
CaCO ₃	53.8	53.8	53.5	53.7	0.2
Total	99.3	99.5	99.5	99.4	

Numbers of ions based on 60

Fe					
Mn					
Mg	2.003	2.009	2.021	2.011	0.009
Ca	1.997	1.991	1.979	1.989	0.009
Total	4.000	4.000	4.000	4.000	

Table 3.7. From figure 3.51. Group analysis of Semail carbonate (SU 15 1) zone 3.

CaMg(CO₃)₂

Blank = beneath detection limit. SMD = standard mean deviation.

	1	2	3	Mean	SMD
FeCO ₃					
MnCO ₃					
MgCO ₃	37.3	36.8	37.2	37.1	0.3
CaCO ₃	62.0	62.5	61.8	62.1	0.3
Total	99.3	99.2	99.0	99.2	

Numbers of ions based on 60

Fe					
Mn					
Mg	1.667	1.646	1.667	1.660	0.012
Ca	2.333	2.354	2.333	2.340	0.012
Total	4.000	4.000	4.000	4.000	

Table 3.8. From figure 3.51. Group analysis of Semail carbonate (SU 15 1) zone 4.

CaMg(CO₃)₂

Blank = beneath detection limit. SMD = standard mean deviation.

	1	2	Mean	SMD
FeCO ₃				
MnCO ₃				
MgCO ₃	41.2	40.8	41.0	0.3
CaCO ₃	58.1	58.7	58.4	0.4
Total	99.3	99.5	66.3	

Numbers of ions based on 60

Fe				
Mn				
Mg	1.830	1.810	1.820	0.014
Ca	2.170	2.190	2.180	0.014
Total	4.000	4.000	2.667	

Table 3.10. From figure 3.53. Group analysis of Semail carbonate (SU 15 4) zone 1.

CaMg(CO₃)₂

Blank = beneath detection limit. SMD = standard mean deviation.

	1	2	3	Mean	SMD
FeCO ₃					
MnCO ₃					
MgCO ₃	44.9	45.4	46.2	45.5	0.7
CaCO ₃	54.2	54.0	52.9	53.7	0.7
Total	99.0	99.3	99.1	99.2	

Numbers of ions based on 60

Fe					
Mn					
Mg	1.983	1.999	1.964	1.982	0.018
Ca	2.017	2.001	2.036	2.018	0.018
Total	4.000	4.000	4.000	4.000	

Table 3.9. From figure 3.53. Group analysis of Semail carbonate (SU 15 4) zone 2.

CaMg(CO₃)₂

Blank = beneath detection limit. SMD = standard mean deviation.

	1	2	3	Mean	SMD
FeCO ₃					
MnCO ₃					
MgCO ₃	36.2	35.5	35.9	35.9	0.4
CaCO ₃	63.6	64.2	63.0	63.6	0.6
Total	99.8	99.6	98.9	99.4	

Numbers of ions based on 60

Fe					
Mn					
Mg	1.615	1.586	1.614	1.605	0.016
Ca	2.385	2.414	2.386	2.395	0.016
Total	4.000	4.000	4.000	4.000	

Table 3.10. From figure 3.54. Group analysis of Semail tremolite (sample SU 15 1).



Blank = beneath detection limit. SMD = standard mean deviation.

	1	2	3	4	5	Mean	SMD
Na ₂ O	0.6	0.6	0.7	0.6	0.6	0.6	0.0
MgO	24.1	24.0	24.1	24.2	23.9	24.1	0.1
Al ₂ O ₃	1.1	1.1	1.1	1.2	1.0	1.1	0.1
SiO ₂	58.4	58.3	58.5	58.7	58.2	58.4	0.2
SO ₃	0.3	0.3	0.3	0.3	0.2	0.3	0.0
K ₂ O	0.0	0.0	0.0	0.0	0.0	0.0	0.0
CaO	12.7	12.6	12.7	12.6	12.9	12.7	0.1
TiO ₂	0.1	0.1	0.1	0.1	0.1	0.1	0.0
Cr ₂ O ₃	0.9	0.9	0.9	1.0	0.9	0.9	0.0
MnO	0.1	0.0	0.0	0.0	0.0	0.0	0.0
FeO	2.2	2.2	2.1	2.1	2.1	2.1	0.1
NiO			Not	tested			
CuO	0.0	0.0	0.0	0.0	0.0	0.0	0.0
Total	100.5	100.2	100.6	100.9	100.0	100.4	0.3

Numbers of ions based on 40

Na	0.028	0.029	0.031	0.028	0.028	0.029	0.002
Mg	0.831	0.832	0.831	0.832	0.832	0.831	0.000
Al	0.031	0.030	0.030	0.033	0.027	0.030	0.002
Si	1.353	1.354	1.355	1.354	1.357	1.355	0.001
S	0.005	0.005	0.005	0.005	0.004	0.005	0.000
K	0.000	0.000	0.000	0.000	0.000	0.000	0.000
Ca	0.314	0.313	0.314	0.312	0.322	0.315	0.004
Ti	0.002	0.002	0.002	0.002	0.002	0.002	0.000
Cr	0.017	0.017	0.017	0.018	0.016	0.017	0.001
Mn	0.001	0.001	0.001	0.000	0.001	0.001	0.000
Fe	0.043	0.042	0.041	0.041	0.040	0.042	0.001
Ni			Not	tested			
Cu	0.000	0.000	0.000	0.001	0.000	0.000	0.000
Total	2.624	2.625	2.628	2.625	2.629	2.626	0.002

Table 3.10. From figure 3.54. Group analysis of Semail pentlandite (sample SU 15 1).



Blank = beneath detection limit. SMD = standard mean deviation.

	1	2	3	4	5	Mean	SMD
Na							
Mg	0.09	0.08	0.10	0.13	0.12	0.104	0.02
Al							
Si	0.10	0.11	0.10	0.11	0.11	0.106	0.01
S	33.06	33.10	33.05	33.02	33.04	33.054	0.03
K							
Ca							
Ti							
Cr							
Mn							
Fe	29.73	29.46	29.61	30.07	29.98	29.77	0.25
Ni	34.37	34.51	34.44	33.53	33.55	34.08	0.50
Cu							
Total	97.35	97.26	97.30	96.86	96.80	97.11	

Note: Value totals were ~99% prior to removal of elements beneath the calculated detection limit.

Table 3.11. From figure 3.57. Group analysis of Semail carbonate (sample SU 15 4) zone 1.



Blank = beneath detection limit. SMD = standard mean deviation.

	1	2	3	Mean	SMD
FeCO ₃					
MnCO ₃					
MgCO ₃	40.1	37.3	40.9	39.4	1.9
CaCO ₃	59.0	62.7	58.5	60.1	2.3
Total	99.1	99.9	99.4	99.5	

Numbers of ions based on 60

Fe					
Mn					
Mg	1.786	1.656	1.814	1.752	0.084
Ca	2.214	2.344	2.186	2.248	0.084
Total	4.000	4.000	4.000	4.000	

Table 3.12. From figure 3.57. Group analysis of Semail carbonate (sample SU 15 4) zone 2.

CaMg(CO₃)₂

Blank = beneath detection limit. SMD = standard mean deviation.

	<u>1</u>
FeCO ₃	
MnCO ₃	
MgCO ₃	44.9
CaCO ₃	<u>54.6</u>
Total	99.5

**Numbers of ions based on
60**

Fe	
Mn	
Mg	1.976
Ca	<u>2.024</u>
Total	4.000

Table 3.13. From figure 3.57. Group analysis of Semail protoanthophyllite (sample SU 15 4) zone 3.



Blank = beneath detection limit. SMD = standard mean deviation.

	1	2	3	Mean	SMD
Na ₂ O			0.1	0.1	
MgO	32.3	32.4	32.6	32.4	0.1
Al ₂ O ₃	4.4	4.5	4.6	4.5	0.1
SiO ₂	54.5	54.1	54.2	54.3	0.2
SO ₃					
K ₂ O					
CaO	1.1	1.1	1.2	1.1	0.1
TiO ₂					
Cr ₂ O ₃	0.6	0.5	0.5	0.5	0.0
MnO					
FeO	6.3	6.2	6.1	6.2	0.1
NiO					
CuO					
Total	99.2	98.8	99.4	99.1	

Numbers of ions based on 24O

Na			0.080	0.080	
Mg	6.714	6.758	6.761	6.744	0.027
Al	0.730	0.742	0.756	0.743	0.013
Si	7.599	7.574	7.545	7.573	0.027
S					
K					
Ca	0.163	0.166	0.179	0.169	0.009
Ti					
Cr	0.061	0.060	0.058	0.060	0.002
Mn					
Fe	0.738	0.726	0.708	0.724	0.015
Ni					
Cu					
Total	16.005	16.026	16.088	16.039	

Note: Ion totals were exactly 16 prior to removing values beneath the detection limit. Ni and Mn were also present at approximately ideal values for protoanthophyllite (0.07) but fell beneath the detection limits for Mn (0.20) and Ni (0.23).

Chapter 4

Table 4.1. From figure 4.14. Group analysis pre-experiment basalt (olivine).

Fe₂SiO₄.

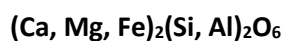
Blank = beneath detection limit. SMD = standard mean deviation.

	1	2	3	Mean	SMD
Na ₂ O		0.4		0.40	0.00
MgO	40.36	40.3	40.2	40.27	0.07
Al ₂ O ₃	0.42	0.3	0.3	0.33	0.06
SiO ₂	38.40	38.6	38.3	38.43	0.14
SO ₃					
K ₂ O					
CaO	0.32	0.3	0.4	0.35	0.02
TiO ₂					
Cr ₂ O ₃					
MnO	0.28	0.3	0.3	0.31	0.02
FeO	20.13	19.9	20.0	20.00	0.11
NiO					
CuO					
Total	99.9	100.1	99.5	99.82	

Numbers of ions based on 6O

Na		0.02			
Mg	1.55	1.55	1.55	1.55	0.00
Al	0.01	0.01	0.01	0.01	0.00
Si	0.99	0.99	0.99	0.99	0.00
S					
K					
Ca	0.01	0.01	0.01	0.01	0.00
Ti					
Cr					
Mn	0.01	0.01	0.01	0.01	0.00
Fe	0.43	0.43	0.43	0.43	0.00
Ni					
Cu					
Total	3.00	3.01	3.00	3.00	

Table 4.2. From figure 4.14. Group analysis pre-experiment basalt (pyroxene/augite).



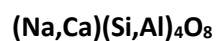
Blank = beneath detection limit. SMD = standard mean deviation.

	1	2	3	Mean	SMD
Na ₂ O	0.81	0.7	0.8	0.75	0.06
MgO	11.54	13.0	11.4	11.97	0.72
Al ₂ O ₃	4.72	2.3	4.7	3.92	1.14
SiO ₂	47.81	49.7	48.0	48.53	0.86
SO ₃					
K ₂ O					
CaO	15.41	12.5	15.9	14.59	1.50
TiO ₂	1.74	0.9	1.7	1.43	0.37
Cr ₂ O ₃					
MnO	0.43	0.5	0.4	0.45	0.03
FeO	18.78	21.0	18.6	19.46	1.12
NiO					
CuO					
Total	101.2	100.6	101.4	101.10	

Numbers of ions based on 60

Na	0.05	0.050	0.056	0.05	0.00
Mg	0.52	0.743	0.646	0.64	0.09
Al	0.21	0.104	0.212	0.18	0.05
Si	1.83	1.909	1.830	1.86	0.04
S					
K					
Ca	0.73	0.513	0.648	0.63	0.09
Ti	0.05	0.026	0.047	0.04	0.01
Cr					
Mn	0.02	0.016	0.014	0.02	0.00
Fe	0.63	0.675	0.591	0.63	0.03
Ni					
Cu					
Total	4.03	4.04	4.04	4.04	

Table 4.3. From figure 4.14. Group analysis pre-experiment basalt (plagioclase/andesine).



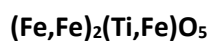
Blank = beneath detection limit. SMD = standard mean deviation.

	1	2	3	Mean	SMD
Na ₂ O	10.76	10.0	10.9	10.56	0.49
MgO	0.20	0.1	0.1	0.17	0.03
Al ₂ O ₃	26.12	26.1	26.0	26.08	0.07
SiO ₂	56.22	56.2	55.8	56.07	0.22
SO ₃					
K ₂ O	0.31	0.4	0.4	0.37	0.05
CaO	9.67	9.6	9.7	9.67	0.05
TiO ₂					
Cr ₂ O ₃					
MnO					
FeO	1.03	1.1	1.0	1.05	0.03
NiO					
CuO					
Total	104.31	103.56	104.04	103.97	

Numbers of ions based on 60

Na	0.69	0.65	0.71	0.68	0.03
Mg	0.01	0.01	0.01	0.01	0.00
Al	1.02	1.03	1.02	1.02	0.00
Si	1.87	1.87	1.86	1.87	0.01
S					
K	0.01	0.02	0.02	0.02	0.00
Ca	0.34	0.34	0.35	0.35	0.00
Ti					
Cr					
Mn					
Fe	0.03	0.03	0.03	0.03	0.00
Ni					
Cu					
Total	3.98	3.95	3.99	3.97	

Table 4.4. From figure 4.14. Group analysis pre-experiment basalt (metal oxide/pseudobrookite).



Blank = beneath detection limit. SMD = standard mean deviation.

	1	2	3	Mean	SMD
Na ₂ O					
MgO	0.83	0.8	0.9	0.85	0.02
Al ₂ O ₃	2.87	3.1	3.1	3.01	0.10
SiO ₂	0.43	0.4	0.4	0.40	0.03
SO ₃					
K ₂ O					
CaO	0.22	0.2	0.2	0.19	0.02
TiO ₂	24.31	24.4	24.5	24.39	0.08
Cr ₂ O ₃					
MnO	0.48	0.5	0.6	0.52	0.05
FeO	68.35	68.7	68.6	68.55	0.14
NiO					
CuO					
Total	97.5	98.1	98.2	97.90	

Numbers of ions based on 60

Na					
Mg	0.06	0.06	0.06	0.06	0.00
Al	0.17	0.18	0.18	0.17	0.01
Si	0.02	0.02	0.02	0.02	0.00
S					
K					
Ca	0.01	0.01	0.01	0.01	0.00
Ti	0.90	0.90	0.90	0.90	0.00
Cr					
Mn	0.02	0.02	0.02	0.02	0.00
Fe	2.81	2.81	2.80	2.81	0.00
Ni					
Cu					
Total	4.00	3.99	3.99	3.99	

Table 4.5. From figure 4.16 and 4.17. Group analysis pre-experiment type 1 pyrrhotite (pyrrhotite).

Fe_(1-x)S (x = 0 to 0.2)

Blank = beneath detection limit. SMD = standard mean deviation. Values are wt. %.

	1	2	3	Mean	SMD
Na					
Mg					
Al					
Si					
S	39.42	39.38	39.36	39.39	0.02
K					
Ca					
Ti					
Cr					
Mn					
Fe	59.2	59.36	59.67	59.41	0.20
Ni					
Cu					
Total	98.62	98.74	99.03	98.80	

Table 4.6. From figure 4.16 and 4.17. Group analysis pre-experiment type 2 pyrrhotite (chalcopyrite).

CuFeS₂

Blank = beneath detection limit. SMD = standard mean deviation.

Values are wt. %.

	1	2	3	Mean	SMD
Na					
Mg		0.08	0.06	0.05	0.01
Al					
Si					
S	34.45	34.29	34.46	34.40	0.08
K					
Ca					
Ti					
Cr					
Mn					
Fe	30.03	30.39	30.17	30.20	0.15
Ni					
Cu	33.86	33.77	33.74	33.79	0.05
Total	98.34	98.53	98.43	98.43	

Table 4.7. From figure 4.16 and 4.17. Group analysis pre-experiment type 3 pyrrhotite (Pyrite).

FeS₂

Blank = beneath detection limit. SMD = standard mean deviation. Values are wt. %.

	1	2	3	Mean	SMD
Na					
Mg					
Al					
Si		0.07		0.07	0.00
S	51.69	51.74	51.76	51.73	0.03
K					
Ca					
Ti					
Cr					
Mn					
Fe	45.68	45.87	45.49	45.68	0.16
Ni					
Cu					
O	1.32	1.17	1.29	1.26	0.06
Total	98.69	98.85	98.54	98.74	

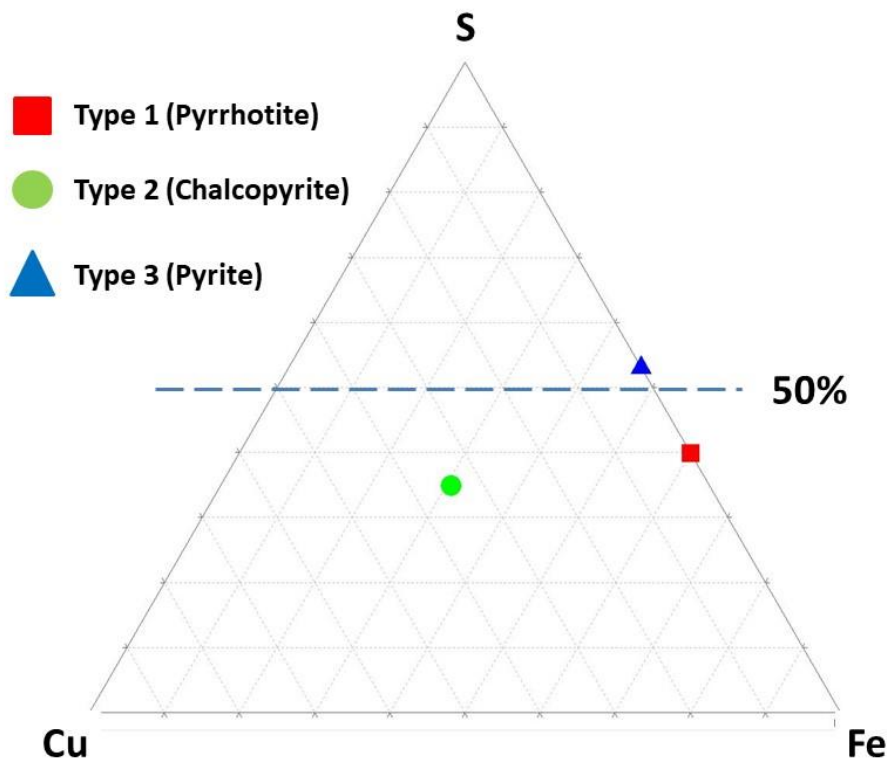


Table 4.8. From figure 4.17 and 4.18. Group analysis pre-experiment pyrrhotite impurity (Calcite).

CaCO₃

	1	2	3	4	5	Mean	SMD
FeCO ₃	0.56		1.14	0.52	0.89	0.62	0.29
MnCO							
MgO			0.24				
CaO	99.06	99.71	98.03	98.68	98.38	98.77	0.65
Total	99.62	99.71	99.41	99.20	99.27	99.64	

Numbers of ions based on 60

Fe	0.02		0.03	0.02	0.03	0.02	0.01
Mn							
Mg			0.02				
Ca	3.98	3.99	3.95	3.98	3.97	3.98	0.01
Total	4.000	4	4.000	4.000	4.000	4.000	

Table 4.9. From figure 4.19 and 4.20. Group analysis pre-experiment olivine.

	1	2	3	Mean	SMD
Na ₂ O	0.2		0.3	0.3	0.0
MgO	22.3	22.5	22.6	22.4	0.2
Al ₂ O ₃	0.3	0.2	0.2	0.2	0.0
SiO ₂	34.1	34.2	34.0	34.1	0.1
SO ₃					
K ₂ O					
CaO					
TiO ₂					
Cr ₂ O ₃					
MnO	0.5	0.6	0.5	0.5	0.0
FeO	42.4	42.6	42.8	42.6	0.2
NiO					
CuO					
Total	99.8	100.1	100.3	100.1	

Numbers of ions based on 40

Na	0.014		0.015	0.014	0.001
Mg	0.962	0.969	0.972	0.967	0.005
Al	0.009	0.008	0.008	0.008	0.001
Si	0.989	0.988	0.981	0.986	0.004
S					
K					
Ca					
Ti					
Cr					
Mn	0.013	0.014	0.013	0.013	0.001
Fe	1.027	1.029	1.033	1.030	0.003
Ni					
Cu					
Total	3.013	3.008	3.022	3.014	

Table 4.10. From figure 4.19 and 4.20. Group analysis of ilmenite.

Fe²⁺TiO₃

Blank = beneath detection limit. SMD = standard mean deviation.

	1	2	3	Mean	SMD
Na ₂ O					
MgO	0.90	0.9	0.9	0.88	0.02
Al ₂ O ₃					
SiO ₂	0.15	0.2	0.2	0.19	0.04
SO ₃					
K ₂ O					
CaO					
TiO ₂	50.79	50.7	50.7	50.74	0.05
Cr ₂ O ₃					
MnO	0.72	0.9	0.9	0.83	0.10
FeO	45.77	45.6	45.4	45.58	0.19
NiO					
CuO					
Total	98.33	98.29	98.05	98.22	

Numbers of ions based on 30

Na					
Mg	0.034	0.034	0.033	0.034	0.001
Al					
Si	0.004	0.004	0.006	0.005	0.001
S					
K					
Ca					
Ti	0.980	0.980	0.980	0.980	0.000
Cr					
Mn	0.016	0.020	0.019	0.018	0.002
Fe	0.982	0.979	0.976	0.979	0.003
Ni					
Cu					
Total	2.016	2.016	2.014	2.015	

Table 4.11. Group analysis post-experiment 1701 type 1 pyrrhotite (pyrrhotite). From figure 4.36.

FeS₂

Blank = beneath detection limit. SMD = standard mean deviation. Values are wt. %.

	1	2	3	Mean	SMD
Na					
Mg					
Al					
Si					
S	39.13	39.21	39.11	39.15	0.05
K					
Ca					
Ti					
Cr					
Mn					
Fe	60.87	60.46	60.06	60.46	0.41
Ni					
Cu					
Total	100	99.67	99.17	99.61	

Table 4.12. Group analysis of 1703 olivine. From figure 4.38.

(Mg,Fe)₂SiO₄

Blank = beneath detection limit. SMD = standard mean deviation.

	1	2	3	Mean	SMD
Na ₂ O	0.3				
MgO	23.0	23.2	22.7	23.0	0.3
Al ₂ O ₃		0.4	0.4	0.4	0.0
SiO ₂	34.2	34.3	34.2	34.2	0.0
SO ₃					
K ₂ O					
CaO					
TiO ₂					
Cr ₂ O ₃					
MnO	0.5	0.6	0.6	0.6	0.1
FeO	41.4	41.5	41.3	41.4	0.1
NiO					
CuO					
Total	99.5	99.9	99.2	99.5	0.4

Numbers of ions based on 40

Na	0.018				
Mg	0.994	0.995	0.980	0.990	0.008
Al		0.013	0.013	0.013	0.000
Si	0.991	0.986	0.992	0.989	0.003
S					
K					
Ca					
Ti					
Cr					
Mn	0.012	0.015	0.016	0.014	0.002
Fe	1.004	0.999	1.002	1.002	0.002
Ni					
Cu					
Total	3.018	3.008	3.002	3.009	0.008

Table 4.13. Group analysis of 1705 olivine (grains). From figure 4.43.

(Mg,Fe)₂SiO₄

Blank = beneath detection limit. SMD = standard mean deviation.

	1	2	3	Mean	SMD
Na ₂ O			0.4		
MgO	21.8	21.8	21.6	21.7	0.1
Al ₂ O ₃	0.9	0.8	0.9	0.9	0.1
SiO ₂	33.9	34.2	33.8	33.9	0.2
SO ₃					
K ₂ O					
CaO					
TiO ₂					
Cr ₂ O ₃					
MnO	0.6	0.5	0.6	0.5	0.1
FeO	41.6	41.6	41.9	41.7	0.1
NiO					
CuO					
Total	98.7	98.9	99.1	98.9	0.2

Numbers of ions based on 40

Na			0.021	0.007	
Mg	0.947	0.945	0.937	0.943	0.005
Al	0.031	0.028	0.032	0.031	0.002
Si	0.988	0.994	0.985	0.989	0.005
S					
K					
Ca					
Ti					
Cr					
Mn	0.014	0.011	0.014	0.013	0.002
Fe	1.016	1.013	1.021	1.017	0.004
Ni					
Cu					
Total	2.996	2.992	3.011	3.000	0.010

Table 4.14. Group analysis post-experiment 1705 iron oxide. From figure 4.43. D.

FeO

Blank = beneath detection limit. SMD = standard mean deviation.

	1	2	3	Mean	SMD
Na ₂ O					
MgO	0.8	0.7	0.7	0.8	0.1
Al ₂ O ₃					
SiO ₂	1.6	1.7	1.8	1.7	0.1
SO ₃					
K ₂ O					
CaO					
TiO ₂					
Cr ₂ O ₃					
MnO	1.0	0.9	1.0	1.0	0.1
FeO	88.7	88.7	88.4	88.6	0.2
NiO					
CuO					
Total	92.1	92.1	92.0	92.1	0.1

Numbers of ions based on 10

Na					
Mg	0.016	0.014	0.013	0.014	0.001
Al					
Si	0.020	0.022	0.023	0.022	0.001
S					
K					
Ca					
Ti					
Cr					
Mn	0.010	0.010	0.011	0.010	0.001
Fe	0.933	0.933	0.930	0.932	0.002
Ni					
Cu					
Total	0.980	0.978	0.977	0.978	0.001

Table 4.15. Group analysis of 1706 olivine in basalt. From figure 4.44.

(Mg,Fe)₂SiO₄

Blank = beneath detection limit. SMD = standard mean deviation.

	1	2	3	Mean	SMD
Na ₂ O					
MgO	40.18	39.78	39.72	39.89	0.25
Al ₂ O ₃	0.15	0.15	0.19	0.16	0.02
SiO ₂	38.06	38.23	37.97	38.09	0.13
SO ₃					
K ₂ O					
CaO	0.41	0.36	0.46	0.41	0.05
TiO ₂					
Cr ₂ O ₃					
MnO	0.34	0.32	0.32	0.33	0.01
FeO	20.04	19.94	19.97	19.98	0.05
NiO	0.29			0.29	
CuO	0.20			0.20	
Total	99.67	98.79	98.63	99.03	

Numbers of ions based on 40

Na					
Mg	1.555	1.547	1.548	1.550	0.004
Al	0.005	0.005	0.006	0.005	0.001
Si	0.988	0.997	0.993	0.993	0.004
S					
K					
Ca	0.011	0.010	0.013	0.011	0.001
Ti					
Cr					
Mn	0.007	0.007	0.007	0.007	0.000
Fe	0.435	0.435	0.437	0.436	0.001
Ni	0.004			0.004	
Cu	0.004			0.004	
Total	3.010	3.001	3.004	3.010	

Table 4.16. Group analysis of 1706 pseudobrookite in basalt. From figure 4.44.



Blank = beneath detection limit. SMD = standard mean deviation.

	1	2	3	Mean	SMD
Na ₂ O	0.40	0.43		0.42	0.02
MgO	0.46	0.38	0.38	0.41	0.05
Al ₂ O ₃	1.61	1.63	1.46	1.56	0.09
SiO ₂	0.39	0.47	0.51	0.46	0.07
SO ₃					
K ₂ O		0.07		0.07	
CaO	0.21	0.15		0.18	0.04
TiO ₂	23.08	22.99	22.79	22.95	0.15
Cr ₂ O ₃					
MnO	0.53	0.62	0.45	0.53	0.08
FeO	68.22	67.13	67.73	67.70	0.55
NiO					
CuO					
Total	94.90	93.88	93.33	94.03	

Numbers of ions based on 50

Na	0.040	0.043		0.042	0.002
Mg	0.036	0.030	0.030	0.032	0.003
Al	0.097	0.099	0.090	0.096	0.005
Si	0.020	0.024	0.027	0.024	0.004
S					
K		0.005		0.005	
Ca	0.012	0.009	0.000	0.007	0.006
Ti	0.894	0.898	0.898	0.897	0.003
Cr					
Mn	0.023	0.027	0.020	0.023	0.004
Fe	2.937	2.916	2.966	2.940	0.025
Ni					
Cu					
Total	4.058	4.052	4.030	4.064	

Table 4.17. Group analysis of 1707 olivine CO₂ + SO₂ (main slice). From figure 4.45.

(Mg,Fe)₂SiO₄

Blank = beneath detection limit. SMD = standard mean deviation.

	1	2	3	Mean	SMD
Na ₂ O	0.30	0.24		0.27	0.04
MgO	22.30	22.34	22.42	22.35	0.06
Al ₂ O ₃	0.30		0.34	0.32	0.03
SiO ₂	34.08	34.01	33.89	33.99	0.10
SO ₃					
K ₂ O					
CaO					
TiO ₂					
Cr ₂ O ₃					
MnO	0.48	0.53	0.54	0.52	0.03
FeO	42.00	41.76	41.49	41.75	0.26
NiO					
CuO					
Total	99.46	98.88	98.68	99.01	

Numbers of ions based on 40

Na	0.017	0.014		0.015	0.002
Mg	0.965	0.973	0.976	0.971	0.005
Al	0.010		0.012	0.011	0.001
Si	0.990	0.994	0.990	0.991	0.002
S					
K					
Ca					
Ti					
Cr					
Mn	0.012	0.013	0.013	0.013	0.001
Fe	1.020	1.020	1.013	1.018	0.004
Ni					
Cu					
Total	3.014	3.013	3.004	3.010	

Appendix 5.

IC - ICPMS data from chapter 4.

Sample Code	Date	Interval Time	Total Time	Solid	Gas	Eh (mV)	Eh (SHE)	pH	Ca	Mg	Na	K	HCO ₃ ⁻	Cl ⁻	SO ₄ ²⁻	NO ₃ ⁻	Cation Total	Anion Total	
Blank	19/05/2015 11:00	h	h						0.4	0.02	0.3	0.03							
1700/1	29/05/2015 15:10	244.2	244.2	Basalt	N ₂	240.8	450.8	7.84	<0.40	<0.02	<0.30	<0.03	n/a	<0.25	<0.25	<0.15	0.23	n/a	
1700/2	12/06/2015 14:00	334.8	579.0			<50.6	159.4	7.40	2.20	0.32	1.70	0.28	<5.00	2.93	2.79	0.44	0.24	0.51	
1700/3	09/07/2015 11:30	645.5	1224.5			206.2	416.2	7.07	2.20	0.31	1.90	0.38	7.25	12.19	2.20	0.30	0.23	0.51	
1700/4	07/08/2015 13:30	698.0	1922.5			168.9	378.9	7.81	1.60	0.31	2.50	0.63	<5.00	3.86	3.85	0.48	0.23	0.20	
1700/5	16/09/2015 10:15	956.8	2879.3			119.7	329.7	7.35	1.20	0.25	2.90	0.83	<5.00	6.47	3.43	0.46	0.23	0.26	
Blank	19/05/2015 11:00	-	0.0	Basalt	CO ₂	216.8	426.8	7.04	1.00	0.21	3.30	0.99	<5.00	1.30	3.72	0.24	0.24	0.12	
1702/1	29/05/2015 15:10	244.2	244.2	Basalt		240.8	450.8	7.84	<0.40	<0.02	<0.30	<0.03	n/a	<0.25	<0.25	<0.15	n/a	n/a	
1702/2	12/06/2015 14:11	335.0	579.2			178.9	388.9	5.33	8.50	1.20	2.10	0.36	35.82	3.64	1.97	0.41	0.62	0.74	
1702/3	09/07/2015 11:35	645.4	1224.6			148.5	358.5	5.80	13.00	1.33	3.30	0.40	<5.00	7.86	1.98	0.25	0.91	0.27	
1702/4	07/08/2015 14:30	698.9	1923.5			194.4	404.4	5.54	9.70	1.13	4.50	0.45	45.48	1.26	2.08	<0.15	0.79	0.83	
1702/5	16/09/2015 11:00	956.5	2880.0			144.6	354.6	5.49	11.40	1.34	5.30	0.51	53.29	14.74	2.19	12.84	0.92	1.54	
Blank	19/05/2015 11:00	-	0.0	Basalt	CO ₂ SO ₂	183.5	393.5	5.43	14.10	1.61	6.50	0.58	65.51	0.71	2.14	<0.15	1.14	1.14	
1706/1	29/05/2015 15:10	244.2	244.2	Basalt		240.8	450.8	7.84	<0.40	<0.02	<0.30	<0.03	n/a	<0.25	<0.25	<0.15	n/a	n/a	
1706/2	12/06/2015 14:40	335.5	579.7			311.4	521.4	3.75	55.00	349.46	6.00	2.66	<5.00	<25.00	2306.57	<15.00	31.91	48.28	
1706/3	09/07/2015 11:50	645.2	1224.8			14.5	224.5	5.64	48.90	353.09	5.90	0.50	<5.00	<25.00	2258.24	<15.00	31.84	47.17	
1706/4	07/08/2015 14:00	698.2	1923.0			14.7	224.7	5.42	48.00	377.22	6.40	0.56	30.79	<25.00	2234.76	<15.00	33.81	47.03	
1706/5	16/09/2015 11:40	957.7	2880.7			15.9	225.9	5.41	47.30	368.51	6.90	6.69	57.19	<25.00	2264.44	<15.00	33.24	48.08	
						38.8	248.8	5.70	48.00	312.22	7.70	0.70	76.12	<25.00	2261.77	<15.00	48.55	48.55	

Sample Code	Date	Interval Time	Total Time	Solid	Gas	Eh	Eh (SHE)	pH	Ca	Mg	Na	K	HCO ₃ ⁻	Cl ⁻	SO ₄ ²⁻	NO ₃ ⁻	Cation Total	Anion Total
Blank	19/05/2015 11:00	.	0.0	Olivine	N ₂	240.8	450.8	7.84	<0.40	<0.02	<0.30	<0.03	n/a	<0.25	<0.25	<0.15	n/a	n/a
1703/1	29/05/2015 15:10	244.2	244.2			26.9	236.9	7.53	4.00	0.34	1.50	2.77	11.13	4.33	0.42	0.35	0.36	0.32
1703/2	12/06/2015 14:15	335.1	579.2			112.5	322.5	6.98	2.80	0.32	1.60	1.71	<5.00	25.25	0.51	0.87	0.28	0.74
1703/3	09/07/2015 11:35	645.3	1224.6			150.9	360.9	7.20	2.20	0.23	1.50	2.01	3.79	4.43	0.60	0.50	0.25	0.21
1703/4	07/08/2015 14:00	698.4	1923.0			154.9	364.9	6.85	2.00	0.28	1.60	2.26	<5.00	0.43	<0.25	<0.15	0.25	0.01
1703/5	16/09/2015 10:40	956.7	2879.7	pH double checked		142.8	352.8	8.92	2.70	0.46	1.60	2.63	<5.00	3.70	0.79	0.34	0.31	0.13
Blank	19/05/2015 11:00	.	0.0	Olivine	CO ₂	240.8	450.8	7.84	<0.40	<0.02	<0.30	<0.03	n/a	<0.25	<0.25	<0.15	n/a	n/a
1705/1	29/05/2015 15:10	244.2	244.2			87.1	297.1	5.91	5.30	23.27	0.90	8.60	127.70	3.62	1.71	0.61	2.44	2.24
1705/2	12/06/2015 14:30	335.3	579.5			38.2	248.2	6.21	2.50	36.53	0.60	8.22	198.90	11.56	1.73	0.36	3.37	3.63
1705/3	09/07/2015 11:45	645.3	1224.8			47.8	257.8	6.15	1.10	47.50	0.90	10.82	241.80	3.39	2.78	0.34	4.29	4.12
1705/4	07/08/2015 14:00	698.3	1923.0			196.6	406.6	5.92	1.50	51.78	0.90	12.40	273.70	7.78	3.35	0.34	4.70	4.78
1705/5	16/09/2015 11:25	957.4	2880.4			78.0	288.0	6.03	1.20	58.33	0.90	12.96	315.70	1.48	4.10	0.30	5.24	5.31
Blank	19/05/2015 11:00	.	0.0	Olivine	CO ₂ + SO ₂	240.8	450.8	7.84	<0.40	<0.02	<0.30	<0.03	n/a	<0.25	<0.25	<0.15	n/a	n/a
1707/1	29/05/2015 15:10	244.2	244.2			46.5	256.5	5.47	8.50	327.39	3.00	7.14	<5.00	<25.00	2246.08	<15.00	27.72	46.76
1707/2	12/06/2015 14:45	335.6	579.8			<12.8	197.2	5.43	2.90	340.90	0.60	6.93	<5.00	<25.00	2275.71	<15.00	28.44	47.38
1707/3	09/07/2015 11:55	645.2	1224.9			20.5	230.5	5.60	2.40	347.17	0.60	9.26	27.23	<25.00	2255.68	<15.00	28.99	47.41
1707/4	07/08/2015 14:00	698.1	1923.0			No sample	No sample	No sample	No sample	No sample	No sample	No sample	No sample	No sample	No sample	No sample	No sample	No sample
1707/5	16/09/2015 11:30	957.5	2880.5			45.2	255.2	5.82	2.20	164.58	0.60	8.20	110.20	<25.00	1108.83	<15.00	1108.83	<15.00

Sample Code	Date	Interval Time	Total Time	Solid	Gas	Eh	Eh (SHE)	pH	Ca	Mg	Na	K	HCO ₃ ⁻	Cl ⁻	SO ₄ ²⁻	NO ₃ ⁻	Cation Total	Anion Total
Blank	19/05/2015 11:00	.	0.0	Basalt + pyrrhotite	N ₂	240.8	450.8	7.84	<0.40	<0.02	<0.30	<0.03	n/a	<0.25	<0.25	<0.15	n/a	n/a
1701/1	29/05/2015 15:10	244.2	244.2			30.1	240.1	5.78	6.30	5.13	2.20	7.33	<5.00	5.96	157.24	<1.50		
1701/2	12/06/2015 14:05	334.9	579.1			72.4	282.4	5.68	8.50	5.25	2.30	0.32	<5.00	35.47	158.68	<1.50		
1701/3	09/07/2015 11:30	645.4	1224.5			115.9	325.9	5.20	10.30	5.19	3.40	0.42	<5.00	6.06	165.67	<1.50		
1701/4	07/08/2015 13:30	698.0	1922.5			396.8	606.8	4.85	12.20	5.34	4.30	0.54	<5.00	28.77	164.63	<1.50		
1701/5	16/09/2015 10:11	956.7	2879.2			148.6	358.6	5.01	15.90	5.28	5.60	0.71	<5.00	<2.50	164.97	<1.50		
Blank	19/05/2015 11:00	.	0.0	Basalt + pyrrhotite	CO ₂	240.8	450.8	7.84	<0.40	<0.02	<0.30	<0.03	n/a	<0.25	<0.25	<0.15	n/a	n/a
1704/1	29/05/2015 15:10	244.2	244.2			6.3	216.3	5.67	7.40	8.05	1.50	0.21	43.55	23.01	210.31	<1.50		
1704/2	12/06/2015 14:25	335.3	579.4			<44.9	165.1	6.25	7.10	7.93	2.30	0.22	76.80	5.84	157.11	<1.50		
1704/3	09/07/2015 11:40	645.2	1224.7			<21.5	188.5	6.17	9.90	8.13	3.60	0.35	<5.00	2.95	172.51	.		
1704/4	07/08/2015 13:45	698.1	1922.7			<28.1	181.9	5.86	12.40	8.29	4.60	0.43	137.70	25.25	178.25	<1.50		
1704/5	16/09/2015 11:20	957.6	2880.3			59.3	269.3	5.79	15.60	8.61	6.00	0.52	176.70	3.51	196.48	<1.50		

Pa6

Sample Code

Sample Code	Date	Interval Time	Total Time	Solid	Gas	Balance	S Balance	Br	NO ₂	HPO ₄ ²⁻	F	TIC (CALC from alk)	Total P	Total S	S Diff	Si	SiO ₂	Ba
Blank	19/05/2015 11:00	-	0.0	Basalt	N ₂	n/a	n/a	<0.05	<0.03	<0.05	0.11	n/a	<0.03	<4.00	97.91	<0.11	<0.24	<0.30
1700/1	29/05/2015 15:10	244.2	244.2			<37.24		0.11	<0.03	<0.05	<0.03	<0.98	0.03	<4.00	123.30	4.15	8.88	3.20
1700/2	12/06/2015 14:00	334.8	579.0			<38.61	2.05	0.10	<0.03	<0.05	<0.03	1.43	<0.03	<4.00	118.39	6.19	13.24	2.00
1700/3	09/07/2015 11:30	645.5	1224.5			7.68	371.71	0.06	<0.03	<0.05	<0.03	<0.98	<0.03	<4.00	132.14	9.53	20.39	1.80
1700/4	07/08/2015 13:30	698.0	1922.5			<7.36	167.06	0.10	<0.03	<0.05	0.03	<0.98	<0.03	<4.00	128.61	11.94	25.54	1.70
1700/5	16/09/2015 10:15	956.8	2879.3			32.18	1486.27	<0.05	<0.03	0.05	0.04	<0.98	<0.03	<4.00	131.06	14.26	30.51	0.90
Blank	19/05/2015 11:00	-	0.0	Basalt	CO ₂	n/a	n/a	<0.05	<0.03	<0.05	0.11	n/a	<0.03	<4.00	97.91	<0.11	<0.24	<0.30
1702/1	29/05/2015 15:10	244.2	244.2			<8.31	16.62	<0.05	<0.03	<0.05	<0.03	7.05	<0.03	<4.00	116.45	6.37	13.63	21.30
1702/2	12/06/2015 14:11	335.0	579.2			54.75	105.47	<0.05	<0.03	<0.05	<0.03	<0.98	<0.03	<4.00	116.54	11.19	23.94	24.30
1702/3	09/07/2015 11:35	645.4	1224.6			<2.47	19.25	0.07	<0.03	<0.05	<0.03	8.95	<0.03	<4.00	117.34	16.51	35.32	16.50
1702/4	07/08/2015 14:30	698.9	1923.5			<25.09	<14.89	0.08	<0.03	<0.05	<0.03	10.49	<0.03	<4.00	118.23	18.98	40.60	16.70
1702/5	16/09/2015 11:00	956.5	2880.0			<0.21	14.64	0.13	<0.03	<0.05	<0.03	12.90	<0.03	<4.00	117.86	21.71	46.44	19.30
Blank	19/05/2015 11:00	-	0.0	Basalt	CO ₂ + SO ₂	n/a	n/a	<0.05	<0.03	<0.05	0.11	n/a	<0.03	<4.00	97.91	<0.11	<0.24	<0.30
1706/1	29/05/2015 15:10	244.2	244.2			<20.41	<19.42	<5.00	<2.50	<5.00	4.85	<0.98	<0.03	753.00	<2.24	271.63	581.10	133.30
1706/2	12/06/2015 14:40	335.5	579.7			<19.40	<17.99	<5.00	<2.50	<5.00	2.99	<0.98	<0.03	731.00	<3.11	248.46	531.53	87.60
1706/3	09/07/2015 11:50	645.2	1224.8			<16.36	<14.91	<5.00	<2.50	<5.00	<2.50	6.06	0.05	723.00	<3.16	223.86	478.90	77.20
1706/4	07/08/2015 14:00	698.2	1923.0			<18.26	<24.64	<5.00	<2.50	<5.00	<2.50	11.26	<0.03	865.00	12.63	194.82	416.78	73.70
1706/5	16/09/2015 11:40	957.7	2880.7					<5.00	<2.50	<5.00	4.03	14.98	<0.03	811.00	6.92	146.14	312.64	65.80

Sample Code	Date	Interval Time	Total Time	Solid	Gas	Balance	S Balance	Br ⁻	NO ₂ ⁻	HPO ₄ ²⁻	F ⁻	TIC (CALC from alk)	Total P	Total S	S Diff	Si	SiO ₂	Ba
Blank	19/05/2015 11:00	-	0.0	Olivine	N ₂	n/a	n/a	<0.05	<0.03	<0.05	0.11	n/a	<0.03	<4.00	97.91	<0.11	<0.24	<0.30
1703/1	29/05/2015 15:10	244.2	244.2			6.52	71.17	0.09	<0.03	<0.05	<0.03	2.19	<0.03	<4.00	103.52	1.04	2.22	2.70
1703/2	12/06/2015 14:15	335.1	579.2			<44.89	<25.91	<0.05	<0.03	<0.05	<0.03	<0.98	<0.03	<4.00	104.25	0.94	2.01	5.50
1703/3	09/07/2015 11:35	645.3	1224.6			8.04	154.19	0.07	<0.03	<0.05	0.03	0.75	<0.03	<4.00	105.02	1.20	2.57	2.40
1703/4	07/08/2015 14:00	698.4	1923.0			90.90	2246.46	<0.05	<0.03	<0.05	<0.03	<0.98	<0.03	<4.00	97.91	1.36	2.91	3.10
1703/5	16/09/2015 10:40	956.7	2879.7	pH double checked	41.02	256.31	<0.05	<0.03	<0.05	0.07	<0.98	<0.03	<4.00	106.60	1.73	3.70	4.90	
Blank	19/05/2015 11:00	-	0.0	Olivine	CO ₂	n/a	n/a	<0.05	<0.03	<0.05	0.11	n/a	<0.03	<4.00	97.91	<0.11	<0.24	<0.30
1705/1	29/05/2015 15:10	244.2	244.2			4.30	11.07	<0.05	<0.03	<0.05	<0.03	25.14	<0.03	<4.00	114.25	22.24	47.58	64.00
1705/2	12/06/2015 14:30	335.3	579.5			<3.67	0.44	<0.05	<0.03	<0.05	<0.03	39.15	<0.03	<4.00	114.43	33.94	72.61	100.20
1705/3	09/07/2015 11:45	645.3	1224.8			1.93	5.81	0.08	<0.03	<0.05	<0.03	47.60	<0.03	<4.00	123.22	42.47	90.86	130.10
1705/4	07/08/2015 14:00	698.3	1923.0			<0.88	2.58	0.09	<0.03	<0.05	<0.03	53.88	<0.03	<4.00	127.98	45.72	97.81	143.40
1705/5	16/09/2015 11:25	957.4	2880.4			<0.67	2.60	0.13	<0.03	<0.05	<0.03	62.14	<0.03	<4.00	134.19	51.06	109.23	156.00
Blank	19/05/2015 11:00	-	0.0	Olivine	CO ₂ + SO ₂	n/a	n/a	<0.05	<0.03	<0.05	0.11	n/a	<0.03	<4.00	97.91	<0.11	<0.24	<0.30
1707/1	29/05/2015 15:10	244.2	244.2			<25.57	<25.59	<5.00	<2.50	<5.00	<2.50	<0.98	0.13	749.00	<0.09	182.75	390.96	79.80
1707/2	12/06/2015 14:45	335.6	579.8			<24.98	<23.55	<5.00	<2.50	<5.00	<2.50	<0.98	0.21	736.00	<3.20	168.66	360.81	63.80
1707/3	09/07/2015 11:55	645.2	1224.9			<24.10	<22.40	<5.00	<2.50	<5.00	<2.50	5.36	0.55	725.00	<3.84	163.46	349.69	47.60
1707/4	07/08/2015 14:00	698.1	1923.0			No sample	No sample	No sample	No sample	No sample	No sample	No sample	No sample	No sample	No sample	No sample	No sample	No sample
1707/5	16/09/2015 11:30	957.5	2880.5			<5.00	<5.00	<5.00	<2.50	<5.00	2.85	21.69	0.18	408.00	9.29	100.98	216.03	42.00

Sample Code

Sample Code	Date	Interval Time	Total Time	Solid	Gas	Balance	S Balance	Br ⁻	NO ₂ ⁻	HPO ₄ ²⁻	F ⁻	TIC (CALC from alk)	Total P	Total S	S Diff	Si	SiO ₂	Ba
Blank	19/05/2015 11:00	.	0.0	Basalt + pyrrhotite	N ₂	n/a	n/a	<0.05	<0.03	<0.05	0.11	n/a	<0.03	<4.00	97.91	<0.11	<0.24	<0.30
1701/1	29/05/2015 15:10	244.2	244.2			%	%	<0.50	<0.25	<0.50	<0.25	<0.98	<0.03	54.00	2.81	9.25	19.79	20.00
1701/2	12/06/2015 14:05	334.9	579.1			%	%	<0.50	<0.25	<0.50	<0.25	<0.98	<0.03	56.00	5.43	12.62	27.00	26.10
1701/3	09/07/2015 11:30	645.4	1224.5			%	%	<0.50	<0.25	<0.50	<0.25	<0.98	<0.03	54.00	<2.39	15.66	33.50	24.60
1701/4	07/08/2015 13:30	698.0	1922.5			%	%	<0.50	<0.25	<0.50	<0.25	<0.98	<0.03	54.00	<1.75	18.11	38.74	26.80
1701/5	16/09/2015 10:11	956.7	2879.2			%	%	<0.50	<0.25	<0.50	<0.25	<0.98	<0.03	61.00	9.74	21.00	44.93	27.80
Blank	19/05/2015 11:00	.	0.0	Basalt + pyrrhotite	CO ₂	n/a	n/a	<0.05	<0.03	<0.05	0.11	n/a	<0.03	<4.00	97.91	<0.11	<0.24	<0.30
1704/1	29/05/2015 15:10	244.2	244.2			%	%	<0.50	<0.25	<0.50	<0.25	8.57	<0.03	58.00	<21.02	11.12	23.79	27.40
1704/2	12/06/2015 14:25	335.3	579.4			%	%	<0.50	<0.25	<0.50	<0.25	15.12	<0.03	58.00	9.59	15.00	32.09	24.40
1704/3	09/07/2015 11:40	645.2	1224.7			%	%	<0.50	<0.25	<0.50	<0.25	<0.98	<0.03	58.00	0.73	18.90	40.43	25.80
1704/4	07/08/2015 13:45	698.1	1922.7			%	%	<0.50	<0.25	<0.50	<0.25	27.11	<0.03	59.00	<0.83	22.07	47.21	27.10
1704/5	16/09/2015 11:20	957.6	2880.3			%	%	<0.50	<0.25	<0.50	<0.25	34.78	<0.03	74.00	11.38	24.98	53.44	32.50

Sample Code	Date	Interval Time	Total Time	Solid	Gas	Sr	Mn	Total Fe	Total Fe	Reduced Fe	Oxidised Fe	Li	Be	B	Al	Ti	V
Blank	19/05/2015 11:00	-	0.0	Basalt	N ₂	<0.40	0.70	<50	<0.05	<0.005	n/a	<3.0	<0.02	<40.00	<4.00	0.10	<0.20
1700/1	29/05/2015 15:10	244.2	244.2			14.80	8.70	128	0.13	0.08	0.05	<3.0	<0.02	105.00	818.00	<0.10	2.10
1700/2	12/06/2015 14:00	334.8	579.0			10.60	5.00	<50	<0.05	0.03	<0.08	<3.0	<0.02	77.00	1121.00	0.20	2.90
1700/3	09/07/2015 11:30	645.5	1224.5			6.90	8.40	88	0.09	0.05	0.04	<3.0	<0.02	72.00	869.00	<0.10	3.10
1700/4	07/08/2015 13:30	698.0	1922.5			5.30	6.20	115	0.12	0.04	0.08	<3.0	<0.02	66.00	977.00	0.30	3.30
1700/5	16/09/2015 10:15	956.8	2879.3			4.00	5.20	88	0.09	0.12	<0.03	<3.0	<0.02	84.00	783.00	0.20	3.90
Blank	19/05/2015 11:00	-	0.0	Basalt	CO ₂	<0.40	0.70	<50	<0.05	<0.005	n/a	<3.0	<0.02	<40.00	<4.00	0.10	<0.20
1702/1	29/05/2015 15:10	244.2	244.2			22.30	103.90	85	0.09	0.09	<0.01	<3.0	0.15	114.00	32.00	<0.10	0.60
1702/2	12/06/2015 14:11	335.0	579.2			30.10	178.90	578	0.58	0.65	<0.07	<3.0	0.10	96.00	37.00	0.20	0.30
1702/3	09/07/2015 11:35	645.4	1224.6			35.20	99.40	275	0.28	0.29	<0.02	<3.0	0.04	93.00	26.00	0.10	0.40
1702/4	07/08/2015 14:30	698.9	1923.5			42.20	118.00	260	0.26	0.22	0.04	<3.0	<0.02	99.00	27.00	<0.10	0.40
1702/5	16/09/2015 11:00	956.5	2880.0			51.30	130.10	150	0.15	0.26	<0.11	<3.0	<0.02	153.00	23.00	<0.10	0.20
Blank	19/05/2015 11:00	-	0.0	Basalt	CO ₂ + SO ₂	<0.40	0.70	<50	<0.05	<0.005	n/a	<3.0	<0.02	<40.00	<4.00	0.10	<0.20
1706/1	29/05/2015 15:10	244.2	244.2			2087.50	8808.30	560282	560.28	127.85	432.43	11.0	0.40	59.00	1001.00	0.40	24.60
1706/2	12/06/2015 14:40	335.5	579.7			2026.40	9243.40	576914	576.91	115.56	461.35	9.0	0.15	57.00	28.00	0.30	5.00
1706/3	09/07/2015 11:50	645.2	1224.8			2040.30	9754.30	603178	603.18	118.00	485.18	14.0	0.04	68.00	12.00	0.30	4.30
1706/4	07/08/2015 14:00	698.2	1923.0			2016.00	9665.40	596768	596.77	99.96	496.81	12.0	0.04	93.00	21.00	0.30	2.90
1706/5	16/09/2015 11:40	957.7	2880.7			2017.70	9899.40	608736	608.74	Cal X		23.0	0.05	<40.00	19.00	0.40	6.70

Sample Code	Date	Interval Time	Total Time	Solid	Gas	Sr	Mn	Total Fe	Total Fe	Reduced Fe	Oxidised Fe	Li	Be	B	Al	Ti	V
Blank	19/05/2015 11:00	-	0.0	Olivine	N ₂	<0.40	0.70	<0.05	<0.05	<0.005	n/a	<3.0	<0.02	<40.00	<4.00	0.10	<0.20
1703/1	29/05/2015 15:10	244.2	244.2			31.60	1.30	<0.05	<0.05	0.01	<0.06	3.0	<0.02	<40.00	102.00	<0.10	0.30
1703/2	12/06/2015 14:15	335.1	579.2			37.80	10.80	<0.05	<0.05	0.01	<0.06	<3.0	<0.02	<40.00	124.00	0.10	0.20
1703/3	09/07/2015 11:35	645.3	1224.6			29.70	2.50	<0.05	<0.05	0.01	<0.06	4.0	<0.02	<40.00	197.00	<0.10	0.40
1703/4	07/08/2015 14:00	698.4	1923.0			29.10	2.00	0.06	0.06	<0.01	0.07	3.0	<0.02	<40.00	109.00	<0.10	<0.20
1703/5	16/09/2015 10:40	956.7	2879.7	pH double checked		37.50	2.00	<0.05	<0.05	0.39	<0.44	4.0	<0.02	<40.00	130.00	0.20	0.40
Blank	19/05/2015 11:00	-	0.0	Olivine	CO ₂	<0.40	0.70	<0.05	<0.05	<0.005	n/a	<3.0	<0.02	<40.00	<4.00	0.10	<0.20
1705/1	29/05/2015 15:10	244.2	244.2			26.10	528.30	0.26	0.26	0.27	<0.01	12.0	<0.02	<40.00	5.00	<0.10	0.30
1705/2	12/06/2015 14:30	335.3	579.5			25.60	944.50	0.34	0.34	0.36	<0.02	13.0	0.03	<40.00	<4.00	<0.10	<0.20
1705/3	09/07/2015 11:45	645.3	1224.8			29.80	1192.20	0.21	0.21	0.20	0.01	24.0	<0.02	<40.00	4.00	<0.10	0.30
1705/4	07/08/2015 14:00	698.3	1923.0			39.50	1307.90	0.10	0.10	0.05	0.06	25.0	<0.02	<40.00	<4.00	0.10	0.30
1705/5	16/09/2015 11:25	957.4	2880.4			35.60	1471.90	0.08	0.08	0.55	<0.47	27.0	<0.02	86.00	<4.00	<0.10	0.50
Blank	19/05/2015 11:00	-	0.0	Olivine	CO ₂ + SO ₂	<0.40	0.70	<0.05	<0.05	<0.005	n/a	<3.0	<0.02	<40.00	<4.00	0.10	<0.20
1707/1	29/05/2015 15:10	244.2	244.2			38.70	9405.70	681.55	681.55	129.73	551.82	18.0	0.69	<40.00	30.00	1.20	1.60
1707/2	12/06/2015 14:45	335.6	579.8			37.70	9805.50	715.13	715.13	119.57	595.57	28.0	0.05	<40.00	17.00	0.60	0.80
1707/3	09/07/2015 11:55	645.2	1224.9			43.30	10075.20	721.20	721.20	117.00	604.20	22.0	0.04	49.00	23.00	2.30	0.80
1707/4	07/08/2015 14:00	698.1	1923.0			No sample	No sample	No sample	No sample	No sample	No sample	No sample	No sample	No sample	No sample	No sample	No sample
1707/5	16/09/2015 11:30	957.5	2880.5			33.30	5594.70	360.98	360.98	Cal X		14.0	<0.02	51.00	<4.00	0.30	0.40

Sample Code	Date	Interval Time	Total Time	Solid	Gas	Sr	Mn	Total Fe	Total Fe	Reduced Fe	Oxidised Fe	Li	Be	B	Al	Ti	V
Blank	19/05/2015 11:00	.	0.0	Basalt + pyrrhotite	N ₂	<0.40	0.70	<50	<0.05	<0.005	n/a	<3.0	<0.02	<40.00	<4.00	0.10	<0.20
1701/1	29/05/2015 15:10	244.2	244.2			28.60	290.50	79407	79.41	88.27	<8.86	<3.0	0.04	66.00	6.00	<0.10	<0.20
1701/2	12/06/2015 14:05	334.9	579.1			38.10	343.60	79304	79.30	85.11	<5.80	<3.0	0.03	50.00	<4.00	<0.10	<0.20
1701/3	09/07/2015 11:30	645.4	1224.5			48.00	312.10	81794	81.79	84.20	<2.41	<3.0	<0.02	43.00	14.00	<0.10	<0.20
1701/4	07/08/2015 13:30	698.0	1922.5			57.90	327.70	78139	78.14	79.02	<0.88	<3.0	0.04	42.00	21.00	<0.10	<0.20
1701/5	16/09/2015 10:11	956.7	2879.2			69.30	322.50	68776	68.78	68.61	0.17	<3.0	<0.02	65.00	10.00	0.20	<0.20
Blank	19/05/2015 11:00	.	0.0	Basalt + pyrrhotite	CO ₂	<0.40	0.70	<50	<0.05	<0.005	n/a	<3.0	<0.02	<40.00	<4.00	0.10	<0.20
1704/1	29/05/2015 15:10	244.2	244.2			19.50	381.50	112410	112.41	118.28	<5.87	<3.0	0.05	47.00	<4.00	<0.10	<0.20
1704/2	12/06/2015 14:25	335.3	579.4			27.10	353.00	206497	206.50	138.50	68.00	<3.0	0.05	42.00	<4.00	<0.10	<0.20
1704/3	09/07/2015 11:40	645.2	1224.7			39.30	249.10	187357	187.36	126.00	61.36	<3.0	<0.02	50.00	8.00	<0.10	<0.20
1704/4	07/08/2015 13:45	698.1	1922.7			47.60	137.70	183118	183.12	111.15	71.97	<3.0	<0.02	61.00	9.00	<0.10	<0.20
1704/5	16/09/2015 11:20	957.6	2880.3			59.70	67.70	168061	168.06	Cal X		<3.0	<0.02	105.00	6.00	<0.10	<0.20

Sample Code	Date	Interval Time	Total Time	Solid	Gas	Cr	Co	Ni	Cu	Zn	Ga	As	Se	Rb	Y	Zr	Nb	Mo
Blank	19/05/2015 11:00	-	0.0	Basalt	N ₂	0.09	<0.04	0.10	<0.40	<7.00	<0.100	<0.070	<0.200	<0.020	<0.010	<0.050	<0.020	<0.030
1700/1	29/05/2015 15:10	244.2	244.2			3.11	0.04	2.30	75.40	21.00	0.600	0.830	0.400	0.510	<0.010	<0.050	<0.020	11.500
1700/2	12/06/2015 14:00	334.8	579.0			0.22	<0.04	1.10	103.30	<7.00	0.800	1.200	0.400	1.030	<0.010	<0.050	<0.020	10.500
1700/3	09/07/2015 11:30	645.5	1224.5			0.28	0.21	2.10	162.20	10.00	0.900	1.580	0.200	2.220	0.080	<0.050	<0.020	7.840
1700/4	07/08/2015 13:30	698.0	1922.5			0.33	0.08	0.90	217.20	29.00	1.100	1.580	0.200	3.180	<0.010	<0.050	<0.020	6.920
1700/5	16/09/2015 10:15	956.8	2879.3			0.37	0.08	0.80	276.00	<7.00	1.300	1.550	0.400	4.090	<0.010	<0.050	<0.020	7.690
Blank	19/05/2015 11:00	-	0.0	Basalt	CO ₂	0.09	<0.04	0.10	<0.40	<7.00	<0.100	<0.070	<0.200	<0.020	<0.010	<0.050	<0.020	<0.030
1702/1	29/05/2015 15:10	244.2	244.2			0.80	1.89	19.50	473.90	107.00	<0.100	0.160	0.200	0.410	0.720	<0.050	<0.020	1.210
1702/2	12/06/2015 14:11	335.0	579.2			0.59	3.07	49.80	723.40	81.00	<0.100	0.150	0.200	0.460	1.190	<0.050	<0.020	0.910
1702/3	09/07/2015 11:35	645.4	1224.6			0.45	3.22	37.10	832.40	81.00	<0.100	0.230	0.300	0.480	0.770	<0.050	<0.020	0.420
1702/4	07/08/2015 14:30	698.9	1923.5			0.62	3.89	39.60	711.50	90.00	<0.100	0.170	0.300	0.550	0.420	<0.050	<0.020	0.340
1702/5	16/09/2015 11:00	956.5	2880.0			0.19	4.00	34.20	895.00	65.00	<0.100	0.130	0.400	0.630	0.550	<0.050	<0.020	0.290
Blank	19/05/2015 11:00	-	0.0	Basalt	CO ₂ + SO ₂	0.09	<0.04	0.10	<0.40	<7.00	<0.100	<0.070	<0.200	<0.020	<0.010	<0.050	<0.020	<0.030
1706/1	29/05/2015 15:10	244.2	244.2			76.58	357.10	1035.90	7.70	583.00	1.100	2.120	0.300	1.020	30.410	<0.050	<0.020	0.730
1706/2	12/06/2015 14:40	335.5	579.7			31.00	361.14	1073.40	0.70	60.00	0.900	1.590	0.200	0.610	26.290	<0.050	<0.020	0.810
1706/3	09/07/2015 11:50	645.2	1224.8			21.08	283.63	788.70	0.80	23.00	0.800	1.700	<0.200	0.650	20.090	<0.050	<0.020	0.810
1706/4	07/08/2015 14:00	698.2	1923.0			14.30	200.14	516.60	2.80	40.00	0.800	1.850	0.200	0.900	18.100	<0.050	<0.020	1.230
1706/5	16/09/2015 11:40	957.7	2880.7			12.80	68.02	272.00	1.50	357.00	0.800	3.040	<0.200	0.740	19.190	<0.050	<0.020	1.230

Sample Code	Date	Interval Time	Total Time	Solid	Gas	Cr	Co	Ni	Cu	Zn	Ga	As	Se	Rb	Y	Zr	Nb	Mo
Blank	19/05/2015 11:00	-	0.0	Olivine	N ₂	0.09	<0.04	0.10	<0.40	<7.00	<0.100	<0.070	<0.200	<0.020	<0.010	<0.050	<0.020	<0.030
1703/1	29/05/2015 15:10	244.2	244.2			0.12	<0.04	4.70	6.30	19.00	0.200	<0.070	<0.200	6.890	<0.010	<0.050	<0.020	73.820
1703/2	12/06/2015 14:15	335.1	579.2			0.16	0.11	8.10	7.90	<7.00	0.100	0.090	<0.200	9.260	<0.010	<0.050	<0.020	116.230
1703/3	09/07/2015 11:35	645.3	1224.6			0.23	<0.04	6.80	4.80	7.00	0.200	0.150	<0.200	11.290	<0.010	<0.050	<0.020	127.790
1703/4	07/08/2015 14:00	698.4	1923.0			0.26	0.06	3.80	0.70	16.00	0.200	0.070	<0.200	12.750	<0.010	<0.050	<0.020	130.870
1703/5	16/09/2015 10:40	956.7	2879.7	pH double checked	0.60	0.04	2.10	1.00	<7.00	0.100	0.200	<0.200	15.860	<0.010	<0.050	<0.020	136.640	
Blank	19/05/2015 11:00	-	0.0	Olivine	CO ₂	0.09	<0.04	0.10	<0.40	<7.00	<0.100	<0.070	<0.200	<0.020	<0.010	<0.050	<0.020	<0.030
1705/1	29/05/2015 15:10	244.2	244.2			1.39	15.45	61.50	1.90	37.00	<0.100	0.090	<0.200	30.740	0.040	<0.050	<0.020	0.930
1705/2	12/06/2015 14:30	335.3	579.5			0.43	40.02	130.30	2.90	38.00	<0.100	0.090	<0.200	47.650	0.140	<0.050	<0.020	0.990
1705/3	09/07/2015 11:45	645.3	1224.8			0.35	38.64	132.70	1.10	22.00	0.100	0.190	<0.200	64.020	0.030	<0.050	<0.020	0.960
1705/4	07/08/2015 14:00	698.3	1923.0			0.56	32.53	107.10	3.00	40.00	0.100	0.180	<0.200	71.320	<0.010	<0.050	<0.020	2.070
1705/5	16/09/2015 11:25	957.4	2880.4			0.54	31.13	90.40	22.20	22.00	0.100	0.190	<0.200	76.440	0.030	<0.050	<0.020	0.420
Blank	19/05/2015 11:00	-	0.0	Olivine	CO ₂ + SO ₂	0.09	<0.04	0.10	<0.40	<7.00	<0.100	<0.070	<0.200	<0.020	<0.010	<0.050	<0.020	<0.030
1707/1	29/05/2015 15:10	244.2	244.2			15.87	555.73	1300.10	0.40	77.00	1.000	3.610	<0.200	24.010	15.730	<0.050	<0.020	1.010
1707/2	12/06/2015 14:45	335.6	579.8			2.02	393.54	1158.70	<0.40	47.00	0.800	2.730	<0.200	34.800	3.980	<0.050	<0.020	1.030
1707/3	09/07/2015 11:55	645.2	1224.9			1.75	239.92	861.50	<0.40	76.00	0.800	3.070	<0.200	48.920	3.460	<0.050	<0.020	1.570
1707/4	07/08/2015 14:00	698.1	1923.0			No sample	No sample	No sample	No sample	No sample	No sample	No sample	No sample	No sample	No sample	No sample	No sample	No sample
1707/5	16/09/2015 11:30	957.5	2880.5			0.39	67.69	434.40	<0.40	348.00	0.500	0.940	<0.200	48.550	0.530	<0.050	<0.020	20.380

Sample Code	Date	Interval Time	Total Time	Solid	Gas	Cr	Co	Ni	Cu	Zn	Ga	As	Se	Rb	Y	Zr	Nb	Mo
Blank	19/05/2015 11:00	-	0.0	Basalt + pyrrhotite	N ₂	0.09	<0.04	0.10	<0.40	<7.00	<0.100	<0.070	<0.200	<0.020	<0.010	<0.050	<0.020	<0.030
1701/1	29/05/2015 15:10	244.2	244.2			0.22	0.60	63.10	2.10	35.00	<0.100	0.120	<0.200	0.770	0.180	<0.050	<0.020	0.610
1701/2	12/06/2015 14:05	334.9	579.1			0.10	0.30	15.10	<0.40	21.00	<0.100	0.130	<0.200	0.440	0.120	<0.050	<0.020	0.780
1701/3	09/07/2015 11:30	645.4	1224.5			0.27	0.13	5.00	<0.40	101.00	<0.100	0.200	<0.200	0.760	0.390	<0.050	<0.020	0.740
1701/4	07/08/2015 13:30	698.0	1922.5			1.27	0.30	7.40	8.10	25.00	<0.100	0.290	<0.200	1.130	1.480	<0.050	<0.020	0.230
1701/5	16/09/2015 10:11	956.7	2879.2			0.38	0.06	4.10	7.70	<7.00	<0.100	0.180	<0.200	1.610	0.990	<0.050	<0.020	0.590
Blank	19/05/2015 11:00	-	0.0	Basalt + pyrrhotite	CO ₂	0.09	<0.04	0.10	<0.40	<7.00	<0.100	<0.070	<0.200	<0.020	<0.010	<0.050	<0.020	<0.030
1704/1	29/05/2015 15:10	244.2	244.2			0.36	0.84	4.60	<0.40	51.00	<0.100	0.110	<0.200	0.290	0.610	<0.050	<0.020	0.560
1704/2	12/06/2015 14:25	335.3	579.4			0.12	0.12	2.70	3.10	50.00	<0.100	<0.070	<0.200	0.370	0.190	<0.050	<0.020	0.660
1704/3	09/07/2015 11:40	645.2	1224.7			0.27	0.09	2.00	<0.40	14.00	<0.100	0.100	<0.200	0.490	0.190	<0.050	<0.020	1.610
1704/4	07/08/2015 13:45	698.1	1922.7			0.45	0.10	2.20	<0.40	18.00	<0.100	0.100	<0.200	0.620	0.110	<0.050	<0.020	0.660
1704/5	16/09/2015 11:20	957.6	2880.3			0.36	0.19	2.20	<0.40	137.00	<0.100	0.090	<0.200	0.800	0.170	<0.050	<0.020	0.280

P

Sample Code	Date	Interval Time	Total Time	Solid	Gas	Ag	Cd	Sn	Sb	Cs	La	Ce	Pr	Nd	Sm	Eu	Gd	Tb
Blank	19/05/2015 11:00	-	0.0	Basalt	N ₂	<0.200	<0.020	<0.300	<0.050	<0.020	<0.010	<0.020	<0.020	<0.200	<0.020	<0.020	<0.010	<0.010
1700/1	29/05/2015 15:10	244.2	244.2			<0.200	<0.020	<0.300	0.300	<0.020	<0.010	<0.020	<0.020	<0.200	<0.020	<0.020	<0.010	<0.010
1700/2	12/06/2015 14:00	334.8	579.0			<0.200	<0.020	<0.300	0.310	0.020	<0.010	<0.020	<0.020	<0.200	<0.020	<0.020	<0.010	<0.010
1700/3	09/07/2015 11:30	645.5	1224.5			<0.200	<0.020	<0.300	0.360	0.050	0.080	0.080	0.030	<0.200	0.020	<0.020	0.020	<0.010
1700/4	07/08/2015 13:30	698.0	1922.5			<0.200	<0.020	<0.300	0.380	0.040	<0.010	<0.020	<0.020	<0.200	<0.020	<0.020	<0.010	<0.010
1700/5	16/09/2015 10:15	956.8	2879.3			<0.200	<0.020	<0.300	0.380	0.050	<0.010	<0.020	<0.020	<0.200	<0.020	<0.020	<0.010	<0.010
Blank	19/05/2015 11:00	-	0.0	Basalt	CO ₂	<0.200	<0.020	<0.300	<0.050	<0.020	<0.010	<0.020	<0.020	<0.200	<0.020	<0.020	<0.010	<0.010
1702/1	29/05/2015 15:10	244.2	244.2			<0.200	0.120	<0.300	0.060	0.040	0.470	0.380	0.140	0.600	0.120	0.030	0.130	0.020
1702/2	12/06/2015 14:11	335.0	579.2			<0.200	0.170	<0.300	<0.050	<0.020	0.820	0.660	0.250	0.900	0.170	0.050	0.230	0.030
1702/3	09/07/2015 11:35	645.4	1224.6			<0.200	0.150	<0.300	<0.050	<0.020	0.610	0.560	0.180	0.700	0.110	0.040	0.160	0.020
1702/4	07/08/2015 14:30	698.9	1923.5			<0.200	0.130	<0.300	<0.050	<0.020	0.320	0.310	0.080	0.200	0.060	<0.020	0.070	<0.010
1702/5	16/09/2015 11:00	956.5	2880.0			<0.200	0.130	<0.300	<0.050	0.030	0.380	0.400	0.080	0.300	0.060	<0.020	0.090	<0.010
Blank	19/05/2015 11:00	-	0.0	Basalt	CO ₂ + SO ₂	<0.200	<0.020	<0.300	<0.050	<0.020	<0.010	<0.020	<0.020	<0.200	<0.020	<0.020	<0.010	<0.010
1706/1	29/05/2015 15:10	244.2	244.2			<0.200	2.050	<0.300	0.440	0.270	43.770	59.860	8.070	34.100	7.090	1.840	8.310	1.160
1706/2	12/06/2015 14:40	335.5	579.7			<0.200	0.090	<0.300	<0.050	0.040	18.620	30.120	5.600	23.400	4.590	1.280	6.000	0.810
1706/3	09/07/2015 11:50	645.2	1224.8			<0.200	0.060	<0.300	<0.050	0.040	13.890	26.320	3.850	16.400	3.300	0.930	4.260	0.600
1706/4	07/08/2015 14:00	698.2	1923.0			9.500	0.080	<0.300	<0.050	0.120	12.860	23.610	3.140	13.700	2.780	0.790	3.530	0.500
1706/5	16/09/2015 11:40	957.7	2880.7			<0.200	0.030	<0.300	<0.050	0.040	12.920	24.430	3.200	13.800	2.830	0.830	3.740	0.520

Sample Code	Date	Interval Time	Total Time	Solid	Gas	Ag	Cd	Sn	Sb	Cs	La	Ce	Pr	Nd	Sm	Eu	Gd	Tb
Blank	19/05/2015 11:00	-	0.0	Olivine	N ₂	<0.200	<0.020	<0.300	<0.050	<0.020	<0.010	<0.020	<0.020	<0.200	<0.020	<0.020	<0.010	<0.010
1703/1	29/05/2015 15:10	244.2	244.2			<0.200	0.030	<0.300	0.070	0.500	0.020	0.020	<0.020	<0.200	<0.020	<0.020	<0.010	<0.010
1703/2	12/06/2015 14:15	335.1	579.2			<0.200	0.040	<0.300	0.050	0.630	<0.010	<0.020	<0.020	<0.200	<0.020	<0.020	<0.010	<0.010
1703/3	09/07/2015 11:35	645.3	1224.6			<0.200	0.020	<0.300	0.060	0.700	<0.010	<0.020	<0.020	<0.200	<0.020	<0.020	<0.010	<0.010
1703/4	07/08/2015 14:00	698.4	1923.0			<0.200	<0.020	<0.300	0.060	0.780	<0.010	<0.020	<0.020	<0.200	<0.020	<0.020	<0.010	<0.010
1703/5	16/09/2015 10:40	956.7	2879.7	pH double checked	<0.200	0.030	<0.300	0.050	1.010	<0.010	<0.020	<0.020	<0.200	<0.020	<0.020	<0.010	<0.010	<0.010
Blank	19/05/2015 11:00	-	0.0	Olivine	CO ₂	<0.200	<0.020	<0.300	<0.050	<0.020	<0.010	<0.020	<0.020	<0.200	<0.020	<0.020	<0.010	<0.010
1705/1	29/05/2015 15:10	244.2	244.2			1.500	0.220	<0.300	0.120	2.520	1.310	1.260	<0.020	<0.200	<0.020	<0.020	<0.010	<0.010
1705/2	12/06/2015 14:30	335.3	579.5			<0.200	0.300	<0.300	<0.050	3.320	0.070	0.040	0.030	<0.200	0.020	<0.020	0.020	<0.010
1705/3	09/07/2015 11:45	645.3	1224.8			0.900	0.280	<0.300	<0.050	4.400	<0.010	<0.020	<0.020	<0.200	<0.020	<0.020	<0.010	<0.010
1705/4	07/08/2015 14:00	698.3	1923.0			<0.200	0.280	<0.300	<0.050	4.880	<0.010	<0.020	<0.020	<0.200	<0.020	<0.020	<0.010	<0.010
1705/5	16/09/2015 11:25	957.4	2880.4			<0.200	0.390	<0.300	<0.050	5.220	0.010	<0.020	<0.020	<0.200	<0.020	<0.020	<0.010	<0.010
Blank	19/05/2015 11:00	-	0.0	Olivine	CO ₂ + SO ₂	<0.200	<0.020	<0.300	<0.050	<0.020	<0.010	<0.020	<0.020	<0.200	<0.020	<0.020	<0.010	<0.010
1707/1	29/05/2015 15:10	244.2	244.2			0.900	0.550	<0.300	0.140	2.640	32.960	46.380	9.210	36.700	6.030	1.480	7.030	0.790
1707/2	12/06/2015 14:45	335.6	579.8			<0.200	0.060	<0.300	<0.050	2.880	3.440	5.680	1.380	5.800	1.160	0.350	1.290	0.170
1707/3	09/07/2015 11:55	645.2	1224.9			<0.200	<0.020	<0.300	<0.050	3.630	3.180	6.000	1.230	5.300	1.090	0.340	1.130	0.150
1707/4	07/08/2015 14:00	698.1	1923.0			No sample	No sample	No sample	No sample	No sample	No sample	No sample	No sample	No sample	No sample	No sample	No sample	No sample
1707/5	16/09/2015 11:30	957.5	2880.5			<0.200	0.050	<0.300	<0.050	3.130	0.690	0.710	0.100	0.300	0.060	0.030	0.090	<0.010

Sample Code	Date	Interval Time	Total Time	Solid	Gas	Ag	Cd	Sn	Sb	Cs	La	Ce	Pr	Nd	Sm	Eu	Gd	Tb
Blank	19/05/2015 11:00	.	0.0	Basalt + pyrrhotite	N ₂	<0.200	<0.020	<0.300	<0.050	<0.020	<0.010	<0.020	<0.020	<0.200	<0.020	<0.020	<0.010	<0.010
1701/1	29/05/2015 15:10	244.2	244.2			10.500	0.070	<0.300	0.080	0.150	1.030	0.940	0.270	0.600	0.040	<0.020	0.080	<0.010
1701/2	12/06/2015 14:05	334.9	579.1			<0.200	0.060	<0.300	<0.050	<0.020	0.230	0.100	0.160	0.300	<0.020	<0.020	0.050	<0.010
1701/3	09/07/2015 11:30	645.4	1224.5			<0.200	<0.020	<0.300	0.050	0.020	0.640	0.510	0.410	1.100	0.100	0.020	0.160	0.010
1701/4	07/08/2015 13:30	698.0	1922.5			<0.200	0.030	<0.300	<0.050	0.050	1.430	1.820	0.960	3.600	0.610	0.140	0.640	0.070
1701/5	16/09/2015 10:11	956.7	2879.2			<0.200	<0.020	<0.300	<0.050	0.040	0.770	1.310	0.490	1.600	0.240	0.070	0.320	0.030
Blank	19/05/2015 11:00	.	0.0	Basalt + pyrrhotite	CO ₂	<0.200	<0.020	<0.300	<0.050	<0.020	<0.010	<0.020	<0.020	<0.200	<0.020	<0.020	<0.010	<0.010
1704/1	29/05/2015 15:10	244.2	244.2			<0.200	0.100	<0.300	<0.050	0.030	0.660	0.410	0.160	0.600	0.100	0.030	0.140	0.020
1704/2	12/06/2015 14:25	335.3	579.4			<0.200	0.070	<0.300	<0.050	0.030	0.050	<0.020	<0.020	<0.200	<0.020	<0.020	<0.010	<0.010
1704/3	09/07/2015 11:40	645.2	1224.7			<0.200	<0.020	<0.300	<0.050	0.020	0.180	0.140	0.040	0.200	0.030	<0.020	0.040	<0.010
1704/4	07/08/2015 13:45	698.1	1922.7			<0.200	<0.020	<0.300	<0.050	<0.020	0.130	0.100	0.030	<0.200	<0.020	<0.020	0.010	<0.010
1704/5	16/09/2015 11:20	957.6	2880.3			<0.200	<0.020	<0.300	<0.050	0.030	0.170	0.190	0.050	<0.200	0.020	<0.020	0.030	<0.010

Sample Code	Date	Interval Time	Total Time	Solid	Gas	Dy	Ho	Er	Tm	Yb	Lu	Hf	Ta	W	Tl	Pb	Th	U
		h	h			$\mu\text{g l}^{-1}$	$\mu\text{g l}^{-1}$	$\mu\text{g l}^{-1}$	$\mu\text{g l}^{-1}$	$\mu\text{g l}^{-1}$	$\mu\text{g l}^{-1}$	$\mu\text{g l}^{-1}$	$\mu\text{g l}^{-1}$	$\mu\text{g l}^{-1}$	$\mu\text{g l}^{-1}$	$\mu\text{g l}^{-1}$	$\mu\text{g l}^{-1}$	$\mu\text{g l}^{-1}$
Blank	19/05/2015 11:00	-	0.0	Basalt	N ₂	<0.010	<0.020	<0.020	<0.010	<0.010	<0.010	<0.020	<0.020	<0.050	<0.020	0.050	<0.020	<0.020
1700/1	29/05/2015 15:10	244.2	244.2			<0.010	<0.020	<0.020	<0.010	<0.010	<0.010	<0.020	<0.020	0.080	<0.020	0.410	<0.020	0.020
1700/2	12/06/2015 14:00	334.8	579.0			<0.010	<0.020	<0.020	<0.010	<0.010	<0.010	<0.020	<0.020	0.080	0.020	1.010	<0.020	0.020
1700/3	09/07/2015 11:30	645.5	1224.5			0.010	<0.020	<0.020	<0.010	<0.010	<0.010	<0.020	<0.020	0.090	<0.020	0.270	<0.020	0.020
1700/4	07/08/2015 13:30	698.0	1922.5			<0.010	<0.020	<0.020	<0.010	<0.010	<0.010	<0.020	<0.020	0.090	<0.020	0.220	<0.020	0.030
1700/5	16/09/2015 10:15	956.8	2879.3			<0.010	<0.020	<0.020	<0.010	<0.010	<0.010	<0.020	<0.020	0.130	<0.020	0.210	<0.020	0.030
Blank	19/05/2015 11:00	-	0.0	Basalt	CO ₂	<0.010	<0.020	<0.020	<0.010	<0.010	<0.010	<0.020	<0.020	<0.050	<0.020	0.050	<0.020	<0.020
1702/1	29/05/2015 15:10	244.2	244.2			0.090	0.030	0.070	<0.010	0.050	0.010	<0.020	<0.020	<0.050	0.090	0.460	<0.020	0.030
1702/2	12/06/2015 14:11	335.0	579.2			0.150	0.040	0.090	0.010	0.060	<0.010	<0.020	<0.020	<0.050	0.080	0.250	<0.020	0.040
1702/3	09/07/2015 11:35	645.4	1224.6			0.100	0.020	0.060	<0.010	0.050	<0.010	<0.020	<0.020	<0.050	0.080	0.250	<0.020	0.020
1702/4	07/08/2015 14:30	698.9	1923.5			0.050	<0.020	0.040	<0.010	0.020	<0.010	<0.020	<0.020	<0.050	0.070	0.110	<0.020	<0.020
1702/5	16/09/2015 11:00	956.5	2880.0			0.060	<0.020	0.040	<0.010	0.020	<0.010	<0.020	<0.020	<0.050	0.090	<0.040	<0.020	0.030
Blank	19/05/2015 11:00	-	0.0	Basalt	CO ₂ + SO ₂	<0.010	<0.020	<0.020	<0.010	<0.010	<0.010	<0.020	<0.020	<0.050	<0.020	0.050	<0.020	<0.020
1706/1	29/05/2015 15:10	244.2	244.2			6.660	1.330	3.820	0.530	3.240	0.520	0.040	<0.020	<0.050	0.060	18.340	0.070	<0.020
1706/2	12/06/2015 14:40	335.5	579.7			4.780	0.960	2.720	0.360	2.060	0.320	0.030	<0.020	<0.050	<0.020	0.130	<0.020	<0.020
1706/3	09/07/2015 11:50	645.2	1224.8			3.700	0.730	2.100	0.280	1.550	0.250	<0.020	<0.020	<0.050	<0.020	0.140	<0.020	<0.020
1706/4	07/08/2015 14:00	698.2	1923.0			3.000	0.620	1.710	0.220	1.230	0.190	<0.020	<0.020	<0.050	<0.020	3.460	<0.020	<0.020
1706/5	16/09/2015 11:40	957.7	2880.7			3.280	0.670	1.890	0.250	1.340	0.210	<0.020	<0.020	<0.050	<0.020	0.060	0.030	0.030









P:

Sample Code	Date	Interval Time	Total Time	Solid	Gas	Dy	Ho	Er	Tm	Yb	Lu	Hf	Ta	W	Tl	Pb	Th	U
Blank	19/05/2015 11:00	-	0.0	Olivine	N ₂	<0.010	<0.020	<0.020	<0.010	<0.010	<0.010	<0.020	<0.020	<0.050	<0.020	0.050	<0.020	<0.020
1703/1	29/05/2015 15:10	244.2	244.2			0.01	0.02	0.02	0.01	0.01	0.01	0.02	0.02	0.05	0.02	0.04	0.02	0.02
1703/2	12/06/2015 14:15	335.1	579.2			µg l ⁻¹	µg l ⁻¹	µg l ⁻¹	µg l ⁻¹	µg l ⁻¹	µg l ⁻¹	µg l ⁻¹	µg l ⁻¹	µg l ⁻¹	µg l ⁻¹	µg l ⁻¹	µg l ⁻¹	µg l ⁻¹
1703/3	09/07/2015 11:35	645.3	1224.6			<0.010	<0.020	<0.020	<0.010	<0.010	<0.010	<0.020	<0.020	0.880	0.030	0.070	<0.020	<0.020
1703/4	07/08/2015 14:00	698.4	1923.0			<0.010	<0.020	<0.020	<0.010	<0.010	<0.010	<0.020	<0.020	0.900	0.030	<0.040	<0.020	<0.020
1703/5	16/09/2015 10:40	956.7	2879.7	pH double checked	<0.010	<0.020	<0.020	<0.010	<0.010	<0.010	<0.020	<0.020	1.010	0.040	0.120	<0.020	<0.020	<0.020
Blank	19/05/2015 11:00	-	0.0	Olivine	CO ₂	<0.010	<0.020	<0.020	<0.010	<0.010	<0.010	<0.020	<0.020	<0.050	<0.020	0.050	<0.020	<0.020
1705/1	29/05/2015 15:10	244.2	244.2			<0.010	<0.020	<0.020	<0.010	<0.010	<0.010	<0.020	<0.020	<0.050	0.190	1.250	<0.020	<0.020
1705/2	12/06/2015 14:30	335.3	579.5			0.010	<0.020	<0.020	<0.010	<0.010	<0.010	<0.020	<0.020	<0.050	0.260	0.210	<0.020	<0.020
1705/3	09/07/2015 11:45	645.3	1224.8			<0.010	<0.020	<0.020	<0.010	<0.010	<0.010	<0.020	<0.020	<0.050	0.330	0.080	<0.020	<0.020
1705/4	07/08/2015 14:00	698.3	1923.0			<0.010	<0.020	<0.020	<0.010	<0.010	<0.010	<0.020	<0.020	<0.050	0.370	0.090	<0.020	<0.020
1705/5	16/09/2015 11:25	957.4	2880.4			<0.010	<0.020	<0.020	<0.010	<0.010	<0.010	<0.020	<0.020	<0.050	0.380	0.040	<0.020	0.030
Blank	19/05/2015 11:00	-	0.0	Olivine	CO ₂ + SO ₂	<0.010	<0.020	<0.020	<0.010	<0.010	<0.010	<0.020	<0.020	<0.050	<0.020	0.050	<0.020	<0.020
1707/1	29/05/2015 15:10	244.2	244.2			3.760	0.670	1.700	0.200	1.100	0.180	0.020	<0.020	0.060	0.250	4.140	0.040	0.050
1707/2	12/06/2015 14:45	335.6	579.8			0.970	0.180	0.520	0.070	0.470	0.080	<0.020	<0.020	0.050	<0.020	0.150	0.020	<0.020
1707/3	09/07/2015 11:55	645.2	1224.9			0.920	0.170	0.480	0.070	0.440	0.080	<0.020	<0.020	0.080	<0.020	0.270	<0.020	<0.020
1707/4	07/08/2015 14:00	698.1	1923.0			No sample	No sample	No sample	No sample	No sample	No sample	No sample	No sample	No sample	No sample	No sample	No sample	No sample
1707/5	16/09/2015 11:30	957.5	2880.5			0.070	<0.020	0.030	<0.010	0.030	<0.010	<0.020	<0.020	<0.050	<0.020	0.040	0.030	<0.020

Sample Code	Date	Interval Time	Total Time	Solid	Gas	Dy	Ho	Er	Tm	Yb	Lu	Hf	Ta	W	Tl	Pb	Th	U
Blank	19/05/2015 11:00	-	0.0	Basalt + pyrrhotite	N ₂	<0.010	<0.020	<0.020	<0.010	<0.010	<0.010	<0.020	<0.020	<0.050	<0.020	0.050	<0.020	<0.020
1701/1	29/05/2015 15:10	244.2	244.2			0.020	<0.020	<0.020	<0.010	0.010	<0.010	<0.020	<0.020	<0.050	<0.020	2.410	0.050	<0.020
1701/2	12/06/2015 14:05	334.9	579.1			0.010	<0.020	<0.020	<0.010	<0.010	<0.010	<0.020	<0.020	<0.050	<0.020	<0.040	0.030	<0.020
1701/3	09/07/2015 11:30	645.4	1224.5			0.080	<0.020	0.030	<0.010	0.020	<0.010	<0.020	<0.020	<0.050	<0.020	0.070	<0.020	<0.020
1701/4	07/08/2015 13:30	698.0	1922.5			0.390	0.070	0.210	0.020	0.180	0.020	<0.020	<0.020	<0.050	<0.020	0.140	<0.020	<0.020
1701/5	16/09/2015 10:11	956.7	2879.2			0.190	0.040	0.120	0.010	0.080	0.010	<0.020	<0.020	<0.050	<0.020	<0.040	0.020	<0.020
Blank	19/05/2015 11:00	-	0.0	Basalt + pyrrhotite	CO ₂	<0.010	<0.020	<0.020	<0.010	<0.010	<0.010	<0.020	<0.020	<0.050	<0.020	0.050	<0.020	<0.020
1704/1	29/05/2015 15:10	244.2	244.2			0.070	<0.020	0.040	<0.010	0.030	<0.010	<0.020	<0.020	<0.050	<0.020	0.440	0.050	<0.020
1704/2	12/06/2015 14:25	335.3	579.4			<0.010	<0.020	<0.020	<0.010	<0.010	<0.010	<0.020	<0.020	<0.050	<0.020	0.040	0.030	<0.020
1704/3	09/07/2015 11:40	645.2	1224.7			0.020	<0.020	<0.020	<0.010	0.010	<0.010	<0.020	<0.020	<0.050	<0.020	0.070	0.020	<0.020
1704/4	07/08/2015 13:45	698.1	1922.7			<0.010	<0.020	<0.020	<0.010	<0.010	<0.010	<0.020	<0.020	<0.050	<0.020	0.060	<0.020	<0.020
1704/5	16/09/2015 11:20	957.6	2880.3			0.030	<0.020	<0.020	<0.010	<0.010	<0.010	<0.020	<0.020	<0.050	<0.020	<0.040	0.020	<0.020

Appendix 6.

Saturation indices from chapter 4.

	1700 Basalt + N₂		1704 Basalt & pyrrhotite + CO₂
	1701 Basalt & Pyrrhotite + N₂		1705 Olivine + CO₂
	1702 Basalt + CO₂		1706 Basalt + CO₂ & SO₂
	1703 Olivine + N₂		1707 Olivine + CO₂ & SO₂

